

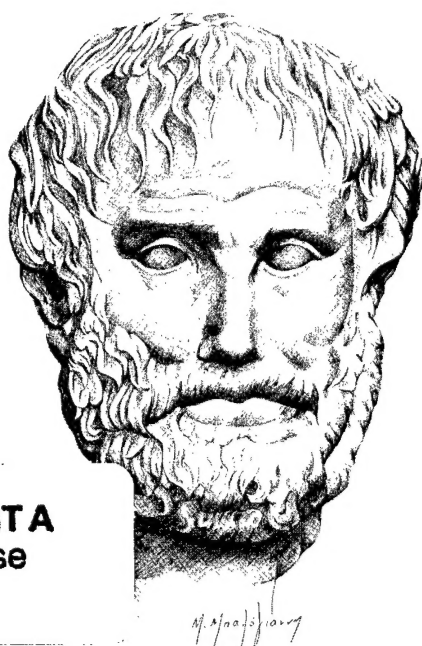
HELLENIC SOCIETY OF THEORETICAL
AND APPLIED MECHANICS (HSTAM)

ARISTOTLE UNIVERSITY
OF THESSALONIKI (AUTH)

6th NATIONAL CONGRESS OF MECHANICS

PROCEEDINGS VOLUME I

EDITORS
E.C.AIFANTIS
A.N.KOUNADIS



DISTRIBUTION STATEMENT A
Approved for Public Release
Distribution Unlimited

20020125 228

*Dedicated to the memory
of P.S.Theocaris*

THESSALONIKI,
JULY 19-21, 2001

6th National Congress of Mechanics

Thessaloniki, 19-21 July 2001

Hellenic Society of Theoretical and Applied Mechanics (HSTAM)

Aristotle University of Thessaloniki (AUT)

PROCEEDINGS

Volume I

Thursday 19 July 2001

Editors: *E. C. Aifantis* and *A. N. Kounadis*

Dedicated to the memory of
P. S. Theocaris

Thessaloniki 13 July 2001

Foreword

It was an honor that HSTAM (Hellenic Society of Theoretical and Applied Mechanics) assigned to the Laboratory of Mechanics of the General Department of AUT the responsibility of organizing the 6th National Congress of Mechanics in cooperation with the Department of Civil Engineering of AUT.

Special thanks to A. Kounadis and D. Beskos, president and secretary of HSTAM respectively, as well as to G. Manolis and D. Talaslidis who served as vice-chairmen of the organizing committee.

The Congress is dedicated to the memory of P. Theocaris whose influence on the Mechanics Community of Greece will remain for many years. My predecessor G. Lianis and A. Armenakas served as honorary chairmen of the Congress. My thanks go to them, as well as to the rest of the members of the organizing committees.

The Congress was organized during a very interesting period of substantial activity in the educational and scientific community in Greece. More than two months before the Congress, the University administration, at first, and the undergraduate student body as a whole, later, opposed certain educational proposals passed by the State, and daily university activities came to a standstill. This had a serious impact on the conference organization including the disruption of usual e-mail correspondence.

It was the determination of my graduate students G. Efremidis and P. Sapalidis, the help of F. Akintayo, K. Kosmidis, K. Kalaitzidou/S. Marras (currently at MTU/USA), the assistance of undergraduate students Th. Atmakidis and D. Dodou, as well as the encouragement of A. Kounadis, which helped me decide not to postpone the meeting. Special thanks go to George Efremidis who took upon himself the responsibility of completing the process of collecting the manuscripts, coordinating the e-mail correspondence, and other organizational details. My colleagues D. Beskos and G. Manolis were always available for consultation and advice. Many faculty of the General Department including its past and newly elected Chairman, as well as the Dean of Engineering were very supportive of this event.

The active participation of the travel agency Aethra, the publisher Giahoudi-Giapouli and the personal involvement of the owner of Philippon Hotel Helena Thoidou, who took the initiative to help with respective arrangements without requiring pre-payment, is worth mentioning. The financial support of the General Department, the College of Engineering, and the Research Committee of AUT, as well as of Democritus University of Thrace is

acknowledged. Also we acknowledge with thanks the financial support of the Ministry of Education, the Ministry of Culture and the Municipality of Thessaloniki. We also hope to have some financial support from the Ministry of Macedonia-Thrace and the Academy of Athens; but, at the time this foreword was composed, we had not yet received a definite decision from these governmental agencies, mainly due to difficulties in communication or decision-making during this unusual period of academic life.

Finally, sincere thanks go to all participants, especially those from abroad invited by HSTAM and myself or personally encouraged by me to attend. They all honored their commitment to participate despite the minimal information that could be distributed due to the aforementioned unforeseen circumstances. Many of the participants facilitated us greatly by pre-registering, thus enabling us to respond to initial financial obligations related to the Congress organization. It should be noted that as a result of the unusual circumstances mentioned above, it was not possible to activate a panel for a thorough review of the papers, which were accepted on the basis of their abstracts only.

Last, but not least, I would like to personally acknowledge the support and encouragement of the Minister of Yugoslavia, Professor Dragoslav Sumarac, for developing in Thessaloniki a Balkan Center of Mechanics with support from ERO and MTU with the participation of leading researchers of Mechanics and Materials of an international stature. In this respect, the sincere interest of Sam Sampath and the continuous help of my students I. Mastorakos, Avraam and Dimitris Konstantinidis in the organization of related research activities at AUT, as well as the scientific support of my student I. Tsagrakis, the research associate Mike Zaiser, and my physics colleague S. Logothetidis at AUT, are gratefully acknowledged.

*Elias C. Aifantis
Chairman*

6th NATIONAL CONGRESS OF MECHANICS

Thessaloniki. 19 – 21 July, 2001

Hellenic Society of Theoretical and Applied Mechanics (HSTAM)
Aristotle University of Thessaloniki (AUT)

ORGANIZING COMMITTEES

• *Chairmanship*

E. Aifantis,	Chairman, AUT
G. Lianis,	Honorary Chairman, Emeritus Professor, AUT
A. Armenakas,	Honorary Chairman, Emeritus Professor, NTUA Past President of HSTAM

• *HSTAM Council*

A. Kounadis,	Academy of Athens / NTUA, President
J. Katsikadelis,	NTUA, Vice-President
D. Beskos,	University of Patras, Secretary General
A. Vakakis,	NTUA, Treasurer
I. Vardoulakis,	NTUA
A. Mavraganis,	NTUA
D. Panayotounakos,	NTUA
H. Georgiadis,	NTUA
V. Koumoussis,	NTUA
G. Papadopoulos,	University of Athens
M. Papadrakakis,	NTUA

• *National Committee*

N. Alikakos,	University of Athens	A. Liolios,	DUTH
N. Aravas,	University of Thessaly	A. Mamalis,	NTUA
A. Bountis,	University of Patras	C. Massalas,	University of Ioannina
I. Dafalias,	NTUA	A. Payatakes,	University of Patras
G. Dassios,	University of Patras	P. Perdikaris,	University of Thessaly
V. Dougalis,	University of Athens	S. Pnevmatikos,	University of Patras
E. Economou,	University of Crete	D. Theodorou,	University of Patras
G. Fytas,	University of Crete	D. Tsahalis,	University of Patras
E. Gdoutos,	DUTH	G. Tsamasphyros,	NTUA
A. Liakopoulos,	University of Thessaly	P. Varotsos,	University of Athens

- ***AUT Committees***

G. Manolis / D. Talaslidis: Vice-Chairmen

A. Anagnostopoulos	G. Kourouklis
J. Antonopoulos	P. Latinopoulos
P. Argyrakis	S. Logothetidis
G. Athanasiadis	G. Manos
Ch. Baniotopoulos	S. Natsiavas
S. Bantis	S. Nychas
K. Bouzakis	M. Pagitsas
N. Charalambakis	C. Panayiotou
A. Charalambopoulos	P. Papadopoulos
J. Ganoulis	G. Penelis
A. Goulas	K. Pitilakis
J. Hadjidemetriou	N. Platakis
S. Ichtiaroglou	G. Theodorou
G. Kanelis	A. Trochidis
A. Karabelas	G. Tsagas
Th. Karakostas	D. Tsipas
A. Kehagias	K. Tsouros
C. Kiparissides	C. Tzimopoulos

- ***Local Arrangements Committee***

Section of Mechanics: S. Ambatjidis, E. Douka, M. Matsikoudi, S. Papargyri

Graduate students: G. Efremidis, P. Sapalidis, F. Akintayo, I. Mastorakos, K. Kosmidis,
K. Kalaitzidou, S. Marras

Undergraduate students: Th. Atmakidis, D. Dodou

TABLE OF CONTENTS

VOLUME I

THERMOMECHANICS OF LOCAL STRUCTURAL REARRANGEMENTS	
<i>G. Maugin</i>	1
QUANTUM PLASTICITY	
<i>K. Valanis</i>	9
ON STRAIN GRADIENTS IN PLASTICITY	
<i>J. Kratochvil</i>	14
ENABLING NONLINEAR COMPUTATIONS THROUGH EFFICIENT TIME-STEPPING	
<i>E. Koronaki, C. Theodoropoulos, A. Boudouvis I. Kevrekidis</i>	21
RHEOLOGY OF DENSE LIGNITE-WATER SUSPENSIONS; TRANSITION STRESSES ON FLOW CURVES	
<i>T. Goudoulas, E. Kastrinakis, S. Nychas</i>	27
COMPUTER SIMULATION OF THE NONLINEAR EVOLUTION OF INCLINED FILM FLOWS	
<i>N. Malamataris, M. Vlachogiannis, V. Bontozoglou</i>	33
AN IMPROVED COASTAL CIRCULATION MODEL BASED ON THE CHARACTERISTIC-GALERKIN TECHNIQUE	
<i>H. Mpimpas, P. Anagnostopoulos</i>	39
ON THE EFFECT OF THE RELATIVE VISCOSITY OF TWO FLUIDS ON THE DYNAMICS OF AXISYMMETRIC CORE-ANNULAR FLOW IN A TUBE	
<i>C. Kouris, J. Tsamopoulos</i>	45
A COMPARISON OF THE ACCURACY OF VARIOUS INTERPOLATION TECHNIQUES FOR PROCESSING RANDOMLY SCATTERED BATHYMETRIC DATA	
<i>N. Volakos, R. Barber</i>	52
INTERRELATION BETWEEN STOKES AND PAPKOVICH - NEUBER EIGENMODES FOR SPHEROIDAL STOKES FLOW	
<i>M. Hadjinicolaou, P. Vafeas</i>	59
NUMERICAL STUDY OF OSCILLATORY FLOW PAST PAIRS OF CYLINDERS AT LOW REYNOLDS AND KEULEGAN-CARPENTER NUMBERS	
<i>P. Anagnostopoulos, A. Koutras, S. Seitanis</i>	66
INVERSE DESIGN OF AERODYNAMIC SHAPES USING ANT COLONY OPTIMIZATION	
<i>T. Zervogiannis, V. Assouti, K. Gagas, A. Kaounis, K. Giannakoglou</i>	72
STRATIFIED TWO -PHASE FLOW OF VAPOUR BOUNDARY LAYER-CONDENSATE FILM OVER A CYLINDER	
<i>D. Smyrniaios, N. Pelekasis, J. Tsamopoulos</i>	78
FLUID DISPLACEMENT BY AIR IN A CAPILLARY TUBE	
<i>Y. Dimakopoulos, J. Tsamopoulos</i>	84

FLOW BETWEEN TWO ROTATING HEATED SPHERES <i>V. Loukopoulos</i>	90
AN EXPERIMENTAL METHODOLOGY FOR ENHANCING 2-D FLOW CHARACTERISTICS IN A 3-D TURBULENT FLOW <i>G. Sideridis, E. Kastrinakis, S. Nychas</i>	96
FORCES FROM JET FLOWS ON INCLINED DISCS <i>J. Demetriou, D. Dimitriou</i>	102
FLOW IN OPEN CHANNELS LINED WITH DIFFERENT MATERIALS <i>J. Demetriou, C. Pourliotis, P. Sarantos</i>	108
AIRLIFT PUMP PERFORMANCE OPTIMISATION FOR DEEP-SEA MINING <i>D. Margaritis</i>	114
BOUNDARY SHEAR IN COMPOUND NON-SYMMETRICAL CHANNELS <i>K. Nanou-Giannarou, J. Demetriou</i>	121
USE OF HEIGHT DENSITY FUNCTION FOR THE EVALUATION OF MEASUREMENTS WITH A LASER DOPPLER ANEMOMETER <i>Th. Panidis</i>	127
DAMAGE MODELS FOR VISCOELASTIC COMPOSITES <i>R. Schapery</i>	134
DAMAGE LOCALIZATION AND FRACTURE IN LAMINATE COMPOSITES <i>P. Ladeveze</i>	140
CYLINDRICAL SHELLS AND THEIR STABILITY (CHOICE OF THE DEFLECTION FUNCTION AND CRITICAL EXTERNAL RADIAL PRESSURE) <i>D. Ruzic, Lj. Markovic</i>	146
ESSENTIAL STRUCTURE OF DAMAGE MECHANICS MODELS <i>D. Krajcinovic</i>	155
FATIGUE OF MATERIALS AND STRUCTURES <i>J. Lemaitre</i>	163
LARGE DEFLECTION ANALYSIS OF BEAMS WITH VARIABLE STIFFNESS. AN ANALOG EQUATION SOLUTION <i>J. Katsikadelis, G. Tsiatas</i>	172
CRUSHING OF SHIP'S BOW STRUCTURE DURING COLLISION WITH BRIDGE PIERS <i>N. Hajdin, R. Mandic</i>	178
BEM SOLUTION OF VISCOPLASTIC PROBLEMS IN METALLIC STRUCTURES IN THE PRESENCE OF TEMPERATURE GRADIENTS <i>C. Provdakis, S. Kourtakis</i>	184
ROCK DISCONTINUITIES IN TUNNEL DESIGN: NUMERICAL SIMULATION OF THE EFFECTS OF FILLED AND OPEN JOINTS <i>C. Stiakakis, Z. Agioutantis, G. Paschalis</i>	191
ON THE NUMERICAL PERFORMANCE OF A SIMPLIFIED METHOD OF ANALYSIS FOR CREEPING STRUCTURES LOADED CYCLICALLY <i>K. Spiliopoulos</i>	198

STATIC AND DYNAMIC ANALYSIS OF SHELL PANELS USING THE ANALOG EQUATION METHOD	
<i>J. Yiotis, J. Katsikadelis</i>	204
NUMERICAL STUDIES OF ANCHORS AND REBARS IN CONCRETE SPECIMENS BY DAMAGE MODELS	
<i>G. Hatzigeorgiou, M. Sfakianakis, D. Theodorakopoulos, D. Beskos</i>	210
ON THE FLEXURAL MODES OF THE BICKFORD BEAM THEORY	
<i>C. Sophocleous, K. Soldatos</i>	216
A REALISTIC ESTIMATION OF THE EFFECTIVE BREADTH OF RIBBED PLATES	
<i>J. Katsikadelis, E. Sapountzakis</i>	222
ON THE STUDY OF TIE PLATES IN PIN CONNECTIONS	
<i>I. Mademlis, S. Marnoutsidis, A. Avdelas</i>	228
THE EFFECT OF DECK ROUGHNESS IN CONJUNCTION WITH OTHER PARAMETERS ON THE DYNAMIC RESPONSE OF STEEL HIGHWAY BRIDGES UNDER VEHICULAR LOADING	
<i>G. Michaltsos, D. Sophianopoulos</i>	234
LQR AND H OPTIMAL STRUCTURAL CONTROL IN ASEISMIC DESIGN	
<i>E. Zacharenakis, K. Arvanitis, A. Soldatos, G. Stavroulakis</i>	240
RELIABILITY BASED OPTIMIZATION USING NEURAL NETWORKS	
<i>M. Papadrakakis, N. Lagaros</i>	246
A NUMERICAL ESTIMATION OF THE INTERRELATION BETWEEN ACCELERATION PARAMETERS AND DAMAGE INDICATORS IN EARTHQUAKE ENGINEERING	
<i>A. Elenas, A. Liolios, L. Vasiliadis, M. Sakellari, P. Koliopoulos</i>	254
ELASTOPLASTIC RESPONSE SPECTRA FOR THE DESIGN OF STRUCTURES SUBJECTED TO EXPONENTIAL BLAST LOADING	
<i>N. Pnevmatikos, C. Gantes</i>	261
ANALYTICAL ESTIMATION OF TOTAL DISPLACEMENT'S COMPONENTS OF R/C SHEAR WALLS WITH ASPECT RATIO 1.0-1.5 SUBJECTED TO SEISMIC LOADS	
<i>T. Salonikios</i>	267
COMPETITION AMONG GENETIC ALGORITHMS TO IMPROVE ROBUSTNESS IN OPTIMIZATION	
<i>C. Dimou, V. Koumousis</i>	275
YUGOSLAV INVESTIGATIONS CONCERNING THE PATCH LOADING ON GIRDERS	
<i>N. Hajdin, B. Coric, N. Markovic, D. Lucic</i>	282
SYNTHESIS OF NEW PHENOLIC POLYMERS VIA ENZYMATIC POLYMERIZATION AND THEIR PROPERTIES	
<i>S. Kobayashi</i>	290
ADAPTIVE FINITE ELEMENT ANALYSIS OF LIMIT-LOAD STATES IN DRY AND SATURATED SOILS	
<i>W. Wunderlich, R. Findei, H. Cramer</i>	298
MEASUREMENT OF THE MECHANICAL PROPERTIES OF MEMS MATERIALS	
<i>W. Sharpe Jr.</i>	306

BEHAVIOR OF PARTICLE REINFORCED COMPOSITES WITH SOFT MATRICES <i>C. Sciammarella, F. Sciammarella</i>	314
INDENTATION FAILURE OF SANDWICH PANELS <i>E. Gdoutos, I. Daniel, K.-A. Wang</i>	320
ESTIMATION OF THE CONCRETE CHARACTERISTICS USING PATTERN RECOGNITION METHODS <i>M. Titsias, D. Fotiadis, A. Likas</i>	327
DESTRUCTIVE AND ULTRASONIC NON-DESTRUCTIVE TESTING OF 28-DAY AND 28-YEAR OLD CONCRETE <i>I. Prassianakis, P. Giokas</i>	333
EXPERIMENTAL QUANTIFICATION OF CRACK TIP PARAMETERS FOR PARTICULATE METAL MATRIX COMPOSITES <i>S. Kourkoulis, V. Kytopoulos</i>	339
ON SELECTING A COMPATIBLE SUBSTITUTE FOR THE KENHCREAE POROS STONE USED IN THE EPIDAUREAN ASKLEPIEION <i>N. Ninis, S. Kourkoulis</i>	348
NON-LINEAR MECHANICS AND BUCKLING ANALYSIS OF COMPOSITE SHELLS WITH EMBEDDED PIEZOELECTRIC ACTUATORS AND SENSORS <i>D. Varelis, D. Saravanos</i>	357
A NEW DESIGN METHODOLOGY FOR HIGH TEMPERATURE STRUCTURAL COMPONENTS MADE OF CONTINUOUS FIBER CERAMIC COMPOSITES EXHIBITING THERMALLY INDUCED ANISOTROPIC DAMAGE <i>D. Vlachos, Y. Pappas, R. De Stefano, V. Kostopoulos</i>	365
EXPERIMENTAL AND THEORETICAL STRESS ANALYSIS OF INCOMPRESSIBLE BONDED ELASTOMERIC DISCS SUBJECTED TO COMPRESSION <i>P. Kakavas</i>	375
OPTICAL DEVICE FOR PROSTATE CANCER DETECTION <i>G. Anastassopoulos, J. Lytras, M. Sunaric, V. Moulitanitis, S. Panteliou, A. Bekos, N. Kalinderis, D. Hatzichristou</i>	381
EXPERIMENTAL VERIFICATION OF SHEAR WALL MODELING USING FINITE ELEMENT ANALYSIS <i>A. Papachristidis, G. Badaloukas, B. Badalouka</i>	388
FAILURE OF A COMPOSITE WITH A BROKEN FIBER <i>D. Zacharopoulos, E. Gdoutos, D. Karalekas</i>	394
MICROMECHANICS OF CARBON FIBRE MODEL COMPOSITES UNDER TENSILE, COMPRESSIVE AND FATIGUE LOADING CONDITIONS <i>C. Koimtzoglou, S. Goutianos, C. Galiotis</i>	401
DYNAMIC BEHAVIOR OF A HANGED CABLE FOR DEEP WATER APPLICATIONS <i>I. Chatjigeorgiou, S. Mavrakos</i>	408
EXPERIMENTS FOR THE ESTIMATION OF UNSATURATED HYDRAULIC CONDUCTIVITY <i>G. Arampatzis, Ch. Tzimopoulos</i>	416

VOLUME II

CONTINUUM THEORY OF SELF-HEALING INTERFACE CRACKS <i>M. Marder, E. Gerde</i>	1
MATERIAL DEGRADATION AND FRACTURE IN HYDRIDE FORMING METALS <i>A. Varias, A. Massih</i>	7
SOME PROBLEMS OF ELECTROMECHANICAL FRACTURE OF DIELECTRIC AND PIEZOELECTRIC BODIES <i>D. Bardzokas, A. Zobnin</i>	13
CONTROL OF DYNAMIC STRESS AND FRACTURE OF PIEZOELECTRIC BODIES WITH CRACKS <i>D. Bardzokas, M. Filshinsky</i>	22
OPTIMIZATION AND SOFT COMPUTING FOR INVERSE AND CRACK IDENTIFICATION <i>G. Stavroulakis, H. Antes</i>	28
MECHANICAL BEHAVIOR OF MULTILAYERED NANOCOMPOSITE FILMS <i>V. Singh, X. Nie, P. Gupta, E. Meletis</i>	33
A COMPARATIVE STUDY OF MECHANICAL PROPERTIES OF STATE-OF-THE-ART AMORPHOUS CARBON FILMS <i>C. Charitidis, S. Logothetidis</i>	40
THE ROLE OF POINT DEFECTS ON THE GROWTH AND BREAKDOWN OF METAL PASSIVE FILMS IN ELECTROLYTE SOLUTIONS <i>M. Pagitsas, A. Diamantopoulou, D. Sazou</i>	46
FAILURE RESISTANCE TO THERMAL SHOCK OF THERMAL BARRIER COATINGS USING THE FINITE ELEMENT METHOD <i>A. Kekatou, V. Sfakiotakis, D. Katsareas, N. Anifantis</i>	52
FINITE ELEMENT ANALYSIS OF THE ELASTIC MECHANICAL BEHAVIOUR OF LDPE FILM <i>D. Briassoulis, E. Schettini</i>	57
ADAPTIVE COMPOSITES INCORPORATING SHAPE MEMORY ALLOY WIRES; RECORDING THE INTERNAL STRESS BY LASER RAMAN SPECTROSCOPY <i>J. Parthenios, G. Psarras, D. Bollas, C. Galiotis</i>	63
A HEMIVARIATION ALINE QUALITY APPROACH TO THE RESISTANCE OF ALUMINIUM RIVETED CONNECTIONS <i>M. Zygomalas, M. J. Kontoleon and C. C. Baniotopoulos</i>	70
ANALYSIS OF "CONVEX ENERGY" STRUCTURAL SYSTEMS UNDER STOCHASTIC LOADING <i>M. Kontoleon, C. Baniotopoulos, M. Betti, C. Borri</i>	78
FRICTION EVOLUTION IN FRACTAL INTERFACES <i>O. Panagouli, E. Mistakidis</i>	84

NUMERICAL STUDY OF THE F.E. MESH DEPENDENCY IN NONCONVEX-NONSMOOTH ENGINEERING PROBLEMS	
<i>E. Mistakidis, N. Politis</i>	90
FUZZY SETS IN ENGINEERING ANALYSIS AND DESIGN	
<i>E. Mistakidis, D. Georgiou</i>	96
BENDING AND WARPING IN FIBER REINFORCED RECTANGULAR BEAMS	
<i>C. Demakos</i>	102
ON THE POTENTIAL REPRESENTATIONS FOR POLYADICS AND ANISOTROPIC MEDIA	
<i>G. Dassios</i>	109
THE APPLICATION OF NOTHER'S THEOREM TO NON-LINEAR ANISOTROPIC ELASTIC-MATERIALS	
<i>J. Jaric, K. Kishimoto, T. Wang, M. Omiya</i>	115
MICROMECHANICAL MODELING OF THE BEHAVIOR OF POROUS SHAPE MEMORY ALLOYS	
<i>D. Lagoudas, P. Entchev</i>	120
VARIATIONAL FORMULATION AND MATERIAL BALANCE LAWS OF DISSIPATIONLESS THERMOELASTICITY	
<i>V. Kalpakides, G. Maugin</i>	126
THE INFINITE ISOTROPIC WEDGE UNDER LINEARLY DISTRIBUTED LOADING	
<i>J. Stabouloglou, E. Theotokoglou</i>	133
SIZE EFFECT ON FAILURE LOAD OF MARBLE BEAMS UNDER THREE POINT BENDING	
<i>I. Vardoulakis, G. Exadaktylos, S. Kourkoulis</i>	140
FINITE ELEMENT TECHNIQUES FOR STRAIN-GRADIENT ELASTICITY PROBLEMS	
<i>E. Amanatidou, N. Aravas</i>	149
THE ELASTIC PUNCH PROBLEM REVISITED	
<i>G. Exadaktylos</i>	155
GRADIENT ELASTIC BERNOULLI-EULER BEAMS IN BENDING AND BUCKLING	
<i>S. Papargyri-Beskou, K. Tsepoura, D. Polyzos, D. Beskos</i>	163
DUAL MODE VIBRATION ISOLATION BASED ON NONLINEAR MODE LOCALIZATION	
<i>X. Jiang, A. Vakakis</i>	170
A FRACTIONAL BROWNIAN MOTION MODEL FOR TIMESERIES PRODUCED BY CONSTANT ENERGY MOLECULAR DYNAMICS SIMULATIONS	
<i>T. Karakasidis, I. Andreadis</i>	177
VIBRATIONAL PROPERTIES OF A $\Sigma 5(310)[001]$ NiO GRAIN BOUNDARY STUDIED BY MOLECULAR DYNAMICS SIMULATION	
<i>T. Karakasidis</i>	183
ANALYTICAL SOLUTION OF THE NONLINEAR DAMPED DUFFING OSCILLATOR	
<i>D. Panayotounakos, G. Exadaktylos, A. Vakakis</i>	189

NONLINEAR EFFECTS ON THE ELASTIC STABILITY OF A COLUMN-FOOTING SYSTEM ON ELASTIC BASE	
<i>Ch. Younis, D. Panayotounakos</i>	196
THE CONTINUOUS TIME HOMOGENEOUS MARKOV SYSTEM WITH FIXED SIZE AS A LINEAR ELASTIC CONTINUUM	
<i>G. Tsaklidis, K. Soldatos</i>	209
STUDY OF THE DYNAMIC CHARACTERISTICS DURING CALLUS FORMATION	
<i>G. Foutsitzi, A. Charalambopoulos, D. Fotiadis, C. Massalas</i>	216
ON THE ELECTROENCEPHALOGRAPHY (EEG) PROBLEM FOR THE ELLIPSOID ALBRAIN MODEL	
<i>G. Kamvyssas, F. Kariotou</i>	222
MATHEMATICAL MODELS FOR BIOMAGNETIC FLUID FLOW AND APPLICATIONS	
<i>E. Tzirtzilakis, N. Kafoussias</i>	227
LAMELLAR INHOMOGENEITIES IN PIEZOELECTRIC SOLIDS	
<i>C. Dascalu, D. Homentcovschi</i>	233
ON A NEW CRACK MODEL FOR PIEZOELECTRIC SOLIDS	
<i>C. Dascalu, D. Homentcovschi, V. Kalpakides, E. Hadjigeorgiou</i>	239
ON THE STOCHASTIC MICROMECHANICAL THEORY OF DISCRETE MATERIAL SYSTEMS	
<i>Y. Haddad</i>	245
A CONSTITUTIVE LAW FOR POWDER COMPACTION	
<i>S. Subramanian, P. Sofronis</i>	251
CONTINUUM MICROPOLAR MODELLING OF DISCONTINUOUS MASONRY-LIKE SYSTEMS	
<i>P. Trovalusci, R. Masiani</i>	257
SOME ASPECTS OF A MICROPOLAR PLASTICITY THEORY	
<i>P. Grammenoudis, Ch. Tsakmakis</i>	263
DESCRIPTION OF PLASTIC ANISOTROPY EFFECTS AT LARGE DEFORMATIONS	
<i>D. Schick, Ch. Tsakmakis</i>	269
"COLD" WORK AND STABILITY IN SOFTENED MATERIALS	
<i>N. Charalambakis</i>	276
SOME BASIC SOLUTIONS TO DYNAMIC PROBLEMS IN RANDOM MEDIA	
<i>C. Karakostas, G. Manolis</i>	280
ANALYSIS OF RAYLEIGH WAVES IN MICRO STRUCTURED SOLIDS BY DIPOLAR GRADIENT ELASTICITY	
<i>H. Georgiadis, I. Vardoulakis, E. Velgaki</i>	289
THE 3D THERMO-ELASTODYNAMIC PROBLEM OF MOVING LOADS IN A HALF - SPACE	
<i>G. Lykotrafitis, H. Georgiadis</i>	295
THE ATTITUDE MOTION OF A CARRIER-ROTOR SYSTEM WITH ALMOST SYMMETRIC INERTIA ELLIPSOID, UNDER BODY-FIXED TORQUES	
<i>K. Dimitrakopoulou, A. Mavraganis</i>	301

GRADIENT ANISOTROPIC DAMAGE IN MMCS FOR BRIDGING LENGTH SCALES BETWEEN MACROSCOPIC RESPONSE AND MICROSTRUCTURE <i>G. Voyiadjis, R. Dorgan</i>	309
TWO SCALE DAMAGE MODEL FOR FATIGUE REPRESENTATION OF GRADIENT EFFECTS <i>R. Desmorat</i>	318
GRADIENT ELASTIC BARS UNDER UNIAXIAL STATIC OR DYNAMIC LOAD <i>K. Tsepoura, S. Papargyri - Beskou, D. Polyzos, D. Beskos</i>	328
EVOLUTION OF PERSISTENT SLIP BANDS IN FATIGUED METALS <i>E. Douka, B. Polyzos, A. Trochidis</i>	335
CRACK IDENTIFICATION IN BEAM STRUCTURES <i>Y. Bannios, E. Douka, A. Trochidis</i>	342
FRACTALS AND FRACTIONAL CALCULUS IN SOLID MECHANICS <i>A. Carpinteri, B. Chiaia, P. Cornetti</i>	349
CHARACTERIZATION OF MATERIALS WITH PORES AND INCLUSIONS AT DIVERSE SCALES <i>G. Frantziskonis</i>	359
SEMI-ANALYTICAL SOLUTION FOR A 1-D SIMPLIFIED THMPC MODELLING OF A NON-SATURATED SOIL <i>M - A. Abellan, J - M. Bergheau, J. M. Huyghe, R. de Borst</i>	365
COMPACT, HIGH-POWER, SYNTHETIC JET ACTUATORS FOR FLOW SEPARATION CONTROL <i>J. Gilarranz, O. Rediniotis</i>	371
LOCALIZED PERIODIC MOTIONS IN SYSTEMS OF COUPLED OSCILLATORS <i>V. Koukouloyannis, S. Ichtiaroglou</i>	379
EFFECT OF THE PARAMETERS ON THE DYNAMIC BEHAVIOR OF A SMALL PARTICLE IN AN ANNULAR DISTRIBUTION OF N BODIES <i>T. Kalvouridis, F. Psarros</i>	385
RESEARCH AND CHALLENGES OF ENGINEERING MECHANICS AND MATERIALS IN THE TWENTY FIRST CENTURY <i>K. Chong, D. Davis</i>	391
DAMAGE MECHANICS APPLICATION ON REPAIR OF DESTROYED STRUCTURES <i>D. Sumarac</i>	397

VOLUME III

COMPUTATIONAL ASPECTS OF MATERIAL INSTABILITIES	
<i>R. de Borst, H. Askes, M. Gutierrez, G. Wells</i>	1
EXPERIMENTAL STUDIES OF PLASTIC INSTABILITIES IN SOLID SOLUTIONS	
<i>H. Neuhaeuser, F. Klose, H. Dierke, A. Ziegenbein, A. Nortmann</i>	9
COMBINED MEASUREMENTS OF ACOUSTIC EMISSION AND LASER EXTENSOMETRY DURING PORTEVIN-LE CHATELIER DEFORMATION IN AN Al-Mg ALLOY	
<i>A. Ziegenbein, F. Chmelik, H. Neuhaeuser</i>	16
SERRATED YIELDING AND NONUNIFORM PLASTIC DEFORMATION OF PORTEVIN - LE CHATELIER EFFECT IN COMMERCIAL Al-Mg ALLOYS	
<i>K. Chihab, H. Ait-Amokhtar</i>	22
TIME SERIES ANALYSIS AND THE DETERMINISTIC STRUCTURE OF THE PLC EFFECT	
<i>D. Kugiumtzis, E. Aifantis</i>	29
SOME DYNAMICAL SYSTEM CONSIDERATIONS FOR DISLOCATIONS	
<i>G. Stagika, S. Ichtiaroglou, E. Aifantis, I. Groma</i>	35
THE DISLOCATION MODEL OF LOCAL BEND	
<i>N. Tokiy, T. Konstantinova, V. Varyukhin, A. Tokiy</i>	40
MULTISCALE PLASTICITY: LINKING DISCRETE AND CONTINUUM APPROACHES	
<i>L. Kubin, B. Devincre</i>	47
MACROSCOPIC MATERIAL BEHAVIOR FROM MICROSCOPIC SIMULATIONS	
<i>S. Luding, M. Laetzel</i>	53
MODELLING OF LAMINATED COMPOSITE STRUCTURES	
<i>A. Fernandes, J. Pouget</i>	61
INVARIANT RELATIONS IN A BOUSSINESQ TYPE EQUATION	
<i>E. Meletlidou, J. Pouget, G. Maugin, E. Aifantis</i>	67
KINK DYNAMICS IN A LONG-RANGE INTERACTION MODEL	
<i>T. Ioannidou, J. Pouget and E. Aifantis</i>	73
MAGNETIC SOLITONS	
<i>P. Sutcliffe</i>	79
THE PROPAGATION OF STRAIN WAVES IN MATERIALS WITH MICROSTRUCTURE	
<i>A. Potapov, V. Rodyushkin</i>	85
GOVERNING EQUATIONS AND BALANCE LAWS FOR MICROPOLAR CONTINUUM	
<i>S. Lisina, A. Potapov, G. Utkin</i>	90
SPLITTING UP OF MULTISTABLE SOLITONS IN SOLIDS	
<i>A. Potapov, V. Kazhaev, S. Gromov</i>	96

MODELING THE CRUSHING OF A CELLULAR MATERIAL

M. Zaiser, E. Aifantis102

APPENDIX WITH THE LATE PAPERS111

AUTHOR INDEX

6th National Congress on Mechanics

Session A

Volume I

THERMOMECHANICS OF LOCAL STRUCTURAL REARRANGEMENTS

G.A.Maugin

Laboratoire de Modélisation en Mécanique, UMR 7607 CNRS,
Université Pierre et Marie Curie, Case 162
4 place Jussieu, 75252 Paris cedex 05, France.

1. SUMMARY

In this contribution we emphasize the relationship between the material Eshelby stress tensor and the notion of local structural rearrangements that are responsible for many of the macroscopically observed irreversible behaviors of solid-like matter (e.g., anelasticity (plasticity, viscoplasticity), damage, phase transitions, growth). All these phenomena take place directly on the material manifold. Such a setting, mainly geometrical and thermodynamical, can be developed from the inclusive notions of uniformity maps, inhomogeneity maps, and material transplants (Epstein-Maugin). This provides a unifying link between two of the most innovative theories of continua of the 20th century, those of material inhomogeneities by W.Noll and J.D.Eshelby, that were at first completely unrelated.

2. INTRODUCTION

So-called *configurational forces*, also called *material forces* in modern continuum mechanics [1]-[2], and more generally *energetic driving forces*, are those "forces" which are associated by duality to the displacement or motion of whatever may be considered a *defect* in a continuum field theory. Conceptually simple examples of such "defects" are dislocations in ordered crystals, cracks and cavities in materials science, propagating fronts in phase-transition problems, shock waves in continuum mechanics, and more generally all manifestations, smooth or abrupt, of changes in material properties. In such a framework, the material symmetry of the physical system is broken by the presence of a field singularity of a given dimensionality (point, line, surface, volume). A general framework has emerged in recent years, basing on inclusive ideas of J.D.Eshelby - hence the coinage of *Eshelbian mechanics* by the author for the mechanics of such forces. In this framework all configurational forces appear as *forces of a non-Newtonian nature*, acting on the material manifold (the set of points building up the material whether discrete or continuous) and *not* in physical space which remains the realm of Newtonian forces and their more modern realizations which usually act per quantity of matter (mass or electric charge). That is, configurational forces act on spatial gradients of properties, on field singularities, *etc.* They acquire a true physical meaning only in so far as the associated expended power is none other

than a *dissipation* ; accordingly, configurational forces are essentially used to formulate *criteria of progress* of defects in accordance with the second law of thermodynamics. Within such a general vision, many irreversible properties of matter (e.g., damage, plasticity, phase transition, growth) are seen as *irreversible local rearrangements* of matter (e.g., material particles in an ordered crystal) that are represented by pure material mappings. Although configurational forces do not live, if we may say so, in the real world, they are “visible” through the duality they enjoy with their thermodynamic partners, material displacements. This is here illustrated by various cases.

3. THE NOTION OF LOCAL STRUCTURAL REARRANGEMENT

In order to make ideas clear let us consider *the case of quasi-statics in the absence of body force* with an elastic energy density given by $W = \bar{W}(\mathbf{F}; \mathbf{X})$ per unit reference volume, where $\mathbf{F} := \partial \chi / \partial \mathbf{X}$ is the deformation gradient, $\mathbf{x} = \chi(\mathbf{X}, t)$ is the sufficiently regular deformation mapping from the reference configuration K_R to the actual configuration K_t , and \mathbf{X} denotes the material point. Then the basic field equation - bulk equilibrium - in the Piola formalism reduces to

$$\text{div}_R \mathbf{T} = \mathbf{0} . \quad (1)$$

Following Epstein and Maugin [3], we consider (thought experiment) the case where the material homogeneity can be artificially removed *at each* material point \mathbf{X} , by effecting a change of reference configuration. This is done at each material point, and the reference change is therefore *local* and generally *not integrable* over the whole body. Such a change is called a *local structural rearrangement*, and this is conceived independently of any action in the actual configuration. Let $\mathbf{K}(\mathbf{X})$ this reference change so that accounting for the accompanying volume change $J_K = \det \mathbf{K}$, it combines mutiplicatively to the right with \mathbf{F} and, for energies, we can write

$$\bar{W}(\mathbf{F}; \mathbf{X}) = J_K^{-1} \tilde{W}(\mathbf{F}\mathbf{K}(\mathbf{X})) = \tilde{W}(\mathbf{F}, \mathbf{K}) . \quad (2)$$

Obviously we can compute the partial derivatives of the last mentioned function \tilde{W} , obtaining thus, as easily checked ,

$$\mathbf{T} = \frac{\partial \tilde{W}}{\partial \mathbf{F}} = \frac{\partial \bar{W}}{\partial \mathbf{F}} , \quad \tilde{\mathbf{b}} = - \frac{\partial \tilde{W}}{\partial \mathbf{K}} = - (\mathbf{T} \cdot \mathbf{F} - W \mathbf{1}_R) \cdot \mathbf{K}^{-T} . \quad (3)$$

Accordingly,

$$\mathbf{b} \equiv \tilde{\mathbf{b}} \cdot \mathbf{K}^T = - \frac{\partial \tilde{W}}{\partial \mathbf{K}} \cdot \mathbf{K}^T \equiv W \mathbf{1}_R - \mathbf{T} \cdot \mathbf{F} . \quad (4)$$

This provides an elegant definition of the quasi-static Eshelby stress via the notion of local structural rearrangement. Assuming that we just know (1), we can then compute the material divergence of \mathbf{b} resulting in (*expl* means the material gradient at fixed field \mathbf{F})

$$\operatorname{div}_R \mathbf{b} + \mathbf{f}^{inh} = \mathbf{0} \quad , \quad \mathbf{f}^{inh} := - \left. \frac{\partial \bar{W}}{\partial \mathbf{X}} \right|_{expl} , \quad (5)$$

where \mathbf{f}^{inh} is the so-called « material force of inhomogeneity » [1]. But we can also compute this material co-vector through the operation

$$\left. \frac{\partial W}{\partial \mathbf{X}} \right|_{expl} = (\nabla_R \mathbf{K}) : \frac{\partial \tilde{W}(\mathbf{F}, \mathbf{K})}{\partial \mathbf{K}} = -(\nabla_R \mathbf{K}) : (\mathbf{b} \cdot \mathbf{K}^{-T}) = \mathbf{b} : \Gamma , \quad (6)$$

where Γ is the (geometrical) *connection* based on the non-integrable mapping \mathbf{K} ; that is, in components (to avoid any misunderstanding):

$$\Gamma_{B,K}^A := -(\mathbf{K}^{-1})_{,B}^\alpha K_{,\alpha,K}^A . \quad (7)$$

Therefore, eqn.(5) also reads [3]

$$\operatorname{div}_R \mathbf{b} = \mathbf{b} : \Gamma . \quad (8)$$

In some geometrical theories of *continuous distributions of dislocations*, the connection Γ is directly related to the *density of dislocations* [1]. Accordingly, we can say that in such « continuously dislocated » elastic bodies, dislocations create a material force density which is responsible for the non-divergence-free nature of the Eshelby stress tensor. Dislocations, which originally are discrete defects, act thus as a materially *distributed inhomogeneity force* in agreement with equation (8). We do not pursue further here this geometrical approach to continuously distributed defects (see more on differential geometry, the notions of material uniformity and homogeneity, the role of material symmetry groups, crystallographic basis, transplants, G -structure, and G -covariance in Epstein and Maugin [4]).

4. ANELASTICITY AS A STRUCTURAL REARRANGEMENT

The identification of the driving force of anelasticity is central to a thermomechanical approach to this type of irreversible behavior. Anelastic behavior is a macroscopic manifestation of microstructural material rearrangements. The corresponding time evolution in fact is the evolution of the distribution of microstructural material inhomogeneities, e.g., dislocation patterns. Prime importance is thus attributed to the *inhomogeneity mapping* \mathbf{K} of Section 2. and its time evolution. The inhomogeneity finite strain and the inhomogeneity velocity gradient can be defined by [4]-[5] $\mathbf{C}_K := \mathbf{K}^{-T} \cdot \mathbf{K}^{-1}$, $\mathbf{C}_K^{-1} = \mathbf{K} \cdot \mathbf{K}^T$, and $\mathbf{L}_K = \dot{\mathbf{K}} \cdot \mathbf{K}^{-1}$, where a superimposed dot denotes partial time differentiation. The local configuration reached after the \mathbf{K} mapping at \mathbf{X} is called the *reference crystal* C_R by Epstein and Maugin [3]. But if \mathbf{K} is taken to represent anelastic effects then by simple composition we see that $\mathbf{F} \cdot \mathbf{K}(\mathbf{X}) = \mathbf{F}_e$ is the *elastic deformation gradient*. But \mathbf{K} being generally non-integrable, this is also the case of \mathbf{F}_e . Accordingly we can write the *Bilby-Lardner-Stroh-Kröner-Lee multiplicative decomposition* $\mathbf{F} = \mathbf{F}_e \cdot \mathbf{F}_p$, $\mathbf{F}_p \equiv \mathbf{K}^{-1}$, where \mathbf{F}_p may be referred to as the *plastic* (in general, *anelastic*) deformation gradient, in fact *not* a true gradient. The thermomechanics then goes as

follows. The original *Clausius-Duhem inequality* per unit volume of the reference configuration K_R reads

$$-(\dot{W} + S\dot{\theta}) + \text{tr}(\mathbf{T} \cdot \dot{\mathbf{F}}) - \theta^{-1} \mathbf{Q} \cdot \nabla_R \theta \geq 0, \quad (9)$$

where S is the entropy per unit reference volume, W is the free energy, θ is the thermodynamical temperature, \mathbf{Q} is the material heat flux, ∇_R denotes the material gradient, and a superimposed dot indicates the material time derivative. We set

$$\begin{aligned} J_e &= \det \mathbf{F}_e, \quad J_p = \det \mathbf{F}_p = J_K^{-1}, \\ \mathbf{C}_e &= \mathbf{F}_e^T \cdot \mathbf{F}_e, \quad \mathbf{C}_p = \mathbf{F}_p^T \cdot \mathbf{F}_p = \mathbf{C}_K, \end{aligned} \quad (10)$$

and consider free energy densities of the following functional dependence

$$W = W(\mathbf{F}, \alpha, \theta) = J_K^{-1} \bar{W}(\mathbf{F} \cdot \mathbf{K}(\mathbf{X}), \alpha) = J_p \bar{W}(\mathbf{F}_e, \alpha), \quad (11)$$

where α denotes the set of internal variables of state (e.g., hardening parameters, perhaps \mathbf{F}_p itself [6]). $\bar{W} = W_i$ now is the free energy density per unit volume of the so-called *intermediate configuration* K_i . The latter therefore is assimilated to our *reference crystal* at \mathbf{X} . This is indeed in agreement with Mandel's [7] concept of isoclinic intermediate configuration. There is in fact more connection to Mandel's theory of finite elastoplasticity than that. Remember that the Mandel stress \mathbf{M} is generally defined by $\mathbf{M} = \mathbf{T} \cdot \mathbf{F}$. We can also define the fully covariant material stress tensor $\bar{\mathbf{S}}$ by $\bar{\mathbf{S}} = -\mathbf{C} \cdot \mathbf{S} \cdot \mathbf{C} = -\mathbf{C} \cdot \mathbf{M}$, where $\mathbf{C} = \mathbf{F}^T \cdot \mathbf{F}$. Then

$$\mathbf{B} := \mathbf{C} \cdot \mathbf{b} = \mathbf{C} \cdot (\mathbf{W} \mathbf{1}_R - \mathbf{T} \cdot \mathbf{F}) = \mathbf{C} \cdot (\mathbf{W} \mathbf{1}_R - \mathbf{S} \cdot \mathbf{C}) = \mathbf{W} \mathbf{C} + \bar{\mathbf{S}} = \mathbf{b}^T \cdot \mathbf{C}, \quad (12)$$

where the last equality results from the symmetry of the Eshelby stress with respect to \mathbf{C} [3]. *Plastic incompressibility* imposes that $J_p = J_K = 1$ and $\text{tr} \mathbf{L}_K = \text{tr} \mathbf{L}_p = 0$, where, in general $\mathbf{L}_p = -\mathbf{K}^{-1} \cdot \mathbf{L}_K \cdot \mathbf{K}$. We note that in plastic-incompressibility conditions the Mandel and Eshelby stresses are just the same but for a change of sign: $\mathbf{M} = -\mathbf{b}$. Furthermore, we can check in general that \mathbf{b} is also symmetric with respect to \mathbf{C}_K , i.e., $\mathbf{b} \cdot \mathbf{C}_K = \mathbf{C}_K \cdot \mathbf{b}^T$. From (9), the laws of state read

$$\mathbf{T} = \frac{\partial W}{\partial \mathbf{F}}, \quad S = -\frac{\partial W}{\partial \theta}, \quad A = -\frac{\partial W}{\partial \alpha}, \quad (13)$$

where A is the thermodynamical force associated with the internal variable(s) α . These state laws can also be eventually written in terms of \bar{W} (per unit volume of K_i , the *intermediate* or *elastically relaxed* configuration). Then we let the reader prove the following expressions of the *intrinsic dissipation*:

- per unit volume of the reference configuration K_R :

$$\Phi_R = -tr(\mathbf{b} \cdot \mathbf{L}_K) + A \dot{\alpha} = tr(\mathbf{M} \cdot \mathbf{L}_K) + A \dot{\alpha} , \quad (14)$$

or

$$\Phi_R = -tr(\mathbf{B} \cdot (\mathbf{L}_K \mathbf{C}^{-1})_s) + A \dot{\alpha} ; \quad (15)$$

- per unit volume of the intermediate configuration K_i :

$$\Phi_i = tr(\mathbf{S}_i \cdot (\mathbf{C}_e \mathbf{L}_p)_s) + A_i \dot{\alpha} . \quad (16)$$

Here \mathbf{S}_i is the second Piola-Kirchoff stress in K_i , and a subscript s denotes the operation of symmetrization. Accordingly, the skewsymmetric parts of $\mathbf{L}_K \mathbf{C}^{-1}$ and $\mathbf{C}_e \mathbf{L}_p$ are left indeterminate in the formulations (15) and (16), respectively. We let the reader verify that

$$\bar{\mathbf{S}} = \mathbf{B} - \mathbf{W} \mathbf{C} = \frac{\partial \tilde{W}}{\partial \bar{\mathbf{E}}} , \quad \tilde{W} = \tilde{W}(\bar{\mathbf{E}}, \alpha, \theta) , \quad \bar{\mathbf{E}} = \frac{1}{2}(\mathbf{1}_R - \mathbf{C}^{-1}), \quad (17)$$

in the first case, and

$$\mathbf{S}_i = 2 \frac{\partial W_i}{\partial \mathbf{C}_e} , \quad W_i = \bar{W}(\mathbf{C}_e, \alpha, \theta), \quad (18)$$

in the second case. Following the principles enunciated in Maugin [8],[9], the thermomechanical formulations (15) and (16) are tantamount to writing the following *evolution laws* for the plastic behavior (regular plasticity surface):

$$(\mathbf{L}_K \mathbf{C}^{-1})_s = \dot{\lambda} \frac{\partial f(\mathbf{B}, A, \theta)}{\partial \mathbf{B}} , \quad \dot{\alpha} = \dot{\lambda} \frac{\partial f(\mathbf{B}, A, \theta)}{\partial A} , \quad (19)$$

and

$$(\mathbf{C}_e \cdot \mathbf{L}_p)_s = \dot{\lambda} \frac{\partial g(\mathbf{S}_i, A_i, \theta)}{\partial \mathbf{S}_i} , \quad \dot{\alpha} = \dot{\lambda} \frac{\partial g(\mathbf{S}_i, A_i, \theta)}{\partial A_i} , \quad (20)$$

with associated flow functions f and g , and plastic multiplier $\dot{\lambda}$; more on these developments in a recent work of Cleja-Tigoiu and Maugin [6]. Early developments using the notion of Eshelby stress tensor as the *driving force* behind plasticity are given in Maugin [10].

5. VOLUMETRIC GROWTH AS A STRUCTURAL REARRANGEMENT

Basing on a recent work by Epstein and Maugin [11], we view volumetric growth as a process that happens to a uniform body, which we describe in terms of a fixed reference configuration. As time goes on, more material of the *same* kind is « squished-in » smoothly into the body, but in such a way that material points preserve their identity. In other words, the process of growth can be seen as an evolution of material-point neighborhoods in a fixed reference configuration, an evolution that finds its expression in temporal changes of density and concomitant distortions of material-point neighborhoods. While preserving the uniform

material properties, the growth process will in general cause the developments of *inhomogeneities*, responsible for *residual stresses* in the body. Other types of growth, such as inclusions and surface growth (accretion), are beyond the scope of this study. Accretive growth is dealt with by Gurtin [12]. Also, we do not deal here with the complicated physical or physiological mechanisms responsible for volumetric growth. In contrast with previous sections, here mass density, even in the reference configuration, can evolve with time. Accordingly, the local mass balance equation reads

$$\left. \frac{\partial \rho_0}{\partial t} \right|_{\mathbf{x}} = \Pi \neq 0, \quad (21)$$

where we ignore diffusion. Epstein and Maugin [13] have shown that, for this theory, the first Piola-Kirchhoff stress \mathbf{T} , and the Eshelby stress tensor \mathbf{b} are left formally unchanged while a *material growth force* $\mathbf{f}^{gr} = \Pi \mathbf{V}$, $\mathbf{V} = -\mathbf{F}^{-1} \cdot \mathbf{v}$, exists in such a way that the balance equation of *canonical* momentum reads

$$\left. \frac{\partial P}{\partial t} \right|_{\mathbf{x}} - (\text{div}_R \mathbf{b} + \mathbf{f}^{inh}) = \mathbf{f}^{th} + \mathbf{f}^{gr}, \quad P = \rho_0 \mathbf{C} \cdot \mathbf{V}, \quad \mathbf{f}^{th} = S \nabla_R \theta. \quad (22)$$

The Clausius-Duhem equation takes its standard form. Now we introduce the inhomogeneity mapping \mathbf{K} called *transplant* in this growth theory with physiological applications. Let $J_K = \det \mathbf{K}$, and ρ_c the truly invariant mass density in C_R so that $\rho_0 = J_K^{-1} \rho_c$. By time differentiation this shows that *growth* (increase in density) corresponds to $\partial(\det \mathbf{K})/\partial t < 0$ and *resorption* (decrease in density) corresponds to the opposite condition. With a simplified functional dependence of W taken as $W = \bar{W}(\mathbf{F}, \theta, \mathbf{X}, t)$ we can write

$$W = J_K^{-1} W_c(\mathbf{F} \cdot \mathbf{K}(\mathbf{X}, t), \theta). \quad (23)$$

We also introduce the following two transplant velocity gradients :

$$\mathbf{L}_K = \dot{\mathbf{K}} \cdot \mathbf{K}^{-1}, \quad \bar{\mathbf{L}}_K = \mathbf{K}^{-1} \cdot \dot{\mathbf{K}} = -\dot{\mathbf{K}}^{-1} \cdot \mathbf{K}. \quad (24)$$

On account of the relationship between ρ_0 and ρ_c we have

$$\left. \frac{\partial \rho_0}{\partial t} \right|_{\mathbf{x}} = -\rho_0 \text{tr} \mathbf{L}_K. \quad (26)$$

Comparing to (21) shows that there is no need for an evolution equation for the volumetric source, once we know the evolution of \mathbf{K} . These must be ruled by the second law of thermodynamics. As a matter of fact, \mathbf{T} and S receiving their classical form as state laws, the reduced dissipation reads as follows :

$$\Phi = \text{tr}(\mathbf{M} \cdot \mathbf{L}_K) - \theta^{-1} \mathbf{Q} \cdot \nabla_R \theta \geq 0, \quad (27)$$

where \mathbf{M} is the material Mandel stress based on \mathbf{T} . The system of constitutive equations must now be closed by a heat conduction law (e.g., Fourier's) and the evolution equation for the transplanted \mathbf{K} . The latter can be envisaged as the general relationship between various arguments :

$$\phi(\mathbf{K}, \dot{\mathbf{K}}, \mathbf{M} \text{ or } \mathbf{b}, \mathbf{F}, \dot{\mathbf{F}}) = 0, \quad \text{reflecting thus some kind of}$$

nonlinear viscoelasticity. Using invariance arguments it can be shown [11] that this can be reduced to the following relationship : $\phi(\bar{\mathbf{L}}_{\mathbf{K}}, \mathbf{b}_c, \mathbf{C}_e, \dot{\mathbf{C}}_e) = 0$, where \mathbf{C}_e and $\dot{\mathbf{C}}_e$ come from $\mathbf{F}_e = \mathbf{F} \cdot \mathbf{K}$ - the elastic deformation gradient, $\bar{\mathbf{L}}_{\mathbf{K}}$ comes from an invariant combination of \mathbf{K} and $\dot{\mathbf{K}}$, and \mathbf{b}_c is given by $\mathbf{b}_c = J_{\mathbf{K}} \mathbf{K}^{-1} \cdot \mathbf{b} \cdot \mathbf{K}$. As a simple example of isotropic behavior for the symmetric part $\bar{\mathbf{L}}_S$ of $\bar{\mathbf{L}}_{\mathbf{K}}$ we have the evolution equation

$$\bar{\mathbf{L}}_S = \varphi_0 \mathbf{1} + \varphi_1 \mathbf{b}_c + \varphi_2 \mathbf{b}_c^2, \quad (28)$$

where the coefficients are functions of the fundamental invariants of \mathbf{b}_c . Such a law, akin to *nonlinear viscoelasticity*, is exploited in finite-element numerical computations of growth by Imatani and Maugin [13].

6. CONCLUSION

The above-given examples are not limitative. Other effects such as smoothly distributed damage and bulk phase transitions can be dealt with in the like manner by adapting the notion of local structural rearrangement. But what is perhaps more important here is to realize that this presentation, starting with the pioneering work of Epstein and Maugin [3], has united in a single framework the deeply thought ideas of W.Noll [14] on material uniformity that were strongly influenced by the early works of Kondo in Japan, Bilby and co-workers in the U.K, and E.Kröner [15] in Germany, and the notion of configurational or material force (e.g., force acting on a field singularity) so ingeniously introduced by J.D.Eshelby [16],[17]. The missing link has been provided by eqns.(4)-(5) that no authors had given before the end of 1989. Then the recognition of the multiplicative decomposition advocated by many authors (among them Bilby, Bullough and Stroh [18], Kröner [15] and Lee [19] as a particular case of inverse inhomogeneity mapping, and the incorporation of all these into a neat thermomechanical framework completed the thermodynamical theory of configurational forces in our view of it [9],[20].

Acknowledgements : This work was carried out within the European TMR networks 96-0062 and 98-0229.

7. REFERENCES

- [1] Maugin, G.A., *Material Inhomogeneities in Elasticity*, Chapman and Hall London (1993).
- [2] Maugin G.A., *Material Forces: Concepts and Applications*, ASME.Appl.Mech.Rev., 48, 213-245 (1994).
- [3] Epstein, M. and Maugin, G.A., The energy-momentum tensor and material uniformity in finite elasticity, Acta Mech., 83, 127-133 (1990).

-
- [4] Epstein, M. and Maugin, G.A., Notions of material uniformity and homogeneity, in *Theoretical and Applied Mechanics* (Proc.ICTAM, Kyoto, 1996), eds.T.Tatsumi *et al*, pp.201-215, Elsevier, Amsterdam (1997).
 - [5] Epstein, M. and Maugin, G.A., On the geometrical material structure of Anelasticity, *Acta Mech.*, 115, 119-131 (1995).
 - [6] Cleja-Tigoiu, S. and Maugin, G.A., Eshelby's stress tensors in finite Elastoplasticity, *Acta Mech.*, 139, 231-249 (2000).
 - [7] Mandel, J., *Plasticité et viscoplasticité*, (Lecture notes) CISM-Springer, Wien (1971).
 - [8] Maugin, G.A., *The Thermomechanics of Plasticity and Fracture*, Cambridge University Press, U.K. (1992).
 - [9] Maugin, G.A., *Thermomechanics of Nonlinear Irreversible Behaviors*, World Scientific Publ., Singapore, and River Edge, N.J. , USA (1999).
 - [10] Maugin, G.A., Eshelby stress in elastoplasticity and fracture, *Int.J.Plasticity*, 10, 393-408 (1994).
 - [11] Epstein, M and Maugin, G.A., Thermomechanics of volumetric growth in uniform bodies, *Int.J .Plasticity*, 16, 951-978 (2000).
 - [12] Gurtin, M.E., The dynamics of solid-solid phase transitions.I. Coherent interfaces, *Arch.Rat.Mech.Anal.*, 123, 305-335 (1993).
 - [13] Imatani, S. and Maugin, G.A., A constitutive model for growing materials and its applications to finite-element analysis, *Trans.ASME. J.Appl .Mech.*, (2001).
 - [14] Noll, W., Materially Uniform simple bodies with inhomogeneities, *Arch.Rat.Mech. Anal.*, **27**, 1-32, 1967.
 - [15] Kröner, E., *Kontinuumstheorie der Versetzungen und Eigenspannungen*, Springer-Verlag, Berlin (1958).
 - [16] Eshelby, J.D., *The force on an elastic singularity*, *Phil.Trans.Roy.Soc.Lond.*, A244, 87-112 (1951).
 - [17] Eshelby, J.D., The elastic energy-momentum tensor, *J.Elast.*, **5**, 321-335(1975).
 - [18] Bilby, B.A., Lardner, L.R.T. and Stroh, A.N., Continuous distributions of dislocations and the theory of plasticity, in *Proc. 10th International Congress of Applied Mechanics* (Brussels, 1956), Vol.III, pp.35-44, Université Libre de Bruxelles, Belgium (1957).
 - [19] Lee, E.H., *Elastic-plastic deformation at finite strain*, *ASME Trans. J.Appl.Mech.*, 36, 1-6 (1969).
 - [20] Kienzler, R. and Maugin, G.A., (eds), *Configurational Mechanics of Materials* (Lecture notes, Sept.2000), CISM-Springer-Verlag, Vienna (2001).

QUANTUM PLASTICITY

Kirk C. Valanis
Endochronics/University of Portland
Vancouver, WA., USA

1. SUMMARY

In this paper we demonstrate that *quantum behavior* is not limited to systems of atomic dimensions but *does in fact occur in macroscopic systems*. Currently, quantum behavior is associated with systems of atomic dimensions. Such systems occupy discrete energy levels and change their energy state by discrete transitions. The energy levels are determined by the solution of the Schrodinger Equation specific to a system. However, *and most surprisingly*, similar behavior is exhibited by metal specimens under stress. Plastic states change in a sudden fashion and *exist only at discrete values of the surface tractions*. Here we show that the tractions are determined by an equation *identical* to that of Schrodinger, derived in the literature by the author. It is demonstrated that the predicted values of the tractions are in excellent agreement with their experimental counterparts published in the literature.

2. INTRODUCTION

It is observed that metal specimens, large in reference to their atomic dimensions - such as soft aluminum specimens in tension or in torsion - under *slow load control*, deform uniformly and continuously, except at specific values of the applied traction, when they deform *spontaneously*, and in an unstable manner, to a new configuration at constant traction. Simultaneously new periodic patterns appear on the surface of the specimens. Such observations have been reported initially by Portevin and Chatelier and since then by other experimentalists. Of these, the work of Lubahn (1961), Dillon (1965) and Sharpe (1966) is given special attention.

This behavior is strongly reminiscent of the quantum behavior of atomic systems. We pose, therefore, the question, whether such behavior may be predicted, or at a minimum depicted, by a differential equation similar in form to the Schrodinger Equation for the quantum behavior of atomic systems.

The purpose of this paper is to show that these discrete material instabilities are predicted by the solution of a partial differential equation, henceforth referred to as the *Quantum Plasticity Equation*. This equation was derived previously by the author (1996,1997,1998) within the scope of the non-affine gradient theory of thermodynamics. There are striking parallels between the unstable phenomenological behavior of metals and the time-independent quantum behavior of atomic systems as we shall illustrate.

3. QUANTUM BEHAVIOR

The Schrodinger Equation

In the case of an elementary particle, quantum behavior is a phenomenon whereby a particle in a time invariant *specific* potential field $U(x_j)$ occupies *only* one of a discrete set of energy states E_n . At the same time the spatial configuration of the particle is given by its wave function ψ which satisfies the Schrodinger Equation, Landau and Lifshitz (1976):

$$(\hbar^2/2m)\nabla^2\psi + [E - U(x_j)]\psi = 0 \quad (1)$$

in R^3 where \hbar is the Planck constant divided by 2π , m is the mass of the particle and ∇^2 is the Laplacian operator. The case of interest here is when $U = 0$, i.e., when the field is null and the particle is in an infinite potential well. This is the case of a 'particle in a box'. In this case:

$$(\hbar^2/2m)\nabla^2\psi + E\psi = 0 \quad (2)$$

and $\psi = 0$ on the walls of the box.

The Quantum Plasticity Equation

The theory of non-affine deformation has as its basis the observation that during an inelastic process, there is a subset of material particles, called the *non-affine phase*, which migrate from their initial neighborhood in the course of deformation. The migration vector field, which determines the configuration of the non-affine phase, is called q_j . The vector field q_j is determined from the equation:

$$\kappa^2 \nabla^2 q_k + s_{kj} q_j = 0 \quad (3)$$

where κ is a material constant and s is the deviatoric stress vector. The boundary condition on q depends on the physics of the surface S . If the surface is impermeable then $q = 0$ on S . If S is permeable then, on S , the normal gradient of q , i.e. $\partial q / \partial n = 0$.

Mathematical Equivalence

Equations (2) and (3) show that the vector q in eq. (3) plays a counter-role to the wave function ψ in eq. (2). The material constant κ replaces $\hbar^2/2m$ and the tensor s replaces the scalar E . In a like fashion, $q = 0$ at an impermeable boundary (but $\partial q / \partial n = 0$ at a permeable surface).

The particle in a box is the atomic analogue of the extension of a box-like macroscopic domain. We illustrate this analogy by pointing out that the eigen-energies E of the Schrodinger Equation are:

$$E = (\pi^2 \hbar^2 / 2m) [(n/a)^2 + (m/b)^2 + (p/c)^2], \quad (4)$$

where a, b, c are the dimensions of the box and n, m, p are integers. The analytical expression for the wave function ψ is given by eq. (4a):

$$\psi = \psi_0 \sin(n\pi x/a) \sin(m\pi y/b) \sin(p\pi z/c) \quad (4a)$$

Correspondingly, the eigen-tensions T of the Quantum Plasticity Equation are:

$$T = (3/2)(\pi^2 \kappa^2) [(n/a)^2 + (m/b)^2 + (p/c)^2], \quad (5)$$

where a, b, c in are the dimensions of the rectangular specimen under tension and with permeable boundaries. The analytical expression for the non-affine displacement q_j is given by eq. (5a):

$$q_j = q_j^0 \cos(n\pi x/a) \cos(m\pi y/b) \cos(p\pi z/c) \quad (5a)$$

4. EXPERIMENTAL VALIDATION

Experiments support the proposition that $n=m=p$, i.e., that the eigen-tractions T at points of instability have 'maximal values'. Thus:

$$\sqrt{T} = \sqrt{T_0} n \quad (6)$$

where

$$T_0 = (3/2)(\pi^2 \kappa^2) [(1/a)^2 + (1/b)^2 + (1/c)^2] \quad (7)$$

Thus, the square root of the tensile stress at the points of instability, is proportional to the ordinal number of its occurrence. The strain jump is uncorrelated!

The scalar T_0 is the *instability coefficient* and is composed of two factors: κ which is a material parameter, which controls the material propensity to instability, and the bracket $[(1/a)^2 + (1/b)^2 + (1/c)^2]$, which accounts for the effect of the specimen geometry on the collapse loads. We note that if we keep the transverse dimensions b and c fixed, then as the length ' a ' increases T_0 becomes independent of specimen size while as ' a ' tends to zero T_0 goes to infinity. Short specimens are more resistant to instability than long ones. The extraordinary result of eq. (6) has been validated by the experiments of Lubahn (1961) who measured the load P rather than the traction T .

Experimentally, instabilities are not discernible until the stress reaches a certain threshold. This means that there is a minimum n_c below which unstable states are not observable, most likely because they lie outside the sensitivity of the apparatus. Thus, in view of eq. (6), we have the following relation:

$$P = P_0 (n_c + r)^2; \quad \sqrt{P} = \sqrt{P_0} (n_c + r) \quad (8a,b)$$

where $r = n - n_c$. A plot of the experimental values of \sqrt{P} vs r gave a straight line. The intercept on the \sqrt{P} -axis gave $\sqrt{P_0} n_c$ while the slope of the plot gave $\sqrt{P_0}$. It was found the $P_0 = 3.889$ while $n_c = 14$. Thus:

$$P = 3.889(14+r)^2; \quad \sqrt{P} = 1.972(14+r) \quad (9a,b)$$

$r = 1, 2, 3, \dots, \infty$. The match between experimental and calculated values is very close despite experimental as well as reading errors. See Table 1 below.

r	0	1	2	3	4	5
Observed P	760	860	980	1120	1260	1420
Calculated P	764	878	998	1122	1263	1407

Table 1. Comparison of experimental and calculated loads in terms of ordinate numbers, after Lubhan

Experiments by Sharpe

Sharpe (1966) tested cylindrical specimens of soft aluminum in tension. The solution to the cylindrical form differs from its cuboidal counterpart. In this case the non-affine displacements field q_j is given by eq. (10):

$$q_z = A J_0(\beta_n r/a) \cos(n\pi z/l) \quad (10)$$

where J_0 , 'a' is the radius and l the length of the cylinder while z is the coordinate along its length. Permeable boundaries were considered.

For 'long' cylinders such as those used by Sharpe, the collapse tractions T_n are given in eq. (11):

$$\sqrt{T_n} = \sqrt{(3C/2a^2)} \beta_n \quad (11)$$

where β_n are the zeros of the Bessel function J_1 . Thus the square roots of the collapse tractions should be proportional to the zeros of J_1 . The theory gives account of the effect of both size and shape on the collapse loads. The constant C was determined from the data and the numerical value of $\sqrt{(3C/2a^2)}$ was found and inserted in eq. (12). Thus:

$$\sqrt{T_n} = 0.0227 \beta_n \quad (12)$$

The *extreme* agreement between the experimental data and the theoretical values T_n is illustrated in Table 2.

Obs. \sqrt{T}	1.59	1.65	1.73	1.80	1.89	1.95	2.01	2.08	2.15	2.23	2.30	2.37
Calc. \sqrt{T}	1.59	1.66	1.73	1.80	1.87	1.94	2.01	2.08	2.08	2.23	2.30	2.37
n	22	23	24	25	26	27	28	29	30	31	32	33

Table 2. Comparison of experimental and calculated loads in terms of ordinate numbers, after Sharpe

Remark. Subsequent analysis of other experimental data, with specific reference to the work of Dillon (1965), involving torsion of hollow and solid cylinders has been reported elsewhere. See Valanis (2000,2001). Agreement of theoretical predictions with experiment was also very close.

5. REFERENCES

- [1] Dillon, W. O., (1965): Experimental data on aluminum as an unstable solid. Proc. 4th International Congress of Rheology (Lee,E.H., ed.) **2**, 377-389.
- [2] Landau, L.D. and Lifshitz, E.N., (1976): Quantum Mechanics. Oxford, Pergamon Press.
- [3] Lubahn,J.D. and Felgar, R.P., (1961): Plasticity and creep in metals. New York, Wiley.
- [4] Sharpe, W.N., Jr, (1966): The Portevin Le Chatelier effect in aluminum single crystals and polycrystals. J. Mech. Phys. Solids, **14**, 187-202.
- [5] Valanis, K.C., (1996): A gradient theory of internal variables. Acta Mechanica, **116**, 1-14.
- [6] Valanis, K.C., (1997): A gradient theory of finite viscoelasticity. Arch. Mech., **49**, 589-609.
- [7] Valanis, K.C., (1998): A gradient thermodynamic theory of self-organization. Acta Mechanica, **127**, (1-23).
- [8] Valanis, K.C., (2000) The Portevin-Le Chatelier Effect. Its prediction and place in gradient thermodynamics. Acta Mechanica, **145**, 95-116.

ON STRAIN GRADIENTS IN PLASTICITY

J. Kratochvíl

Department of Physics, Faculty of Civil Engineering,
Czech Technical University, 166 29 Prague 6, Czech Republic

1. SUMMARY

The recent renewed interest in the strain gradient plasticity has been motivated mainly by the experimental evidence that plastic flow processes in crystalline solids are inherently size dependent. However, similarly as in the previous attempts to introduce formally strain gradients into plasticity the current theories have failed to reflect the underlying physical mechanisms. Their range of validity has remained uncertain. The two major problems in the gradient theories are the choice of the gradients which are to be used and the formulation of adequate constitutive equations for them. This paper indicates that the problems can be overcome by putting the theoretical framework in correlation with microscopic observations. For the case of shear bands it is shown that an advanced non-local plasticity model need not be a curve fitting procedure providing that the constitutive equations for additional degrees of freedom (strain gradients, directors) are based on knowledge of the mechanism which dominates the studied plastic deformation process.

2. INTRODUCTION

In the paper [1] Dillon and Kratochvíl stated that at the scale of the order of micrometers the theory of plasticity should be formulated as a non-local theory due to interaction among dislocations. The formulation has been accomplished by introducing strain gradients into the theory of plasticity. However, the formal attempt [1], based on a vague interpretation of the plastic strain gradients and lacking correlation with microscopic observations, has failed to reflect the underlying physical mechanisms. The observations reveal that the non-local character of plasticity is a result of a complex self-organization of dislocations. The self-organization process leads to the formation of dislocation structures with a characteristic length scale. Plastic deformation is carried by glide dislocations which are flexible line defects. The stress needed to move a glide dislocation segment is influenced by the self-force which can be expressed through a dislocation curvature and the line tension. The incorporation of the dislocation curvature introduces plastic strain gradients into the plasticity theory [2]. However, the curvature is just one of the factors governing the nonlocal character of the crystal plasticity at mesoscale. The other factors are the properties of stored dislocations, namely, the processes controlling fluxes of the stored dislocations. There is not enough space here to analyze the problem in more detail; the reader is referred to the literature on dislocation patterning [2-8]. Instead, the difficulties of the strain gradient theories

of plasticity will be explained through a somewhat simpler problem of plastic strain localization.

The conventional solid mechanics fails to describe localization of deformation in a realistic way. It provides a criterion for the occurrence of strain localization in a form of deformation bands, however, it predicts infinitesimal width of the bands. The later effect results in a pathological mesh-size dependence of FEM simulations of the strain localization. A framework aimed to provide a more realistic description of plastic strain localization has been proposed by Aifantis [9], Triantafyllidis and Aifantis [10], and Coleman and Hodgdon [11,12]. In [9-12] the process of localization is studied within the context of constitutive theories that involve second order deformation gradients. The implicit underlying idea is that the material microstructure (dislocation arrangements, damage, micro voids, etc.) could generate higher order gradients in stress-strain relations through approximate constitutive equations. However, the introduced phenomenological constants which are of dimension of length and which control the band width have not been related to the microstructure in any of the models [9-12]. These models suggest the criterion for the occurrence of the deformation bands, as the conventional theory does; additionally they predict the band width and the evolution of the bands in the post localization stage. However, for the specific forms of the constitutive equations assumed, the predicted shape and the evolution of the shear band profiles are not in agreement with observation on metals [13,14]. While the bell-shaped profiles predicted by the strain gradient models [9-12] grow with deformation, the shear bands observed in single crystal and polycrystalline metals consist of micro bands and propagate across samples by increasing their length and width through activation of new micro bands, whereas the former ones become inactive [13,14]. In the next section an approximate non-local theory of plasticity of the Cosserat type will be presented, which reflects the observations and gives the characteristic length of the Cosserat framework a concrete physical meaning.

3. COSSERAT MODEL OF SHEAR BANDS

The results of the detailed experimental and theoretical analysis of shear banding in copper single crystals and mild steel polycrystals have been summarized in [14]. In both of the materials studied the observed processes of shear banding were similar. The SEM in situ observation on Cu single crystals [13,15] has revealed that a macro-band on the sample scale, whose thickness could reach several millimeters, consists of a set of short parallel micro shear bands regularly spaced about $0.5 \mu\text{m}$. The micro-bands are approximately parallel to one of the slip systems. The structural studies in mild steel polycrystals have shown that similarly to the single crystals a macro-band in the polycrystal consists of a set of densely spaced micro-bands which are able to penetrate grain boundaries and propagate through several grains with only a small deviation. The thickness of the macro bands increases due to the activation of new micro bands in the adjacent matrix of the polycrystal. The micro bands do not follow a particular crystallographic direction in the individual grains. They consist of slips locally chosen from the large number of slip systems available in the b.c.c. structure. The choice seems to be governed by optimization of the shear band orientation according to the laws of continuum mechanics.

The measurements revealed that the macro bands consists of saturated and active zones which divide each macro-band in two parallel parts. The saturated zone is formed by the deactivated micro shear bands and its thickness grows with increasing straining. In the active zone new micro bands are activated. The active zone shifts with the increasing strain and its

thickness remains constant. The Cosserat theory of shear banding has proved to be a convenient tool for modeling the strain profiles of the bands. This theory was proposed already in [16-18] but was applied for the first time to interpretation of the detailed experimental data in [14]. The comparison has indicated that the Cosserat model is a promising theoretical tool for analyzing the localization processes. The additional degree of freedom of the Cosserat type (directors) are customary related to density of dislocations [14,17,18]. It is supposed that the lattice curvature represented by the gradient of the field of directors is caused by the geometrically necessary dislocations trapped in a volume element of a certain unspecified characteristic size.

An alternative interpretation of Cosserat directors has been proposed in [19,20]. It is based on the observed mesostructure of macro-bands which consist of micro bands. Work hardening of the micro bands which limits their shearing capacity and the fact that a new micro band can be activated only at a characteristic distance apart control the mesoscale flexibility of the material. This feature can be expressed through the Cosserat constitutive equations. Let us consider a mesoscale volume element of a linear dimension l represented e.g. by the mesh size of the micro grid used in the measurements of the macro band profiles [14]. Let l be large enough in comparison with the distance d between the neighboring micro bands ($d \approx 0.5 \mu\text{m}$). A new micro-band is activated in the vicinity of the already formed band when the local critical resolved shear stress reaches a value τ_{crit} . Each micro band carries a plastic shear γ_B . When n micro bands enter the mesoscale volume element they cause curvature of the material in an analogous way as geometrically necessary crystal dislocations bend a crystal. The average material curvature can be expressed by component K of the curvature tensor

$$K = \frac{n\gamma_B w}{l^2} \quad (1)$$

At the mesoscale the 'Burgers vector' of the micro band is $\gamma_B w$; w is the width of the micro band ($w \approx 0.1 \mu\text{m}$). Angle $\theta = n\gamma_B w/l$ measures the rotation of the material fiber (micro grid) with respect to the direction perpendicular to the shear band plane. Note that the angle θ and curvature component K depend on the chosen size l of the volume element partly filled with the micro-bands; for the same number n of the penetrating micro bands the angle θ decreases with increasing l .

A micro band at the level n is activated when the couple stress component μ equals

$$\mu = nd\tau_{crit} \quad (2)$$

Unlike the stress τ_{crit} , the couple stress μ is able to distinguish that the activation takes place at the level n . The equilibrium condition for the couple stress transfers the activation signal among the volume elements. By excluding n from Eqns. (1) and (2) we get the constitutive equation for the couple stress component written in the usual form (G is shear modulus)

$$\mu = GL^2 K \quad (3)$$

where the phenomenological characteristic length L is

$$L = l \sqrt{\frac{\tau_{crit} d}{G \gamma_B w}} \quad (4)$$

Hence, L depends not only on the characteristic material length scales, i.e. on the distance d between the neighboring micro bands and the mesoscale 'Burgers vector' $\gamma_B w$ (the length of the surface step produced by an average micro band), but also on the chosen size l of the mesoscale volume element given by the method of measurements. This size can be identified with the mesh size of the micro grid used in the interferometric measurements of the band profiles [14].

The suggested interpretation is close to the interpretation of the Cosserat additional degrees of freedom in terms of geometrically necessary dislocations. The principle difference is that instead of the geometrically necessary dislocations the micro-bands are considered as the main factors. The essential feature is that in both single crystals and polycrystals each micro band carries only certain amount of shear before it gets saturated by hardening, and that other micro bands are activated at the characteristic distance d from the neighboring ones. As a consequence, the mesoscale flexibility of the material is limited and the macro bands are of finite width. The interpretation would remain valid even if the micro bands were less ordered. It is interesting to note that a similar micro band structure of macro bands appears also in many polymers [21] despite the fact that the mechanism of plastic flow is much different than in case of metals, as there exit no dislocations here.

The observation that micro bands have limited shearing capacity and are activated at the characteristic distance d from neighboring ones can be probably understood by analogy to the formation of the Lüders bands. The simplest form of the Lüders bands, which appear in many alloy crystals and e.g. in neutron irradiated Cu, is an analogy to the active zone of a macro shear band. The Lüders band front advances by adding new slip bands parallel to the old ones. At present the propagation of the Lüders bands is better understood [22] than that of the shear bands. The distance of the location of the next activation ahead from the Lüders band front is controlled by the local stress produced as a consequence of surface slip steps. The strong notch stresses at the growing slip step are shielded by the produced dislocations moving into the crystal. The calculations have shown, Hampel et al. [23], that the resulting shear stress in the neighboring slip planes has maximum at distances corresponding quite well to the observed most frequent slip line and slip band distances. In case of the Lüders bands the new slip band starts to operate with a very rapid motion of the first dislocation group through the virgin crystal with destructible obstacles causing local softening followed by hardening through successive activation of further neighboring dislocation groups. Analogously, in a shear banding of a pre-deformed material the intensive shear in a lamella of localized deformation first disintegrates the original deformation substructure and then massive production of dislocations causes a 'traffic jam' which results in hardening. In both cases the elementary distances between the slip or micro shear bands (distance d entering equations (2)), which seem to be controlled by the notch effect of the surface steps, and the amount of slip carried by the individual slip lines or micro-bands ($\gamma_B w$ entering (1)) can serve as the convenient intrinsic length scale of a phenomenological model of plastic localization processes.

4. CURRENT STRAIN GRADIENT THEORIES OF PLASTICITY

The recent renewed interest in the strain gradient plasticity [24,25], has been motivated mainly by the experimental evidence that plastic flow processes in crystalline solids are inherently size dependent over a scale that ranges from a fraction of a micrometer to hundreds of micrometers. For example, the scaled shear strength of copper wires in torsion increases with diminishing wire diameter in the range 100 μm to 10 μm by almost a factor of three, while the data for uniaxial tensile behavior of the wires, for which imposed gradients are absent, show essentially no size effect [24,25]. In this context, the constitutive description of the material is proposed to depend both on the strain and the strain gradient. The interpretation is based on notions of incompatible lattice deformations and geometrically necessary dislocations. According to Fleck et al. [24,25] the dislocations that control the flow strength are stored in deformed materials for two reasons: (i) In crystalline materials strained uniformly the dislocations are accumulated by random trapping. These are referred by the authors as statistically stored dislocations. (ii) When a crystalline material is subjected to a plastic strain gradient, geometrically necessary dislocations must be additionally stored. Plastic strain gradients appear in a plastically deformed solid either because of the geometry (e.g. a strain field near a crack tip) and loading conditions (e.g. torsion), or because the material itself is plastically inhomogeneous (e.g. non-deformable phases).

The above mentioned interpretation can be approximately used if the dislocations are averaged over volumes of linear dimension far greater than μm . At the micrometer scale dislocation structures are observed. Strained crystalline materials behave as composites with lots of intrinsic geometrically necessary dislocations. At that scale the strain is never uniform and intrinsic stress gradients are very high. The externally imposed strain gradients could correspond to some geometrically necessary dislocations in a rough averaged sense. In this context it is interesting to note that the too rough averaging, as already recognized by Kosevich [26], has caused that the theory of continuous distribution of dislocations (from which the relation between strain gradients and density of geometrically necessary dislocation has been derived) did not provide any adequate theoretical framework for plasticity.

As seen in the previous section the correlation of the theoretical framework with microscopic observations can substantially improve the formulation and physical meaning of constitutive relations of the nonlocal plasticity. On the other hand the attempts based just on the phenomenological arguments, e.g. [1,9-12], have proved to be inadequate. From that point of view it seems that unless the current attempts to formulate a strain gradient theory of plasticity are confronted with detailed microscopic observations they will remain to be a pure phenomenology, merely able to describe the observed size-dependent macroscopic behavior by curve-fitting with the validity range uncertain.

Acknowledgement: The research was supported by the project VZ J00021, and partially by the project GAUK 164/1999/B MAT/MFF.

5. REFERENCES

- [1] Dillon, O. W. and Kratochvíl J., A strain gradient theory of plasticity, *International Journal of Solids and Structures* 6, 1513-1533 (1970).
- [2] Kratochvíl, J. and Saxlová, M., Dislocation pattern formation and strain hardening in solids, *Physica Scripta T49*, 399-404 (1993).

- [3] Walgraef, D. and Aifantis, E. C., Dislocation patterning in fatigued metals as a result of dynamical instabilities, *Journal of Applied Physics* 58, 688-691 (1985).
- [4] Aifantis, E. C., On the dynamical origin of dislocation patterns, *Materials Science and Engineering* 81, 563-574 (1986).
- [5] Kratochvíl, J. and Libovický, S., Dipole drift mechanism of early stages of dislocation pattern formation in deformed metal single crystals, *Scripta metallurgica* 20, 625-1630 (1986).
- [6] Glazov, M., Llanes, L. M. and Laird, C., Self-organized dislocation structures (SODS) in fatigued metals, *physica status solidi (a)* 149, 297-321 (1995).
- [7] Malygin, G. A., Dislocation self-organization process and crystal plasticity, *Progress in Physics* 169, 979-1010 (1999).
- [8] Kratochvíl, J., Self-organization model of localization of cyclic strain into PSBs and formation of dislocation wall structure, *Materials Science and Engineering A* (2001), in the press.
- [9] Aifantis, E. C., On the microstructural origin of certain inelastic models, *Transactions of ASME, Journal of Engineering Materials and Technology* 106, 326-330 (1984).
- [10] Triantafyllidis, N. and Aifantis, E.C., A gradient approach to localization of deformation in hyperelastic materials, *Journal of Elasticity* 16, 225-237 (1986).
- [11] Coleman, B. D. and Hodgdon, M. L., On shear bands in ductile materials, *Archive for Rational Mechanics and Analysis* 90, 219-247 (1985).
- [12] Coleman, B. D. and Hodgdon, M. L., On the localization of strain in shearing motions of ductile materials, *Res Mechanica* 23, 223-238 (1988).
- [13] Yang, S. and Rey, C., Shear band post-bifurcation in oriented copper single crystals, *Acta metallurgica and materialia* 42, 2763-2774 (1994).
- [14] Labbé, E., Hoc, T. and Rey, C., A simplified crystallographic approach of bifurcation for single crystals and polycrystals, in *Proceedings of Euromech-Mecamat on Mechanism of Materials with Intrinsic Length Scale*, A. Bertram, S. Forest and F. Sidoroff (Eds.), Otto-von-Guerlicke University, Magdeburg-Germany (1998) 211-218.
- [15] Dubois, P., Gasparini, M., Rey, C. and Zau, A., Crystallographic analysis of shear bands initiation and propagation in pure metals, *Archives of Mechanics* 40, 25-32 (1988).
- [16] De Borst, R., Simulation of strain localization: A reappraisal of the Cosserat continuum, *Engineering Computations* 8, 317-332 (1991).
- [17] Forest, S., Cailletaud, G. and Sievert, R., A Cosserat theory for elastoviscoplastic single crystals at finite strain, *Archives of Mechanics* 49, 705-736 (1997).
- [18] Forest, S., Modeling slip, kink and shear banding in classical and generalized single crystal plasticity, *Acta materialia* 46, 3265-3281 (1998).
- [19] Kratochvíl, J., Labbé, E., Rey, C. and Yang, S., On physically motivated mesoscale Cosserat model of shear band formation, *Scripta materialia* 41, 761-766 (1999).
- [20] Kratochvíl, J., On intrinsic length scales in plasticity, in *Proceedings of PLASTICITY'99, The Seventh Int. Sym. On Plasticity and Its Current Applications*, A. Khan (Ed.), Net Press, Fulton, Maryland (1999) 1017-1020.
- [21] Van Der Giessen, E., Localized plastic deformation in glassy polymers, *European Journal of Mechanics A/Solids* 16, special issue, 87-106 (1997).
- [22] Neuhäuser, H. and Hampel, A., Observation of Lüders bands in single crystals, *Scripta metallurgica and materialia* 29, 1151-1157 (1993).
- [23] Hampel, A., Kammler, Th. and Neuhäuser, H., Structure and kinetics of Lüders band slip in Cu 5 to 15 at % Al single crystals, *physica status solidi* 135, 405-416 (1993).

- [24] Fleck, N. A., Müller, G. M., Ashby, M.F. and Hutchinson, J. W., Strain gradient plasticity: Theory and experiment, *Acta metallurgica and materialia* 42, 475-487 (1994).
- [25] Fleck, N. A. and Hutchinson, J. W., Strain gradient plasticity, *Advances in Applied Mechanics* 33, 295-361 (1997).
- [26] Kosevich, A. M., Dynamical theory of dislocations, *Uspechy Fiziceskich Nauk* 4, 579-609 (1964).

ENABLING NONLINEAR COMPUTATIONS THROUGH EFFICIENT TIME-STEPPING

E. D. Koronaki¹, C. Theodoropoulos², A.G. Boudouvis¹ and I.G. Kevrekidis²

¹Department of Chemical Engineering
National Technical University of Athens, Athens 15780, Greece

²Department of Chemical Engineering
Princeton University, Princeton NJ 08544, USA

1. SUMMARY

The Recursive Projection Method (RPM) is implemented in this study in order to accelerate the convergence of two time-stepping schemes to stable steady states, as well as to enable them to compute mildly unstable ones. This approach forms the basis for the computer-assisted stability and bifurcation analysis of the nonlinear dynamic behavior of the underlying system model. The effect of the size of the time step in the overall procedure is explored and the interplay of the spectra of the underlying system and of the time-stepping scheme with the RPM convergence is emphasized.

2. INTRODUCTION

The semi-discretization of time-dependent, nonlinear PDEs results in (often large) systems of coupled nonlinear ODEs (or DAEs). Equilibrium solutions of the original PDEs can be asymptotically obtained by integrating the resulting ODEs (or DAEs) to steady state. This approach, when combined with appropriate continuation algorithms, constitutes a systematic path towards the computer-assisted stability and bifurcation analysis of the nonlinear dynamic behavior of the underlying system model. The efficacy of this "direct simulation" approach is inextricably linked to the particular numerical time integration scheme used. Time integration can become very slow (and eventually fail) to converge at certain parameter values that are close to bifurcations. The Recursive Projection Method (RPM), proposed by Shroff and Keller [1], is implemented in this study in order to accelerate the rate of the time-stepper approach to steady state and also guarantee convergence under certain conditions. In this work, the Galerkin/finite element method for spatial discretization is combined with two time integration schemes. The illustrative example consists in locating spatially non-uniform steady states of the Bratu problem in one dimension. The time-steppers employed are a) the forward Euler (FE) scheme and b) an implicit-explicit one-step scheme (IE) proposed by Akrivis et al.[2].

The effect of the size of the time steps used and its interplay with RPM-assisted convergence is explored for both time-steppers. This is correlated with the structure of the eigenvalue

spectra of the underlying model problem as well as the time-stepper. Numerical investigation shows that for a wide range of time steps, the RPM enhanced the convergence rate of both schemes to the corresponding steady states and even allowed the computation of unstable solutions. In addition, the most dangerous eigenvalues of the time integration schemes were detected with significant accuracy with the help of the RPM. It is observed that the RPM-assisted convergence of the IE scheme, is not affected by spatial discretization, while, in contrast to the RPM-assisted convergence of the FE scheme [3] which can be - and is - severely affected.

3. THE RECURSIVE PROJECTION METHOD

In this section, a brief discussion of the Recursive Projection Method is offered. The method is described in detail in [1] and a family of related "Newton-Picard" methods in several theses (e.g. [4]). Steady state solutions of the parameter-dependent dynamical system:

$$\dot{u} = f(u, \lambda) \quad (1)$$

are also solutions of the fixed point iterative procedure:

$$U^{n+1} = F(U^n, \lambda), F: \mathbb{R}^N \times \mathbb{R} \rightarrow \mathbb{R} \quad (2)$$

F denotes a system time-stepper, a result of numerical integration over a time interval T - the reporting horizon of the time-stepper - of the semi-discretization, through finite elements on a mesh of N grid points, of eqn. (1); as initial condition is taken the steady state solution for $\lambda = 0$.

The RPM stabilizes, under certain assumptions, fixed point iterative procedures, such as (2) by determining and isolating the subspace, P , corresponding to the directions in which the map is slowly contracting or even slowly expanding. The original procedure is then modified by performing Newton's method on the subspace P while on its orthogonal complement, Q , the fixed point iteration (2) continues to converge. The fixed point iteration (2) is stable when all the eigenvalues of the matrix $F_U(U, \lambda)$ lie in the unit disk.

Then the stabilized iterative procedure takes the form:

1. $p^{(0)} = PU^{(0)}(\lambda), q^{(0)} = QU^{(0)}(\lambda)$
2. Do until convergence:
 - (a) Newton step: $p^{(v+1)} = p^{(v)} + (I - PF_U(U^{(v)}, \lambda) P)^{-1} (P F(U^{(v)}, \lambda) - p^{(v)}),$
 - (b) Fixed point iteration: $q^{(v+1)} = Q F(U^{(v)}, \lambda)$
3. $u^*(\lambda) = p^{(v_{\text{final}})} + q^{(v_{\text{final}})} \equiv p^* + q^*$

The main assumption is the existence of a gap between the "strongly stable" and the "slow" eigenvalues of the linearization around the fixed point in question. For the method to work, the dimension, m , of this latter "slow" subspace should be comparatively low (typically $O(10)$ eigenvalues). While this may appear restrictive, there is a large class of dissipative system models for which this is a case of interest close to primary instabilities.

4. TIME INTEGRATION SCHEMES

The test case in this study is the Bratu problem in one dimension [5]:

$$\dot{u} = u_{xx} + \lambda e^u = f(u, \lambda), \text{ with } u(0) = u(1) = 0 \quad (4)$$

λ is a parameter. The initial condition is the steady state solution for $\lambda=0$.

4.1 The forward Euler scheme

Applying the forward Euler (FE) scheme in the above equation, results in the following:

$$(u^{n+1} - u^n) / \Delta t = u_{xx}^n + \lambda e^{u^n} \Rightarrow u^{n+1} = u^n + \Delta t \cdot f(u, \lambda) \quad (5)$$

Discretization in space is done using the Galerkin/finite element method with quadratic basis functions, $\{\phi_i\}_{i=1}^N$. Finally, U^{n+1} at each time step is:

$$U^{n+1} = A^{-1} b \quad (6)$$

$$A_{ij} \equiv \int_0^1 \phi^i \phi^j dx, \quad b_i \equiv \int_0^1 \phi^i u^n dx + \lambda \Delta t \left[\int_0^1 \phi^i e^{u^n} dx - \int_0^1 u_x^n \frac{d\phi^i}{dx} dx \right], \quad i, j = 1, \dots, N \quad (7)$$

In the case of the forward Euler scheme, the stability condition is $\Delta t/h^2 < 1$, where $h=1/N$.

4.2 The one-step implicit-explicit Euler scheme

The one-step implicit-explicit scheme (IE) [2], is stable, consistent and very efficient and it is applied to equation (5), as follows:

$$(u^{n+1} - u^n) / \Delta t = u_{xx}^{n+1} + \lambda e^{u^n} \Rightarrow u^{n+1} - \Delta t \cdot u_{xx}^{n+1} = u^n + \lambda \cdot \Delta t \cdot e^{u^n} \quad (8)$$

The Galerkin/finite element method yields: $U^{n+1} = A^{-1} b$, where:

$$A_{ij} = \Delta t \int_0^1 \frac{d\phi^i}{dx} \frac{d\phi^j}{dx} dx + \int_0^1 \phi^i \phi^j dx, \quad b_i = \int_0^1 \phi^i u^n dx + \lambda \cdot \Delta t \int_0^1 \phi^i e^{u^n} dx \quad i, j = 1, \dots, N \quad (9)$$

5. RESULTS AND DISCUSSION

The aim of this study is the efficient location of steady states of eqn. (4) using RPM-assisted time integration with the schemes mentioned in section 3. The operator f is discretized on a spatial grid of 200 points and $F(U^n, \lambda)$ is the result of time integration over a time interval T for each n . As criterion for convergence to steady state the condition $|F(U^{n+1}, \lambda) - F(U^n, \lambda)| < \varepsilon = 10^{-5}$ is used.

The RPM-assisted time-stepping is first implemented in conjunction with an algorithm that allows continuation on the physical parameter of the system λ . The solution branch is shown in Figure 1. To continue past the turning point, which appears at $\lambda = 3.512$, the arc-length continuation algorithm is employed, as described in [1]. In this case $T = 0.01$.

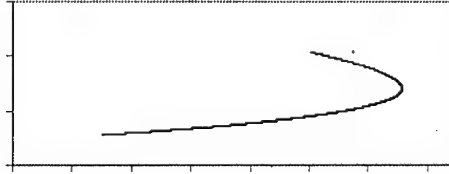


Figure 1. The solution branch computed using the RPM

Implementation of the RPM acceleration procedure results in reducing the number of iterations performed until convergence to the steady state. This happens even in the case of the, very stable, IE scheme. For two parameter values close the turning point at $\lambda = 3.512$, the number of iterations needed to converge to steady state, are shown in Table 1.

λ	iterations	iterations with RPM
3.3	290	16
3.5	888	21

Table 1. Number of iterations of the IE scheme performed with and without RPM

The dimension of the unstable subspace detected by the RPM, in this case, does not exceed $m = 2$. The RPM has the same effect on the less stable FE scheme. For $\lambda = 3.3$ the number of iterations needed for steady state are 2870, whereas with the RPM only 30 are performed overall. In each example, $T = 0.01$.

In the case of continuation on λ , an orthonormal basis, $Z \in \mathbb{R}^{N \times m}$, of the unstable subspace, is computed when the number of fixed point iterations exceeds a preset value, taken here $n_{\max} = 10$. This becomes necessary for $\lambda = 3.2$ and the dimension of the subspace is $m = 2$. Continuation on λ takes place, maintaining the same basis and updating only when it becomes necessary. In the present implementation, the basis is not updated, since no other singularity becomes imminent, and the iterations of the time-stepper at subsequent parameter values are as few as 3 or 4.

Apart from accelerating the convergence of the time-stepper to steady state, the RPM has the attractive feature of enabling the study of the nonlinear character of the system. The small $m \times m$ matrix $H = Z^T F_U Z$ contains approximations of the most dangerous eigenvalues of the time-stepper F and by monitoring that, it is possible to find the critical parameter value. This is illustrated more clearly in Table 2, where the largest eigenvalue of the matrix H is shown at different parameter values. The turning point appears when a real eigenvalue becomes equal to 1.

Parameter, λ	3.2	3.4	3.5	3.51	3.511
largest eigenvalue	0.96588	0.97837	0.99203	0.99781	0.9985

Table 2. The value of the leading eigenvalue for different λ , approximated by the RPM

The leading eigenvectors of the original PDE, are also successfully reconstructed from the eigenvectors of the small Jacobian, H , as shown in Figure 2. The reconstructed eigenvectors are in agreement with the ones computed directly from the full Jacobian of the discretized steady state problem.

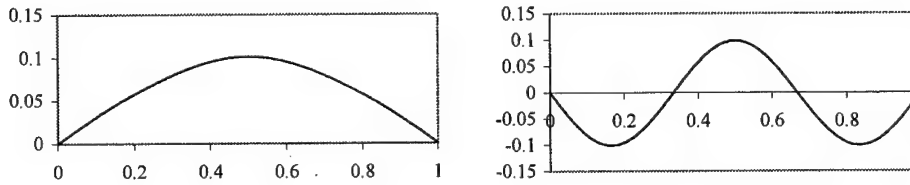


Figure 2. Approximations of the leading eigenvectors of the PDEs reconstructed by the matrix H at $\lambda=3.2$.

The dimension of the slow subspace detected by the RPM is influenced by the reporting horizon, T . The eigenvalues of the “perfect” time stepper, μ_i , for a linear problem or for the linearization of our problem at the steady state, are related to the eigenvalues of the full Jacobian of the steady state problem, λ_i , according to the relation $\mu_i = e^{\lambda_i T}$. Therefore, T should be big enough so that the unstable modes will decay fast. The effect of the time step on the size of the basis, is significant since for $T = 0.0001$ the dimension of the unstable subspace is $m = 9$ and $m = 10$ for the FE and IE schemes respectively, whereas for $T = 0.01$, it is found that the corresponding values are $m = 1$ and $m = 2$.

When the spatial discretization becomes finer, the dimension of the slow/unstable subspace detected by the RPM applied to the FE scheme, increases significantly (making preconditioning necessary [3]). This happens because as the discretization becomes finer, the eigenvalues of the Laplacian become large and negative and the eigenvalues of the FE time stepper start exiting the unit circle through -1, making the slow/unstable subspace “fatter” and eventually destroying convergence. This is not the case for the IE scheme for which the slow/unstable subspace dimension remains the same, namely $m = 2$, for a number of grid sizes. The number of iterations also remains the same as shown in table 3. The computations are performed at parameter value $\lambda = 3.0$ and $T = 0.1$.

Grid points	number of iterations
101	13
201	14
401	13
801	13

Table 3. Number of iterations of the IE scheme with RPM for several spatial discretizations.

6. CONCLUSIONS

Acceleration of the convergence to steady states of (even very stable) time-stepping schemes, has been demonstrated in this work. This is done at little extra cost with the Recursive Projection Method, which has the additional benefit of enabling nonlinear stability/bifurcation calculations circumventing the calculation of the full system. When combined with a stable scheme, like the one-step Implicit-Explicit used here, it becomes a powerful tool for efficient steady state computation even for high dimensional systems, since big (even inaccurate) time steps can be used as long as the dimension of the slow/unstable subspace is small. The true value of detection of steady states through RPM-assisted time-stepping, lies in the fact that it is applicable to “black-box”, commercial time integration codes, even microscopic, i.e. Lattice-Boltzmann, time-steppers [6], the accuracy of which is not usually possible to control.

Acknowledgements: This work is partially supported by the General Secretariat for Research and Technology of Greece through the IIENEΔ program, the Air Force Office of Scientific Research of the USA and the State Scholarships Foundation of Greece. The authors would like to thank Dr K. Lust for the valuable discussions.

7. REFERENCES

- [1] Shroff, G. M. and Keller H. B., Stabilization of unstable procedures: The Recursive Projection Method, *SIAM J. Numer. Anal.*, 31, 1099-1120 (1993).
- [2] Akrivis, G., Crouzeix, M., Makridakis, C., Implicit-Explicit Multistep Finite Element Methods for nonlinear parabolic problems, *Math. Comp.*, 67, 457-477, (1998).
- [3] Davidson, B. D., Large-scale continuation and numerical bifurcation for partial differential equations, *SIAM J. Numer. Anal.*, Vol. 34, No. 5, 2008-2027, (1997).
- [4] Lust, K., *Numerical bifurcation analysis of periodic solutions of partial differential equations*, PhD thesis, K.U. Leuven, 1997.
- [5] Seydel, R., *From equilibrium to chaos*, Elsevier, New York, 1988.
- [6] Theodoropoulos, C., Quian, Y.-H. and Kevrekidis, I. G., “Coarse” stability and bifurcation analysis using time-steppers: A reaction-diffusion example, *Proceedings of the National Academy of Sciences*, Vol. 97, no. 18, 9840-9843 (2000).

RHEOLOGY OF DENSE LIGNITE-WATER SUSPENSIONS; TRANSITION STRESSES ON FLOW CURVES

T. B. Goudoulas, E. G. Kastrinakis, S. G. Nychas
Department of Chemical Engineering
Aristotle University of Thessaloniki, GR-54006 Thessaloniki, Greece

1. SUMMARY

Aspects of dense Lignite-Water Slurry (LWS) rheology were investigated using a controlled stress rheometer, with parallel plate geometry. Measurements of the flow curves were carried out for various ascending times, shear rates and testing times. In the ascending part of the flow curves a transition point was observed, which was characterized by a local maximum stress, σ_{tr} . The variation of the transition point with respect to solids loading, shear stress region and testing time was investigated. For the interpretation of the data, structural aspects of the LWS were considered.

2. INTRODUCTION

The objective in Coal-Water Slurries (CWS) technology is the preparation of a relatively stable dense suspension of coal in aqueous medium having the higher possible solids loading with acceptable rheological behavior. The rheological properties of CWS were investigated in the past, especially in countries having large deposits of coal like USA (Turian et al. [1]) and Australia (Tudor et al. [2]). Numerous investigators were interested in utilising the CWS as alternative fuels. It is common that CWS are characterised by broad particle size distributions and their rheological behavior is non-Newtonian affected by a number of parameters. For example, the relative viscosity, η_r , or the appearance of a yield stress depends on the ratio of the solids volume fraction, ϕ , to the maximum achieved solids volume fraction, ϕ_m , i.e. ϕ/ϕ_m (Botsaris and Astill [3]; Roh et al. [4]; Turian et al. [1]). Shear induced structure in concentrated suspensions of spherical particles has been reported in the past (Watanabe et al. [5]). Leighton and Acrivos [6] found a short-term increase in the viscosity upon initial shearing of the suspension in a Couette device with bob and cup. This behavior was attributed to a shear-induced migration of particles across the width of the gap of the device. In the present investigation, dense LWS were studied with respect to their rheological behaviour at high and low shear stresses, where the slurries exhibit different behavior.

3. EXPERIMENTAL

The starting material was dried lignite powder produced at the Public Power Corporation (P.P.C.), Ptolemais, Briquettes factory. Among the dominant parameters affecting the rheological behavior of the slurries are the physicochemical properties of the particles and the pH of the slurries. Therefore, in the dispersion process, i.e. the adsorption of chemical additives and stability of the slurry, the humidity content and the ratio of carbon to oxygen

(C/O) of the lignite is important (Botsaris and Astill [3]; Roh et al. [4]). The C/O ratio is related to the adsorption of the additives on the surface of the particles. In this work this ratio was approximately 50/21, on a dry basis. Also the higher the humidity content, the lower will be the achieved solids concentration (Turian et al. [1]). The slurryfication process started with the wet grinding of the lignite together with the additives in a ball mill. Surfactants and polyelectrolytes were used as additives in the slurryfication process to achieve acceptable rheological behaviour. Two types of stabilizers were used in the preparation of the slurries, an ionic and a non-ionic polymer. Recent published work report that this type of polyelectrolyte show a high ζ -potential for a wide range of salt concentrations and effectively results in a long-term stabilization of the slurries (Furusawa et al. [7]). The surfactant chosen for this work was a non-ionic alkylphenolpolyethylene oxide, produced by Aldrich®. The total amount of additives in the slurries was less than 1wt% of the solids.

The achieved lignite load in the slurries was approximately up to 47.5 wt% or in volume fraction ϕ equal to 0.44. The concentrations in volume fraction depends on the density of the lignite and on the volume of water, which will be absorbed upon contact with water. The specification of this parameter is not an easy task, since the lignite is a porous material. In the present work the volume fraction ϕ of lignite was determined with an accuracy of $\pm 2\%$. An important parameter, of the present work, is the particle size distribution (p.s.d.) of the lignite particles in the slurries. Slurries were prepared having a unimodal or bimodal p.s.d while the p.s.d. of the lignite slurries was measured by the light scattering method with a Malvern Instruments M.07 system. An example of a bimodal p.s.d. of prepared slurries is given in Figure 1. The rheological tests were performed with a Carri-Med CLS 100 controlled stress rheometer, using parallel plate geometry.

In order to examine the shape of lignite particles, scanning electron microscope photographs (S.E.M.) were taken from slurries of various size distributions. A S.E.M. photo from a sample having a unimodal distribution with a maximum particle size $38 \mu\text{m}$, appears in Figure 2. The shape of the lignite particles in some cases deviates considerably from the spherical shape. Spherical shape and uniform size of particles are critical assumptions in most established rheological models for dense suspensions.

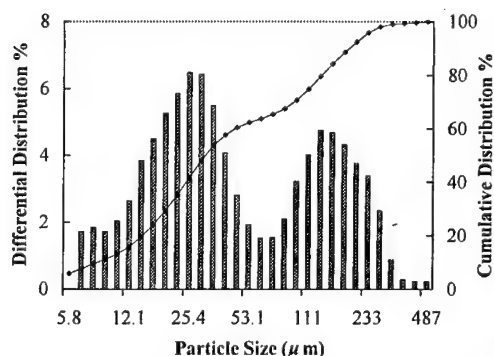


Figure 1. A bimodal p.s.d. of the prepared slurries

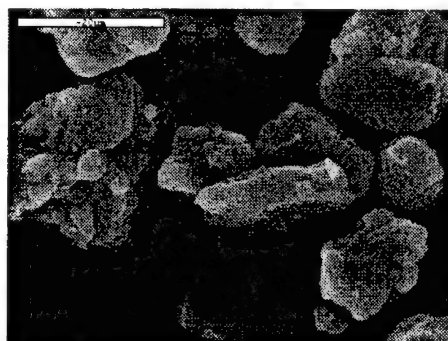


Figure 2. S.E.M. of a unimodal distribution of lignite particles (top size equal to $38 \mu\text{m}$)

4. RESULTS AND DISCUSSION

Systematic viscosity measurements revealed a different behavior of the samples during the ascending and the descending part of applied stresses, in the equilibrium flow curve. The

suspension shows a typical thixotropic loop during the implementation of the first flow run, while in consecutive runs the extent of the loop is reduced and a transition point with a local maximum becomes evident. Figure 3 shows a typical flow curve of a LWS sample corresponding to the first run together with the flow curve of the eighth run. On this latter flow curve an arrow indicates the transition point.

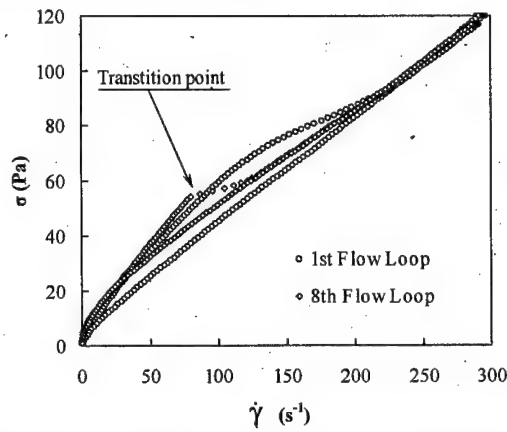


Figure 3. A typical flow curve of a LWS sample

The position of the transition point on the flow curve depends, among others, on the lignite concentration in the slurry. This effect is depicted in Figure 4, where the ascending parts of the flow curves appear for solids concentration of 38 wt% and up to 46.3 wt%. The samples were subjected to the same shear history of consecutive runs, with the same time duration of the loop, equal to 9min. The curves in Figure 4 correspond to the 4th consecutive run, while the ratio R/Gap was 20mm/3mm, where R was the disk radius and Gap was the distance between the rotating disk and the plate. The transition stress appears beyond a certain solids concentration. In the examined slurry the critical solids concentration, where the transition point becomes evident, was approximately 42 wt%.

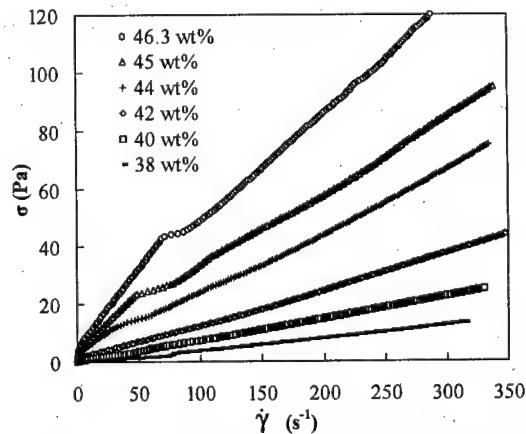


Figure 4. The effect of the solids loading on the transition stress point

In Figure 5 a sample was subjected to six consecutive flow runs; for all these runs the maximum shear stress, σ_{\max} , and the duration of the run (flow loop) were the same. For a better presentation, the region around the transition points appears magnified in Figure 5. It can be seen that the transition stress increases with the number of the runs or the testing time.

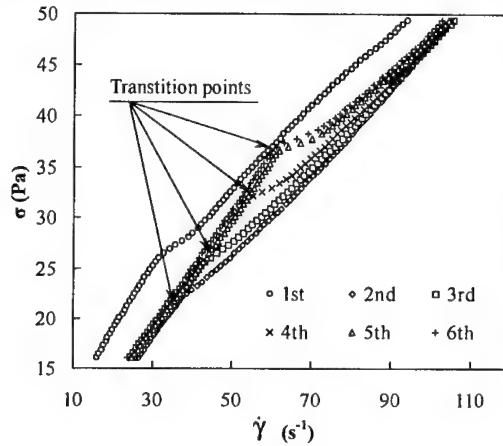


Figure 5. The effect of the consecutive runs or the testing time on the ascending curve

The shear stress range and the duration of the ascending or descending parts of a flow curve influence the position of the transition point. Figure 6 shows ascending parts of the flow curves for three samples of a LWS having the same concentration of 46.3 wt%, corresponding to the sixth run and for three shear stress ranges with $\sigma_{\max} = 40, 80$ and 120 Pa. The ascending part duration of all flow curves, t_a , was 2 min while the duration of the hold point ($\sigma_{\max} = \text{const.}$) equal to 1 min. It can be observed that the shear stress at the transition point increases with the increase of the applied σ_{\max} . In Figure 6, beyond the transition points, the three ascending parts of the curves are almost identical.

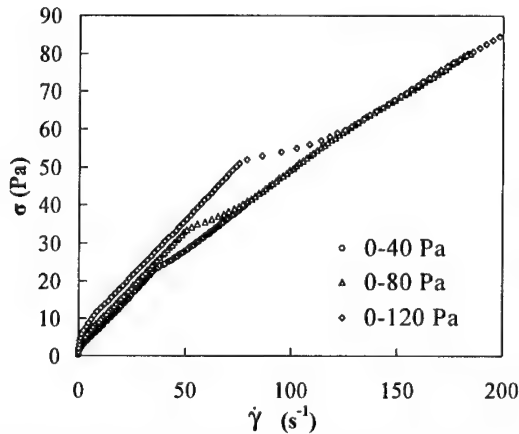


Figure 6. Ascending curves for three shear stress ranges for the same ascending time and solids concentration

It was discussed above that σ_{tr} depends strongly upon ϕ and total time of shearing, shear stress range and weakly on the flow loop time (Figures 3 and 4). Another parameter of

dynamic nature, which influences the σ_{tr} is the applied shear stress rate, E , in the ascending part of the flow curve. Considering for example the stress range between zero and 80 Pa with the t_a equal to 4 min, the corresponding applied shear stress rate E is calculated as: $E = 80 \text{ Pa}/4 \text{ min} = 20 \text{ Pa/min}$. Hence, the parameters t_a and σ_{max} are correlated in one parameter, E . Figure 7 shows the σ_{tr} -data as a function of the time at which the transition occurs, for various rates E . It can be observed that data corresponding to the same E are found on the same curve even for different σ_{max} . As E increases the corresponding transition time decreases.

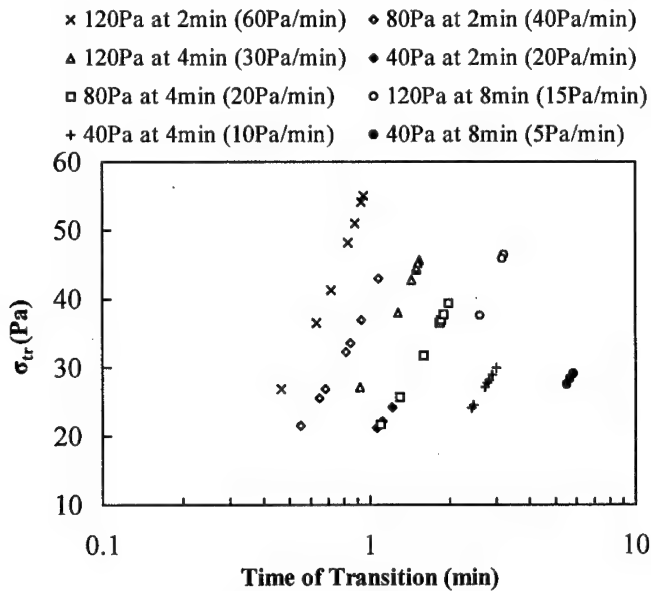


Figure 7. The σ_{tr} -data as a function of the time at which the transition occurs

In the following an effort is made to interpret the rheological behavior of dense LWS presented above. The first flow loop mainly serves to brake up the initial structure of the suspension and to distribute the suspending particles. During the second loop the condition of the sample is favourable for the initiation of a different shear induced structure. This explanation is based on the fact that the transition stress is evident from the second flow loop (Figure 3). From the data presented above, two shear regions with different behavior were observed. The high shear region, is the one where the controlling parameters are ϕ and $\dot{\gamma}$. These two parameters are related to the hydrodynamic forces on the particles, i.e. viscous drag force and particle-liquid interaction. These forces cause orientation in the flow field of the irregular shape particles. As one proceeds towards the other region of low shear rates, additional forces become evident. These forces are attractive van der Waals and/or friction forces due to interactions between the particles. In the high shear region, a state of dispersed particles in the suspending medium results. By decreasing the shear rates $\dot{\gamma}$ the controlling forces of the low shear region contribute to develop a different structure with local clusters of particle concentrations. As Jomha et al. [8] state, a shear rate gradient may also develop a gradient of osmotic pressure, which can cause particle migration away from regions of high shear. As $\dot{\gamma}$ decreases toward zero, the particle clusters increase in size with a consequent increase of the viscosity, i.e. higher slope of the flow curve before the transition point (Figure 3). The irregular shape and the polydisperse size distribution of the particles contribute also to the structure formation in dense suspensions as Jogun and Zukoski [9] reported.

In Figure 3 the higher slope of the curve before the transition point suggests that the structure is present in the beginning of the flow. The gradual increase of the shear stresses must exceed a value at which the formed compact structure brakes up, resulting in a decrease of the measured viscosity (lower slope of the curve). This value is the transition stress, σ_{lr} . After that, the hydrodynamic forces predominate and the structure of the suspension attains the dispersed state described above.

5. CONCLUSIONS

The rheological behavior of dense Lignite-Water Slurries was studied using a controlled stress rheometer. The study included the measurement of the flow curves for various testing times and various shear stress ranges. Moreover, the position of the transition point, which was identified in the ascending part of the flow curves, was further studied. It was found that the shear stress at which the transition occurs, depends upon solids concentration and shear stress range. It was also found that the shear stress rate under which the slurry is tested is an important parameter of its rheological behavior. In an attempt to interpret the rheological data, structural aspects of the LWS were considered.

Acknowledgements: The authors wish to thank the State Scholarships Foundation of Greece (I.K.Y.) for the support to T.B.G. The authors would like to thank the FORTH-CPERI for the technical support of the electron microscopy and particles size distributions. Also the P.P.C. of Greece for providing us with the lignite samples.

6. REFERENCES

- [1] Turian R.M., Fakhreddine M.K., Avramidis K.S. and Sung D.-J., Yield stress of coal-water mixtures, *Fuel* 72, 1313-1318 (1993).
- [2] Tudor P.R., Atkinson D., Crawford R.J. and Mainwaring D.E., The effect of adsorbed and non-adsorbed additives on the stability of coal-water suspensions, *Fuel* 75, 443-452 (1996).
- [3] Botsaris G.D. and Astill K.N., Effect of the interaction between particles on the viscosity of coal water slurries. *Proceedings 6th Intern. Symp. on Coal Slurry Combustion and Technology*, Orlando, June 25-27, 304-309 (1984).
- [4] Roh N.-S., Shin D.-H., Kim D.-C. and Kim J.-D., Rheological behavior of coal-water mixtures. 1 Effects of coal type, loading and particles size, *Fuel* 74, 1220-1225 (1995).
- [5] Watanabe H., Yao M.-L., Osaki K., Shikata T, Niwa H., Morishima Y., Balsara N.P. and Wang H., Nonlinear rheology and flow induced structure in a concentrated spherical silica suspensions, *Rheologica Acta* 37, 1-6 (1998).
- [6] Leighton D. and Acrivos A., The shear-induced migration of particles in concentrated suspensions. *J. Fluid Mechanics* 181, 415-439 (1987).
- [7] Furusawa K., Ueda M., Chen M. and Tabori N., A new concept for coal water mixture stabilization using a polyelectrolyte, *Colloid & Polymer Science* 273, 490-495 (1995).
- [8] Jomha A.I., Merrington A., Woodcock L.V., Barnes H.A. and Lips A., Recent developments in dense suspension rheology, *Powder Technology* 65, 343-370 (1991).
- [9] Jogun S. and Zukoski C.F., Rheology and microstructure of dense suspensions of plate-shape colloidal particles, *J. Rheology* 43, 847-871 (1999).

COMPUTER SIMULATION OF THE NONLINEAR EVOLUTION OF INCLINED FILM FLOWS

N.A.Malamataris, M.Vlachogiannis and V.Bontozoglou
Department of Mechanical and Industrial Engineering
University of Thessaly, GR-38334 Volos, Greece

1. SUMMARY

The linear and nonlinear evolution of disturbances, introduced at the inlet of a liquid film flowing along an inclined plane wall, is studied numerically with the Galerkin finite element method. The numerical results are in satisfactory agreement with available predictions of linear stability analysis and with experimental data of the entire evolution process. In addition, the computations provide detailed information on the structure of the free surface flow.

2. INTRODUCTION

Wave evolution on an inclined or vertical falling film is an open-flow hydrodynamic instability, which has attracted the attention of many investigators. It has long been established that interfacial waves on film flows enhance heat and mass transfer rates in process equipment such as condensers, falling film evaporators, absorption columns and two-phase flow reactors. On the contrary, the formation of waves on the surface of coating films results in degradation of their properties and is highly undesirable.

Much of the information available for the problem is based on experiments. A technique introduced in the pioneering work of Kapitza & Kapitza (1949) and subsequently adopted by many investigators (Alekseenko et al. 1985; Liu & Gollub (1994) is to facilitate observations of wave development by applying a constant-frequency disturbance at the inlet. In this way regular waves are produced, whose form depends to a large extent on the frequency of the forcing. These studies have demonstrated that saturated periodic waves result from high-frequency disturbances, whereas low-frequency disturbances evolve directly into solitary waves.

On the contrary, direct numerical simulations of film flow by solution of the full Navier-Stokes equations are not very numerous. The pioneering work of Bach & Villadsen (1984) was followed by few efforts (Kheshgi & Scriven 1987; Ho & Patera 1990; Salamon et al. 1994), mostly restricted to low Reynolds numbers ($Re < 10$). More recently, Ramaswamy et al. (1996) presented computations of film flow by a Galerkin finite-element method. In the present work we follow a similar approach, using the Galerkin finite element method and employing at outflow the free boundary condition developed by Malamataris & Papanastasiou (1991) and also used by Malamataris & Bontozoglou (1999). We present results as a function of forcing frequency at the inlet, both for the initial linear growth of very small disturbances and for the subsequent nonlinear evolution of larger disturbances. Direct comparison of computations with data confirms satisfactory agreement.

3. PROBLEM FORMULATION AND SOLUTION

Gravity-driven flow down a plane with inclination ϕ relative to the horizontal is considered. The mean volumetric flow rate per unit span is denoted by Q and the Re number is defined as $Re=Q/\nu$ where ν is the kinematic viscosity, $\nu=\mu/\rho$. The location of the free surface generally varies in space and time and is described by the function $y=h(x,t)$, where x is the streamwise coordinate and y is the normal coordinate starting from the wall. Similarly, the local volumetric flow rate is denoted by $q(x,t)$.

The classical Nusselt solution for uniform flow with thickness $H = (3\nu^2 Re / g \sin \phi)^{1/3}$ - where g is the magnitude of gravity- and parabolic x -velocity profile is given by

$$u(x, y, t) = \frac{g \sin \phi H^2}{\nu} \left(\frac{y}{H} - \frac{1}{2} \frac{y^2}{H^2} \right) \quad (1)$$

A complete description of the flow is provided by the continuity and the Navier-Stokes equation. The boundary conditions are no-slip and no-penetration along the wall and a balance of forces and the kinematic condition along the free surface. We use the free boundary condition at the outflow (Malamataris & Papanastasiou, 1991) and introduce constant-frequency disturbances at the inlet by imposing the conditions

$$h(0, t) = 1 + A \cos 2\pi f t \quad (2)$$

$$u(0, y, t) = \frac{3q(0, t)}{h(0, t)} \left(\frac{y}{h(0, t)} - \frac{1}{2} \frac{y^2}{h(0, t)^2} \right) \quad (3)$$

Numerical solution by finite-elements involves expansion of the unknown u and v velocities, pressure, p , and free surface location, h , in terms of Galerkin basis functions as follows:

$$u = \sum_{i=1}^9 u_i \phi_i, \quad v = \sum_{i=1}^9 v_i \phi_i, \quad h = \sum_{i=1}^3 h_i \phi_i, \quad p = \sum_{i=1}^4 p_i \psi_i \quad (4)$$

The residuals are evaluated numerically using nine-point Gaussian integration. A system of non-linear algebraic equations results, which is solved with the Newton-Raphson iterative method. Finally, time integration is performed with the Crank-Nicolson scheme.

4. RESULTS AND DISCUSSION

The results of this work are presented in the following way: First, the initial linear evolution of very small disturbances is studied numerically and compared with the results of linear stability analysis and with relevant data. Next, the nonlinear evolution of larger disturbances as a function of forcing frequency is systematically investigated. Finally, detailed information on the flow structure is extracted from the simulations.

Computational linear stability analysis

The temporal linear stability theory of film flow has developed over many years, by both asymptotic (Benjamin (1957); Yih (1963)) and computational methods (Anshus & Goren (1966); Orszag (1971)). However, it is now well established that the primary film instability is convective and is thus better represented by a spatial analysis. Recent relevant publications include the detailed spatial growth-rate data taken by Liu et al. (1993) and the extensive numerical results of Brevdo et al. (1999).

In this work, we impose an infinitesimal disturbance of specific frequency at the entrance (initial amplitude equal to 0.2% of the Nusselt film thickness) and follow its spatio-temporal

evolution. In accordance with the convective nature of the instability, the disturbance is expected to remain periodic in time and grow or decay exponentially with fetch. We have chosen a film with $Re=15.33$ and $We=12.13$ at an inclination $\phi=4.6^\circ$. These conditions correspond to the data taken by Liu et al. (1993), who used a 50% glycerol-water solution

Our results indicate the development of a specific wavenumber, with the wave amplitude depending exponentially on fetch in the inception region. A comparison of our computations with the data of Liu et al. (1993) and the numerical predictions of Brevdo et al. (1999) is shown in figures 1a and 1b. Figure 1a depicts the phase speed of the developing linear mode. All three curves show the same trend, with a minimum phase speed around dimensionless wavenumber $k=0.12$. Our computed values are in close agreement with the numerical predictions of Brevdo et al. (1999) and exhibit a small systematic deviation from the data of Liu et al. (1993).

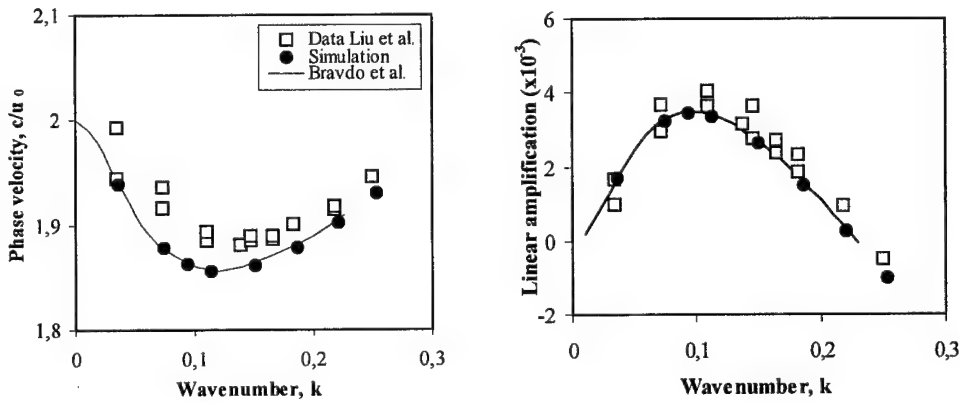


Figure 1: The phase velocity (a) and growth rate (b) of linear disturbances.

The linear growth rate is shown in figure 1b. All three sets of data show the same trend, with maximum amplification around $k=0.12$ or a frequency of 3 Hz and cut-off frequency a little higher than 6 Hz. Again, the maximum growth rate presently computed is in close agreement with the numerical predictions of Brevdo et al. (1999) and differs somewhat from the measurements. The reason for this small discrepancy is not presently clear. It is noted, however, that the height differences measured by Liu et al. (1993, their fig. 13) for the determination of the growth rate are in the limit of accuracy of their experimental technique, and the confidence intervals of the data include our computational values.

Nonlinear evolution as a function of forcing frequency

Having confirmed the satisfactory accuracy of the simulation in the linear limit, we proceed to compute the spatio-temporal evolution of stronger inlet disturbances. It has been noted both in experimental (Liu et al. 1993) and in computational studies (Bach & Villadsen 1984) - and is also confirmed by our results - that the qualitative features of downstream evolution are independent of the exact form of the inlet disturbance, and an increase of the disturbance amplitude has as a sole effect an acceleration of the evolution with fetch.

In all subsequent computations we have used a constant inlet disturbance with amplitude equal to 2% of the Nusselt film thickness. This value - which is an order of magnitude higher than that used in the linear stability analysis - helps to keep the flow domain down to a reasonable size for the available computational power. In the comparisons with experiments, we have not made a systematic effort to fine tune the initial disturbance amplitude so as to bring the computed and measured evolution with fetch to exact agreement, because this is an extremely time consuming procedure. However, we have performed representative tests, which have shown that this manipulation is straightforward.

Next, we fix all flow variables and vary the frequency of the inlet disturbance in the range 1-7 Hz. Our goal is to reproduce quantitatively experimental observations on the dependence of the final stationary waveforms on the forcing frequency, and also to capture the entire spatial development leading from linear disturbances to the nonlinear stationary solutions. In particular, we set the simulation results in perspective with the detailed measurements of Liu & Gollub (1994). The simulations performed refer to a film with $Re=19.33$ and $We=5.43$ at an inclination $\phi=6.4^\circ$ and inlet disturbances with frequency 1. Hz, 1.5 Hz, 3. Hz, 4.5 Hz and 7. Hz. Due to space limitations, only the runs corresponding to disturbance frequencies $f=4.5$ Hz and 1.5 Hz are presented.

Computational results for the frequency, $f=4.5$ Hz, are shown in Figure 2. An exponential disturbance growth is initially observed, which is gradually arrested by nonlinear effects. However, the free surface does not equilibrate to a constant waveform but develops a distinct overtone (superharmonic). The secondary peak first appears as an instability at the middle of the tail of the periodic wave, but moves faster than the primary crest and is eventually placed in front of it. The evolution appears as a preliminary effort towards creation of solitary humps with front-running ripples, which is mitigated by the proximity of the preceding and the following crests. This phenomenon corresponds to the quasi-periodic wave regime reported by Ramaswamy et al. (1996).

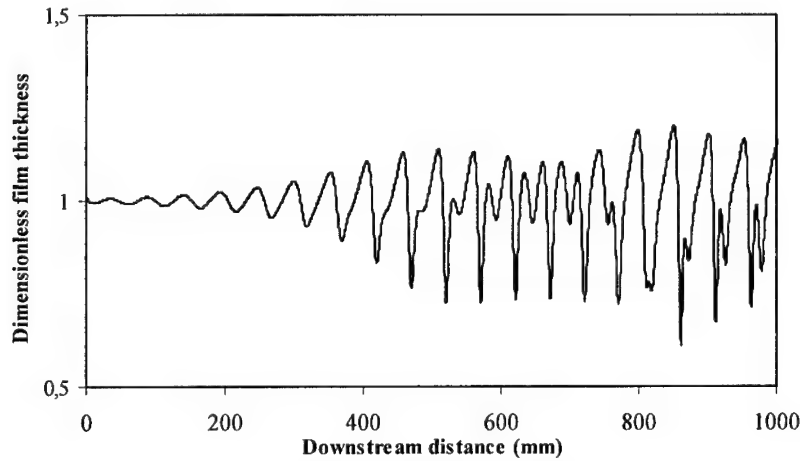


Figure 2: Spatial development of the a disturbance with frequency $f=4.5$ Hz.

Next, we present simulation results for the lowest frequency reported by Liu & Gollub (1994), $f=1.5$ Hz. Shown in Figure 3a is a snapshot of the free surface which exhibits the formation downstream of a series of stationary solitary waves. The evolution leading to a solitary hump is more clearly demonstrated in Figure 3b, where five consecutive profiles at equidistant time intervals are superimposed. A gradual bending-forward of the crest is observed, which triggers the development of front-running ripples. The number of ripples increases with the height of the crest. In general, the numerical procedure reproduces satisfactorily the experimentally observed evolution.

5. CONCLUSIONS

The nonlinear evolution of disturbances, introduced at the inlet of a liquid film flowing along an inclined plane, is studied numerically with the Galerkin finite-element method. Implementation of the free boundary condition at outflow allowed us to formulate the

simulation as an initial value problem with streamwise evolution, which is directly relevant to experimental observations.

Introducing very small inlet perturbations, we are able to simulate an extensive linear growth region and confirm the agreement of computed phase speeds and growth rates with predictions of stability analysis and with experimental observations. Introducing stronger perturbations, the entire nonlinear evolution with fetch is computationally recovered, and is found to agree with the detailed measurements of Liu & Gollub (1994). In particular, low-frequency disturbances lead to solitary waves and high-frequency disturbances to saturated periodic waves. The degenerate structure of the intermediate frequency range is also accurately captured.

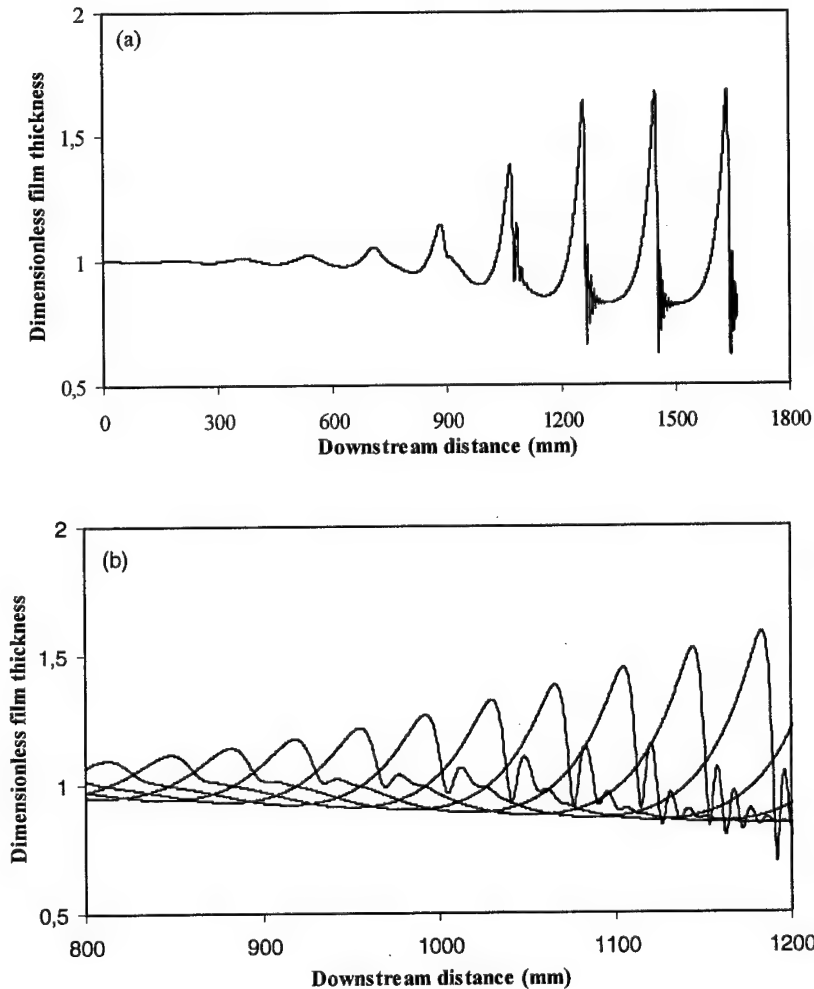


Figure 2: (a) Spatial development of the a disturbance with frequency $f=1.5$ Hz. (b) The free surface at five consecutive time steps, indicating the gradual formation of a solitary hump.

6. REFERENCES

- [1] ALEKSEENKO, S. V., NAKORYAKOV, V. Y. & POKUSAIEV, B. G. 1985 Wave formation on a vertical falling liquid film. *AIChE J.* **31**, 1446-1460.
- [2] ANSHUS, B. E. & GOREN, S. L. 1966 A method of getting approximate solutions to the Orr-Sommerfeld equation for flow on a vertical wall. *AIChE J.* **12**, 1004-1008.
- [3] BACH, P. & VILLADSEN, J. 1984 Simulation of the vertical flow of a thin wavy film using a finite element method. *Intl. J. Heat Mass Transfer* **27**, 815-827.
- [4] BENJAMIN, T. B. 1957 Wave formation in laminar flow down an inclined plane. *J. Fluid Mech.* **2**, 554-574.
- [5] BREVDO, L., LAURE, P., DIAS, F. & BRIDGES T. J. 1999 Linear pulse structure and signaling in a film flow on an inclined plane. *J. Fluid Mech.* **396**, 37-71.
- [6] HO, L.-W. & PATERA, A. T. 1990 A Legendre spectral element method for simulation of unsteady incompressible viscous free-surface flows. *Comp. Meth. Appl. Mech. Eng.* **80**, 355-366.
- [7] KAPITZA, P. L., KAPITZA, S. P. 1949 Wave flow of thin fluid layers of liquid. *Zh. Eksp. Teor. Fiz.* **19**, 105-20; also in *Collected Works of L. P. Kapitza*, ed. D. Ter Haar. Oxford: Pergamon (1965).
- [8] KHESHGI, H. S. & SCRIVEN, L. E. 1987 Disturbed film flow on a vertical plate. *Phys. Fluids* **30**, 990-997.
- [9] LIU, J., PAUL & J. D., GOLLUB, J. P. 1993 Measurements of the primary instabilities of film flow. *J. Fluid Mech.* **250**, 69-101.
- [10] LIU, J. & GOLLUB, J. P. 1994 Solitary wave dynamics of film flows. *Phys. Fluids* **6**, 1702-1712.
- [11] MALAMATARIS, N. A. & BONTZOZOGLOU, V. 1999 Computer Aided Analysis of Viscous Film Flow along an Inclined Wavy Wall. *J. Comput. Phys.* **154**, 372-392.
- [12] MALAMATARIS, N. T. & PAPANASTASIOU, T. C. 1991 Unsteady free surface flows on truncated domains. *Ind. Engng. Chem. Res.* **30**, 2210-2219.
- [13] ORSZAG, S. A. 1971 Accurate solution of the Orr-Sommerfeld stability equation. *J. Fluid Mech.* **50**, 689-703.
- [14] RAMASWAMY, B., CHIPPADE, S. & JOO, S. W. 1996 A full-scale numerical study of interfacial instabilities in thin-film flows. *J. Fluid Mech.* **325**, 163-194.
- [15] SALAMON, T. R., ARMSTRONG, R. C. & BROWN, R. A. 1994 Traveling waves on inclined films: Numerical analysis by the finite-element method. *Phys. Fluids* **6**, 2202-2220.
- [16] YIH, C.-S. 1963 Stability of a liquid film down an inclined plane. *Phys. Fluids* **6**, 321-330.

AN IMPROVED COASTAL CIRCULATION MODEL BASED ON THE CHARACTERISTIC-GALERKIN TECHNIQUE

H. Mpimpas and P. Anagnostopoulos

Department of Civil Engineering

Aristotle University of Thessaloniki, GR-54006 Thessaloniki, Greece

1. SUMMARY

A numerical solution for shallow water flow based on the depth averaged Navier-Stokes equations for the prediction of coastal circulation in a coastal area is presented. The finite element method is advantageous for the solution of the shallow water equations in many cases, because of its versatility to model complicated geometries like coastlines, islands and strongly varying bathymetry. To reduce the numerical problems associated with the solution of these equations, such as the appearance of spurious $2\Delta x$ waves on the water surface, the characteristic-Galerkin technique was employed. The Smagorinsky equation was applied for the modeling of turbulence, whereas a constant eddy viscosity coefficient throughout the domain was also tested. The comparison of the new algorithm with the standard Galerkin method shows that the characteristic-Galerkin model improves considerably the circulation pattern and reduces drastically the $2\Delta x$ waves.

2. INTRODUCTION

The shallow water equations in depth-averaged form have been successfully applied to many engineering problems, particularly in areas such as estuarine and coastal hydrodynamics. These equations are often coupled with advection-diffusion models of biochemical processes. The finite element method [1] is ideally suited for the simulation of water circulation in lakes, estuaries and gulfs, characterized by complicated geometries and bathymetries. However, various difficulties associated with the numerical solution of the shallow water equations must be resolved. A serious problem in the numerical treatment is the appearance of spurious $2\Delta x$ waves [2] in the water surface elevation for realistic small values of turbulent viscosity coefficients, introducing instability to the values of water velocities.

An efficient technique to reduce this instability is to use the characteristic-Galerkin procedure, which minimizes considerably the $2\Delta x$ waves. This algorithm has been used successfully to treat numerically the advection-diffusion equation for pollutant transport in one and two dimensions ([3], [4]). The numerical simulations were conducted for two different conditions of turbulence modeling. In the first case the Smagorinsky equation was applied, while in the second a constant eddy viscosity coefficient throughout the domain was used. As an application, the wind-induced coastal circulation is solved numerically in a domain of simple geometry. Simulations were conducted for both the simple and the

characteristic-Galerkin technique, with the Smagorinsky model and the constant eddy viscosity in each case.

3. MATHEMATICAL FORMULATION

The shallow water equations in their depth-averaged form, can be written as:

$$\begin{aligned} \frac{\partial u}{\partial t} + \frac{u}{\partial x} \frac{\partial u}{\partial x} + \frac{v}{\partial y} \frac{\partial u}{\partial y} - f v = -g \frac{\partial n}{\partial x} + \frac{\tau_{sx}}{\rho H} - \frac{\tau_{bx}}{\rho H} + 2 v_T \frac{\partial^2 u}{\partial x^2} + \\ v_T \frac{\partial}{\partial y} \left(\frac{\partial u}{\partial y} + \frac{\partial v}{\partial x} \right) \end{aligned} \quad (1)$$

$$\begin{aligned} \frac{\partial v}{\partial t} + \frac{u}{\partial x} \frac{\partial v}{\partial x} + \frac{v}{\partial y} \frac{\partial v}{\partial y} + f u = -g \frac{\partial n}{\partial y} + \frac{\tau_{sy}}{\rho H} - \frac{\tau_{by}}{\rho H} + 2 v_T \frac{\partial^2 v}{\partial y^2} + \\ v_T \frac{\partial}{\partial x} \left(\frac{\partial u}{\partial y} + \frac{\partial v}{\partial x} \right) \end{aligned} \quad (2)$$

$$\frac{\partial n}{\partial t} + \frac{\partial(uH)}{\partial x} + \frac{\partial(vH)}{\partial y} = 0 \quad (3)$$

where u and v are the velocity components in the x and y direction, h is the mean sea level from the bottom, n is the time depended water elevation, H is the quantity $h+n$, f is the Coriolis parameter and v_T is the eddy viscosity defined by the Smagorinsky model as [5]:

$$v_T = (C_s \Delta)^2 |\bar{S}| \quad (4)$$

in which Δ is the filter width (proportional to the grid size), C_s is the Smagorinsky constant ($C_s=0.1$), and $|\bar{S}| = (2\bar{S}_{ij} \bar{S}_{ij})^{1/2}$ is the magnitude of the large scale tensor:

$$\bar{S}_{ij} = \frac{1}{2} \left(\frac{\partial u_i}{\partial x_j} + \frac{\partial u_j}{\partial x_i} \right) \quad (5)$$

for $i, j=1, 2$.

The shear forces on the water surface are expressed in terms of the components of the wind velocity W_x and W_y as:

$$\tau_{sx} = \kappa \cdot \rho \cdot W_x \cdot \sqrt{W_x^2 + W_y^2} \quad \tau_{sy} = \kappa \cdot \rho \cdot W_y \cdot \sqrt{W_x^2 + W_y^2} \quad (6)$$

The bottom friction term is given by the well-known Chezy formula:

$$\tau_{bx} = \frac{\rho \cdot g \cdot u \cdot \sqrt{u^2 + v^2}}{C^2} \quad \tau_{by} = \frac{\rho \cdot g \cdot v \cdot \sqrt{u^2 + v^2}}{C^2} \quad (7)$$

where ρ is the water density, κ is an empirical coefficient ($10^{-6} \sim 3 \cdot 10^{-6}$) and C is the Chezy coefficient.

4. THE NUMERICAL PROCEDURE

Equations (1) and (2) can be written, using the summation convention in a compact form as:

$$\frac{\partial u_i}{\partial t} + \frac{\partial F_{ij}}{\partial x_j} + g \frac{\partial n}{\partial x_i} + \frac{\partial G_{ij}}{\partial x_j} + Q_i = 0 \quad (8)$$

where $F_{ij} = u_i u_j$, G_{ij} represents the eddy viscosity terms and Q_i contains the water surface and bottom friction terms. The application of the characteristic-Galerkin procedure to equation (8) along the characteristic paths, in explicit form, yields [6]:

$$\begin{aligned} \frac{\Delta u_i}{\Delta t} + \frac{\partial F_{ij}}{\partial x_j} + g \frac{\partial n}{\partial x_i} + \frac{\partial G_{ij}}{\partial x_j} + Q_i + \frac{\Delta t}{2} u_k \frac{\partial}{\partial x_k} \left(\frac{\partial F_{ij}}{\partial x_j} + Q_i \right) + \\ \frac{g \Delta t}{2} u_k \frac{\partial}{\partial x_k} \left(\frac{\partial n}{\partial x_i} \right) = 0 \end{aligned} \quad (9)$$

for $i, j, k=1, 2$.

Then the standard Galerkin procedure is applied for the spatial discretization of equations (3) and (9). The split-time integration scheme [2] was used for the solution of the resulting algebraic equations.

5. APPLICATION AND RESULTS

The water velocity field was obtained by solving the depth averaged shallow-water equations in a rectangular shallow enclosure (1300 m length, 1400 m width, 5 m depth), using the finite element technique for north wind of velocity 5 m/s. The starting conditions were zero velocities and water elevations through the computational domain.

The circulation pattern, using the Smagorinsky turbulence model, for the standard Galerkin method is depicted in Fig. 1(a), while for the characteristic-Galerkin method in Fig. 1(b). Figure 2(a) shows the circulation pattern obtained from the standard Galerkin method using a constant eddy viscosity coefficient ($\nu_T=1 \text{ m}^2/\text{s}$), while Fig. 2(b) shows the circulation pattern for the characteristic-Galerkin technique.

In Figures 3(a) and 3(b) the water surface elevations are depicted, using the Smagorinsky turbulence model, for both the standard Galerkin and the characteristic-Galerkin procedure respectively. The water surface elevations, using a constant eddy viscosity coefficient ($\nu_T=1 \text{ m}^2/\text{s}$), for both techniques (standard Galerkin and characteristic-Galerkin), are depicted in Figures 4(a) and 4(b).

It is obvious that the use of the characteristic-Galerkin model improves drastically the results, which, in the case of the standard Galerkin procedure are unacceptable. A serious reduction of the $2\Delta x$ waves occurs, whereas the circulation distribution improves considerably, even for the low value of turbulent viscosity coefficient used herein. The water velocities obtained from the constant eddy viscosity simulation are higher than those obtained from the Smagorinsky model for turbulence. Comparison of Figures 3(b) and 4(b) shows that the

solution based on the Smagorinsky model yields low amplitude $2\Delta x$ irregularities, which are not present in the case of constant eddy viscosity. This is because the eddy viscosity coefficient in Smagorinsky method is variable, and lower than the constant value ($1 \text{ m}^2/\text{s}$) in some cases.

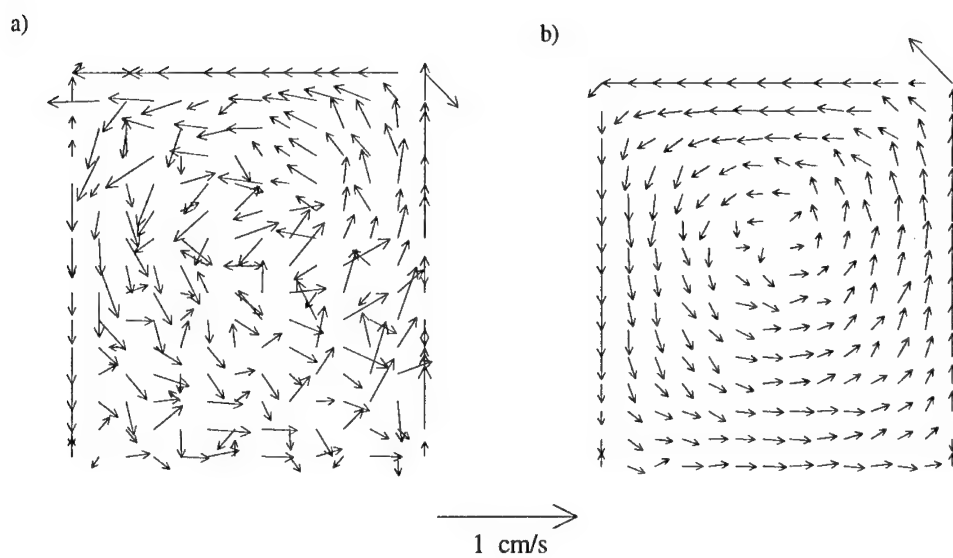


Figure 1: Circulation patterns, using the Smagorinsky turbulence model, for:
a) standard Galerkin method, b) for characteristic-Galerkin method.

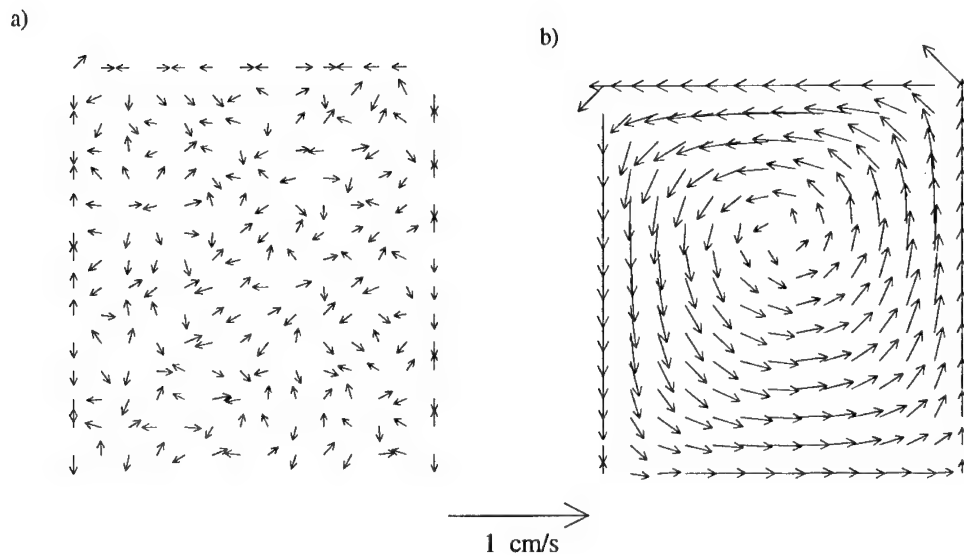


Figure 2: Circulation patterns, using a constant eddy viscosity coefficient ($\nu_T=1 \text{ m}^2/\text{s}$), for:
a) standard Galerkin method, b) for characteristic-Galerkin method.

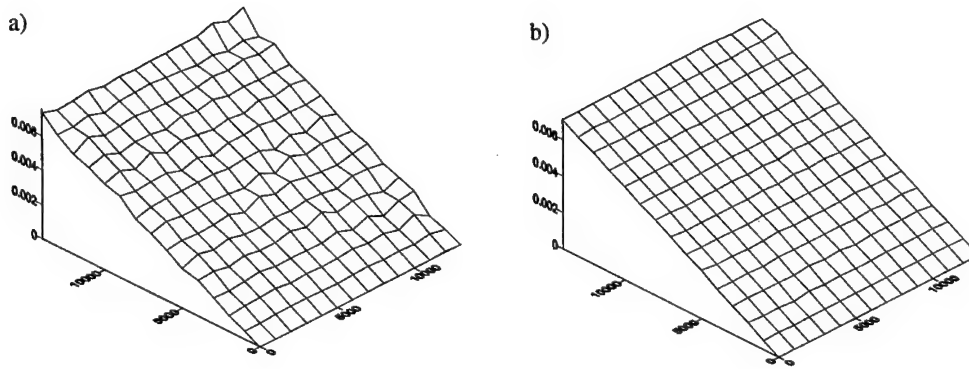


Figure 3: Water surface elevation, using the Smagorinsky turbulence model, for:
a) standard Galerkin method, b) characteristic-Galerkin method.

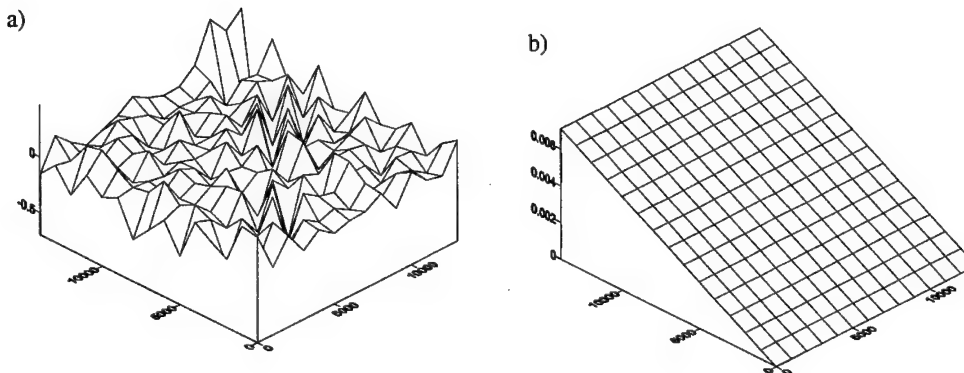


Figure 4: Water surface elevation, using a constant eddy viscosity coefficient ($\nu_T=1 \text{ m}^2/\text{s}$), for:
a) standard Galerkin method, b) characteristic-Galerkin method.

6. CONCLUSIONS

A finite element model was applied to the shallow water equations for the study of wind-induced coastal circulation in a simple rectangular domain. To overcome various problems arising from a numerical solution, such as the appearance of $2\Delta x$ waves, the characteristic-Galerkin formulation was employed, and the results were compared with those of the standard Galerkin technique. In both formulations the Smagorinsky model was used for the improvement of turbulence modeling, in addition to the constant eddy viscosity approximation. The results show that the characteristic-Galerkin method almost obliterates the $2\Delta x$ waves and improves drastically the circulation distribution in the flow domain. The use of Smagorinsky model for turbulence seems to yield more realistic results, compared to those obtained assuming a constant eddy viscosity coefficient.

7. REFERENCES

- [1] Zienkiewicz, O. C. and Taylor, R. L., *The Finite Element Method*, Fourth ed., McGraw-Hill, London (1991).
- [2] Anagnostopoulos, P. and Mpimpas, H., Numerical solution of wind-induced circulation- Effect of time integration scheme, in *Proc. of 4th Greek National Congress on Mechanics Vol. 2*, P.S. Theocaris and E.E. Gdoutos (Eds), Xanthi, Greece (1995) 897-905.
- [3] Mpimpas, H., Anagnostopoulos, P. and Ganoulis, J., Comparison of three numerical schemes for the solution of the advection-dispersion equation, in *Proc. of 5th National Congress of Mechanics Vol. 2*, P.S. Theocaris, D.I. Fotiadis and C.V. Massalas (Eds), Ioannina, Greece (1998) 990-997.
- [4] Mpimpas, H., Anagnostopoulos, P. and Ganoulis, J., Modelling of water pollution in the Thermaikos gulf with fuzzy parameters, *Ecological Modelling*, in press.
- [5] Smagorinsky, J., General circulation experiments with the primitive equations, I. The basic experiment, *Mon. Weather Rev.* 91, 99-165 (1963).
- [6] Zienkiewicz, O. C. and Wu, J., A general explicit or semi-explicit algorithm for compressible and incompressible flows, *Int. J. for Numerical Methods in Engineering* 35, 457-479 (1992).

ON THE EFFECT OF THE RELATIVE VISCOSITY OF TWO FLUIDS ON THE DYNAMICS OF AXISYMMETRIC CORE-ANNULAR FLOW IN A TUBE

Charalampos Kouris and John Tsamopoulos

Laboratory of Computational Fluid Dynamics

Department of Chemical Engineering, University of Patras, Patras 26500, GREECE.

e-mail: tsamo@chemeng.upatras.gr, FAX: +(3061) 993-255

1. SUMMARY

Nonlinear dynamics of the concentric, two-phase flow of two immiscible fluids in a circular tube is studied. A pseudo-spectral numerical method is coupled with an implicit second order time-integration scheme to solve the complete mass and momentum conservation equations as an initial value problem. The simulations originate with the analytical solution for the pressure driven, steady, Core-Annular Flow (CAF) in a tube. The volume fraction of each fluid in the tube and the total flow rate of both fluids are imposed. Furthermore, the length of the tube is taken to be as long as computationally possible in order to allow for multiple waves of different lengths to develop and interact as reported in experiments [1] and in earlier weakly nonlinear analyses [2], [3]. Distinct results are obtained in the following two cases:

1) When the viscosity ratio of the fluid in the annulus to that in the core of the tube is smaller than 1, $\mu < 1$, gravity acts against the applied pressure gradient and other parameter values are such that the experimentally obtained flow charts indicate that both phases retain their integrity, but the original steady flow is unstable. Then it was found that indeed traveling waves develop with slightly sharper crests (pointing towards the annular fluid) than troughs, the so-called "bamboo waves". Despite the uneven interface, the flow in the core fluid closely resembles Poiseuille flow, but in the annular fluid small recirculation zones develop at the level of each crest. As the Reynolds number or the flow rate of the core fluid increase, the average wavelength and the amplitude of these waves decrease, whereas the holdup ratio of the core to the annular fluid approaches 2. For large values of interfacial tension, waves with even different wavelength move with the same velocity, whereas for small values, they attain variable velocities and approach or repel each other but no wave merging or splitting is observed.

2) When $\mu \geq 1$, the steady CAF is linearly unstable and it is necessary to keep the ratio of the thickness of the annulus to the radius of the tube small so that the solutions remain uniformly bounded. The resulting waves, the so-called "saw-tooth waves", generally travel in the same direction and faster than the interface, except for the case with $\mu=1$ for which they are stationary with respect to the unperturbed interface. Depending on parameter values and initial conditions, waves move with the same velocity or interact with each other exchanging their amplitudes or merge and split giving rise to either chaotic or organized solutions. For fluids of equal viscosities and densities ($\mu=\rho=1$) and for $Re=0.0275$ and $W=145.4$, small

amplitude waves are predicted. The increase of μ by almost two orders of magnitude does not affect their amplitudes, but increases their temporal period linearly. Varying W by more than three orders of magnitude increases their amplitudes proportionately, while their period increases with the logarithm of W . Similar to that is the effect of increasing Re . The present analysis confirms and extends results based on long wave expansions, which lead to the Kuramoto-Sivashinsky equation and its variations.

This two-phase flow has been studied extensively, because it simulates important technological and scientific problems such as the so-called “lubricated pipelining”, a technique employed to facilitate the transportation of viscous oil through a pipeline using water [1]. Similarly it arises in heat exchangers operating with supersaturated steam, in oil recovery from underground rocks by injecting steam or water, in trickle-bed reactors for reforming oil at high pressure, etc.

2. GOVERNING EQUATIONS

We examine the axisymmetric CAF of two incompressible, Newtonian fluids in a pipe of constant and circular cross-section with radius \hat{R}_2 . The region $0 \leq \hat{r} \leq \hat{R}_1(\hat{z}, \hat{t})$ is occupied by the core fluid (fluid 1) with viscosity and density $(\hat{\mu}_1, \hat{\rho}_1)$, while the annular fluid (fluid 2) with properties $(\hat{\mu}_2, \hat{\rho}_2)$ is located in the region $\hat{R}_1(\hat{z}, \hat{t}) \leq \hat{r} \leq \hat{R}_2$, where (\cdot) denotes dimensional quantities. The position vector of the fluid/fluid interface is defined by:

$$\hat{\mathbf{R}}_1 = \underline{e}_r \hat{R}_1(\hat{z}, \hat{t}) + \underline{e}_z \hat{z} \quad (2.1)$$

The components of the velocity vector of each fluid, are denoted as:

$$\underline{\hat{U}}_i = (\hat{U}_i, 0, \hat{W}_i) = \underline{e}_r \hat{U}_i + \underline{e}_\theta 0 + \underline{e}_z \hat{W}_i \quad (2.2)$$

where $(\hat{r}, \hat{\theta}, \hat{z})$ are the cylindrical coordinates, $(\underline{e}_r, \underline{e}_\theta, \underline{e}_z)$ are the corresponding unit normal vectors while \underline{e}_z is directed opposite to gravity, and \hat{t} denotes time. The equations that govern the motion of both fluids, $i=1, 2$, and the fluid/fluid interface are the following:

$$\nabla \cdot \underline{\hat{U}}_i = 0 \quad (2.3)$$

$$\hat{\rho}_i \frac{D \underline{\hat{U}}_i}{D \hat{t}} = -\nabla \hat{P}_i + \nabla \cdot \hat{\underline{\tau}}_i - \hat{\rho}_i g \underline{e}_z \quad (2.4)$$

$$\frac{D \hat{\mathbf{R}}_1}{D \hat{t}} = \underline{\hat{U}}_1(\hat{\mathbf{R}}_1(\hat{z}, \hat{t}), \hat{t}) \quad (2.5)$$

The stress tensor of each Newtonian fluid is defined as usual, $\hat{\underline{\tau}}_i = \hat{\mu}_i (\nabla \underline{\hat{U}}_i + \nabla \underline{\hat{U}}_i^T)$. This set of equations is solved subject to the boundary conditions of no slip, no penetration of the tube wall and continuity of velocities and stresses at the fluid-fluid interface. In the axial direction, we impose that the velocity field, the stress tensor of both fluids as well as the fluid/fluid interface are periodic functions with period the length of the computational domain, \hat{L} . In order to achieve a well-defined set of equations, we impose that the volume of the core fluid as well as their total volumetric flow rate remain constant in time. Upon making dimensionless the governing equations, using as characteristic velocity, \hat{W}_o , one half the average velocity in each cross section, the following six dimensionless numbers arise: The Reynolds number, $Re = \Lambda \hat{\rho}_1 \hat{R}_2 \hat{W}_o / \hat{\mu}_1$; the inverse Weber number, $w = \hat{\tau} / (\hat{\rho}_1 \hat{W}_o^2 \hat{R}_2)$; the inverse Froude number, $F = (g \hat{R}_2) / (\Lambda \hat{W}_o^2)$; the viscosity ratio, $\mu = \hat{\mu}_2 / \hat{\mu}_1$; the density ratio, $\rho = \hat{\rho}_2 / \hat{\rho}_1$; and the ratio of volumes of each fluid, v_1 / v_2 , where the aspect ratio, $\Lambda = 2\pi \hat{R}_2 / \hat{L}$, also appears and is set for computational reasons.

3. TRANSFORMATIONS AND NUMERICAL IMPLEMENTATION

The above equations are solved in the streamfunction-vorticity, $(\hat{\psi}_i, \hat{\Omega}_i)$ formulation, in each fluid, so the respective mass balances are identically satisfied. We also employ the following non-orthogonal, body-fitted coordinate transformation $(r, z, t) \rightarrow (x_1, x_2, \tau)$.

$$\text{Core fluid: } x_1 = 1 - 2 \frac{r}{R_1(z, t)}, x_2 = z, \tau = t \quad (3.1)$$

$$\text{Annular fluid: } x_1 = -1 + 2 \frac{r - R_1(z, t)}{1 - R_1(z, t)}, x_2 = z, \tau = t \quad (3.2)$$

This normalization is essential in order to transform the boundaries of the regions that each fluid occupies to coordinate lines in the new transformed space given the spectral method that we have adopted for the numerical solution of this problem and the need to exactly impose the boundary conditions on a deforming surface. The bounds of the new independent variables are the following:

$$-1 \leq x_1 \leq 1, 0 \leq x_2 \leq 2\pi, \tau \geq 0 \quad (3.3)$$

In order to solve numerically the resulting set of equations we use a pseudo-spectral method. This method is preferred because of its exponential rate of convergence with mesh refinement and for its easy implementation. We approximate every dependent variable by using Chebyshev polynomials and Fourier modes in the x_1 and x_2 directions, respectively. The grid points in the x_1 -direction are defined by the following relation:

$$x_{1k} = \cos\left(\pi \frac{k}{N}\right) \quad 0 \leq k \leq N \quad (3.4)$$

where N is the highest-order of Chebyshev polynomial that we use while the grid points in the x_2 -direction are taken to be equidistant i.e.:

$$x_{2l} = \frac{2\pi l}{M}, \quad 0 \leq l \leq M-1 \quad (3.5)$$

So, every dependent variable in the transformed space, indicated by f , is approximated as a sum of products of Chebyshev polynomials, C_i , and Fourier modes, F_j , i.e.:

$$f(x_1, x_2, \tau) = \sum_{i=0}^N \sum_{j=0}^{M-1} a_{ij}(\tau) C_i(x_1) F_j(x_2) \quad (3.6)$$

The derivative of each function represented by eq. (3.6), is evaluated by differentiating term by term its spectral expansion, while the unknowns of the above expansion are evaluated by exactly satisfying the differential equations at the collocation points. By using M and N collocation points in the axial and radial direction, respectively, the total unknowns are $4MN+M$. Typical (and more than sufficient for numerical convergence) values of M and N are 111 and 11 (in each fluid), respectively, which result in 4995 unknowns. The time integration is performed by using the implicit, second order accurate, Adams-Moulton method with typical time step $0.5 \cdot 10^{-3}$. In order to reduce the time required to invert the final Jacobian matrix at every time step, which is a full matrix with approximately $2.5 \cdot 10^7$ entries, we adopt the modified Newton-Raphson technique. The required CPU time for each dynamic simulation is of the order of 3-4 weeks in an ALPHA-DEC DS20 Workstation.

4. RESULTS AND DISCUSSION: Bamboo waves

Experiments with very viscous oil in the core and water in the annulus, both flowing against gravity and for a rather wide range of flow rates demonstrate that initially small and random disturbances of the cylindrical interface increase in amplitude and finally saturate assuming the bamboo shape, [1]. This wave shape is composed of sharper crests than troughs and the crests are directed from the more viscous to the less viscous fluid. A good indication of the

flow regime is given by the hold up ratio, defined as the ratio of the imposed flow rates to the ratio of volumes occupied by each phase

$$h = \frac{\hat{Q}_1 / \hat{Q}_2}{\hat{V}_1 / \hat{V}_2} \quad (4.1)$$

For perfect (steady) CAF $h=2$ and it decreases from this value as bamboo waves evolve. Earlier theoretical analyses [4], [5], did not obtain satisfactory agreement with experiments mainly because they made fairly restrictive assumptions about the interface shape, the fluid properties or the operating conditions. As we are interested in simulating as closely as possible the development of the bamboo waves we use herein the same conditions under which the experiments were performed, [1]. These were conducted in a long tube of circular cross section of inner radius $\hat{R}_2 = 0.48$ cm. They used oil of viscosity $\hat{\mu}_1 = 6.01$ poise and density $\hat{\rho}_1 = 0.905$ gr/cm³ flowing in the core of the tube and surrounded by water of viscosity $\hat{\mu}_2 = 0.01$ poise and density $\hat{\rho}_2 = 0.995$ gr/cm³. Thus, throughout we use $\mu = 0.00166$ and $\rho = 1.0995$. The surface tension of the oil-water system is $\hat{\tau} = 8.54$ dyn/cm [1], or $\hat{\tau} = 26$ dyn/cm, [4]. Given the experimentally imposed volumetric flow rates of oil and water \hat{Q}_1, \hat{Q}_2 , respectively, the characteristic velocity and the resulting Re are calculated first:

$$\hat{W}_o = \frac{\hat{Q}_1 + \hat{Q}_2}{2\pi\hat{R}_2^2}, \quad Re = \frac{\Lambda}{2\pi} \frac{\hat{Q}_1 + \hat{Q}_2}{\hat{R}_2(\hat{\mu}_1 / \hat{\rho}_1)} \quad (4.2), (4.3)$$

The last parameter that we should set is the ratio of the volumes occupied by each fluid. This is not reported in the experiments [1], instead we deduce it from the definition of the hold up ratio, eq. (4.1), and the fact that in the related experiments it remained constant, $h=1.39$:

$$V = \frac{\hat{V}_1}{\hat{V}_T} = \left(1 + 1.39 \frac{\hat{Q}_2}{\hat{Q}_1} \right)^{-1} \quad (4.4)$$

where \hat{V}_1, \hat{V}_2 , and \hat{V}_T are the volumes occupied by the core fluid, the annular fluid and their summation, respectively, while V denotes the volume fraction occupied by the core fluid in the tube.

We present only certain aspects of one of the several simulations of the corresponding experiments, the one with $\hat{Q}_1=429$, $\hat{Q}_2=200$ cm³/min. A photograph of this experiment, showing the saturated shape of the interface can be seen in [1]. This photograph is used in order to estimate the average wavelength of the bamboo wave so as to set the length of our computational domain. It turns out that the average wavelength equals 1.225 cm, which is 2.552 times the radius of the tube. Having computed this, we set the length of the domain equal to 20.833 times the tube radius expecting in this way to compute a bamboo wave having about 8 crests. With these data we compute the characteristic velocity from eq. (4.2) to be $\hat{W}_o = 7.242$ cm/s, whereas the values of the dimensionless numbers with $\hat{\tau} = 26$ dyn/cm are $h=1.39$, $A=0.3016$, $Re=0.1579$, $W=1.141$, $F=29.77$, $V=0.6068$. Linear stability theory reveals that the perfect CAF for these dimensionless numbers is unstable, since several eigenvalues have positive real part. The most unstable eigenvalue corresponds to the Fourier mode having wave number equal to 7, while the growth rate of the mode having wave number 6 is only by 0.7% smaller than the growth rate of the most dangerous one.

The volumetric flow rate of the core fluid computed at the entrance of the tube is a good measure of the flow field. Here our initial condition is the steady flow field of the perfect CAF. Because of this, even up to $t \sim 15$ the flow cannot be distinguished from the perfect CAF, i.e. a long incubation period is needed before instability sets in through numerical truncation error. After $t \sim 15$, the exponential deviation from the perfect core-annular flow

becomes visible and at about $t \sim 22$ the instability seems to have saturated as the core flow rate reaches a periodic pattern. We graphically compute the average oscillation period and we find it to equal to 0.501, while linear stability theory predicts that the period of oscillation of the Fourier modes having wave numbers 5, 6 and 7 are $2\pi/10.708=0.587$, 0.459 and 0.374, respectively. Thus, the graphically computed oscillation period of the saturated bamboo wave is closer to the mode with wave number 6 than to any other mode. The wave speed computed using the same figure is found to be $2\pi/(6 \cdot 0.501)=2.088$ times the characteristic velocity of the flow. The time-averaged flow rate also indicates that the onset of the bamboo waves results in the deceleration of the oil.

In fig. 1 we show the instantaneous streamlines of the flow as well as the interface at $t=27.049$ for $\hat{\tau}=8.54$ dyn/cm. Clearly the waves are not all exactly the same and generally the crests are slightly sharper in their front than in their back. It is a non-deforming wave, which travels downstream with a constant velocity. In the core fluid the streamlines are almost straight indicating that the flow there resembles Poiseuille flow. Also, it can be seen that the interface intersects different streamlines revealing in this way the unsteady nature of the flow. In part of the annular fluid the streamlines remain straight, whereas small vortices arise in it and where each crest is located. Combining the fact that the annular flow rate attains its minimum value at a crest with the steady translation of the interface we conclude that, if recirculation can arise in the annulus, it will do so at a crest. In the present case this is even clearer, since $Q_2 \sim 0$ at the crest forcing the axial velocity to change sign along the radius, whereas $Q_2 > 0$ at the trough. For further results and details see [6].

Saw-tooth waves

We present only certain characteristics from one representative simulation for the case with $\mu \geq 1$. The other parameter values have been set so that the interface does not break or fold and so that earlier approximate analyses, [2], [3], are tested and extended. The parameter values used are: $\rho=\mu=1$, $A=0.1$, $Re=0.0275$, $W=145.4$, $V=0.826$. Linear stability theory, performed as described elsewhere, [7], [8], predicts that the perfect CAF for these dimensionless numbers is unstable, since there are several eigenvalues having positive growth rates and that the computational domain includes at least 8 times the most unstable mode. In fact, we first performed this linear stability analysis and after finding the wavelength of the most unstable wave, we set the length of the domain to be at least 8 times that and, thus, $A=0.1$. In order to validate our numerical scheme of solution we have integrated the non-linear governing set of equations in both space and time using as initial condition the perfect CAF seeded with the most unstable eigenvector for these values of the dimensionless numbers. Since the perfect CAF is unstable the flow departs from it and after a transient period the instability is arrested leading to saturation. We can graphically compute the temporal oscillation frequency, which is found to equal 5.572, while the one predicted by the linear theory equals 5.568. Similarly we compute the linear growth rate, which graphically equals 0.02548, while using linear theory it is 0.02734. So, our numerical scheme is validated. Under the present parameter values the perfect CAF is unstable due to capillarity as the viscosity ratio equals unity and the Reynolds number is relatively small. Despite the fact that capillarity induces the instability in the linear regime, capillarity in conjunction with the imposed flow capture it preventing in this way rupture of the fluid/fluid interface and as a result shear induced stabilization is effective. In the absence of imposed flow, the instability would have broken the interface. Because of the small amplitude of these waves the holdup ratio does not deviate appreciably from its value for perfect CAF.

In fig. 2 we present the time evolution of the interface for initial condition seeded with a random disturbance. The time difference between successive snapshots is $\Delta t=2$ while the first one corresponds to time $t=152$. Significant wave interaction can be seen. This observation is in accordance with the analyses by [2] for no viscosity stratification that introduces dispersion, and [3] for small values of the capillary parameter, which show that the governing equation of motion of the interface is the Kuramoto-Sivashinsky equation, which admits chaotic solutions. The interaction between neighboring waves leads to their splitting and merging, which do not diminish as time evolves.

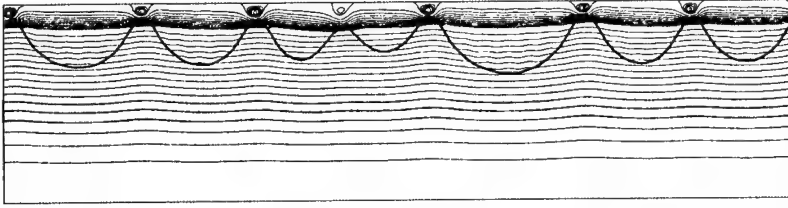


Figure 1: Wave interface (thicker line) and streamlines in both fluids in a fully developed bamboo wave at $t=27.049$ for $\hat{r} = 8.54$. The upper and lower horizontal lines are the tube wall and the axis of symmetry, respectively. Flow is from left to right and gravity opposes it.

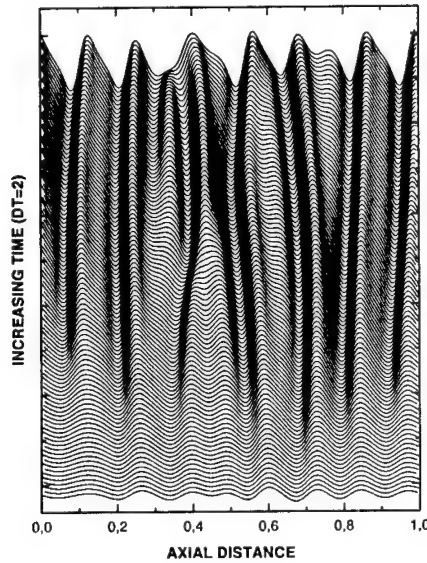


Figure 2: Development of the interfacial wave for initial condition that of perfect CAF seeded with a random disturbance (time increases upwards)

Acknowledgement: This work was supported by the EPET II program (Grant 88/1998).

5. REFERENCES

- [1] Bai R., Chen, K. & Joseph, D.D., *J. Fluid Mech.* **240**, 97-132, (1992).
- [2] Papageorgiou D., Maldarelli C. & Rumschitzki D., *Phys. Fluids*, **A2(3)**, 340-352, (1990).
- [3] Kerchman V., *J. Fluid Mech.*, **290**, 131-166, (1995).
- [4] Bai, R., Kelkar, K. & Joseph D.D., *J. Fluid Mech.* **327**, 1-34, (1996).
- [5] Li, J. & Renardy, Y. *J. Fluid Mech.*, **391**, 123-149, (1999).
- [6] Kouris, Ch. & Tsamopoulos, J., *Phys. Fluids*, **13(4)**, 841-859, (2001).
- [7] Kouris, Ch. & Tsamopoulos, J. *Chem. Engng Sci.*, **55(22)**, 5509-5530, (2000).
- [8] Kouris, Ch. & Tsamopoulos, J., *J. Fluid Mech.*, **432**, 31-68, (2001).

A COMPARISON OF THE ACCURACY OF VARIOUS INTERPOLATION TECHNIQUES FOR PROCESSING RANDOMLY SCATTERED BATHYMETRIC DATA

N. P. Volakos

School of Aeronautical, Civil and Mechanical Engineering
University of Salford, Salford, M5 4WT, United Kingdom

R. W. Barber

Computational Science and Engineering Department
Daresbury Laboratory, Daresbury, Warrington, Cheshire, WA4 4AD, United Kingdom

1. SUMMARY

As part of the development of a hydrodynamic model of a natural water body such as an estuary or coastal sea, spot depths must be assigned to all nodes of the computational grid. This paper presents the results of a statistical analysis of the accuracy of three basic techniques, offered by Thompson & Johnson [1], for interpolating between scattered depth data. The methods tested include bilinear interpolation, inverse-power interpolation and Taylor series interpolation. Initially, the ability of each method to reproduce analytically-generated surfaces was investigated and it was found that all methods performed well with dense bathymetric data. However, some of the interpolation techniques were found to have critical flaws when processing sparsely scattered depth points containing rapid changes in gradient.

2. INTRODUCTION

In estuaries and near coastal regions the available depth data (or bathymetry) obtained from nautical charts will vary in spatial resolution between well surveyed shipping channels and sparsely surveyed surrounding shallows. Often, however, the flow behaviour in the shallow near-shore region has a significant effect on the overall hydrodynamics of the flow domain. It is therefore important that the method of interpolation from the measured bathymetry onto the nodes of the hydrodynamic mesh is as accurate as possible and uses the available depth data to best effect. The choice of an inappropriate depth interpolation method is likely to be a major source of error in any hydrodynamic model.

This paper investigates the accuracy of three basic interpolation techniques provided in the WESCORA computer code (Thompson & Johnson [1], Johnson & Thompson [2]). The WESCORA code uses depth interpolation as a precursor to depth-dependent grid adaptation but the interpolation methods discussed are also widely applicable to both 2-D and 3-D hydrodynamic schemes.

3. DEPTH INTERPOLATION

Depth interpolation is the assignment of representative values of depth to each node of a computational grid from a randomly scattered set of bathymetric data points. The interpolated depth of the sea bed can then be used in the continuity equation of a shallow water equation model or to establish the lower boundary of a 3-D hydrodynamic scheme.

In theoretical studies, the bed of the domain may be flat or have a prescribed known shape which can be found using analytical methods. However, when modelling a natural water body such as a river, estuary or coastal sea, bathymetric data will come from a nautical chart in the form of a series of surveyed spot depths. These spot depths will not coincide with the nodes of the computational grid and therefore interpolation must be employed to obtain representative values of depth at each grid node.

Thompson & Johnson [1] implemented three basic methods for interpolating between scattered depth points. The methods assume that the depth at a particular grid node is only dependent upon those surrounding spot depths which are nearest to it. Therefore a number of depth points must be located around the grid node before interpolation can be performed. The rules for choosing depth points to surround a fixed (x,y) position, P , are illustrated in Figure 1:

- 1st point P_1 nearest depth point to P .
- 2nd point P_2 nearest depth point such that the vector P_2P forms an obtuse angle with P_1P .
- 3rd point P_3 nearest depth point lying between the projections beyond P of P_1P and P_2P .
- 4th point P_4 nearest depth point lying within one of the sectors $P_1P_2P_3$, $P_1P_3P_2$ or $P_2P_3P_1$.
- 5th point P_5 nearest unused depth point to P .

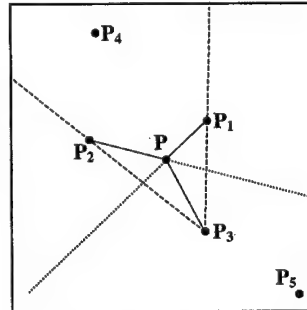


Figure 1: Choosing depth points to surround a fixed (x,y) position, P

To enforce these criteria, algorithms are employed which consider the vectors and angles between groups of points. If there is no depth point satisfying the above criteria then the nearest unused data point is chosen.

If the grid node in question lies near the boundary it may well be impossible to find depth points that surround it, in which case all interpolation methods will effectively extrapolate for the depth at that node. Extrapolation is a risky procedure as it can easily lead to false results. In order to overcome this problem, extra depth points can be added to the bathymetric data along the coastal perimeter and open boundaries. This ensures that the depth is always computed using interpolation.

The three methods of interpolation considered in the present study are as follows:

(a) *Bilinear interpolation*: The bed is assumed to be planar with the equation of the plane given by:

$$\bar{h}(x, y) = a + bx + cy + dxy \quad (1)$$

The coefficients a , b , c and d can be found by knowing the location of 4 spot depths, or if the xy term is ignored, the coefficients a , b and c can be found using 3 spot depths. The

interpolated depth, \bar{h} , at a grid node is then found by substituting the x - and y - coordinates of the node into equation (1).

(b) *Inverse-power interpolation*: The interpolated depth, \bar{h} , at the grid node at (x,y) is given by a weighted average of the surrounding depth points depending on an inverse power of their distance away:

$$\bar{h}(x, y) = \frac{\sum_{i=1}^n \frac{h(x_i, y_i)}{d_i^m}}{\sum_{i=1}^n \frac{1}{d_i^m}} \quad (2)$$

where n is the number of depth points used,

m is the power at which the weight decreases with distance (usually 2 or 3),

$h(x_i, y_i)$ is the depth at data point P_i

and d_i is the distance of the depth point P_i from the grid node.

(c) *Taylor series interpolation*: Suppose that (x_p, y_p) is the nearest depth point to the grid node at (x,y) . Then the interpolated depth at (x,y) is given by:

$$\begin{aligned} \bar{h}(x, y) = & h(x_p, y_p) + [x - x_p] h_x(x_p, y_p) + [y - y_p] h_y(x_p, y_p) \\ & + \frac{1}{2} [x - x_p]^2 h_{xx}(x_p, y_p) + \frac{1}{2} [y - y_p]^2 h_{yy}(x_p, y_p) + [x - x_p][y - y_p] h_{xy}(x_p, y_p) \end{aligned} \quad (3)$$

This equation contains five unknowns, the five derivatives of h at the depth point (x_p, y_p) . These are determined using Taylor series expansions about (x_p, y_p) to five other surrounding depth points. Thus if the five nearest points to (x_p, y_p) are (x_i, y_i) $i=1, \dots, 5$ then:

$$\begin{aligned} h(x_i, y_i) = & h(x_p, y_p) + [x_i - x_p] h_x(x_p, y_p) + [y_i - y_p] h_y(x_p, y_p) \\ & + \frac{1}{2} [x_i - x_p]^2 h_{xx}(x_p, y_p) + \frac{1}{2} [y_i - y_p]^2 h_{yy}(x_p, y_p) + [x_i - x_p][y_i - y_p] h_{xy}(x_p, y_p) \end{aligned} \quad (4)$$

which is a system of 5 equations for the 5 unknowns. If fewer derivatives are included in equation (3) then respectively fewer equations of the form shown in (4) are required. Taylor series interpolation may also be utilised with two (or more) sets of interpolation points. In this case the above process is performed a second time with those depth points used in the first sweep removed and the coefficients of the matrix of derivatives of h at (x_p, y_p) selectively updated.

4. VALIDATION TESTS

In order to assess the accuracy of each form of interpolation, a domain is required with known analytical bathymetry and a grid generated within its perimeter. The various interpolation methods are used to predict the depth at each grid node which can then be compared with the analytical depth at the grid node position. The accuracy of the various interpolation methods can be expressed in terms of the standard deviation of the depth error. If $h_{i,j}$ is the analytical value of depth at grid node (i,j) and $\bar{h}_{i,j}$ is the interpolated value of depth at the same node then the standard deviation of the interpolation, σ , is defined by:

$$\sigma = \sqrt{\frac{\sum_{i,j}^n (h_{i,j} - \bar{h}_{i,j})^2}{n}} \quad (5)$$

where n is the total number of nodes in the grid. A comparison index is also evaluated which expresses the standard deviation for each interpolation method as a ratio of the best observed value.

Initially the domain chosen was a slice of a sphere of non-dimensionalised radius 100 (see Figure 2). The maximum depth was 29.29 and the maximum gradient was unity. A boundary-fitted grid of 30 by 30 cells was generated and 1000 scattered data points were chosen at random positions within the perimeter and assigned depth values equal to the analytical bathymetry of the basin. An extra 120 data points of zero depth were equally spaced around the perimeter to overcome the problems arising from data extrapolation. The results of the various interpolation schemes are illustrated in Table 1 and Figures 3 & 4.

Table 1: Standard deviation for various interpolation methods

Interpolation method	Standard Deviation	SD Index
Bilinear 3 points	0.09592	3.817
Bilinear 4 points	0.32422	12.902
Inverse Square 2 points	0.49854	19.839
Inverse Square 3 points	0.38087	15.156
Inverse Square 4 points	0.44056	17.531
Inverse Square 5 points	0.49455	19.680
Inverse Cube 2 points	0.56223	22.373
Inverse Cube 3 points	0.48399	19.259
Inverse Cube 4 points	0.51495	20.492
Inverse Cube 5 points	0.54121	21.536
Inverse Fourth 2 points	0.61998	24.671
Inverse Fourth 3 points	0.56554	22.504
Inverse Fourth 4 points	0.58033	23.093
Inverse Fourth 5 points	0.59085	23.512
Taylor 2 points 1 set	2.24031	89.149
Taylor 3 points 1 set	1.45179	57.771
Taylor 4 points 1 set	0.26331	10.478
Taylor 5 points 1 set	0.05342	2.126
Taylor 2 points 2 sets	0.32548	12.952
Taylor 3 points 2 sets	0.32837	13.067
Taylor 4 points 2 sets	0.08090	3.219
Taylor 5 points 2 sets	0.02513	1.000
Nearest point	0.92128	36.661

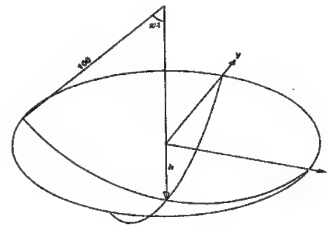


Figure 2: Three-dimensional representation of spherical bathymetry

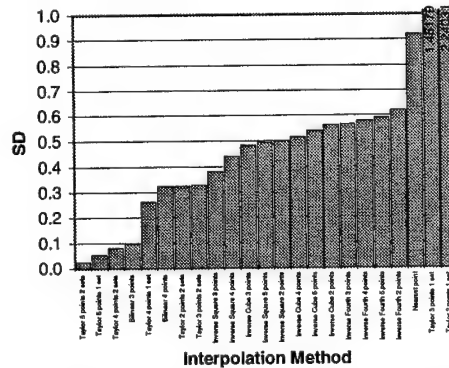


Figure 3: Graphical representation of standard deviation for various interpolation methods

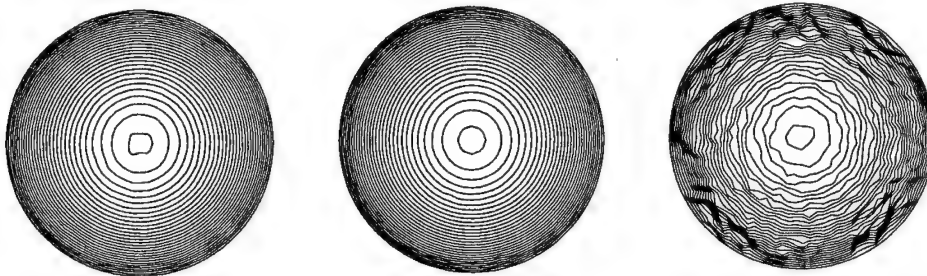


Figure 4: Depth contours for bilinear interpolation using 3 depth points (left), Taylor series interpolation using 5 depth points with 2 sets (middle) and inverse power interpolation using 4 depth points with $m=4$ (right)

A second hypothetical domain was chosen with a sinusoidal bathymetry prescribed by:

$$h(x, y) = 2\sin(x)\sin(y) \quad \begin{cases} 0 \leq x \leq 360^\circ \\ 0 \leq y \leq 360^\circ \end{cases} \quad (6)$$

A Cartesian mesh having 60 by 60 cells was applied within the perimeter of the domain and 4000 scattered data points were chosen at random positions within the perimeter. Each data point was assigned a depth equal to the analytical value calculated from equation (6). An extra 240 data points of zero depth were again assigned along the perimeter. The results of the interpolation tests are presented in Table 2 and Figures 6 & 7.

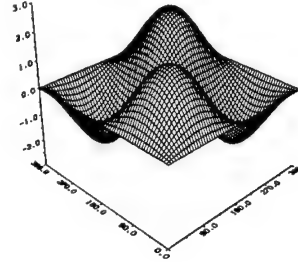


Table 2: Standard deviation for various interpolation methods

Interpolation method	Standard Deviation	SD Index
Bilinear 3 points	0.00486	1.303
Bilinear 4 points	0.02844	7.624
Inverse Square 2 points	0.02938	7.877
Inverse Square 3 points	0.02241	6.009
Inverse Square 4 points	0.02623	7.032
Inverse Square 5 points	0.02935	7.870
Inverse Cube 2 points	0.03330	8.928
Inverse Cube 3 points	0.02865	7.681
Inverse Cube 4 points	0.03067	8.223
Inverse Cube 5 points	0.03242	8.691
Inverse Fourth 2 points	0.03663	9.819
Inverse Fourth 3 points	0.03333	8.935
Inverse Fourth 4 points	0.03432	9.202
Inverse Fourth 5 points	0.03529	9.462
Taylor 2 points 1 set	0.25192	67.541
Taylor 3 points 1 set	0.11997	32.165
Taylor 4 points 1 set	0.31009	83.135
Taylor 5 points 1 set	0.01575	4.223
Taylor 2 points 2 sets	0.01530	4.101
Taylor 3 points 2 sets	0.01590	4.264
Taylor 4 points 2 sets	0.01239	3.323
Taylor 5 points 2 sets	0.00373	1.000
Nearest point	0.05448	14.606

Figure 5: Three-dimensional representation of sinusoidal bathymetry

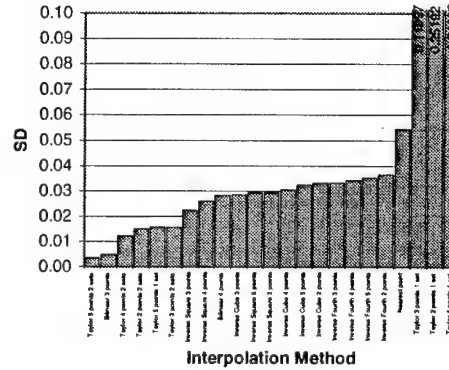


Figure 6: Graphical representation of standard deviation for various interpolation methods

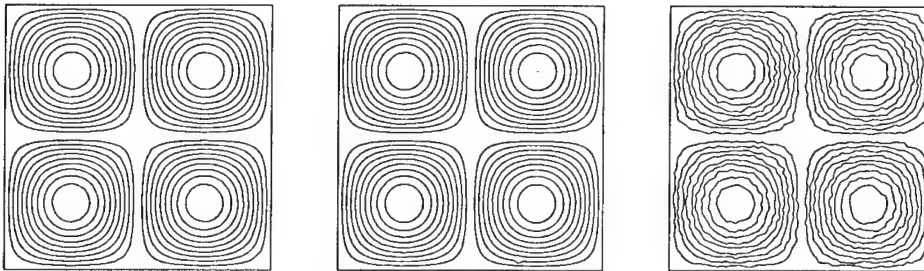


Figure 7: Depth contours for bilinear interpolation using 3 depth points (left), Taylor series interpolation using 5 depth points with 2 sets (middle) and inverse power interpolation using 4 depth points with $m=4$ (right)

Finally the northern part of the Gulf of Thermaikos (Greece) was chosen to test the interpolation techniques on a real domain. Unfortunately there are no analytical methods available to obtain the depth at an arbitrary (x,y) position in the gulf. Instead 600 random depth points from Hellenic Naval Chart No. 255 (approximately one-third of the total number of surveyed spot depths) were reserved for comparison purposes. The remaining bathymetric data were then used to interpolate the depth at the points that were previously set aside. The results of the analysis are illustrated in Table 3 and Figures 8 & 9.

Table 3: Standard deviation for various interpolation methods

Interpolation method	Standard Deviation	SD Index
Bilinear 3 points	1.88311	1.000
Bilinear 4 points	13.21911	7.020
Inverse Square 2 points	2.24706	1.193
Inverse Square 3 points	2.06359	1.096
Inverse Square 4 points	2.13189	1.132
Inverse Square 5 points	2.27356	1.207
Inverse Cube 2 points	2.38980	1.269
Inverse Cube 3 points	2.23552	1.187
Inverse Cube 4 points	2.25302	1.196
Inverse Cube 5 points	2.33408	1.239
Inverse Fourth 2 points	2.51653	1.336
Inverse Fourth 3 points	2.38965	1.269
Inverse Fourth 4 points	2.37568	1.262
Inverse Fourth 5 points	2.41736	1.284
Taylor 2 points 1 set	423.12696	224.695
Taylor 3 points 1 set	31.89027	16.935
Taylor 4 points 1 set	148.84615	79.043
Taylor 5 points 1 set	75.93301	40.323
Taylor 2 points 2 sets	3.16881	1.683
Taylor 3 points 2 sets	3.64144	1.934
Taylor 4 points 2 sets	2.98405	1.585
Taylor 5 points 2 sets	4.14484	2.201
Nearest point	3.23704	1.719

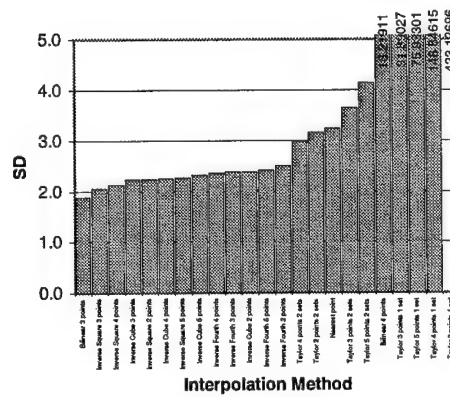


Figure 8: Graphical representation of standard deviation for various interpolation methods



Figure 9: Depth contours for bilinear interpolation using 3 depth points (left), Taylor series interpolation using 5 depth points with 2 sets (middle) and inverse power interpolation using 4 depth points with $m=4$ (right)

5. CONCLUSIONS

This paper has presented a comparison of three basic techniques for interpolating between randomly scattered depth data. Results are presented for analytical test geometries and the complex bathymetry in the northernmost part of the Gulf of Thermaikos. The tests indicate that Taylor series interpolation is the most accurate technique when the bathymetry varies smoothly in space. However, if the surveyed depth points contain rapid changes in gradient, the Taylor series algorithm is prone to overshoot the supplied bathymetry data, producing spurious peaks and troughs in the interpolated depth field. Under these circumstances, the bilinear technique becomes the most accurate interpolation procedure. A review of the overall accuracy of each of the methods reveals that bilinear interpolation appears to be the most robust approach for a wide range of coastal bathymetries.

6. REFERENCES

- [1] Thompson, J.F. & Johnson, B.H., Development of an adaptive boundary-fitted coordinate code for use in coastal and estuarine areas, *Misc. Paper HL-85-5, U.S. Army Engineer Waterways Experiment Station*, Vicksburg, Mississippi, U.S.A., 1985.
- [2] Johnson, B.H. & Thompson, J.F., Discussion of a depth-dependent adaptive grid generator for use in computational hydraulics, *Proc. Int. Conf. on Numerical Grid Generation in Computational Fluid Dynamics*, pp. 629-640, 1986.

INTERRELATION BETWEEN STOKES AND PAPKOVICH – NEUBER EIGENMODES FOR SPHEROIDAL STOKES FLOW

Maria Hadjinicolaou

Hellenic Open University, Sahtouri 16, GR-262 22 Patras, Greece

Panayiotis Vafeas

Department of Chemical Engineering, University of Patras and ICEHT/FORTH
GR-265 00 Patras, Greece

1. SUMMARY

The study of Stokes flow through a swarm of particles is of great theoretical and practical interest. The analytical expressions obtained for the flow fields are very useful for determining important engineering quantities in many applications like heat or mass transfer. Since the flow was assumed to be axisymmetric, spheroidal geometry is employed. The two different complete representations of the flow fields are considered here. The first one is obtained through the theory of generalized eigenfunctions, according to which the stream function is given in full series expansion in terms of semiseparable eigenmodes. The second one, also valid in non-axisymmetric geometries, is the Papkovitch-Neuber differential representation, where the flow fields are provided in terms of harmonic spheroidal eigenfunctions. In the present work, connection formulae are obtained which relate the spheroidal harmonic eigenfunctions of the Papkovitch-Neuber representation, considering rotational symmetry, with the semiseparable spheroidal stream eigenfunctions.

2. INTRODUCTION

The steady and creeping flow of an incompressible, viscous fluid is described by the well-known Stokes equations (1851), connecting the biharmonic vector velocity with the harmonic scalar pressure field [1]. For many interior and exterior flow problems involving small particles, spheroidal geometry [2] provides very good approximation. Therefore, in many important applications the flow is considered to be axisymmetric [3] since relative physical problems enjoy rotational symmetry. Such motions are characterized from the existence of a stream function [1], which is employed in order to obtain the velocity and the pressure field. The complete solution of the equation for Stokes flow in spheroidal coordinates can be obtained through the theory of generalized eigenfunctions and this stream function enjoys the representation of a full series expansion in terms of semiseparable eigenmodes [4]. On the other hand, Papkovitch (1932) and Neuber (1934) proposed a differential representation of the flow fields in terms of harmonic functions [3,5]. This representation holds true also for non-axisymmetric problems. In the interest of producing ready-to-use basic functions for Stokes flow in spheroidal coordinates, we calculate the Papkovitch-Neuber eigensolutions, generated by the appropriate spheroidal eigenfunctions [6] (excluding singularities on the axis of symmetry) where the full series expansion is being demonstrated. Furthermore, connection

formulae are obtained through which any solution of the Stokes system, given in terms of semiseparable eigenfunctions, can be transformed to the Papkovitch-Neuber eigensolutions. We show that this procedure is not invertible since these formulae interrelate each Papkovitch-Neuber potential with a specific combination of semiseparable eigenfunctions. We are, also, focused to prolata spheroids, since the results for oblate spheroids are obtained through a known transformation [2].

3. STATEMENT OF THE PROBLEM – PROLATE SPHEROIDS

The governing equations of the steady, non-axisymmetric (3-D), creeping flow ($Re \ll 1$) of an incompressible (density $\rho = \text{const.}$), viscous (dynamic viscosity $\mu = \text{const.}$) fluid, around particles embedded within smooth, bounded domains $\Omega(R^3)$, are given by a pair of partial differential equations connecting the biharmonic velocity field $\mathbf{v}(\mathbf{r})$ (harmonic vorticity $\boldsymbol{\omega}(\mathbf{r}) = \nabla \times \mathbf{v}(\mathbf{r})$) with the harmonic total pressure field $P(\mathbf{r})$, where \mathbf{r} stands for position vector

$$\mu \Delta \mathbf{v}(\mathbf{r}) = \nabla P(\mathbf{r}), \quad \mathbf{r} \in \Omega(R^3) \quad (1)$$

$$\nabla \cdot \mathbf{v}(\mathbf{r}) = 0, \quad \mathbf{r} \in \Omega(R^3) \quad (2)$$

Equation (1) states that, for creeping flow, the generated pressure is compensated by the viscous forces while equation (2) secures the incompressibility of the fluid.

Given a fixed positive number $c > 0$, which we consider to be the semifocal distance of our system, we define the prolata spheroidal coordinates (η, θ, φ) , $0 \leq \eta < +\infty$, $0 \leq \theta \leq 2\pi$, $0 \leq \varphi < 2\pi$ where introducing the simple transformation $\tau = \cosh \eta$, $1 \leq \tau < +\infty$ and $\zeta = \cos \theta$, $-1 \leq \zeta \leq 1$ are given as follows ($\mathbf{r} = (x_1, x_2, x_3)$) [2]

$$x_1 = c\sqrt{\tau^2 - 1}\sqrt{1 - \zeta^2} \cos \varphi, \quad x_2 = c\sqrt{\tau^2 - 1}\sqrt{1 - \zeta^2} \sin \varphi, \quad x_3 = c\tau\zeta \quad (3)$$

To every fixed value of $\tau \in (1, +\infty)$, τ_0 , there corresponds the unique prolata spheroid

$$S_{\tau_0} : \frac{x_1^2 + x_2^2}{c^2(\tau_0^2 - 1)} + \frac{x_3^2}{c^2\tau_0^2} = 1 \quad (4)$$

with major semiaxes (on the axis of symmetry) $\alpha_3(\tau) = c\tau$, minor semiaxes $\alpha_1(\tau) = c\sqrt{\tau^2 - 1}$ and eccentricity $\varepsilon(\tau) = 1/\tau$.

The outward unit normal vector on the surface of the spheroid $\tau = \tau_0$, is furnished by the formula

$$\hat{\mathbf{n}}(\tau_0) = \frac{1}{\sqrt{\tau_0^2 - \zeta^2}} \left(\tau_0 \sqrt{1 - \zeta^2} \cos \varphi, \quad \tau_0 \sqrt{1 - \zeta^2} \sin \varphi, \quad \sqrt{\tau_0^2 - 1} \zeta \right) \quad (5)$$

where for any nondegenerate spheroid, S_{τ_0} , it is $\tau_0 > 1$. Furthermore, $|\zeta| \leq 1$. Hence, the expression $(\tau^2 - \zeta^2)$ is always bounded away from zero for all points exterior to S_{τ_0} , as well as on S_{τ_0} .

Papkovich-Neuber [5] proposed the following differential representation of the solutions for Stokes flow, in terms of harmonic potentials $\Phi(\mathbf{r})$, $\Phi_0(\mathbf{r})$ ($\Delta \Phi(\mathbf{r}) = 0$, $\Delta \Phi_0(\mathbf{r}) = 0$, $\mathbf{r} \in \Omega(R^3)$)

$$\mathbf{v}(\mathbf{r}) = \Phi(\mathbf{r}) - \frac{1}{2} \nabla(\mathbf{r} \cdot \Phi(\mathbf{r}) + \Phi_0(\mathbf{r})), \quad \mathbf{r} \in \Omega(R^3) \quad (6)$$

$$P(\mathbf{r}) = -\mu \nabla \cdot \Phi(\mathbf{r}), \quad \mathbf{r} \in \Omega(R^3) \quad (7)$$

where the differential operators ∇ , Δ , in prolate spheroidal coordinates, assume the forms

$$\nabla = \frac{1}{c\sqrt{\tau^2 - \zeta^2}} \left[\sqrt{\tau^2 - 1} \hat{\tau} \frac{\partial}{\partial \tau} - \sqrt{1 - \zeta^2} \hat{\zeta} \frac{\partial}{\partial \zeta} \right] + \frac{1}{c\sqrt{\tau^2 - 1}\sqrt{1 - \zeta^2}} \hat{\phi} \frac{\partial}{\partial \phi} \quad (8)$$

$$\Delta = \frac{1}{c^2(\tau^2 - \zeta^2)} \left\{ \frac{\partial}{\partial \tau} \left[(\tau^2 - 1) \frac{\partial}{\partial \tau} \right] + \frac{\partial}{\partial \zeta} \left[(1 - \zeta^2) \frac{\partial}{\partial \zeta} \right] \right\} + \frac{1}{c^2(\tau^2 - 1)(1 - \zeta^2)} \frac{\partial^2}{\partial \phi^2} \quad (9)$$

and $\hat{\tau}$, $\hat{\zeta}$, $\hat{\phi}$ denote the coordinate vectors of the system.

On the other hand, the development of the *Stokes Theory* [1], for axisymmetric flows, has the advantage that demands only one potential (Stokes stream function $\psi(\mathbf{r})$, $\mathbf{r} \in \Omega(R^2)$) when one seeks solutions for Stokes flow, but restricts the dimensions to two. $\psi(\mathbf{r})$ satisfies the well-known equation of motion

$$E^4 \psi(\mathbf{r}) = 0, \quad \mathbf{r} \in \Omega(R^2) \equiv \{(\tau, \zeta) : \tau > 1, -1 \leq \zeta \leq 1\} \quad (10)$$

where in prolate geometry, the operator E^2 is given by the expression

$$E^2 = \frac{1}{c^2(\tau^2 - \zeta^2)} \left[(\tau^2 - 1) \frac{\partial^2}{\partial \tau^2} + (1 - \zeta^2) \frac{\partial^2}{\partial \zeta^2} \right] \quad (11)$$

The vector velocity field for $\tau > 1$, $|\zeta| \leq 1$ has the form

$$\mathbf{v}(\tau, \zeta) = v_\tau(\tau, \zeta) \hat{\tau} + v_\zeta(\tau, \zeta) \hat{\zeta} \quad (12)$$

and the components of the velocity are expressed in terms of the Stokes stream function via

$$v_\tau(\tau, \zeta) = \frac{1}{c^2 \sqrt{\tau^2 - \zeta^2} \sqrt{\tau^2 - 1}} \frac{\partial \psi(\tau, \zeta)}{\partial \zeta}, \quad v_\zeta(\tau, \zeta) = \frac{1}{c^2 \sqrt{\tau^2 - \zeta^2} \sqrt{1 - \zeta^2}} \frac{\partial \psi(\tau, \zeta)}{\partial \tau} \quad (13)$$

while the total pressure field is provided as a function of an arbitrary constant pressure, P_0

$$P(\tau, \zeta) = P_0 + \frac{\mu}{c} \left\{ \int_{\infty}^{\tau} \frac{1}{(\tau'^2 - 1)} \frac{\partial (E^2 \psi(\tau', \zeta))}{\partial \zeta} d\tau' - \int_0^{\zeta} \frac{1}{(1 - \zeta'^2)} \frac{\partial (E^2 \psi(\tau, \zeta'))}{\partial \tau} d\zeta' \right\} \quad (14)$$

The vorticity field is easily confirmed to be expressed as

$$\omega(\tau, \zeta) = \nabla \times \mathbf{v}(\tau, \zeta) = \frac{\hat{\phi}}{h_\phi} E^2 \psi(\tau, \zeta) = \frac{\hat{\phi}}{c\sqrt{\tau^2 - 1}\sqrt{1 - \zeta^2}} E^2 \psi(\tau, \zeta) \quad (15)$$

showing that irrotational fields are described by a stream function $\psi(\tau, \zeta)$ which satisfies the equation $E^2 \psi(\tau, \zeta) = 0$. Hence, every axisymmetric Stokes flow problem is being solved once the Stokes stream function $\psi(\mathbf{r})$, $\mathbf{r} \in \Omega(R^2)$ is known.

Our goal is to derive connection formulae between the corresponding potentials after the interrelation of the *Papkovich-Neuber* axisymmetric flow fields with those of *Stokes Theory*.

4. PAPKOVICH-NEUBER AND STOKES PROLATE SPHEROIDAL POTENTIALS

Introducing the eigenfunctions $S_n^{m,(i)}(\tau, \zeta)$ of the i th kind ($i=1,2,3,4$), of order n ($n=0,1,2,\dots$) and of degree m ($m=0,1,2,\dots, n$) in terms of the associated Legendre functions [6] of the first ($P_n^m(x)$, $x=\tau, \zeta$) and the second ($Q_n^m(x)$, $x=\tau, \zeta$) kind via the formulae

$$S_n^{m,(1)}(\tau, \zeta) = P_n^m(\tau)P_n^m(\zeta), \quad S_n^{m,(3)}(\tau, \zeta) = Q_n^m(\tau)P_n^m(\zeta) \quad (\text{regular on the } x_3\text{-axis}) \quad (16)$$

$$S_n^{m,(2)}(\tau, \zeta) = P_n^m(\tau)Q_n^m(\zeta), \quad S_n^{m,(4)}(\tau, \zeta) = Q_n^m(\tau)Q_n^m(\zeta) \quad (\text{singularities on the } x_3\text{-axis}) \quad (17)$$

for every $\tau > 1$ and $|\zeta| \leq 1$, the following complete representation of the Papkovitch-Neuber potentials which belong to the kernel space of the operator Δ (equation (9)), is obtained

$$\Phi(\mathbf{r}) = \sum_{n=0}^{\infty} \sum_{m=0}^n \sum_{i=1}^4 \sum_{s=e,o} \left[c_n^{m,(i)s} u_n^{m,(i)s}(\mathbf{r}) \right], \quad \mathbf{r} \in \Omega(R^3) \quad (18)$$

$$\Phi_0(\mathbf{r}) = \sum_{n=0}^{\infty} \sum_{m=0}^n \sum_{i=1}^4 \sum_{s=e,o} \left[d_n^{m,(i)s} u_n^{m,(i)s}(\mathbf{r}) \right], \quad \mathbf{r} \in \Omega(R^3) \quad (19)$$

where $c_n^{m,(i)s} = (a_n^{m,(i)s}, b_n^{m,(i)s}, c_n^{m,(i)s})$ and $d_n^{m,(i)s}$ denote the vector and the scalar constant coefficients of the harmonic potentials $\Phi(\mathbf{r})$, $\Phi_0(\mathbf{r})$, respectively, while

$$u_n^{m,(i)s}(\mathbf{r}) = S_n^{m,(i)}(\tau, \zeta) f^{ms}(\varphi) \quad \text{with} \quad f^{ms}(\varphi) = \begin{cases} \cos m\varphi, & s=e \\ \sin m\varphi, & s=o \end{cases}, \quad \varphi \in [0, 2\pi) \quad (20)$$

with s characterizing the even (e) and odd (o) part of the potentials.

On the other hand, any Stokes stream function can be represented [4] as

$$\psi(\tau, \zeta) = \sum_{n=0}^{\infty} \sum_{i=1}^4 \left[A_n^i \Theta_n^{(i)}(\tau, \zeta) + B_n^i \Omega_n^{(i)}(\tau, \zeta) \right], \quad \tau > 1, \quad |\zeta| \leq 1 \quad (21)$$

where the sum with the A -coefficients represents an element of the space $\ker E^2$ (separable solutions), whereas the sum with the B -coefficients stands for a function that is mapped to the space $\ker E^2$ under the action of the operator E^2 (equation (11)) (semiseparable solutions [4]). The eigenfunctions $\Theta_n^{(i)}(\tau, \zeta)$ and $\Omega_n^{(i)}(\tau, \zeta)$ of kind $i=1,2,3,4$ and order $n=0,1,2,\dots$ are provided through the Gegenbauer functions of the first and the second kind, using the theory of the generalized eigenfunctions, developed in [4]. The regular-on-the-axis solutions of equation of motion (equation (10)), are restricted to the proper subspace of $\ker E^4$, which is spanned by the eigenfunctions of odd kind and of order greater than or equal to two.

5. INTERRELATION BETWEEN STOKES AND PAPKOVICH – NEUBER EIGENMODES – THE PROLATE AND OBLATE SPHEROID

Taking into account that the flow fields $\mathbf{v}(\mathbf{r})$ and $P(\mathbf{r})$ are given by the two different representations (6), (7) ($\mathbf{r} \in \Omega(R^3)$) and (12), (13), (14) ($\mathbf{r} \in \Omega(R^2)$), the idea is to find transmission relations from one representation to the other. Specifically, for given velocity and pressure through the Stokes potential $\psi(\mathbf{r})$, $\mathbf{r} \in \Omega(R^2)$ (equation (21)), we seek for the equivalent Papkovitch-Neuber potentials $\Phi(\mathbf{r})$, $\Phi_0(\mathbf{r})$, $\mathbf{r} \in \Omega(R^3)$ (equations (18), (19)) which results with the same flow fields. In order to answer this question we proceed as

follows. Substituting equations (18) and (19) to Papkovitch-Neuber representation (6), (7) we derive relations for the flow fields in 3-D domains, furnished by the formulae

$$\mathbf{v}(\mathbf{r}) = \frac{1}{2} \sum_{n=0}^{\infty} \sum_{m=0}^n \sum_{i=1}^4 \sum_{s=e,o} \left\{ \mathbf{c}_n^{m,(i)s} u_n^{m,(i)s}(\mathbf{r}) - [\mathbf{c}_n^{m,(i)s} \cdot \mathbf{r} + d_n^{m,(i)s}] \nabla u_n^{m,(i)s}(\mathbf{r}) \right\} \quad (22)$$

for the velocity field, for every $\mathbf{r} \in \Omega(R^3)$, while for the total pressure field

$$P(\mathbf{r}) = -\mu \sum_{n=0}^{\infty} \sum_{m=0}^n \sum_{i=1}^4 \sum_{s=e,o} \left\{ \mathbf{c}_n^{m,(i)s} \cdot \nabla u_n^{m,(i)s}(\mathbf{r}) \right\}, \quad \mathbf{r} \in \Omega(R^3) \quad (23)$$

where in prolate spheroidal coordinates the operator ∇ is given by equation (8) and also

$$\begin{aligned} \mathbf{c}_n^{m,(i)s} = \frac{1}{\sqrt{\tau^2 - \zeta^2}} & \left\{ \left[a_n^{m,(i)s} \cos \varphi + b_n^{m,(i)s} \sin \varphi \right] \tau \sqrt{1 - \zeta^2} + c_n^{m,(i)s} \zeta \sqrt{\tau^2 - 1} \right] \hat{\mathbf{r}} \\ & + \left[a_n^{m,(i)s} \cos \varphi + b_n^{m,(i)s} \sin \varphi \right] \zeta \sqrt{\tau^2 - 1} - c_n^{m,(i)s} \tau \sqrt{1 - \zeta^2} \right] \hat{\boldsymbol{\zeta}} \Big\} \\ & + (-a_n^{m,(i)s} \sin \varphi + b_n^{m,(i)s} \cos \varphi) \hat{\boldsymbol{\varphi}} \end{aligned} \quad (24)$$

and

$$(\mathbf{c}_n^{m,(i)s} \cdot \mathbf{r}) = c \left[(a_n^{m,(i)s} \cos \varphi + b_n^{m,(i)s} \sin \varphi) \sqrt{\tau^2 - 1} \sqrt{1 - \zeta^2} + c_n^{m,(i)s} \tau \zeta \right] \quad (25)$$

Since the Papkovitch-Neuber representation refers to 3-D flow fields, we have to reduce the dimensions to two, considering rotational symmetry, in order to make the interrelation with the Stokes representation (2-D) possible. This is attainable and requires the same velocity on every meridian plane. That is, the velocity is independent of the angle φ

$$\partial \mathbf{v}(\mathbf{r}) / \partial \varphi = \mathbf{0}, \quad \mathbf{r} \in \Omega(R^2) \quad (26)$$

moreover, the velocity lacks of azimuthal component

$$\hat{\boldsymbol{\varphi}} \cdot \mathbf{v}(\mathbf{r}) = 0, \quad \mathbf{r} \in \Omega(R^2) \quad (27)$$

Applying equations (26) and (27) to the velocity field (22), we obtain relations for the Papkovitch-Neuber constant coefficients, which reflect the required rotational symmetry

$$a_n^{m,(i)s} = b_n^{m,(i)s} = 0, \quad n \geq 0, \quad m = 0, 1, \dots, n, \quad i = 1, 2, 3, 4, \quad s = e, o \quad (28)$$

$$c_n^{m,(i)s} = d_n^{m,(i)s} = 0, \quad n \geq 0, \quad m = 1, 2, \dots, n, \quad i = 1, 2, 3, 4, \quad s = e, o \quad (29)$$

Due to physical arguments which concerns most usual axisymmetric Stokes flow problems, we are interested in fields regular on the axis of symmetry (x_3 -axis, $\zeta = \pm 1$). Therefore, the terms involving Legendre and Gegenbauer functions of the second kind [6] must be excluded, i.e. all the eigenfunctions of even kind $S_n^{(i)}(\tau, \zeta)$, $\Theta_n^{(i)}(\tau, \zeta)$ and $\Omega_n^{(i)}(\tau, \zeta)$, $i=2, 4$, $n=0, 1, 2, \dots$ and the leading two eigenfunctions of odd kind, $\Theta_n^{(i)}(\tau, \zeta)$, $\Omega_n^{(i)}(\tau, \zeta)$, $i=1, 3$, $n=0, 1$, should be vanished. Thus, the following constant coefficients are set to nil

$$c_n^{(i)} = d_n^{(i)} = 0 \quad \text{and} \quad A_n^i = B_n^i = 0, \quad n \geq 0, \quad i = 2, 4 \quad (30)$$

$$A_0^i = B_0^i = A_1^i = B_1^i = 0, \quad i = 1, 3 \quad (31)$$

After long and tedious calculations, we interrelate the flow fields in view of equations (6), (7) with (18), (19) and equations (12), (13), (14) with (21) in addition with equations (28), (29), (30) and (31), using certain recurrence and orthogonality relations for the Legendre and the Gegenbauer functions [6]. What is actually happening is that the connection of the velocity and pressure fields has been transferred to the corresponding connection of the constant coefficients of the potentials (18), (19) and (21)

$$c_n^{(i)} = \frac{1}{c^2} \left[\frac{1}{(2n+3)(n+1)(n+2)} B_{n+2}^i - \frac{1}{(2n-1)(n-1)n} B_n^i \right], \quad n \geq 2, \quad i=1,3 \quad (32)$$

$$d_n^{(i)} = -\frac{1}{c} \left\{ \frac{2}{n(n+1)} A_{n+1}^i + \frac{1}{(2n-1)^2 (2n+3)^2} \left[\frac{(n+1)(2n-1)^2}{(2n+5)(n+2)} B_{n+3}^i - \left(4 + \frac{3}{n(n+1)} \right) B_{n+1}^i - \frac{n(2n+3)^2}{(2n-3)(n-1)} B_{n-1}^i \right] \right\}, \quad n \geq 2, \quad i=1,3 \quad (33)$$

and

$$d_1^{(i)} = -\frac{1}{c} \left\{ A_2^i + c^2 \left[-c_0^{(i)} + \frac{2}{25c^2} \left(\frac{1}{21} B_4^i - \frac{2}{3} B_2^i \right) \right] \right\}, \quad i=1,3 \quad (34)$$

$$\text{while specifically } B_2^3 = B_3^3 = c_1^{(3)} = 0 \text{ and also } c_0^{(i)}, d_0^{(i)} \in R, \quad i=1,3, \quad c_1^{(1)} \in R \quad (35)$$

Irrotational flows force, in addition, the constant coefficients B_n^i και $c_n^{(i)}$, $n \geq 2$, $i=1,3$ to become zero as it is dictated by equations (15), (21), and (32).

The corresponding results for the oblate spheroidal geometry can be readily obtained through the simple transformation [6]

$$\tau \rightarrow i\lambda \quad \text{and} \quad c \rightarrow -i\bar{c} \quad (36)$$

where $0 \leq \lambda \equiv \sinh \eta < +\infty$ and $\bar{c} > 0$ are the new characteristic variables of this system.

6. CONCLUSIONS

In this work a method for connecting two differential representations for axisymmetric Stokes flow is developed. Based on this method we examine the Papkovitch-Neuber and the Stokes representations, which offer solutions for such problems in spheroidal geometry. Furthermore, connection formulae are obtained by interrelating the flow fields using the corresponding potentials in terms of spheroidal eigenfunctions. Work under progress involves extension to harmonic *ellipsoidal* eigenfunctions [6] for the Papkovitch-Neuber representation and their Stokes flow counterparts in order to solve Stokes flow boundary problems involving small ellipsoidal particles moving within Stokes fluids.

7. REFERENCES

- [1] Fox R.W., McDonald A.T., *Introduction to Fluid Mechanics*, John Wiley & Sons, Inc., Third Edition, New York (1985).
- [2] Moon P., Spencer E., *Partial Differential Equations*, Health & Comp., Lexington (1969).
- [3] Xu X. and Wang M., *General Complete Solutions of the Equations of Spatial and Axisymmetric Stokes Flow*, Quart. J. Mech. Appl. Math., 44, 537-548 (1991).

- [4] Dassios G., Hadjinicolaou M. and Payatakes A.C., *Generalized Eigenfunctions and Complete Semiseparable Solutions for Stokes Flow in Spheroidal Coordinates*, Quart. of Appl. Math., Vol. LII, 1, 157-191 (1994).
- [5] Neuber H., *Ein neuer Ansatz zur Lösung räumlicher Probleme der Elastizitätstheorie*, Z. Angew. Math. Mech., 14, 203-212 (1934).
- [6] Hobson E.W., *The Theory of Spherical and Ellipsoidal Harmonics*, Chelsea Publishing Company, New York (1965).

NUMERICAL STUDY OF OSCILLATORY FLOW PAST PAIRS OF CYLINDERS AT LOW REYNOLDS AND KEULEGAN-CARPENTER NUMBERS

P. Anagnostopoulos, A. Koutras, and S. Seitanis
Department of Civil Engineering,
University of Thessaloniki, GR-54006 Thessaloniki, Greece

1. SUMMARY

The numerical study of oscillatory flow past a pair of cylinders is conducted herein. The finite element technique was favored for the solution of the Navier-Stokes equations, in the formulation where the stream function and the vorticity are the field variables. The streamlines and the vorticity contours were used for the flow visualization, and the unsteady in-line and transverse forces exerted on the cylinders were evaluated. The solution revealed the effect of the spacing of the cylinders on the flow pattern and on the hydrodynamic forces exerted on the cylinders.

2. INTRODUCTION

The numerical solution of oscillatory flow past a pair of cylinders placed transversely to the oncoming flow is attempted in the present study. In the oscillatory flow the flow velocity varies sinusoidally according to the relationship

$$U(t) = U_m \sin \varphi, \quad \varphi = 2\pi t/T \quad (1)$$

where U_m is the maximum flow velocity, T the oscillation period and t the instant from the inception of the flow oscillation. The planar oscillatory flow past a cylinder is controlled by two dimensionless numbers, the Keulegan-Carpenter number (KC) and the Reynolds number (Re). KC is defined as

$$KC = U_m T/D \quad (2)$$

where D is the cylinder diameter. The Reynolds number is given by

$$Re = U_m D/\nu \quad (3)$$

where ν is the kinematic viscosity of the fluid. The ratio of these two numbers is known as the frequency parameter, β , and is defined as

$$\beta = Re/KC = D^2/\nu T \quad (4)$$

The greatest part of related studies refers to flow past single cylinders. Experiments at low

KC have revealed that the flow can be classified into a number of different flow regimes, governed mainly by KC and dependent also on Re (Bearman et al. [1], Williamson [2], Sarpkaya [3], Tatsuno and Bearman [4]). At $KC \ll 1$ the flow remains attached, symmetrical and two-dimensional. As KC increases, the flow separates from the cylinder and remains symmetrical until KC reaches a critical threshold, whose value depends on the frequency parameter. If this critical KC is exceeded, the flow becomes asymmetric and various vortex shedding flow regimes are observed, at which the number of vortices shed in each oscillation cycle increases with the Keulegan-Carpenter number.

Apart from the experimental, several computational studies of the phenomenon have been conducted. Baba and Miyata [5], Murashige et al. [6], Wang and Dalton [7] and Justesen [8] used finite difference schemes, whereas Skomedal et al. [9], Graham and Djahansouzi [10] and Smith and Stansby [11] the discrete vortex method. More recently, Iliadis and Anagnostopoulos [12, 13] presented results of oscillatory flow past a cylinder with the finite element technique.

Experimental investigation of oscillatory flow past pairs of cylinders has been conducted by Williamson [2], and numerical by Skomedal et al. [9] and Koutras et al. [14]. The flow pattern past pairs of cylinders is more complicated than the one for flow past a single cylinder due to the hydrodynamic interference, which depends on the arrangement and the distance between the two cylinders.

In the study by Koutras et al. [14] the solution was confined to KC numbers extending up to 4, for which the flow remains symmetrical with respect to the horizontal axis of symmetry of the computational domain. In the present work KC numbers in the range between 5 and 10 are considered, for which asymmetries in the flow pattern are observed, whereas the value of the frequency parameter was 50, equal to that of the relevant study by Koutras et al. The two cylinders were placed transversely to the oncoming flow, whereas the spacing of their centers was varying between 1.2 to 5 diameters, forming a gap ranging between 0.2 to 4 diameters. The gap to diameter ratio will be denoted as g . The mathematical model of the problem consists of the well-known Navier-Stokes equations. In the present investigation the finite element technique was favored for the solution of these equations, in the formulation where the stream function and the vorticity are the field variables. The characteristic-Galerkin technique was employed for the temporal discretization, in an attempt to improve the approximation of time derivatives. The pressure distribution throughout the flow field was obtained from the solution of Poisson's equation. Unstructured meshes were employed for the solution of each configuration, generated by the advancing front technique.

3. THE COMPUTATIONAL TECHNIQUE

The equations of motion of a viscous incompressible fluid, in case that the stream function, Ψ , and the vorticity, ω , are the field variables, can be written as

$$\nabla^2 \Psi = -\omega \quad (5)$$

$$\frac{\partial \omega}{\partial t} + \frac{\partial \Psi}{\partial y} \frac{\partial \omega}{\partial x} - \frac{\partial \Psi}{\partial x} \frac{\partial \omega}{\partial y} = \nu \nabla^2 \omega \quad (6)$$

Equation (5) is of Poisson's type, whereas equation (6) is the well-known advection-diffusion equation. The characteristic-Galerkin technique, described by Zienkiewicz and Taylor [15],

was employed for an improved approximation of the time derivative in equation (6). Its application to equation (6), as explained by Seitanis and Anagnostopoulos [16], yields

$$\frac{\Delta\omega}{\Delta t} + \frac{\partial\Psi}{\partial y} \frac{\partial\omega}{\partial x} - \frac{\partial\Psi}{\partial x} \frac{\partial\omega}{\partial y} = \nabla^2\omega + \frac{\partial}{\partial x} \left[\frac{u^2 \Delta t}{2} \frac{\partial\omega}{\partial x} \right] + \frac{\partial}{\partial y} \left[\frac{v^2 \Delta t}{2} \frac{\partial\omega}{\partial y} \right] + uv\Delta t \frac{\partial^2\omega}{\partial x \partial y} \quad (7)$$

where u and v are the two components of the fluid velocity, determined in terms of Ψ as:

$$u = \partial\Psi/\partial y \text{ and } v = -\partial\Psi/\partial x.$$

From the application of the standard Galerkin technique for each element in equations (5) and (7) and the assembly for all elements, the following matrix equations are obtained

$$[K_1]\{\Psi\}_n = [K_2]\{\omega\}_n + \{R_1\} \quad (8)$$

$$\left[[K_3] + \frac{1}{\Delta t} [K_4] \right] \{\omega\}_{n+1} = \frac{1}{\Delta t} [K_4] \{\omega\}_n - \{R_2\} - \{R_3\} \quad (9)$$

where n and $n+1$ are two successive time levels, separated by the interval Δt . The coefficient matrices $[K_1]$, $[K_2]$, $[K_3]$ and $[K_4]$ are of square form, whereas $\{R_1\}$, $\{R_2\}$, $\{R_3\}$ and $\{R_4\}$ are column matrices (vectors).

For the determination of vorticity on the surface of the cylinders the equation of Stokes was used, whereas the pressure throughout the solution domain was evaluated from the solution of Poisson's equation, as explained by Iliadis and Anagnostopoulos [12]. From the distribution of pressure and shear on the surface of the cylinders the hydrodynamic forces F_x^* and F_y^* in the in-line and transverse direction were determined. The normalization of forces F_x^* and F_y^* by the quantity $0.5\rho U_m^2 D$ yields the dimensionless values F_x and F_y .

4. APPLICATION AND RESULTS

The first task for the solution is the generation of the computational grid. For each spacing between the cylinders a suitable mesh of three-node triangular elements was constructed, using the advancing front technique (Seitanis et al. [17]).

For each KC number the computational procedure was conducted for twenty oscillation cycles. The flow pattern is not symmetrical with respect to the horizontal axis of symmetry, and does not remain periodic at subsequent cycles. The KC number equal to 6 was selected for the presentation of the results, for a transverse spacing between the centers of the two cylinders equal to 1.4 and 2 diameters (g equal to 0.4 and 1). The streamlines and vorticity contours were generated from the nodal values of the stream function and vorticity, and are presented for the twentieth cycle at $\phi=90^\circ$ in Fig. 1. We can see that for $g=0.4$ the displacement of the two vortices flanking the gap is greater than those at the opposite side, forming a narrow passage between the cylinders. For $g=1$ the vortices formed at either side of each cylinder do not vary substantially, whereas vortices formed during previous cycles are still detectable. Finally, the unsteady in-line and transverse forces on the cylinder were calculated from the pressure and shear around the cylinder surface, and are depicted for the last ten cycles in Fig. 2. The aperiodicity of the flow field at subsequent cycles is reflected on the time histories of the hydrodynamic forces. The amplitude of both the in-line and the

transverse force is larger for $g=0.4$.

The rms values of F_x and F_y for KC ranging between 0.1 and 10 derived from the force traces are illustrated in Fig. 3. The values of F_x (rms) and F_y (rms) are larger for $g=0.4$, whereas the F_y (rms) values become very close for KC between 5 and 6.

5. CONCLUSIONS

A numerical study of viscous oscillatory flow past pairs of cylinders was conducted. The distance between the cylinders affects the flow pattern and the hydrodynamic forces exerted on the cylinders. The rms values of both the in-line and the transverse force increase when the spacing between the cylinders is reduced.

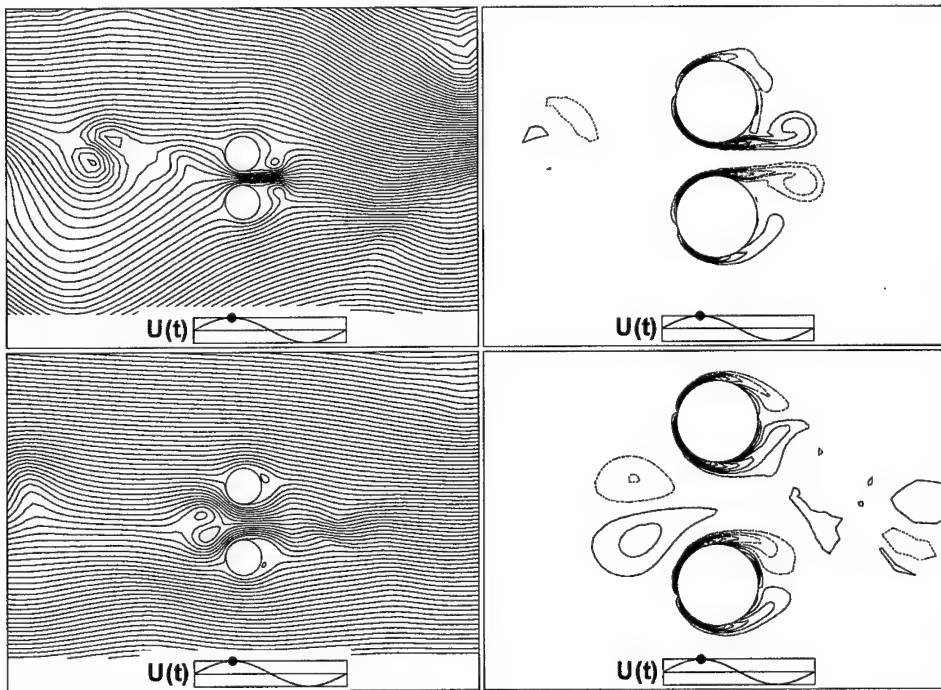


Figure 1: Streamlines (left) and vorticity contours (right), for $\phi=90$ degrees; $g=0.4$ (upper frames), $g=1$ (lower frames).
The solid lines represent positive and the dashed lines negative vorticity.

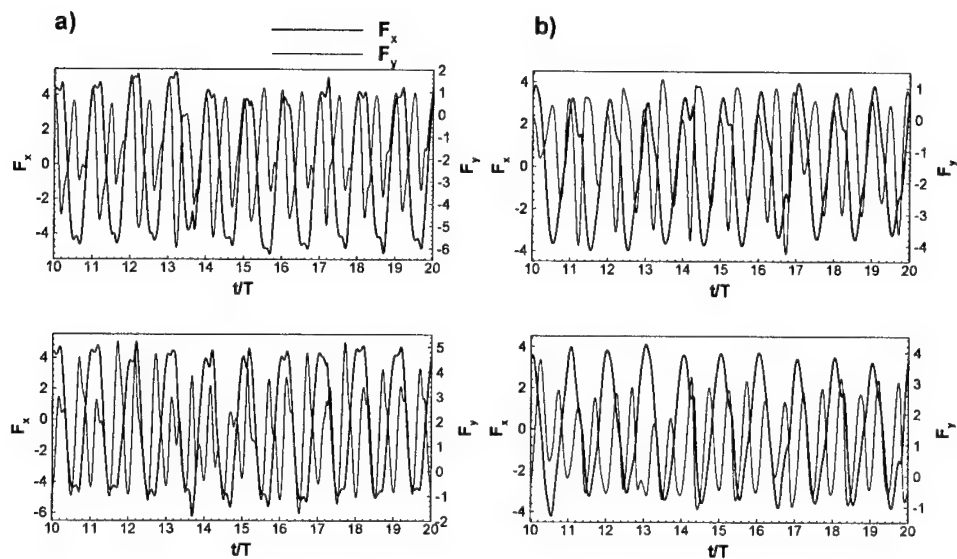


Figure 2: In-line and transverse forces on the cylinders; a) $g=0.4$ and b) $g=1$.
The upper graph corresponds to the upper and the lower to the lower cylinder.

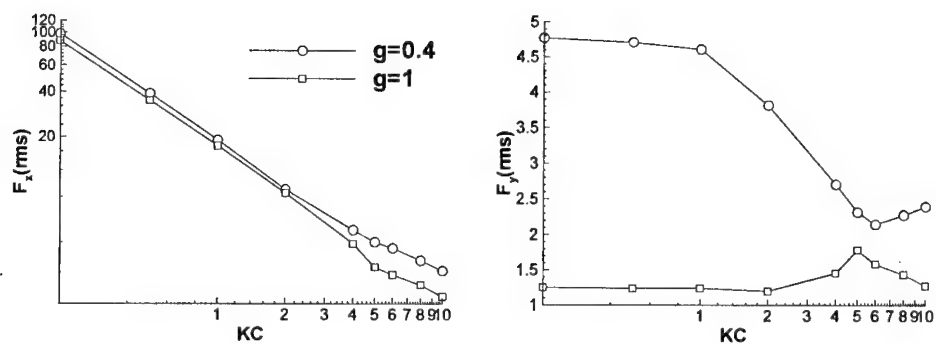


Figure 3: Rms value of the in-line and transverse force vs KC.

6. REFERENCES

- [1] Bearman, P. W., Graham, J. M. R., Naylor, P. and Obasaju, E. D., The role of vortices in oscillatory flow about bluff bodies, in *Proc. of the Int. Symposium on Hydrodynamics in Ocean Engineering*, The Norwegian Inst. of Technology, Trondheim, Norway (1981) 621-635.
- [2] Williamson, C. H. K., Sinusoidal flow relative to circular cylinders, *J. Fluid Mech.*, 155, 141-174 (1985).
- [3] Sarpkaya, T., Forces on a circular cylinder in viscous oscillatory flow at low Keulegan-Carpenter numbers, *J. Fluid Mech.*, 165, 61-71 (1986).
- [4] Tatsuno, M. and Bearman, P. W., A visual study of the flow around an oscillating cylinder at low Keulegan-Carpenter number and low Stokes numbers, *J. Fluid Mech.*, 211, 157-182 (1990).
- [5] Baba, N. and Miyata, H., Higher-order accurate difference solutions of vortex generation from a circular cylinder in an oscillatory flow, *J. Comput. Phys.*, 69, 362-396 (1987).
- [6] Murashige, S., Hinatsu, M. and Kinoshita, T., Direct calculations of the Navier-Stokes equations for forces acting on a cylinder in oscillatory flow, in *Proc. of the 8th Int. Conf. on Offshore Mech. and Arctic Engineering Vol. 2*, The Hague (1989) 411-418.
- [7] Wang, X. and Dalton, C., Oscillating flow past a rigid circular cylinder: A finite difference calculation, *J. of Fluids Engineering (ASME)*, 113, 377-383 (1991).
- [8] Justesen, P., A numerical study of oscillating flow around a circular cylinder, *J. Fluid Mech.*, 222, 157-196 (1991).
- [9] Skomedal, N. G., Vada, T. and Sortland, B., Viscous forces on one and two circular cylinders in planar oscillatory flow, *Appl. Ocean Res.*, 11, 114-134 (1989).
- [10] Graham, J. M. R. and Djahansouzi, B., 1989, Hydrodynamic damping of structural elements, in *Proc. of the 8th Int. Conf. on Offshore Mech. and Arctic Engineering Vol. 2*, The Hague (1989) 289-293.
- [11] Smith, P. A. and Stansby, P. K., Viscous oscillatory flows around cylindrical bodies at low Keulegan-Carpenter numbers using the vortex method, *J. Fluids and Struct.*, 5, 339-361 (1991).
- [12] Iliadis, G. and Anagnostopoulos, P., Viscous oscillatory flow around a circular cylinder at low Keulegan-Carpenter numbers and frequency parameters, *Int. J. for Numerical Methods in Fluids*, 26, 403-442 (1998).
- [13] Iliadis, G. and Anagnostopoulos, P., Numerical visualization of oscillatory flow around a circular cylinder at $Re=200$ AND $KC=20$ - An aperiodic flow case, *Communications in Numerical Methods in Engineering*, 14, 181-194 (1998).
- [14] Koutras, A., Anagnostopoulos, P. and Seitanis, S., Numerical solution of oscillatory flow past a pair of cylinders, in *Proc. of the 8th National Conference of the Hellenic Hydrotechnic Association*, Athens (2000) 85-92.
- [15] Zienkiewicz, O. C. and Taylor, R. L., *The Finite Element Method*, 4th Ed., McGraw-Hill, London (1991).
- [16] Seitanis, S. and Anagnostopoulos, P., Numerical visualization of cross-flow past two staggered rows of cylinders, in *Proc. of the 3rd National Congress on Computational Mechanics Vol. 2*, N. Aravas and J.T. Katsikadelis (Eds), Volos (1999) 803-810.
- [17] Seitanis, S. A., Rorris, L. P., Iliadis, G. D. and Anagnostopoulos, P., Unstructured mesh generation for domains with irregular boundaries, in *Proc. of 5th National Congress on Mechanics Vol. 1*, P.S. Theocaris, D.I. Fotiadis and C.V. Massalas (Eds), Ioannina (1998) 444-451.

INVERSE DESIGN OF AERODYNAMIC SHAPES USING ANT COLONY OPTIMIZATION

T. Zervogiannis, V. Assouti,
K. Gagas, A. Kaounis and K.C. Giannakoglou

National Technical University of Athens,
P.O. Box 64069, Athens 157 10, GREECE.
e-mail :kgianna@central.ntua.gr

1 SUMMARY

In the past, Ant Colony Optimization methods have been used to solve combinatorial optimization problems, like the well known Traveling Salesman Problem. This paper introduces a novel extension of the conventional method which is capable of solving optimization problems with continuous search spaces for the free variables. For this purpose, various notions which are implicit to the Ant Colony Optimization techniques are modified in conformity with the particularities of search problems in continuous spaces. The proposed method will be used for the design of aerodynamic shapes, isolated airfoils or compressor cascade airfoils.

2 INTRODUCTION

The Ant Colony Optimization (*ACO*) method is a recently proposed metaheuristic. In the past, it has been used to solve stochastic combinatorial optimization problems, [1], [2], such as the Traveling Salesman Problem (*TSP*) or routing problems. In all these problems, integer numbers should be arranged in the proper order which ensures the minimization of a functional. In the (*ACO*) method, ants stand for agents with search capabilities similar to those of real ants. They act synergetically, i.e. in populations, seeking for the optimum route. A new population of ants comes after the previous one and inherits coded information about the quality of previously evaluated routes. Information is communicated in the form of pheromone trails laid down by the previous populations. Pheromone trails affect ants' decisions about where to go next, with a probability which is proportional to the amount of pheromone.

This paper aims to extend the *ACO* methods' capabilities to new scientific areas, such as the inverse or optimum design of aerodynamic shapes. In the past, other optimization methods, such as Genetic Algorithms (*GAs*), have been widely used for the design of ducts of airfoils, [3]. The aim is to design shapes along which the pressure (or velocity) distribution at given flow conditions matches a target one. The shape parameterization, which points out the design variables, is an evident prerequisite.

Computational Fluid Dynamics (*CFD*) tools are employed for the evaluation of candidate solutions. In contrast to combinatorial problems, the inverse design of a shape (*IDS*) is a problem with continuous search spaces for the design variables and a likely complex solution landscape.

The use of *ACO* in this kind of problems is, in fact, novel. To the authors knowledge, this could be the first use of *ACO* in a problem with real (continuous) free parameters. The concept is simple; provided that we do possess an effective *ACO* method (and the relevant software) for solving the *TSP* problem, modifications should be employed so as to transform the *IDS* problem to an equivalent *TSP*. The route length, which is the cost function in the *TSP*, is taken to be the deviation of the pressure or velocity distribution along the shape contour from the target one.

For the readers which are not familiar with the *ACO* method, this will be presented below at length. Then, its novel implementation to the *IDS* problem will be described, followed by indicative results.

3 THE *ACO* METHOD

Ants, though almost blind animals, are capable of finding the shortest path from their nest to areas rich in food. Many individuals, perhaps almost the entire ant colony, should cooperate to achieve this goal. In the search of the shortest route to the food, ants use to exploit pheromone trails which are laid on the ground by each one of them as they move. Pheromone is a substance easily traced by subsequent ants, which are likely to follow the trail rather than move randomly. When an ant follows an existing pheromone trail, the latter will be further reinforced by its own pheromone. Thus, a frequently used trail becomes more attractive and is likely to be followed by a continuously increasing number of ants. The ants' behaviour in search of food is the concept of the so-called *ACO* method. This is a population-based algorithm, where pheromone trails define the feedback of information between ants. Since moving ants act independently, *ACO* is readily amenable to parallelization.

The amount of pheromone a moving agent lays on the ground can be computed in various ways. We will present one of them on the basis of the *TSP* problem. In the *TSP*, given n towns (with known coordinates) the salesman should visit all of them once and then return to the starting town, with the minimum route length.

A possible way for solving the *TSP* using *ACO* is through as many ants as the number of towns (n agents). Each ant starts its route from a different town. The next town to be visited is chosen with a probability p_{ij} that depends on the distance d_{ij} between the current i and the next j town to be visited (already visited towns are excluded) and the amount of pheromone τ_{ij} laid on the connecting edge. This probability is expressed as follows:

$$p_{ij} = \frac{\tau_{ij}^\alpha d_{ij}^{-\beta}}{\sum_j \tau_{ij}^\alpha d_{ij}^{-\beta}} \quad (1)$$

The inverse of the distance between two towns (d_{ij}^{-1}) is usually referred to as visibility. Upon completion of n (closed) tours by the current population agents, the pheromone trails τ_{ij} are updated as $\tau_{ij}^{new} = \rho \tau_{ij}^{old} + \Delta \tau_{ij}$, where $(1 - \rho)$ is the evaporation coefficient.

The pheromone quantity $\Delta\tau_{ij}$, contributed by the k -th ant which rounded off its tour with length D_k is $\Delta\tau_{ij} \propto D_k^{-1}$ if the k -th ant used edge (i, j) , otherwise $\Delta\tau_{ij} = 0$.

4 INVERSE DESIGN OF AIRFOILS

The inverse design of airfoils can be envisaged as a minimization problem which employs: (a) one or more targets; here the target is to achieve the desired pressure coefficient distribution over the airfoil walls, at given flow conditions, (b) the parameterization of the airfoil contour; Bezier-Bernstein polynomials are used where the ordinates of the Bezier points are the design variables of degrees of freedom (*dofs*), (c) the evaluation tool; incompressible fluids and irrotational flows are assumed, modelled through a simple and non-costly tool, i.e.. the panel method, [4]; however, the method may readily incorporate more accurate tools (Navier-Stokes or Euler equations solvers), in a straightforward manner, (d) the optimization tool, which in our case is a novel *ACO* method, as it will be described in the next paragraph.

5 THE EXTENDED *ACO* ALGORITHM

Let the airfoil contour be described using two Bezier curves, one for the pressure side (from the trailing to the leading edge, with n_1 control points) and the other for the suction side (in the opposite direction, with n_2 control points). Leading and trailing edge points are kept fixed. Fixed is also the abscissa of any other control point giving rise to $n = n_1 + n_2 - 4$ *dofs*. In the example of fig. 1 (left), $n_1 = 5$, $n_2 = 5$ and $n = 6$; vertical lines indicate the search space for the ordinates of the n Bezier control points. Let also assume that the combined effects of the Bezier polynomial and flow solver on the n *dofs*, $\vec{Y} = (y_1, \dots, y_n)$, yields a curve (i.e. the pressure distribution) that should minimize its deviation from the target curve. Both curves are shown in fig. 1 (right), for the airfoil pressure side. In this example, the payoff value associated with \vec{Y} is the area enclosed by the two curves (plus the corresponding area for the suction side).

Under the previous assumptions, we should first cast the *IDS* problem illustrated in fig. 1 as an equivalent *TSP* (to be referred to as *eTSP*), which will then be solved through the modified *ACO* algorithm. In the *eTSP* the salesman should visit n territories, instead of n towns. Ants should mimic this itinerary. The territories associated with each *dof* are the vertical lines in fig. 1. The sequence of the territories to be visited is known and the tour is closed. The optimization method should locate the sequence of visiting points over each territory so that the total path be of minimum length. For the path followed by an ant, the term "length" is used metaphorically and stands for the cost associated with the corresponding airfoil. To compute this cost, the evaluation software described in the previous paragraph should be used.

In the *ACO* algorithm, eq. 1, the probability with which the next destination is chosen by an ant depends on two parameters, namely the distance d and the pheromone trail τ . The former represents a sort of *local* data (correlating the actual position of an agent and the towns that are likely to be visited next) whereas the latter stands for *global* information (i.e. information related to the evaluation of \vec{Y} as a whole). Local data can be defined in many ways. Here, we will assume that the relative position of the k^{th} and $(k+1)^{th}$ Bezier points is associated with the hatched area shown in fig. 1. This

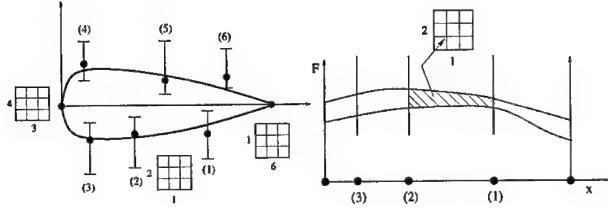


Figure 1: Design of airfoils using Bezier points. Global and local costs and the grids for storing probabilities.

can readily be generalized for all *dofs*. So, the global cost associated with an agent tour and the corresponding airfoil shape splits to partial or “local” costs using separators that can either be defined by the user or set automatically (vertical separators in fig. 1, right). A noticeable feature of the proposed method is that information is stored in a discrete way, though it is used as a continuous field. One grid for storing local (i.e. distances) and another one for storing global (feromone trails) data are needed for each pair of consecutive territories (i.e. *dofs*), fig. 1.

A cycle corresponds to n tours with n agents, each starting from a different territory. The closed tour by any agent corresponds to n values $\vec{Y} = (y_1, \dots, y_n)$ and yields an airfoil shape. Through its evaluation, global and local (or partial) costs are computed. These are pieces of information that should be stored over the aforementioned grids. On each grid, for instance the k^{th} one, the y_k and y_{k+1} values are used to locate a point on this grid. The $\tau_{k,k+1}$ and $d_{k,k+1}$ values are computed as the inverse of the global and the corresponding local cost, respectively. Then, all grid nodes are given a feromone and distance value by employing a 2D exponential decay based on distances measured over the grid. At the end of the cycle, pheromone is allowed to evaporate, using a law similar to the one employed in the standard *ACO*. Probabilities are stored over the same nodes by post-processing the stored pheromone and distance values.

The exploitation of the probabilities stored over the grid nodes during the search is simple. The k^{th} agent starts from a point (not necessarily coinciding with a grid node) on the k^{th} grid, determined in a probabilistic way on the basis of the nodal probability values. Then, each agent moves in the clockwise direction. Its next station on the next territory can be found by entering the grid with the abscissa (known from the previous station) and by computing the ordinate in a probabilistic way.

6 RESULTS

First, an assessment of the present method in the conventional *TSP* problem will be given. In the Eilon’s 50-town problem, [5], the best computed route is shown in fig. 2. The minimum computed route length is equal to 428.1. This is similar to results exposed in other works, [5], by means of *ACO* or *GAs*.

The redesign of the symmetric isolated *NACA12* airfoil, at zero and 10° incidence as well as the redesign of the *NACA65* cascade airfoil (stagger angle= 30° , solidity=1.25, inlet flow angle= 48°) have been analyzed using the proposed method. Results are presented in figs. 3, 4 and 5. Using the known airfoil shapes and the panel method

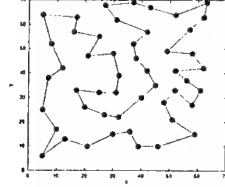


Figure 2: Optimum solution to the Eilon's 50-town *TSP*.

solver, we have first computed the pressure distributions over their contours, at the aforesaid flow conditions. These have been used as target distributions, so the sought for airfoil shapes were known beforehand. In all cases, $\alpha = \beta = 0.8$ and $\rho = 0.5$. In the *NACA12* case, $n_1 = n_2 = 8$ whereas in the *NACA65* one $n_1 = 9$ and $n_2 = 8$.

As it may be seen from the comparison of the best predicted and target distributions (or even by comparing starting and predicted airfoils), our method gives very satisfactory results. The cost of the three redesigns is illustrated in fig 6. In this figure, the abscissa stands for calls to the evaluation *CFD* tool which determines the computing cost of the optimization method. To avoid all misunderstanding, we should point out that the use of the panel method leads to almost negligible computing cost per evaluation, but the last figure is a very good indication of the computing cost in case of a more *CPU*-demanding *CFD* method (eg. Navier-Stokes solver).

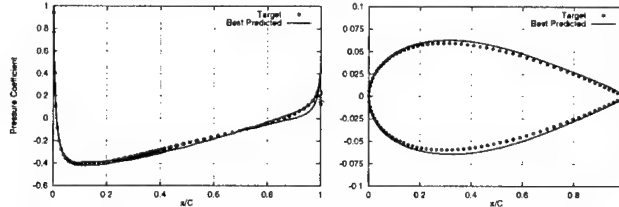


Figure 3: Redesign of the *NACA12* isolated profile at zero incidence: target and best computed pressure coefficient distribution along with the corresponding airfoil shapes.

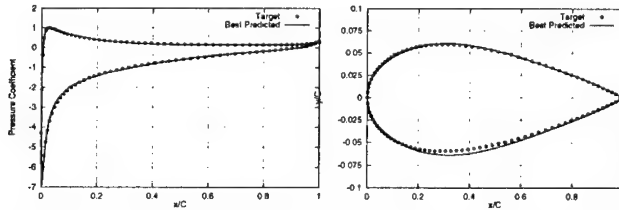


Figure 4: Redesign of the *NACA12* isolated profile at 10° incidence: target and best computed pressure coefficient distribution along with the corresponding airfoil shapes.

7 CONCLUSIONS

A new method has been proposed for optimization problems involving degrees of freedom that may vary over continuous search spaces. Such a typical problem is the inverse

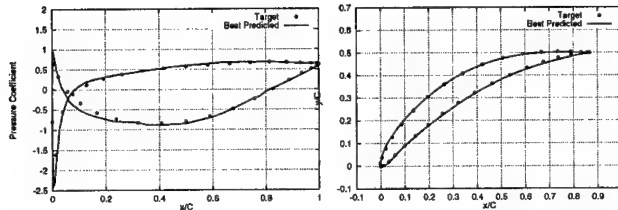


Figure 5: Redesign of the *NACA66* compressor cascade: target and best computed pressure coefficient distribution along with the corresponding airfoil shapes.

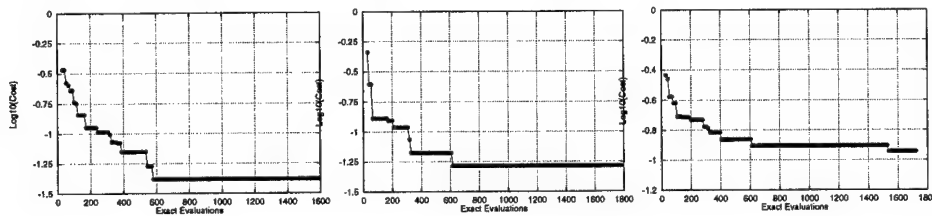


Figure 6: Convergence histories.

design of aerodynamic shapes. The new method is based on the Ant Colony Optimization algorithm, used so far only for combinatorial optimization problems. The new method required the definition of quantities that mimic any quantity that appears in the traditional *ACO* method. In this respect, global and local costs have been defined and used after being stored on properly defined grids. The method proved to be an effective optimization tool for the inverse design of isolated airfoils or cascades.

References

- [1] M. Dorigo, V. Maniezzo, and A. Coloni. The ant system: Optimization by a colony of cooperating agents. *IEEE Transactions on Systems, Man and Cybernetics - Part B*, 26:1–13, 1996.
- [2] N. Monmarche, Venturini, and M. G. Slimane. On how *pachycondyla apicalis* ants suggest a new search algorithm. *Future Generation Computer Systems*, 16:937–946, 2000.
- [3] K.C. Giannakoglou. Acceleration of genetic algorithms using artificial neural networks - theoretical background. Von-Karman Institute LS 2000-07, May 2000.
- [4] J.L. Hess. Panel methods in computational fluid dynamics. *Annu. Rev. Fluid Mech.*, 22:255–274, 1990.
- [5] V.M. Kureichickl, V.V. Miagkikh, and A.P. Topchy. Genetic algorithm for solution of the traveling salesman problem with new features against premature convergence. Proc. of GA + SE'96, Gursuf, Ukraine, 1996.

STRATIFIED TWO-PHASE FLOW OF VAPOUR BOUNDARY LAYER- CONDENSATE FILM OVER A CYLINDER

D. N. Smyrniaios¹, N. A. Pelekasis² and J. A. Tsamopoulos³

Laboratory of Computational Fluid Mechanics

Department of Chemical Engineering

University of Patras, GR-26500 Patras, Greece

¹e-mail: smyrniaios@chemeng.upatras.gr, ²e-mail: pel@chemeng.upatras.gr

³e-mail: tsamo@chemeng.upatras.gr

1. SUMMARY

The current study examines the steady two-dimensional laminar flow of a stream of saturated vapor flowing over a cylinder that is kept at a uniform temperature, below the saturation temperature. Owing to the temperature difference between the vapor stream and the solid surface a film of condensate is generated that flows along the surface due to shear, pressure-drop and gravity. In the limit as the boundary layer and film thickness remain smaller than the radius of curvature of the surface a simplified lubrication-type formulation describes the temperature and flow fields in the film, whereas the usual boundary layer formulation is applied in the vapor boundary layer. As the effect of adverse pressure drop becomes more pronounced it is shown that the solution exhibits two different types of singularity in the rear part of the cylinder. The first one takes place in the vapor phase in a region where very small velocities prevail in conjunction with vanishing shear rate, giving rise to an off-wall separation. The second one is a typical Goldstein singularity, it appears at the tube wall and it is associated with vanishing skin friction (wall shear) and rapidly increasing film thickness. Preliminary comparison of the computed heat transfer coefficient with experimental measurements indicate that heat transfer is enhanced when either one of the two types of singularity takes place, owing to flow recirculation.

2. INTRODUCTION

Laminar film condensation is of great practical importance in many technical applications such as the design and optimal operation of condensers, heat exchangers, wetted wall towers etc. In general, it affects the operation of contact devices where saturated vapor is used as a means for transferring heat. Early studies applied elements of boundary layer theory in order to account for vapor stream-condensate film interaction in the context of free, [1], and forced convection, [2]. Fujii et al., [3], examined the combined effect of forced and free convection on the heat transfer for flow of a stream of saturated vapor over a horizontal cylindrical tube taking the direction of the oncoming vapor stream to be parallel with gravity. Ignoring the effect of pressure drop in the flow of the condensate and assuming a simplified form of the

velocity profile in the vapor boundary layer they were able to calculate the heat transfer coefficient and compare it against their own experimental observations with favorable results, especially for slow free stream velocities of the oncoming vapor stream. More recently, Rose [4], improved the model developed by Fujii et al., in the limit of large suction velocities across the vapor-condensate interface, by accounting for pressure drop in the condensate. Thus, they were able to capture flow separation in the downstream region of the flow, in the form of the classical Goldstein singularity appearing at the tube wall, and predict the heat transfer coefficient for large free stream velocities of the vapor stream. The present study accounts for the effect of vapor-condensate interaction for both low and large suction velocities at the interface and for the effect of pressure drop in the condensate for the same combined forced and free convection over the same cylindrical geometry that was tackled in [3] and [4]. In this fashion the flow and temperature fields are obtained in the two phases until a point of singularity (indicating flow separation or flow recirculation in general) is reached. In addition, the location of the singularity is mapped, at the wall or near the interface depending on the problem parameters, and a connection is attempted between that location and certain discrepancies between predicted and experimentally observed values of the Nusselt number.

2. PROBLEM FORMULATION

The laminar film condensation of a stream of saturated vapor, temperature T_s , on a horizontal cylindrical tube that is maintained at subcooled conditions, temperature $T_w < T_s$, is examined. The oncoming vapor stream is approaching the tube with a free stream velocity, U_∞ , which is taken to be aligned with gravity for simplicity. Owing to the temperature difference between the vapor stream and the tube, vapor condensation takes place giving rise to a film of condensate that flows down the cylindrical tube surface, Fig. 1.

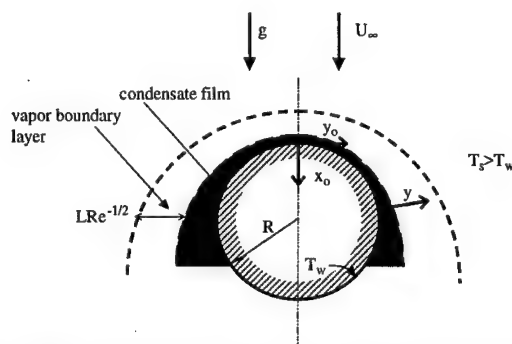


Figure 1: Schematic representation of the flow pattern under consideration.

The vapor stream is considered to be isothermal at its saturation temperature which is determined by the operating pressure of the process. The temperature of the film is allowed to vary from the saturation temperature at the interface down to the wall temperature. With the exception of viscosity and thermal conductivity all other properties of the condensate are taken to be independent of the local temperature level and acquire values that are obtained at saturation conditions using steam tables. Taking advantage of the similarity of the current problem with that of the boundary layer flow of air past solid surfaces in the presence of rainfall, the methodology developed by Smyrniotis, Pelekasis and Tsamopoulos, [5], is adopted. Thus, in the vapor phase the governing equations, assuming that the cylinder radius,

$R=L/\pi$, is much larger than the boundary layer thickness, take the familiar form of the classical boundary layer equations for flow past a flat plate.

At the vapor-condensate interface, $y_s = \epsilon H(x)$, $y_c = H(x)$ we have:

continuity of tangential velocity,

$$u_s = \frac{u_f}{U_\infty} u_c \quad (1)$$

continuity of mass flow across the interface,

$$v_s = \frac{u_f}{U_\infty} \frac{H_f}{L Re^{-1/2}} \left[\frac{\rho_{cs}}{\rho_{ss}} v_c - \left(\frac{\rho_{cs}}{\rho_{ss}} - 1 \right) \frac{dH}{dx} u_c \right] \quad (2)$$

continuity of tangential and normal stress (ignoring the action of surface tension),

$$\frac{\partial u_s}{\partial y_s} = \frac{\partial u_c}{\partial y_c} \frac{\mu_{cs}}{\mu_{ss}} \frac{u_f}{U_\infty} \frac{L Re^{-1/2}}{H_f}, \quad P_c = P_s \quad (3a, b)$$

balance between the latent heat liberated due to condensation at the interface and the heat conducted across the interface and into the condensate,

$$-\frac{k_{cs} \Delta T}{H_f} \frac{\partial \Theta_c}{\partial y_c} = h_{fg} \rho_{cs} u_f \frac{H_f}{L} \left(v_c - \frac{dH}{dx} u_c \right) \quad (4)$$

(with h_{fg} denoting the latent heat of condensation per unit mass of steam) and saturation conditions for the temperature field,

$$\Theta_s = \Theta_c = 1 \quad (5)$$

In the film of condensate the problem formulation becomes,

x-momentum

$$\epsilon^2 \frac{\rho_{cs}}{\rho_{ss}} \left(\frac{\mu_{ss}}{\mu_{cs}} \right)^2 \left(u_c \frac{\partial u_c}{\partial x} + v_c \frac{\partial u_c}{\partial y_c} \right) = \frac{1}{Fr} \left(\frac{\rho_{cs}}{\rho_{ss}} - 1 \right) \left(\sin \beta \frac{\partial x}{\partial x_0} - \cos \beta \frac{\partial x}{\partial y_0} \right) - \quad (6)$$

$$\frac{dP_c}{dx} + \frac{1}{\epsilon} \frac{\partial}{\partial y_c} \left(\mu_c \frac{\partial u_c}{\partial y_c} \right), \quad Fr = \frac{U_\infty^2}{gL}$$

y-momentum and continuity

$$\frac{\partial P_c}{\partial y_c} = 0, \quad \frac{\partial u_c}{\partial x} + \frac{\partial v_c}{\partial y_c} = 0 \quad (7a, b)$$

differential heat transfer equation including inertia terms and transverse conduction

$$\epsilon^3 Pr \frac{\rho_{cs}}{\rho_{ss}} \left(\frac{\mu_{ss}}{\mu_{cs}} \right)^2 \left(u_c \frac{\partial \Theta_c}{\partial x} + v_c \frac{\partial \Theta_c}{\partial y_c} \right) = \frac{\partial}{\partial y_c} \left(k_c \frac{\partial \Theta_c}{\partial y_c} \right), \quad Pr = \frac{c_{p,cs} \mu_{cs}}{k_{cs}} \quad (8)$$

no slip, no penetration and constant temperature, at the periphery of the cylindrical tube,

$$y_c = 0, \quad u_c = v_c = 0, \quad \Theta_c = 0 \quad (9)$$

Balancing terms in the tangential stress balance, eq. (3a), and the heat balance at the interface, eq. (4), we obtain a measure for the film thickness, H_f , and the film velocity u_f ,

$$\varepsilon = \frac{H_f}{L Re^{-1/2}} = \left(\frac{c_{pcs} \Delta T}{Pr h_{fg}} \right)^{1/3} \left[\left(\frac{\mu_{cs}}{\mu_{ss}} \right)^2 \frac{\rho_{ss}}{\rho_{cs}} \right]^{1/3} \quad (10)$$

$$\frac{u_f}{U_\infty} = \frac{H_f}{L Re^{-1/2}} \frac{\mu_{ss}}{\mu_{cs}} \quad (11)$$

More details on the problem formulation as well as the numerical solution are given in Smyrniotis, Pelekasis and Tsamopoulos, [6].

3. RESULTS

Once the operating fluid is determined and the bulk pressure of the process is chosen, the saturation temperature, T_s , of the system is fixed and so are the thermophysical properties of the two phases at saturation. Thus, the density and viscosity ratios, ρ_{ss}/ρ_{cs} , μ_{ss}/μ_{cs} as well as the Prandtl number, Pr , acquire specific values. Next, the wall temperature, T_w , and free stream velocity, U_∞ , are assigned values thus setting ε and Fr as the last two problem parameters. As ε increases the film thickness increases as well and, contrary to the findings reported in [4] where flow separation was observed only when

$$\frac{\rho_{ss}}{\rho_{cs}} \frac{U_\infty^2}{g 2R} = Fr \frac{\pi}{2} > \frac{1}{8} \quad (12)$$

here separation is observed for a much wider range of values with the difference that in the present study two different types of separation are observed. In the downstream region and for small values of ΔT the flow exhibits a separation point at the tube wall as a result of the adverse pressure gradients that develop in this region. In particular, as the separation point is approached the shear stress at the tube wall vanishes and an inflection point appears in the vapor stream. In addition, the film thickness starts increasing abruptly, an effect also observed in [4], and computations cannot proceed further. These are all typical effects of the Goldstein singularity that signal the onset of recirculation and, possibly, separation. As ΔT increases the film thickness increases as well and the inertia of the condensate has a lubricating effect on the flow thus pushing the separation point further downstream. The lubricating effect of the film has also been observed in [2] in a study of laminar film condensation over a cylindrical surface in the absence of gravity.

Further increase of ε results in the appearance of a region with vanishing velocities and shear rate near the fluid/fluid interface, i.e. of a singularity of a different type than the one discussed above which appears at the tube wall. In this case, the film thickness does not exhibit such an abrupt increase. More specifically, near the film-vapor interface a region of vanishingly small velocities and shear rates appears indicating the tendency for back-flow to appear. Computations cannot capture this part of the flow because the boundary layer formulation is no longer valid and an interactive boundary layer formulation has to be adopted which is in the scope of a future study. As ε further increases the lubricating effect of the film persists pushing the point of singularity downstream.

A similar transition from a wall singularity to an off wall singularity is observed when Fr is decreased, or equivalently, as the free stream velocity is reduced corresponding to gradually eliminating the component of forced convection from the flow. Due to its orientation, gravity opposes the adverse pressure gradients in the downstream region hence weakening the wall

singularity. For large values of Fr forced convection dominates and wall separation is observed. Below a certain threshold value, the off wall singularity that was described in the previous paragraph appears again in the downstream region. In fact as Fr further decreases, the singularity disappears, the Nusselt limit is captured and integration of the flow until the trailing edge of the tube becomes possible. Figure 2 shows the loci of the points that separate the two different regions in (Fr, ε) space where one or the other type of singularity appears, for different values of the operating pressure or the saturation temperature, T_s , for the steam-water system. For a given saturation temperature the points belong to a curve that separates the two regions in such a way that for large values of Fr , large free stream velocities, and small values of ε , thin film, "wall separation" takes place. An interesting aspect of Figure 2 is that upon proper redefinition of Fr and ε as,

$$\varepsilon' = \left(\frac{C p_{cs} \Delta T}{Pr h_{fg}} \right)^2 \left(\frac{\rho_{cs}}{\rho_{ss}} \right)^{3/2} \left(\frac{\mu_{cs}}{\mu_{ss}} \right)^{1/2}, \quad Fr' = \frac{U_\infty^2}{gL} \left/ \left(\frac{\rho_{cs}}{\rho_{ss}} - 1 \right) \right. \quad (13)$$

the curves separating the two regions tend to collapse into one.

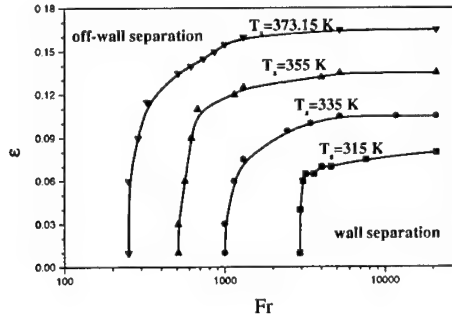


Figure 2: Loci of threshold points separating regions of "off-wall separation" from those where "wall separation" is observed in the (Fr, ε) space for different values of the saturation temperature, T_s , for the steam-water system.

Finally, the effect of Fr and ε on the heat transfer coefficient for the system steam-water is shown in figure 3. In particular, increasing the temperature difference between the vapor stream and the wall (larger ε) results in smaller heat transfer coefficients, $Nu_{\pi/2}$, and larger skin friction coefficients, $C_{f,\pi/2}$ (figure 4), averaged over the front portion of the tube. On the other hand, increasing the free stream velocity (larger Fr) results in a thinner condensate and, consequently, smaller heat transfer coefficient and skin friction. The same pattern is obtained for different saturation temperatures. Overall the above behavior suggests a combination of, relatively, small temperature differences and moderate free stream velocities for optimum operation of the entire heat transfer process. Comparison with experimental data, [6], indicates that heat transfer is enhanced when either one of the two types of singularity takes place owing to flow recirculation. It is conjectured that the appearance of a 'singular point' is associated with a change in the dominant heat transfer mechanism in the vertical direction from conduction to convection (due to the formation of eddies in the bulk of the condensate), which enhances heat transfer. The latter is an issue for future study by means of the interactive boundary layer formulation, [7].

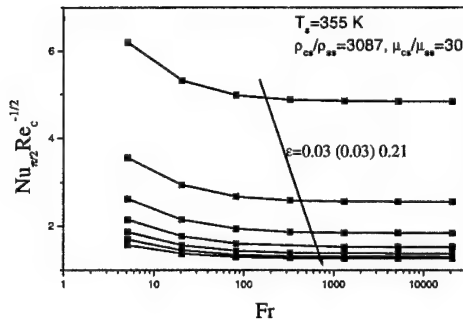


Figure 3: Variation of $Nu_{\pi/2} Re_c^{-1/2}$ with increasing Fr for different values of ϵ

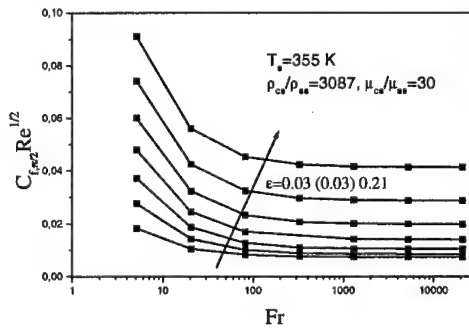


Figure 4: Variation of $C_{f,\pi/2} Re_c^{1/2}$ with increasing Fr for different values of ϵ .

Acknowledgement: This work was partially supported under the EPEAEK program (Grand number 51) of the Ministry of Education of Greece and by the University of Patras Research Foundation through the "Karatheothori" research program.

4. REFERENCES

- [1] KOH, J. C. Y. SPARROW, E. M. & HARTNETT, J. P. 1961 The two phase boundary layer in laminar film condensation. *Int. J. Heat Mass Transfer* **2**, 69-82.
- [2] BECKETT, P. & POOTS, G. 1972 Laminar flow condensation in forced flows. *Q. J. Mech. Appl. Maths.* **25**, 125-152.
- [3] FUJII, T. UEHARA, H. & KURATA, C. 1972 Laminar filmwise condensation of flowing vapour on a horizontal cylinder. *Int. J. Heat Mass Transfer.* **15**, 235-246.
- [4] ROSE, J. W. 1983 Effect of pressure gradient in forced convection film condensation on a horizontal tube. *Int. J. Heat Mass Transfer* 39-46.
- [5] SMYRNAIOS, D. N., PELEKASIS, N. A. & TSAMOPOULOS, J. A. 2000 Boundary layer flow past solid surfaces in the presence of rainfall. *J. Fluid Mech.* **425**, 79-110.
- [6] SMYRNAIOS, D. N., PELEKASIS, N. A. & TSAMOPOULOS, J. A. Stratified two-phase flow of vapour boundary layer-condensate film over a cylinder. Submitted for publication to the *Phys. Fluids*.
- [7] TIMOSHIN, S.N. & VAGANOV, A.V. Boundary-layer separation and transcritical two-fluid flows. Personal communication. Submitted to the *J. Fluid Mech*

FLUID DISPLACEMENT BY AIR IN A CAPILLARY TUBE

Y. E. Dimakopoulos¹, J. A. Tsamopoulos²

Laboratory of Computational Fluid Mechanics, Department of Chemical Engineering
University of Patras, GR-26500 Patras, Greece

¹e-mail: dimako@chemeng.upatras.gr ²e-mail: tsamo@chemeng.upatras.gr

1. SUMMARY

The present theoretical study examines the displacement of a more viscous fluid by highly pressurized air in a cylindrical tube with a four to one contraction at its downstream end. During this process a long, round-ended bubble is created, due to fluid adherence to the tube wall. This is known as fingering instability and it is often encountered in practical applications, such as enhanced oil recovery, production of hollow membranes and gas-assisted injection molding. To simulate numerically this process, we have chosen the finite element method, together with a system of elliptic partial differential equations, capable of generating a boundary-fitted finite element discretization of the flow domain. It is shown that both the finger profile and the thickness of the deposited material on the tube wall are affected by the properties of the displaced fluid and the flow conditions. In particular, increasing the Reynolds number, the deposited material becomes thinner and the finger profile steeper. For sufficiently low Reynolds numbers and high Capillary numbers, that is high tip velocities, the fraction of the liquid deposited on the wall of the tube, reaches an asymptotic value of 0.60, a theoretical verification of the experiments by Cox [1].

2. INTRODUCTION

Although fluid displacement by air in a capillary has been studied experimentally for many years (G.I. Taylor [2], Cox [1] & [3], Kolb & Cerro [4]), its theoretical study has been restricted to simplified and usually steady state models (Bretherton [5], Huzyak & Koelling [6]). Early on, Taylor [1] examined the effect of the Capillary number, when $Ca < 2$, for sufficiently low Reynolds numbers in cylindrical tubes with circular cross-sections and lengths about 1000 times their radii. He observed that for the higher displacing speeds the fractional coverage on the walls of the tubes (fraction of fluid remaining attached to the wall) reached an asymptotic value of 0.56. He also proposed distinctly different streamline patterns depending upon the fractional coverage. Latter on, Cox [2] extended Taylor's experiments at higher Ca and found that the asymptotic value of the fractional coverage was 0.6. Kolb and Cerro [4] performed experiments in tubes with square cross-sections. They found that the coating of square capillaries displayed many of the same phenomena as in circular capillaries. In particular, the behavior of square and circular cross-sections was nearly identical for

$Ca > 0.7$. The effect of the square cross-section became important as Ca was decreased. The first theoretical study of gas-bubble penetration was performed by Bretherton [5], who studied the steady motion of a bubble for Ca numbers very close to zero applying the methods of matched asymptotic expansions. Huzyak & Koelling [6] studied the effects of fluid elasticity on the hydrodynamic fractional coverage which is an increasing function of Deborah for all $De > 1$. At $De \approx 5$ the fractional coverage was 30% greater than that for a Newtonian fluid.

The motivation for the present work is a new forming process for polymer melts, the so-called Gas-Assisted Injection Molding. The process takes place in a mold filled with a polymer melt. Gas at high pressure is injected through the polymer, causing the continuing deformation of the free surface. As a result, hollow parts can be produced with higher strength to weight ratio, improved surface finish and lower frozen in (residual) stresses.

3. PROBLEM FORMULATION

Figure 1 shows a section of the tube between its axis of symmetry and its wall (lower and upper horizontal lines, respectively), partially filled with a viscous fluid, while the rest of the tube is occupied by air. The fluid sticks to the tube wall, forming a three phase contact line. At start up the pressure in the air is increased abruptly and displacing of the fluid is initiated. The radius and the length of the primary tube are a , b_1 , while a_c , b_2 are the radius and the length of the tube with the smaller radius. Scaling lengths with a , pressure with the air pressure $\overline{P_{ext}}$, velocities with $a^2 \overline{P_{ext}} / (L_{eq} \mu)$, the following three dimensionless groups arise: the Reynolds number $Re = \rho a^3 \overline{P_{ext}} / (L_{eq} \mu^2)$, the Capillary number $Ca = a^2 \overline{P_{ext}} / (\sigma L_{eq})$ and $\varepsilon = a / L_{eq}$, where L_{eq} is equal to b_1 for a straight tube, and $b_1 + b_2$ for a constricted tube. The viscosity and the density of the fluid that is being displaced are denoted by μ and ρ , respectively.

Governing equations

The governing equations that describe displacement of an incompressible Newtonian fluid under isothermal conditions and with negligible gravitational effects are the Navier-Stokes equations and the continuity equation. Written in dimensionless form they are:

$$Re \frac{D\mathbf{v}}{Dt} - \nabla \cdot \underline{\underline{\sigma}} = 0 \quad (1)$$

$$\nabla \cdot \mathbf{v} = 0 \quad (2)$$

where $\frac{D}{Dt} = \varepsilon \frac{\partial}{\partial t} + \mathbf{v} \cdot \nabla$ is the material derivative and $\underline{\underline{\sigma}} = -\frac{P}{\varepsilon} \mathbf{I} + (\nabla \mathbf{v} + (\nabla \mathbf{v})^T)$ is the total stress tensor.

Boundary and Initial conditions

The appropriate boundary conditions are: The velocity field must be (a) bounded at the centerline ($\mathbf{n} \cdot \mathbf{v} = 0$, $\mathbf{t} \cdot \underline{\underline{\sigma}} = 0$), (b) zero at the tube wall ($\mathbf{v}_r = 0$, $\mathbf{v}_z = 0$), and (c) fully developed far downstream ($\mathbf{v}_r = 0$, $\mathbf{n} \cdot \nabla \mathbf{v} = 0$). At the free surface the velocity field should also satisfy a

local balance between viscous stresses, surface tension and gaseous pressure: $\mathbf{n} \cdot \underline{\underline{\sigma}} = \frac{2H}{Ca} \mathbf{n} - \frac{1}{\varepsilon} \mathbf{n}$,

where $2H$ is twice the mean curvature of the free boundary. Initially, fluid is assumed to be stationary under constant pressure and its free surface in contact with the air is flat.

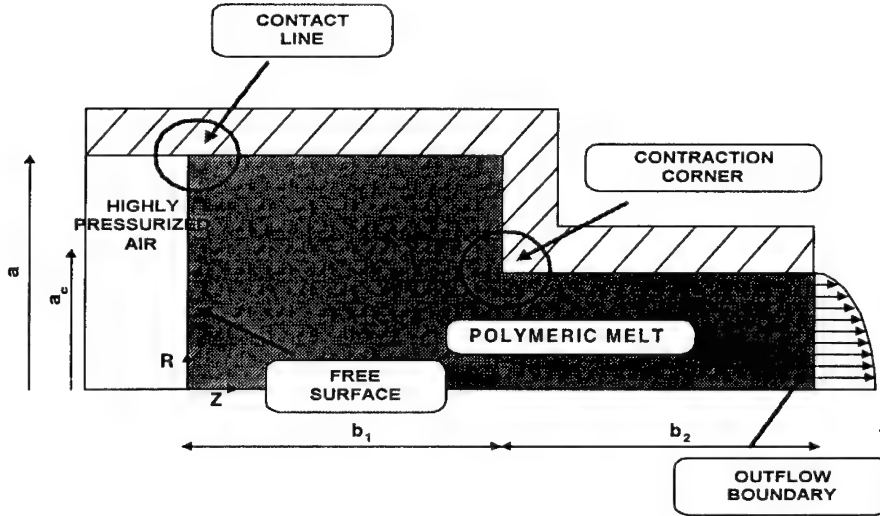


Figure 1. Constricted tube filled with partially fluid, displaced by air at high pressure.

4. NUMERICAL SOLUTION

The presence of a highly deformable free surface, a time dependent control-volume and the stress-singular points (at the three phase contact line and the corners of the tube wall) demand an accurate, robust and flexible numerical method. The one we have chosen, is the mixed finite element method, together with a system of elliptic partial differential equations, capable of generating a boundary-fitted (Lagrangian) finite element discretization. Grid points become finite element nodes mapped subparametrically. For convenience, the computational domain is split into three regions, the tube with the smaller radius, its extension into the main tube and the remaining volume of the main tube and, then, these regions are patched together.

The node distribution scheme is the most important, single factor for the success of this numerical simulation. Earlier researchers developed similar mesh generation schemes (Tsiveriotis & Brown [7] and Christodoulou & Scriven [8]). These resulted in meshes composed of quadrilateral elements such that (a) their corners were almost orthogonal, (b) they followed a harmonic distribution in space, and (c) they were regularized so that the ratio of their neighboring sides did not exceed certain limits. Because of the time dependent nature of the present problem and the extreme deformations that we need to simulate, we modified their mesh generation scheme. We included the first two criteria in the equation generating the radial distribution of nodes and only the second criterion in the axial distribution of nodes:

$$\nabla \cdot (\epsilon_{11} \sqrt{\frac{R_\xi^2 + Z_\xi^2}{R_\eta^2 + Z_\eta^2}} \nabla \xi + \epsilon_{12} \nabla \xi) = 0, \quad (3)$$

$$\Delta \eta = 0 \quad (4)$$

where (R, Z) are the components of the position vector in the physical domain, (ξ, η) are the components of the position vector in the computational domain, and ϵ_{11} , ϵ_{12} are empirically chosen parameters. Equations (3), (4) constitute an anisotropic transformation that is able to capture the great deformation in the Z direction. Even with this scheme it proved necessary to

split each quadrilateral into two triangles. This procedure started with the quadrilateral lying next to the intersection of the axis of symmetry and the air/fluid interface by drawing its main diagonal emanating from this intersection point. In the same fashion and direction all quadrilaterals were converted into triangles, see figure 2a.

As boundary conditions for eqs (3) and (4) we use: (a) On fixed parts of the boundary (tube walls and exit of the tube) the equation that defines the boundary curve replaces the mesh generation equation associated with the coordinate that is constant on that boundary. (b) The remaining degree of freedom is used to control the node distribution along the boundary. (c)

At the free surface the two boundary conditions are the kinematic equation $\frac{DR}{Dt} = \underline{v}$ and a generalized distribution $s(\xi) = \int_0^\xi \sqrt{w_1 R_\xi^2 + w_2 Z_\xi^2} d\xi$, where w_1, w_2 are weight functions, which have to be adjusted by trial and error to optimize performance. Previous researchers, [7] & [8], used an equidistribution condition on the free surface ($w_1=w_2=1$) which is useful and accurate only when the deformation of the free surface is not very large. In our case Z_ξ becomes much larger than R_ξ , and their scheme produces unsatisfactory results. So we must use weights such that $w_1 \gg w_2$, in order to prevent strong repulsion of the nodes from the front of the bubble or from the neighbor of the contact line, where the curvature of the surface is large.

The velocity field is represented by quadratic basis functions, while the node coordinates and the pressure are approached by linear elements (6/3 formulation). For integration in time the implicit Euler method is used. The resulting system of the coupled non-linear equations is solved using the Newton-Raphson iterative method.



(a)



(b)

Figure 2. (a) Close up of the discretized in triangles domain using equations (3) & (4), (b) Close up of the discretized in quadrilaterals domain using the proposed by Christodoulou & Scriven equations ($Re=0$, $Ca=5 \times 10^3$, $\tau=44$, $b_1/a=16$, $b_2/a=4$, $a_c/a=0.25$)

5. DISCUSSION OF RESULTS

Figure 2(a) shows a snapshot of the discretized flow domain in the neighborhood of its tip, when the maximum penetration of the air is about five radii ($Re=0$, $Ca=5 \times 10^3$, $\tau=44$, $b_1/a=16$,

$b_2/a=4$, $a_c/a=0.25$). To obtain converged results, 130 elements in the Z direction and 36 in the R direction have been used, resulting in 40000 unknowns. The currently applied elliptic mesh generation scheme, eqs (3) & (4) and fig. 2a, is clearly more flexible than that originally proposed by Christodoulou & Scriven [8], fig. 2b. The mesh generation proposed in [8] was based on the minimization of an orthogonality functional in both the R and Z directions, resulting in the creation of very restrictive meshes. Such meshes do not allow control of mesh spacing, this becomes apparent in fig.2(b). Here two distinct regions inside the domain develop, which are separated by a transition zone composed of very large and highly deformed (skewed) elements, although their aspect ratios remain close to 1. Also, close to the free surface there is a high concentration of elements having very high aspect ratios. All these are quite disadvantageous for the accuracy of the accurate calculation for the flow field.

The evolution of the free surface, for the same set of parameters and using our mesh generation scheme, is shown in figure 3. Flow takes place from left to right. It is clear that the streamlines smoothly follow the solid wall, except near the air/fluid interface and the tube contraction. Apparently there is no flow far upstream from the front of the flow, near the contact line, and that a few diameters in front of the finger tip the flow field becomes parabolic. At early times the free surface has a parabolic form, which later on becomes a round-ended bubble, leaving a fraction of mass stuck on the tube wall.

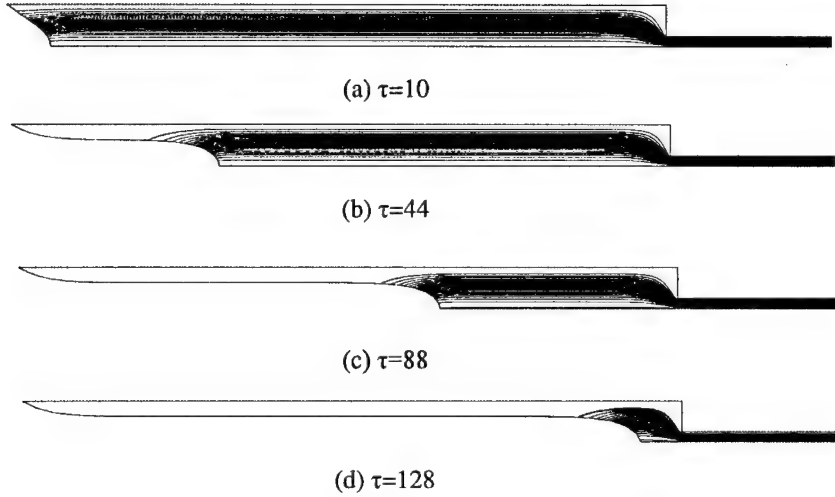


Figure 3. Sequence of streamlines in the liquid that is being displaced by the gas, at different time instances for ($Re=0$, $Ca=5 \times 10^3$, $b_1/a=16$, $b_2/a=4$, $a_c/a=0.25$).

In figure 4 we show the effect of the imposed capillary number on the tip velocity, which is represented by the local tip capillary number ($Ca_{tip} = \mu U_{tip} / \sigma$). Three distinct regions are apparent. In the first region the velocity increases exponentially, because of the step change in the applied pressure. Then, the tube contraction provides large resistance to the flow and stabilizes the front development and its velocity for a long distance. When the front of the bubble reaches the end of the primary tube ($\tau \sim 120$), the velocity increases abruptly (third region). For all the values of Ca given in fig.4, the fractional coverage is about 0.60 in accordance with Cox [1].

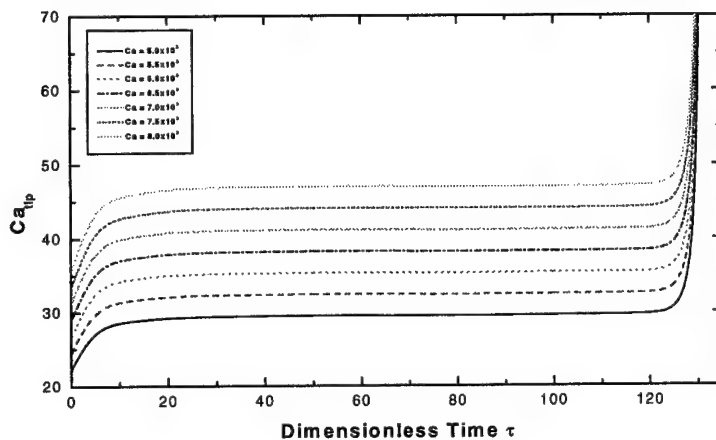


Figure 4. Local tip capillary number as a function of dimensionless time for the imposed Ca indicated in the figure insert ($Re=0$, $\tau=44$, $b_1/a=16$, $b_2/a=4$, $a_c/a=0.25$).

Acknowledgement: This work was partially supported by the EPET II program (Grant number, 88/1998) and the EPEAEK program (Grant number, 51).

5. REFERENCES

- [1] B.G. Cox, On driving a viscous fluid out of a tube, *J. Fluid Mech.*, **14**, 81, (1962).
- [2] G.I. Taylor, Deposition of a viscous fluid on the wall of a tube, *J. Fluid Mech.*, **10**, 161 (1961).
- [3] B.G. Cox, An experimental investigation of the streamlines in viscous fluid expelled from a tube, *J. Fluid Mech.*, **20**, 193, (1964).
- [4] W.B. Kolb and R.L. Cerro, Coating the inside of a capillary of square cross section, *Chem. Eng. Sc.*, **46**(9), 2181, (1991).
- [5] F.P. Bretherton, The motion of long bubbles in tubes, *J. Fluid Mech.*, **10**, 166-188 (1961).
- [6] P.C. Huzyak and K.W. Koelling, The penetration of a long bubble through a viscoelastic fluid in a tube, *J. NonNewt. Fluid Mech.*, **71**, 73, (1997).
- [7] K. Tsiveriotis and R.A. Brown, Solution of Free-Boundary problems using Finite-Element/Newton methods and locally refined grids: Application to analysis of solidification microstructure, *Int. J. Num. Meth. Fluids*, **14**, 827, (1993).
- [8] K.N. Christodoulou and L.E. Scriven, Discretization of free surface flows and other moving boundary problems, *J. Comp. Phys.*, **99**, 39, (1992).

FLOW BETWEEN TWO ROTATING HEATED SPHERES

V. C. Loukopoulos

Department of Physics

University of Patras, Patras 26500, Greece

1. SUMMARY

The steady motion in a spherical shell is studied in the presence of heat when the boundaries are rotating. The secondary motion as well as the Nusselt number along a meridional line on the outer boundary are affected by the relative rotation of the two spheres.

2. INTRODUCTION

The present work considers the steady motion of a viscous incompressible fluid contained between two concentric heated spheres that rotate about their vertical diameter with different angular velocities. Such configurations are of interest in geophysical and meteorological problems, in which the geometry and the rotation play an important role on the fluid motion. The convective flow in an annular conduit and the effects of this type of the flow in a catheterized artery was studied by Karahalios [1], [2]. The problem of heat transfer with flow between two concentric rotating spheres was considered by Bhatnagar and Vayo [3] for small Reynolds numbers and for a set of values of the Prandtl and of the Eckert number. In their study they neglected the effect of gravitational forces but they considered the effect of heat by viscous dissipation. The results they presented were for $Re \leq 0.6$. Zhang and Gubbins [4], [5] examined the thermal convection in the Earth's core under the action of laterally varying temperature in the lower mantle and the effect of such non – uniform boundary conditions on convective instability.

Though the problem is of general interest in rotating fluid mechanics, our motivation is concerned with several connections to geophysics, such as the possible relation of connection in the Earth's mantle to the movement of the continents.

In the present work we study the flow properties of a viscous incompressible fluid between two concentric spheres that rotate about their common vertical diameter with different angular velocities and that have constant but different surface temperatures. The approximate solutions of the equations of motion and energy are obtained either analytically or numerically. In the analytic solution the flow properties, such as stream function, axial velocity function and temperature are each expressed in a series of the Reynolds and of the Grashoff number of the flow $Re = \Omega_0 \alpha^2 / \nu$ and $Gr = \alpha^3 \beta g (T_1 - T_2) / \nu^2$ respectively where $Re < 150$ and $Gr < 10$ and α is the radius of the outer sphere, Ω_0 is a typical angular velocity, ν the coefficient of kinematic viscosity, β is the thermal expansion coefficient of the

fluid, g is the acceleration of gravity, T_1 is the temperature of the inner sphere and T_2 is the temperature of the outer sphere, where $T_1 > T_2$.

3. EQUATIONS OF MOTION AND ENERGY

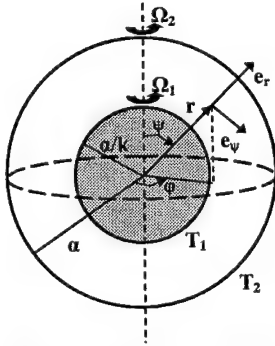


Figure 1. Spherical annulus.

We consider the steady flow of a viscous incompressible fluid between two concentric spheres, rotating about their vertical diameter with different angular velocities Ω_1 and Ω_2 , where subscripts 1 and 2 correspond to the inner and to the outer sphere. Let in addition $r_1 = \alpha/k$ and $r_2 = \alpha$ be their radii where $k > 1$ and T_1 and T_2 ($T_1 > T_2$) their temperature assumed constant. The flow is symmetric about the axis of rotation and hence all quantities are independent of the azimuthal angle ϕ . The non-dimensional equations of motion and energy are

$$D^4 f = \frac{1}{r^2 \sin \psi} \left[\frac{\partial(f, D^2 f)}{\partial(r, \psi)} - \frac{2}{r \sin \psi} D^2 f \left(\frac{\partial f}{\partial r} r \cos \psi - \frac{\partial f}{\partial \psi} \sin \psi \right) \right] - R_e \frac{2\chi}{r^3 \sin^2 \psi} \left(\frac{\partial \chi}{\partial r} r \cos \psi - \frac{\partial \chi}{\partial \psi} \sin \psi \right) + G_r \left(\frac{\partial \Theta}{\partial r} r \sin^2 \psi + \frac{\partial \Theta}{\partial \psi} \sin \psi \cos \psi \right) \quad (1)$$

$$D^2 \chi = \frac{1}{r^2 \sin \psi} \frac{\partial(f, \chi)}{\partial(r, \psi)}, \quad (2)$$

$$\nabla^2 \Theta = P_r \frac{1}{r^2 \sin \psi} \frac{\partial(f, \Theta)}{\partial(r, \psi)}, \quad (3)$$

where $D^2 = \frac{\partial^2}{\partial r^2} - \frac{\cos \psi}{r^2 \sin \psi} \frac{\partial}{\partial \psi} + \frac{1}{r^2} \frac{\partial^2}{\partial \psi^2}$, $\frac{\partial(a, b)}{\partial(x, y)} = \frac{\partial a}{\partial x} \frac{\partial b}{\partial y} - \frac{\partial a}{\partial y} \frac{\partial b}{\partial x}$ and R_e is the Reynolds number of the flow, G_r is the Grashoff number, P_r is the Prandtl number, f is the stream function χ is the axial velocity function and Θ is the temperature. The boundary conditions of the flow are

$$f = \frac{\partial f}{\partial \psi} = 0 \quad \text{on both boundaries,} \quad (4)$$

$$\chi = R_e^{1/2} \frac{1}{k^2} \sin^2 \psi \frac{\Omega_1}{\Omega_0} \quad \text{at } r = 1/k \text{ (inner boundary),} \quad (5)$$

$$\chi = R_e^{1/2} \sin^2 \psi \frac{\Omega_2}{\Omega_0} \quad \text{at } r = 1 \text{ (outer boundary),}$$

$$\Theta = 1 \quad \text{at } r = 1/k, \quad \Theta = 0 \quad \text{at } r = 1. \quad (6)$$

4. METHODS OF SOLUTION

In the present work equations (1) to (3) have been solved both analytically and numerically. For the approximate analytic solution we suppose that χ , f and Θ can be expanded as power series in the Reynolds number and in the Grashoff number when both are small, as follows

$$\begin{aligned}\chi &= \chi_0 + R_e \chi_{10} + G_r \chi_{11} + R_e^2 \chi_{20} + R_e G_r \chi_{21} + G_r^2 \chi_{22} + \dots, \\ \Theta &= \Theta_0 + R_e \Theta_{10} + G_r \Theta_{11} + R_e^2 \Theta_{20} + R_e G_r \Theta_{21} + G_r^2 \Theta_{22} + \dots, \\ f &= R_e f_{10} + G_r f_{11} + R_e^2 f_{20} + R_e G_r f_{21} + G_r^2 f_{22} + \dots.\end{aligned}\tag{7}$$

In this way each one of equations (1) to (3) is split into a number of differential equations that are solved analytically. The output of the analytical calculations is compared with that of the numerical calculations and the comparison shows that the validity of the analytical solution is limited within the range $R_e < 150$ and $G_r < 10$.

For the approximate numerical solution we construct a grid of mesh points with constant radial and angular mesh sizes $h = (1 - 1/k)/N$ and $\ell = \pi/L$ where N and L are integers indicating the density of the grid of mesh points. We next denote all quantities at a typical set of grid points (r_0, ψ_0) , $(r_0 + h, \psi_0)$, $(r_0, \psi_0 + \ell)$, $(r_0 - h, \psi_0)$ and $(r_0, \psi_0 - \ell)$ by the subscripts 0, 1, 2, 3 and 4 respectively and replace equations (1) to (3) by central differences. We are therefore led to an algebraic system of equations in which the matrix of the coefficients of the unknowns may be diagonally dominant. Diagonal dominance is a sufficient condition for convergence for iterative procedures such as the Gauss - Seidel or the over - relaxation are. In the present work the matrix corresponding to the system of equations derived by (1) to (3) was always diagonally dominant and a relaxation parameter ω of order 10^{-1} or 10^{-2} was found necessary for convergence.

We write

$$D^2 f = -\zeta \tag{8}$$

After lengthy manipulations we finally construct the following equation from equation (1)

$$a_1 \zeta_1 + a_2 \zeta_2 + a_3 \zeta_3 + a_4 \zeta_4 + a_0 \zeta_0 = -2h^2 G, \tag{9}$$

where ζ is the vorticity and a_i are known coefficients.

The boundary conditions for the vorticity function in finite - difference form are

$$\begin{aligned}\zeta(1/k, \psi) &= -\frac{3f(1/k + h, \psi)}{h^2} - \frac{\zeta(1/k + h, \psi)}{2}, \\ \zeta(1, \psi) &= -\frac{3f(1 - h, \psi)}{h^2} - \frac{\zeta(1 - h, \psi)}{2}.\end{aligned}\tag{10}$$

Following the same procedure for Eqs. (2), (3) and (8) we finally take

$$n_1 \chi_1 + n_2 \chi_2 + n_3 \chi_3 + n_4 \chi_4 + n_0 \chi_0 = 0, \tag{11}$$

$$m_1 f_1 + m_2 f_2 + m_3 f_3 + m_4 f_4 + m_0 f_0 = -h^2 \zeta_0, \tag{12}$$

$$d_1\Theta_1 + d_2\Theta_2 + d_3\Theta_3 + d_4\Theta_4 + d_0\Theta_0 = 0, \quad (13)$$

where the n_i , m_i and d_i ($i = 0, 1, 2, 3, 4$) are coefficients of the unknowns χ , f , and Θ .

The system of equations (9) and (11) to (13) is solved numerically by employing the under relaxation method at all internal points of the annular region $1/k < r < 1$, $0 < \psi < \pi$ subject to boundary conditions that are either known *a priori* (Eqs (4) – (6)) or are calculated by Eqs (10).

5. RESULTS AND DISCUSSION

The results obtained by the analytic approximation are valid when $R_e < 150$ and $G_r < 10$. This is based on the comparison with analogous results of ours calculated numerically. In all Figures the Grashoff number is constant and the Froude number $F_r = \frac{R_e^2}{G_r}$ varies.

In the numerical approximation, results have been obtained with the radius ratio being equal to $k = 2$ and for the Prandtl number $P_r = 1$. The Reynolds number and the Grashoff number can vary in the range $1 < R_e < 5000$ and $1 < G_r < 10^6$ respectively. In fact, convergence could be obtained for $R_e \leq 5000$ whereas no problem was related with the value of the Grashoff number.

In Figures 2a to 2c the streamline pattern, based form henceforth on the numerical solution, is presented for $G_r = 1000$ and for various Froude numbers when $k = 2$ and the outer sphere is stationary, so that the relative effect of the centrifugal force on the buoyancy force is demonstrated. In Figures 3a to 3c the streamline pattern is presented for $k = 2$ when the inner sphere is stationary and in Figures 4a to 4c and 5a to 5c we show the azimuthal isovelocity curves for the previously mentioned cases.

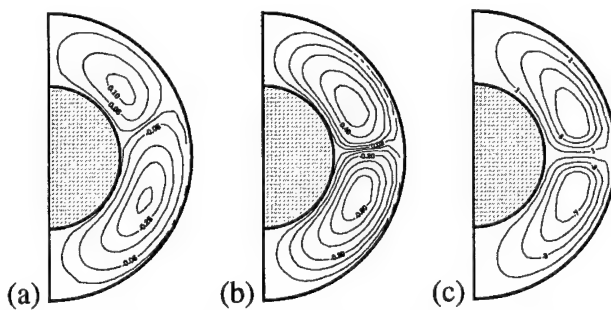


Figure 2. Stream function pattern for $\Omega_1 = \Omega_0$, $\Omega_2 = 0$ and $k = 2$.

((a) $F_r = 10$, (b) $F_r = 40$, (c) $F_r = 1000$, $G_r = 1000$).

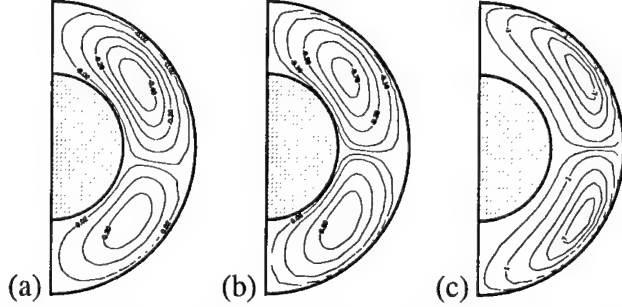


Figure 3. Stream function pattern for $\Omega_1 = 0$, $\Omega_2 = \Omega_0$ and $k = 2$.

((a) $F_r = 10$, (b) $F_r = 40$, (c) $F_r = 1000$, $G_r = 1000$).

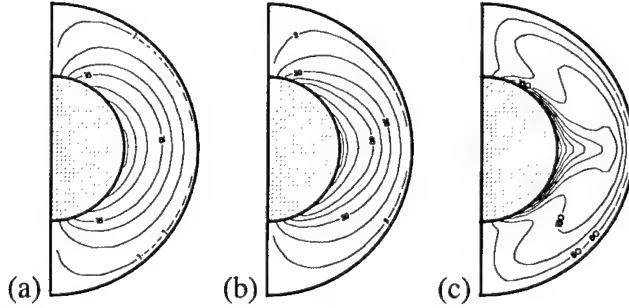


Figure 4. Isovelocity curves pattern for $\Omega_1 = \Omega_0$, $\Omega_2 = 0$ and $k = 2$.

((a) $F_r = 10$, (b) $F_r = 40$, (c) $F_r = 1000$, $G_r = 1000$).

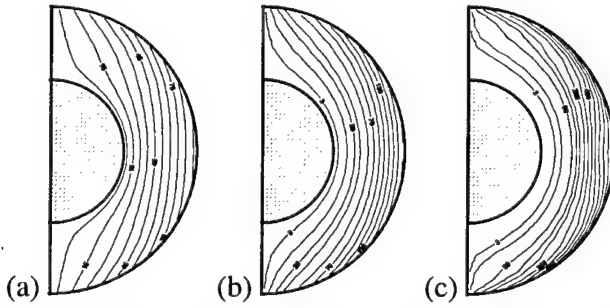


Figure 5. Isovelocity curves pattern for $\Omega_1 = 0$, $\Omega_2 = \Omega_0$ and $k = 2$.

((a) $F_r = 10$, (b) $F_r = 40$, (c) $F_r = 1000$, $G_r = 1000$).

In Figure 6 we show the variation of the Nusselt number $N_u = \frac{\partial \Theta}{\partial r}$ along a meridian line on the outer boundary for various Froude numbers when $k = 2$ and $\Omega_2 = 0$. When the Froude number is large, the heat loss is great owing to the development of large centrifugal forces. Finally in Figure 7 we have plotted the variation of the Nusselt number along a meridional line on the outer shell when $\Omega_1 = 0$ and $\Omega_2 = \Omega_0$.

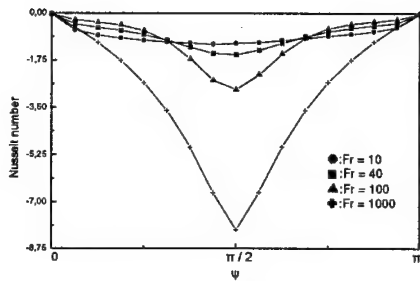


Figure 6. Nusselt number for $\Omega_1 = \Omega_0$, $\Omega_2 = 0$ and $k = 2$. ((a) $F_r = 10$, (b) $F_r = 40$, (c) $F_r = 100$, (d) $F_r = 1000$, $G_r = 1000$).

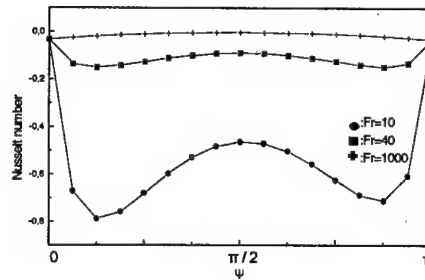


Figure 7. Nusselt number for $\Omega_1 = 0$, $\Omega_2 = \Omega_0$ and $k = 2$. ((a) $F_r = 10$, (b) $F_r = 40$, (c) $F_r = 1000$, $G_r = 1000$).

6. CONCLUSION

In this work we study the effect of natural convection on the motion of a fluid contained between two concentric rotating and heated spheres. Our results refer mainly to the specific configurations in which the annular distance is equal to the radius of the inner sphere ($k = 2$). We show that the secondary flow is strongly affected by the relative rotation of the spherical shells as well as by the magnitude of the Froude number. Finally, we deduce that the temperature distribution within the fluid and the rate of heat loss along a meridional line on the outer boundary follows the form of the azimuthal isovelocity curves.

7. REFERENCES

- [1] Karahalios, G.T., *Mixed convection flow in a heated curved pipe with core*, Physics of fluids **A2**, 2164 – 2175 (1990).
- [2] Karahalios, G.T., *Some possible effects of a catheter on the arterial wall*, Medical Physics **17**, 922 – 925 (1990).
- [3] Bhatnagar, R. K. and Vayo, H. W., *Heat transfer in a Viscous Liquid Between Concentric Rotating Spheres*, ZAMM **69**, 227 – 242 (1989).
- [4] Zhang, K. and Gubbins, D., *On convection in the Earth's core forced by lateral temperature variations in the lower mantle*, Geophysics Journal International. **108**, 247 – 255 (1992).
- [5] Zhang, K. and Gubbins, D., *Convection in a rotating spherical fluid shell with an inhomogeneous temperature boundary condition at infinite Prandtl number*, Journal of Fluid Mechanics **250**, 209 – 232 (1993).

AN EXPERIMENTAL METHODOLOGY FOR ENHANCING 2-D FLOW CHARACTERISTICS IN A 3-D TURBULENT FLOW

G.A. Sideridis, E.G. Kastrinakis, and S.G. Nychas

Department of Chemical Engineering

Aristotle University of Thessaloniki, GR-54006 Thessaloniki, Greece

1. SUMMARY

The present experimental work is aimed at enhancing the 2-D characteristics of the coherent flow in the wake of a cylinder. It has been observed that two factors have significant role in that issue: the flow Reynolds number based on the cylinder's diameter, R_D and the its surface roughness. The criteria selected for evaluation of the two-dimensionality of the flow were the velocity power spectral density distribution and the coherent kinetic energy term $\overline{q_c^2}$ ($= \overline{u_c^2} + \overline{v_c^2}$, where u_c and v_c are the coherent contributions to the streamwise and vertical velocity components). With R_D near the value of 2000 and with roughness on the cylinder's surface, the velocity psd displayed a scaling region with slope close to -3 , the theoretical result for pure 2-D flow. Furthermore, at the same conditions, $\overline{q_c^2}$ was found significantly increased.

2. INTRODUCTION

Real turbulent flows are essentially 3-D. Under certain circumstances, they might develop some 2-D characteristics, in which case they are referred to as quasi 2-D. Typical examples are the large-scale flows in the atmosphere and in the oceans where velocity fluctuations are significant only in planes parallel to the earth's surface. It has been observed that the velocity power spectral density (psd) distribution of these quasi 2-D flows contains a scaling region which follows a power law with exponent different from $-5/3$, the value for isotropic, 3-D turbulence. Their value is closer to -3 , the classical theoretical result for 2-D turbulence [1]. Hence, it may be deduced that a successful experimental simulation of a quasi 2-D flow should have as a prerequisite the existence of the scaling region with exponent close to -3 . A flow with particular interest, due to its widely spread applications, is that in the wake of a cylinder. Although this flow is 3-D, it has an inherent 2-D character, associated with the periodically appearing large-scale structures, the von Karman street of vortices [2], [3]. A cylinder in cross-flow configuration may be regarded as a continuous source of coherent spanwise vortices travelling downstream. From that point of view, enhancing the 2-D characteristics of the flow would result in stronger, more coherent vortices, capable of surviving over longer distances in the streamwise direction.

Based on the above, the present work had two main targets: first, the production in a wind tunnel of a flow behind a cylinder with a velocity psd displaying a distinct scaling region with slope near -3 and then, the isolation of the periodic, coherent flow and the examination for

increased values of the coherent kinetic energy term $\overline{q_c^2} = \overline{u_c^2} + \overline{v_c^2}$ (u_c and v_c are the coherent flow streamwise and normal velocity components).

3. EXPERIMENTAL PROCEDURE

The experimental part of the present work was performed in an open-return, suction type wind tunnel with test section dimensions $0.5 \times 0.5 \times 2 \text{ m}^3$ and free-stream turbulence level about 0.4%. A circular cylinder with length equal to the width of the test section was placed normal to the flow. Using hot wire anemometry with an X-type, double wire probe,³ the streamwise and vertical velocity components were measured simultaneously across the wake of the cylinder. The cylinder's diameter D and the velocity defect U_d (defined in Fig. 1) were used for normalization. Measurements were taken at two values of the Reynolds number based on D ($R_D = 2000, 4000$) at the locations: $x/D = 5, 20, 40$ and 60 .

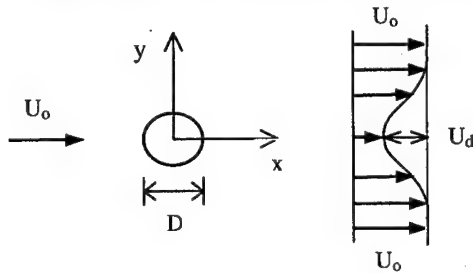


Figure 1. Definition of the reference axes and the velocity defect U_d in the wake.

4. RESULTS

Velocity power spectral density distributions.

A series of preliminary measurements with the same experimental set up indicated that the velocity psd can have a scaling region with slope near the value -3 under two conditions: the cylinder has rough surface (using a high-grade sandpaper glued on its surface) and the Reynolds number is close to 2000. Fig. 2 shows a group of present velocity psd's, all produced at $R_D=2000$ and $y/D=1$. Each diagram displays three curves: the actual velocity psd (denoted by $n=0$) and two others, which have been derived by multiplication of the ordinates of the original velocity psd curve by f^n (f denotes the corresponding values of frequency and n , the anticipated slope of the scaling region). This transformation forces the part of the spectrum with slope $-n$ to appear horizontal. It is evident from the data presented in Fig. 2 that at all measurement stations, except the last, the effect of roughness is the formation in the scaling region of a section with slope close to -3 . On average, the bandwidth of that section is about 500Hz. Also shown in Fig. 2 are distinct peaks at the Strouhal frequency of the flow, thus designating the presence of von Karman vortices. The fact that these peaks reduce in height with streamwise distance implies that the strength of the coherent vortices decays likewise. Furthermore, comparison at the same x/D location of peaks from the two cases considered, i.e. with and without roughness, indicates that with roughness, the presence of the coherent structures is stronger. This is more apparent at $x/D=40$.

Similarly, Fig. 3 shows velocity psd distributions at $R_D=4000$. Here, the effect of roughness appears to be negligible, since in all cases shown, no significant parts of the scaling region with slope other than $-5/3$ can be distinguished. In addition, the peaks at the Strouhal frequency of the flow at each x/D location, appear to have almost the same length,

irrespectively of the presence or not of roughness. It is thus implied that in both cases, with and without roughness, coherent vortices of similar strength are present in the flow, having similar decaying rates.

Coherent kinetic energy.

The coherent flow in the wake of the cylinder, having a strong periodic nature, was isolated from the overall flow using a phase-averaging method, similar to that described in [4]. Its application implies that any time-dependent flow quantity $S(t)$ consists of an overall time-mean value \bar{S} , a periodic fluctuation component s_c , associated with the coherent flow, and a random fluctuation component s_r . Phase-averaged results obtained from the $S(t)-\bar{S}$ time series refer to the periodic component s_c , since the random component s_r disappears by definition.

Applying this methodology to both streamwise and normal velocity components in the wake $U(t)$ and $V(t)$, the distribution of the coherent components u_c and v_c over one shedding period were obtained. Then, each of the quantities u_c^2 and v_c^2 was averaged again over one shedding period and the results were added together to evaluate the coherent flow kinetic energy parameter $\overline{q_c^2} = \overline{u_c^2} + \overline{v_c^2}$ (an overbar denotes averaging over one shedding period).

Distributions of $\overline{q_c^2}$ across the wake, at $x/D = 5, 10, 20, 40$ normalized by the velocity defect U_d , are shown in Fig. 4. It is evident that at $R_D=2000$ the effect of roughness is a substantial increase of $\overline{q_c^2}/U_d^2$, especially close to the cylinder. On the contrary, at $R_D=4000$, the distribution of $\overline{q_c^2}/U_d^2$ at every x/D location is almost identical with and without roughness. It is noted here that at the last measurement station, at $x/D=60$, the values of $\overline{q_c^2}/U_d^2$ in all cases considered are negligible.

5. CONCLUSIONS

The main conclusions of the present work are the following:

- i) It is possible to augment the quasi 2-D nature of the large-scale coherent structures in the wake of a cylinder by adding roughness on its surface.
- ii) The effectiveness of the roughness is very sensitive to the Reynolds number. In the present work, it was significant only within a narrow range of R_D values near 2000.
- iii) With $R_D=2000$ and roughness on the cylinder's surface, the coherent structures in the wake displayed increased kinetic energy content and a lower decay rate.

6. REFERENCES

- [1] Tennekes, H., Turbulent flow in two and three dimensions, *Bull. Amer. Meteor. Soc.*, 59, 22-78 (1978).
- [2] Hussain, A.K.M.F. and Hayakawa, M., Eduction of large-scale organized structures in a turbulent plane wake, *J. Fluid Mech.*, 180, 193-229 (1987).
- [3] Sideridis, G.A., Kastrinakis, E.G. and Nychas S.G., Turbulence production and transport in quasi 2-D wake / boundary layer interaction, *AIAA J*, 38(2), 259-266 (2000).
- [4] Matsumura, M. and Antonia, R.A., Momentum and heat transport in the turbulent intermediate wake of a circular cylinder, *J. Fluid Mech.*, 250, 651-668 (1993).

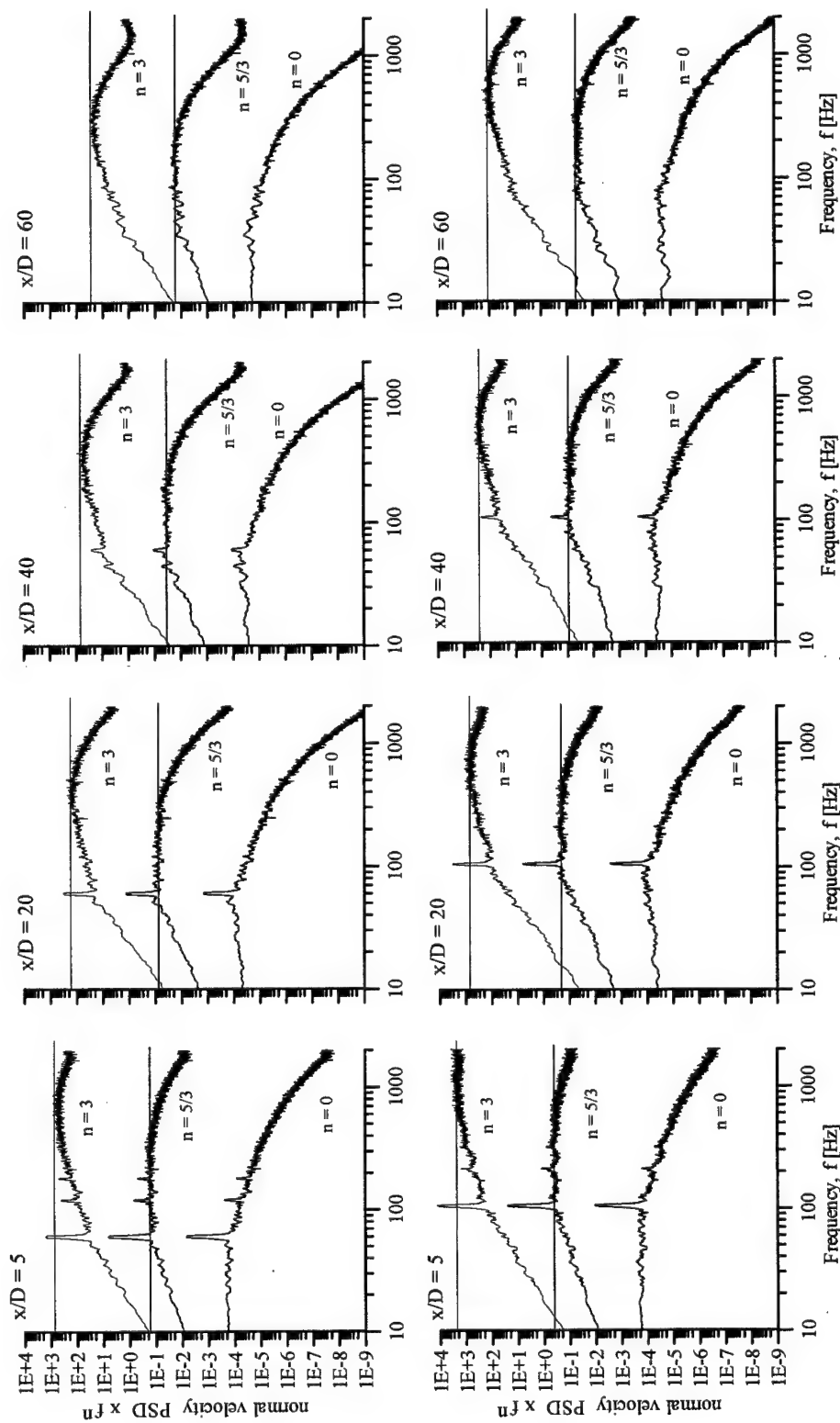


Figure 2. Normal velocity power spectral density distributions at $Re=2000$. Upper row: without roughness. Lower row: with roughness.

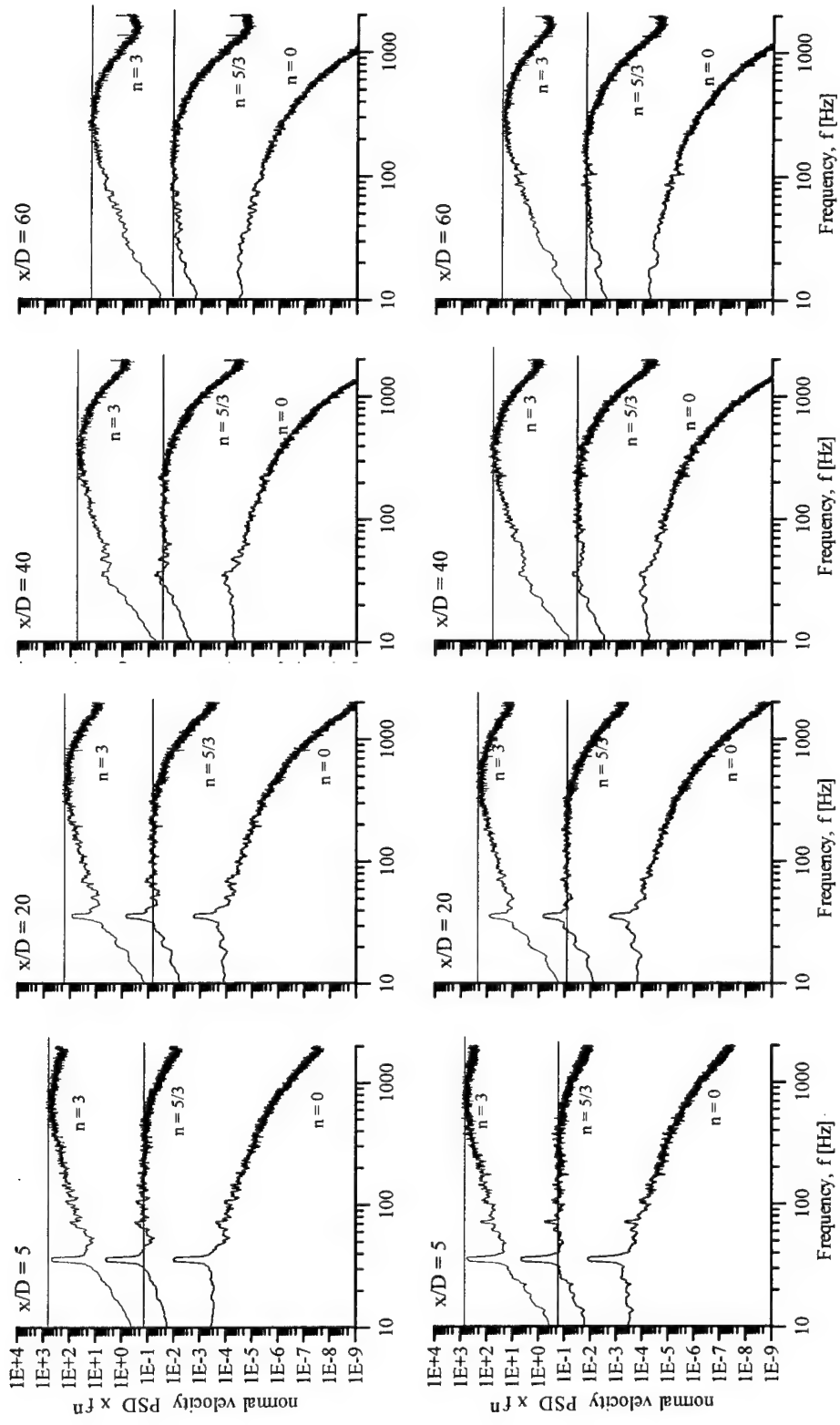


Figure 3. Normal velocity power spectral density distributions at $R_D=4000$. Upper row: without roughness. Lower row: with roughness.

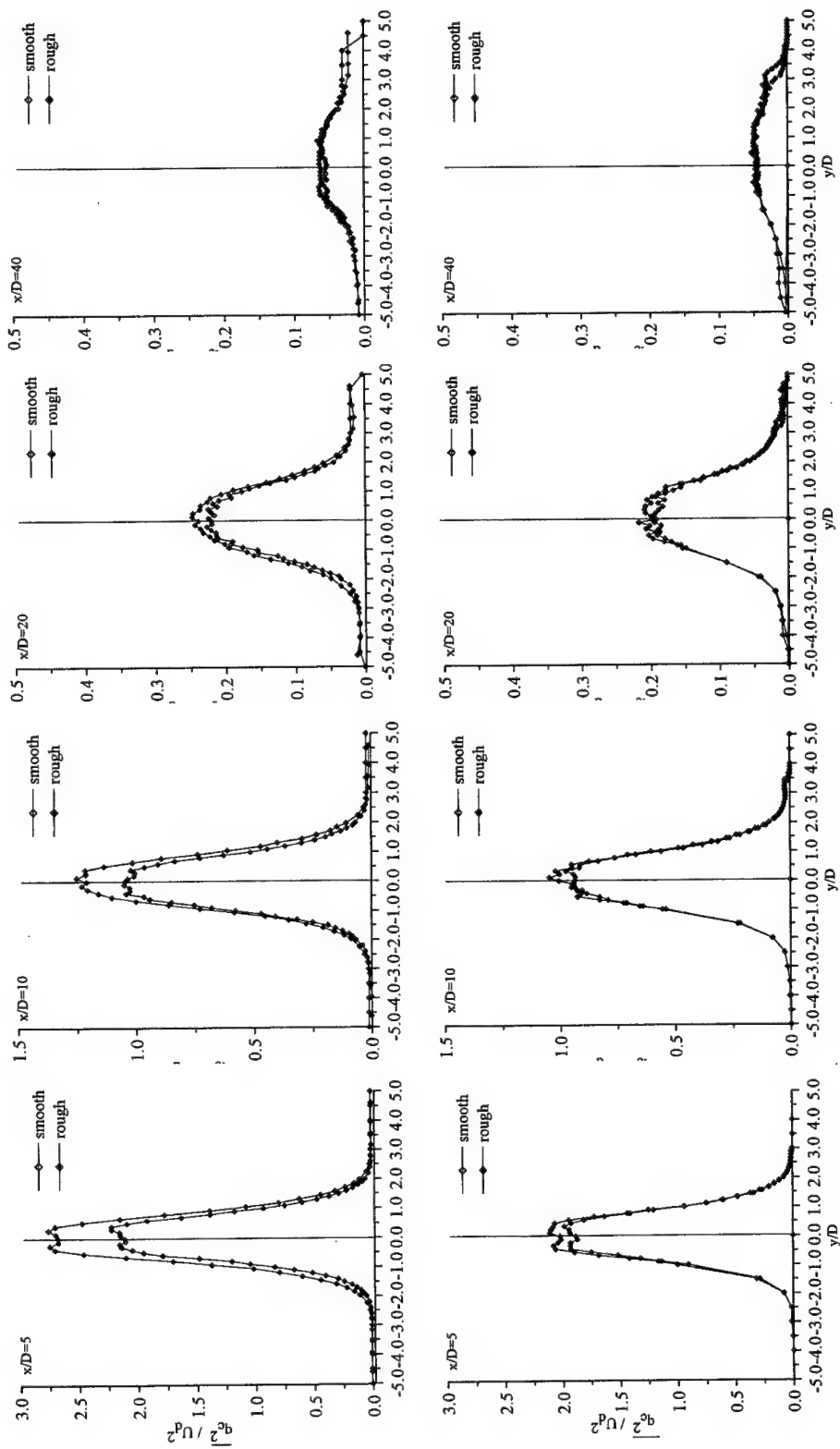


Figure 4. Distributions across the wake of the coherent kinetic energy term q_c^2/U_d^2 . Upper row: $Re_D=2000$. Lower row: $Re_D=4000$.

FORCES FROM JET FLOWS ON INCLINED DISCS

J. D. Demetriou

Department of Civil Engineering
N.T.U.A, GR 15780, Athens, Greece

D. J. Dimitriou

Mechanical Engineering Department
Imperial College of Science, Technology and Medicine
GBR SW7-2BX, London, U.K.

1. SUMMARY

In this paper a number of measurements and the analysis of them are presented, concerning the forces exercised on inclined discs from jet flows. A number of empirical equations are presented giving the forces and their dependence on the initial momentum flux, the distance and the disc geometry. It is believed that the results are useful for design purposes.

2. INTRODUCTION

An interesting technical problem is concerning the determination of the forces on smooth symmetrical bodies which are placed on the axis of a steady jet flow, issuing from a pipe exit into an initially quiescent ambient consisting from the same fluid.

In this work a number of experimental measurements and the analysis of them are presented, concerning the axial force, exercised on an inclined smooth plan circular disc from the flow of a round turbulent fluid jet. The practical purpose of this research is to contribute to the determination of the above force on deflectors, or to the design of discs placed in the sea against the jets issuing from the ports of a diffuser - in order to maximize the dilution of pollutants.

Figure 1 shows the flow geometry. The angle of the inclination of the thin disc to the jet axis is ϕ , the pipe exit has a diameter d_o , and the smooth disc has a diameter D and is placed at a distance x from the pipe exit. The axial force, which is due to pressures and shear stresses on the disc, is F while the density of both fluids is ρ_o , the kinematic viscosity is ν_o , and the exit jet velocity is V_o . The exit discharge is $Q_o = V_o(\pi d_o^2)/4$, the corresponding momentum flux is $M_o = \rho_o Q_o$, and the exit Reynolds number is $Re_o = V_o d_o / \nu_o$. When the Reynolds number is large enough the jet flow and momentum diffusion are turbulent.

In the case of undisturbed jet flow, i.e. without the disc, the jet has an initial conical region near the exit, the core, with a length around $8d_0$, within which the flow velocities are constant in each cross section. Further down the jet flow has in each cross section a maximum centerline velocity, u_m , which is quickly reducing when x distances are increasing. The discharge on each cross section is greater than Q_0 , because of fluid entrainment from the ambient. From a large number of previous measurements it has been found that beyond the core,

$$u_m/V_0 = C(x/d_0)^{-1}, \quad (1)$$

where $C \approx 6.2$.

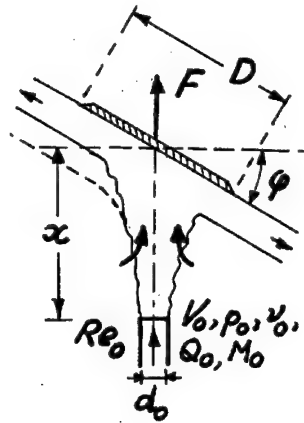


Figure 1. Flow geometry

If a symmetrical body such as a disc is placed on the flow axis, then the jet behavior is disturbed around the body. This means that the jet behavior is not dramatically changed far from the body, and eq.(1) is still holding there.

N. Ackermann and R. Undan had measured in 1970 the forces on discs without an inclination, $\phi=0$, [1], while T. Papathanassiadis and J. Demetriou also presented in 1984 some measurements with horizontal discs, [2]. In both papers the results were in good agreement among them, showing that the force F is decreasing when x is increasing-no matter the fluid medium.

In the paper by Papathanassiadis et al is was proved that

$$F/M_0 \sim (2C^2/\pi x^2) \cdot (\pi D^2/4) \quad (2)$$

and their results were worked out in double logarithmic scales, F/M_0 (vertical axis) versus $A = [(2C^2/\pi x^2) \cdot (\pi D^2/4)]^{1/2} = (C/\sqrt{2}) \cdot (D/x) \approx 4.384 \cdot (D/x)$ on the horizontal axis. The same method

of data presentation and analysis is followed in the present paper, separately for each angle φ , while it appears reasonable that $F=0$ when $\varphi=90^\circ$.

An interesting distinction between the discs at any angle φ , is that of "small" and "large" discs. When D is relatively large and x is small-but always further from the core ($x>8d_0$), then D/x is large and the disc is considered as large. For $\varphi=0$ the jet is symmetrically deflected, and a simple application of one dimensional analysis for a weightless and ideal fluid shows that for large discs $F/M_0=1$. For other angles φ the same result could hold if the deflected flow had the same thickness around the disc perimeter. This is not true because the flow thickness is not constant throughout, Fig.1-dashed line. Thus F/M_0 takes various limiting values K for various angles φ . K actually consists a measure of the fluid thickness variation along the disc periphery and comprises also a shear stress contribution on the disc.

When D is relatively small and x is large then D/x is small and the body is considered as small. This fact does not arise another limiting value for F/M_0 in terms of A , simply because the flow overcomes the disc and creates a wake field behind it.

3. EXPERIMENTS AND DATA ANALYSIS

In this experimental work air jets were vertically issuing from a round exit into the atmospheric air of the laboratory, with relatively small velocities, $V_0<60$ m/sec. The exit velocities were measured through a Pitot tube, the discs were made from various smooth materials and were placed at various x distances from the exit. With the aid of a balance placed over each disc, its weight was measured with and without a flow, and the difference of the two values corresponded to the force F exercised on each disc. It is estimated that the percentage errors of all measurements were less than $\pm 3\%$.

Four groups of runs were organized with $\varphi=0^\circ - 30^\circ - 45^\circ - 60^\circ$. For each angle φ the disc diameters were $D=36-30-25-22.7-20-15-14.5-10-5-2$ cm, and the exit diameters were $d_0=6.45-2.5-1$ cm, in various combinations among them. More than 800 force measurements were performed, although they are not all used in the present work. The Reynolds numbers varied between 134,200 and 27,000, while x/D varied between 7.3 and 0.55 and x/d_0 varied between 60 and 8.

Figure 2 shows the F results in dimensionless terms of A and F/M_0 for each angle φ . Each group of experimental points is well represented by a curve which tends, for large A values, to a limiting value of F/M_0 , $F/M_0=K$. In Figure 3 the corresponding K values are examined versus the angles φ , and the

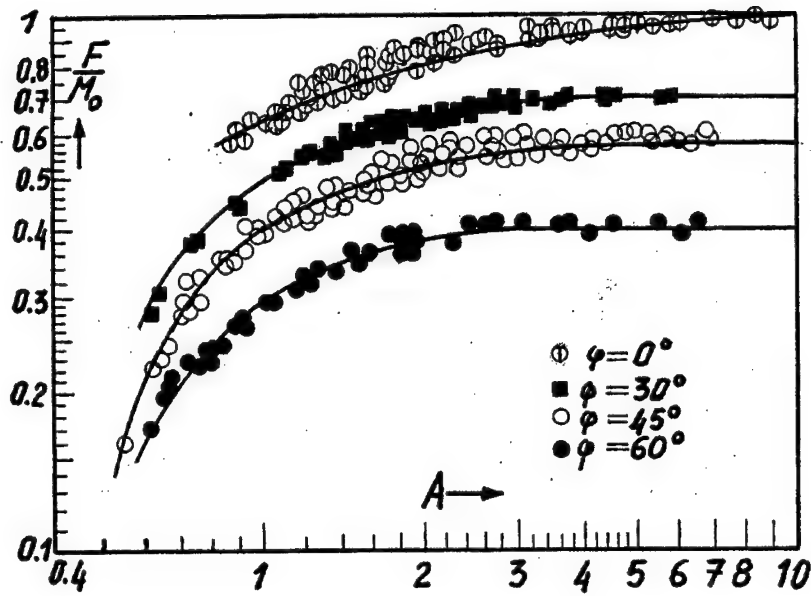


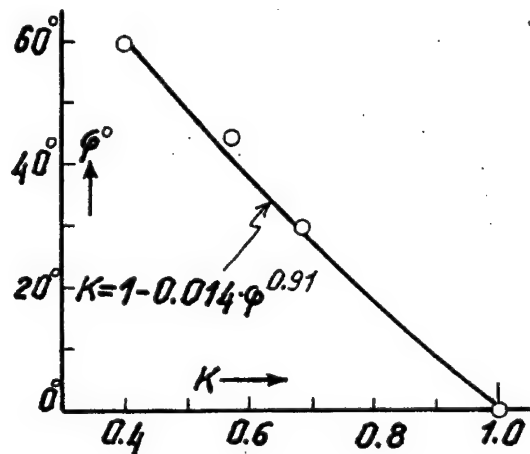
Figure 2. Force measurements

simple empirical equation

$$K = 1 - 0.014\phi^{0.91} \quad (3)$$

is determined.

Moreover, for each curve of Fig.2 another empirical equation of the form

Figure 3. K versus ϕ

$$F/M_o = K \cdot a \cdot A^b \quad (4)$$

may be assumed, where a and b are functions of the angle φ .

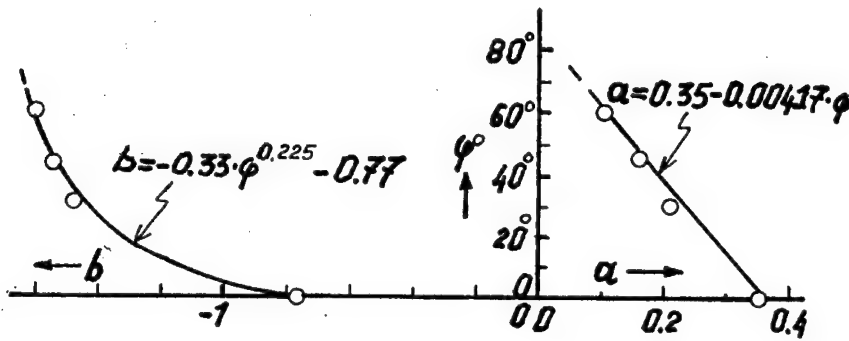


Figure 4. a and b functions

Figure 4 shows a and b values versus the angle φ , and two simple equations are deduced

$$a = 0.35 - 0.00417 \cdot \varphi \quad (5)$$

$$b = -0.33 \cdot \varphi^{0.225} - 0.77 \quad (6)$$

The final expression for F/M_o comes after the combination of eq. (3), (4), (5) and (6) for angles φ with $0^\circ \leq \varphi \leq 60^\circ$,

$$F/M_o = (1 - 0.014 \cdot \varphi^{0.91}) - (0.35 - 0.00417 \cdot \varphi) \cdot [4.384 \cdot D/x]^{-(0.33 \cdot \varphi^{0.225} + 0.77)} \quad (7)$$

4. CONCLUSIONS

In this paper a number of measurements and the analysis of them are presented, concerning the forces exercised on inclined smooth discs from pipe jet flows. The results are dimensionlessly presented in Fig. 2, and equations (3), (4), (5), (6), or (7), are concluded. The forces are depending on the initial exit velocity, on the disc and pipe diameters, on disc distances and inclination angles, and on the fluids' density. It is believed that the results are useful for design purposes.

5. REFERENCES

- [1] Ackermann N., Undan R., *Forces from submerged jets*, ASCE, Hyd. Div., HY11, pp 2231 – 2239 (1970).
- [2] Papathanassiadis T., Demetriou J., *Forces on bodies within jet flows*, Scientific Papers, National Technical University of Athens, Vol. 8, N° 1-4, pp. 29-40 (1984).

FLOW IN OPEN CHANNELS LINED WITH DIFFERENT MATERIALS

J. D. Demetriou

Department of Civil Engineering
Nat.Tech.University of Athens, Gr-15780, Athens, Greece

C. Pourliotis

Department of Civil Engineering
Nat.Tech.University of Athens, Gr-15780, Athens, Greece

P. Sarantos

Civil Engineer, Nat.Tech.University of Athens
Matzagriotaki 110, Kallithea, Gr-17676, Athens, Greece

1. SUMMARY

This paper presents a number of experimental measurements in rectangular open channel flows, concerning the relation among the Manning resistance coefficient and the geometry of the flow and roughness elements. The case of rough walls and nearly smooth bottom is investigated, and a number of pertinent equations are given. The results may be useful to the hydraulic engineer when designing open channels.

2. INTRODUCTION

The design of one-dimensional open channels is mainly based upon information provided by experimental measurements in the hydraulics laboratory. In practice, it is usual for the hydraulic engineer to deal with open channels lined with different materials, e.g. a smooth concrete or asphalt bottom and two lateral symmetric walls from stone, brick, plaques or other rough materials

If the roughness of a channel is everywhere (bottom, lateral walls) the same, then the Manning resistance coefficient n is usually considered as of unique value and constant throughout, $n = \text{const.}$ Thus, the well established empirical Manning equation for the uniform flows is used in the form of

$$Q = E \cdot V = E \cdot (1/n) R^{2/3} J_0^{1/2},$$

where E = liquid cross section (m^2), $R = E/P$ = hydraulic radius (m), P = wetted perimeter (m), J_0 = channel slope along the flow- which usually is very small, and Q = discharge (m^3 / sec). The constancy of n means that this parameter is independent of the flow depth and is only

related to the nature of the roughness elements on the entire internal area of the channel boundaries.

In case of different roughnesses because of different lining materials, it is common in the hydraulic calculations to determine a constant "hydraulic mean" or "equivalent" resistance coefficient, $n_E = \text{const.}$, on the entire wetted perimeter.

Although, the above practice does not reveal some interesting resistance details, mainly about the dependence of n (for a flow depth y) on other flow parameters.

In two previous papers by the first author with or without other writers, in 1999, [1], and in 2000, [2], it was experimentally concluded that in the case of a rough bottom and two symmetrical smooth walls in a rectangular open channel, n depends upon the parameters of the channel when flowing full (reference values y_f , n_f), the width of the channel (b), and the relative bottom roughness. In those papers a number of equations were given based on the experimental roughness which was realized with the use of transverse - uniformly distributed rubber strips on the entire bottom, with constant heights $h = k$ or $h = 2k$ ($k = 4\text{mm}$) and at constant distances λ , where the relative roughness λ/h was varying between 6,25 and 100. The method of transverse artificial strips was explained in 1959 by V.T.Chow in his book, [3], and was used by D.Knight and A.McDonald in 1979, [4], by D.Knight et al in 1988, [5], and others. The above conclusions were also confirmed from the reanalysis of a number of data taken from the papers by previous investigators and worked out in the papers [1] and [2].

In this investigation the bottom is considered as nearly smooth and the walls as rough. Fig. 1 shows the geometry of the uniform flow in the rectangular channel. The flow depth is y (with corresponding resistance coefficient n), the maximum channel flow depth is y_f (with corresponding resistance coefficient n_f), b is the channel width, while the roughness elements are constructed from hard rubber strips, with cross sections $k \times k$, and glued at various distances λ (axis to axis): In each experiment λ was kept constant in the entire length of the walls, but the relative roughness λ/k was changing from one experiment to the next experiment.

The area of any liquid cross section is considered as $E = b \cdot y$, while $P = b + 2y$, $R = E/P$, $Re = V \cdot 4R/\nu$, $V = Q/E$ = average cross section velocity, ν = kinematic viscosity, $Fr = V \cdot (g \cdot y)^{-1/2}$. All flows have $Re \gg Re_{crit.}$ (entirely turbulent flows), and $Fr < 1$ (subcritical flows).

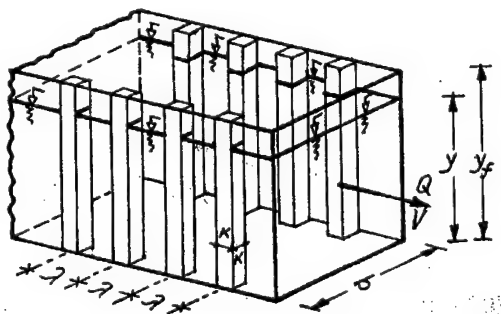


Figure 1. Flow geometry

Based on dimensionless reasoning it can be shown that in general

$$n/n_f = s(y/y_f, y_f/b, \lambda/k, Re, Fr)$$

where s means function. The above qualitative equation is reduced to

$$n/n_f = s(y/y_f, y_f/b, \lambda/k) \quad (1)$$

because of the nature of the flow, which is always here turbulent and subcritical.

In the previously mentioned papers [1] and [2] eq. (1) was determined in a quantitative form, concerning the flows in a rectangular channel with a rough bottom and two lateral and symmetrical vertical smooth walls.

As it will be shown in the present paper, when the walls are rough and the bottom is smooth, the qualitative form of eq. (1) is similar, although its quantitative form is somewhat different.

3. EXPERIMENTAL MEASUREMENTS AND DATA ANALYSIS

The details of the experimental channel can be found in the two previous papers [1] and [2]. The discharges were accurately and systematically measured with the aid of a differential manometer, the flow depths with a number of level gauges, while the uniform flow was realized through the use of an end sluice gate. The measurements concerned the water temperature (and thus ν), the discharges Q and Q_f and the depths y and y_f , for various λ/k ratios. E, P, R and $V (= Q/E)$ were calculated, while from the Manning equation the resistance coefficients n and n_f were deduced. It is estimated that the mean percentage error of all measurements did not exceed $\pm 3\%$.

A large number of runs were organized with $\kappa = 4\text{mm}$, $\lambda/\kappa = 12.5-25-50-100-\infty$ (smooth case), $41,200 < Re < 193,300$, $0.250 < Fr < 0.660$, $3\text{cm} < y < 36\text{cm}$, $4\text{l/sec} < Q < 52\text{ l/sec}$, $34\text{cm/sec} < V < 59\text{ cm/sec}$, $0.40 < y_f/b < 1.46$, $0.143 < y/y_f < 1.0$. In each run, in order to determine the uniform flow depth (for a particular set of Q and λ/k values), 5 depths were measured along the channel and then, if those depths did not differ more than 1 mm, i.e. if it was secure that the flow was practically uniform, the average depth was calculated and considered as the final uniform flow depth for this particular values of Q , λ/k (and n).

Fig 2 shows an example from the initial measurements with $k = 4\text{mm}$, $\lambda = 100\text{mm}$, and various y depths.

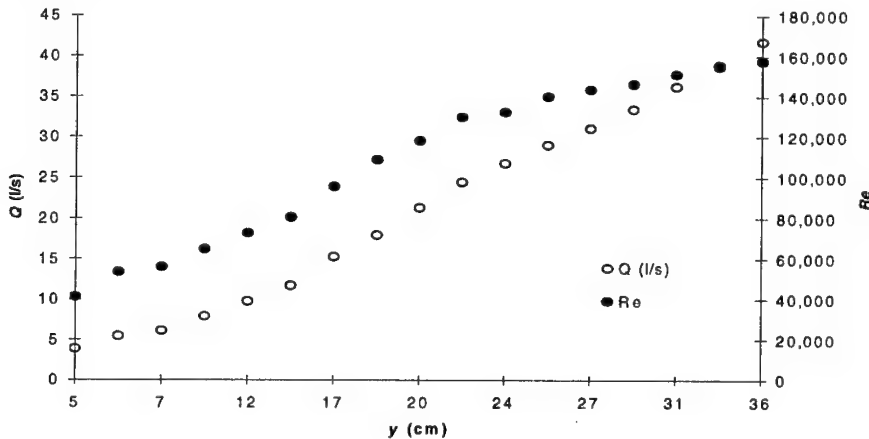


Figure 2. Initial measurements

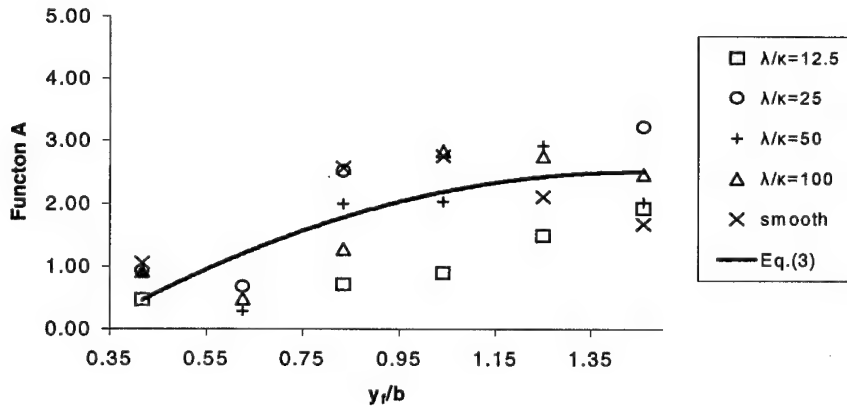
In order to analyze the experimental data the following empirical equation was used,

$$n / n_f = A (y / y_f)^B [1 - (y / y_f)]^C + (y / y_f) \quad (2)$$

where , A,B,C are functions of the flow parameters, and $n / n_f = 1$ when $y / y_f = 1$. A,B,C, may be determined if the ratios y_f / b and λ / κ are related to them for all measurements.

From preliminary tests it was concluded that A and B are mainly related to y_f / b , while C is rather related to λ / κ . This result, which is holding here for $\kappa = 4\text{mm}$ (small roughness elements), is also confirmed from more recent laboratory measurements with $\kappa = 8\text{mm}$ (high roughness elements) which are not presented here.

Figure 3,4 and 5 present the relations between A and B versus y_f / b , and C versus λ / κ .

**Figure 3 . Relation between A and y_f / b .**

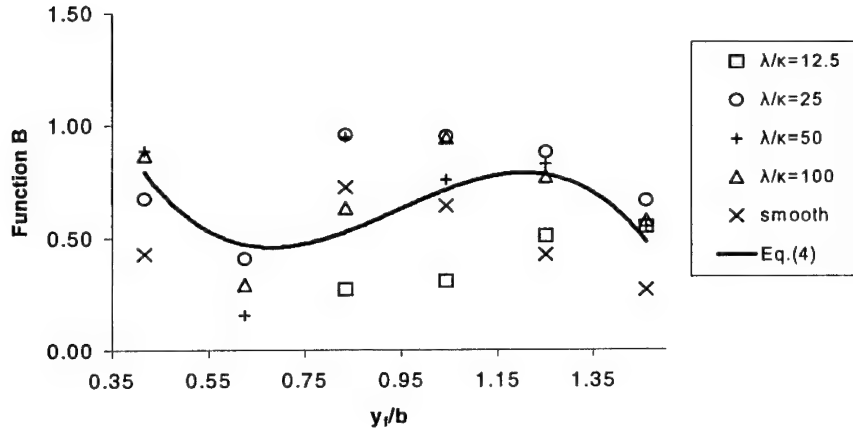


Figure 4 . Relation between B and y_f/b .

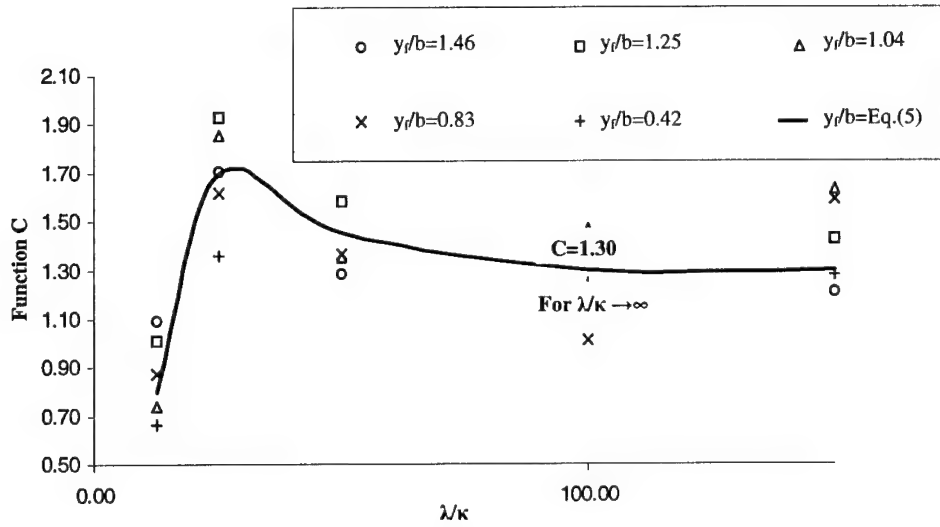


Figure 5. Relation between C and λ/κ .

From the above diagrams the following empirical expressions are determined

$$A = 1.923 \cdot (y_f/b)^2 + 5.5712 \cdot (y_f/b) - 1.5274, \quad (3)$$

$$B = 1.558 \cdot (y_f/b)^3 + 12.89 \cdot (y_f/b)^2 - 11.211 \cdot (y_f/b) + 3.5561, \quad (4)$$

$$C = -9941 \cdot (\lambda/\kappa)^3 + 784.5 \cdot (\lambda/\kappa)^2 - 5.4 \cdot (\lambda/\kappa)^{-1} + 1.3, \quad (5)$$

and are combined with eq. (2).

The above expressions are somewhat different from corresponding expressions in [1] and [2].

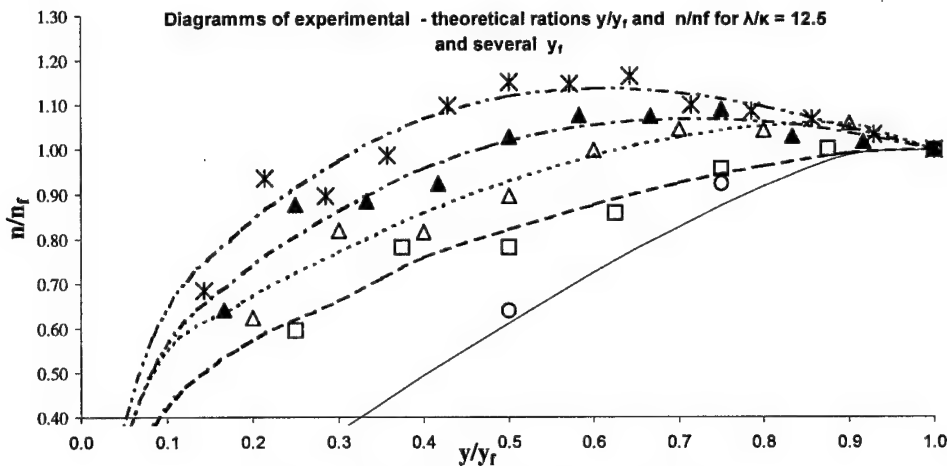


Figure 6. Relations between n/n_f , y/y_f and λ/κ

Finally, Fig. 6 presents an example of the application of the above equations, showing that the determined curves are satisfactorily presenting the experimental results.

Unfortunately the present results cannot be compared with other results, because of the lack of previous experimental results from earlier investigators.

4. CONCLUSIONS

This paper presents a number of experimental measurements in rectangular open channel flows with rough walls and nearly smooth bottoms, concerning the dependence of Manning n coefficient upon the geometries of flows and roughnesses. The empirical eq. (2) gives the relation among all pertinent parameters, accompanied by eqs (3),(4),(5). It is believed that the results are useful to the hydraulic engineer when designing open channels.

5. REFERENCES

- [1] Demetriou J.D., Manassakis E.J., Dimitriou D.J., *Resistance Coefficient Change in Open Channels*, 4th National Congress of the Greek Committee for the Water Management, Abstracts, Vol. B, p.p 91-97, Volos-Greece, June 1999.
- [2] Demetriou J.D., *Irrigation Channels With Differential Roughness*, 2nd National Congress of Agricultural Mechanics, Abstracts, p.p. 42-49, Volos, Greece, September 2000.
- [3] Chow V.T. *Open Channel Hydraulics*, McGraw Hill, 1959, p.p. 194-197.
- [4] Knight D.W. and McDonald A.J., *Hydraulic Resistance of Artificial Strip Boundaries* ASCE, J.Hydr.Eng.105(6), 1979, pp 675-690.
- [5] Knight D.W., Demetriou J.D., Hamed M.E., *Hydraulic Analysis of Channels with Flood Plains*, Int. Conference on the Hydraulic Aspects of Floods, BHRA, Sept.1988, London, 7 pages.

AIRLIFT PUMP PERFORMANCE OPTIMISATION FOR DEEP-SEA MINING

D. P. Margaritis

Assist. Prof., Dr-Eng., Fluid Mechanics Lab.,
Mechanical Engineering and Aeronautics Dept., University of Patras,
GR-26500 Patras, Greece

1. SUMMARY

The object of the present study is to access and optimise the performance of an airlift pump under predetermined operating conditions, and especially to estimate the effect of the pipe diameter and injection depth to the airlift pump efficiency. In the numerical modelling, the gas-liquid-solid three-phase flow in an airlift pump is described by a system of differential equations, which derives from the fundamental conservation equations of continuity and momentum. The effect of the shape and size of particles derives from the different relationships used for the drag coefficient calculation. The numerical simulation results clearly show a very good agreement with experimental and computational data of other researchers. This approach leads to a more general mathematical model, which is applicable to a wide range of installations, from small to very large systems, suitable for deep-sea mining.

2. INTRODUCTION

The airlift method has been known since the end of the 18th century. It has since been used for the lifting of water, wastewater and aggressive fluids, for the transportation of solids and more recently of radioactive fluids in nuclear fuel recycling plants. It is based on the principle of injecting a compressed gas, usually air, into the conveying pipe causing thus the gradual lifting of the liquids or the solid-liquids mixture.

There have been numerous publications suggesting calculation procedures for the design and the satisfactory operation of an airlift pump. Chaziteodorou [1] presented a systematic review concerning the applications and developments of the airlift pump. Weber [2,3,4] and Dedegil [2,5] presented a calculation model for an airlift pump and the principles of airlift techniques. The technology of artificial lift methods has been presented by Brown [6]. Yet all the above studies depend either on experimental data or empirical correlation factors leading to results without general validity.

A general calculation method for the three-phase flow and a design model for an airlift pump installation presented by Margaritis and Papanikas [7]. This method can be used in simulation of an airlift system for pumping liquids or solid-liquid mixtures. The object of the present paper is to access and optimise the behaviour of an airlift pump, and especially to estimate the effect of the geometry and flow conditions to the airlift pump efficiency, for deep-sea mining.

3. PHYSICAL MODELLING AND DESIGN OF AN AIR-LIFT PUMP

The airlift pump consists of two vertical pipes. One for pumping liquid or a mixture of liquid and solid particles and a parallel one for the injection of the gas phase. The main pipe is divided into three parts, the suction part L_S , the raising part or injection depth L_I and the third one and so-called discharge part L_D , (figure 1). Considering the pressure at the free surface of the feed tank to be p_o and in the storage tank to be p_n , the pressure balance can be written as

$$p_o + \rho_L g(L_S + L_I) = p_n + \Delta p_{Tot} \quad (1)$$

where Δp_{Tot} are the total pressure losses along the three parts of the pipe, due to the frictional, accelerational and gravitational component of the pressure gradient, and ρ_L is the liquid phase density.

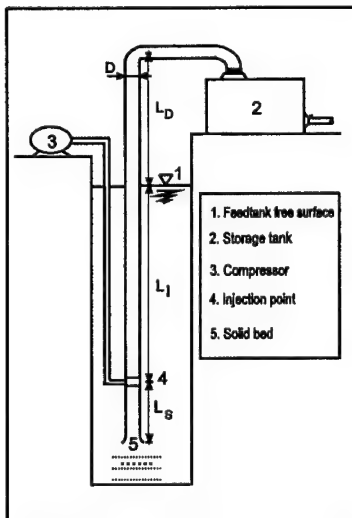


Figure 1. Airlift pump installation

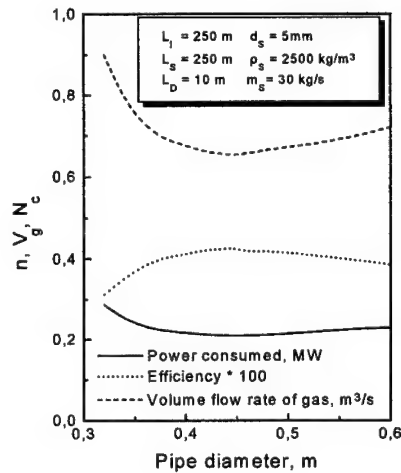


Figure 2. Optimisation of the pipe diameter of an airlift pump installation

In the suction part, pressure losses are calculated as an integral whole, and in the other two sections, the pressure losses should be calculated step-by-step because of the expansion of the gas phase, using the following equation:

$$\Delta p_S = \int_0^{L_S} \frac{dp}{dx} dx = \Delta p_{\Delta x} L_S, \quad \Delta p_{I,D} = \sum_1^k \left(\frac{\Delta p}{\Delta x} \right)_k \Delta x, \quad k = \frac{L_I + L_D}{\Delta x} \quad (2)$$

A very important quantity is the pump or lifting efficiency, which is defined as the ratio of the gained power N_G over the consumed power N_C , that is $\eta = N_G/N_C$, given by the equations

$$N_C = \int_{p_o}^{p_I} \frac{M_G}{\rho_G} dp = M_G R T \ln \left(\frac{p_I}{p_o} \right) \quad N_G = C M_S g \left((L_S + L_I) \left(1 - \frac{\rho_S}{\rho_L} \right) + L_D \right) + (1 - C) g L_D M_L \quad (3)$$

with ρ_G the density and M_G the mass flow rate of the gas phase. The gained power is defined as the increase of the potential energy of the liquid or the solid phase, with $C=0$ for pumping liquids and $C=1$ for pumping solids, ρ_s , ρ_L the density and M_s , M_L the mass flow rate of solid and liquid phase respectively.

4. MATHEMATICAL MODELLING FOR SEPARATED THREE PHASE FLOW

To make the problem one-dimensional, which is approximately the case in practice, the following assumptions are made for the mathematical formulation of the airlift mechanism. The planes of equal velocity and equal pressure should be normal to the pipe axis. The transport of the solid particles occurs primarily through water. No particular shape of bubbles or solid particles is assumed, due to the generalised relationship used for the calculation of the drag coefficients. Finally an isothermal change of state is assumed for air. This assumption is justified only if the three phases flow very slowly through the pipe.

For a separated three-phase flow model, one should consider the balance equations for flow through the vertical pipe element of length dx and cross-sectional area A , divided into the subareas with cross section A_s , A_G , A_L , for solid, gas and liquid phase, respectively. Due to the gas-phase expansion, we have to transform the system of equations to a system of differential equations and to treat a step-by-step calculation procedure, using a suitable numerical method. The governing equations are the momentum and the continuity equations for the individual phases, ($i=1,2,3$), in differential form:

$$-\frac{dp}{dx} = \sum_{i=1}^3 \left(\rho_i a_i g + \rho_i a_i u_i \frac{du_i}{dx} + \left(\frac{dp}{dx} \right)_{FR,i} \right) \quad (4)$$

$$u_i \rho_i \frac{da_i}{dx} + u_i a_i \frac{d\rho_i}{dx} + \rho_i a_i \frac{du_i}{dx} = 0 \quad \text{with} \quad \frac{d\rho_1}{dx} = \frac{d\rho_3}{dx} = 0 \quad \text{and} \quad \sum_{i=1}^3 \frac{da_i}{dx} = 0 \quad (5)$$

The absolute velocity of the solid and gas phase, with $i=1,2$, and the relative velocity of particles in differential form, are

$$\frac{du_i}{dx} = \frac{du_3}{dx} + (-1)^i \frac{du_{i,r}}{dx} \quad \frac{du_{i,r}}{dx} = \left(\frac{4}{3} \frac{d_i g}{C_{D,i}} \left(\frac{\rho_i}{\rho_3} - 1 \right) \right)^{\frac{1}{2}} \frac{1}{2a_3^{\frac{1}{2}}} \frac{da_3}{dx} \quad (6)$$

For the rising velocity of bubbles, we have to consider in addition the change of the bubble diameter due to the expansion of the gas-phase. For an isothermal expansion of gas, with $d_{2,0}$ the initial bubble diameter at the injection point where the pressure is p_0 and the compressibility factor is Z_0 , the rising velocity of bubbles in differential form is

$$\frac{du_{2,r}}{dx} = \left(\frac{4}{3} \frac{d_{2,0} g a_3}{C_{D,2}} \right)^{\frac{1}{2}} \left(\frac{p_0}{p} \frac{Z}{Z_0} \right)^{\frac{1}{6}} \left(\frac{\rho_3 + 2\rho_2}{6(2\rho_3 - \rho_2)^{\frac{1}{2}}} \left(Z^{-1} \frac{dZ}{dp} - p^{-1} \right) \right) \frac{dp}{dx} + \left(\frac{\rho_3 - \rho_2}{4\rho_3 a_3^2} \right)^{\frac{1}{2}} \frac{da_3}{dx} \quad (7)$$

According to the airlift principle, the gas phase is supplied at the injection point under pressure p_i and it is expanded to the nominal pressure p_n of the storage tank. Differentiating equation of state and assuming an isothermal expansion, for the calculation of the compressibility factor Z as a function of pressure, (Schlichting [8], Chaziteodorou [1]), we get

$$\frac{dZ}{dx} = \left(\frac{dp}{dx} - \frac{p}{\rho_2} \frac{d\rho_2}{dx} \right) \frac{Z}{p}, \quad Z(p) = 1 - 5.8198 \cdot 10^{-4} \left(\frac{p_1}{p_n} \right) + 2.809 \cdot 10^{-6} \left(\frac{p_1}{p_n} \right)^2 \quad (8)$$

The calculation of the drag coefficient, $C_{D,i}$, of solid particles or the bubbles is based on a generalised form, similar to that proposed by Margaris and Papanikas [9],

$$C_{D,i} = \sum_{j=1}^3 B_j Re_i^{j-3/2} \quad Re_i = \frac{\rho_3 |u_i - u_3| d_i}{\mu_3} \quad | i = 1, 2 \quad (9)$$

where the slip velocity between the corresponding two phases, $u_i - u_3$, is used in the Reynolds number and B_j are constants, given in Table 1, depending upon the shape of the particles and the values of the Reynolds number Re_i (Molerus [10], Muschelknautz [11], Clift et al. [12]).

Table 1. Constants B_j for the calculation of the drag coefficient of particles or bubbles.

Constants B_1 B_2 B_3	Reynolds range	Characteristic dimension	Shape of particle	Reference
24 0 0	$Re_i < 0.1$	diameter	sphere	Stokes
24 4 0.4	$Re_i < 10^4$	diameter	sphere	Molerus
21.5 6.5 0.23	$0.5 < Re_i < 10^3$	diameter	sphere	Muschelknautz
24 6 0.35	$0.5 < Re_i < 800$	$1.5 \times a$ $a = \text{largest dimen.}$	polyhedron	Muschelknautz
23 6 0.5	$0.5 < Re_i < 600$	$1.08 \times dz$ $dz = \text{diam. of base}$	cylinder $l/dz = 1$	Muschelknautz
27 4.5 0.65	$0.5 < Re_i < 400$	$1.24 \times a$, $a = \text{edge}$	cube	Muschelknautz

In the framework of the present paper a Runge-Kutta 4th order method was used in order to solve the above system of differential equations for the gas-liquid-solid flow. The variables, which must be defined, for the solution of the gas-liquid-solid flow, are the physical properties of the phases, the geometry of the pipe and the desired mass flow rate of solids. For these conditions, the computational algorithm calculates the necessary mass flow rate of gas.

5. RESULTS AND DISCUSSION

For validation purposes of our analysis, a large number of results were compared against both experimental and computed data by other researchers [2,3,4,7]. The average deviation of our results is 5% for the solid flow rate and 0.3% for the liquid flow rate, while the corresponding values of other researchers are 10% and 15%, respectively. The difference is due to the fact that their analysis is based on empirical or mechanistic model, while our analysis is based on the fundamental equations of fluid mechanics.

An operation curve of an airlift pump shows mass flow rate of solids and pump efficiency as a function of gas flow rate delivered by the compressor (figure 3). The most significant geometric parameter is the pipe diameter, its magnitude has a great effect in the airlift efficiency and it is obvious that an optimisation of the system is very important (figure 2). It should also be noted that for different mass flow rates of solids different optimum diameters would result. The optimum design of an airlift system should aim to obtain not always the maximum efficiency but

a high enough efficiency for a wide range of applications, which means a wide range of mass flow rates of particles.

Generally the increase in the gas injection depth L_I , results in an increase of the amount of solids that can be pumped followed by a parallel decrease of the maximum pump efficiency, as related to the power consumed (figure 4). On the other hand, by increasing the injection depth L_I , for pumping a certain quantity of solids, we can also increase the total submerged length, $L_I + L_S$. But as the injection depth increases the suction part decreases, eventually reaching the limit where the gas injection point is at the same level with the solid bed. This phenomenon is of great importance to large-scale installations, such as deep-sea mining. The purpose of the airlift designer is to combine all the above geometric and functional parameters in order to achieve at first the maximum efficiency, while the solids flow rate is large enough, and on the other hand to maintain a satisfactory efficiency over a large range of gas flow rates.

6. CONCLUSIONS

An applied **Air Lift Model Analysis** for air-water-solid flow has been developed. Based on a system of differential equations, derived from the fundamental equations of continuity and momentum conservation, this model has a very good performance and a more general mathematical form, compared to other models. This model has been combined in an easily used computer code, named **ALMA**, which is a very useful tool for the optimum design of airlift pump installations.

The optimisation of the installation is the more important feature of the code. This means that the code can calculate the optimum value for the pipe diameter, injection depth, shape and size of particles and bubbles, and the other parameters in order to minimise the energy consumption. The results of the present analysis are in good agreement with the existing data in the literature, but in order to approximate the phenomenon better an extended modelling is in progress now. Taking into account the flow regimes that may exist in the pipeline, as well as the influence of the solid particles to the development of the flow regimes, this extended modelling is expected to contribute more to the optimum design of the airlift pump installations.

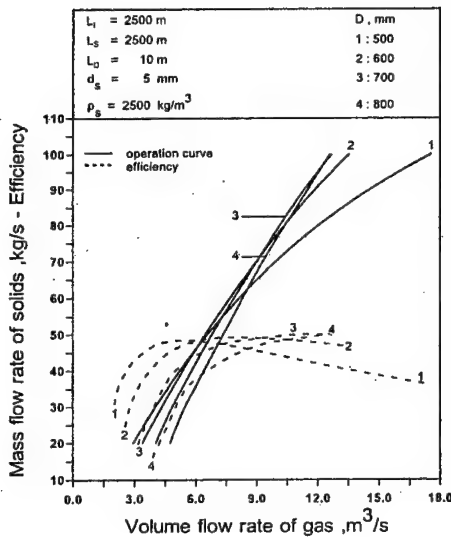


Figure 3. Influence of the pipe diameter on the airlift pump efficiency

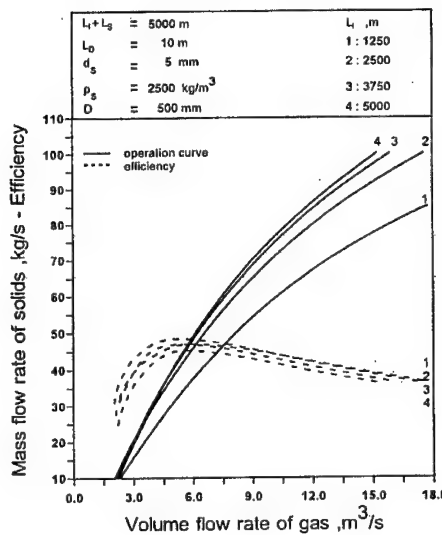


Figure 4. Influence of the injection depth on the airlift pump efficiency

7. REFERENCES

- [1] Chaziteodorou, G., «Fundamentals of Oceanic Mining», Dr. Riederer-Verlag, Stuttgart, (1977).
- [2] Weber, M., and Dedegil, Y., «Transport of solids according to the airlift principle», Fourth International Conference on the Hydraulic Transport of Solids in Pipes, May 18-21, Alberta, Canada, paper H1, (1977).
- [3] Weber, M., Dedegil, Y., and Feldle, G., «New experimental results regarding extreme operating conditions in air lifting and vertical transport of solids according to the jet lift principle and its applicability to deep-sea mining», Fifth International Conference on the Hydraulic Transport of Solids in Pipes, May 8-11, Hanover, Germany, paper F7, (1978).
- [4] Weber, M., «Vertical Hydraulic conveying of solids by airlift», Journal of Pipelines, pp.137-152, (1982).
- [5] Dedegil, Y., «Principles of airlift techniques». Encycl. of Fluid Mechanics, pp.383-397, (1986).
- [6] Brown, K. E., «The Technology of Artificial Lift Methods», Pennwell Publ. Co., Vol. 1-4, (1977-1984).
- [7] Margaritis, D.P. - Papanikas, D.G., «A Generalized Gas-Liquid-Solid Three-Phase Flow Analysis for Airlift Pump Design», Transactions of the ASME, Journal of Fluid Engineering, Vol. 119, No 4, pp. 995-1002, (1997).
- [8] Schlichting, H., «Grenzschichttheorie», 3, Aufl. Karlsruhe, (1958).
- [9] Margaritis, D., and Papanikas, D., «Effect of particle drag coefficient on the boundary layer of particulate gas flow over a flat plate», Z. Flugwis. Weltraumforschung, Band 13, Heft 2, pp. 73-79, (1989).
- [10] Molerus, O., «Fluid-Feststoff-Stroemungen», Berlin, Springer Verlag, (1982).

- [11] Muschelknautz, E., «*Druckverlust bei der Flugfoerderung*» Chem. Ing. Techn. 58, pp. 788-799, (1986).
- [12] Clift, R., Grace, J. R. and Weber, M. E., «*Bubbles, Drops and Particles*», Academic Press, Inc., (1978).

BOUNDARY SHEAR IN COMPOUND NON-SYMMETRICAL CHANNELS

K. J. Nanou-Giannarou

Dept. of Water Resources, Hydraulics and Maritime Engineering
Faculty of Civil Engineering, National Technical University of Athens, Greece

J. D. Demetriou

Dept. of Water Resources, Hydraulics and Maritime Engineering
Faculty of Civil Engineering, National Technical University of Athens, Greece

1. SUMMARY

The present work deals with the investigation, presentation and analysis of experimental results, concerning the boundary shear stress distribution and the friction factor determination in a uniform flow within a smooth open channel with compound cross section, comprising a rectangular main channel and a non-symmetrical rectangular flood plain.

2. ΠΕΡΙΛΗΨΗ

Στην παρούσα εργασία ερευνώνται, παρουσιάζονται και αναλύονται πειραματικά αποτελέσματα με σκοπό τον προσδιορισμό της κατανομής διατμητικών τάσεων ορίου και τον υπολογισμό του συντελεστή τριβής μέσα σε λείο ανοικτό αγωγό σύνθετης μη συμμετρικής διατομής, αποτελούμενης από την ορθογωνικής μορφής κυρίως κοίτη και μία επίσης ορθογωνική πλημμυρική κοίτη.

3. INTRODUCTION

The distribution of boundary shear stresses from flows in complex cross sections is still poorly understood. As a result, knowledge concerning the momentum transfer within the cross section is limited, despite the practical interest involved. In the case of compound channel, the lateral momentum transfer between regions of different depth considerably modifies the primary flow field. Consequently it is important to accurately specify this interaction between the pertinent flow fields.

One of the pioneering works in the flow within compound non-symmetrical channels was that of Rajaratnam-Ahmadi [1], who performed a large number of experiments to investigate the interaction between main channel and flood plain in a wide channel. Stephenson-Kolovopoulos [2] presented a method of separating the flow of the compound channel by using an interface, while Tominaga-Nezu [3] studied in detail the turbulent characteristics of a compound non-symmetrical channel. Naot-Nezu-Nakawaga ([4] and [5]) attempted in their two works to explain the hydrodynamic behavior of flow in compound non-symmetric channels. More recently Pang [6] analyzed energy losses in such flows while Sofialides-

Prinos [7] simulated numerically the flow and studied the impact of roughness in the problem. In this study the works of Knight-Demetriou [8], Knight-Hamed [9] and Myers-Brennan [10] on compound symmetrical channels have been used for comparison reasons.

A first presentation of the present work, concerning the structure of the velocity field, the proportion of the total flow that occurs in the various sub-areas of the cross-section and an estimation of Manning' n coefficient, momentum β and kinetic energy α correction factor, has been recently presented by the authors [11]. In the present investigation experimental results by HR Wallingford [12] have also been used.

4. THE EXPERIMENTS

Experimental Apparatus

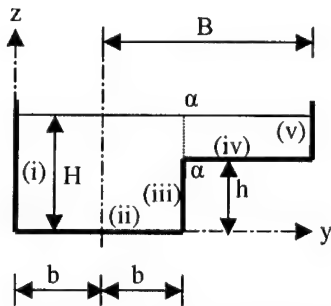


Table 1	
$B+b$	381 mm
J_o	$9.66 \cdot 10^{-4}$
h	76 mm
$2b$	152 mm
$B-b$	229 mm
H	84÷188 mm

Figure 1: Typical cross section of a non-symmetrical channel with one flood plain

The experiments were performed in a 15 m flume, 610 mm wide, with a constant bed slope of $9.66 \cdot 10^{-4}$. A non-symmetrical cross section was used with a main channel 152 mm wide and a flood plain 229 mm wide. The typical cross section of the channel and geometrical symbols are presented in Figure 1. The dimensions are shown in Table 1. Both the main channel and the flood plain were constructed from smooth perspex and their roughness elements are considered as identically distributed.

Uniform flow was achieved for any given discharge, by adequately adjusting a tailgate at the downstream end of the flume. Discharge was measured by a Venturi meter with two differential manometers, one for high and one for low discharge flows. Velocities were recorded using a Novar streamflow miniature electronic current meter with a propeller diameter of approximately 13 mm. Shear tractive stresses τ_o (local values) were measured with the Preston technique in conjunction with the velocity readings near the wetted perimeter.

Experimental Procedure

During the present work the ratio B/b was constant, $B/b \cong 4.013$, the height H varied between 84 and 188 mm, while h was constant -equal to 76 mm. Measurements were organized in 7 experimental runs, each one with different height H . The most important geometrical non-dimensional parameter of the flow was considered to be ([11]) the ratio H^* of the depth $(H-h)$ of the flood plain to the depth H of the main channel:

$$H^* = \frac{H-h}{H} \quad (1)$$

Important non-dimensional parameters are the Reynolds number, $Re = (V_{mean} * 4R) / \nu$ and the Froude number, $Fr = V_{mean} / (g * t_\mu)^{1/2}$, where V_{mean} = mean velocity, R = hydraulic radius, ν = kinematic viscosity of water, g = gravitational acceleration, t_μ = mean hydraulic depth. In the present work Re and Fr numbers varied as follows:

$$3.47 \cdot 10^4 < Re < 1.46 \cdot 10^5$$

$$0.550 < Fr < 0.459$$

i.e. the flows were fully turbulent and subcritical.

After calculating the shear stress values on the wetted perimeter, the total shear force and the mean experimental boundary shear stress have been computed. The latter was compared with the mean shear stress $\tau_{o\mu} = g * \rho * R * J_E$, obtained from the energy gradient J_E and the experimental shear stress values were adequately corrected.

5. DISCHARGE RESULTS

For the examined cross-sections the discharges of the main channel and the flood plain are related to the total discharge as shown in the two plots of Figure 2. More details may be found in reference [11]. In the present plot a comparison is made with other works ([7], [12]) in compound non-symmetrical cross-sections. The indexes mc and fp refer to the main channel and flood plain correspondingly.

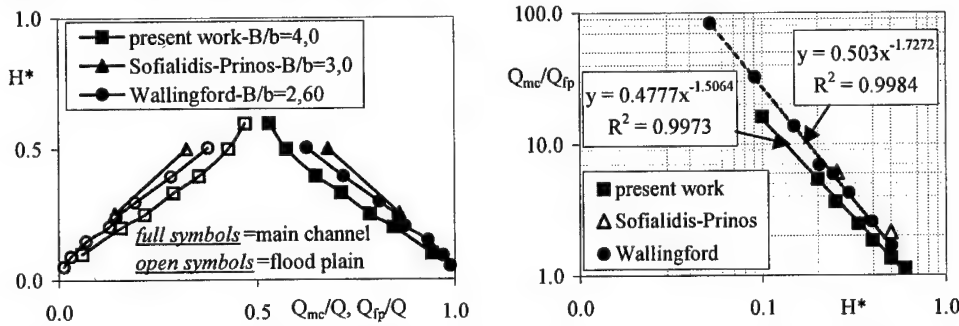


Figure 2: Non-dimensional discharges Q_{mc}/Q , Q_{fp}/Q and Q_{mc}/Q_{fp} as a function of H^*

6. BOUNDARY SHEAR STRESS RESULTS

The experimental shear stress distributions on each sub-element of the wetted perimeter were numerically integrated to give the mean boundary shear stress and shear force value. For convenience, the wetted perimeter was divided in five parts according to the flow direction (Figure 1): (i) The main channel left wall (ii) The main channel bed (iii) The main channel right wall (iv) The flood plain bed and (v) The flood plain (right) wall. For each run local shear stresses τ_o were calculated and plotted in dimensionless form:

- $(y/(B+b), \tau_o/\tau_{o\mu})$ for the channel and flood plain beds and
- $(\tau_o/\tau_{o\mu}, z/H)$ for the channel and flood plain walls

where y is the horizontal coordinate for points on the channel bed and z is the vertical coordinate for points on the walls.

In Figure 3 the shear stress distribution on the channel and flood plain beds is presented, while in Figures 4, 5 the shear stress distribution on the left wall of the main channel and the right walls of the main channel and flood plain are shown correspondingly.

Figure 6 represents the percentage of the shear force of each sub-element to the total force of the cross-section as a function of parameter H^* . These results are qualitatively the same, as those found by other works for compound, both symmetrical and non-symmetrical cross-sections ([3], [4]).

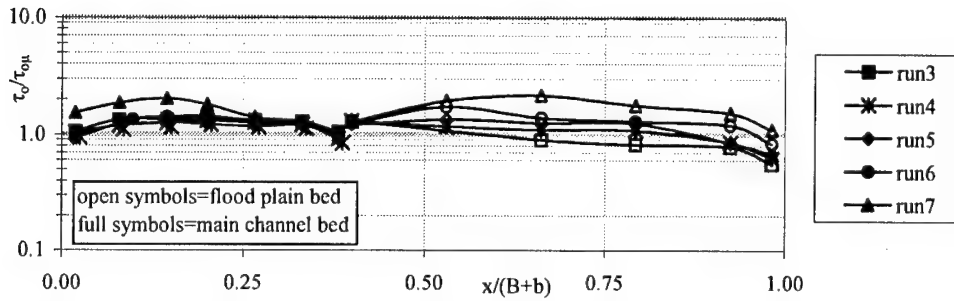


Figure 3: Boundary shear stress distribution on the main channel and flood plain beds (sub-elements ii and iv)

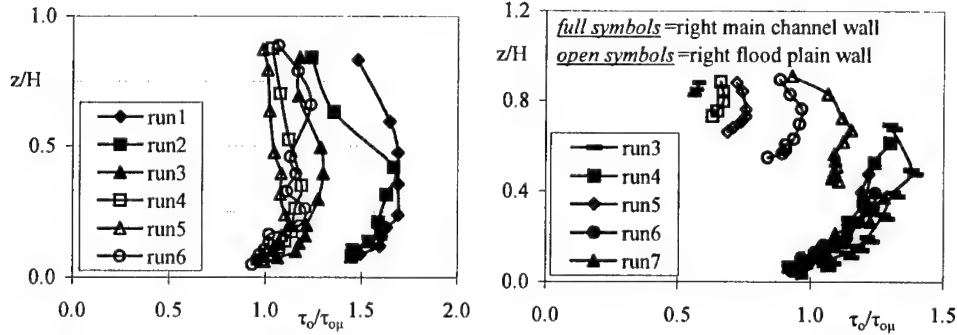


Figure 4: Boundary shear stress distribution on the main channel left wall (sub-element i)

Figure 5: Boundary shear stress distribution on the main channel and flood plain left walls (sub-elements iii, iv)

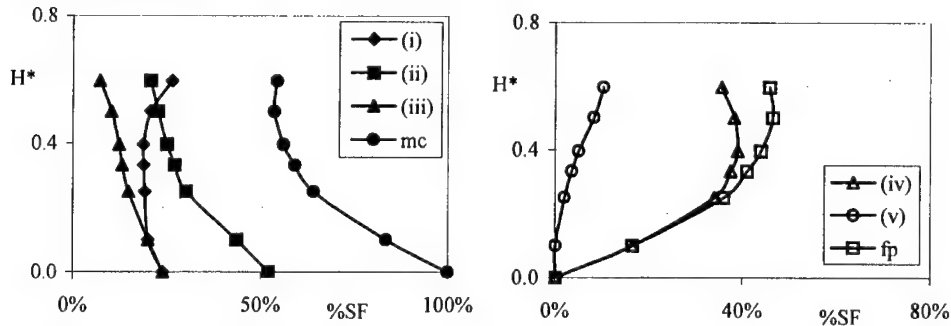


Figure 6: Percentage of the shear force of each sub-elements to the total force of the compound channel (a) for the main channel and (b) the flood plain, as a function of parameter H^*

In Figure 7 the ratio of the shear forces on the main channel and on the flood plain is plotted as a function of the ratio (i) of the corresponding Reynolds numbers and (ii) of the discharges, also of the main channel to the flood plain. It can be seen a good linear relationship between them exists and the numerical values of the mean experimental shear forces of the main channel and of the flood plain may easily be computed. By taking into account the equations of Figures 2 and 7, an easy to use relationship is deduced:

$$\frac{SF\%_{mc}}{SF\%_{fp}} = 0.133 \cdot (H^*)^{-1.5064} + 0.7871 \quad \text{or} \quad (2)$$

$$\frac{SF\%_{mc}}{SF\%} = \frac{0.133 \cdot (H^*)^{-1.5064} + 0.7871}{0.133 \cdot (H^*)^{-1.5064} + 1.7871} \quad \text{and} \quad \frac{SF\%_{fp}}{SF\%} = \frac{1}{0.133 \cdot (H^*)^{-1.5064} + 1.7871} \quad (3)$$

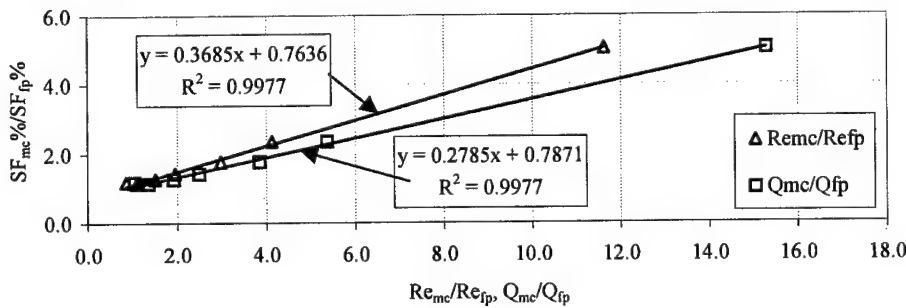


Figure 7: Ratio of the shear forces on the main channel to the flood plain as a function of the ratio of the Reynolds numbers and of the discharges of the main channel to the flood plain

7. FRICTION FACTOR CALCULATION

A very interesting aspect of the problem is the calculation of the friction factor f of the total cross-section and its behavior for the various parameters of the problem. The friction factor may be calculated by combining Darcy-Weisbach equation, with the calculation of mean shear stress obtained from the energy gradient. Experimental results from other researchers for compound non-symmetrical cross-sections are also plotted on the same graph. The relation between the friction factor f and Reynolds number is presented in the log-log diagram of Figure 8. The well-known Prandtl equation for a smooth rectangular channel is plotted on the same graph. As can be seen from Fig. 8, the behavior of friction factor f for compound channels, with larger values of Reynolds number, conforms very well to the Prandtl equation. For smaller values of Re , the behavior is the same with that, which was found by other researchers [3], [4], [5], [9]. Although this is not theoretically explained, it seems that the reason for this behavior change in channels with small height H , is the way with which the hydraulic radius R is defined and calculated. For smaller water depths, the flood plain is physically almost not influencing the behavior of the main channel, because it shows some independent-non-compound characteristics. However the hydraulic radius takes into account the whole cross-section and this may explain the prediction of a smaller f , from that computed by Prandtl equation.

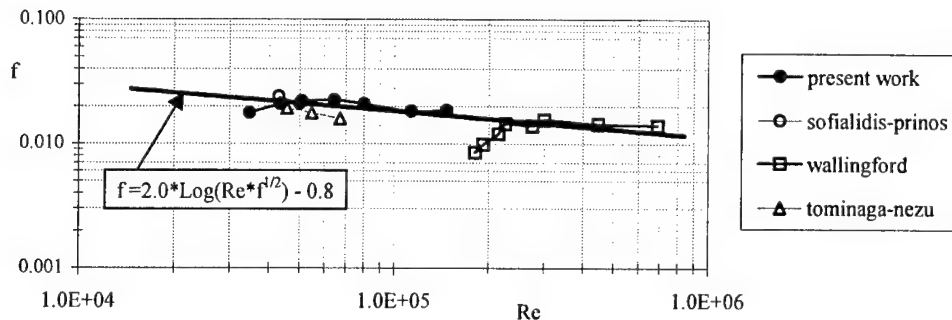


Figure 8: Friction factor f for compound non-symmetrical channels

8. CONCLUSIONS

In the present work experimental velocity and shear stress results in a channel with compound non-symmetrical cross-section have been elaborated. The results were qualitatively similar to those predicted by other works both for symmetrical and non-symmetrical cross-sections. An easy-to-use analytical relation is given, which permits the calculation of the mean shear stress of the main channel and of the flood plain as a function of the mean shear stress of the compound cross-section. More work is necessary, especially in the direction of modeling and numerical prediction of the flow behavior.

9. REFERENCES

- [1] Rajaratnam N. and Ahmadi R., 1981, Hydraulics of Channels with Flood Plains. *J. Hydr. Eng. (ASCE)*, 19(1), pp. 43-60.
- [2] Stephenson D., Kolovopoulos P., 1990, Effects of Momentum Transfer in Compound Channels. *J. Hydr. Eng. (ASCE)*, 116(2), pp. 1512-1522.
- [3] Tominaga A., Nezu I., 1991, Turbulent Structure in Compound Open-Channel Flows. *J. Hydr. Eng. (ASCE)*, 117(1), pp. 21-41.
- [4] Naot D., Nezu I. and Nakagawa H., 1993, Calculation of Compound Open-Channel Flow. *J. of Hydr. Eng. (ASCE)*, 122(11), 1418-1426.
- [5] Naot D., Nezu I. and Nakagawa H., 1996, Hydrodynamic Behavior of Partly Vegetated Open Channels. *J. of Hydr. Eng. (ASCE)*, 122(11), 625-633.
- [6] Pang B., 1998, River Flood Flow and its Energy Loss. *J. of Hydr. Eng. (ASCE)*, 124(2), 228-231.
- [7] Sofialidis D. and Prinos P., 1999, Turbulent Flow in Open Channels with Smooth and Rough Flood Plains. *J. of Hydr. Research*, 37(5), 615-640.
- [8] Knight D. and Demetriou J., 1983, Flood Plain and Main Channel Flow Interaction. *J. of Hydr. Eng. (ASCE)*, 109(8), 1073-1092.
- [9] Knight D. and Hamed M., 1984, Boundary Shear in Symmetrical Compound Channels. *J. of Hydr. Eng. (ASCE)*, 110(10), 1412-1430.
- [10] Myers W. R. and Brennan E. K., 1990, Flow Resistance in Compound Channels. *J. of Hydr. Research*, Vol. 28, 141-155.
- [11] Demetriou J. and Nanou-Giannarou K., 2000, Water Flow in Compound Non-symmetrical Channels, *Proceedings of the 8th Panhellenic Congress of the Hellenic Hydrotechnical Union*, June 2000, Athens, Greece (in Greek)
- [12] HR Wallingford, 1992, SERC Flood Channel Facility, Experimental Data-Phase A, Volume 1, Report SR 314.

USE OF HEIGHT DENSITY FUNCTION FOR THE EVALUATION OF MEASUREMENTS WITH A LASER DOPPLER ANEMOMETER

Th. Panidis

Mechanical Engineering and Aeronautics Department
University of Patras, GR 265 00 Rion-Patras, Greece, e_mail: panidis@mech.upatras.gr

1. SUMMARY

In the present work the height density function is introduced as a means to analyze the measuring volume properties for Laser Doppler Anemometry (LDA) and Phase Doppler Anemometry (PDA) systems in order to provide unbiased estimators for the reduction of flow data as well as error estimation. To illustrate the capabilities of the methodology the height density function of an ellipsoid is derived and used to estimate the cross sectional area of the measuring volume of a LDA system as a function of velocity direction.

2. INTRODUCTION

Laser Doppler Anemometry (LDA) [1] is a non-intrusive, optical technique for local, time evolving measurements of velocities in fluids. Two parallel Laser beams are focused on a control volume. Light scattered on seeding particles is collected on a photo-detector. Interference due to scattering from two beams with different propagating unit vectors results to a signal with frequency proportional to the local velocity of the flow. Phase Doppler Anemometry (PDA) [2] is an extension of LDA technique measuring the size and velocity of small spherical particles, in dispersed two phase flows. The velocity measurement is accomplished as in LDA, but collecting the scattered field in different directions using at least two photodetectors PDA is capable to provide size information based on the phase difference of the signals.

LDA and PDA signal processing systems are capable to evaluate the properties of a particle crossing the measuring volume depending on the particle trajectory and velocity magnitude. For this reason the sensitivity of these systems is different for different directions, introducing a bias to the measurements. Since in most processing systems a particle is evaluated only once during its passage through the measuring volume the important parameter is the effective cross sectional area in each direction [3,4,5]. In this work the height density function is introduced and is used for the estimation of the effective cross sectional area of LDA measuring volumes as a function of the velocity magnitude and direction.

3. DEFINITION OF THE HEIGHT DENSITY FUNCTION

Let us consider two surfaces $S_1(x, y, z)$ and $S_2(x, y, z)$ single valued for (x, z) in an area A_i on the xz plane. The height between the surfaces in direction y is

$$H(x, z) = |y_{S_1}(x, z) - y_{S_2}(x, z)| \quad (1)$$

We define a characteristic function

$$\left. \begin{aligned} k(L, x, z) &= 1 & \text{if } H(x, z) \leq L \\ k(L, x, z) &= 0 & \text{if } H(x, z) > L \end{aligned} \right\} \quad \text{for } 0 \leq L < \infty \quad (2)$$

The integral

$$A(L) = \iint_{A_i} k(L, x, z) dx dz \quad (3)$$

defines the part of A_i which corresponds to height less than L and is a positive, increasing function.

We define the cumulative height distribution function, $G(L)$, as

$$G(L) = \frac{A(L)}{A_i} \quad (4)$$

For the segments where $G(L)$ is continuous, we define the height density function, $g(L)$, as

$$g(L) = \frac{dG}{dL} = \frac{1}{A_i} \cdot \frac{dA}{dL} \quad (5)$$

If $G(L)$ has a discontinuity at L_d with increase $\Delta G(L_d)$ (indicating that a part of S_2 , corresponding to a projection area $A_i \Delta G(L_d)$, is the same as a corresponding part of S_1 displaced by $\pm L_d$ in direction y) then we define the height density function, $g(L)$ at L_d as

$$g(L_d) = \Delta G(L_d) \cdot \delta(L - L_d) = \frac{1}{A_i} \cdot \Delta A(L_d) \cdot \delta(L - L_d) \quad (6)$$

where δ is the Dirac delta.

If in place of L we use $l = L/L_c$, where L_c is a characteristic length then we are able to define the corresponding normalized (nondimensional) height distribution and density functions. In the following we will work exclusively with the normalized version of these functions.

Some properties of the height distribution and density functions are given in the following:

$$g(l) \geq 0 \quad (7)$$

$$\int_0^\infty g(l) dl = 1 \quad (8)$$

$$G(l_0) = \int_0^{l_0} g(l) dl \quad (9)$$

$$\iint_{A_i} H(x, z) dx dz = A_i \cdot L_c \int_0^\infty l \cdot g(l) dl = V \quad (10)$$

where V is the volume bounded by S_1 , S_2 and the surface produced by the extrusion of the boundary of A_i in y direction.

Moreover if l_{max} is the maximum normalized height in A_i

$$g(l) = 0 \quad \text{for } l > l_{max} \quad \text{and} \quad \int_0^{l_{max}} g(l) dl = 1 \quad (11)$$

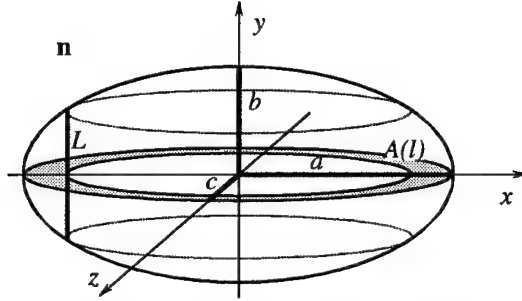


Figure 1. Derivation of the height distribution function for an ellipsoid

4. THE HEIGHT DENSITY FUNCTION OF AN ELLIPSOID

Let us now determine the height distribution, G , and density, g , functions in the direction of axis y for an ellipsoid (see figure 1) given by the equation

$$\frac{x^2}{a^2} + \frac{y^2}{b^2} + \frac{z^2}{c^2} = 1 \quad (12)$$

The height corresponding to a point (x, z) within its projection on the xz plane is $L = 2|y|$, and the maximum $L_{max} = 2b$ is reached for $x = z = 0$. Using $L_c = L_{max}$ to normalize the height $l = L/L_{max}$, it is straightforward to prove that the projection area corresponding to height less than l is

$$A(l) = \pi ac - \pi \left(a\sqrt{1-l^2} \right) \left(c\sqrt{1-l^2} \right) = \pi ac l^2 \quad (13)$$

Confining A_l in the domain of the ellipsoid's projection area, A_{tot} , The height distribution can readily be determined

$$G(l) = \frac{A(l)}{A_{tot}} = l^2 \quad (14)$$

and differentiating

$$g(l) = \frac{dG}{dl} = \frac{dl^2}{dl} = 2l \quad (15)$$

It can be proved that theses equations give the height distribution, G_n , and density, g_n ,

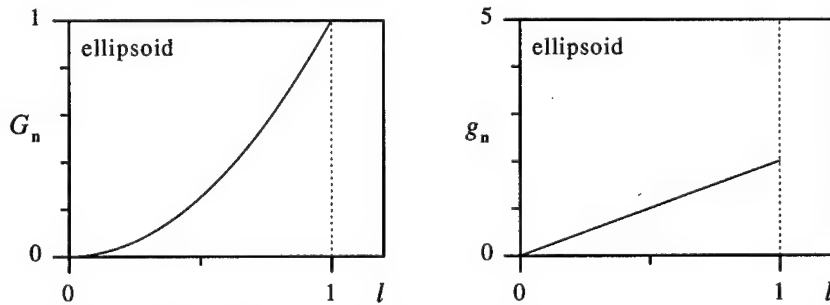


Figure 2. The height distribution, G_n , and height density, g_n , functions for an ellipsoid

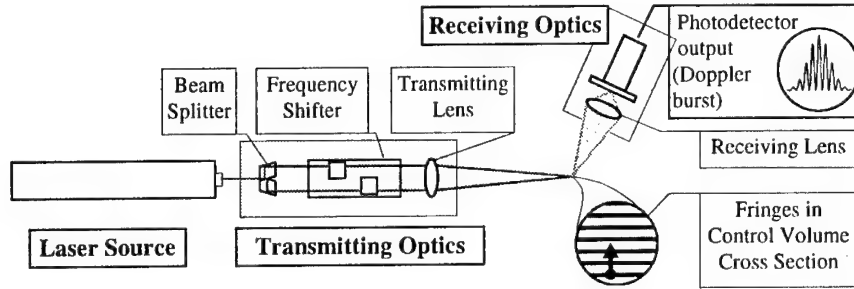


Figure 3. A typical Laser Doppler Anemometry system

functions for an ellipsoid in any direction, \mathbf{n} , given that $L_{n,max}$ is the maximum height in direction \mathbf{n} and $A_{n,tot}$ is the area of the ellipsoid's projection on a plane normal to \mathbf{n} (figure 2).

5. LASER DOPPLER ANEMOMETRY

A typical Laser Doppler Anemometry (LDA) system is shown in figure 3. A laser beam is split in two equal beams, which are focused at the measuring location. The measuring volume is the part of the intersection of the beams seen by the photodetector. If the receiving optics are in the forward or backward direction and the beam angle is not very small (in which case the beam intersection would be very long) the optics usually see the whole beam intersection and it is customarily assumed [1,2] that the measuring volume is an ellipsoid (figure 4) of dimensions

$$\Delta x = \frac{d_m}{\cos(\theta/2)}, \quad \Delta y = d_m, \quad \Delta z = \frac{d_m}{\sin(\theta/2)} \quad (16)$$

where d_m is the beam waist diameter at the focal point. A convenient way to outline the principle of operation, sufficient for the purpose of the present study, is based on the fringe pattern "created" at the beam intersection due to the interference of the two beams. The fringe planes are parallel to each other at a constant spacing, d_f , which is a function of the beam wavelength, λ , and the beam angle, θ . They are normal to the plane of the beams and parallel to the beam bisector. Small seeding particles in the flow with properties securing that they follow precisely the fluid flow, pass through the control volume, that is through the fringe pattern. A photodetector focused on the control volume selects light scattered by every particle. The signal thus produced is confined in a Gaussian envelope (due to the Gaussian distribution of the intensity in the beam, the Doppler burst in figure 3) and its frequency, f_D , is equal to the inverse of the time that the particle takes to pass through two successive fringe planes. Based on the evaluation of the signal frequency, LDA measures the flow velocity component in direction \mathbf{n}_f , normal to the fringe planes (x axis in figure 4), as

$$u_{n_f} = \frac{\lambda}{2\sin(\theta/2)} f_D = d_f f_D \quad (17)$$

To distinguish flow direction a frequency difference of the beams is introduced with a frequency shifter making the fringes to move normal to their planes with a constant velocity. Thus the velocity – frequency relationship is shifted and stationary particles in the control volume produce a signal with frequency equal to the shift frequency, $f_{f.s.}$, whereas particles moving in the same direction or against the fringe movement produce lower or higher frequencies respectively.

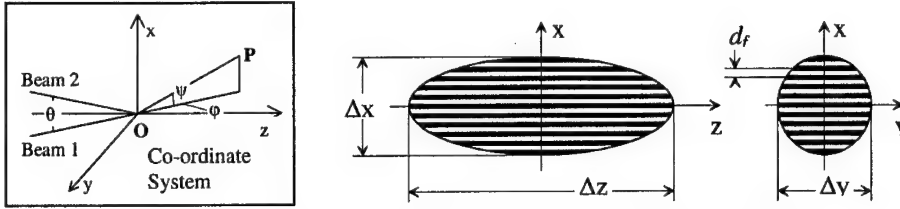


Figure 4. The measuring volume of a LDA and the coordinate system.

Evaluation of Doppler signals

Let us suppose that at a particular point in a flow the probability density function of the x component of the velocity, u_x , is $B(u_x)$. The corresponding probability density function of the u_x velocity measurements is

$$B_m(u_x) = B(u_x) \frac{E_m(u_x)}{\int_{-\infty}^{\infty} B(u_x) E_m(u_x) du_x} \quad (18)$$

where $E_m(u_x)$ is the efficiency of the system to measure u_x which may introduce a bias to the measurements. Using a LDA system $E_m(u_x)$ may be evaluated as proportional to the data rate achieved for each velocity u_x .

Let us now suppose a measuring volume in a flow uniformly seeded with small monosized particles (much smaller than the measuring volume dimensions) with concentration of c particles per volume, securing that only one particle will be in the measuring volume at any time. The data rate for a LDA system measuring a velocity \mathbf{u} in direction \mathbf{n} dominating the measuring volume for a fraction of time will be

$$R(\mathbf{u}) = c |\mathbf{u}| A_{n,eff} \quad (19)$$

Correspondingly in an isotropic turbulent flow with probability density functions $B(u_x)$, $B(u_y)$, $B(u_z)$, for the three velocity components the corresponding efficiency of the system to measure a specific magnitude u_x is

$$R(u_x) = c \int_{-\infty}^{\infty} \int_{-\infty}^{\infty} B(u_y) B(u_z) \sqrt{u_x^2 + u_y^2 + u_z^2} A_{n,eff} du_y du_z \quad (20)$$

and the corresponding probability density function of the u_x velocity measurements is

$$B_m(u_x) = B(u_x) \frac{c \int_{-\infty}^{\infty} \int_{-\infty}^{\infty} B(u_y) B(u_z) \sqrt{u_x^2 + u_y^2 + u_z^2} A_{n,eff} du_y du_z}{\int_{-\infty}^{\infty} B(u_x) c \int_{-\infty}^{\infty} \int_{-\infty}^{\infty} B(u_y) B(u_z) \sqrt{u_x^2 + u_y^2 + u_z^2} A_{n,eff} du_y du_z du_x} \quad (21)$$

Processing systems are able to evaluate the Doppler frequency if the photodetector's signal has a sufficient number of signal periods, that is if a particle has crossed a sufficient number of fringes. For a system with no frequency shift a particle following a certain trajectory will cross the same number of fringe plane regardless of its velocity. If N_{min} is the minimum number of fringes for a valid measurement then the minimum length of a particle trajectory moving in direction \mathbf{n} within the measuring volume, normalized with the maximum height of

the measuring volume ellipsoid in this direction should be

$$l_{min}(\mathbf{n}) = \frac{L_{min}(\mathbf{n})}{L_{max}(\mathbf{n})} = \frac{N_{min} d_f}{|\sin(\angle \mathbf{n}, \mathbf{n}_f)| L_{max}(\mathbf{n})} = \frac{N_{min} d_f}{|\sin \psi| L_{max}(\mathbf{n})} = \frac{L_{min}(\mathbf{n}_f)}{|\sin \psi| L_{max}(\mathbf{n})} \quad (22)$$

Assuming that every particle which crosses the measuring volume is evaluated if its

trajectory length is larger than corresponding $l_{\min}(\mathbf{n})$ then the effective cross sectional area is

$$A_{n,eff} = A_{n,tot} - A_n(l_{\min}(\mathbf{n})) = A_{n,tot}(1 - G_n(l_{\min}(\mathbf{n}))) \quad (23)$$

It can be analytically derived that for the optical setup described in the preceding section the maximum height of the ellipsoid in direction \mathbf{n} given by the angles φ, ψ is

$$L_{\max}(\mathbf{n}(\varphi, \psi)) = 2\Delta x \Delta y \Delta z \sqrt{\frac{(1 - \tan^2 \varphi)(1 - \tan^2 \psi)}{\Delta x^2 \Delta y^2 - \Delta x^2 \Delta z^2 + \Delta z^2(1 - \tan^2 \varphi)(\Delta x^2 - \Delta y^2 \tan^2 \psi)}} \quad (24)$$

and the corresponding projection area is:

$$A_{n,tot}(\varphi, \psi) = \pi \sqrt{\frac{\Delta x^2 \Delta y^2 - \Delta x^2 \Delta z^2 + \Delta z^2(1 - \tan^2 \varphi)(\Delta x^2 - \Delta y^2 \tan^2 \psi)}{(1 - \tan^2 \varphi)(1 - \tan^2 \psi)}} \quad (25)$$

Based on these derivations the normalized effective cross sectional area, for various ratios of the minimum length to be travelled by a particle in x direction to the measuring volume maximum height in the same direction, is plotted in figure 5. The graphs are referring to a conventional LDA forward scatter optical setup with beam displacement 50mm, transmitting optics focal length 110mm and beam waist diameter 88 μ m. These graphs show that $A_{n,eff}$ is varying significantly with flow direction, especially for large $L_{\min}(\mathbf{n}_f)/L_{\max}(\mathbf{n}_f)$ ratios, indicating that bias may be introduced in LDA measurements. In fact the problem is not so grave as figure 5 indicates since usually the velocity direction fluctuates in a rather small solid angle. Besides the use of frequency shifting is capable in most cases to alleviate the problems associated with large $L_{\min}(\mathbf{n}_f)/L_{\max}(\mathbf{n}_f)$ ratios. These effects have to be studied further.

6. CONCLUSIONS

The height distribution and density functions have been introduced and their forms for an ellipsoid have been derived. These derivations have been used to estimate the cross sectional area of the measuring volume of a LDA system as a function of velocity direction. The results indicate significant bias of the measurements in flows with velocity direction changes

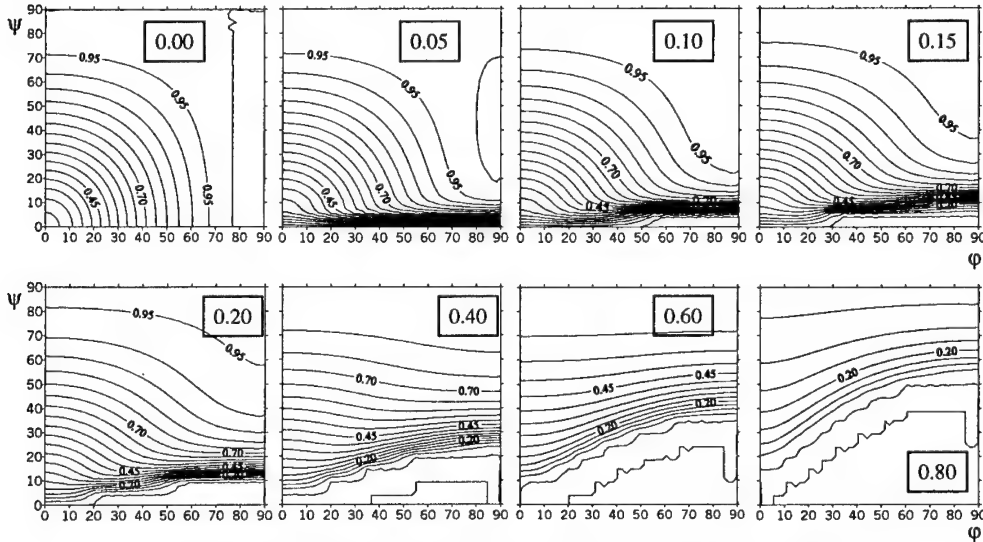


Figure 5. $A_{n,eff}(\varphi, \psi)$ iso-area lines for various $L_{\min}(\mathbf{n}_f)/L_{\max}(\mathbf{n}_f)$ ratios

in the absence of frequency shifting. Further studies are needed for the correct estimation of the error and the development of data reduction estimators that may alleviate the bias.

7. REFERENCES

- [1] Durst, F. , Melling, A. and Whitelaw, J.H., *Principles and Practice of Laser-Doppler anemometry*. Academic Press (1976).
- [2] Crowe, C., Sommerfeld, M. and Tsuji, Y., *Multiphase Flows with Droplets and Particles*, CRC Press (1998).
- [3] Qiu, H.-H. and Sommerfeld, M., A reliable method for Determining the Measurement Volume Size and Particle Mass Fluxes Using Phase-Doppler Anemometry, *Experiments in Fluids* 13, 393-404 (1992).
- [4] Hardalupas, Y. Taylor, A.M.K.P. and Whitelaw, J.H., Measurement of Droplet Flux and Concentration with Phase -Doppler Anemometry, in *20th Anniversary of Phase Doppler Anemometry, Erlangen* (1995).
- [5] Panidis, Th., Giannoulis, D. and Emmanouilidis, A.,: Locus of centres method considerations for concentration and flux measurements with a phase doppler anemometer, in *Two-Phase Flow Modelling and Experimentation 3*, G.P. Celata et al (Eds), *Edizioni ETS, Pisa*, (1999) 1385-1391.

6th National Congress on Mechanics

Session B

Volume I

DAMAGE MODELS FOR VISCOELASTIC COMPOSITES

R. A. Schapery

Department of Aerospace Engineering
The University of Texas at Austin, 78712, USA

1. SUMMARY

Homogenized constitutive equations, damage evolution equations and some related experimental results for viscoelastic composite materials with constant or growing damage are described. Behavior of both fiber and particle-reinforced composites is discussed. The essential assumptions in the models are that there is one dominant creep function, the reinforcement phase is very stiff relative to the matrix, and the composite is linearly viscoelastic when the damage is constant. We also discuss a study in which acoustic emissions have been used to obtain evidence on damage growth in a fiber composite and how they are affected by different loading histories; this work includes a comparison of theory and experiment on load history effects.

Space does not allow for an extended bibliography. However, it is hoped that publications cited in this paper will assist the interested reader in becoming familiar with the broader relevant literature. Similarly, figures that illustrate the comparison of theory and experiment and other aspects of the discussion are not included here, but they are in the cited literature and will be used in the lecture.

2. INTRODUCTION

Many technically important composites consist of one or more polymeric viscoelastic phases which are reinforced with relatively high modulus particles and/or fibers. These composites often exhibit a considerable amount of distributed damage in the form of microcracks prior to global failure. When there is a high volume fraction of particle reinforcement (as in asphalt concrete or solid propellant) or fiber reinforcement (as in many structural composites) microcracks may develop at low loads, but are arrested and do not necessarily lead to failure until high loads or very long times are reached.

Here we are concerned with models for damage evolution and the effect of distributed damage on homogenized constitutive equations for viscoelastic composites. Broad-spectrum viscoelastic behavior is allowed for in order to develop realistic models of polymer composites. Linear behavior, apart from damage growth effects, is assumed. Multiple creep functions, nonlinear viscoelasticity and viscoplasticity with damage growth are taken into account in [1].

Models for void formation in constrained rubber and particle-filled rubber date back to the pioneering work of Gent and Lindley [2] and Farris [3], respectively. This early work

neglected viscoelastic effects. More recent theoretical and experimental studies by Schapery et al. [4 -7] have accounted for broad-spectrum viscoelastic behavior of filled rubber and asphalt concrete.

Models and some experimental studies for viscoelastic behavior of fiber-reinforced plastics with growing damage have been addressed by Bocchieri [8], Schapery and Sicking [9] and Weitsman et al. [10, 11].

3. COMPOSITES WITH STRAINS PROPORTIONAL TO ONE CREEP FUNCTION

Constant Damage: Let us consider first a linear constitutive equation having constant damage, with ϵ and σ as the strain and stress tensors, respectively,

$$\epsilon = \{Sd\sigma\} + \epsilon_T \quad (1)$$

where S is a fully symmetric, fourth order creep compliance tensor and ϵ_T is the strain tensor due to temperature and moisture (and other absorbed substances which may affect the strains). The braces are abbreviated notation for a linear hereditary integral. Although the most general form could be used, allowing for general aging effects, we shall use the familiar form for thermorheologically simple materials because the composite discussed later in this section exhibits this behavior with constant or growing damage:

$$\{fdg\} = \int_0^t f(\xi - \xi') \frac{\partial g}{\partial t'} dt' = \int_0^\xi f(\xi - \xi') \frac{\partial g}{\partial \xi'} d\xi' \quad (2)$$

where it is assumed $f = g = 0$ for $t < 0$ and

$$\xi \equiv \int_0^t dt'' / a_T[T(t'')], \quad \xi' = \xi(t') \quad (3)$$

Also, $a_T(T)$ is the temperature-dependent shift factor. If the temperature is constant in time then $\xi - \xi' = (t - t') / a_T$. Physical aging [12] may be taken into account by introducing explicit time-dependence in a_T ; i.e. use $a_T = a_T(T, t'')$ in Eq.(3). The effect of plasticizers, such as moisture, may also be included in a_T . When Eq.(2) is used with Eq.(1), f and g are components of the creep compliance and stress tensors, respectively.

In certain important cases, the creep compliance components are proportional to one function of time,

$$S = kD \quad (4)$$

where k is a constant, *dimensionless* tensor and $D = D(\xi)$ is a creep compliance (taken here to be that obtained under a uniaxial stress state). Isotropic materials with a constant Poisson's ratio satisfy Eq.(4). If such a material has mechanically rigid reinforcements and/or holes (of any shape), it is easily shown by dimensional analysis that its homogenized constitutive equation satisfies Eq.(4); in this case the stress and strain tensors in Eq.(1) should be interpreted as volume-averaged quantities. The Poisson's ratio for polymers at temperatures which are not close to their glass-transition temperature, T_g , is nearly constant; except at time or rate extremes, above T_g Poisson's ratio is essentially one-half, while below T_g it is commonly in the range 0.35-0.40 [13].

Equations (1) and (4) give

$$\boldsymbol{\varepsilon} = \{Dd(\mathbf{k}\boldsymbol{\sigma})\} + \boldsymbol{\varepsilon}_T \quad (5)$$

The inverse is

$$\boldsymbol{\sigma} = \mathbf{k}_I \{E d\boldsymbol{\varepsilon}\} - \mathbf{k}_I \{E d\boldsymbol{\varepsilon}_T\} \quad (6)$$

where $\mathbf{k}_I = \mathbf{k}^{-1}$ and $E = E(\xi)$ is the uniaxial relaxation modulus which, for $t > 0$, satisfies $\{DdE\} = \{EdD\} = 1$.

In relating solutions of elastic and viscoelastic boundary value problems, and for later use with growing damage, it is helpful to introduce the *dimensionless* quantities

$$\boldsymbol{\varepsilon}^R \equiv \frac{1}{E_R} \{E d\boldsymbol{\varepsilon}\}, \quad \boldsymbol{\varepsilon}_T^R \equiv \frac{1}{E_R} \{E d\boldsymbol{\varepsilon}_T\}, \quad \mathbf{u}^R \equiv \frac{1}{E_R} \{E d\mathbf{u}\} \quad (7)$$

where E_R is an arbitrary constant with dimensions of modulus, called the *reference modulus*; also $\boldsymbol{\varepsilon}^R$ and $\boldsymbol{\varepsilon}_T^R$ are so-called *pseudo strains* and \mathbf{u}^R is the *pseudo displacement*. Equation (6) becomes

$$\boldsymbol{\sigma} = C\boldsymbol{\varepsilon}^R - C\boldsymbol{\varepsilon}_T^R \quad (8)$$

where $C \equiv E_R \mathbf{k}_I$ is like an elastic modulus tensor; its elements are called *pseudo moduli*. Equation (8) reduces to that for an elastic material by taking $E = E_R$; it reduces to the constitutive equation for a viscous material if E is proportional to a Dirac delta function of ξ . The inverse of Eq.(8) gives the pseudo strain $\boldsymbol{\varepsilon}^R$ in terms of stress,

$$\boldsymbol{\varepsilon}^R = \hat{\mathbf{S}}\boldsymbol{\sigma} + \boldsymbol{\varepsilon}_T^R \quad (9)$$

where $\hat{\mathbf{S}} = C^{-1} = \mathbf{k} / E_R$. The physical strain is given in Eq.(5).

Growing Damage: The correspondence principle (CPII in [14, 15]), which relates elastic and viscoelastic solutions, shows that Eqs.(1)-(9) remain valid, under assumption Eq.(4), with damage growth when the damage consists of cracks whose faces are either unloaded or have loading that is proportional to the external loads; this is true even with general aging effects. With growing damage \mathbf{k} , C and $\hat{\mathbf{S}}$ are time-dependent because they are functions of one or more damage measures; the strain $\boldsymbol{\varepsilon}_T$ may also depend on damage. The fourth-order tensor \mathbf{k} must remain inside the convolution integral in Eq.(5), just as shown. This position is required by the correspondence principle. The elastic-like Eqs.(8) and (9) come from Eq.(5), and thus have the appropriate form with growing damage. However, with healing of cracks, pseudo stresses replace pseudo strains because \mathbf{k} must appear outside the convolution integral in (5) [14, 15].

The damage evolution equations are based on viscoelastic crack growth equations and, in a more general context, on nonequilibrium thermodynamic equations. Specifically, let

W^R and W_C^R denote pseudo strain energy density and pseudo complementary strain energy density, respectively,

$$W^R = \frac{1}{2} C (\epsilon^R - \epsilon_T^R) (\epsilon^R - \epsilon_T^R) - F, \quad W_C^R = \frac{1}{2} \hat{S} \sigma \sigma + \epsilon_T^R \sigma + F \quad (10)$$

so that

$$W_C^R = -W^R + \sigma \epsilon^R \quad (11)$$

and

$$\sigma = \partial W^R / \partial \epsilon^R, \quad \epsilon^R = \partial W_C^R / \partial \sigma \quad (12)$$

The function F is a function of damage and physical variables that cause residual stresses such as temperature and moisture.

Let us assume here that the damage is fully defined by a set of scalar internal state variables (ISVs), S_p ($p = 1, 2, \dots, P$) instead of tensor ISVs. Thermodynamic forces, which are like energy release rates, are introduced,

$$f_p \equiv -\partial W^R / \partial S_p = \partial W_C^R / \partial S_p \quad (13)$$

where the equality of these derivatives follows directly from the total differential of Eq.(11).

Although more general forms could be used, the evolution equations for $\dot{S}_p \equiv dS_p / d\xi$ are commonly assumed in the form $\dot{S}_p = \dot{S}_p(S_q, f_p)$ in which \dot{S}_p may depend on one or more S_q ($q = 1, \dots, P$), but on only one force f_p . The entropy production rate due to damage is non-negative if $\sum_p f_p \dot{S}_p \geq 0$, thus satisfying the Second Law of thermodynamics. It is assumed

that when $|f_p|$ is less than some threshold value (which may be zero) then $\dot{S}_p = 0$.

The use of tensor ISVs is discussed and compared with scalar ISVs by Schapery [1]. The form of the equations in this section is equally valid for tensor and scalar ISVs.

Application to Filled Rubber: Damage Growth in particle-reinforced rubber has been characterized using a power law when $f_p > 0$,

$$\dot{S}_p = (f_p)^{\alpha_p} \quad (14)$$

where α_p is a positive constant, and $\dot{S}_p = dS_p / d\xi$. (For the composite in [6, 7] two ISVs, with $\alpha_1 = 4.5$ and $\alpha_2 = 6$, were used.) A coefficient depending on S_p may be included in Eq.(14); but it does not really generalize the equation because a simple change of the variable S_p may be used to eliminate the coefficient.

This composite is usually isotropic in the undamaged state. However, except for pure hydrostatic tension or compression, it becomes anisotropic as a result of stress-induced

damage. The experimental method used in [6] to characterize the composite consisted of testing rectangular bars at several values of constant tensile strain rate while under several levels of confining pressure and at several temperatures. This type of loading caused the material to be transversely isotropic with damage, in which the axis of isotropy is coincident with direction of tensile straining. In [7] these results were used to develop three-dimensional constitutive and damage evolution equations, while retaining the transverse isotropy assumption. These equations were then used in a finite element code (ABAQUS) to predict the nonuniform mechanical state of rectangular plates with and without holes and macro-cracks. Local, transverse isotropy was assumed, with the isotropy axis oriented in the direction of the local maximum principle stress (considering the full history of loading).

4. GENERALIZATION FOR FIBER COMPOSITES

In many uses of fiber composites the fiber deformations cannot be neglected. Even if the fibers are elastic and much stiffer than the matrix, the constitutive and damage evolution equations in Section 3 do not necessarily apply. The primary theoretical issue is that the correspondence principle with growing damage, as discussed in Section 3, is not rigorously applicable. However, in unidirectional composites the primary effect of fiber deformation (for relatively stiff fibers) may be taken into account by modifying the normal stress acting in the fiber direction σ_1 . This leads to a correspondence principle with growing damage like that discussed in Section 3 [9]. The modified constitutive equations take the form of Eq.(6), but with σ_1 replaced by $\sigma_1 - E_1 \epsilon_1$, where σ_1 , E_1 and ϵ_1 are the stress, axial modulus and strain, respectively, in the fiber direction. This modified constitutive equation may then be used in applications involving multidirectional laminates and in damage evolution equations. Acoustic emission (AE) monitoring and waveform analysis have been used to study experimentally the effect of loading history on microcracking in a carbon/epoxy fiber composite [8]. Theoretical predictions of microcracking, based on a viscoelastic crack growth model, were confirmed by the AE data.

5. CONCLUSIONS

Continuum damage models (but not micromechanical models) of varying degrees of complexity exist for viscoelastic composites. However, the only substantial experimental support for these models is for initially isotropic particle-filled rubber. Even here, though, more experimental work is needed, especially in multiaxial stress states, including studies in which there is significant rotation of the principal stress directions. Experimental studies in support of damage model validation for viscoelastic fiber composites is practically nonexistent. Durability analysis of fiber composites is still quite limited because of the lack of established viscoelastic damage models.

6. REFERENCES

- [1] Schapery, R.A., Nonlinear viscoelastic and viscoplastic constitutive equations with growing damage, *International Journal of Fracture* 97, 33-66 (1999).
- [2] Gent, A.N. and Lindley, P.B., Internal rupture of bonded rubber cylinders in tension, *Proc. R. Soc. A* 249, 195-205 (1958).
- [3] Farris, R.J., The character of the stress-strain function for highly filled elastomers, *Trans. Soc. Rheology* 12(2), 303-314 (1968).

- [4] Schapery, R. A., Models for damage growth and fracture in nonlinear viscoelastic particulate composites, *Proc. Ninth U.S. National Congress of Applied Mechanics*, Book No. H00228 (Y.H. Pao, ed.), ASME, New York, 237-245 (1982).
- [5] Park, S.W., Kim, Y.R. and Schapery, R.A., A viscoelastic continuum damage model and its application to uniaxial behavior of asphalt concrete, *Mechanics of Materials* 24, 241-255 (1996).
- [6] Park, S.W. and Schapery, R.A., A viscoelastic constitutive model for particulate composites with growing damage, *International Journal of Solids and Structures* 34, 931-947 (1997).
- [7] Ha, K. and Schapery, R.A., A three-dimensional viscoelastic constitutive model for particulate composites with growing damage and its experimental validation, *International Journal of Solids and Structures* 35, 3497-3517 (1998).
- [8] Bocchieri, R.T., Time-dependent deformation of a nonlinear viscoelastic rubber-toughened fiber composite with growing damage, Ph.D. Dissertation, The University of Texas at Austin (May, 2001).
- [9] Schapery, R.A. and Sicking, D.L., On nonlinear constitutive equations for elastic and viscoelastic composites with growing damage, In: *Mechanical Behavior of Materials*, (Edited by A. Bakker), Delft University Press, Delft, 45-76 (1995).
- [10] Abdel-Tawab, Kh. and Weitsman, Y.J., A coupled viscoelasticity/damage model with application to swirl-mat composites, *International Journal of Damage Mechanics* 7(4), 351-380 (1998).
- [11] Elahi, M. and Weitsman, Y.J., On the mechanical response of a random chopped fiber mat/polymeric resin composite: data and model, *Mechanics of Time-Dependent Materials* 3, 219-244 (1999).
- [12] Struik, L.C.E., *Physical Aging in Amorphous Polymers and Other Materials*, Elsevier, Amsterdam (1978).
- [13] Schapery, R.A., Viscoelastic behavior and analysis of composite materials, In: *Mechanics of Composite Materials*, (Edited by G.P. Sendeckyj), Academic Press, New York, 85-168 (1974).
- [14] Schapery, R.A., On viscoelastic deformation and failure behavior of composite materials with distributed flaws, In: *1981 Advances in Aerospace Structures and Materials*, (S.S. Wang and W.J. Renton, eds.), ASME, AD-01, 5-20 (1981).
- [15] Schapery, R.A., Correspondence principles and a generalized J integral for large deformation and fracture analysis of viscoelastic media, *International Journal of Fracture* 25, 195-223 (1984).

DAMAGE LOCALIZATION AND FRACTURE IN LAMINATE COMPOSITES

Pierre Ladevèze

LMT-Cachan

ENS Cachan/CNRS/Université Paris 6

61, avenue du Président-Wilson Cachan 94235, France

1. SUMMARY

A major challenge in composite design is to calculate the intensities of the damage mechanisms at any point of a composite structure subjected to complex loading and at any time until final fracture subsequent to strain and damage localization. One approach for laminated composites is based on what we call a damage mesomodel, for which the characteristic length is the thickness of the elementary ply; macrocracks are simulated as completely damaged zones. At the present time, micromechanics approaches for the prediction of final fracture and localization are far from complete.

After having presented the basic aspects of the meso- and micromodels, we will attempt to connect the micromechanics and the mesomechanics of laminated composites in order to get a better understanding and prediction of localization and final fracture.

In the end, the main questions which remain open will be discussed.

Keywords: laminate, localization, fracture, mesomechanics, micromechanics.

2. INTRODUCTION

A preliminary step, which has been done in previous studies, is to define what we call a mesomodel of a laminate. On the mesoscale, characterized by the thickness of a ply, the laminate's structure is described, as in Ladevèze [1], as a stacking sequence of homogeneous layers throughout the thickness and the interlaminar interfaces. The main damage mechanisms are described as: fiber breakage, matrix microcracking and debonding of adjacent layers (see Figure 1).

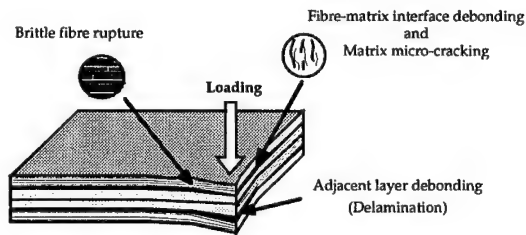


Figure 1: Damage and failure mechanisms

The single-layer model includes both damage and (visco)plasticity [2]. The interlaminar interface is represented by a two-dimensional mechanical model which ensures the transfer of traction and displacement from one ply to the next. Its mechanical behavior depends on the angle between the fibers of two adjacent layers [3] [4]. The state-of-the-art of models based on damage mechanics can be found in [5].

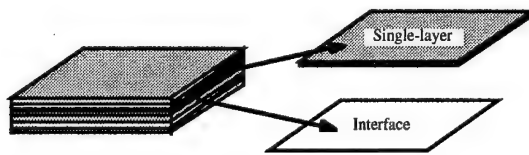


Figure 2: Mesomodeling of a laminate

It is well-known that the simulation of fracture using a continuum damage model leads to severe theoretical and numerical difficulties [6] [7]. A second step, which has also been completed, is to overcome these difficulties. For laminates and, more generally, for composites, we proposed the concept of "mesomodel" in which the state of damage is considered uniform within each mesoconstituent. For laminates, damage is uniform throughout the thickness of each layer. In addition, we introduce continuum damage models with delay effects combined with dynamic analysis [8]. Various comparisons with experimental results have been made [9] [10] [11] [12] [13] [14].

The example concerns a composite plate made of carbon fiber (T300) and epoxy resin [914] (Allix [30]). The in-plane dimensions of the plate are 125 mm & 75 mm and the stacking

sequence is $[45_2, 0_2, -45_2, 90_2]_s$. The impact is achieved by a mass of 2.9 kg at a velocity of 2.2 m/s, which corresponds to an energy of 7J.

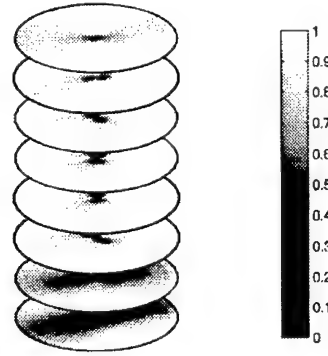


Figure 3: Transverse macrocracks in the plies after a low-velocity impact

Another approach is to use micromechanics models, which are closely connected to microobservations of the different microcracking mechanisms [15] [16] [17] [18] [19] [20] [21] [22] [23] [24] [25] [26] [27]. The first scenario takes into account matrix microcracking, which is parallel to the fibers of the central layer. The second scenario involves a diffuse delamination, whereas the third one takes into account microdeteriorations at the fiber-matrix interfaces only, but not through the ply's thickness.

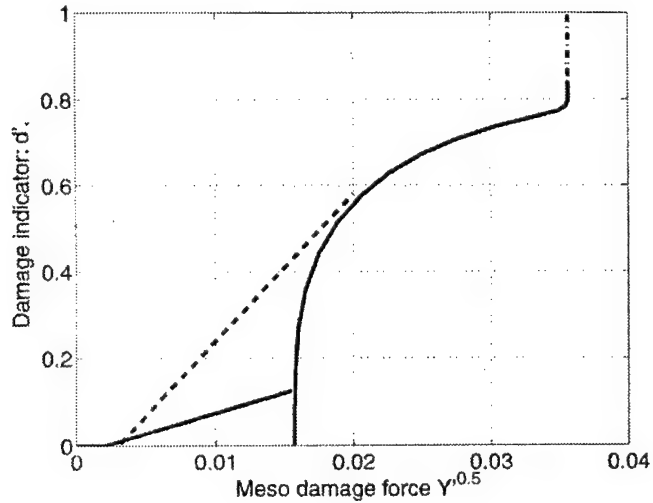


Figure 4: Different scenarios on the microscale for a damaged interior layer

However, today, this approach is far from being complete for the prediction of final fracture and localization.

In [28] [29], an attempt to completely connect the micromechanics and mesomechanics of laminated composites was made in order to get a better understanding and prediction of

fracture. The central and crucial point of discussion is the main homogenization assumption which leads to the mesomodel: for any stacking sequence and for any loading, the laminate can be described in terms of two elementary constituents: the single layer and the interface. Numerous finite element calculations were performed to simulate the behavior of various stacking sequences and various load configurations, including thermal stresses. Approximate quantities and relations for the ply's material were introduced using the mesomodel as a guide. These quantities and relations are approximately independent of the characteristics of the adjacent parts, *i.e.* they depend (approximately) only on the characteristics of the cracked ply considered. The error is generally a few percentage points, 10 being the maximum. Consequently, the mesomodel, after minor modifications, appears to be completely compatible with classical micromechanics models and related to basic material characteristics. Figure 5 shows the material's mesodamage curve for a single-layer T300-914. This curve relates the transverse mesodamage variable d' to the associated damage force; it depends partially on the thickness.

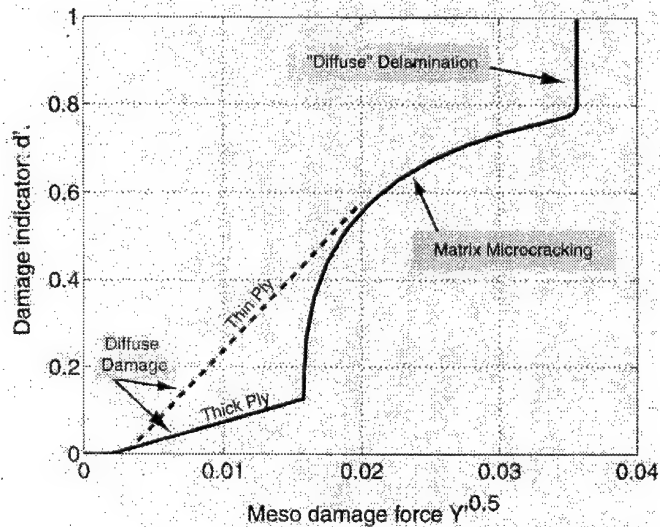


Figure 5: Mesodamage evolution law $d' \Leftrightarrow \sqrt{Y'}$ for T300-914 material

In conclusion, several open questions will be discussed.

3. REFERENCES

- [1] Ladevèze, P., On the damage mechanics of composites, in *Comptes-rendus des JNC5*, C. Bathias and D. Menkès, *Pluralis Publication* (Ed), Paris, 667-683 (1986) (In french).
- [2] Ladevèze, P. and Le Dantec, E., Damage modelling of the elementary ply for laminated composites, *Composites Science and Technology*, V. 43-3, 257-267 (1992).
- [3] Allix, O. and Ladevèze, P., Interlaminar interface modelling for the prediction of laminate delamination, *Composite Structures*, V. 22, 235-242 (1992).

- [4] Allix, O., L  v  que, D., Perret, L., Interlaminar interface model identification and forecast of delamination in composite laminates, *Composites Science and Technology*, V. 56, 671-678 (1998).
- [5] Voyiadjis, G., Ju, J. W., Chaboche, J. L., Damage mechanics in engineering materials, *Elsevier* (Eds) (1998).
- [6] Mazars, J. and Bazant, Z., Cracking and damage-strain localisation and size effect, *Elsevier* (Eds) (1989).
- [7] Bazant, Z., Bettmar, Z., Jirasck, M., Fracture and damage in quasi brittle structures, *Elsevier* (Eds) (1994).
- [8] Ladev  ze, P., About a damage mechanics approach, in *Mechanics and Mechanisms of Damage in Composite and Multimaterials*, D. Baptiste (Ed) (MEP), 119-142 (1989).
- [9] Ladev  ze, P., A damage computational approach for composites: basic aspects and micromechanical relations, *Computational Mechanics*, 17, 142-150 (1995).
- [10] Ladev  ze, P., Modelling and computation until final fracture of laminate composites, in *Recent Developments in Durability Analysis of Composite Systems*, A. H. Cardon *et al.* (Eds), Balkema, 39-47 (2000).
- [11] Ladev  ze, P., Allix, O., Gornet, L., L  v  que, D., Perret, L., A computational damage mechanics approach for laminates: identification and comparison with experimental results, in *Damage Mechanics in Engineering Materials*, G. Voyiadjis, J. W. Ju, J. L. Chaboche (Eds), 481-500 ((1998).
- [12] Ladev  ze, P., Moes, N., Douchin, B., Constitutive relation estimators for (visco) plastic finite element analysis with softening, *Comput. Methods Appl. Mech. Engrg.*, 176, 247-264 (1999).
- [13] Ladev  ze, P., Allix, O., De  , J. F., L  v  que, D., A mesomodel for localisation and damage computation in laminates, *Comput. Methods Appl. Mech. Engrg.*, 183, 105-122 (2000).
- [14] Allix, O. and De  , J. F., Delay-damage modelling for fracture prediction of laminated composites under dynamic loading, *Engrg. Trans.*, 45, 29-46 (1997).
- [15] Hashin, Z., Analysis of cracked laminates: a variational approach, *Mechanical of Materials*, V. 4, 121-136 (1985).
- [16] Hashin, Z., Analysis of stiffness reduction of cracked cross-ply laminates, *Engineering Fracture Mechanisms*, V. 25, 771-778 (1986).
- [17] Nairn, J. and Hu, S., Matrix microcracking, in *Damage Mechanics of Composite Materials*, Talreja (Ed), 187-243 (1994).
- [18] Nairn, J., Matrix microcracking in composites, in *Polymer Matrix Composites*, Taljera-Manson (Eds), Ch. 13 (2000) (In press).
- [19] Laws, N. and Dvorak, G. J., Progressive transverse cracking in composite laminates, *Journal of Composite Materials*, V. 22, 900-916 (1988).
- [20] Flaggs, D. L. and Kural, M. H., Experimental determination of the *in situ* transverse lamina strength in graphite/epoxy laminates, *Journal of Composite Materials*, V. 16, 103-115 (1982).
- [21] Parvisi, A. and Bailey, J. E., On multiple transverse cracking in glass-fiber epoxy cross-ply laminates, *Journal of Material Sciences*, V. 13, 2131-2136 (1978).
- [22] Reifsnider, K. L., Stiffness reduction mechanism in composite materials, in *ASTM-STP* 75 (1980).
- [23] Talreja, R., Transverse cracking and stiffness reduction in composite laminates, *Journal of Composite Materials*, V. 19, 355-375 (1985).
- [24] Tan, S. C. and Nuismer, R. J., A theory for progressive matrix cracking in composites laminates, *Journal of Computational Materials*, V. 23, 1029-1047 (1989).

- [25] Tong, J., Guild, F. J., Ogin, S. L., Smith, P. A., On matrix crack growth in quasi-isotropic laminates – I. Experimental investigation, *Composites Science and Technology*, V. 57, 1527-1535 (1997).
- [26] Takeda, N., McCartney, N., Ogiwara, S., The application of a ply-refinement technique to the analysis of microscopic deformation in interlaminar-toughened laminates with transverse cracks, *Composites Science and Technology*, V. 60, 231-240 (2000).
- [27] Joffe, R. and Varna, J., Analytical modelling of stiffness reduction in symmetric and balanced laminates due to cracks in 90° layer, *Composites Science and Technology*, V. 59, 1641-1652 (1999).
- [28] Ladevèze, P. and Lubineau, G., On a damage mesomodel for laminates: micro-mesorelations, possibilities and limits, *Composites Science and Technology* (2001) (To appear).
- [29] Ladevèze, P. and Lubineau, G., An enhanced mesomodel for laminates based on micromechanics, *Composites Science and Technology* (2001) (To appear).
- [30] Allix, O., Composite damage mesomodel for impact problem, *Composites Science and Technology* (2001) (To appear).

CYLINDRICAL SHELLS AND THEIR STABILITY (CHOICE OF THE DEFLECTION FUNCTION AND CRITICAL EXTERNAL RADIAL PRESSURE)

D. D. Ruzic

Faculty of Mechanical Engineering
University of Belgrade, YU-11120 Belgrade, Yugoslavia;
Faculty of Mechanical Engineering, Srpsko Sarajevo, Republika Srpska

Lj. S. Markovic

MAIER MASCHINENBAU, D-78564 Wehingen, Germany

1. SUMMARY

An overview of the research concerning the theoretical approach to the loss of stability of a cylindrical shell subjected to the external radial pressure is presented. Previously the authors derived a certain general formula for such a case showing that the procedure can be applied to various boundary conditions (symmetrical, both fixed or simply supported ends, as well as the nonsymmetrical, one fixed and the other simply supported end). The generality of the derived expression consists in the fact that different known formulae for the described boundary conditions appear to be just its particular cases. After that it was shown that the Lateral Stability Function must be taken into account in the calculations of the critical pressure. Different forms and types of the deflection functions were investigated as well as their influences on the form of the expression for the critical pressure. The deflection function was assumed in the form of the potential series, then in the form of the sinusoidal function and finally as an exponential function. For all cases the expressions for the critical pressure are derived and shown.

2. INTRODUCTION

An interesting and important practical engineering problem, studied by several authors is the problem of the loss of stability of a cylindrical shell subjected to the external radial pressure. Several expressions for the critical load were proposed by different authors (Mises formula for simply supported ends [1], [2], [3], W. Nash and V. A. Nagaev formulae for fixed ends [2]). The two last mentioned formulae applied to the same shell give different critical pressures. The authors of this paper tried and derived [4], [5], [6] a more general, may be more correct, expression valid for different end supports, and giving the previously mentioned formulae just as its particular cases.

The starting point are partial differential equations for the considered shell problem [1], [2]

$$\frac{D}{h} \nabla^4 w = \frac{1}{R} \frac{\partial^2 \Phi}{\partial x^2} - \frac{q R}{h} \frac{\partial^2 w}{\partial y^2} ; \quad \nabla^4 \Phi = \frac{-E}{R} \frac{\partial^2 w}{\partial x^2}. \quad (1)$$

$w(x, y)$ - deflection function, x and y - circumferential and longitudinal coordinates, $\Phi(x, y)$ - stress function, h, R, L , and D - shell thickness, radius, length and bending stiffness, E - Young's modulus. The deflection function is assumed in the form [4], [5]

$$w = w(\xi, y) = \Psi(\xi) \sin a y. \quad (2)$$

$\xi = x/L$ - dimensionless longitudinal coordinate, n - number of waves in the circumferential direction, $a = n/R$ - reduced number of waves, $\Psi(\xi)$ is introduced [4], [5] as

$$\Psi(\xi) = \{[g(\xi) - g(0)] \cdot [g(\xi) - g(L)]\}^2. \quad (3)$$

It can, in general case, satisfy even mixed boundary conditions, and the function $g(\xi)$ must satisfy some functional equations. If the integrals of the form

$$\lambda(\xi, \pm a) = \int e^{\pm a \xi L} \frac{d^2 \Psi(\xi)}{d\xi^2} d\xi \quad (4)$$

are introduced the Lateral Stability Function (LSF) [4], [5] can be defined as

$$\bar{\theta}(\xi, a) = \frac{1}{4 a L} \frac{\partial}{\partial \xi} \left[e^{a \xi L} \int \lambda(\xi, -a) d\xi - e^{-a \xi L} \int \lambda(\xi, a) d\xi \right] \quad (5)$$

The application of the Bubnov-Galerkin method leads to the relation connecting the external radial pressure q in its dimensionless form \bar{q} to the LSF.

$$\bar{q} = \frac{q}{E} \left(\frac{R}{h} \right)^2 = \frac{K_1}{C_0 n^2} \left[D_2 - 2D_1 n^2 + D_0 n^4 + \int_0^L \bar{\theta}(\xi, n) \Psi(\xi) d\xi \right] \quad (6)$$

The critical number of waves is determined from the integral equation

$$2D_2 - 2D_0 n^4 = \int_0^L \Psi(\xi) \left[n \frac{\partial \bar{\theta}(\xi, n)}{\partial n} - 2\bar{\theta}(\xi, n) \right] d\xi \quad (7)$$

$$D_r = \frac{C_r}{12 K_1^2 K_2^{2r} (1 - \nu^2)}, \quad (r = 0, 1, 2) \quad (8)$$

$$C_r = \int_0^L \Psi(\xi) \frac{d^{2r} \Psi(\xi)}{d\xi^{2r}} d\xi, \quad (r = 0, 1, 2) \quad (9)$$

$$K_1 = \frac{R}{h}; \quad K_2 = \frac{L}{R} \quad (10)$$

D_r are the new proposed [4] generalized dimensionless shell stiffness coefficients depending on the shell geometry through the coefficients $K_i, (i=1,2)$, on the assumed deflection function defined by (2) and (3) through the generalized constants $C_r, (r=0,1,2)$ and on material constants E and ν . For $K_1^2 K_2^{2r} = 1$ the coefficients D_r reduce to the bending stiffness $D = Eh^3 / 12(1-\nu^2)$ depending only on h, E and ν , and the constants C_r reduce in the same case to Eh^3 . The critical number of waves n_{CR} introduced into the equation connecting the external load and the LSF, gives the general expression for the critical pressure in the form [4], [5], [6]

$$\bar{q}_{CR} = \frac{q_{CR}}{E} \left(\frac{R}{h} \right)^2 = \frac{K_1}{C_0 n_{CR}^2} \left[D_0 n_{CR}^4 - 2D_1 n_{CR}^2 + D_2 + \int_0^l \bar{\theta}(\xi, n_{CR}) \Psi(\xi) d\xi \right] \quad (11)$$

The generality of the expression (11) for the critical pressure was explained in [5] and [6] and it will be mentioned here only in the condensed way.

2.1. Shell with built in ends. The formula proposed by V. A. Nagaev is obtained if the function $\Psi(\xi)$ defined by (3) is introduced in the form [4], [5]

$$\Psi(\xi) = \xi^2 (1-\xi)^2 \quad (12)$$

and the LSF [4], [5] as its consequence is

$$\bar{\theta}(\xi, a) = \frac{24}{(aL)^4} \quad (13)$$

The formula proposed by W. Nash is obtained if $\Psi(\xi)$ is assumed in the form [4], [5]

$$\Psi(\xi) = \sin^2 \pi \xi \quad (14)$$

giving as its consequence the LSF [4], [5] as

$$\bar{\theta}(\xi, a) = -\frac{8\pi^4 \cos 2\pi \xi}{[(aL)^2 + 4\pi^2]^2} \quad (15)$$

2.2. Shell with simply supported ends. The expression known as the Mises formula [1], [2], [3] will be obtained from the function $\Psi(\xi)$ assumed in the form [4], [6]

$$\Psi(\xi) = \sin \pi \xi \quad (16)$$

giving the LSF in the form [4], [6]

$$\bar{\theta}(\xi, a) = \frac{\pi^4 \sin \pi \xi}{[(aL)^2 + \pi^2]^2} \quad (17)$$

3. INFLUENCE OF THE LATERAL STABILITY FUNCTION ON THE FORM OF THE CRITICAL PRESSURE

The influence of the form of the LSF on the critical pressure can be estimated from the integral equation (7) for the determination of the critical number of waves. If the LSF can not be eliminated from the considerations, as it is the fact because of its coupling with the functions $\Psi(\xi)$, its influence on the results can be examined and analyzed in the way that follows. The expression for the pressure defined by (6) will be decomposed into two parts q_1 and q_2 where only the part q_2 depends on the LSF

$$q_{total} = q_1 + q_2 \quad (18)$$

$$q_1 = \frac{K_1}{C_0 n^2} [D_2 - 2D_1 n^2 + D_0 n^4] \quad (19)$$

$$q_2 = \frac{K_1}{C_0 n^2} \left[\int_0^1 \bar{\theta}(\xi, n) \Psi(\xi) d\xi \right] \quad (20)$$

If the LSF is not taken into the consideration it is easy to obtain the critical number of waves n_{2CR} from (19) and in that case the critical pressure becomes

$$(\bar{q}_2)_{CR} = \frac{2K_1}{C_0} (\sqrt{D_0 D_2 - D_1}) = \frac{I}{6C_0 K_1 K_2^2 (1-\nu^2)} (\sqrt{C_0 C_2} - C_1) \quad (21)$$

The influence of the LSF can now be estimated from the relative difference

$$\Delta(q_2, q_{total}) = \frac{(\hat{q}_2)_{CR} - (\hat{q}_{total})_{CR}}{(\hat{q}_{total})_{CR}} \quad (22)$$

This expression was calculated for the shell with fixed ends, with $K_2 = 1$ (a short shell) and for $K_1 = 100, 200, \dots, 700$. and the formulae proposed by Nagaev and by Nash were applied. For the considered shell the relative difference (22) was in the first case (Nagaev) between 0.62 and 0.84 and in the second case (Nash) between 0.99 and 1.00 and it became obvious that the LSF must be taken into account even if it is causing the difficulties during the calculations.

4. INFLUENCE OF THE FORM OF THE DEFLECTION FUNCTION ON THE CRITICAL PRESSURE

Following the previous conclusions about the influence of the LSF different forms of the Deflection Function (DF) were taken into account and their consequences on the critical pressure were examined. A shell with fixed ends will be here considered.

4.1. Deflection function in the form of the potential series. The deflection function in the form

$$\Psi(\xi) = \xi^m (1-\xi)^m = \sum_{k=0}^m (-1)^k \binom{m}{k} \xi^{m+k} \quad (23)$$

after being introduced into (9) will have as its consequence

$$C_0 = \sum_{k=0}^{2m} \frac{(-1)^k \binom{2m}{k}}{2m+k+1} \quad (24)$$

$$C_1 = \frac{m(m-1)}{2m-1} + \frac{2m(2m-1)}{4m-1} + \sum_{k=0}^{2m-2} \frac{(-1)^{k+1} \binom{2m-1}{k} [m-1)k^2 + (4m^2 - m - 1)k + 2m^2(2m-1)]}{(k+1)(2m-k-1)(2m+k)} \quad (25)$$

$$C_2 = m(m-1) \left(\sum_{k=0}^{2m-4} \frac{R_k}{2m+k+1} + \frac{A}{2m-3} + \frac{B}{2m-2} + \frac{C}{4m-4} + \frac{D}{4m-3} \right) \quad (26)$$

where the coefficients A, B, C, D and R_k are

$$A = (m-2)(m-3); B = (-2m)(m-1)(m-2) \quad (27)$$

$$C = (-8)(m-1)(4m^2 - 8m + 3); D = 4(4m^2 - 8m + 3)$$

$$R_k = (-1)^k \binom{2m-3}{k} \left\{ \frac{24(m-1)}{2m-k-2} + 12(m-2) \left(4 + \frac{2m-k-3}{k+1} + \frac{4k}{2m-k-2} \right) + \frac{(m-2)(m-3)(2m-k-3)}{2m-3} \left[24 + \frac{(2m-k-4)(2m+7k+11)}{(k+1)(k+2)} + \frac{16k(4m-k-5)}{(2m-k-3)(2m-k-2)} \right] \right\} \quad (28)$$

It must be underlined that the coefficients (28) are always integers. The LSF and the critical pressure are now defined by (29) and (30) where δ_i , α_i and S are coefficients defined by some cumbersome expressions. The derived expressions will be shown for $m=2$ and $m=3$

$$\bar{\theta}(\xi, a) = \frac{1}{4(aL)^m} \left\{ \sum_{k=0}^{m-2} \left[\frac{(a\xi L)^k}{k!} \sum_{r=0}^m \frac{(m+r-k-2) \binom{m}{r} (m+r-k-2)! ((-1)^{k+m} + (-1)^r)}{(aL)^r} \right] + \sum_{m-1}^{2m-4} \left[\frac{(a\xi L)^k}{k!} \sum_{r=k-m+4}^m \frac{(m+r-k-2) \binom{m}{r} (m+r-k-2)! ((-1)^{k+m} + (-1)^r)}{(aL)^r} \right] \right\} \quad (29)$$

$$\bar{q} = \frac{K_1}{C_0 n^2} \left(n^4 D_0 - 2n^2 D_1 + D_2 + \sum_{i=4}^m \frac{\delta_i}{4n^i K_2^i} + \sum_{i=2}^m \frac{\alpha_i}{4n^{m+i} K_2^{m+i}} + \frac{S}{4n^{m+1} K_2^{m+1}} \right) \quad (30)$$

4.1.1. Case m = 2. The equation for the pressure is

$$\bar{q} = \frac{K_1}{C_0 n^2} \left(n^4 D_0 - 2n^2 D_1 + D_2 + \frac{4}{5(nK_2)^4} \right) \quad (31)$$

$$C_0 = \frac{1}{630} \quad D_0 = \frac{1}{7560(1-\nu^2)K_1^2} \quad D_1 = \frac{12}{K_2^2} D_0 \quad D_2 = \frac{42}{K_2^2} D_1 \quad (32)$$

representing the Nagaev's formula but in much simpler form than it is usually shown.

4.1.2. Case m = 3. The equation for the pressure becomes

$$\bar{q} = \frac{K_1}{C_0 n^2} \left(n^4 D_0 - 2n^2 D_1 + D_2 + \frac{2}{35(nK_2)^4} - \frac{72}{7(nK_2)^6} \right) \quad (33)$$

$$C_0 = \frac{1}{12012} \quad D_0 = \frac{1}{144144(1-\nu^2)K_1^2} \quad D_1 = -\frac{16}{K_2^2} D_0 \quad D_2 = -\frac{44}{K_2^2} D_1 \quad (34)$$

4.2. Deflection function in the sinusoidal form. The deflection function in the form

$$\Psi(\xi) = \sin^m(\pi\xi) \quad (35)$$

where m must be the natural number greater than 1 in order to permit the boundary conditions to be satisfied, after the development of the *sine* function and its introduction in (9) gives

$$C_0 = \frac{\binom{2m-1}{m}}{2^{2m-1}}; C_1 = \frac{-m\pi^2}{2^{2m-2}} \binom{2m-3}{m-2}; C_2 = \frac{m^2\pi^4(3m-4)\binom{2m-5}{m-2}}{(m-1)2^{2m-3}} \quad (36)$$

After the calculation of the integrals $\bar{\lambda}$ defined by (4) the LSF is obtained for even and odd values of m and the integral from (11) depending on the LSF becomes respectively

$$\int_0^1 \bar{\theta}(\xi, n) \Psi(\xi) d\xi = \frac{\pi^4}{2^{2m-1}} \sum_{k=0}^{\frac{m-1}{2}} \frac{\binom{m}{k}^2 (m-2k)^4}{[nK_2]^2 + \pi^2(m-2k)^2} \quad (m \text{ even number}) \quad (37)$$

$$\int_0^1 \bar{\theta}(\xi, n) \Psi(\xi) d\xi = \frac{\pi^4}{2^{2m-1}} \sum_{k=0}^{\frac{m-1}{2}} \frac{\binom{m}{k}^2 (m-2k)^4}{[nK_2]^2 + \pi^2(m-2k)^2} \quad (m \text{ odd number}) \quad (38)$$

The lateral pressure is then defined by (39) for even and by (40) for odd values of m .

$$\hat{q} = \frac{K_I}{n^2 C_0} \left[n^4 D_0 - 2n^2 D_1 + D_2 + \frac{\pi^4}{2^{2m-1}} \sum_{k=0}^{\frac{m-1}{2}} \frac{\binom{m}{k}^2 (m-2k)^4}{[nK_2]^2 + \pi^2 (m-2k)^2} \right] \quad (39)$$

$$\hat{q} = \frac{K_I}{n^2 C_0} \left[n^4 D_0 - 2n^2 D_1 + D_2 + \frac{\pi^4}{2^{2m-1}} \sum_{k=0}^{\frac{m-1}{2}} \frac{\binom{m}{k}^2 (m-2k)^4}{[nK_2]^2 + \pi^2 (m-2k)^2} \right] \quad (40)$$

The derived expressions are here calculated and shown for the coefficients $m=2$ and $m=3$.

4.2.1. Case $m=2$. Only the LSF and the lateral pressure equation will be shown

$$\bar{\theta}(\xi, n) = \frac{-8\pi^4 \cos(2\pi\xi)}{[nK_2]^2 + 4\pi^2} \quad (41)$$

$$\hat{q} = \frac{K_I}{n^2 C_0} \left[n^4 D_0 - 2n^2 D_1 + D_2 + \frac{2\pi^4}{[nK_2]^2 + 4\pi^2} \right] \quad (42)$$

representing the Nash formula in the form that is modified and simpler than the common one.

4.2.2. Case $m=3$.

$$\bar{\theta}(\xi, n) = \frac{3\pi^4 \sin(\pi\xi)}{4[nK_2]^2 + \pi^2} - \frac{81\pi^4 \sin(3\pi\xi)}{4[nK_2]^2 + 9\pi^2} \quad (43)$$

$$\hat{q} = \frac{K_I}{n^2 C_0} \left[n^4 D_0 - 2n^2 D_1 + D_2 + \frac{9\pi^4}{32[nK_2]^2 + \pi^2} + \frac{81\pi^4}{32[nK_2]^2 + 9\pi^2} \right] \quad (44)$$

4.3. Deflection function in the exponential form. After that a very logical step was to try to find out some other classes of functions that will give the acceptable equations for the lateral pressure. It was concluded from (4) that an exponential function of the first order could be used for that purpose and using the appropriate assumptions the function $g(\xi)$, the DF, $C_i, (i=0,1,2)$, the LSF and the lateral pressure equation were obtained in the forms

$$g(\xi) = e^\xi - e^{I-\xi} \quad (45)$$

$$\Psi(\xi) = (e^\xi - e^{I-\xi} + e - I)^2 (e^\xi - e^{I-\xi} - e + I)^2 \quad (46)$$

$$C_0 = \frac{1}{12}(-13e^8 + 32e^6 + 432e^4 + 352e^2 + 37) = 31.8013,$$

$$C_1 = \frac{-4}{3}(e^8 + 4e^6 - 72e^4 + 52e^2 - 1) = 371.11673, \quad (47)$$

$$C_2 = \frac{32}{3}(e^8 - 14e^6 + 72e^4 + 38e^2 - 1) = 16,467.262.$$

$$\bar{\theta}(\xi, n) = \frac{256}{T_2} [e^{4\xi} + e^{4(1-\xi)}] - \frac{32}{T_1} [e^2 + 1](e^{2\xi} + e^{2(1-\xi)}) \quad (48)$$

$$T_j = [(nK_2)^2 - 4]^2 \quad (49)$$

$$\hat{q} = \frac{K_1}{C_0 n^2} \left\{ n^4 D_0 - 2n^2 D_1 + D_2 - \frac{H_1}{[(nK_2)^2 - 4]^2} + \frac{H_2}{[(nK_2)^2 - 16]^2} \right\} \quad (50)$$

$$H_1 = \frac{32}{3}(e^2 + 1)(e^6 - 3e^4 - 21e^2 - 1) = 7,469;$$

$$H_2 = \frac{64}{3}(e^8 - 8e^6 + 24e^4 + 8e^2 - 1) = 23,936 \quad (51)$$

It is necessary to underline that (51) according to the authors' knowledge represents a new equation for the pressure.

5. CONCLUSION

It can be concluded that a certain general formula for the critical external radial pressure around a cylindrical shell is derived. The explained procedure can be applied to shells with different types and combinations of boundary conditions, and the Lateral Stability Function must be taken into account during the calculations of the critical pressure. A new proposed form of the deflection function is giving as its consequence a new formula for the critical pressure and experimental results will show which one between existing and new proposed expressions is approaching the real situation.

6. REFERENCES

- [1] Timoshenko, S.P., Gere, J.M., *Theory of elastic stability*, 2nd ed., McGraw Hill (1961).
- [2] Vol'mir, L., *Stability of elastic systems* (in Russian), Gos.izd.fiz-mat. lit., Moscow (1963).
- [3] Umanskij, A.A. red. *Designer's Manual, Selected chapters*, (in Serbian), Gradjevinska knjiga (1980).
- [4] Markovic Lj., S., *Determination of limit equilibrium state for radially compressed cylindrical shell with various boundary conditions* (in Serbian), Ph D Thesis, Fac. Mech. Eng., Univ. of Belgrade (1999).
- [5] Ruzic, D.D., Markovic, Lj. S., *A general formula for critical external radial pressure around a circular cylindrical shell with built in ends*, Recent Advances in Mechanics, Xanthi, Greece (1998).

- [6] Ruzic, D.D., Markovic Lj., S., *Cylindrical shell with arbitrary supported ends (Stability under radial external load)*, 4th Euromech Solid Mechanics Conference, Metz, France (2000).
- [7] Ruzic, D.D., Markovic Lj., S., *New formula for the critical external radial pressure around the cylindrical shell*, ICTAM 2000, Chicago, USA (2000).

ESSENTIAL STRUCTURE OF DAMAGE MECHANICS MODELS

Dusan Krajcinovic
Mechanical and Aerospace Engineering
Arizona State University, USA

1. SUMMARY

This paper provides my view of damage mechanics objective, accomplishes and the relation with other models of solid mechanics, thermodynamics and statistical physics. The fact that the estimates of damage are has a value only as the overture for specimen failure is still accepted by many authors. Finally, the introduction of the meso-scale texture and coupling between macro and meso scales is necessary for development of better models.

2. INTRODUCTION

Damage mechanics, born in Russia where Lazar Kachanov's [1] study was published, grown, in my personal judgement, more in quantity of papers than in new ideas that were not pilfered from plasticity. This is not to say that the Cachan School in France was not successful in the promotion of damage mechanics in industry. This success was, for some reasons, not duplicated on the other shore of Atlantic Ocean. Even if some wanted to use one of many models of damage mechanics, which are not related to a class of materials and process, it would be very difficult to select the proper model. Too many damage parameters and a damage entity, defined by tensors of all orders, would make no sense even if they were identified and measurable. Some of these models are not objective, assumptions are carelessly elevated to rank of principles and the model limitations not mentioned.

In my opinion a damage mechanics model must provide a useful estimate of the effect of nucleation, propagation and clustering of microcracks on deformation, residual strength and failure mode and onset of the considered damage or aged material and structure. A crack is a microcrack if its size is similar to the material micro-texture size (such as grain boundary length in polycrystalline materials). Since the material morphology in which microcrack is embedded disordered crack geometry cannot be defined by few parameters. Hence, damage must measured indirectly from their effect on the macro-scale deformation. This truism is crucial for the model development since the input is statistical while the output is either deterministic or statistical depending on the damage density.

Serious models of damage mechanics must be based on the principles (if not the models) fracture mechanics, physics of disorder materials and thermodynamics of dissipative processes that can be either “close” or “far” from the equilibrium. Finally, the process of renormalization from statistical micro and meso models must be related to the continuum models which still the war-horse of the industry and engineering design.

3. MACRO-SCALE MODELS

In the course of a structure design, which is subjected to given applied external internal loads and/or displacements as a function of time, is typically discretized into many finite elements (FE). The stress-strain relation, assuming that the strains are moderate and strain infinite small, is

$$\bar{\epsilon} = \bar{S}(\bar{D}) : \bar{\sigma} \quad (1)$$

where \bar{S}_{ijmn} is the effective compliance tensor which depend on the microcrack density \bar{D} and the bar over the symbol stands for the macro-scale value. Assumed, that the strain $\bar{\epsilon}_{ij}$ is at minimum C^1 continuous the strain rate is from (1)

$$\dot{\bar{\epsilon}} = \dot{\bar{S}}(\bar{D}) : \bar{\sigma} + \bar{S}(\bar{D}) : \dot{\bar{\sigma}} \quad (2)$$

Assuming that the flow rule exists the infinitesimal increment of the effective compliance of the material is

$$d\bar{S}_{ijmn} = 2\lambda \frac{\partial \Omega(\bar{\Gamma}, \bar{T}, \bar{D})}{\partial \bar{\Gamma}_{ij} \partial \bar{\Gamma}_{mn}} = \lambda \frac{\partial \Omega(\bar{\Gamma}, \bar{T}, \bar{H})}{\partial \bar{\Gamma}_{ijmn}} \quad (3)$$

where λ is the proportionality constant (i.e. rate of some monotonically increasing scalar parameter selected as an appropriate measure accumulated at current instant, Ω a potential and T the temperature. The thermodynamic force $\bar{\Gamma}$ is conjugate to the selected measure of the accumulated damage \bar{S}_{ijmn} since entropy production inequality is

$$T\dot{\eta} = \frac{1}{2} \dot{\bar{S}}_{ijmn} \bar{\sigma}_{ij} \bar{\sigma}_{mn} - \dot{\bar{U}}^s = \Gamma_{ijmn} \dot{\bar{S}}_{ijmn} - \dot{\bar{U}}^s \geq 0 \quad (4)$$

(Krajcinovic 1997). In (4), dot above symbol stands for the rate, T the absolute temperature, \bar{U}^s the energy of internal surfaces (of cracks), and thermodynamic force that drives damage

$$\Gamma_{ijmn} = \frac{1}{2} \bar{\sigma}_{ij} \bar{\sigma}_{mn} \quad (5)$$

from (3). Selection of the effective compliance tensor $\bar{S}_{ijmn}(\bar{D})$ as repository of accumulated history H is consistent to the proposed goals since the compliance can be measured in situ and laboratory (Audoin and Baste [2]).

In general, the stresses, strain, stress and compliance tensor must be decomposed (Krajcinovic [3]) since the closed microcracks do not effect the deformation. In a short review it suffices mention the decomposition and state its necessity at the price of cumbersome model. However, the number of assumptions required to develop above deterministic continuum model and simultaneously shrink its range of applications is many. The more important assumptions that limit model's application are:

- Deformation of the specimen and evolution of damage are driven by the *volume average* of stresses, strains and free surface energy \bar{U}^s (that resists microcrack propagation).
- The representative volume element (RVE) exists.
- Flow potential Ω in (6) and (7) and damage surface actually exists.
- The deformation process is "close" to equilibrium and its attractor state minimizes the energy of the elastic strain.

These assumptions are satisfied only when the specimen is *statistically homogeneous*, i.e. when the deformation depends on average of all fields and precise locations of stress fluctuations and resistance to crack propagation fields [3]. Since the thermodynamic state does not depend on the spatial distribution of fields each state is equilibrated and defined by the manifold $\{\bar{\epsilon}, \bar{S}, \bar{T}\}$ when the stress is controlled or $\{\bar{\sigma}, \bar{S}, \bar{T}\}$ when the strain is controlled. According to the statistical physics and thermodynamics (see Carrod [4]) a state is in equilibrium when can be defined by a minimum of macroscopic parameters, which are in this case, macroscopic stresses, effective macroscopic compliance (as a measure of dissipated energy used to form internal surface within the material) and temperature. The dissipative thermodynamical process in this case can be viewed as the temporal sequence of equilibrated states and the above model belongs to the class of thermodynamic with internal variable(s) (see Krajcinovic [3] and Lemaitre and Chaboche [5]).

A mechanician in trade will, therefore, start with the thermodynamics as a basis of the model, select a damage parameter, assume that the flow potential exists, and introduce as many of fitting "material parameters" to duplicate a set of macroscopic stress-strain curves. However, this continuum model, often used and not always understood, will be predictive in general only when the parameters fits the physics of the process on finer scales.

4. MEAN-FIELD MESO-SCALE MODELS

When the mean-field models of statistical physics a quarter century ago burst into solid mechanics research many hoped for a new class of models which will solve all unsolved problems of solid mechanics. Mesomechanical fracture mechanics inquire into the relation between the material parameters and microcracks density should help in the selection of the physically reasonable damage parameter.

A model belongs to class of mean-field models if variables are approximate by their average values deduce self-consistently (Chaikin and Lubensky [6]). A typical meso-scale damage mechanics sees a damage material as an ensemble of microcracks embedded within a homogeneous, elastic, continuum matrix. The external surfaces of this volume are subjected to the homogeneous tractions or deformation related to the macroscopic stresses and strains. Assuming that volume is statistically homogeneous the position of individual microcracks is irrelevant and the problem of many cracks is reduced to the superposition of many individual cracks within the effective material. In other words, the effect of all cracks on a given crack is reduced to their effect on the parameters of the continuum matrix.

The objective of this model is to deduce the effective (macroscopic) parameters of this volume and related this parameters to the density of the microcracks. This volume and its parameters are then mapped on the "point" of the continuum to define the parameters in the

damaged state. This mapping is objective only if the parameters of the volume do not depend on the volume size, i.e. if the volume is equal or larger than the representative volume element (RVE) defined above. Assumption of translation invariance of these models (i.e. positions of cracks) ignores cooperative processes and local fluctuations of stresses, strains and free surface energy of the material. It severely limits of their application to the insignificantly modest level of microcrack densities. However, these models provide the link between thermodynamics, fracture mechanics and basic statistics of the problems and provide a very useful test for elimination of rogue models.

To deduce the essential form of damage mechanics models it is necessary to consider a problem for which the analytical solution is possible. Assuming that all cracks are penny-shaped and the distribution of crack radii and orientations are not correlated the statistics of damage is reduced to the distributions of microcrack orientation $w_\phi(\phi, \theta)$ (rosette) and their radii $w(a)$. Damage tensors can be derived from empirical function $w_\phi(\phi, \theta)$, deduced from measurements, by expanding it into a Fourier-type series of the certain families of Laplace harmonics (see [3]).

The next task is to derive the effective compliance and stiffness tensors of a damage RVE. Using the recipe of fracture mechanics (Budiansky and Connell 1976) the effective compliance tensor \bar{S}_{ijmn} of the RVE attributed to the presence of damage can, in this case, be derived by adding the contributions of microcracks in all planes in the form

$$\begin{aligned}\bar{S}_{ijmn} &= \bar{S}_{ijmn}^o + \frac{8(1-\bar{\nu})}{3(2-\bar{\nu})\bar{\mu}} \omega \int_0^{2\pi(\pi/2)} \int_{-\pi/2}^{\pi/2} F_{ijmn}(\bar{\mu}, \bar{\nu}; \phi, \theta) \cos \phi \, d\phi \, d\theta = \\ &= \bar{S}_{ijmn}^o + \frac{8(1-\bar{\nu})}{3(2-\bar{\nu})\bar{\mu}} \omega \Theta_{ijmn}(\bar{\mu}, \bar{\nu}; \phi, \theta) = \bar{S}_{ijmn}^o + \bar{S}_{ijmn}^* \end{aligned} \quad (6)$$

where superscript “*” stands for the contribution of damage and while the superscript “o” stands for the initial (pristine) state. The expression (6), derived using the tools of the linear elastic fracture mechanics, ignore microcracks interaction [3] and effect of damage on the isotropy of the matrix. The components of the distribution of density in directions defined by angles ϕ and θ fourth order tensor $\Theta_{ijmn}(\bar{\mu}, \bar{\nu}; \phi, \theta)$, defined as the product $\bar{S}_{ijmn}^* w_\phi(\phi, \theta)$, are determined by solving the double integral in (6). Finally, the scalar parameter

$$\omega = N \langle a^3 \rangle = 4\pi \bar{\rho} \quad (7)$$

known as Budiansky-O’Connell parameter, is defined as a product of the number of microcracks per volume N and the volume average of the cube of microcrack radii. The accuracy of three mesomechanical scalar models based on the scalar, second and fourth orders tensors of damage distribution were evaluated by Krajcinovic and Mastilovic [8]. Expression (7) summarize the most dangerous deficiency of mean-field models by stating that very many small microcrack have the same effect as smaller large microcracks that is true only at very small microcracks and their density and strongly damage tolerant materials.

To complete the micromechanical model, developed above, it is necessary to relate the rate of effective parameters of the RVE to the nucleation and propagation of microcracks. The flow potential (6) can be derived using the assumption of the *local dependence* (Rice [8] and [9])

from free complementary energy $\Psi(\bar{\sigma}, \bar{D})$ of the considered volume V , attributed to the irreversible changes of the material texture

$$d^c \Psi \equiv [\Psi(\bar{\sigma}, \bar{D} + d\bar{D}) - \Psi(\bar{\sigma}, \bar{D})] = \sum_{\alpha=1}^N f_{\alpha}(\bar{\sigma}, \bar{D}) d\xi_{\alpha} \quad (8)$$

In (8) f_{α} are thermodynamic forces conjugate to the set of internal variables ξ_{α} . In the case of damage, attributed to N randomly scattered microcracks within the volume V , the expression (29) in [8]) is

$$\sum_{\alpha=1}^N f_{\alpha}(\bar{\sigma}, \bar{D}) d\xi_{\alpha} \approx \int_L [(G - 2\gamma) d\ell] dL \quad (9)$$

where G is the elastic energy release rate familiar from the fracture mechanics, γ the surface free energy, L locus of all points on the crack front and $d\ell$ local advance of the crack front (or tip in two-dimensional problems). Assuming that the integrand is a weak function of L , i.e. if the shape of the crack does not change, from (9)

$$f_{\alpha} \approx (G - 2\gamma)_{\alpha} \quad \text{and} \quad \dot{\xi}_{\alpha} \approx \dot{A}_{\alpha}^* \quad (10)$$

where A_{α}^* is the microcrack surface area and \dot{A}_{α}^* the rate of crack propagation. The thermodynamic force (affinity) conjugate to the increase of a given microcrack is therefore defined

$$A = G - 2\gamma \quad (11)$$

The corresponding rate of the effective compliance of the volume V that is attributed to the microcrack propagation is

$$d\bar{S}_{ijmn} = \frac{1}{V} \int_L \left[\frac{\partial^2 G(\bar{\sigma}, H)}{\partial \bar{\sigma}_{ij} \partial \bar{\sigma}_{imn}} d\ell \right] dL \quad (12)$$

A microcrack will propagate in a stable fashion when

$$A = 0 \quad \text{and} \quad \dot{A} < 1$$

and unstable when

$$A = 0 \quad \text{and} \quad \dot{A} > 1 \quad (13)$$

When the thermodynamic affinity is negative, $A < 0$, the crack will not propagate at all.

Assume that the microscopic relation between the thermodynamic force f_{α} and rate of increase the surface area of microcrack α \dot{A}_{α}^* is $\dot{\xi}_{\alpha} = \Phi(f_{\alpha}, T, \xi)$ the macroscopic (continuum) flow potential reads

$$\Omega(\bar{\sigma}, T, \xi) = \frac{1}{V} \int_0^f \xi_{\alpha}(\mathbf{f}, T, \xi) df_{\alpha} \quad (14)$$

where \mathbf{f} stands for all N thermodynamic forces f_{α} , ($1 \leq \alpha \leq N$), collectively. According to expression (14) the macroscopic flow potential is a superposition of all microscopic flow potentials ξ_{α} . The rate of effective compliance attributed to microcracks is

$$\dot{S}_{ijmn}^* = \frac{\partial \Omega(\Gamma, T, \xi)}{\partial \Gamma_{ijmn}} \quad (15)$$

where Γ is the thermodynamic force defined in (5).

Assuming that all assumptions are justified the relations between stresses and strains is

$$\bar{\epsilon}_{ij} = \bar{S}_{ijmn}(H) \bar{\sigma}_{mn} + \bar{\epsilon}_{ij}^p \quad \text{and} \quad \dot{\bar{\epsilon}}_{ij} = \bar{S}_{ijmn}(H) \dot{\bar{\sigma}}_{mn} + \dot{\bar{S}}_{ijmn}(H) \bar{\sigma}_{mn} + \dot{\bar{\epsilon}}_{ij}^p \quad (16)$$

where $\bar{\epsilon}_{ij}^p$ is the plastic strain, at first glance conveniently similar to the traditional equations of plasticity. However, this model is justified only when the volume is statistically homogeneous and damage evolves by microcrack nucleation typical only when the damage density is modest and not of important in engineering.

5. STATISTICAL MESO-SCALE MODELS

The onset, rate and direction microcrack propagation depends on the local, rather than average, stress and material cohesive strength is an obvious truism. Since the material texture is on mesoscopic scale not homogenous the process of damage evolution must be based on the random variable $G[\sigma(x)]/R(x)$ where the numerator is the *local* release energy and the denominator the *local* cohesive energy of material. The distribution bandwidth of the random variable $R(x; \bar{D})$ is the measure of the damage tolerance that controls the level of material brittleness.

The onset of microcrack propagation, its direction and retardation depends on the micro-features of the material. Assuming that the cohesive strength grain boundary of the material is inferior to those of the grains most microcracks will be of inter-granular type. Grain faces of the polycrystal form a Delaunay division of simplexes is the topological inverse or dual to the Voronoi froth (division) [10]. Since the number of facets per grain is a random variable the Voronoi and Delaunay lattices of most engineering material are random graphs. Finally, the bonding along grain boundaries depend on imperfections, relative disclination of anisotropy of planes of elastic symmetries of joined grains, impurities, pores at triple junction and atomic defects. Thus, the length and cohesive strength of grain boundaries of most engineering materials are also random variables.

The simplest model of damage in this class of damage-tolerant material on the micro-scale is a Delaunay lattice (or graph) of particles, in which the grain mass is lumped, connected by links that are perpendicular to grain boundaries depicted dual by the edges of Voronoi cell. Hence, a broken link represents the microcrack perpendicular to the link. Quenched material disorder, that can be topological, geometrical and structural, is introduced by the distribution of link type, lengths, strengths and effect of defects smaller than the residual (or link) length is introduced through links strengths. Finally, the parameters of lattice are derived such that the elastic deformation of the lattice and the actual material are equal.

Damage evolution simulation on a lattice, which is based on the Hamiltonian mechanics, in the general case of elongation control, is not as simple as it likes. Damage evolution during which microcracks nucleate, propagate and join into clusters is a primer for those who want to understand thermodynamics of internal variables. As demonstrate in Krajcinovic [11] this dissipative, non-stationary, non-linear and non-equilibrium process is actually a temporal

sequence of equilibrated states (of stationary damage) connected by non-equilibrium, dissipative and non-stationary process during which the energy released by broken link propagate in the form of stress wave through the lattice. A state is equilibrated when its manifold $\{\bar{\sigma}, \bar{D}, \bar{T}\}$, at a given value of controlled macro-strain $\bar{\epsilon}$, is defined by the minimum of macro-parameters. This criterion is satisfied when the thermodynamic affinity is negative, i.e. when $A < 0$ or $\bar{D} = \text{const.}$. Distributions of link force in an equilibrated state must satisfy the principle of minimum energy. Thus, the process is driven by averages of stresses, damage and temperature and has both this potential (3) and attractor state of minimum entropy.

In contrast, non-stationary parts of the process damage evolution, during which $\dot{\bar{D}} > 0$ and $\bar{\epsilon} = \text{const.}$, can depend on the stress wave which magnitude decrease with the distance from the source since $G(x, t)$ where t is time. In this case damage evolution depends also on the dynamic parameters and the material-damping rate on the micro-scale. Moreover, the phenomenon of avalanche becomes important at larger damage density. Avalanche is defined as the number of links that are broken links at the constant applied elongation $\bar{\epsilon} = \text{const.}$ In other words, avalanche of n -order will occur when $\max(A_i) = 1$ take place n times at constant elongation of lattice. Avalanches of small order, where the order is equal to the number of links broken at same applied elongation, is not necessary a sign of the imminent failure. Hence, the process will be dependent on the macro-parameters until the damage clusters are small. Nevertheless, the dynamic distribution of released energy and avalanches favor clustering of damage and large damage densities. As the clusters grow the models of cooperative phenomena, which introduce the correlation length defined as the distance at which the fluctuations are correlated, must replace the mean-field theory. The dependence of the lattice performance on the lattice size is one of the sign of this transition.

Finally, in the softening phase of the lattice deformation is the sign that the size of the largest cluster (macroscopic crack in tension and fault in compression) is comparable to the specimen size L , i.e. that the correlation length $\xi \approx L$. Having in mind the primary dependence of the mechanics of the lattice on the on a fractal object, such as large cluster of microcracks, it is obvious that the deformation process in the softening phase is statistical. Moreover, the thermodynamics process is far-from equilibrium, potential and attractor state do not exist.

6. RENORMALIZATION

Lattice models have several advantages in the process of bridging from meso- to macro-scale. Its application is not confined to small damage density, their tractability dependent on the simplest geometry of microcracks and assumption of homogeneous, elastic, isotropic matrix. Thus the lattice is the only renormalization road, already tested and found trustworthy in many fields of physics, which can be used to bridge the gap between micro-, meso- and macro-scale.

Consider, as an example, a finite square plate made of damage-tolerant elastic material subjected along all boundaries to non-homogeneous displacements u_x and u_y which are quasi-statically increased until the plate failure. The plate is divided into a large number of square sub-elements such that the macroscopic elongation applied to its boundaries can be

considered to be homogeneous. The sub-element has to contain a large enough number of grains and provide for the resolution length comparable to the grain facet radius. Thus, each sub-element is subjected to uniform, but different, elongations in x and y directions.

The object of simulation is not only to produce several stress-strain curves that look great as transparent on a meeting but also to define universal exponents of the scaling functions and crossovers in the process. For example, the hardening phase of damage-elongation of lattice is at modest damage scales as $\bar{D}(L,u) \propto u^\beta$ and $\bar{D}(L) \propto L^\alpha$ at the peak of the stress-strain curve. Using Family and Vicsek [12] scaling function is $\bar{D}(L,u) \propto L^\alpha f(u)$. The universal exponent α is derived by plotting curves $\log(\bar{D}/L^\alpha)$ vs. $\log(u/L^z)$ such that curves for all lattice sizes collapse on a one curve. The crossover elongation is defined as $u_c \propto L^z$ where the dynamic exponent z is $\alpha = z\beta$. Dynamic scaling requires a very precise simulation, very precise of the interplay between different mechanical mechanisms and very good software.

7. CONCLUSIONS

These short strolls through damage mechanics, in my opinion, shows some defects of current development, interesting future and further growth of this baby of solid mechanics. This development will be based on the statistical models needed to reach the finite goal of bridging of scales, which is tailored for the damage mechanics.

8. ACKNOWLEDGEMENTS

The author gratefully acknowledges the research grant from the Engineering Science Division of the Army Research Office that made this work possible.

9. REFERENCES

- [1] Kachanov, L.M., On the time to failure under creep conditions, in *Izv. AN SSSR, Otd. Tekhn. Nauk*, No. 8, 26-31, (1958).
- [2] Audion, B. and Baste, S., Ultrasonic evaluation of stiffness tensor changes and associate anisotropic damage in ceramic composite, in *J. Appl. Mech.*, Vol. 61, 309-316, (1994).
- [3] Krajcinovic, D., *Damage Mechanics*, Elsevier, Amsterdam, (1996).
- [4] Garrod, C., *Statistical Mechanics and Thermodynamics*, Oxford Univ. Press, New York, (1995).
- [5] Lemaitre, J. and Chaboche, J.L., *Mecanique des Materiaux Solides*, Dunod, Paris, (1982).
- [6] Chaikin, P.M. and Lubensky, T.C., *Principles of Condensed Matter Physics*, Cambridge Univ. Press, New York, (1995).
- [7] Krajcinovic, D. and Mastilovic, S., Some fundamental issues of damage mechanics, *Mech. Mater.*, Vol. 21, 217-230, (1995).
- [8] Rice, J.R., Continuum Mechanics and Thermodynamics of Plasticity, in *Constitutive Equations*, A.S. Argon (Ed), MIT Press, Cambridge, MA, 23-79, (1975).
- [9] Rice, J.R., Inelastic Constitutive Relations for Solids, *J. Mech. Phys. Solids*, 433-455, (1971).
- [10] Zallen, R., *Physics of Amorphous Solids*, John Wiley & Sons, New York, 1983.
- [11] Krajcinovic, D., Thermodynamics of damage evolution and failure, in writing.

FATIGUE OF MATERIALS AND STRUCTURES

J. Lemaitre

Prof. Em. University Paris 6, LMT-Cachan,
61, avenue du Président Wilson 94235 Cachan, France

ABSTRACT

A short overview upon the phenomenon of fatigue is presented. An historical background shows that the studies on fatigue started only in the middle of the 19th Century with A. Wölher as a pioneer. The different physical and experimental effects are reviewed in a second part : discrepancy, scale, surface effects, initial conditions, mean stress, history of stress, temperature... In a third part, a two scale model, based on elasto-plasticity coupled to damage, is formulated to fulfill most of the effects mentioned.

1. HISTORICAL BACKGROUND

The recognition of the phenomenon of fracture of materials is as old as human activities but fracture under repetition of loads has been identified only in the 19th century. It seems that the first tests under repeated tensions up to 100 000 cycles were made on mine chains by Albert in Germany around 1830. It seems also that the word "fatigue" was mentioned for the first time by Poncelet during a conference given to engineers at Metz (France) in 1839. Rankine, working in England on railways, used also the word "Fatigue" in 1843. But this is A. Wöhler (1819-1914) who really gave the starting point on research upon fatigue by his idea to plot his many test results on steels, obtained at the railway factory of Hannover, as the stress amplitude to fracture in tension, function of the number of stress cycles applied. The **Woehler curve** was born around 1860 [1] (figure 1).

This was fatigue under uniaxial periodic loading in tension-compression at a mean stress equal to zero and at room temperature. It took about a century to be able to deal with multiaxial variable or random loading at high temperature ! The reason is that so many effects involved did oppose for a long time a clear view on quantitative theories.

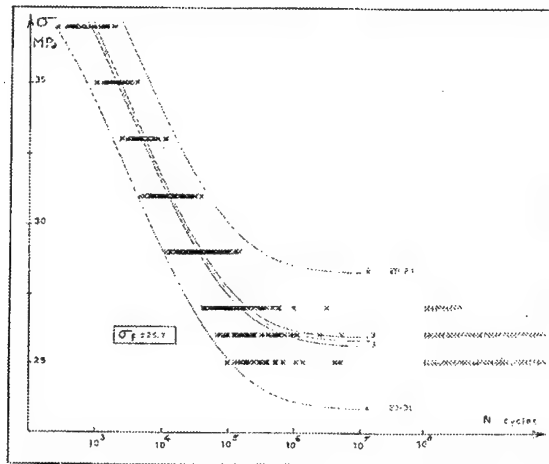


Fig. 1 : Woehler curve of XC10 Steel (Doc. CETIM)

- Soon after Wöhler, Fairbain in England (1864), Baushinger in Germany (1886) has to work on fatigue in bending for bridges and railways and it was difficult to relate properly the fatigue strength in bending to the fatigue strength in tension.
- Around 1900 Ewing and his coworkers in England showed by microscopic observations that fatigue on iron is related to plastic slip bands, but at a macro or mesoscopic scale no measurement can give an indication on the progression of fatigue : nothing between virginity and fracture !
- Many attempts were made to relate fatigue to an increase of the internal damping of metals (Lechatelier 1909, Boudouard 1910, in France) but the effect is so small that it is practically useless.
- The first book devoted to fatigue was published by H.G. Cough only in 1926 [2]. It is about at that time that the local character of fatigue was identified in relation with the large stress concentrations at sharp notches. This helped very much to design better structures against fatigue by smooth variations of geometry in the drawing of mechanical components [3].
- Soon, the studies on fatigue were stimulated by the need of light structures in aeronautics and safer design in general. The necessity of coordination, rules and standards was taken over by national organizations such as : Bureau of Aeronautics (1941), American Society for Testing Materials (1949), American Society of Metals (1953) in USA ; Institution of Metallurgists (1955), Institution of Mechanical Engineers (1956) in England ; Société Française de Métallurgie (1956) in France. All those Societies published important documents at the indicated dates.
- A nice synthesis of all possible aspects of fatigue of metals is in the book "La fatigue des métaux" published by R. Cazaud in 1937 and reedited in 1943, in 1948, and rewritten by G. Pomey, P. Rabbe and Ch. Janssen in 1969 [4].

- During the last three decades, most of the studies were devoted to the fatigue limit and to fatigue criteria :

. Does it exist a stress below which the number of cycles may reach infinity ? Recent works at number of cycles as large as 10^{12} or 10^{13} seems to show that the answer could be no [5]. Nevertheless for practical purposes the fatigue limit is taken as the stress which corresponds to 10^6 or 10^7 cycles.

. Which scalar function, called criterion, of the stress components of a multiaxial state of stress is equivalent to a case of uniaxial stress of tension-compression ? Among many criteria proposed those of Sines (1959), Crossland (1956), Dang Van [6] use the amplitude of the shear stress, octaedral A_{II} or maximum and the hydrostatic stress σ_H by its mean or maximum value.

$$A_{II} = \frac{1}{2} \left[\frac{3}{2} (\sigma_{ijMAX}^D - \sigma_{ijmin}^D) (\sigma_{ijMAX}^D - \sigma_{ijmin}^D) \right]^{1/2}$$

$$\sigma_H = \frac{1}{3} \sigma_{kk}$$

with the stress tensor σ_{ij} decomposed in $\sigma_{ij} = \sigma_{ij}^D + \sigma_H \delta_{ij}$

- More modern researches use micromechanics in modeling the evolution of the fatigue damage from an initial undamaged state to a mesocrack initiation. An example is given in section 3.

2. SO MANY EFFECTS INVOLVED IN FATIGUE !

2.1. Effect of micro-defects in the material

Fatigue as nucleation and growth of micro-cracks is always localized at a very small scale where micro-defects such as inclusions or precipitates or grain boundaries play an important role. Their statistic distribution in size and location induces a large uncertainty in the fatigue initiation which cause a very large **discrepancy** in tests results. For the same history of stress on different specimens made similarly from the same material, the number of cycles to fracture may vary from a factor 10 : (results with a relative error of 1000 %!). This is the signification of the many points in figure 1. The consequence is that to speak of fatigue, obliges to speak of probabilities. An other consequence due to the presence of micro-defects is the **scale effect** : the probability to find a bigger defect in a large piece of metal is larger than in a small piece. The Weibull theory is a good model to take into consideration this scale effect [7].

2.2. Effect of the quality of surfaces

It is recognized by physicists that fatigue is related to plasticity by means of slip bands. As the slips occur more easily in surface crystals than inside, because they are not constrained in one direction by other crystals, the **fatigue meso-cracks always initiate in surface** if the stress field is uniform. Then, the quality of surfaces plays an important role, a rough surface may induce a number of cycles to fracture 10 times less than a smooth surface for the same history of stress. This is a reason to increase the strength to fatigue by a good polishing, by a superficial hardening of shot peening and to avoid corrosion as much as possible.

2.3. Effect of initial conditions

Most of the time in engineering, due to metal forming, machining, or assembly, the material of mechanical components is not in its “natural state”. Fields of strain hardening, damage and **residual stresses** may exist. They, of course, influence the fatigue strength. For example an **overstress** may increase the fatigue strength if it is not too large in comparison to the fatigue limit because it hardens the material, but it may decrease the fatigue strength for larger values because it damages the material ! Beside, a cyclic **understress** below the fatigue limit may increase this fatigue limit because cyclic microplasticity decreases the residual stresses.

2.4. Effect of stress intensity

The main causal variable of fatigue is the amplitude of stress $\Delta\sigma = \sigma_{MAX} - \sigma_{min}$ but in tension-compression the mean value of the loading $\bar{\sigma} = \frac{1}{2}(\sigma_{MAX} + \sigma_{min})$ plays also an important role. It is usually represented by the Goodman's diagram : the amplitude of stress giving a certain value of the number of cycles to fracture decreases as the mean value increases [8].

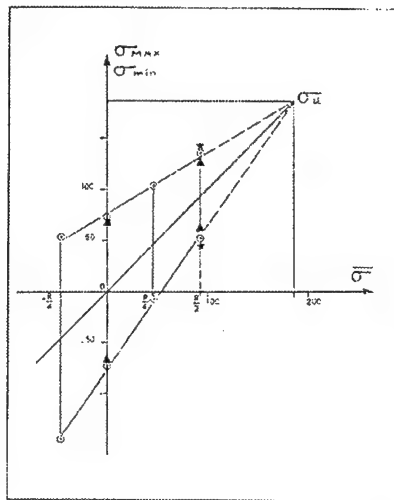


Fig. 2 : Goodman's diagram of a 35NCD 16 steel for 10^6 cycles (Doc. CETIM)

The intensity of the maximum stress induces :

- no plasticity at mesoscale for numbers of cycles to fracture $N_R > 10^5$; this is the range of **high cycle fatigue** generally related to stresses.

Plasticity at mesoscale for numbers of cycles to fracture $N_R < 10^4$; this is the range of **low cycle fatigue** generally related to the amplitude of plastic strain like the Law of Manson- Coffin [9], [10].

$$N_R = \left(\frac{\Delta \epsilon_p}{M} \right)^c$$

Where M and c are two material parameters

2.5. Effect of the history of loading

So far, we spoke about results obtained for periodic loading which is often not the case in practical applications. Due to the fact that the state of plasticity at time t depends upon the whole history of the loading for $\tau < t$, the accumulation of fatigue damage due to different sequences of loading depends upon the order of appearance of the sequences. This is called the **non linear accumulation** of damage. A sequence of large stress is more damageable at the beginning of a fatigue process than at the end. Nevertheless, due to the complexity in modeling this phenomenon, the linear accumulation rule of Palmgreen-Miner is often used

$$\sum \frac{n_i}{N_{Ri}} = 1$$

Where n_i is the number of cycles of a stress $\sigma_{i(t)}$

N_{Ri} is the number of cycles to fracture which would exist for the same stress $\sigma_{i(t)}$ periodic up to fracture.

When the loading is considered as **random** a difficulty arises to define what is a cycle and how to accumulate the damage due to "small" and "large" cycles of realizations of the stochastic process. The best solution is to forgive about cycles and to consider a damage function of time. To obtain statistics upon the probability to fracture, the only way to solve non linear differential equations modeling damage with random input is the Monte-Carlo method.

2.6. Effect of multiaxial state of stress

This is still an open problem due to the lack of tests results. There has been millions of tests in tension-compression, in rotating bending but only a few in tension-torsion or in biaxial tension because the machines did not exist up to about 1970, and even now, not so many are in operation. Furthermore fatigue tests take much time : 10^7 cycles at 5 Hertz takes 23 days ! An actual important problem is fatigue under **non proportional loading** when the principal directions of stress vary. It seems that, like in plasticity, there is a micro-cross-hardening which increases the fatigue strength. Considering multiaxial stress, the notion of cycle is also difficult to define which is an other reason to forgive it !

2.7. Effect of temperature

At room temperature, for almost all materials, the frequency of loading does not give any effect. This is not any more the case at elevated temperature when creep occurs in place of plasticity. There is an interaction, a **non linear interaction**, between the "pure" fatigue damage intragranular in metals and the "pure" creep damage intergranular during holding periods of constant stress for example.

2.8. Fatigue crack growth

When a mesocrack has initiated by fatigue (a size of $\cong 0.2$ to 1mm in metals) it may grow under the same variable loading, this is the field of application of **fracture mechanics**. The most common law for crack propagation is Paris law which gives the crack length a in plane stress condition as a function of the stress intensity factor amplitude ΔK [11].

$$\frac{da}{dN} = C \Delta K^\eta$$

$K = \sigma_\infty \sqrt{\pi a}$ for an “infinite sheet” loaded in mode I by a stress σ_∞ normal to the crack line
 C and η are material parameters.

3. CONSTITUTIVE EQUATIONS FOR FATIGUE DAMAGE

- The fatigue damage is localized at micro-scale much smaller than the mesoscale of the Representative Volume Element. Then, a geometrical model is a micro-inclusion embedded in a meso RVE (figure 3).
- The high cycle fatigue occurs with plasticity at micro scale but not at mesoscale. It is considered that the model has a fatigue limit σ_f for a Number of cycles reaching infinity. Then, the inclusion has the same elasto-plastic and damage properties than the RVE except it is weak by its yield limit taken as the fatigue limit σ_f (figure 3).

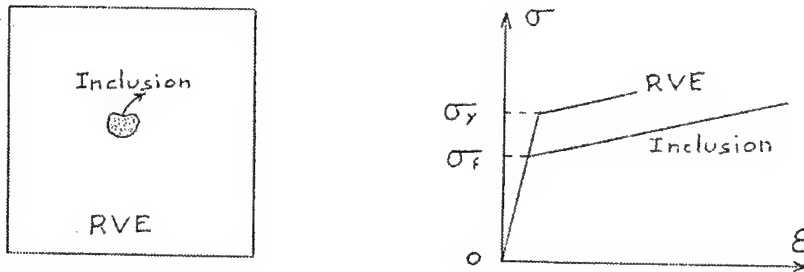


Fig. 3 : The two scale damage model [12]

- If the meso-stress in the RVE is below the yield stress σ_y this is the high cycle fatigue regime, if the meso-stress is larger than σ_y this is the low cycle fatigue regime. If the micro-stress in the inclusion is below its yield stress σ_f there is no fatigue.
- Knowing the stress at mesoscale σ_{ij} the stress in the inclusion σ_{ij}^μ is calculated by use of Kröner's law of localization.

$$\sigma_{ij}^\mu = \sigma_{ij} - aE(\varepsilon_{ij}^{\mu p} - \varepsilon_{ij}^p) \quad \text{with } a_{(v)} \equiv 0.4$$

Where E is the Young's modulus of elasticity

- The damage law activated in the inclusion is governed by the total elastic energy (shear + hydrostatic) somewhat similar to some fatigue criteria and by the plastic strain as observed. It has a strong thermodynamical support [13] :

$$D_{ij} = \left(\frac{\bar{Y}^\mu}{S} \right)^s \left| \dot{\varepsilon}^{\mu p} \right|_{ij} \quad \text{if } p^\mu > p_D$$

. D_{ij} is the Damage second rank tensor. The norm D of the Damage vector $D_{ij}n_j$ is the measure of the microcrack surface density in the plane of normal \vec{n} : $0 \leq D < 1$.

There is a mesocrack initiation when D reaches a critical value D_c , a material parameter.

. \bar{Y}^μ is the effective strain energy

. $|\dot{\epsilon}^{\mu p}|_{ij}$ are the absolute values of the principal values of the plastic strain rate

. p^μ is the accumulated plastic strain : $p^\mu = \left(\frac{3}{2} \dot{\epsilon}_{ij}^{\mu p} \dot{\epsilon}_{ij}^{\mu p} \right)^{1/2}$

p_D is the Damage threshold, a material parameter

. S and s are two material parameters.

- The complete set of constitutive equations to be solved as a post processor to find the condition of a crack initiation $D = D_c$ are :

Total strain $\epsilon_{ij}^\mu = \epsilon_{ij}^{\mu e} + \epsilon_{ij}^{\mu p}$

Elasticity $\epsilon_{ij}^{\mu e} = \frac{1+\nu}{E} \bar{\sigma}_{ij}^\mu - \frac{\nu}{E} \bar{\sigma}_{kk}^\mu \delta_{ij}$

Plasticity $\dot{\epsilon}_{ij}^{\mu p} = \frac{\partial f^\mu}{\partial \sigma_{ij}^\mu} \dot{\lambda}$, $f^\mu = (\bar{\sigma}_{ij}^\mu X_{ij}^\mu)_{eq} - \sigma_f$

Linear kinematic hardening $\dot{X}_{ij}^\mu = \frac{2}{3} C \dot{\epsilon}_{ij}^{\mu p}$

Damage $\dot{D}_{ij} = \left(\frac{\bar{Y}^\mu}{S} \right)^s |\dot{\epsilon}^{\mu p}|_{ij}$ if $p_\mu > p_D$

Localization $\sigma_{ij}^\mu = \sigma_{ij} - aE(\epsilon_{ij}^{\mu p} - \epsilon p_{ij}^p)$

. $\bar{\sigma}_{ij}^\mu$ is the effective stress : $\bar{\sigma}_{ij}^\mu = \sigma_{ij}^\mu / (1 - D)$ for isotropic damage

. The material parameters are

E and ν for elasticity

σ_f and C for plasticity

S, s, p_D, D_c for damage

The integration of these constitutive equations in one material point (RVE) where the stress σ_{ij} is known as a function of time is made by the classical elasto-plastic scheme of Newton-Raphson with elastic predictor and plastic corrector. It is an integration, step by step in time, for each cycle. A "jump in cycles" procedure save computer time in avoiding to calculate all the ($10^5, 10^6, 10^7$!) cycles. It is not as simple as a magic formula ! but this is the price to pay in order to model most of the properties mentioned in the section 2 :

- The statistical effect of microdefects may be taken into account by considering the fatigue limit, yield stress at microlevel, as a random variable but it needs an identification which can come from the discrepancy of a Woehler curve [14]. The scale effect is not obtained.
- The surface effect may be obtained by considering the inclusion at a boundary of the RVE, the only change is in the law of localization [15].

- Non trivial initial conditions may be introduced by initial values of the Damage D_o and of the plastic strain p_o . The effect of an overstress is obtained but not the effect of understressing.
- The effect of mean stress in tension is contained in the plastic properties of the model and considering a kinematic hardening gives no effect of mean stress in shear which is in accordance with experiments. High cycle fatigue is when the matrix is elastic and low cycle fatigue when it is elasto-plastic.
- The non linear accumulation is also a consequence of the irreversibility character of plasticity and damage. It is mainly due to the existence of a damage threshold.
- The model is formulated in three dimensions. It gives the effects of triaxiality and also the better strength in compression than in tension by introduction of an effective stress acting on principal values differently when they are positive or negative.
- The non linear creep-fatigue interaction is obtained by changing the plastic constitutive equation into visco-plasticity depending upon temperature [16].

Let us conclude that the main difficulty, like often in mechanics of materials, is in the identification of material parameters for each material and temperature considered.

4. REFERENCES

- [1] Wöhler A., Zeit für Bauwesen Vol 8, 10, 13, 16, 20. 1858-1870 Engineering (1871).
- [2] Cough H.G., *The fatigue of metals*. Benn, London (1926).
- [3] Caquot A., L'exploitation par l'ingénieur de la résistance de la matière, Bulletin de la Société des Ingénieurs Civils de France (Sept-Oct) (1933).
- [4] Cazaud R., Pomey G., Rabbe P., Janssen C., *La fatigue des métaux*. Dunod Paris (1969).
- [5] Bathias C., Miller K.J., Stauzl-Tschegg S., *Gigacycle fatigue*, Special Vol. 22 n°7 FFEMS (1999).
- [6] Dang Van K., Multiaxial fatigue criteria based on a multiscale approach. *Handbook of Materials Behaviors Models* (J. Lemaitre ed) Academic Press (2001).
- [7] Weibull W., A statistical theory of the strength of Materials Roy. Swed. Inst. Eng. Res. 151 (1939).
- [8] Goodman J., *Mechanics applied to Engineering* Longman's, Greens and Co, London (1914).
- [9] Manson S.S., *Mechanics Applied to Engineering* Longman's, Greens and Co, London (1954).
- [10] Coffin L.F., A study of the effect of cyclic thermal stresses in a ductile metal. Trans ASME 76, 931 (1954).
- [11] Paris P.C., Erdogan F., A critical analysis of crack propagation laws. J. Bas.Eng. Trans ASME 85- 528-534 (1963).
- [12] Lemaitre J., Sermage J.P., Desmorat R., A two scale damage concept applied to fatigue. Int. J. Fracture, 97 : 67-81 (1999).
- [13] Lemaitre J., Desmorat R., Sauzay M., Anisotropic damage law of evolution. Eur. J. Mech A/Solids 19 : 187-208 (2000).

-
- [14] Hild F., A probabilistic approach to fracture in high cycle fatigue. *Handbook of Materials Behaviors Models* (J. Lemaitre ed) Academic Press (2001).
 - [15] Sauzay M., Lemaitre J., Desmorat R., Une prise en compte de l'effet de surface en fatigue polycyclique. Proc. Congrès Français de Mécanique, Toulouse (1999).
 - [16] Sermage J.P., Lemaitre J., Desmorat R., Multiaxial creep-fatigue under anisothermal conditions *Fatigue Fract.Engng Mater Struct* 23. 241-252 (2000).

LARGE DEFLECTION ANALYSIS OF BEAMS WITH VARIABLE STIFFNESS. AN ANALOG EQUATION SOLUTION

J. T. Katsikadelis and G. C. Tsiatas

Department of Civil Engineering
National Technical University of Athens, GR-15773, Greece

1. SUMMARY

The Analog Equation Method (AEM) is employed to analyze the Bernoulli-Euler beam with variable stiffness undergoing large deflections. In this case the transverse deflections influence the axial force and the resulting governing differential equations are coupled and nonlinear with variable coefficients. The pertinent differential equations are derived by considering the equilibrium of the deformed beam element. The resulting boundary value problem is solved using the AEM. According to this method the two coupled nonlinear differential equations are replaced by two uncoupled linear ones pertaining to the axial and transverse deformation of a substitute beam with unit axial and bending stiffness, respectively, under fictitious load distributions. Beams with constant and varying stiffness are analyzed under various boundary conditions and loadings to illustrate the merits of the method as well as its applicability, efficiency and accuracy. Useful results are drawn concerning the simplified equation derived from the equilibrium in the deformed configuration.

2. INTRODUCTION

The load deflection response of beams undergoing large deformations involves the solving of coupled nonlinear differential equations, which become more complicated when the stiffness of the beam is variable. Closed form solutions cannot be obtained when general boundary conditions are considered unless these are simplified on the basis of certain mathematical adjustments. Therefore recourse to numerical solutions is inevitable. The FEM has been successfully employed to the solution of beam with constant cross-section. However, beams with non-uniform cross-section are often approximated by a large number of small uniform elements replacing the continuous variation with a step law. In this way it is always possible to obtain acceptable results and the error can be reduced as much as desired by refining the mesh. Nevertheless, the computational effort can become excessive and the nonlinear solution procedure may fail to converge.

In this paper, an accurate direct solution to the governing coupled nonlinear differential equations is presented, which permits the application of nonlinear boundary conditions. The solution procedure developed is based on the concept of the analog equation applied to nonlinear problems [1,2]. Several beams are analyzed under various boundary conditions and load distributions, which illustrate the method and demonstrate its efficiency and accuracy.

Moreover, the validity of certain simplifications, which are adopted in the literature to reduce the nonlinearity of the equations, is also investigated.

3. GOVERNING EQUATIONS

Consider an initially straight beam of length l having variable cross-section $A(x)$ and consisting of a linearly elastic material. The axis x coincides with the neutral axis of the beam, which is bent in its plane of symmetry xz by the combined action of the distributed load $p_x = p_x(x)$ and $p_z = p_z(x)$ in the axial and transverse directions as well as by the distributed moment $m = m(x)$. Moderate large deflections result from the nonlinear kinematic relation, which retains the square of the slope of the deflection, while the strain component remains still small compared with the unity. Namely,

$$\epsilon_x = u_{,x} + \frac{1}{2} w_{,x}^2 + z\kappa \quad (1)$$

where $u = u(x)$ and $w = w(x)$ are the axial and transverse displacement, respectively, and κ is the curvature of the deflected axis. The governing equations are derived by considering the equilibrium of the deformed element.

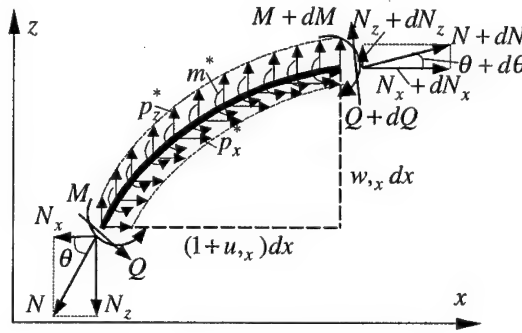


Fig. 1: Forces and moments acting on the deformed element

Thus, referring to Fig. 1 and taking into account that

$$p_x^* = p_x dx / ds, \quad p_z^* = p_z dx / ds, \quad m^* = m dx / ds, \quad ds = \sqrt{(1 + u_{,x})^2 + w_{,x}^2} dx \quad (2a,b,c,d)$$

we obtain the equilibrium equations as

$$N_{x,x} = -p_x, \quad N_{z,x} = -p_z, \quad M_{,x} = Q + m \quad (3a,b,c)$$

Moderate large deflections result by assuming $u_{,x}, w_{,x} \ll 1$, which implies

$$ds = dx, \quad \cos \theta = \frac{1 + u_{,x}}{\sqrt{(1 + u_{,x})^2 + w_{,x}^2}} \approx 1, \quad \sin \theta = \frac{w_{,x}}{\sqrt{(1 + u_{,x})^2 + w_{,x}^2}} \approx w_{,x} \approx \theta \quad (4a,b,c)$$

Moreover, the axial elongation ϵ and the curvature κ are given as

$$\epsilon = u_{,x} + \frac{1}{2} w_{,x}^2, \quad \kappa = \frac{d\theta}{ds} \approx \theta_{,x} \approx w_{,xx} \quad (5a,b)$$

Therefore, the stress resultants, that is the the axial force and the beding moment are given as

$$N = EA \left(u_{,x} + \frac{1}{2} w_{,x}^2 \right), \quad M = -EI w_{,xx} \quad (6a,b)$$

From Fig. 1, we have

$$N_x = N \cos \theta - Q \sin \theta \approx N - Q w_{,x}, \quad N_z = N \sin \theta + Q \cos \theta \approx N w_{,x} + Q \quad (7a,b)$$

Substituting eqns (7) into eqns (3a,b) and using eqn (3c) to eliminate Q yields

$$N_{,x} - (M_{,x} w_{,x})_{,x} + (m w_{,x})_{,x} = -p_x, \quad M_{,xx} + (N w_{,x})_{,x} = -p_z + m_{,x} \quad (8a,b)$$

The governing equations in terms of the displacements are obtained by introducing eqns (6) into eqns (8). Thus we have

$$\left[EA \left(u_{,x} + \frac{1}{2} w_{,x}^2 \right) \right]_{,x} + (EI w_{,xxx} w_{,x})_{,x} + (m w_{,x})_{,x} = -p_x \quad (9a)$$

$$(EI w_{,xx})_{,xx} - \left[EA \left(u_{,x} + \frac{1}{2} w_{,x}^2 \right) w_{,x} \right]_{,x} = p_z + m_{,x} \quad (9b)$$

The pertinent boundary conditions are

$$a_1 u(0) + a_2 N_x(0) = a_3 \quad \bar{a}_1 u(L) + \bar{a}_2 N_x(L) = \bar{a}_3 \quad (10a,b)$$

$$\beta_1 w(0) + \beta_2 N_z(0) = \beta_3 \quad \bar{\beta}_1 w(L) + \bar{\beta}_2 N_z(L) = \bar{\beta}_3 \quad (11a,b)$$

$$\gamma_1 w_{,x}(0) + \gamma_2 M(0) = \gamma_3 \quad \bar{\gamma}_1 w_{,x}(L) + \bar{\gamma}_2 M(L) = \bar{\gamma}_3 \quad (11c,d)$$

where $a_k, \bar{a}_k, \beta_k, \dots, \bar{\gamma}_k$ are specified constants. The above boundary conditions describe the most general boundary conditions including elastic supports.

Solution of the boundary value problem (9), (10) and (11) is not available in the literature due to the difficulty arising from the presence of the term $EI w_{,xxx} w_{,x} = Q w_{,x}$, which expresses the influence of the shear force Q on N_x . Existing solutions approaches circumvent this difficulty by neglecting this nonlinear term. This assumption yields $N_x \approx N$ and it is equivalent to deriving the equilibrium equations by referencing to the undeformed element. This is rather obvious in a beam column loaded only by axial forces. However, the validity of this assumption should be investigated in the presence of the transverse load p_z .

In this paper a direct solution of the coupled strongly nonlinear differential equations (9) subjected to the nonlinear boundary conditions (10)-(11) is developed. The solution procedure is based on the concept of the analog equation [2] as applied in the next section. This computational tool, besides its capability to solve accurately the problem at hand, enables the investigation of the influence of term $Q w_{,x}$ on N validating, thus, the assumption made by earlier investigators.

4. THE AEM SOLUTION

The AEM is applied to the problem at hand as follows. Let $u = u(x)$ and $w = w(x)$ be the sought solution of eqns (9), which are two and four times differentiable, respectively, in $[0, l]$. Noting that eqn (9a) is of the second order with respect to u and of fourth order with respect to w we obtain by differentiating

$$u_{,xx} = b_1(x), \quad w_{,xxxx} = b_2(x) \quad (12a,b)$$

Equations (12) indicate that the solution of eqns (9) can be established by solving eqns (12) under the boundary conditions (10)-(11), provided that the fictitious load distributions b_1, b_2 are first determined. This is achieved by writing the solution of eqns (12) as

$$u = c_1x + c_2 + \int_0^L G_1(x, \xi) b_1(\xi) d\xi \quad (13a)$$

$$w = c_3x^3 + c_4x^2 + c_5x + c_6 + \int_0^L G_2(x, \xi) b_2(\xi) d\xi \quad (13b)$$

where c_i ($i=1,2,\dots,6$) are coefficients to be determined from the boundary conditions and $G_i(x, \xi)$ ($i=1,2$) are the free space Green's functions of eqns (13) obtained as particular solutions of

$$G_{1,xx} = \delta(x - \xi), \quad G_{2,xxxx} = \delta(x - \xi) \quad (14a,b)$$

with $\delta(x - \xi)$ being the Dirac function. After integration of eqns (14) we obtain [3]

$$G_1 = \frac{1}{2}|x - \xi|, \quad G_2 = \frac{1}{12}|x - \xi|(x - \xi)^2 \quad (15a,b)$$

The derivatives of u and w are obtained by direct differentiation of eqns (14). Namely

$$u_{,x} = c_1 + \int_0^L G_{1,x}(x, \xi) b_1(\xi) d\xi, \quad u_{,xx} = b_1(x) \quad (16a,b)$$

$$w_{,x} = 3c_3x^2 + 2c_4x + c_5 + \int_0^L G_{2,x}(x, \xi) b_2(\xi) d\xi \quad (17a)$$

$$w_{,xx} = 6c_3x + 2c_4 + \int_0^L G_{2,xx}(x, \xi) b_2(\xi) d\xi \quad (17b)$$

$$w_{,xxx} = 6c_3 + \int_0^L G_{2,xxx}(x, \xi) b_2(\xi) d\xi, \quad w_{,xxxx} = b_2(x) \quad (17c,d)$$

Subsequently, the interval $[0, l]$ is divided into N equal constant elements, having length l/N , on which the N nodal points placed at the middle of the elements. Equations (16) and (17) are discretized and applied to the N nodal points. This yields

$$u = c_1x_1 + c_2 + G_1b_1, \quad u_{,x} = c_1 + G_{1,x}b_1, \quad u_{,xx} = b_1 \quad (18a,b,c)$$

$$w = c_3x_3 + c_4x_2 + c_5x_1 + c_6 + G_2b_2, \quad w_{,x} = 3c_3x_2 + 2c_4x_1 + c_5 + G_{2,x}b_2 \quad (19a,b)$$

$$w_{,xx} = 6c_3x_1 + 2c_4 + G_{2,xx}b_2, \quad w_{,xxx} = 6c_3 + G_{2,xxx}b_2, \quad w_{,xxxx} = b_2 \quad (19c,d,e)$$

where $G_1, G_{1,x}, \dots, G_{2,xxxx}$ are $N \times N$ known matrices, originating from the integration of the kernels $G_1(x, \xi), G_2(x, \xi)$ and their derivatives on the elements; $u, u_{,x}, \dots, w_{,xxxx}$ are vectors including the values of u, w and their derivatives at the nodal points; b_1, b_2 are also vectors containing the values of the fictitious loads at the nodal points and $x_1 = \{x_1, x_2, \dots, x_N\}^T$, $x_2 = \{x_1^2, x_2^2, \dots, x_N^2\}^T$, $x_3 = \{x_1^3, x_2^3, \dots, x_N^3\}^T$ are vectors containing the abscissas of the nodal points and their first and second powers. Finally, collocating eqns (9) at the N nodal points and substituting the derivatives from eqns (18) and (19) yields $2N$ nonlinear algebraic equations

$$F_1(b_1, b_2, c) = p_x, \quad F_2(b_1, b_2, c) = p_z \quad (20a,b)$$

in which $c = \{c_1, c_2, \dots, c_6\}^T$. After the substitution of the relevant derivatives in the boundary conditions, we obtain six additional equations

$$f_i(\mathbf{b}_1, \mathbf{b}_2, \mathbf{c}) = 0 \quad i = 1, 2, \dots, 6 \quad (21)$$

Eqns (20) and (21) constitute a set of $N + 6$ nonlinear algebraic equations which are solved numerically to yield $\mathbf{b}_1, \mathbf{b}_2$ and \mathbf{c} .

5. NUMERICAL EXAMPLES

On the base of the procedure described in previous section a FORTRAN program has been written and several beams have been analyzed. The nonlinear equations have been solved by minimization of the function

$$S(\mathbf{b}_1, \mathbf{b}_2, \mathbf{c}) = \sum_{i=1}^N \{ [F_1^i(\mathbf{b}_1, \mathbf{b}_2, \mathbf{c}) - p_x^i]^2 + [F_2^i(\mathbf{b}_1, \mathbf{b}_2, \mathbf{c}) - p_z^i]^2 \} + \sum_{j=1}^6 f_j(\mathbf{b}_1, \mathbf{b}_2, \mathbf{c})^2 \quad (22)$$

The numerical results for beams with rectangular cross-section $b \times h$ are presented using the non-dimensional quantities

$$\bar{u} = u/h, \quad \bar{w} = w/h, \quad \bar{\sigma} = \sigma l^2 / Eh^2, \quad \bar{p} = pl^4 / Eh^5 \quad (23)$$

in which l denotes the length of the beam and σ the bending or the axial stress.

A clamped-clamped beam with length $l = 1.0m$, subjected to a uniform load, has been analyzed ($N = 21$). The employed data are: $E = 2.1 \times 10^8 kN/m^2$, $b = 0.01m$, $h_0 = 0.03m$ and $p_x = 0$, $m = 0$. Two cases of thickness variation have been studied (i) $h = h_0(1/2 + x/l)$ and (ii) $h = h_0$. In both cases the volume V of the material has been kept unchanged, that is $V = bh_0l$. The results for $h = h_0$ have been obtained also by neglecting the nonlinear term $Qw_{,x}$ (undeformed)

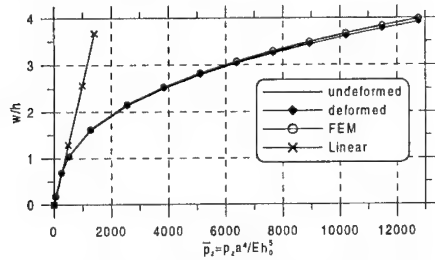


Fig. 2: Central deflection versus load

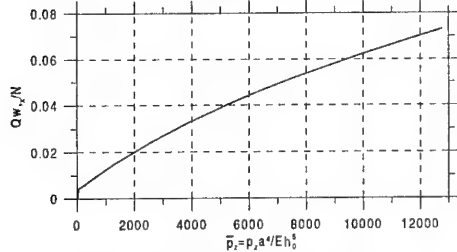


Fig. 4: $Qw_{,x} / N$ versus load

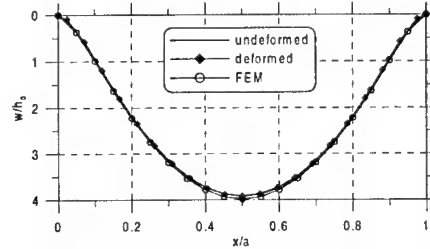


Fig. 3: Profile of the deflection for $\bar{p}_z = 12758$

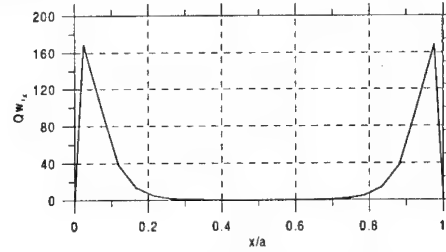


Fig. 5: Profile of $Qw_{,x}$ for $\bar{p}_z = 12758$

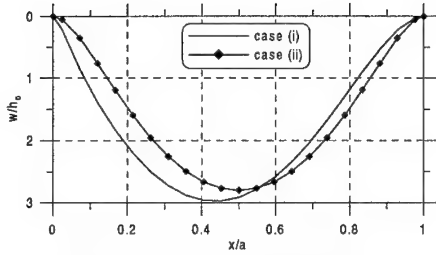


Fig. 6: Profile of the deflection

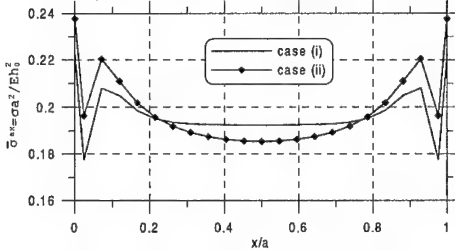


Fig. 8: Profile of the axial stresses

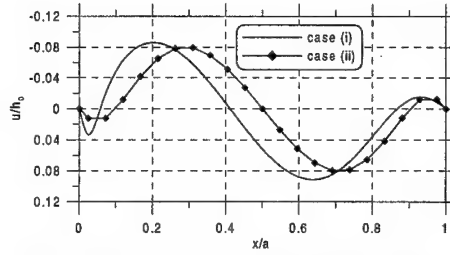


Fig. 7: Profile of the axial displacement

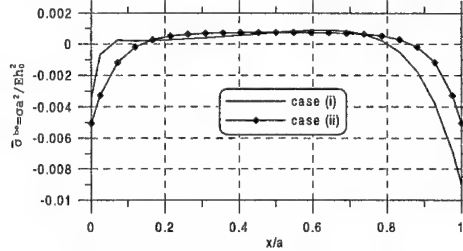


Fig. 9: Profile of the bending stresses

element) and are presented in Fig. 2 and Fig. 3 as compared with those obtained by the FEM using the NASTRAN code. From Fig. 4 and Fig. 5 an important conclusion is drawn concerning the dropping of the term $Qw_{,x}$. Namely, though the quantities Q and $w_{,x}$ are not individually negligible their product $Qw_{,x}$ is negligible as compared with N . The results for both cases of thickness variation, under the uniform load $\bar{p}_z = 5103$, are shown in Fig. 6 through Fig. 9.

6. REFERENCES

- [1] Katsikadelis, J. T., The analog equation method-A powerful BEM-based solution technique for solving linear and nonlinear engineering problems. in *Boundary Elements XVI, CLM Publications, Southampton* (1994) 167-182.
- [2] Katsikadelis, J. T. and Nerantzaki, M. S. The boundary element method for nonlinear problems. *Engineering Analysis with Boundary Elements* 23, 365-373 (1999).
- [3] Banerjee, P. K. and Butterfield R., *Boundary Element Methods in Engineering Science*, Mc Graw-Hill, London (1981).

CRUSHING OF SHIP'S BOW STRUCTURE DURING COLLISION WITH BRIDGE PIERS

Nikola Hajdin

Serbian Academy of Sciences and Arts, 11000 Belgrade, Yugoslavia

Rastislav Mandic

Faculty of Civil Engineering

University of Belgrade, 11000 Belgrade, Yugoslavia

1. SUMMARY

In this paper a model for predicting crushing properties of a ship's structure during collision with bridge piers is presented. The model is mainly oriented for the analysis of vessels on inland waterways. The theoretical predictions are compared with the results of experimental investigation performed in Germany. At the final part of the paper an influence of some parameters on impact forces during ship collision with bridge piers is investigated.

2. INTRODUCTION

Vessel collisions with bridges represent great threat to public safety. An excellent review of various phenomena related to ship impact in bridge piers is given in reference [2]. However, most of these investigations are devoted to sea going ships. Considerably different vessel sizes and structures make these results not applicable for the collision problems on rivers and canals. The crushing properties of ships structure represent the principle factor influencing impact actions during collision. In this paper a method that the authors used for the predicting of crushing force - deformation (indentation) response of a river ship during head-on-bow impact is explained.

3. MECHANICAL MODEL

The analytical model we developed is based on the Darmstadt experimental investigations of a typical Rhine river ship [1]. The results of the research of 1 : 6.5 size model show that the crushing force on the contact between bridge pier and a ship's bow is dominated by properties of deck and bottom structures. In order to model the process of folding observed in [1], deck and bottom structures are discretized in to the finite number of folding sections (Fig. 1) Each folding section k is modelled with two transverse elements (I and II) and a compressed longitudinal element ($a-b-c$) which buckles elasto-plastically out of deck's (bottom's) plane. The reaction of each folding section due to controlled deformation (defined by a single parameter u_F) has the following characteristic components:

$$R_F^{(k)} = R_{SI}^{(k)} + R_{SII}^{(k)} + R_w^{(k)} \quad (1)$$

The first and the second component in Eqn.(1) denote reaction forces from transverse elements *I* and *II* respectively. The last component is from the longitudinal element.

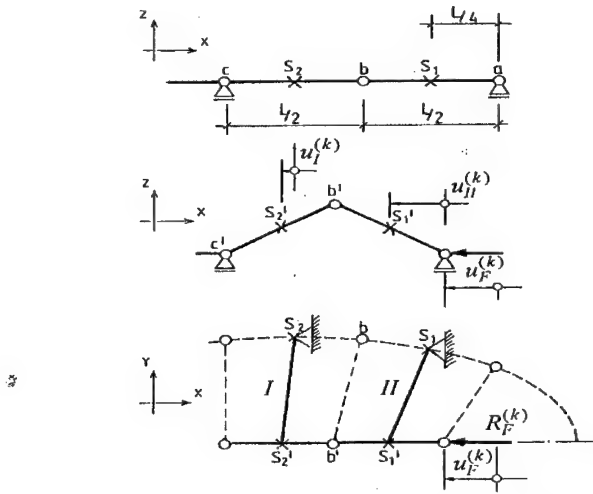


Figure 1. Model of a ship's structure

The longitudinal element is modelled with two bars having infinitely large flexural stiffness. The total flexural deformation is modelled by using a rotational spring lumped in the middle of the element (node *b*). In elastic regime rotational stiffness coefficient c_{rot} is calculated according to:

$$c_{rot} = \frac{\pi^2 EI}{4L} \quad (2)$$

It is assumed that only moderate rotations of bars take place. i.e: $\cos\psi \approx 1 - \psi^2$. The relationship between element force R_w and element deformation u_F may be expressed in the form:

$$u_F = \frac{R_w L}{EA} + \frac{2}{L} (\eta w_0)^2 \quad \eta = \frac{1}{1 - \frac{R_w}{R_{cr}}} \quad (3)$$

where R_{cr} denotes Euler's buckling load. In Eqn. 3 w_0 denotes initial imperfection (displacement along *z* axis). In order to study a plastic response of the element the following yield condition is utilized in the middle of the each element:

$$\frac{M}{M_p} + \frac{N}{N_p} = 1 \quad (4)$$

where N_p and M_p are the axial plastic force and the full plastic bending moment respectively, while $N = R_w$ and $M = R_w w$. The deformation - force relationship in the post-critical (softening) regime is given with:

$$u_F = \frac{2}{L} \left(\frac{M_p}{N_p} \right)^2 \left(\frac{N_p}{R_w} - 1 \right)^2 \quad (5)$$

The schematic view of a transverse element may be seen from the figure 2. It is important to realize that in order to obtain an upper bound of restititional force, displacements of supports due to deformation of ships structure are neglected.

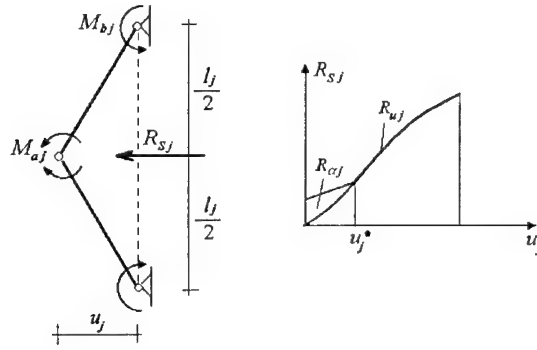


Figure 2. Transverse element and its response

At early stages of deformation transverse elements are mainly subjected to bending. However, during further deformation process of deformation transverse elements behave like ties. This implies that the total reaction of a transverse element due to deformation can be evaluated according to:

$$R_{sj} = R_{\alpha j} + R_{uj} \quad (6)$$

The first component in the Eqn. (6) results from bending of transverse elements in plastic regime. It is calculated from:

$$R_{\alpha j} = \frac{4}{l_j} (M_{aj} + M_{bj}) \quad (7)$$

In the above relation we have:

$$u_j = 0 \quad M_{aj} = M_{aj}^* \quad \text{and} \quad u_j \geq u_j^* \quad M_{aj} = 0 \quad (8)$$

where M_{aj}^* denotes full plastic moment in the case of pure bending. The deformation u_j^* relates to the deformation associated with total plastic axial force. A linear variation of $R_{\alpha j}$ between the values u_j and u_j^* is assumed in order to estimate interaction between bending moments and axial forces. The same expression is used at beam ends.

The component R_{uj} results from axial stressing. It is evaluated from the element relative stretch (dilatation):

$$\epsilon_j = \frac{l_j^* - l_j}{l_j} = \sqrt{1 + \frac{4u_j^2}{l_j^2}} - 1 \quad (9)$$

and appropriate stress-strain constitutive law. In our study steel yield stress 400MPa, hardening modulus 0.5GPa and rupture strain 20% are used. A characteristic form of force-deformation function for transverse element is given in the figure 2.

Step by step procedure is used to evaluate the total response. Note that for active folding section (denoted with k) the increments of deformation which define the response of transverse elements calculated from rigid body kinematics have the following form:

$$\begin{aligned}\Delta u_I^{(k)} &= 0.25 \Delta u_F^{(k)} \\ \Delta u_{II}^{(k)} &= 0.75 \Delta u_F^{(k)}\end{aligned}\quad (10)$$

In the case when condition $L=L_{min}$ (maximum possible folding of a longitudinal element) is satisfied the next folding section $k+1$ becomes active. The angle between longitudinal bars of the element k does not change during the further process of deformation, so we have:

$$\Delta u_j^{(k)} = u_F^{(k)} \quad j = I, II \quad (11)$$

The force-indentation relationships for deck and bottom structures are obtained by the summation over all active sections.

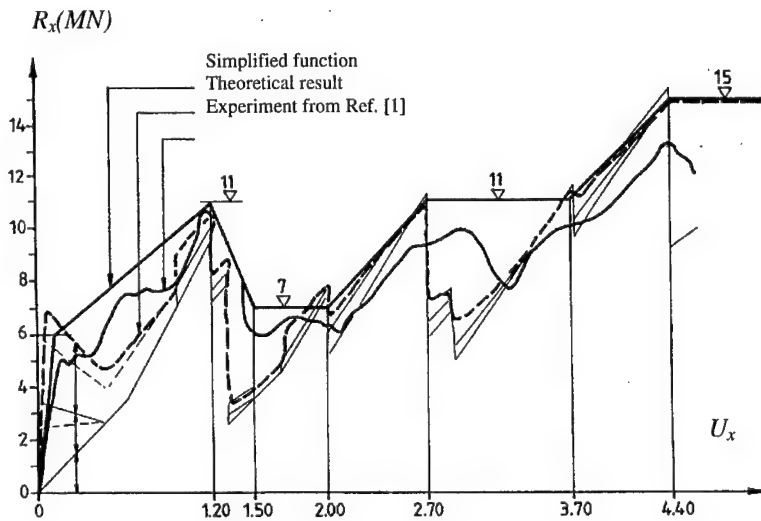


Figure 3. Crushing force - indentation function

The total crushing force is obtained according to:

$$R_x = R_x^D + R_x^B \quad (12)$$

where superscripts B and D refer to bottom and deck respectively. In Fig. 3. total force-deformation function for BS6 class Rhine river ship is compared with the results of experimental investigations from reference [1]. The simplified force-deformation function (published for the first time in [3]) which is used in dynamic analysis is also presented.

4. IMPACT FORCE - TIME FUNCTIONS

In most cases deformation of a pier during a collision is relatively small in comparison to deformation of a vessel and impact actions may be evaluated by treating impacted structures as infinitely stiff. The impact force-time functions presented in figure 4. are obtained by using this assumption and the simplified force deformation relationship from figure 3. The ship mass and impact velocities are varied as the parameters. However, note that in the cases of piers with considerable flexibility, coupled problem of ship-bridge interaction during collision have to be treated.

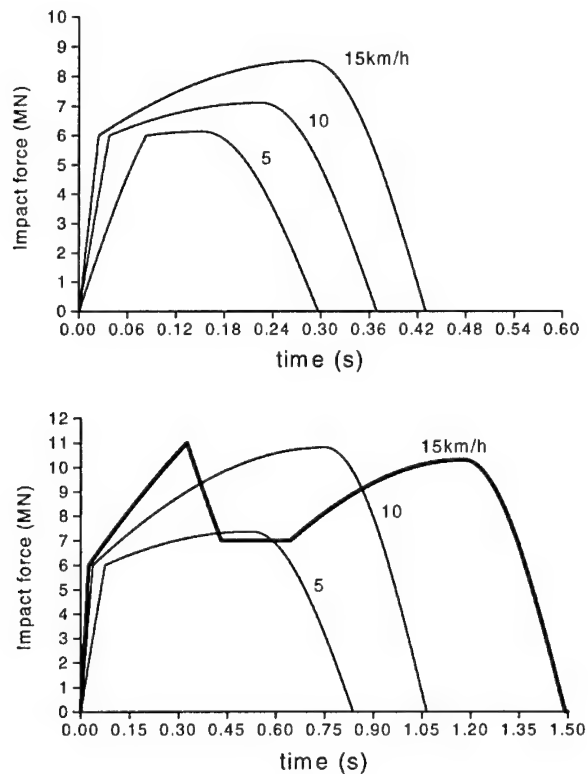


Figure 4. Impact force-time functions for a ship with total mass of 500t (above) and 2400t (below) for impact velocities 5, 10 and 15km/h

5. FINAL REMARKS

In the case of head-on-bow vessel impact on bridge piers crushing properties of ship's structures have dominant influence on impact actions. However, in the case of sideways (skew) impact, dynamics of a vessel during the impact is more complicated. Due to rotation and lateral motion of a vessel the influence of surrounding water becomes important. It is particularly characteristic in shallow waters. In [4,5] this problem is solved by introducing added (hydrodynamic) mass in the analysis and the problem of skew impact is presented in details.

6. REFERENCES

- [1] Maier-Dörnberg K. E. *Theoretische und experimentelle Untersuchungen zum Schiffsstoß vom Motorgüterschiffen (Spitzbug) auf Bauwerke*, 2 Teilbericht, TH Darmstadt, Dezember 1988.
- [2] Saul, R., Svenson, H., *On the theory of ship collision against bridge piers*, IABSE proceedings P-51/82:
- [3] *Empfehlung für durch Schiffsanprall gefährdeten Bauwerken*, Kanton Basel Stadt, Baudepartment, Dezember 1992.
- [4] Hajdin, N. Mandic, R., Ship collision with bridges - a contribution to the standardization of vessel impact forces for bridges on the Danube, Proceedings of the Second International Conference "Bridges over the Danube", Bucharest (1995) 113-119
- [5] Hajdin, N., Mandic, R. Ship collision with civil engineering structures, Bulletin de l'Academie Serbe des Sciences et des Artes (to appear)
- [6] Yang, P. D. C., Caldwell, J. B., Collision Energy absorption of ship's bow structures, International Journal of Impact Engineering 7, (1988) 181-196.

BEM SOLUTION OF VISCOPLASTIC PROBLEMS IN METALLIC STRUCTURES IN THE PRESENCE OF TEMPERATURE GRADIENTS

C. P. Providakis and S. Kourtakis

Department of Applied Sciences
Technical University of Crete, GR-73100 Chania, Greece

1. SUMMARY

A boundary element formulation for the solution of the time-dependent inelastic problems arising in creeping metallic plates at high temperatures is presented in this paper. The formulation allows the use of theories of inelastic deformation using state variables for characterizing the time-dependent behaviour of metals and alloys under thermal loading conditions. The deformation of the plate is simulated using a viscoplastic model developed by Hart to describe the material behaviour. The accuracy and efficiency of the proposed method is demonstrated by obtaining stress and strain distribution for certain selected sample problems of thick walled cylinders under radial temperature gradients. Simulation portrayed by the present formulation is further compared with other numerical and analytical solutions obtained for different thermal stressing rates.

2. INTRODUCTION

Remarkable progress has been made in the technological applications of metal and alloys at elevated temperatures and a great amount of research has been prompted in the area of their high temperature inelastic behaviour. This high temperature inelastic behaviour of metals is well known that is a time dependent and highly nonlinear phenomenon. Classical creep theories[1, 2] are incapable of explaining phenomena that are exhibited by metals and alloys at elevated temperatures, such as history-dependence, time-dependent strain recovery, softening upon unloading, and creep-plasticity interactions. These theories are therefore inadequate for accurate high-temperature design applications[3-5].

A new generation of constitutive models has been proposed during the past decade to overcome the shortcomings of the models defined previously[6-11]. The new mathematical feature of these theories is that the nonelastic strain rates are expressed as functions of the current values of stress, temperature and certain well defined state variables. Hart's is one of several state variable constitutive theory models of inelastic deformations that have been proposed recently. Hart's model[6, 7] has been extensively tested for uniaxial time varying loading on various metals and alloys and the correlation between theory and experiment has generally been found to be very good and shown to faithfully represent experimentally observed material behaviour in a variety of applications.

Mukherjee and his co-workers presented a boundary element method (BEM) formulation for the solution of boundary value problems with material behaviour governed by the Hart's constitutive model. They used a rate formulation of the governing differential equation of the problem. The spatial integration of the relevant was then carried out by using the finite element or boundary element method [12-16]. The applications of these works were limited to two-dimensional isothermal inelastic deformation problems. In Morjaria and Mukherjee[17] was presented a finite element (FEM) solution of inelastic boundary value problems in the presence of transient thermal stresses with material behaviour governed by the state variable constitutive model due to Hart. In this analysis, the temperature field was obtained by solving the unsteady diffusion equation subjected to a prescribed temperature or heat flux boundary conditions.

In Providakis[18-19] and Morjaria et al [16] demonstrated that the BEM is a very powerful method with several potential advantages over the FEM for solving nonlinear time-dependent inelastic deformation problems. One of the main advantages is that the number of unknowns in the final algebraic system of equations is proportional to the number of boundary elements in BEM as opposed to the total number of nodes in FEM. However, one of the most difficult problem in BEM-related problems was the numerical simulation of domain-based effects (e.g. inertial and interior loading effects, nonelastic and thermal strain effects). This is caused by the existence of domain integrals in the formulation which can only seldom be directly transferred into boundary integrals forms. In high temperature and time-dependent creeping problems, domain integrals arise due to thermal and inelastic term effects. Several approaches have been developed to deal with domain integrals, including internal cells and dual reciprocity methods. From the users point of view dual reciprocity method, are attractive since they do not require an internal mesh. Several successful applications based on the dual reciprocity boundary element method (DRBEM) exist for thermoelastic and heat transfer problems. Nevertheless, computations on general time dependent, high temperature, inelastic deformation problems is still far more successful with the use of internal discretization. Even though discretization of the domain must be carried out in this kind of nonlinear problems, this is necessary only for the evaluation of certain integrals with known integrands.

The present paper presents a direct formulation of the boundary element method for the solution of time-dependent nonlinear inelastic deformations of metallic structural components including both plasticity and creep and subjected to arbitrary thermal loading histories at high temperatures. A rate formulation of the governing differential equations has been used by combining the Hart's constitutive state variable model. The boundary element method generates the time rates of change of displacements and stresses at any time step. The time histories of the quantities of interest are then obtained by using a march forward time integration scheme with automatic time-step control. The boundary element formulation uses a spatially linear description of the relevant variables over each boundary element and is capable of solving any planar problem. Numerical examples are presented here for plane strain deformation problems for cylinders subjected to radial temperature gradient loads.

3. BOUNDARY ELEMENT FORMULATION

The Navier equation for the displacement rates for plane stress, in the presence of non-elastic strain are

$$\dot{u}_{i,kk} + \frac{1+\nu}{1-\nu} \dot{u}_{k,ki} = -\frac{\dot{F}_i}{G} + 2\dot{\epsilon}_{ij,j}^n + \frac{2\nu}{1-\nu} \dot{\epsilon}_{kk,i}^n + \frac{2(1+\nu)}{1-\nu} (\alpha \dot{T})_{,i} \quad (1)$$

where F_i is the prescribed body force per unit volume G , ν and α are the shear modulus, Poisson's ratio and coefficient of linear thermal expansion, respectively, u_i is the displacement vector. Suitable traction and displacement rate boundary conditions must be prescribed. For the plane strain case ($\epsilon_{zz}=0$) the integral representation of the solution of a point P on the boundary of the body (with $\dot{F}_i = 0$) has the form

$$\begin{aligned} (\delta_{ij} - C_{ij}) \dot{u}_i(P) = & \int_{\Gamma} [U_{ij}(P, Q) \dot{t}_j(Q) - T_{ij}(P, Q) \dot{u}_j(Q)] d\Gamma_Q + \\ & + \int_{\Omega} [X_{jki}(P, Q) \dot{\epsilon}_{jk}^n(q) + \hat{X}_{jki} \delta_{jk} \alpha \dot{T}(Q)] d\Omega_q \end{aligned} \quad (2)$$

where δ_{ij} is the Kronecker delta, P, Q are boundary points, q is interior point, Γ and Ω are the boundary and the surface of the body, respectively. The kernels U_{ij}, T_{ij} , X_{jki} and \hat{X}_{jki} are known singular solutions due to a point load in an infinite elastic solid in plane strain[20]. The traction and displacement rates are denoted by \dot{t} and \dot{u} , respectively. The coefficients of C_{ij} are known functions of the included angle at the boundary corner at P , the angle between the bisector of the corner angle and the x -axis. Equation (2) is a system of integral equations for the unknown traction and displacements rates in terms of their prescribed values on the boundary, and the non-elastic strain rates. The unknown quantities only appear on the boundary of the body and the volume integral are known at any time through the constitutive equations.

The stress rates can be obtained by direct differentiation of equation (2) resulting in

$$\begin{aligned} \sigma_{ij}(p) = & \int_{\Gamma} [\bar{U}_{ijk}(p, Q) \dot{t}_k(Q) - \bar{T}_{ijk}(p, Q) \dot{u}_k(Q)] d\Gamma_Q - \\ & - 2G \dot{\epsilon}_{ij}^n(p) - 3K \alpha \dot{T}(p) \delta_{ij} + \int_{\Omega} [\bar{X}_{ijkl}(p, q) \dot{\epsilon}_{kl}^n(q) + \bar{\hat{X}}_{ijkl}(p, q) \delta_{kl} \alpha \dot{T}(q)] d\Omega_q \end{aligned} \quad (3)$$

where G and K are the shear and bulk modulus, respectively, and \bar{X}_{ijkl} and $\bar{\hat{X}}_{ijkl}$ are inelastic and temperature effect kernel functions which are defined in Ref. 20.

For the purposes of this paper the temperature on the surface of the body is assumed to change slowly in time and thermal steady state conditions are assumed to exist throughout the surface of the body at each time step. Thus, the temperature field is assumed to be given by the solution of the appropriate steady state diffusion equation subject to slowly varying surface temperatures.

After applying a boundary nodal point collocation procedure to equation (2) one can obtain for any point ξ on the boundary the following system of equations in matrix form

$$[A]\{\dot{u}\} = [B]\{\dot{t}\} + \{\dot{b}\} + \{\dot{b}^T\} \quad (4)$$

where the coefficients of matrices $[A]$ and $[B]$ contain integrals of the type

$$\int_{\Delta S_N} T_{ij}^*(P_M, Q) dS_q, \int_{\Delta S_N} U_{ij}^*(P_M, Q) dS_q \quad (5)$$

and the vectors $\{\dot{b}\}$ and $\{\dot{b}^T\}$ involves X_{jki}^* and \hat{X}_{jki}^* integrals terms for the nonelastic strain and temperature rates. However, the vector $\{\dot{b}\}$ is known at any time through the constitutive equations of Hart's viscoplastic model [6-8] while the vector $\{\dot{b}^T\}$ through the assumed solution of the appropriate steady state diffusion equation subject to slowly varying surface temperatures and half of the total number of components of $\{\dot{u}\}$ and $\{\dot{\tau}\}$ are prescribed through the boundary condition. The other half are unknowns.

The initial distribution of the state variables have to be prescribed while the initial value of the nonelastic strain is set to zero. Thus, the only existed strains at time step $t=0$ are elastic and thermal and the initial stresses and displacements can be obtained from the solution of the corresponding thermoelastic problem. Thus, the initial rates of all the relevant variables are now known and their values at a new time Δt can be obtained by integrating forward in time. The rates are then obtained at time Δt and so on, and finally the time histories of all the variables can be computed.

4. NUMERICAL RESULTS

A computer program has been written to automate the solution procedure described in the last section of this paper. It is capable of solving a variety of planar bodies subjected to high temperature loading. Numerical results are presented here for a long thick-walled cylinder of internal and external radii a and b under plain strain deformation conditions and subjected to internal and external thermal loading increasing at a constant rate. The temperature rate field at a point with a distance r from the centre of the cylinder is assumed to be given by the equation

$$\dot{T} = \frac{1}{\ln(b/a)} (\dot{T}_b \ln(r/a) + \dot{T}_a \ln(b/r)) \quad (6)$$

which actually is the solution of steady state diffusion equation subject to slowly varying internal and external surface temperatures $T_a(t)$ and $T_b(t)$, respectively. The material of the plate is the 304 stainless steel at 400 °C. Symmetry of the spatial cylindrical geometry was taken into account and thus only one quarter of the cylinder was discretized. The thermal loading at the internal and external surfaces has a magnitude of $T_a(t=0)$ and $T_b(t=0)$, respectively at zero time step and increases at some constant temperature rate.

The numerical example analysed here is a uniform long thick-walled cylinder of radius ratio 1.5 in plane strain. The initial temperature throughout the cylinder is 100 °C. The inside curved surface of the cylinder is heated at a constant temperature rate $\dot{T}_a(t=0) = 6 \text{ } ^\circ\text{C/hr}$ while the outside surface is kept at a fixed temperature of 100 °C.

Figure 1 depicts the redistribution of thermoviscoplastic circumferential stress along the radial dimension as obtained by the present method and the analytical solution presented in Kumar and Mukherjee[21] for the circumferential stress distribution. Good agreement

between the present boundary element results and the analytical ones confirms correct boundary element implementation for this kind of problems. In addition to the above remark one can see from the stress profiles as shown in Figure 1 that both of the viscoplastic solutions are qualitatively the same with those obtained in classical plasticity theory and show two yield fronts, the first starting at the inside and the second at the outside of the cylinder.

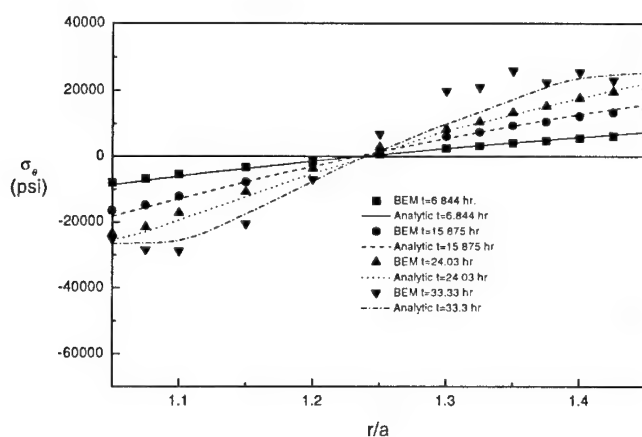


Figure 1: Redistribution of circumferential stress along the radial dimension of the thick walled cylinder in plane strain.

5. CONCLUSIONS

In this paper we have presented a direct formulation of the boundary element method for the analysis of creeping metallic structures subjected to pure thermal loading with time dependent temperature gradient. An analytical solution of the problem is also presented in order to validate the results of the present boundary element method. The details for the integration and solution strategies to solve the initial-boundary value problems have been provided.

On the basis of the good agreement between the analytical and boundary element results the proposed BEM is proved to be a powerful tool for the solution of these complicated non-linear problems of practical importance. The BEM program is quite general and can solve very common problems as in heat-exchanger metallic tubes and pressure vessels.

Several such analyses involving complex geometries and extended to severe loadings which combine the pure thermal loading present case with time dependent mechanical loading are underway.

Acknowledgements: The authors is grateful to Professors D.E Beskos for encouragement and helpful discussions during the course of this work.

6. REFERENCES

- [1] Rabotnov, Y.N., Creep Problems in Structural Members, North-Holland, Amsterdam, 1969.
- [2] Penny, R. K. and Marriott, D.L., Design for Creep, McGraw-Hill, London, 1971.
- [3] Krempl, E., The interaction of rate and history dependent effects and its significance for slow cyclic inelastic analysis at elevated temperatures, Nuclear Engineering and Design, 29(1), 125-134, 1974.
- [4] Krempl, E., Cyclic-creep – an interpretive literature survey, Welding Res. Coun. Bull., 195, 63-123, 1974.
- [5] Onat, E.T. and Fardshisheh, F., Representation of creep of metals, Oak Ridge Natl Lab. Rep. 4783, 1972.
- [6] Hart, E.W., A Phenomenological theory for plastic deformation of polycrystalline metals, Acta Metallurgica, 18(6), 599-610, 1970.
- [7] Hart, E.W., Li, C.Y., Yamada, H. and Wire, G.L., Phenomenological theory: A guide to constitutive relations and fundamental deformation properties in Constitutive Equations in Plasticity, A.S. Argon, (Ed.), MIT Press, Cambridge Mass., 149-197, 1976.
- [8] Hart, E.W., Constitutive relations for the nonelastic deformation of metals, Journal of Engineering Materials and Technology Trans. ASME, Series H, 98(3), 193-202, 1976.
- [9] Miller, A., An inelastic constitutive model for monotonic, cyclic and creep deformation: Part I – Equations development and analytical procedures, Journal of engineering materials and Technology Trans. ASME, Series H, 98(2), 97-105, 1976.
- [10] Miller, A., An inelastic constitutive model for monotonic, cyclic and creep deformation: Part II– Application to type 304 Stainless Steel, Journal of Engineering Materials and Technology Trans. ASME, Series H, 98(2), 106-113, 1976.
- [11] Lagneborg, R., A modified recovery-creep model and its evaluation, Metal Science Journal, 6, 127-133, 1972.
- [12] Kumar, V. and Mukherjee, S., A boundary integral equation formulation for time-dependent inelastic deformation in metals, Int. J. Mech. Sc., 19, 713-724, 1977.
- [13] Mukherjee, S. and Kumar, V., Numerical analysis of time-dependent inelastic deformation in metallic media using the boundary integral equation method, ASME J. Appl. Mech., 45, 785-790, 1978.
- [14] Morjaria, M. and Mukherjee, S., Improved boundary integral equation method for time dependent inelastic deformation in metals, Int. J. Num. Meth. Engng., 15, 97-111, 1980.
- [15] Morjaria, M., Sarihan, V. and Mukherjee, S., Comparison of boundary element and finite element methods in two-dimensional inelastic analysis, Res Mechanica, 1, 3-20, 1980.
- [16] Kumar, V., Morjaria, M. and Mukherjee, S., Numerical integration of some stiff constitutive models of inelastic deformation, ASME J. Engng. Mat. Tech., 102, 92-96, 1980.
- [17] Morjaria, M. and Mukherjee, S., Finite element analysis of time-dependent inelastic deformation in the presence of thermal stresses, Int. J. Num. Meth. Engng., 17, 909-921, 1981.
- [18] Providakis, C.P., Creep analysis of V-notched metallic plates: boundary element method, Theor. Appl. Fract. Mech., 32(1), 1-7, 1999.
- [19] Providakis, C.P., Boundary element analysis of creeping V-notched metallic plates in bending, Engng. Fract. Mech., 64(2), 129-140, 1999.

- [20] Mukherjee, S., Corrected boundary integral equations in planar thermoelastoplasticity, *Int. J. Solids Structures*, 13, 331-335, 1977.
- [21] Kumar, V. and Mukherjee, S., Creep analysis of metallic structures in the presence of thermal gradients using newer constitutive relations, *J. Pres. Vessel Tech. Trans. ASME*, 272-280, 1977.

ROCK DISCONTINUITIES IN TUNNEL DESIGN: NUMERICAL SIMULATION OF THE EFFECTS OF FILLED AND OPEN JOINTS

C. Stiakakis, Z. Agioutantis and G. Paschalis
Department of Mineral Resources Engineering
Technical University of Crete

1. SUMMARY

A set of parallel rock discontinuities intersecting a circular opening in elastic and homogeneous material at 45 degrees is modeled in 2D space using the finite element method. Two cases are discussed; in the first case discontinuities are modeled as very thin material layers with elastoplastic behavior (i.e. infill material), while in the second case the discontinuities are modeled as open joints (no infill material), by using contact elements, i.e. elements that allow for shearing when in compression, but which exhibit negligible tensile strength when in tension. Results are compared and critically evaluated.

2. INTRODUCTION

Rock masses in nature contain numerous discontinuities in the form of cracks, joints, faults, bedding, etc. These discontinuities play a dominant role in the behavior of the rock masses and the structures that are constructed in them [1]. To assess the stability of these structures is a very complex task since the overall properties of the rock mass and the discontinuities must be known and modeled correctly. In order to select the modeling method for a jointed rock mass containing a structure, the difference in scale between the joint size and that of structure to be analyzed should be evaluated, as well as whether an implicit continuum solution or an explicit description of the discontinuum is appropriate [2].

When the implicit method is utilized, the discontinuous rock mass is considered as an equivalent continuum medium and appropriate constitutive relationships are applied. Then the model can be solved as an anisotropic or multilaminated material utilizing all available techniques to describe these states. When the explicit method is implemented, the behavior of the jointed rock mass is directly addressed. The mathematical model that describes the material incorporates procedures and elements to address the discontinuous nature of the rock. The numerical simulation of the explicit method may include contact elements, joint stiffness elements, constraint elements, distinct elements, etc. [2]

3. MODEL FORMULATION

In this study, both implicit and explicit modeling methods for discontinuous rock masses are applied for assessing the stability of a circular opening in a discontinuous medium. The models were created and solved using the MARC-MENTAT suite of programs for linear and non-linear finite element analysis of structures [3]. The only assumption that is introduced for the implicit method is that the differences between the intact rock and the joints are reflected by the material properties. Thus, the rock mass is modeled as an anisotropic continuous material. In the case of the explicit method, a discrete finite element analysis is applied using contact-friction elements to specify the discontinuities in the intact rock.

For the first case, two constitutive material models are used. The first is the perfectly elastic material that can be described using Young's modulus (E), and Poisson's ratio (ν). The second is the elastic-perfectly plastic model, where, if the stress is below the yield stress of the material, it behaves elastically and stress is proportional to strain. After the stress becomes greater than the yield stress, the material no longer exhibits elastic behavior and the stress-strain relationship becomes nonlinear [3]. The yield stress is the point that separates the elastic from the plastic behavior. Due to the fact that the material that describes the discontinuities is subjected to a multiaxial state of stress, yield conditions are defined instead of a yield point. Although, there can be many forms of yield conditions, in this analysis the generalized linear Mohr-Coulomb failure criterion is utilized. This criterion describes elastic-plastic behavior, based on a yield surface that exhibits hydrostatic stress dependence. Such behavior is observed in a wide class of soils and rock-like materials [3].

In the second case, contact-friction elements are used to model the discontinuities of the rock mass. The analysis of contact behavior is complex because of the requirement to accurately track the motion of multiple geometric bodies as well as the motion due to the interaction of these bodies after contact occurs. The numerical objective is to detect the motion of the bodies, apply a constraint to avoid penetration and apply appropriate boundary conditions to simulate the frictional behavior [3]. A discrete finite element analysis incorporates the ability to solve contact problems [1], while at the same time includes large deformation effects and repeated contact and separation between the bodies at the interface. The basic conditions of contact along the interface of the bodies are that penetration cannot occur, and, as a result, contact forces are developed and act along that region. These forces are equal and opposite and the normal tractions can only exert compressive action, (while no tensile state can occur) and the tangential tractions satisfy Coulomb's law of friction [4].

4. MODEL GEOMETRY

As a comparison of the implicit and explicit formulations for modeling discontinuities in a "continuous rock" medium, the following geometry is considered: In the center of a square rock mass of size 40x40 m, a circular opening with radius ($r = 5\text{m}$) is formed. The opening is intersected by a parallel set of joints, which dip 45° from the horizontal. These joints intersect both the rock mass and the opening where appropriate (Figure 1). Thus, an implicit and an explicit model were created based on this geometry.

In the implicit formulation, each joint is described by a very thin layer (about 5-10mm), whose elements are modeled, with different material properties from that of the intact rock.

In the explicit formulation, contact elements are used to model the discontinuities. The same material properties are assigned to the rock mass, however, in place of the joints, an interface

between the two rock faces is generated using contact-friction elements.

5. MATERIAL MODEL ASSUMPTIONS AND BOUNDARY CONDITIONS

As already mentioned, required properties for the elastic materials are the modulus of elasticity and Poisson's ratio. In the case of the elastic-perfectly plastic material, the generalized linear Mohr-Coulomb criterion is applied as defined by the angle of friction (ϕ) and cohesion (c). For the contact analysis (model 2) the program requires the distance tolerance for contact between nodes to occur, the friction coefficient of the interface, and the relative velocity of the slip surface. The latter is used for overcoming numerical difficulties of the friction model. Table 1 summarizes the range of the material properties for each model.

Table 1. Material properties and discretization for models 1 & 2							
Model 1	Total Elements	Total Nodes	E (GPa)	Poisson's Ratio	Frict. angle (deg)	Cohesion (kN/m ²)	
Material 1	1986	2058	40	0.25	-	-	
Material 2			10	0.25	35	10	
Model 2					Friction coef.	Dist. Tolerance (m)	Slid. velocity (m/s)
Material 1	2170	2460	40	0.25	0.5	0.004	0.01
Material 2			10	0.25	0.5	0.004	0.01

All the values of the material and model properties are representative for the respective materials (rock and infill material) [5]. Each model is discretized using four node isoperimetric quadrilateral elements. It should be noted that in the second model, contact properties were also assigned to the elastic elements surrounding (for a depth of a few cm) the friction interface. For both models plain strain conditions were assumed.

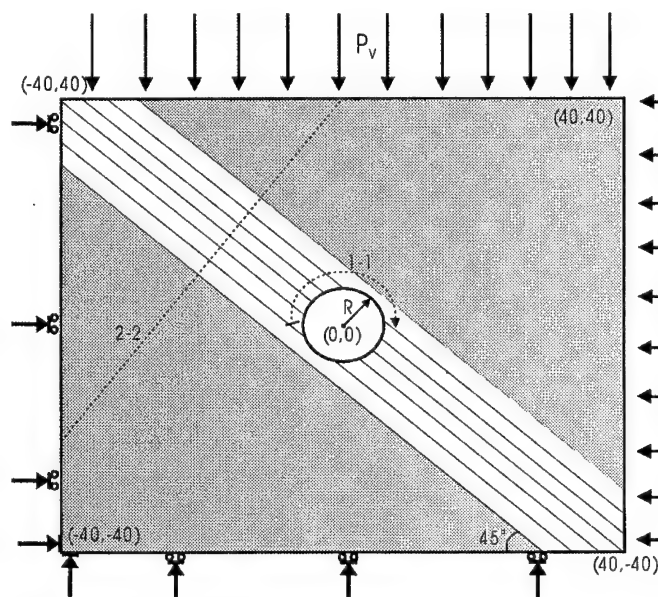
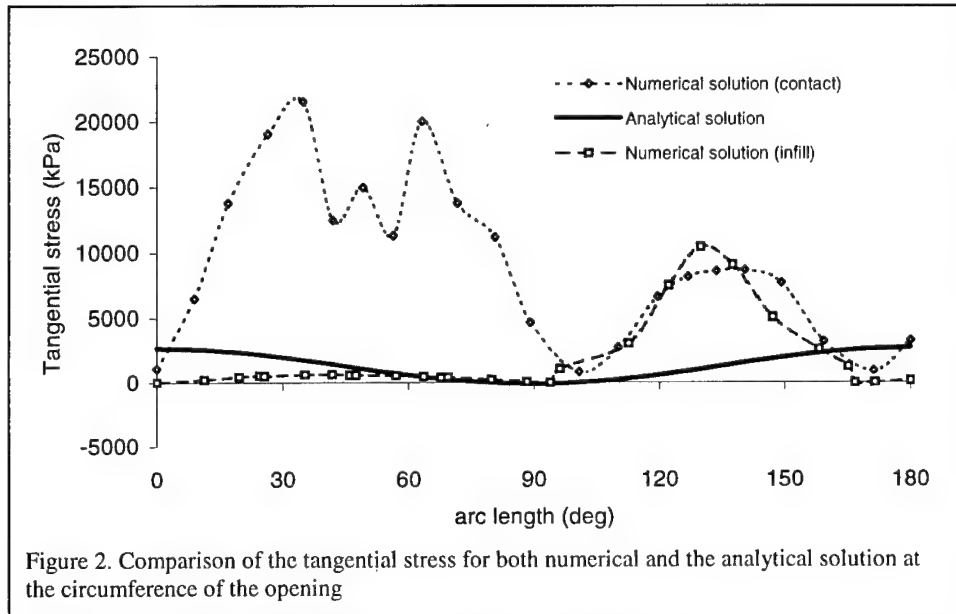


Figure 1. Model Geometry

Each model is subjected to a vertical edge load of 1000kPa and a horizontal edge load of 300kPa. These values were based on the depth from the surface of the opening and the presumed specific gravity of the rock mass.

Boundary conditions were for both models as follows: rolling nodes on the horizontal (x) direction at the base of the model and rolling nodes on the vertical (y) direction (left side of the model) as shown



in Figure 1. The bottom left node is fixed in terms of displacement.

6. RESULTS

The distribution of stresses and displacements are plotted for models 1 and 2 (a) along the circumference of the opening (section 1-1, Figure 1) and (b) perpendicular to the discontinuity plane in a distance of 2 diameters for the center of the openings (section 2-2, Figure 1).

Figure 2 presents the distribution of the tangential stresses (for both models) in the upper half circular portion of the opening, from left to right (0-180°) as well as the closed form solutions obtained by Kirsh's equations. Results for the contact model show very high values of tangential stress in the circumference of the opening, between 10-90°. The stress values of the infill model are lower than the values of closed form solution for the same arc length. At about 100° all solutions are very close and thereafter, both numerical solutions are very much alike and higher than the analytical. Figure 3 presents vertical displacements for the same section (1-1), for both models. Results indicate that although the

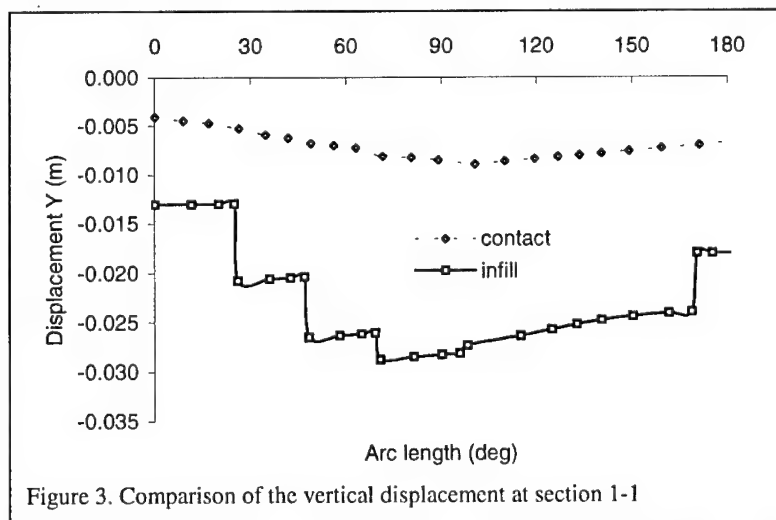


Figure 3. Comparison of the vertical displacement at section 1-1

stresses are much higher in the contact model, the displacement regime is exactly the opposite. In the infill model the displacements are much higher than the contact model. Large differences in displacements are associated

with material changes from "hard" to "softer". On the other hand the displacements of the contact model appear to be much smaller along that profile. This means that although the stress field is high, if there is competent rock mass between the discontinuities then the opening may be stable without support measures. Similar results are obtained for the horizontal displacements.

Figures 4 and 5 present the distribution of the horizontal and vertical stresses for both models for section 2-2, thus highlighting the effects of the two types of discontinuities on the stress distribution. Results show that the two models differ substantially only in the proximity of the discontinuities. In this region it is evident that in the contact model, high stresses are developed contrary to the infill model where the stress field is much smoother. This can be attributed to the elastic-plastic behavior of the fill material due to its yielding. The stress field that results after yielding and the plastic deformation of the fill material is much lower than that in the contact model. In regions far from the discontinuities both models respond in the same manner.

7. CONCLUSIONS

An underground opening is modeled in a discontinuous medium using two types of discontinuity models. In the finite element implementation, a set of parallel rock discontinuities

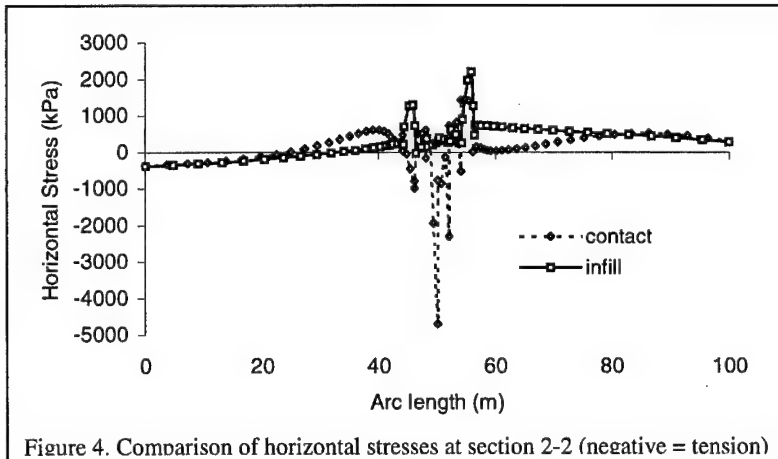


Figure 4. Comparison of horizontal stresses at section 2-2 (negative = tension)

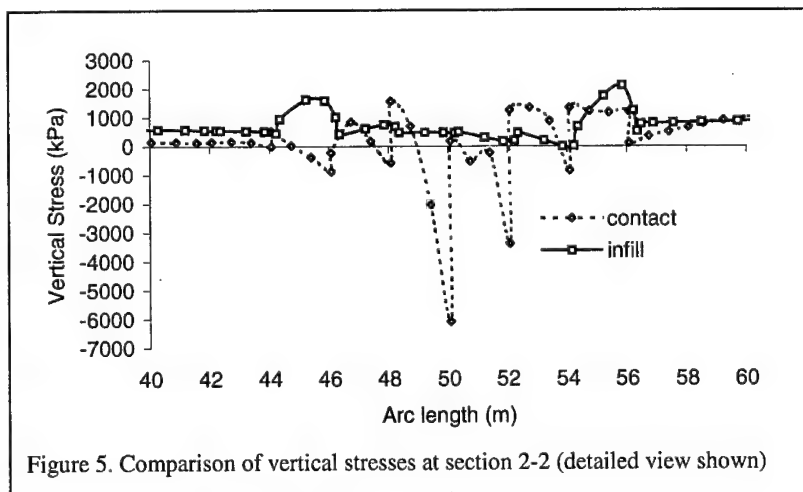


Figure 5. Comparison of vertical stresses at section 2-2 (detailed view shown)

s inclined at 45 degrees from the horizontal, were created in 2D space, intersecting the circular opening as well as the surrounding material. Two cases are discussed; in the first case discontinuities are modeled

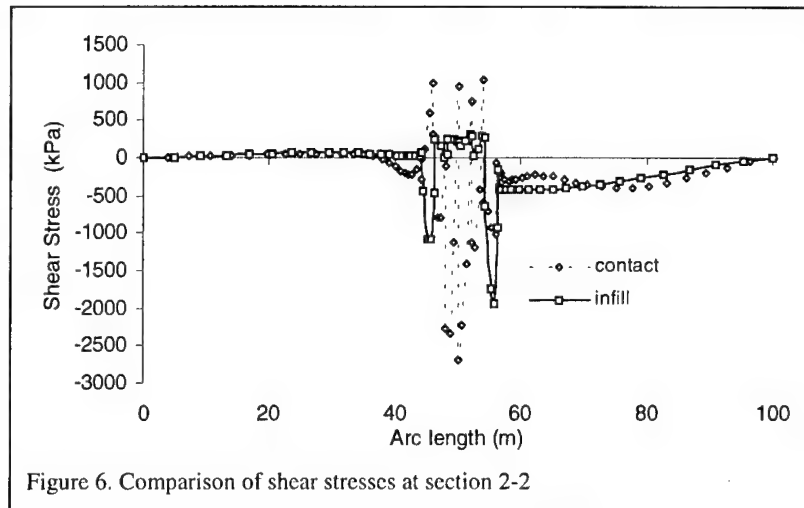


Figure 6. Comparison of shear stresses at section 2-2

as very thin material layers with elastoplastic behavior (i.e. infill material), while in the second case the discontinuities are modeled as open joints (no infill material), by using contact elements.

The two models show significant differences between them. The contact model exhibits high stress values in the region of the discontinuities (both at edge of the opening and away from the opening). This is probably due to the large distinct bodies that are formed between the discontinuities, in accordance with the small (0.5) friction coefficient, and the 45 degrees incline. The material in the contact model is assumed elastic, so high values of stress can be present although they seem high for real rock masses. If the material is assumed elastoplastic, or governed by a yielding criterion suitable for rocks, then probably the stresses would not reach very high values.

In the infill model, the stress field is lower than that of the contact model. This is probably due to the yielding of the fill material and its subsequent plastic deformation. For this reason the displacements were higher in the infill model, especially at the interface of elements with different material properties.

This study is a first step for the evaluation of applicable methods for modeling underground openings in discontinuous rock masses without utilizing homogenized properties for the rock mass. Much has to be done in this direction for such models to yield realistic and accurate results. Further analysis will study the effects of dilatancy of the infill material during yielding, appropriate rock yielding criteria and different friction parameters for rock discontinuities.

8. REFERENCES

1. Kawamoto T. and Aydan, O., "A review of numerical analysis of tunnels in discontinuous rock masses", *International Journal of Numerical and Analytical Methods in Geomechanics*, 23, pp. 1377-1391, 1999.
2. Lei XY, Swoboda G, and Zeng G., "Application of contact-friction interface element to tunnel excavation in faulted rock", *Computers and Geotechnics* 17 (1995).
3. MARC – MENTAT "Theory and user information", Volume A, 2000.

4. Youakim, S.A.S, El-Metewally, S.E.E, and Chen, W.F., "Nonlinear analysis of tunnels in clayey/sandy soil with a concrete lining", *Engineering Structures*, 22 pp. 707-722, 2000.
5. Paschalis, G., "Numerical Simulation of single and conjugate underground openings in continuous and discontinuous rock", Diploma Thesis, Department of Mineral Resources Engineering, Technical University of Crete, 2001 (in Greek).

ON THE NUMERICAL PERFORMANCE OF A SIMPLIFIED METHOD OF ANALYSIS FOR CREEPING STRUCTURES LOADED CYCLICALLY

K.V. Spiliopoulos

Institute of Structural Analysis & Seismic Research
National Technical University of Athens
Zografou Campus, 157-73, Athens, Greece

1. SUMMARY

In the present work the numerical performance of a new simplified method of analysis to structures that creep under cyclic loading is investigated. This method may be applied to find the steady state stress distribution in any structure. This stress may be split into an easy to find cyclic elastic stress in response to the applied load and an unknown residual stress distribution. This residual stress is decomposed into Fourier series and an iterative way is set up to find the unknown Fourier coefficients. This is accomplished by evaluating the time derivatives of the residual stresses at discrete time points inside the cycle. An iterate of the coefficients is then performed by integrating over a cycle period. For convergence to take place, an indirect update of the coefficients is performed based on a special acceleration numerical scheme whose convergence characteristics are discussed in the paper. The whole procedure is formulated using the finite element method and an example of application to a plane stress concentration problem is included.

2. INTRODUCTION

In order to predict the complete behaviour of structures subjected to cyclic loading and are made of a material that exhibits non-linear creep, laborious and time consuming time stepping calculations must be performed. Very often these methods are also numerically unstable.

If one is interested in the long term inelastic behaviour of the structure that occurs after the stress becomes cyclic, simplified methods may be used instead. Ponter [1] has developed a simplified method for cyclic loads that have a very short cycle period. For such loads it is natural to assume that there is no time for any stress redistribution inside the cycle and the residual stress may be considered constant. Then an iterative method may be established that seeks to find this constant in-time residual stress distribution by integrating the creep strains

over a complete cycle and updating the residual stress at the end of the cycle (Ponter & Brown [2]).

The present work discusses the numerical implementation of a new simplified method that has been recently suggested by Spiliopoulos [3] and can be applied to any cyclic loading of any period for creeping structures. This method is based on the decomposition into Fourier series with respect to time of the cyclic residual stress. The unknown terms of this series are approximated in an iterative way with the aid of the time derivative of the residual stress at some time points inside the cycle. The satisfaction of equilibrium and compatibility at these time points provides a means to estimate these derivatives. The finite element method is used as a framework to combine these two conditions of statics and kinematics. An update of the Fourier coefficients then occurs by integrating over the whole cycle period. The update occurs in an indirect way using a special procedure with an acceleration parameter that is necessary for the procedure to converge. The values of this parameter used for a smooth convergence of the process as applied to a plate with a hole loaded in its own plane are also discussed as a numerical example.

3. CYCLIC RESIDUAL STRESS

Frederick and Armstrong [4] proved a theorem that for a cyclic mechanical loading, i.e.

$$P(t) = P(t + T) \quad (1)$$

and for a structure made of a stable material, such as one that exhibits nonlinear creep with a convex creep surface ϕ , like the n -power creep law:

$$\dot{\epsilon}_r^{cr} = \frac{1}{n+1} \frac{\partial \phi}{\partial \sigma} \quad (2)$$

a cyclic state of stress will be reached after many applications of loading cycles. (The entities in bold letters denote vectors evaluated at the Gauss points of a structure which has been discretized using the finite element method. Matrices are also denoted by bold letters).

The stress in the structure may be decomposed into two parts: an elastic one, assuming completely elastic behaviour, which is in equilibrium with the external loading and is therefore cyclic and a second part being a residual stress which is self-equilibrating and is due to the inelastic material behaviour.

Using the above theorem, it is obvious that the long term residual stress is itself cyclic, i.e.

$$\rho(t) \rightarrow \rho(t + T) \quad (3)$$

Since any periodic function may be decomposed into its Fourier series, the residual stress, as a function of time, may be expressed as:

$$\rho(t) = \frac{a_0}{2} + \sum_{k=1}^{\infty} \left(a_k \cos \frac{2k\pi t}{T} + b_k \sin \frac{2k\pi t}{T} \right) \quad (4)$$

where $\mathbf{a}_0, \mathbf{a}_k, \mathbf{b}_k$ are the Fourier coefficients of the expansion and if they are known the distribution of the residual stress is also known. The numerical procedure of the next section will show how these coefficients may be calculated in an iterative way.

4. NUMERICAL PROCEDURE

The three stress components at the Gauss points σ^{el} are evaluated by performing a linear elastic finite element analysis. Thus the elastic stresses $\sigma^{el}(t)$ are evaluated at discrete time points inside the cycle. Denoting by (μ) the current iteration, the discrete form of the Fourier coefficients $\mathbf{a}_0^{(0)}, \mathbf{a}_k^{(0)}, \mathbf{b}_k^{(0)}, k = 1, 2, \dots$, are given initial values, normally zero.

1. Evaluate residual stresses, using (4):

$$\rho^{(\mu)}(t) = \frac{\mathbf{a}_0^{(\mu)}}{2} + \sum_{k=1}^{\infty} (\mathbf{a}_k^{(\mu)} \cos \frac{2k\pi t}{T} + \mathbf{b}_k^{(\mu)} \sin \frac{2k\pi t}{T}) \quad (5)$$

2. Calculate creep strain rates using a form of creep law (4):

$$(\dot{\epsilon}_r^{cr}(t))^{(\mu)} = f(\sigma^{el}(t) + \rho^{(\mu)}(t)) \quad (6)$$

3. Calculate residual displacement rates, with $\mathbf{K}, \dot{\mathbf{R}}, \mathbf{B}, \mathbf{D}$ being the stiffness matrix, time rate of the nodal load vector, compatibility and elasticity matrix respectively.

$$\mathbf{K}\dot{\mathbf{r}}^{(\mu)}(t) = \dot{\mathbf{R}}(t) + \int_V \mathbf{B}'\mathbf{D}(\dot{\epsilon}_r^{cr}(t))^{(\mu)} dV \quad (7)$$

4. Calculate derivatives of the residual stresses:

$$\dot{\rho}^{(\mu)}(t) = \mathbf{D}\mathbf{B}\dot{\mathbf{r}}^{(\mu)}(t) - \dot{\sigma}^{el}(t) - \mathbf{D}(\dot{\epsilon}_r^{cr}(t))^{(\mu)} \quad (8)$$

5. Calculate the following expressions:

$$\mathbf{g}_k^{(\mu)} = -\frac{1}{k\pi} \int_0^T [\dot{\rho}^{(\mu)}(t)] \sin \frac{2k\pi t}{T} dt \quad (9)$$

$$\mathbf{u}_k^{(\mu)} = \frac{1}{k\pi} \int_0^T [\dot{\rho}^{(\mu)}(t)] \cos \frac{2k\pi t}{T} dt \quad (10)$$

$$\mathbf{s}_0^{(\mu)} = \frac{1}{2} \mathbf{a}_0^{(\mu)} - \sum_{k=1}^{\infty} \mathbf{g}_k^{(\mu)} + \sum_{k=1}^{\infty} \mathbf{a}_k^{(\mu)} + \int_0^T [\dot{\rho}^{(\mu)}(t)] dt \quad (11)$$

6. Update the Fourier coefficients using the following formulae (Isaacson & Keller [5]):

$$a_k^{(\mu+1)} = \vartheta g_k^{(\mu)} + (1-\vartheta) a_k^{(\mu)} \quad (12)$$

$$b_k^{(\mu+1)} = \vartheta u_k^{(\mu)} + (1-\vartheta) b_k^{(\mu)} \quad (13)$$

$$\frac{a_0^{(\mu+1)}}{2} = \vartheta s_0^{(\mu)} + (1-\vartheta) \frac{a_0^{(\mu)}}{2} \quad (14)$$

7. Is the following Euclidean error norm satisfied? If not go back to 2

$$\frac{\|\rho^{(\mu+1)}(T)\|_2 - \|\rho^{(\mu)}(T)\|_2}{\|\rho^{(\mu+1)}(T)\|_2} \leq \epsilon_s \quad (15)$$

5. NUMERICAL EXAMPLE – Plate with a hole

The cyclic residual stress of a square plate of dimensions 10x10cm having a circular hole of radius of 1 cm has been found using the numerical procedure that was described above. The plate is loaded symmetrically by a uniform loading along one of its edges. Due to the symmetry only one quarter of the structure needs to be analyzed (Fig.1). 98 eight-noded isoparametric elements with 3x3 Gauss integration points for each of them are used to discretize the structure.

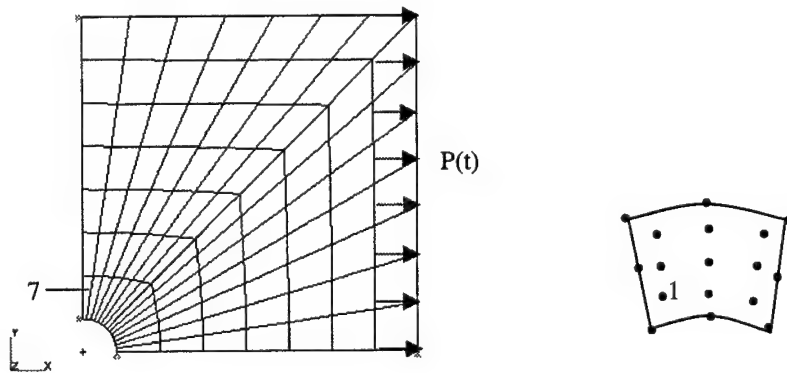


Figure 1: Finite element discretization and typical 8-noded element with 3x3 integr. points

The loading is assumed to vary according to:

$$P(t) = P_o \sin^2\left(\frac{\pi t}{T}\right) \quad (16)$$

The loading variation with time over four cycles is shown in Fig. 2

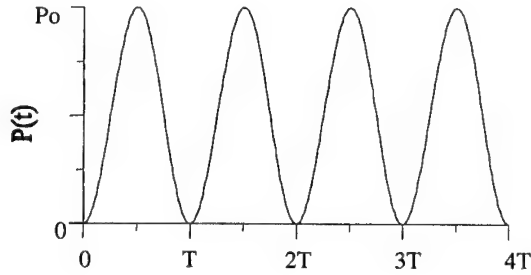


Figure 2: Load variation with time

The material constants that have been used are $K=636 \times 10^{-10}$ (SI units), $n=3.0$, $E=2100$ dN/mm², where K is the constant in the uniaxial equivalent creep law. The material was assumed incompressible with Poisson's ratio equal to $\mu=0.4999$. P_0 was taken equal to 100 dN/mm².

The elastic stress at the Gauss point 1 of the element 7 shown in Fig.1 turns out to be 2.5 times the value of the external load which is applied at the far end vertical edge. This value is quite near the theoretical one which, for an infinite plate, at the bottom left node of this element (on the circular edge) should be 3-times the value of the external load.

The error tolerance of $\varepsilon_S = .99 \times 10^{-5}$ was used as a stopping criteria. Twenty terms of the Fourier series, together with fifty time points inside the cycle were used. As for the values of the convergence parameter ϑ , it was found that smooth convergence towards the final cyclic state occurred for values less than or equal to 0.1. Good convergence behaviour can be seen in Fig.3 for the value of $\vartheta = 0.1$. The variation of the cyclic residual state of stress σ_{xx} with time at the Gauss point 1 of element 7 is shown in Fig.4.

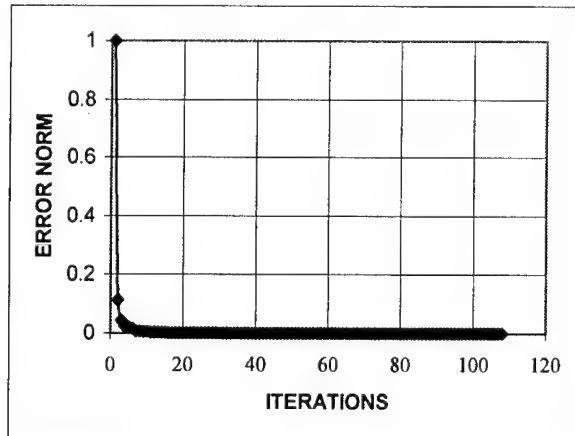


Figure 3: Convergence of iterations for $\vartheta = 0.1$

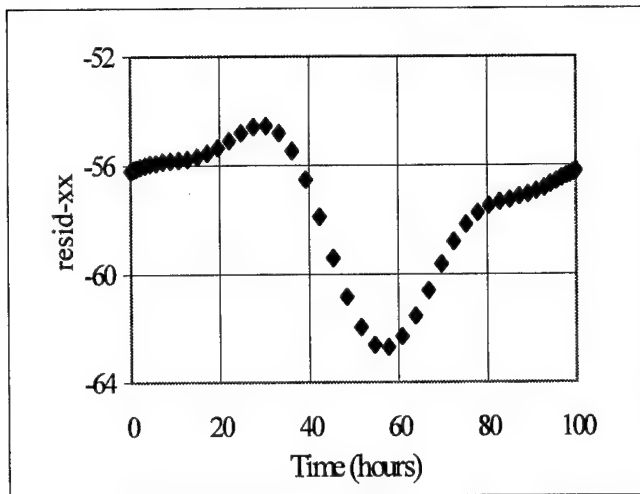


Figure 4: Cyclic residual stress variation (in dN/mm^2) inside a 100 hrs cycle

For values of ϑ around 0.01 convergence towards the cyclic state of stress occurred in about 500 iterations. On the other hand virtually no convergence occurred for values of ϑ above 0.1. For a direct update ($\vartheta = 1$), divergence occurred almost after four iterations.

6. CONCLUSIONS

The numerical implementation of a simplified method of analysis to find the long term cyclic stress for creeping structures was demonstrated. After its decomposition in Fourier series, the cyclic residual stress was found by estimating the coefficients of the series in an iterative way using a special acceleration scheme. The convergence parameter plays a key role in the fast or even no convergence of the procedure. The process, thus, alleviates the problem of having to follow extremely consuming and often numerically unstable time stepping procedures.

7. REFERENCES

- [1] Ponter, A.R.S., The analysis of cyclically loaded creeping structures for short cycle times, *International Journal of Solids & Structures*, 12, 809-825 (1976).
- [2] Ponter, A.R.S. and Brown, P.R., The finite element solution of rapid cycling creep problems, *International Journal for Numerical Methods in Engineering*, 12, 1001-1024 (1978).
- [3] Spiliopoulos, K.V., Simplified methods for the steady state inelastic analysis of cyclically loaded structures, in *Inelastic Analysis of Structures Under Variable Loads: Theory & Engineering Applications*, D. Weichert and G. Maier (Ed), *Kluwer Academic Publishers, Dordrecht* (2000) 213-232.
- [4] Frederick, C.O. and Armstrong, P.J., Convergent internal stresses and steady cyclic states of stress, *Journal of Strain Analysis*, 1, 154-169 (1966).
- [5] Isaacson, E. and Keller, H.B., *Analysis of Numerical Methods*, J. Wiley, New York (1966).

STATIC AND DYNAMIC ANALYSIS OF SHELL PANELS USING THE ANALOG EQUATION METHOD

A. J. Yiotis and J. T. Katsikadelis

Department of Civil Engineering

National Technical University, Zografou Campus GR-157 73 Athens, Greece

1. SUMMARY

A boundary-only method is presented for the static and dynamic analysis of shell panels, based on the Analog Equation Method (AEM). The three displacement components are established by solving two membrane and one plate bending problems subjected to fictitious loads under the same boundary conditions. The fictitious loads are established using the BEM. Numerical results are presented which illustrate the efficiency and the accuracy of the proposed method.

2. INTRODUCTION

There are several investigations involved in the application of BEM to solve shell problems, mainly using the D/BEM method [1]. In general the shell problems are formulated in terms of the displacement components. The proposed method is based on the concept of the Analog Equation. This method has been employed to a variety of engineering problems [2,3]. In this paper it is illustrated for the cylindrical shells.

3. GOVERNING EQUATIONS

The Flugge type differential equations are used, which for a typical thin-walled cylindrical shell of uniform thickness h , made of an isotropic, linearly elastic material, are written as

$$u_{,xx} + \frac{1-\nu}{2} u_{,ss} + \frac{1+\nu}{2} v_{,xs} + \frac{\nu}{R} w_{,x} - \frac{h^2}{12R} [w_{,xxx} - \frac{1-\nu}{2} R (\frac{w_{,xs}}{R} + \frac{u_{,s}}{R^2})_{,s}] = -\frac{1-\nu^2}{Eh} (q_x - \rho h \ddot{u}) \quad (1a)$$

$$v_{,ss} + \frac{1-\nu}{2} v_{,xx} + \frac{1+\nu}{2} u_{,xs} + (\frac{w}{R})_{,s} + \frac{h^2}{12R^2} [\frac{3(1-\nu)}{2} v_{,xx} - \frac{(3-\nu)}{2} R w_{,xxx} - R_{,s} (w_{,ss} + \frac{w}{R^2} + \frac{R_{,s}}{R^2} \nu)] = -\frac{1-\nu^2}{Eh} (q_s - \rho h \ddot{v}) \quad (1b)$$

$$\begin{aligned} \nabla^4 w + \frac{w_{,ss}}{R^2} + \left(\frac{w}{R^2}\right)_{,ss} + \frac{w}{R^4} - \frac{1}{R} u_{,xxx} + \frac{1-\nu}{2} \left(\frac{u_{,xs}}{R}\right)_{,s} - \frac{3-\nu}{2} \left(\frac{v}{R}\right)_{,xss} + \left(\frac{R_{,s}}{R^2} v\right)_{,ss} \\ + \frac{R_{,s}}{R^4} v + \frac{12}{h^2} \frac{1}{R} (v_{,s} + \frac{w}{R} + \nu u_{,x}) = -\frac{12(1-\nu^2)}{Eh^3} (-q_z + \rho h \ddot{w}) \end{aligned} \quad (1c)$$

with $\nabla^4 = \frac{\partial^4}{\partial x^4} + 2 \frac{\partial^2 \partial^2}{\partial x^2 \partial s^2} + \frac{\partial^4}{\partial s^4}$ and u, v, w being the axial, circumferential and radial displacements; R is the radius of curvature of the cross-section of the shell; ρ is the mass density and q_x, q_s, q_z are the components of the body force in the axial, circumferential and radial directions, respectively.

In the present analysis we consider cylindrical shell panels with rectangular plan form under the following boundary conditions.

a. On curved edges

$$N_x = 0, \quad v = 0, \quad w = 0, \quad \delta_1 w_{,x} + \delta_2 M_x = 0 \quad (2a)$$

b. On straight edges

$$\alpha_1 u + \alpha_2 N_{sx} = \alpha_3, \quad \beta_1 v + \beta_2 \left(N_s - \frac{M_s}{R}\right) = \beta_3 \quad (3a,b)$$

$$\gamma_1 w + \gamma_2 Q_{s,eff} = \gamma_3, \quad \delta_1 w_{,s} + \delta_2 M_s = \delta_3 \quad (3c,d)$$

where $\alpha_i(p), \beta_i(p), \gamma_i(p), \delta_i(p)$ $p \in C$ ($i=1,2,3$) are functions specified on the boundary and $N_x, N_s, N_{sx}, M_x, M_s, M_{xs}, M_{sx}, Q_s, Q_{s,eff}$ are the stress resultants given as

$$N_x = \frac{Eh}{(1-\nu^2)} \left[u_{,x} + \nu \left(v_{,s} + \frac{w}{R} \right) - \frac{h^2}{12} \frac{1}{R} w_{,xx} \right] \quad (4a)$$

$$N_s = \frac{Eh}{(1-\nu^2)} \left[v_{,s} + \nu u_{,x} + \frac{w}{R} + \frac{h^2}{12} \frac{1}{R} \left(w_{,ss} + \frac{w}{R^2} + \frac{R_{,s}}{R^2} v \right) \right] \quad (4b)$$

$$N_{sx} = \frac{Eh}{2(1+\nu)} \left[u_{,s} + v_{,x} + \frac{h^2}{12R} \left(w_{,xs} + \frac{u_{,s}}{R} \right) \right] \quad (4c)$$

$$M_x = -D \left\{ w_{,xx} + \nu \left[w_{,ss} - \left(\frac{v}{R} \right)_{,s} \right] - \frac{1}{R} u_{,x} \right\}, \quad M_s = -D \left(w_{,ss} + \frac{w}{R^2} + \frac{R_{,s}}{R^2} v + \nu w_{,xx} \right) \quad (4d,e)$$

$$M_{sx} = -\frac{D(1-\nu)}{2} \left(2w_{,xs} - \frac{v_{,x}}{R} + \frac{u_{,s}}{R} \right) \quad (4f)$$

$$Q_s = -D \left[w_{,sss} + w_{,xss} + \left(\frac{w}{R^2} \right)_{,s} - (1-\nu) \frac{1}{R} v_{,xx} + \left(\frac{R_{,s}}{R^2} v \right)_{,s} \right], \quad Q_{s,eff} = Q_s + M_{sx,x} \quad (4g,i)$$

$$D = \frac{Eh^3}{12(1-\nu^2)} \quad (5)$$

For the dynamic problem the displacements and the velocities must satisfy the given initial conditions.

4. THE ANALOG EQUATION METHOD AS A BOUNDARY-ONLY METHOD

According to the concept of the analog equation [4], eqns (1) are replaced by two Poisson and one biharmonic equation

$$\nabla^2 u_i = b_i(x, s, t) \quad i = 1, 2, \quad \nabla^4 w = b_3(x, s, t) \quad (6a, b)$$

where $b_i(x, s, t)$ ($i=1, 2$) and $b_3(x, s, t)$ are the fictitious sources, which are approximated as [5]

$$b_i = \sum_{j=1}^M \alpha_j^{(i)} f_j \quad i = 1, 2, 3 \quad (7)$$

where f_j is a set of approximation functions and $\alpha_j^{(1)}$, $\alpha_j^{(2)}$, $\alpha_j^{(3)}$ $3M$ unknown time dependent coefficients. We look for a solution of the form $\bar{u}_i + u_i^p$ and $\bar{w} + w^p$, where \bar{u}_i ($u_1 = u, u_2 = v$) and \bar{w} are the homogeneous and u_i^p and w^p the particular solutions. The particular solutions are obtained as

$$u_i^p = \sum_{j=1}^M \alpha_j^{(i)} \hat{u}_j \quad i = 1, 2, \quad w^p = \sum_{j=1}^M \alpha_j^{(3)} \hat{w}_j \quad (8a, b)$$

where \hat{u}_j , \hat{w}_j are particular solutions of the equations

$$\nabla^2 \hat{u}_j = f_j \quad i = 1, 2, \quad \nabla^4 \hat{w}_j = f_j \quad (9a, b)$$

The homogeneous solutions are obtained from the three boundary value problems

$$\nabla^2 \bar{u} = 0 \quad \text{in } \Omega, \quad \alpha_1 \bar{u} + \alpha_2 \frac{\partial \bar{u}}{\partial n} = 0 - (\alpha_1 \sum_{j=1}^M \alpha_j^{(1)} \hat{u}_j + \alpha_2 \sum_{j=1}^M \alpha_j^{(1)} \frac{\partial \hat{u}_j}{\partial n}) \quad \text{on } \Gamma \quad (10a, b)$$

$$\nabla^2 \bar{v} = 0 \quad \text{in } \Omega, \quad \bar{v} = 0 - \sum_{j=1}^M \alpha_j^{(2)} \hat{v}_j \quad \text{on } \Gamma \quad (11a, b)$$

$$\nabla^4 \bar{w} = 0 \quad \text{in } \Omega, \quad \bar{w} = 0 - \sum_{j=1}^M \alpha_j^{(3)} \hat{w}_j \quad \text{on } \Gamma \quad (12a, b)$$

$$\delta_1 \frac{\partial \bar{w}}{\partial n} + \delta_2 \nabla^2 \bar{w} = 0 - (\delta_1 \sum_{j=1}^M \alpha_j^{(3)} \frac{\partial \hat{w}_j}{\partial n} + \delta_2 \sum_{j=1}^M \alpha_j^{(3)} \nabla^2 \hat{w}_j) \quad \text{on } \Gamma \quad (12c)$$

Thus, writing the solutions of the homogeneous equations (10a), (11a), (12a) in integral form, the solutions of eqns (6) are given as

$$cu_i = - \int_C (u^* \bar{u}_{i,n} - \bar{u}_i u_{,n}^*) ds + \sum_{j=1}^M \alpha_j^{(i)} \hat{u}_j \quad i = 1, 2 \quad (13)$$

$$cw = - \int_C (\Lambda_1 \bar{w} + \Lambda_2 \bar{w}_{,n} + \Lambda_3 \nabla^2 \bar{w} + \Lambda_4 \nabla^2 \bar{w}_{,n}) ds + \sum_{j=1}^M \alpha_j^{(3)} \hat{w}_j \quad (14)$$

where the kernels u^* , $\Lambda_i = \Lambda_i(r)$, $i = 1, \dots, 4$, $r = |Q - P|$, are given as

$$\begin{aligned}
u^* &= \frac{1}{2\pi} \ln r, \quad \Lambda_1(r) = -\frac{\cos \varphi}{2\pi r}, \quad \Lambda_2(r) = \frac{\ln r + 1}{2\pi}, \\
\Lambda_3(r) &= -\frac{1}{8\pi} r (2 \ln r + 1) \cos \varphi \\
\Lambda_4(r) &= \frac{r^2 \ln r}{8\pi}, \quad r = |Q - P|, \quad \varphi = \text{angle}(r, n)
\end{aligned} \quad (15a, b, c, d, f, g)$$

with $r = |Q - P| = [(\xi - x)^2 + (\eta - s)^2]^{1/2}$ the distance between any two points $P(x, s) \in \Omega \cup C$, $Q(\xi, \eta) \in \Omega \cup C$ and $c = 1$ if $P \in \Omega$, $c = \alpha/2\pi$ if $P \in C$; α is the interior angle between the tangents to the boundary at point P . We note that for points where the boundary is smooth $c = 1/2$.

The first, second and third derivatives of the displacements for points inside Ω ($c = 1$) are obtained by direct differentiation of eqns (13) and (14) ($c = 1$). For example, the first derivatives are obtained as

$$u_{i,k} = - \int_C (u_{i,k}^* \bar{u}_{i,n} - \bar{u}_{i,n}^* u_{i,k}) ds + \sum_{j=1}^M \alpha_j^{(i)} \hat{u}_{j,k} \quad i=1,2 \quad k=1,2 \quad (16)$$

$$w_{,k} = - \int_C (\Lambda_{1,k} \bar{w} + \Lambda_{2,k} \bar{w}_{,n} + \Lambda_{3,k} \nabla^2 \bar{w} + \Lambda_{4,k} \nabla^2 \bar{w}_{,n}) ds + \sum_{j=1}^M \alpha_j^{(3)} \hat{w}_{j,k} \quad k=1,2 \quad (17)$$

Using the BEM with N constant elements, discretizing eqns (13) and (14) and applying them to the N boundary nodal points yield

$$\frac{1}{2} \bar{u}_i = \mathbf{H} \bar{u}_i - \mathbf{G} \bar{u}_{i,n} + \hat{\mathbf{U}} \boldsymbol{\alpha}^{(i)} \quad i=1,2 \quad (18)$$

$$\frac{1}{2} \bar{w} = -(\Lambda_1 \bar{w} + \Lambda_2 \bar{w}_{,n} + \Lambda_3 \nabla^2 \bar{w} + \Lambda_4 \nabla^2 \bar{w}_{,n}) + \hat{\mathbf{W}} \boldsymbol{\alpha}^{(3)} \quad (19)$$

where, \mathbf{H} , \mathbf{G} , Λ_1 , Λ_2 , Λ_3 , Λ_4 are $N \times N$ known matrices; $\hat{\mathbf{U}}$ and $\hat{\mathbf{W}}$ are known $N \times M$ matrices, and $\boldsymbol{\alpha}_j^{(i)}$, ($i=1,2$), $\boldsymbol{\alpha}_j^{(3)}$ are the vectors of the unknown coefficients. Moreover, applying the boundary conditions to the N boundary nodal points after elimination of \bar{u}_i , $\bar{u}_{i,n}$, \bar{w} , $\bar{w}_{,n}$, $\nabla^2 \bar{w}$, $\nabla^2 \bar{w}_{,n}$ we obtain

$$\mathbf{u}_i = \mathbf{U}_i \boldsymbol{\alpha}^{(i)}, \quad \mathbf{u}_{i,k} = \mathbf{U}_{i,k} \boldsymbol{\alpha}^{(i)}, \quad \mathbf{u}_{i,kl} = \mathbf{U}_{i,kl} \boldsymbol{\alpha}^{(i)} \quad i=1,2 \quad k,l=1,2 \quad (20a, b)$$

$$\mathbf{w} = \mathbf{W} \boldsymbol{\alpha}^{(3)}, \quad \mathbf{w}_{,k} = \mathbf{W}_{,k} \boldsymbol{\alpha}^{(3)}, \quad \mathbf{w}_{,kl} = \mathbf{W}_{,kl} \boldsymbol{\alpha}^{(3)}, \quad \mathbf{w}_{,klm} = \mathbf{W}_{,klm} \boldsymbol{\alpha}^{(3)} \quad k,l,m=1,2 \quad (21a, b)$$

where $\mathbf{U}_i, \dots, \mathbf{W}_{,k}$ are known matrices.

Differentiation of (20a), (21a) with respect to time yields

$$\ddot{\mathbf{u}}_i = \mathbf{U}_i \ddot{\boldsymbol{\alpha}}^{(i)} \quad i=1,2, \quad \ddot{\mathbf{w}} = \mathbf{W} \ddot{\boldsymbol{\alpha}}^{(3)} \quad (22, 23)$$

Finally, writing eqns (1) in matrix form and substituting eqns (20), (21), (22), (23), we obtain the equation of motion

$$\mathbf{M} \ddot{\boldsymbol{\alpha}} + \mathbf{C} \dot{\boldsymbol{\alpha}} + \mathbf{K} \boldsymbol{\alpha} = \mathbf{g} \quad (24)$$

where \mathbf{M} , \mathbf{C} , \mathbf{K} are generalized mass, damping, and stiffness matrices; \mathbf{g} is a vector including the $3M$ values of the external force and $\boldsymbol{\alpha}$ is the vector of the $3M$ coefficients to be determined.

Note that in the absence of inertia and damping forces $\mathbf{M} = \mathbf{C} = 0$ and eqn (24) becomes $\mathbf{K}\mathbf{a} = \mathbf{g}$ which represents the static problem. For free, undamped vibrations it is $\mathbf{g} = \mathbf{C} = 0$ and setting $\mathbf{a}(\mathbf{t}) = \mathbf{A}e^{i\omega t}$ in eqn (24) we obtain $(\mathbf{K} - \omega^2\mathbf{M})\mathbf{A} = 0$, from which the eigenfrequencies and mode shapes are established by solving a typical eigenvalue problem of linear algebra.

5. NUMERICAL RESULTS

The employed approximation functions f_j are the multiquadrics [6], which are defined as

$$f_j = \sqrt{r^2 + c^2} \quad r = \sqrt{(x - x_j)^2 + (s - s_j)^2} \quad (j = 1, 2, \dots, M) \quad (25a, b)$$

where c is an arbitrary constant and x_j, s_j the collocation points. The particular solutions of eqns (9a), (9b) are

$$\hat{u}_j = -\frac{c^3}{3} \ln(c\sqrt{r^2 + c^2} + c^2) + \frac{1}{9}(r^2 + 4c^2)\sqrt{r^2 + c^2} \quad (26)$$

$$\begin{aligned} \hat{w}_j = & -\frac{1}{12} \ln(c\sqrt{r^2 + c^2} + c^2) c^3 (r^2 + c^2) + \frac{7}{60} c^5 \ln(c\sqrt{r^2 + c^2} + c^2) \\ & -\frac{1}{12} c^5 + \frac{1}{12} c^3 r^2 - \frac{7}{60} c^4 \sqrt{r^2 + c^2} + \frac{1}{225} (r^2 + c^2)^{5/2} + \frac{2}{45} c^2 (r^2 + c^2)^{3/2} \end{aligned} \quad (27)$$

Static analysis of a circular cylindrical simply supported shell (barrel vault problem)

A circular cylindrical shell (barrel vault problem) with all edges simply supported and subjected to uniform normal pressure has been analyzed. The numerical results have been obtained with $N = 84$, $M = 72$. The radial deflections at the mid-shell have been calculated and compared with a FEM solution. The results from both solutions are shown in graphical form in Fig.1 and are found in very good agreement with the FEM results. The employed data are $E = 2.1 \times 10^7 \text{ KN/m}^2$, $h = 0.20 \text{ m}$, $R = 10.00 \text{ m}$, $l = 24.54 \text{ m}$, $\nu = 0.25$, $\varphi = 70.30^\circ$.

Free, undamped vibrations of a simply supported shell

The free, undamped vibrations of the simply supported circular cylindrical shell of the example 1 have been studied. The computed first 6 eigenfrequencies are presented in Table 1 as compared with results obtained with a FEM solution. The results are in very good agreement.

Table 1. Eigenfrequencies $\Omega = R\omega\sqrt{(1-\nu^2)\rho/E}$ of the shell of the example 1

n	Present	FEM
1	0.251	0.251
2	0.333	0.327
3	0.391	0.391
4	0.413	0.422
5	0.516	0.494
6	0.558	0.553

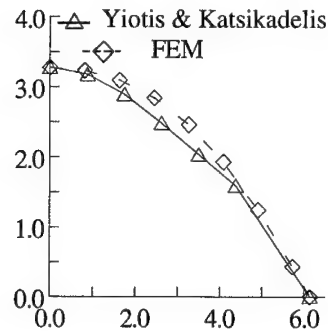


Fig. 1: Radial deflection ($w \times 10^4 m$) of a simply supported shell under normal uniform pressure.

6. CONCLUSIONS

The basic conclusions that can be drawn from this investigation are the following:

The shell analysis problem is converted to the solution of two Poisson's problems and one biharmonic, which can be solved with the BEM using the well-known static fundamental solutions.

The proposed formulation has been converted to a boundary-only BEM by using the multiquadrics functions.

7. REFERENCES

- [1] Beskos, D. E., Static and dynamic analysis of shells, in *Boundary Element Analysis of Plates and Shells*, D. E. Beskos (Ed.), Springer-Verlag, Berlin (1991), 93-1401.
- [2] Katsikadelis, J. T., and Nerantzaki, M. S., "The Boundary Element Method for Nonlinear Problems", *Engineering Analysis with Boundary Elements*, (invited paper to Special Issue), 23, pp. 365-373, (1999).
- [3] Katsikadelis, J. T., and Nerantzaki, M. S., A Boundary-Only Solution To Dynamic Analysis of Non-homogeneous Elastic Membranes, *Computer Modeling in Engineering Science*, 1, 3, pp. 1-9, (2000).
- [4] Katsikadelis, J. T., The analog equation method-a powerful BEM-based solution technique for solving linear and nonlinear engineering problems, in *Boundary Element Method XVI*, C. A. Brebbia (Ed.), CLM Publications, Southampton (1994), pp. 167-182.
- [5] Nardini, D. and Brebbia, C.A., New approach to vibration analysis using boundary elements, in *Boundary Elements Methods in Engineering*, C.A. Brebbia (Ed.), Springer-Verlag, Berlin (1982), pp. 313-336.
- [6] Goldberg, M. A., Chen, C. S., and Kapur, S. P., Improved multiquadric approximation for partial differential equations, *Engineering Analysis with Boundary Elements*, 18, pp. 9-17, (1996).

NUMERICAL STUDIES OF ANCHORS AND REBARS IN CONCRETE SPECIMENS BY DAMAGE MODELS

G. D. Hatzigeorgiou, M. G. Sfakianakis, D. D. Theodorakopoulos, D. E. Beskos

Department of Civil Engineering
University of Patras, GR-265 00 Patras, Greece

1. SUMMARY

A finite element methodology is developed for the prediction of the response of typical pull-out experimental tests of anchors and rebars in normal and fiber reinforced concrete specimens under full bonding conditions, assuming static and dynamic loading including the strain rate effect. The inelastic material behaviour is simulated with the aid of the continuum damage theory. The theoretical part of the developed models and their application to the prediction of the experimental response are presented. The model predicted behaviour is found in good agreement with the experimental one.

2. INTRODUCTION

Anchors and rebars embedded in concrete are used as load transfer mechanisms in the construction industry. The knowledge of the failure mode of anchors and rebars embedded in concrete and being under tension is very important for the establishment of rational design rules. In most cases of daily practice both anchors and rebars are embedded in concrete without connection with the main concrete reinforcement. In these cases, the typical failure mode is a pulled out concrete cone under the application of a tensile load in the anchor or the rebar. In order to delay this failure mechanism, as the applied load increases, several types of anchors have been developed associated with the way they are inserted in concrete as well as with the type of steel-concrete contact established. Among them, the most widely used in practice are the full bonded anchors and rebars, with or without headed stud, as well as the chemical anchors with a chemical epoxy resin acting in the interface between concrete and anchor in order to improve the bond strength. Usually, the full bonding conditions are found in the case of cast in place (C.I.P.) anchors or rebars. The post installed (P.I.) anchors or rebars are characterized by lower bond strength, unless they are equipped by special expansion mechanisms.

In order to characterize the bond behaviour, experimental studies, widely known as pull-out tests, were performed in the background of a recent research project [1]. The tests were performed using normal and high performance concrete with steel fibers. A wide variety of concrete types were used in the experimental part of this research. Two types of rebars and three different industrial types of anchors were used in pull-out tests.

For the numerical simulation of the concrete behaviour during the pull-out tests, two finite element models have been developed by the present authors in the framework of the above project [2]. Both models incorporate simple damage theories according to which the decrease of the strength of a material is governed by a continuous damage function, the value of which ranges between zero (undamaged stress state) and unity (completely loss of material coherence). The basic parameter in these damage theories is a stress or strain measure, which is usually expressed in terms of principal stresses or strains for each material. The developed

finite elements have been introduced to the open library of a global 3-D FEM code, developed by the authors.

3. CONCRETE MODEL DEVELOPMENT

From the plethora of existing theories for modelling the mechanical behavior of plain concrete (elastoplastic, viscoplastic, microplane, damage), one is interested in a theory simple enough for efficient computations, yet capable of simulating all the basic characteristics of concrete behavior (different strengths in tension and compression, softening branch, localization of deformation, strain-rate effects). Thus, the continuum damage theory was selected as the basis of the concrete model development. More specifically, two damage models are used in this work: a) The simple isotropic elastic-damage model of Oñate (1997) [3], which is very simple but restricted to predominantly tensile states of stress, and b) A more complicated anisotropic damage model, which can be thought of as a combination of the elastic-damage part of the elastoplastic-damage model of Faria and Oliver (1993) [4] with two damage indices (one for compression and one for tension) and the damage theory of Mazars (1986) [5], which unifies appropriately these two indices into one index. This is the FOM (Faria-Oliver-Mazars) model. A brief description of these two models follows below.

The Oñate model

For this model, the total stress tensor σ is defined as a function of the undamaged (elastic) stress tensor $\bar{\sigma}$ according to the following relation

$$\sigma = (1-d)\bar{\sigma} = (1-d)D\varepsilon \quad (1)$$

where D is the elasticity matrix and d is the damage index given by an evolution law.

The damage evolution law is a function of a scalar norm r , which corresponds to an equivalent stress measure. Its exponential form, suitable for the prediction of the triaxial damage surface of fig. 1(a), is given by

$$d = 1 - \frac{r_o}{r} \exp \left[A \left(1 - \frac{r}{r_o} \right) \right] \quad (2)$$

In (2), r_o is a threshold value for the onset of damage, and term A depends on material properties, such as the modulus of elasticity E , the fracture energy G_f , the tensile strength f_t and the characteristic element length l^* of the concrete.

The scalar norm r , which corresponds to an equivalent stress, is given by the relation

$$r = \left(\theta + \frac{1-\theta}{n} \right) [\bar{\sigma}^T D \bar{\sigma}]^{1/2} \quad (3)$$

where θ is a function of the effective (undamaged) principal stresses.

The limit damage surface and uniaxial stress-strain curve for this model under 2-D conditions are shown in fig. 1(a). More details about the numerical implementation of eq. (1)-(3) can be found in references [3].

The Faria-Oliver-Mazars (FOM) model

In this model the damage evolution law d of eq. (1) is defined as a linear combination of two damage indices d^+ and d^- for tension and compression, respectively, i.e.,

$$d = a^+ d^+ + a^- d^- \quad (4)$$

$$d^+ = 1 - \frac{r_0^+}{\tau^+} e^{A^+ \left(1 - \frac{\tau^+}{\tau_0^+}\right)}, \quad d^- = 1 - \frac{r_0^-}{\tau^-} (1 - A^-) - A^- e^{B^- \left(1 - \frac{\tau^-}{\tau_0^-}\right)} \quad (5)$$

where a^+ , a^- are scalar norms as functions of principal strains, A^+ , A^- are parameters similar to A in the Oñate model, r_0^+ , r_0^- are threshold values for the onset of damage and τ_0^+ , τ_0^- are scalar norms, which correspond to equivalent stress measures, similar to the scalar norm r of the Oñate model.

Figure 1(b) shows the limit damage surface and the uniaxial stress-strain curve for the FOM model under 2-D conditions. More details about the numerical implementation of eq. (4)-(5) can be found in references [4],[5].

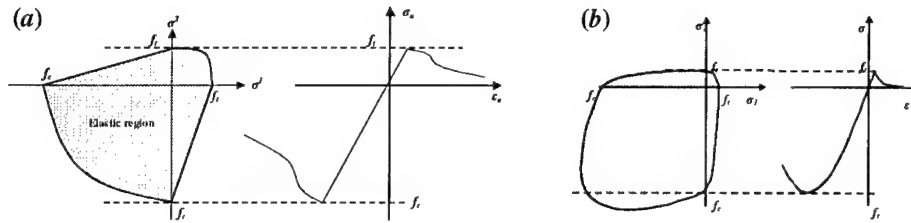


Figure 1: Limit damage surface under 2-D conditions and uniaxial stress-strain curve for: (a) Oñate model, (b) Faria-Oliver-Mazars (FOM) model.

By looking at fig. 1(a) and 1(b) of the two models one can easily observe that the Oñate model cannot take into account the biaxiality effect (increase of strength in compression-compression), while the FOM model can take that into account. However, the Oñate model coincides with the FOM model for uniaxial tension and is very close to it for tension dominated states of stress. Since pull-out tests of rebars and anchorages are tension dominated, both models have been validated and used in subsequent computations.

Strain-rate effects

Concrete exhibits a rate dependent behavior when submitted to high speed straining for which visible effects are the significant increase of dynamic strengths and the decrease of nonlinearity on the stress-strain response curves, when compared to what is observed on static tests. Observational experience shows that rate sensitivity is mainly due to the fact, that growth of internal microcracking (for a particular level of strain) is retarded at high strain rates. Being known, that the concrete (and other geomaterials) damage is essentially due to the nucleation and growth of microvoids and microcracks, it is comprehensible, that a diminishing of microcracking with increasing strain-rate will induce a reduction in macroscopic nonlinear behavior and an increase of dynamic strengths.

The strain-rate concrete behavior simulation under dynamic loading can be obtained from a suitable modification of the Oñate and FOM damage models. This modification requires the computation of equivalent tensile and compressive strain-rate at every time step.

$$\dot{\epsilon}_{eq}^+ = \frac{(\epsilon_{eq}^+)_{N+1} - (\epsilon_{eq}^+)_N}{t_{N+1} - t_N} = \frac{|\Delta \epsilon_{eq}^+|}{\Delta t}, \quad \dot{\epsilon}_{eq}^- = \frac{(\epsilon_{eq}^-)_{N+1} - (\epsilon_{eq}^-)_N}{t_{N+1} - t_N} = \frac{|\Delta \epsilon_{eq}^-|}{\Delta t} \quad (6)$$

where ϵ_{eq}^\pm are scalar norms of principal strains of the form

$$\epsilon_{eq}^+ = \sqrt{\frac{\max(\epsilon_1, \epsilon_2, \epsilon_3)}{\sum_{i=1}^3 \langle \epsilon_i \rangle}} \sqrt{\sum_{i=1}^3 \langle \epsilon_i \rangle^2}, \quad \epsilon_{eq}^- = \sqrt{\frac{\min(\epsilon_1, \epsilon_2, \epsilon_3)}{\sum_{i=1}^3 \langle \epsilon_i \rangle}} \sqrt{\sum_{i=1}^3 \langle \epsilon_i \rangle^2} \quad (7)$$

From the above equivalent strain-rates, the dynamic to static strength ratios are computed for compressive and tensile states. These ratios arise from experimental tests. In the proposed methodology, the experimental results of Suaris & Shah (1985) [6] have been adopted. Polynomial regression of these results gives

$$\frac{f_{t,dyn}}{f_{t,st}} = R_t = 2.2989 + 0.5302[\log_{10}(\dot{\epsilon}_{eq}^+)] + 0.0855[\log_{10}(\dot{\epsilon}_{eq}^+)]^2 + 0.0056[\log_{10}(\dot{\epsilon}_{eq}^+)]^3 \quad (8)$$

$$\frac{f_{c,dyn}}{f_{c,st}} = R_c = 1.4090 + 0.1708[\log_{10}(\dot{\epsilon}_{eq}^-)] + 0.0235[\log_{10}(\dot{\epsilon}_{eq}^-)]^2 + 0.0011[\log_{10}(\dot{\epsilon}_{eq}^-)]^3 \quad (9)$$

An appropriate introduction of ratios R_t and R_c in the static damage models, gives them a strain-rate dependency. For more details one can see reference [7].

Effect of fibers in concrete

Experimental evidence shows that steel fibers in concrete improve its mechanical behavior and lead to a high performance concrete. In general, fibers increase the strength and especially the ductility of plain concrete. The latter is manifested in a stress-strain diagram for tension by a shifting of the peak stress to higher strains and especially by increased values of stress in the softening branch.

The main parameters defining the effect of the steel fibers in concrete are the volume fraction of fibers V_f , the length of fibers l_f , the diameter of fibers d_f and the length efficiency factor of fibers η_L . The introduction of the effect of fibers in the two plain concrete models is made in a rather empirical way by simply replacing the plain concrete strength f_t and the fracture energy G_f by their corresponding counterparts $f_{t,f}$ and $G_{f,f}$ respectively. In particular, the $G_{f,f}$ is given in the form

$$G_{f,f} = G_f \left(1 + Q \eta_L V_f \frac{l_f}{d_f} \right) \quad (10)$$

On the basis of experiments, one can find the coefficient Q to be equal to 25. Equation (10) gives values for $G_{f,f}$ which can be from 4 to 20 times the corresponding value G_f of plain concrete.

4. NUMERICAL AND EXPERIMENTAL RESULTS

The two developed finite element models were used to simulate the experimental response of rebar and anchor pull-out tests in the background of a research program [1]. The following figures show the experimental vs the analytical stress or load – displacement curve for each test. Two failure modes were noticed for the cylindrical rebar specimens which correspond to the boundary conditions of the specimens. The cylinder bond failure mode corresponds to confined specimens. In this case a pulled out concrete cone was noticed. The cylinder splitting failure mode corresponds to a full splitting of the unconfined concrete specimens. Due to symmetry, only one fourth of the specimens was modelled by 20-noded solid finite elements. The boundary conditions were those of the experimental setup. Analogous considerations were taken into account for the analysis of the prismatic concrete blocks for the anchor pull-out tests.

Figure 2 shows the predicted response versus the experimental one for rebar pull-out tests for the same type of normal concrete under static load conditions and for two different failure modes and bond lengths. Figure 3 shows rebar pull-out tests for two different types of high

performance (fiber reinforced) concrete and for cylinder splitting failure mode. Figure 4 shows anchor pull-out tests under static loading for normal and high performance concrete

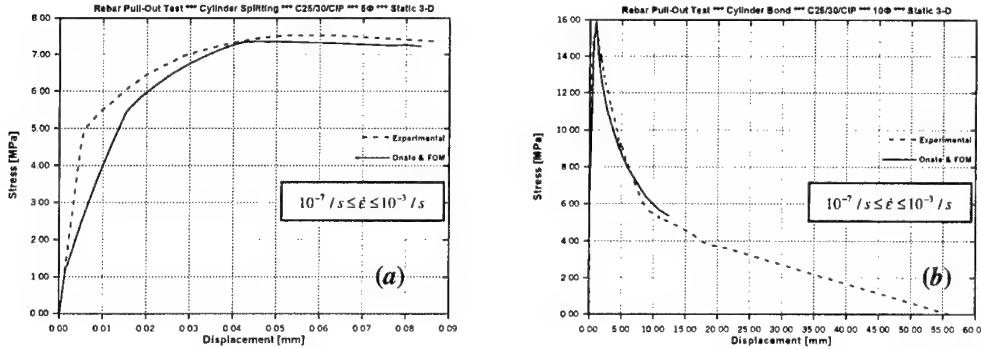


Figure 2. Rebar pull-out tests for normal concrete C25/30 (a) Cylinder Splitting, Bond length 5Φ (b) Cylinder Bond, Bond Length 10Φ .

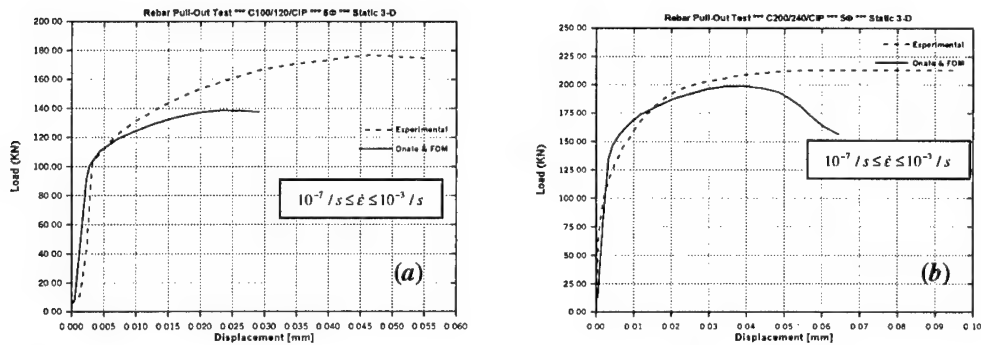


Figure 3. Rebar pull-out tests for fiber reinforced concrete, cylinder splitting failure mode, bond length 5Φ (a) C100/120, (b) C200/240.

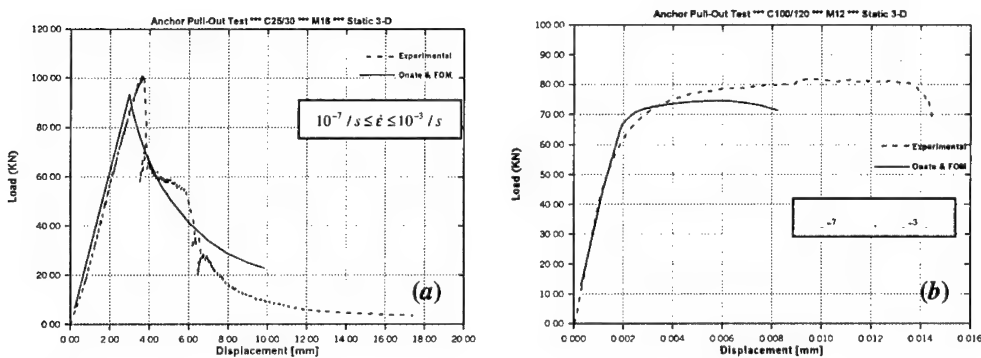


Figure 4. Anchor pull-out tests, (a) normal concrete C25/30, anchor type A, diameter M16 mm, (b) fiber reinforced concrete C100/120, anchor type B, diameter M12 mm.

for two types of industrial anchors with different geometric shape and diameters for the mechanical interlocking with the concrete.

The extremely low bond-slip behaviour was neglected because of the full bonding conditions of the specimens. Since the nature of the pull-out tests is tension dominated, both models, Oñate and FOM, give the same numerical results. It must be noted that the Oñate damage model is a subcase of the FOM model in the case where the term a^- of eq. (4) equals to zero. Finally, the predicted model behaviour is found in good agreement with the experimental one.

7. CONCLUSIONS

In the present work the description of two concrete models and their application to the prediction of the experimental results of pull-out tests were presented. The inelastic behaviour was successfully simulated by the continuum damage theory for brittle materials. The proposed models are stable and accurate since they are based on simple continuous functions of the damage evolution law, a fact that eliminates any numerical errors due to classical integration of the stresses over the finite element volume.

The model predicted behaviour was found to be from good to excellent agreement with that of the experimental pull-out tests. The two damage based concrete models of Oñate and FOM were implemented into 2-D and 3-D finite element method (FEM) codes capable of analysing static and dynamic problems.

Acknowledgements: The authors wish to thank the European Commission for its support through the BRITE-EURAM/ANCHR research program. In particular, the authors wish to thank the research groups of ENEL and Ispra/JRC (Italy) for giving them the experimental curves presented in some of the figures.

8. REFERENCES

- [1] BRITE/EURAM Project ANCHR, Final Report, Mar. 2001.
- [2] D. D. Theodorakopoulos, D.E. Beskos, M.G. Sfakianakis, G. Hatzigeorgiou & A. Sarkoula, BRITE/EURAM Project ANCHR, Final Report of the University of Patras Group, Mar. 2001.
- [3] Oñate, E. (1997), Reliability Analysis of Concrete structures: Numerical and Experimental Studies, Monography, CIMNE No 107, Barcelona.
- [4] Faria, R. & Oliver, X. (1993), A rate dependent plastic – damage constitutive model for large – scale computations in concrete structures, Monografia No 17, CIMNI, Spain.
- [5] Mazars, J., (1986), A description of micro – and macroscale damage on concrete structures, Engng. Fracture Mech., 25, 5-6, pp. 729-737.
- [6] Suaris, W. and Shah, S.P. (1985), Constitutive model for dynamic modelling of concrete, J. Eng. Mech, ASCE, 116, pp.1020-1035.
- [7] G. D. Hatzigeorgiou, Seismic Inelastic Analysis of Underground Structures by Boundary and Finite Elements, Doctoral Dissertation, Univ. of Patras, April 2001, in Greek.
- [8] Sundara Raja Iyengar, K.T. et al (1996), Parametric sensitivity of fracture behavior of concrete, Nuclear Engng Design, 163, pp. 397-403.

ON THE FLEXURAL MODES OF THE BICKFORD BEAM THEORY

C. Sophocleous

Department of Mathematics and Statistics
University of Cyprus, CY-1678 Nicosia, Cyprus

K. P. Soldatos

University of Nottingham, Pope Building, Nottingham, NG7 2RD, U.K.

1. SUMMARY

In this paper we present a general two-degrees-of-freedom theory that describes the plane flexural motion of shear deformable elastic beams. For a specific form of the shape function involved in the theory, we derive the frequency equations and the associated beam characteristic functions and we briefly present some new numerical results for a couple of different boundary conditions applied on the beam ends.

2. INTRODUCTION

This study deals with the construction of the frequency equations and the characteristic functions of a general two-degrees-of-freedom theory that describes the plane flexural motion of shear deformable beams made of homogeneous or layered orthotropic material, the latter being arranged in the form of a symmetric lay-up. The governing equations of the theory involve a general shape function of the transverse beam co-ordinate parameter, the a-posteriori choice of which specifies the distribution of the transverse shear strain or stress along the beam thickness. Different choices of this shape function produce, as particular cases, the corresponding governing equations of different beam theories. These include the differential equations of the classical, Euler-Bernoulli beam theory [1,2] as well as the corresponding equations of the shear deformable theories due to Timoshenko [3,4] and Bickford [5]. Since corresponding developments of the Timoshenko beam theory are already available in the literature [6], the example application considered in this study deals with the Bickford beam theory [5].

The Euler-Bernoulli and the Timoshenko beam models are quoted by employing a constant (zero) or a linear form, respectively, of the shape function involved in the present general beam theory and are both described by a fourth-order ordinary differential equation. In contrast, the parabolic form of the shape function employed in the Bickford beam theory yields a differential equation of the sixth order. The frequency equations, the characteristic functions and the orthogonality conditions of this theory have been constructed analytically

and may be found in [7], for the complete set of classical end boundary conditions. Here, some new numerical results are presented and discussed for a couple of these sets of end boundary conditions.

3. BASIC THEORY

We consider a homogeneous orthotropic or symmetrically laminated elastic beam of length L and thickness h and we assume that its middle-axis coincides with the Ox axis of a Cartesian co-ordinate system $Oxyz$. We assume that the cross-section of the beam has a rectangular shape with unit width. We also assume that the beam is deformed in the Oxz plane only, so that the formulation begins with the following displacement approximation:

$$U(x, y, z, t) = -zw_{,x} + \phi(z)u_1(x, t), \quad W(x, y, z, t) = w(x, t). \quad (1)$$

For the purpose of this study, the shape function $\phi(z)$ is defined as follows [5]:

$$\phi(z) = z \left(1 - \frac{4z^2}{3h^2} \right). \quad (2)$$

It can be shown that, by using either a variational approach or the generalised vectorial approach presented in [8], the beam equations of motion take the form [7],

$$\begin{aligned} D_{11}^c w_{,xxxx} + D_{11}^a u_{1,xxx} &= (\rho_0 w - \rho_2 w_{,xx} + \rho_{11} u_{1,x})_{,tt}, \\ -D_{11}^a w_{,xxx} + D_{11}^{aa} u_{1,xx} - A_{55}^a u_1 &= (\rho_{11} w_{,x} + \rho_{02} u_1)_{,tt}, \end{aligned} \quad (3)$$

where the appearing inertia and rigidity coefficients are defined as follows:

$$\begin{aligned} \rho_i &= \int_{-h/2}^{h/2} \rho^{(k)} z^i dz, \quad \rho_{ij} = \int_{-h/2}^{h/2} \rho^{(k)} z^i [\phi(z)]^j dz, \\ (A_{11}^c, D_{11}^c, D_{11}^a, D_{11}^{aa}) &= \int_{-h/2}^{h/2} Q_{11}^{(k)} (1, z^2, z\phi(z), \phi^2(z)) dz, \\ A_{55}^a &= \int_{-h/2}^{h/2} Q_{55}^{(k)} [\phi'(z)]^2 dz. \end{aligned}$$

Here, ρ 's and Q 's are the material density and the reduced elastic stiffnesses in the k th layer of the beam [9], respectively, whereas a prime represents ordinary differentiation.

Since we deal with free flexural vibrations only, we substitute

$$w/L = \bar{w}(\xi) \cos(\omega t), \quad u_1 = \bar{u}(\xi) \cos(\omega t), \quad (0 \leq \xi = x/L \leq 1) \quad (4)$$

into equations (3) to obtain,

$$\begin{aligned} \frac{d^4 \bar{w}}{d\xi^4} - \frac{D_{11}^a}{D_{11}^c} \frac{d^3 \bar{w}}{d\xi^3} &= \bar{\omega}^2 \left(\bar{w} - \frac{\rho_2}{\rho_0 L^2} \frac{d^2 \bar{w}}{d\xi^2} + \frac{\rho_{11}}{\rho_0 L^2} \frac{d\bar{u}}{d\xi} \right), \\ \frac{D_{11}^a}{D_{11}^c} \frac{d^3 \bar{w}}{d\xi^3} - \frac{D_{11}^{aa}}{D_{11}^c} \frac{d^2 \bar{u}}{d\xi^2} + \frac{A_{55}^a L^2}{D_{11}^c} \bar{u} &= -\bar{\omega}^2 \left(\frac{\rho_{11}}{\rho_0 L^2} \frac{d\bar{w}}{d\xi} - \frac{\rho_{02}}{\rho_0 L^2} \bar{u} \right), \end{aligned} \quad (5)$$

where the appearing non-dimensional frequency parameter is defined as follows:

$$\bar{\omega}^2 = \omega^2 \frac{\rho_0 L^4}{D_{11}^c}. \quad (6)$$

Equations (5) can be uncoupled to give,

$$\begin{aligned} &\left[\left(\frac{D_{11}^a}{D_{11}^c} \right)^2 - \frac{D_{11}^{aa}}{D_{11}^c} \right] \frac{d^6 v}{d\xi^6} + \left[\left(2 \frac{D_{11}^a}{D_{11}^c} \frac{\rho_{11}}{\rho_0 L^2} - \frac{D_{11}^{aa}}{D_{11}^c} \frac{\rho_2}{\rho_0 L^2} - \frac{\rho_{02}}{\rho_0 L^2} \right) \bar{\omega}^2 + \frac{A_{55}^a L^2}{D_{11}^c} \right] \frac{d^4 v}{d\xi^4} + \\ &\left[\left(\frac{A_{55}^a L^2}{D_{11}^c} \frac{\rho_2}{\rho_0 L^2} + \frac{D_{11}^{aa}}{D_{11}^c} \right) \bar{\omega}^2 + \left(\left(\frac{\rho_{11}}{\rho_0 L^2} \right)^2 - \frac{\rho_2 \rho_{02}}{\rho_0^2} \right) \bar{\omega}^4 \right] \frac{d^2 v}{d\xi^2} + \\ &\left[\frac{\rho_{02}}{\rho_0 L^2} \bar{\omega}^4 - \frac{A_{55}^a L^2}{D_{11}^c} \bar{\omega}^2 \right] v = 0, \end{aligned} \quad (7)$$

where v stands for both \bar{w} and \bar{u} .

4. FREQUENCY EQUATIONS AND CHARACTERISTIC FUNCTIONS

In addition to the equations of motion (3), a variational approach (Hamilton's principle) yields all possible sets of variationally consistent boundary conditions that can be applied on the beam ends ($\xi=0, 1$). Using the non-dimensional variables \bar{w} and \bar{u} , these sets of boundary conditions are expressed as follows:

1. Clamped end: $\bar{w} = \bar{w}_{,\xi} = \bar{u} = 0$;
2. Simply supported: $\bar{w} = \bar{w}_{,\xi\xi} = \bar{u}_{,\xi} = 0$;
3. Free: $\bar{w}_{,\xi\xi\xi} - \frac{D_{11}^a}{D_{11}^c} \bar{u}_{,\xi\xi} + \bar{\omega}^2 \left(\frac{\rho_2}{\rho_0 L^2} \bar{w}_{,\xi} - \frac{\rho_{11}}{\rho_0 L^2} \bar{u} \right) = \bar{w}_{,\xi\xi} = \bar{u}_{,\xi} = 0$; and
4. Guided: $\bar{w}_{,\xi\xi\xi} - \frac{D_{11}^a}{D_{11}^c} \bar{u}_{,\xi\xi} = \bar{w}_{,\xi} = \bar{u} = 0$.

The number (three) in each set of end conditions matches the order (six) of the differential equation (7) that only even derivatives of the dependent variable. Hence, the corresponding auxiliary equation has three double roots, λ_1^2 , λ_2^2 and λ_3^2 say, the long expressions of which are given in [7]. It turns out that $\lambda_1^2 < 0$ and $\lambda_3^2 > 0$, whereas $\lambda_2^2 > 0$ if $0 \leq \bar{\omega} < \eta_B$ or $\lambda_2^2 < 0$ if $\bar{\omega} > \eta_B$, with $\eta_B = 12 \left(\frac{L}{h} \right)^2 \sqrt{\frac{14 Q_{55}}{17 Q_{11}}}$. In the lower of these frequency regimes ($0 \leq \bar{\omega} < \eta_B$) the general solution of (7) is therefore as follows:

$$v = B_1 \cos(\lambda_1 \xi) + B_2 \sin(\lambda_1 \xi) + B_3 \cosh(\lambda_2 \xi) + B_4 \sinh(\lambda_2 \xi) + B_5 \cosh(\lambda_3 \xi) + B_6 \sinh(\lambda_3 \xi),$$

and has a corresponding, slightly modified expression in the upper frequency regime [7]. Relations between the arbitrary constants of integration that appear in the solutions thus obtained for \bar{w} and \bar{u} are found by using equations (5).

Frequency equations as well as corresponding characteristic functions are then constructed analytically, by employing these solutions obtained for \bar{w} and \bar{u} in conjunction with different combinations of end conditions. Complete lists of such analytical results can be found in [7] for ten different sets of end boundary conditions. The orthogonality condition that the characteristic functions obey are also presented in [7] together with some preliminary numerical results. Here some new numerical results are next discussed for beams having both their ends free (FF beams) or one end clamped and the other free (CF beams).

5. NUMERICAL RESULTS

Table 1. The first six frequency parameters $\bar{\omega}$ of a CF beam for several values of the stiffness and aspect ratios.

h/L	Q_{11}/Q_{55}	I	II	III	IV	V	VI
0.15	80	2.6250279	9.4292057	18.910568	28.553320	39.571558	51.585809
	50	2.8653592	10.959488	22.470757	33.900672	46.475457	59.743468
	10	3.3369055	16.675002	37.879085	60.722211	84.434930	108.22758
	2	3.4657253	20.101854	51.025224	89.470617	132.50910	178.15489
0.1	80	3.0139958	12.225438	25.497783	38.732913	52.920712	67.894098
	50	3.1721366	13.978696	30.001223	46.259414	63.252238	80.782576
	10	3.4321417	19.038147	46.277355	78.060185	112.09764	147.04620
	2	3.4932695	21.100603	56.059184	102.83773	158.22841	219.58113
0.05	80	3.3647301	17.294999	39.779883	64.301466	89.736856	115.54189
	50	3.4182172	18.639695	44.626388	74.310674	105.66079	137.62181
	10	3.4942763	21.139364	56.233688	103.19741	158.63708	219.70026
	2	3.5102613	21.787320	60.093911	115.31600	185.81074	269.56019
0.02	80	3.4901289	20.979159	55.327305	100.51922	152.99359	209.93951
	50	3.4996397	21.350727	57.429011	106.71642	165.99096	232.27034
	10	3.5124916	21.882212	60.697133	117.35908	190.76914	279.37532
	2	3.5150907	21.994213	61.429621	119.93913	197.34107	293.12088
0.01	80	3.5094605	21.753608	59.874558	114.54603	183.85643	265.49483
	50	3.5118849	21.856304	60.529249	116.77462	189.30131	276.35499
	10	3.5151319	21.996012	61.441423	119.98071	197.44667	293.34029
	2	3.5157839	22.024390	61.629856	120.65833	199.21816	297.16044
EBBT		3.5160150	22.034492	61.697214	120.90192	199.85953	298.55553

In this section we present the first six natural frequency parameters of a CF (clamped-free) and a FF (free-free) Bickford beam. These are tabulated in Tables 1 and 2, respectively, for several realistic values of h/L and Q_{11}/Q_{55} ratios. The bottom row of both Tables presents the corresponding frequency parameters obtained on the basis of the Euler-Bernoulli beam theory (EBBT).

Both tables show that, for the thinnest ($h/L = 0.01$) and less reinforced, essentially isotropic beam ($Q_{11}/Q_{55} = 2$), there is a good agreement between the corresponding frequency parameters based on the Euler-Bernoulli theory and the Bickford theory. The frequency parameters of Bickford's theory decrease however continuously with increasing the beam thickness or the beam reinforcement. For example, when $h/L = 0.15$ and $Q_{11}/Q_{55} = 80$ in the CF beam case (Table 1) the first frequency of Bickford beam becomes as low as 25% whereas its fifth and sixth frequencies are as low as 20% and 17% of the corresponding Euler-Bernoulli theory counterparts, respectively. Similar conclusions can be observed in the FF beam case (Table 2).

In the previous section we have seen that the solution of equation (7) can take one of two general forms depending on whether $0 \leq \bar{\omega} < \eta_B$ (lower regime) or $\bar{\omega} > \eta_B$ (upper regime).

Table 2. The first six frequency parameters $\bar{\omega}$ of a FF beam for several values of the stiffness and aspect ratios. The results indicated with a star fall into the upper frequency regime.

h/L	Q_{11}/Q_{55}	I	II	III	IV	V	VI
0.15	80	12.610913	20.998286	31.551959	41.146692	69.977940*	82.706760*
	50	14.477683	25.182181	37.509483	48.904518	63.394368	67.999224
	10	19.259512	41.904709	66.168860	89.942635	113.86000	135.51384
	2	20.920207	52.328031	92.051140	136.14766	182.51301	229.71054
0.1	80	15.868259	28.843467	42.871736	56.589368	72.048600	87.520185
	50	17.498927	33.969952	51.117339	67.874193	85.774950	103.79654
	10	20.775917	49.862528	83.937740	119.37050	155.14640	190.86964
	2	21.680730	56.834269	104.63551	161.21032	223.78574	290.36337
0.05	80	19.983588	44.408736	70.620153	96.693860	122.93801	149.42580
	50	20.751641	48.911381	80.884937	113.49187	146.21851	179.00605
	10	21.930929	57.863840	106.88770	164.73890	228.22262	295.08498
	2	22.192064	60.320650	115.96687	187.07262	271.64470	367.69598
0.02	80	21.928964	57.496770	105.22556	160.45503	219.94571	281.64413
	50	22.085760	58.924444	110.24447	172.07201	241.08635	314.70712
	10	22.300238	61.005459	118.23862	192.53203	282.38678	386.14279
	2	22.343900	61.448801	120.05983	197.58941	293.56459	407.40309
0.01	80	22.259507	60.541640	116.31171	187.25483	271.02802	365.26499
	50	22.300254	60.948341	117.93790	191.61397	280.26421	382.01677
	10	22.354939	61.503532	120.21804	197.93943	294.22266	408.50978
	2	22.365925	61.616529	120.69039	199.28264	297.27750	414.51329
EBBT		22.373285	61.672823	120.90339	199.85945	298.55554	416.99079

Hence, two different frequency equations are obtained for each set of boundary conditions (a complete list can be found in [7]). Numerical calculations show that in the case of FF Bickford beam, when $h/L = 0.15$ and $Q_{11}/Q_{55} = 2$ the first eight frequencies fall into the lower frequency regime, while if $h/L = 0.15$ and $Q_{11}/Q_{55} = 80$ only the first four fall into the lower regime. In Table 2 the frequencies marked with a "*" fall into the upper frequency regime.

Acknowledgments: The work reported in this paper was supported by the University of Cyprus. We would like to express our gratitude to our Universities for the reciprocal hospitality shown.

6. REFERENCES

- [1] Rayleigh J. W. S., *The Theory of Sound*, London, McMillan (1877-1878).
- [2] Bishop R. E. D. and Johnson D. C., *The Mechanics of Vibration*, Cambridge University Press (1960).
- [3] Timoshenko S. P., On the correction for shear of the differential equation for transverse vibration of prismatic bars, *Philosophical Magazine* **41**, 744-746 (1921).
- [4] Timoshenko S. P., On the transverse vibration of bars of uniform cross section, *Philosophical Magazine* **43**, 125-131 (1922).
- [5] Bickford W. B., A consistent higher-order beam theory, *Developments in Theoretical and Applied Mechanics* **11**, 137-150 (1982).
- [6] Huang T. C., The effect of rotary inertia and of shear deformation on the frequency and normal mode equations of uniform beams with simple end conditions, *Journal of Applied Mechanics* **28**, 579-584 (1961).
- [7] Soldatos K. P. and Sophocleous C., On Shear Deformable Beam Theories: The Frequency and Normal Mode Equations of the Homogeneous Orthotropic Bickford Beam, *Journal of Sound and Vibration*, (in press) (2001).
- [8] Soldatos K. P., Vectorial approach for the formulation of variationally consistent higher-order plate theories, *Composites Engineering* **3**, 3-17 (1993).
- [9] Jones, R.M., *Mechanics of Composite Materials*, Hemisphere, New York (1975).

A REALISTIC ESTIMATION OF THE EFFECTIVE BREADTH OF RIBBED PLATES

J. T. Katsikadelis

Department of Civil Engineering,
National Technical University, Zografou Campus, GR-157 73 Athens, Greece

E. J. Sapountzakis

Department of Civil Engineering,
National Technical University, Zografou Campus, GR-157 73 Athens, Greece

1. SUMMARY

In this paper a realistic estimation of the effective breadth of a stiffened plate is presented. For the estimation of the effective breadth the adopted model contrary to the models used previously takes into account the resulting inplane forces and deformations of the plate as well as the axial forces and deformations of the beam, due to combined response of the system. After the solution of the plate – beams system is achieved, the distribution of the axial stresses across the plate, resulting from both the bending and the inplane action of the plate, is obtained. Integrating this distribution across the plate the values of the effective breadth are obtained. The influence of these values from the beam stiffness and their variation along the longitudinal direction of the plate are shown as compared with those obtained from various codes through numerical examples with great practical interest.

2. INTRODUCTION

In this paper a realistic estimation of the effective breadth of a stiffened plate is presented. Various definitions of the effective breadth have been given from various researchers depending on the intensity of the approximating constant stress (theoretical stress at the beam edge or at the axis of the stiffening beam) and the inclusion or not of the beam width [1-4]. For the estimation of the effective breadth or the effective width of stiffened plates, approximate methods such as the finite strip method [2], energy methods or the FEM have been employed. In all the aforementioned methods the adopted model for the analysis of the plate - beams system neglects the shear forces at the interfaces and the resulting inplane forces and deformations of the plate as well as the axial forces and deformations of the beam. This assumption results in discrepancies from the actual response of the stiffened plate.

In this paper the analysis of the stiffened structure is achieved by adopting a model in which the stiffening beams are isolated from the plate by sections parallel to the lower outer surface of the plate. The forces at the interface, which produce lateral deflection and inplane

deformation to the plate and lateral deflection and axial deformation to the beam, are established using continuity conditions at the interface. The solution of the arising plate and beam problems, which are nonlinearly coupled, is achieved using the Analog Equation Method (A.E.M.) [5]. After the solution of the plate – beams system is achieved, the distribution of the axial stresses across the plate, resulting from both the bending and the inplane (arising from the shear forces at the interfaces) action of the plate, is obtained. Integrating this distribution across the plate and following the aforementioned definition of the effective breadth we obtain its values in the longitudinal direction of the plate. The influence of these values from the beam stiffness and their variation along the longitudinal direction of the plate are shown as compared with those obtained from various codes through numerical examples with great practical interest.

3. STATEMENT OF THE PROBLEM

Consider a thin elastic plate having constant thickness h_p , occupying the domain Ω of the x, y plane and stiffened by a set of parallel beams. The plate may have J holes while its boundary $\Gamma = \bigcup_{j=0}^J \Gamma_j$ may be piecewise smooth (Fig.1). For the sake of convenience the x_n axis is taken parallel to the beams. The plate is subjected to the lateral load, $x : \{x, y\}$ and is supported on its boundary, whereas the beams may have point supports.

For the solution of the problem at hand and the evaluation of the distribution of the axial stresses across the plate the method presented by Sapountzakis and Katsikadelis in [5] is adopted here. According to this method the stiffening beams are isolated from the plate by sections in the lower outer surface of the plate, while tractions at the fictitious interfaces are taken into account. These tractions result in the loading of the beam as well as the additional loading of the plate. Their distribution is unknown and is established by imposing displacement continuity conditions at the interfaces.

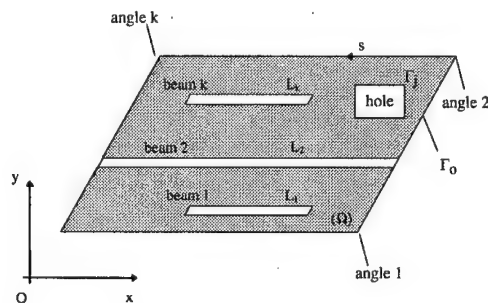


Fig.1. Two dimensional plate region Ω .

The integration of the tractions along the width of the beam result in line forces per unit length which are denoted by q_x , q_y and q_z . Taking into account that the torsional stiffness of the beam is small, the traction component q_y , in the direction normal to the beam axis is ignored. The other two components q_x and q_z produce the following loadings along the trace of each beam.

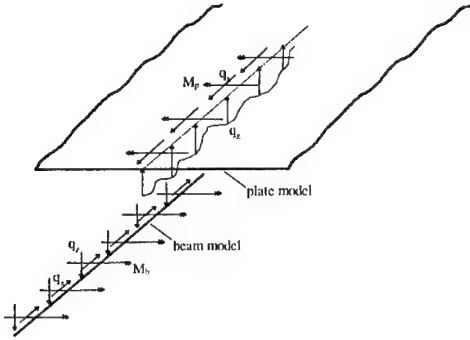
a. In the plate

- (i) A lateral line load $-q_z$ at the interface.
- (ii) A lateral line load $-\partial M_p / \partial x$ due to the eccentricity of the component q_x from the middle surface of the plate. $M_p = q_x h_p / 2$ is the bending moment.
- (iii) An inplane line body force q_x at the middle surface of the plate.

b. In each beam

- (i) A transverse load q_z .
- (ii) A transverse load $\partial M_b / \partial x$ due to the eccentricity of q_x from the neutral axis of the beam cross section.
- (iii) An inplane axial force q_x .

The structural models of the plate and the beams are shown in Fig.2.



On the base of the above considerations the response of the plate and of the beams may be described by the following boundary value problems.

a. For the plate.

The plate undergoes transverse deflection and inplane deformation. Thus, for the transverse deflection we have

Fig.2. Structural model of the plate and the beams.

$$D \nabla^4 w_p - \left(N_x \frac{\partial^2 w_p}{\partial x^2} + 2N_{xy} \frac{\partial^2 w_p}{\partial x \partial y} + N_y \frac{\partial^2 w_p}{\partial y^2} \right) = g - \sum_{k=1}^K \left(q_z^{(k)} + \frac{\partial M_p^{(k)}}{\partial x} \right) \delta(y - y_k) \quad \text{in } \Omega \quad (1)$$

$$\alpha_1 w_p + \alpha_2 V_n = \alpha_3 \quad \beta_1 \frac{\partial w_p}{\partial n} + \beta_2 M_n = \beta_3 \quad \text{on } \Gamma \quad (2a,b)$$

where $w_p = w_p(\mathbf{x})$ is the transverse deflection of the plate; $D = E_p h_p^3 / 12(1 - \nu^2)$ is its flexural rigidity with E_p being the elastic modulus and ν the Poisson ratio; $N_x = N_x(\mathbf{x})$, $N_y = N_y(\mathbf{x})$, $N_{xy} = N_{xy}(\mathbf{x})$ are the membrane forces per unit length of the plate cross section and α_i , β_i ($i = 1, 2, 3$) are functions specified on the boundary Γ .

Since linear plate bending theory is considered, the components of the membrane forces N_x , N_y , N_{xy} do not depend on the deflection w_p . They are given as

$$N_x = C \left(\frac{\partial u_p}{\partial x} + \nu \frac{\partial v_p}{\partial y} \right) \quad N_y = C \left(\nu \frac{\partial u_p}{\partial x} + \frac{\partial v_p}{\partial y} \right) \quad N_{xy} = C \frac{1 - \nu}{2} \left(\frac{\partial u_p}{\partial y} + \frac{\partial v_p}{\partial x} \right) \quad (3a,b,c)$$

where $C = E_p / (1 - \nu^2)$; $u_p = u_p(\mathbf{x})$ and $v_p = v_p(\mathbf{x})$ are the displacement components of the middle surface of the plate and are established by solving the plane stress problem, which is described by the following boundary value problem (Navier's equations of equilibrium)

$$\nabla^2 u_p + \frac{1 + \nu}{1 - \nu} \frac{\partial}{\partial x} \left[\frac{\partial u_p}{\partial x} + \frac{\partial v_p}{\partial y} \right] + \frac{1}{G_p} q_x \delta(y - y_k) = 0 \quad \nabla^2 v_p + \frac{1 + \nu}{1 - \nu} \frac{\partial}{\partial y} \left[\frac{\partial u_p}{\partial x} + \frac{\partial v_p}{\partial y} \right] = 0 \quad \text{in } \Omega \quad (4a,b)$$

$$\gamma_1 u_n + \gamma_2 N_n = \gamma_3 \quad \delta_1 u_t + \delta_2 N_t = \delta_3 \quad \text{on } \Gamma \quad (5a,b)$$

in which $G_p = E_p / 2(1 + \nu)$ is the shear modulus of the plate; N_n , N_t and u_n , u_t are the boundary membrane forces and displacements in the normal and tangential directions to the boundary, respectively; γ_i , δ_i ($i = 1, 2, 3$) are functions specified on Γ .

b. For each beam.

Each beam undergoes transverse deflection and axial deformation. Thus, for the transverse deflection we have

$$E_b I_b \frac{d^4 w_b}{dx^4} - N_b \frac{\partial^2 w_b}{\partial x^2} = q_z - \frac{\partial M_b}{\partial x} \quad \text{in } L_k, k = 1, 2, \dots, K \quad (6)$$

$$a_1 w_b + a_2 V = a_3 \quad b_1 \frac{\partial w_b}{\partial x} + b_2 M = b_3 \quad \text{at the beam ends } x = 0, l \quad (7a,b)$$

where $w_b = w_b(x)$ is the transverse deflection of the beam; $E_b I_b$ is its flexural rigidity; $N_b = N_b(x)$ is the axial force at the neutral axis; V , M are the reaction and the bending moment at the beam ends, respectively and a_i , b_i ($i = 1, 2, 3$) are coefficients specified at the boundary of the beam.

Since linear beam bending theory is considered, the axial force of the beam does not depend on the deflection w_b . The axial deformation of the beam is described by solving independently the boundary value problem i.e.

$$E_b A_b \frac{\partial^2 u_b}{\partial x^2} = -q_x \quad \text{in } L_k, k = 1, 2, \dots, K \quad (8)$$

$$c_1 u_b + c_2 N = c_3 \quad \text{at the beam ends } x = 0, l \quad (9)$$

where N is the axial reaction at the beam ends.

Eqns. (1), (4a), (4b), (6), (8) constitute a set of five coupled partial differential equations including seven unknowns, namely $w_p, u_p, v_p, w_b, u_b, q_x, q_z$. Two additional equations are required, which result from the continuity conditions of the displacements in the direction of the z and x axes at the interfaces between the plate and the beams. These conditions can be expressed as

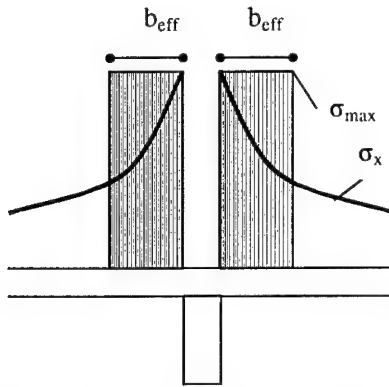
$$w_p = w_b \quad u_p - \frac{h_p}{2} \frac{\partial w_p}{\partial x} = u_b + \frac{h_b}{2} \frac{\partial w_b}{\partial x} \quad (10a,b)$$

It must be noted that the coupling of eqns (1) and (4a,b), as well as of eqns (6) and (8) is nonlinear due to the terms including the unknown membrane and axial forces, respectively.

After the solution of the aforementioned nonlinear system of equations and the evaluation of the unknown plate w_p and beam w_b deflection, the displacement components u_p, v_p of the middle surface of the plate, the axial deformation of the beam u_b and the interface forces

q_x, q_z , the distribution of the axial stresses across the plate is obtained. These stresses result from superposition of the bending and the inplane action of the plate and are given as

$$\sigma_x = -\frac{E}{1-\nu^2}z \left(\frac{\partial^2 w_p}{\partial x^2} + \nu \frac{\partial^2 w_p}{\partial y^2} \right) + C(u_p + w_p) \quad (11)$$



Integrating across the plate the evaluated distribution of the axial stresses given from eqn.(11) the effective breadth is estimated according to Timoshenko and Goodier [3] following Fig.3 and applying the following relation

$$b_{eff} = \frac{\int \sigma_x dy}{\sigma_e} \quad (12)$$

Fig.3. Timoshenko and Goodier [3] effective breadth definition.

4. NUMERICAL SOLUTION

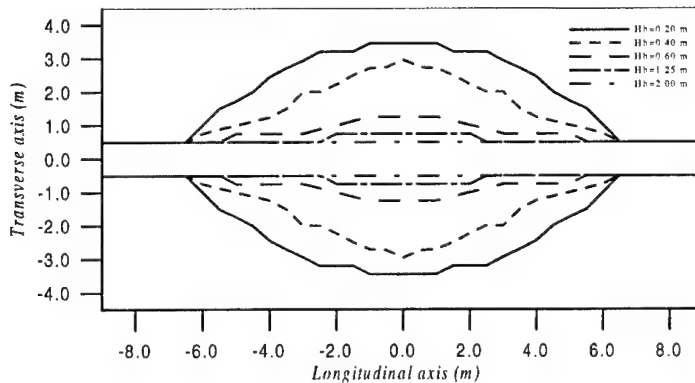


Fig.4. Effective breadth according to the definition of Timoshenko and Goodier [3] of the stiffened plate for various heights of the stiffening beam.

5. NUMERICAL EXAMPLE

A rectangular plate with dimensions $a \times b = 18.0 \times 9.0 \text{ m}$ subjected to a uniform load $g = 10 \text{ kN/m}^2$ and stiffened by a beam with width 1.0 m through the centerline of the plate has been studied. The plate is simply supported along its small edges, while the other two edges are free.

The numerical solution of the aforementioned plate and beam problems is accomplished by developing the Analog Equation Method (AEM) as this is presented in Sapountzakis and Katsikadelis [5].

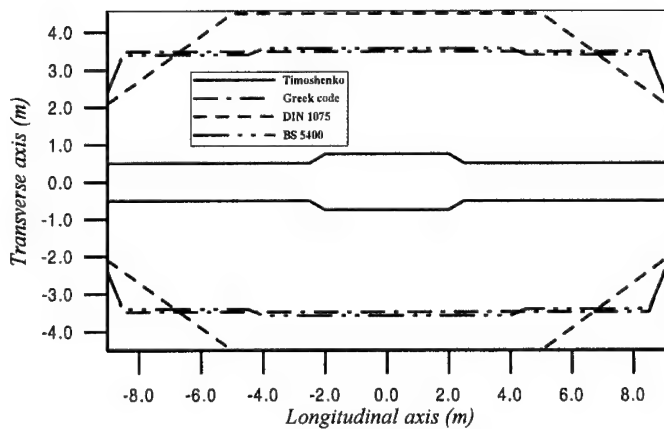


Fig.5. Effective breadth for $h_b = 1.25$ m compared with the recommendations of various codes.

The estimated values of the effective breadth according to Timoshenko and Goodier [3] for different heights of the stiffening beam are presented in Fig.4. Moreover in Fig.5 the estimated values of the effective breadth for the beam height $h_b = 1.25$ m according to Timoshenko and Goodier [3] are presented as compared with those obtained from various codes. The discrepancy between the estimated values and the code proposed ones is remarkable.

6. CONCLUDING REMARKS

- The values of the effective breadth are not constant along the stiffening beam increasing from the supported edges to the center of the stiffened structure. Also, the variation of the effective breadth is significantly reduced as the beam height is increased.
- The discrepancy between the estimated values of the effective breadth using the presented procedure and the code proposed ones is remarkable. It is worth here noting that the code proposed values are independent from the height of the stiffening beam.

7. REFERENCES

- [1] Schade, H.A., The Effective Breadth of Stiffened Plating under Bending Loads, *Transactions of the Society of Naval Architects and Marine Engineers*, 1951, 59, 403-420.
- [2] Wang, X. and Rammerstorfer, F.G., Determination of Effective Breadth and Effective Width of Stiffened Plates by Finite Strip Analysis, *Thin-Walled Structures*, Vol.26, No.24, 1996, 261-286.
- [3] Timoshenko, S.P. and Goodier, J.H., *Theory of Elasticity*, Mc-Graw-Hill, 1951, 262-268.
- [4] Lee, J.A.N., Effective Width of Tee-Beams, *The Structural Engineer*, January 1962, 21-27.
- [5] Sapountzakis, E.J. and Katsikadelis, J.T., Analysis of Plates Reinforced with Beams, *Computational Mechanics*, 2000, 26, 66-74.

ON THE STUDY OF TIE PLATES IN PIN CONNECTIONS

I. Mademlis, S. Marnoutsidis and A. V. Avdelas
Department of Civil Engineering,
Aristotle University, GR-54006 Thessaloniki, Greece

1. SUMMARY

The objective of this paper is the study of tie plates in pin connections. Because of the fundamental concept of the behaviour of pin connections, there is a significant clearance between the tie plate hole and the pin. The stress-state of the assemblage has been determined by the use of the finite element method. The results of the analysis have been compared with both the specifications of Eurocode 3 and with some experimental data.

2. INTRODUCTION

Connections are essential elements of a structure and extensive research is done in recent years on their behaviour. Pin connections are widely used in steel structures. Tie plates are used not only in pin connections but also as components of lifting modules and bridge restrainers [1]. In certain cases, as e.g. in bracings and in bridge restrainers, tie plates are not supposed to carry any load under normal loading conditions. They must respond to loading only under seismic or other horizontal excitation. The particular behaviour of tie plates in such cases has not been studied very well.

Pin connections are often used in steel structures. Among the reasons for their wide use are their limited construction demands and their predictable behavior, since they do not carry moments. Furthermore, the boundary conditions of the nodes can be easily simulated, during the analysis of the structure. In spite of their advantages, the theoretical and experimental study of the behavior of pin connections is not as extensive as it would be expected. A similar study, but in a different context can be found in [2]. A typical example of their application is given in Figure 1.

For the study of the response to loading of tie plates in pin connections, the finite element method has been used. The linear response of the connected plates, under static loads, has been examined keeping under consideration the dimensions of the plates proposed by Eurocode 3 (EC3) [3]. Between the diameter of the hole d_0 and the diameter of the pin d , relation $d_0 > d$ is always valid (Figure 2). Because of this, the contact between the pin and the connected plates is unilateral and not obstructed, the system can be freely rotated around the longitudinal axis of the pin and, finally, shear is the critical form of failure.

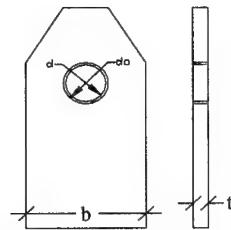
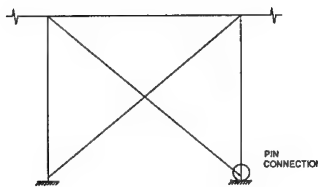


Figure 1: Typical use of pin connection Figure 2: Thickness t and length b of tie plate

3. ANALYSIS

The problem has been studied by the use of two-dimensional analysis. The simulation has been carried out in the SAP2000 finite element program [4]. For the analysis of the model, shell elements have been used. The z-axis has been assigned to the thickness t of the tie plate under consideration. The basic shape of the tie plate model has been designed using AutoCad R14 and imported in the finite element program. After that, the meshing of the elements has been realized, especially of the area near and around the hole, where a $7,5^\circ$ step has been used [7]. To each of the nodes of the contour in the radial direction spring supports have been assigned and equivalent uniform tension loads were enforced at the down part of the plate. The tension or compression of the spring supports determined whether there is contact or not respectively. As it has been shown by the analysis, the contact area is divided symmetrically by the Y-axis, forming an angle of 150° .

The unilateral contact between the pin and the plates and the loading of the plates have been taken into account by the application of appropriate assumptions in order to simulate real conditions. Two basic simplifications have been taken into account for the determination of the geometry of the contact area: a) Friction has been ignored. Thus, only radial interaction between pin and plate was considered. b) Because of the crucial role of the above load condition to the response of the connection, the study has been carried out by using different values of the tension load in the Y direction. It must be noted that the nonlinearities introduced by this unilateral contact phenomena have as a result that the contact areas between the pin and the boundary of the hole are not a priori known. For the solution of the Linear Complementarity Problem that is formulated in each solution step [5], a Quadratic Programming algorithm has been used [6].

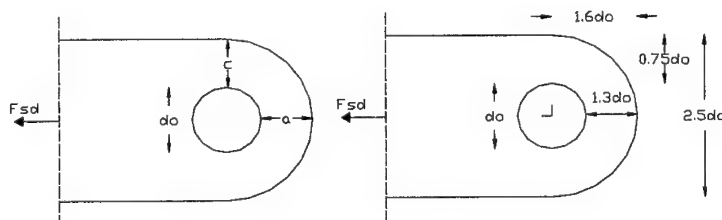


Figure 3: Geometric conditions for tie plates in pin connections [3]

The forces that correspond to each of the elements of the connection are transmitted from the pin to the plates and vice versa (depending on which plate is examined) through the contact area. For the study of the plates, the load has been applied to the shells included in the contact area in the form of an equivalent uniform load. The direction of the load vector coincides with the one of the local axis 2. By rotating the local axis of each shell at the radial direction, compatibility of the adopted load enforcement with the hypothesis of radial interaction between the pin and the plates has been obtained.

4. NUMERICAL STUDY

For the numerical study, the behavior of several cases of pin connections has been examined with the geometric characteristics of the plates and the different qualities of the materials as changing factors. The geometric characteristics of the plates have been defined according to the relevant clauses of EC3 [3], where in Table 6.5.6 the following relations are given for pin connections (Figure 3):

Type A: Constant thickness t

$$a \geq \frac{F_{sd}\gamma_{Mp}}{2tf_y} + \frac{2d_0}{3} : c \geq \frac{F_{sd}\gamma_{Mp}}{2tf_y} + \frac{d_0}{3} \quad (1)$$

Type B: Constant geometry

$$t \geq 0.7 \sqrt{\frac{F_{sd}\gamma_{Mp}}{f_y}} : d_0 \leq 2.5t. \quad (2)$$

Obviously, the above relations are satisfied for many values of the parameters used (a , c , d , t , F_{sd}). In order to give an overall qualitative view, the critical cases will be examined next. This has been done in accordance with the following steps:

- The values of diameters d and d_0 , that will be studied, have been specified.
- For each diameter d_0 , the minimum value of the thickness t has been determined, according to the second of relations (2).
- The limit load F_{cr} , which corresponds to a tie plate of given thickness t , has been determined in each case from the first of relations (2).
- Cases where the pin moment $M_{sd} \{f(t, F_{sd})\}$ is greater than the design resistance M_{rd} have been rejected.
- For the above values of d_0 and t and for $F_{sd} = F_{cr}$ the limit values of lengths a and c have been calculated from relations (1).
- For the plates, steel S235, S275 and S355 have been used. The material of the pin has been taken as 8.8 and 10.9.

In all cases, the comparison of the yield stress f_y to the maximum Von Mises stresses has been used as a failure criterion. First, the above have been solved for the loads proposed by EC3 (F_{ec3}). Next, the limit load (F_{res}) that every plate can resist, depending to its geometric characteristics, has been calculated. In the cases where $F_{res} < F_{ec3}$, the modifications imposed to the geometry of the plates have been defined by the shape of the failure mode.

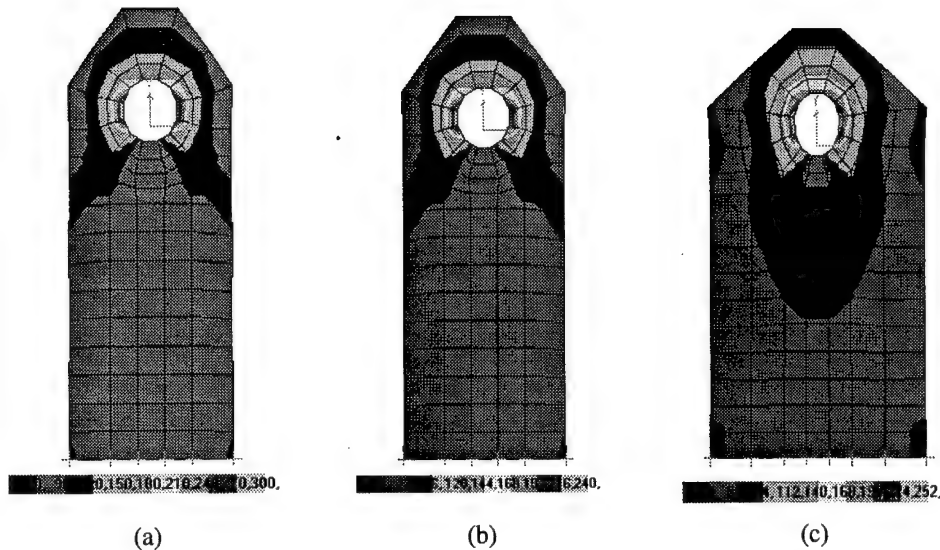


Figure 4: Stress conditions: S235, $d_0 = 30\text{mm}$, $t = 22\text{ mm}$

Under the given loads, the shape of the hole becomes oval and the maximum stresses appear at the 0° and 180° areas, tension failure of the plate occurs [8, 9]. The values of the stresses at these areas are defined by length c . In the case of failure, length c is modified in such a way that the plate is able to withstand the load proposed by EC3. In Figure 4 the stress conditions of the deformed shape for a typical case are presented: (a) for the loads and geometric characteristics given by EC3, (b) for the failure load according to the simulation and the geometric characteristics given by EC3 and (c) for the loading according to EC3 and for the length c modified in such a way that the plate does not fail.

From the combination of the second of relations (1) with the first of relations (2), relation (3) is obtained

$$c = t + \frac{d_0}{3}. \quad (3)$$

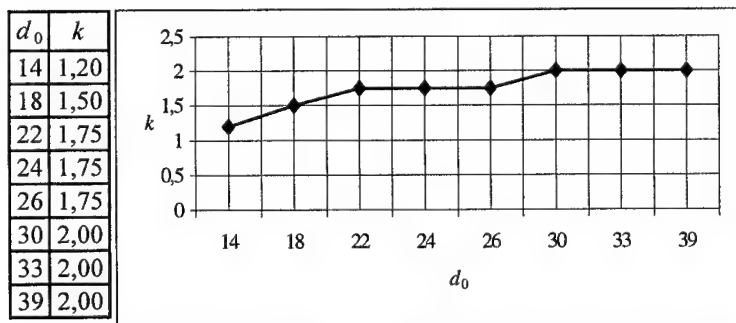
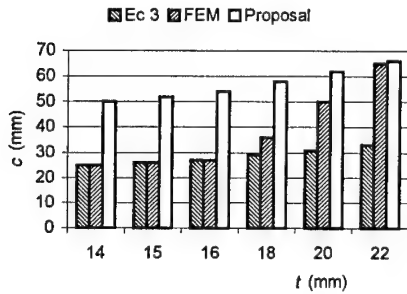
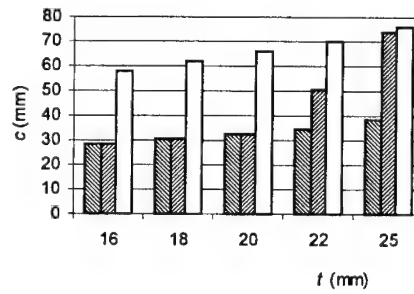
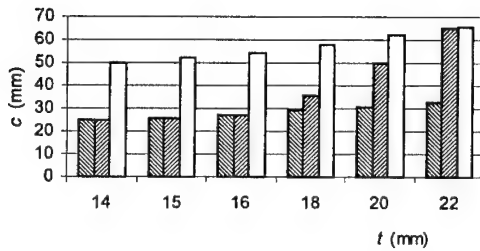
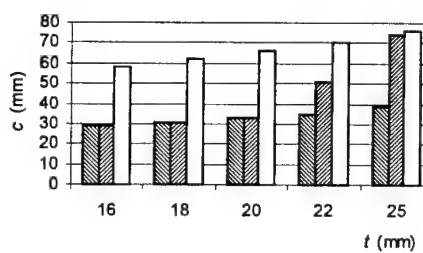
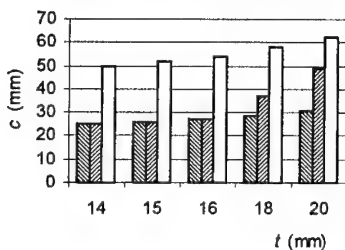
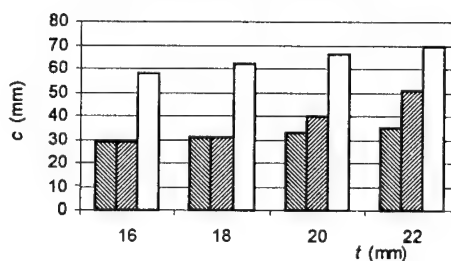


Figure 5: Values of the proposed factor k

The results derived from the study which is presented here, show that the above relation for c is not valid in some critical cases. For this reason, a modification of the relation is proposed. It must be noted that the criterion for the modification is the diameter of the hole. In the cases where EC3 is valid, the above modification contributes to the improvement of the safety of the structure. This modification takes the form of a factor k with the values given in the table of Figure 5. This factor would multiply the second part of relation (3) that takes the form

$$c = k \left[t + \frac{d_0}{3} \right]. \quad (4)$$

The above modification is valid for both the 8.8 and 10.9 material qualities of the pin, with the only difference that, because of the smaller strength of the pin material, some of the cases are excluded for the first one.

Figure 6a: $d_0=33$ mm (S235)Figure 7a: $d_0=39$ mm (S235)Figure 6b: $d_0=33$ mm (S275)Figure 7b: $d_0=39$ mm (S275)Figure 6c: $d_0=33$ mm (S355)Figure 7c: $d_0=39$ mm (S355)

Some indicative results of the procedure developed in order to achieve the aims of this paper are presented above, in diagrams of the implicated parameters.

5. CONCLUSIONS

A change has been proposed in a formula which is extensively used in steel structures. This change has been based upon the two-dimensional finite element analysis of the problem. The reliable study of the problem under consideration was feasible in the two-dimensional space due to the geometry and the loading conditions of the connections. The low value of the ratio thickness t over length b and the symmetry of the plates contributed to the simplification of the problem. The correctness of the assumptions that have been used for the study of the problem, has been verified by applying the basic concepts of the suggested simulation to a similar problem for which both computational and experimental data exist [10].

6. REFERENCES

- [1] Obata, M., Suzuki, S., Goto, Y. and Matsuura, S., Ultimate behaviors of tie plates as bridge restrainer, *ASCE Journal of Struct. Eng.*, V. 117, 10, 2884-2899 (1991).
- [2] Efraimides, S.A., Sakellariadou, H.I., Bisbos, C.D. and Panagiotopoulos, P.D., On the computation of the stress state in the plate of a steel pin connection taking into account the unilateral contact between the plate and the pin, in *Proceedings of 2nd National Congress on Computational Mechanics, Vol. 1*, D.A. Sotiropoulos and D.E. Beskos (Eds.), Technical University of Crete (1996) 454-461.
- [3] ENV1993-1-1, Eurocode 3: Design of Steel Structures - Part 1.1: General Rules and Rules for Buildings, CEN, Brussels (1992).
- [4] Sap 2000 NonLinear Manuals, Version 6.1, Computers and Structures Inc. (1997).
- [5] Panagiotopoulos, P.D., *Inequality Problems in Mechanics and Applications. Convex and Nonconvex Energy Functions*, Birkhäuser Verlag, Basel, Boston (1985).
- [6] Avdelas, A.V., The unilateral contact problem. A treatment by the use of the Keller direct method, in *Proceedings of 1st National Congress on Mechanics, Vol. 1*, T.E.E., Athens (1986) 207-234.
- [7] Ramadan, H.M., Mourad, S.A., Rashed, A.A. and Bode, H., Finite element modeling and experimental testing of single shear bolted joints, in *Advances in Civil and Structural Engineering Computing for Practice*, B.H.V. Topping (Ed.), Civil-Comp Press, Edinburgh (1998) 117-124.
- [8] Stark, J., Bijlaard, F. and Sedlacek, G., Bolted and welded connections in steel structures, in *Connections in Steel Structures*, R. Bjorhovde, J. Brozzetti and A. Colson (Eds.), Elsevier, London (1988) 8-17.
- [9] Chung, K.F. and Ip, K.H., Finite element modeling of cold-formed steel bolted connections, in *CD of the Proceedings of the 2nd European Conference on Steel Structures*, J. Studnička, F. Wald and J. Macháček (Eds.), Czech Technical University in Prague, Prague (1999) paper Nr 232.
- [10] Pasternak, H. and Komann, S., Shear behaviour of rosette joints -Tests and finite element analysis, in *CD of the Proceedings of the 2nd European Conference on Steel Structures*, J. Studnička, F. Wald and J. Macháček (Eds.), Czech Technical University in Prague, Prague (1999) paper Nr 077.

THE EFFECT OF DECK ROUGHNESS IN CONJUNCTION WITH OTHER PARAMETERS ON THE DYNAMIC RESPONSE OF STEEL HIGHWAY BRIDGES UNDER VEHICULAR LOADING

G. T. Michaltsos and D. S. Sophianopoulos

Laboratory of Metal Structures, Department of Civil Engineering
National Technical University of Athens, GR-10682 Athens, Greece

1. SUMMARY

An analytical treatment of the dynamic response of steel highway bridges is developed, under the action of moving vehicles, emphasizing on the effect of deck roughness and vehicle characteristics. Employing a saw-tooth surface roughness simulation on a single axle, two-mass vehicle model, it is found that low-width roughness combined with increasing vehicle speed dramatically increase the flexural deflections, a finding of immense importance for structural design purposes.

2. INTRODUCTION

Highway bridges traversed by moving vehicles are subjected to time-dependent forces, which are affected by numerous parameters of the structure and vehicles. One of these parameters is the road surface (deck) roughness, dealt with excessively in the recent literature. Most of the relevant studies adopt the Power Spectral Density (PSD) functions for roughness as modified by Wang and Huang [7] or the simpler harmonically varying surface irregularity presented in Cheng et al [2]. Among these one must quote the significant contributions by Fafard et al [3], Cheng and Lee [2], Huang and Wang [4], Kou and DeWolf [5] as well as by Yang et al [6]. Their findings have shown that the foregoing parameter is one of the most important factors affecting elastic dynamic response, especially applicable to steel highway bridges. The most common vehicle simulations used in the aforementioned citations are either the simple one-axle two degrees of freedom (DOFs) model or the sophisticated HS20-44 truck design model specified by AASHTO, with 11 independent DOFs.

In the present study, via the former vehicle model and a saw-tooth roughness simulation, a fully analytical treatment of the vibration of steel highway bridges under vehicular loading is presented, leading to significant findings of great importance for structural design purposes. A more detailed parametric study of the whole scientific subject would undoubtedly lead to even more useful results, which could be directly incorporated into Code Specifications, concerning asphalt deck quality and allowable vehicle speed when crossing a steel highway bridge, which performs elastically in the majority of cases.

3. MATHEMATICAL FORMULATION

Modeling of deck roughness and moving vehicle

In order to perform a fully analytical, yet comprehensive, treatment of the forced vibration of bridges with rough decks under vehicular loading, we simulate the roughness by a saw-tooth model shown in Fig.1a. This approach - though quite simplifying compared with the PSD functions often used in the relevant literature - is realistic and representative for the majority of asphalt surfaces in use through the last decade. Furthermore, the well known two-axle sprung-unsprung two-mass (M, m_0), spring-damper (k_v, c_v) model of Fig.2b is chosen for the simulation of the moving vehicle, which is considered crossing the bridge with constant velocity v .

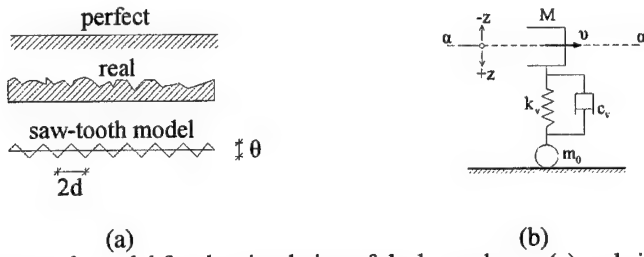


Figure 1 : Saw-tooth model for the simulation of deck roughness (a) and single axle moving vehicle model (b).

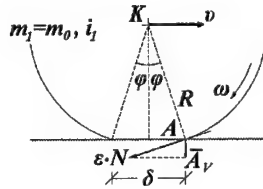


Figure 2 : Impact forces between rough deck and vehicle wheel.

In as much as, the main problem in dealing with the models adopted is to evaluate the forces developing on the bridge due to the impact of the tires on the rough deck as well as to establish the behavior of the bridge interacting with the vehicle simulation. In doing the former, one must resort to the principles of rotational impact theory, one of which clearly dictates that when two rigid bodies, with angular velocities and moments of inertia $\omega_{i,f}$ and I_i , $i=1,2$ respectively collide against each other, after their impact the new angular velocity of the first body is given by the relation

$$\omega_{1,\alpha} = \frac{(I_1 - \epsilon I_2) \omega_{1,f} + (1 + \epsilon) I_2 \omega_{2,f}}{I_1 + I_2} \quad (1)$$

where ϵ is the percentage of the remaining energy after the impact, varying usually between 0.70 and 0.90. Furthermore, when a vehicle travels on an asphalt road surface, there always exists a flat part in full contact with the deck of with δ , as shown in Fig.3. For the tire-deck impact it is evident that

$$I_2 = \infty, \quad \omega_{2,f} = 0, \quad \omega_1 = v/R, \quad I_1 = m_0 R / \sqrt{2} \quad (2)$$

Substituting the latter into eq.(2) we may find that the impact force on the deck is equal to

$$\bar{A}_v = \frac{\varepsilon m_0 v}{4} \frac{\delta}{R} \quad (3)$$

Forced vibration analysis

Let us consider the elastic undamped forced vibration of a simply supported bridge of length ℓ with constant cross-section, mass per unit length m and flexural rigidity EI , acted upon by the vehicle model adopted, moving across its rough deck (according to the aforementioned simulation) with constant velocity v , as depicted in Fig.3.

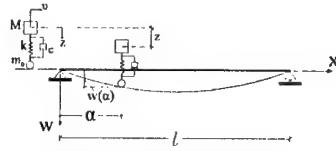


Figure 3 : Geometry and sign convention of a simply supported bridge acted upon by the chosen vehicle model.

The governing equation of motion is thus given by the following expression

$$EI w''''(x, t) + m \ddot{w}(x, t) = (P_v + P_{imp}) \delta(x - a) \quad , \quad a = vt \quad (4)$$

where

$$\left. \begin{aligned} P_v &= Mg - M\ddot{z} + m_0 g - m_0 \ddot{w} \\ P_{imp} &= \bar{A}_v \sum_{i=1}^s \delta(t - t_i) \end{aligned} \right\} \quad (5)$$

are the dynamic forces due to the vehicle and roughness respectively, with

$$\left. \begin{aligned} t_i &= t_{i-1} + 2d/v \\ M\ddot{z} &= K[w(\alpha) - z] + c[\dot{w}(\alpha) - \dot{z}] \end{aligned} \right\} \quad (6)$$

For a bridge initially at rest, the solution of (4) is the sum of its particular solutions due to P_v and P_{imp} to be evaluated. In doing this, it is well known that the modal expression of the flexural deflection of a beam as in Fig.3. under the action of a constant force $P = (M + m_0)g$ crossing its span with constant velocity v is given by:

$$\left. \begin{aligned} w_n(x, t) &= \sum_n X_n(x) P_n(t) \quad \text{where} \quad X_n(x) = \sin \frac{n\pi x}{\ell} \\ P_n(t) &= \frac{2(M + m_0)g}{m\ell} \frac{1}{\omega_n^2 - \Omega_n^2} \left[\sin \Omega_n t - \frac{\Omega_n}{\omega_n} \sin \omega_n t \right] \quad , \quad \Omega_n = \frac{n\pi v}{\ell} \end{aligned} \right\} \quad (7)$$

Considering at first the effect of the moving vehicle, and introducing the latter expression as a first approximation, combination of eqs.(4), (6) and (7) yields

$$EIw'''' + m\ddot{w} = \left[(M + m_0)g - M\ddot{z} - m_0 \sum_n X_n(\alpha) \ddot{P}_n(t) \right] \delta(x - \alpha) \quad (8)$$

$$M\ddot{z} + c\dot{z} + Kz = c \sum_n X_n(\alpha) \dot{P}_n(t) + K \sum_n X_n(\alpha) P_n(t) \quad (9)$$

Seeking solutions of the form

$$w(x, t) = \sum_n X_n(x) T_n(t) \quad , \quad z(t) = \sum_n \Pi_n(t) \quad (10)$$

and equalizing the same modes we get:

$$\ddot{\Pi}_n(t) + 2\beta\dot{\Pi}_n(t) + \gamma^2 \Pi_n(t) = \Phi_n(t) \quad (11)$$

where

$$\left. \begin{aligned} \Phi_n(t) &= 2\beta X_n(\alpha) \dot{P}_n(t) + \gamma^2 X_n(\alpha) P_n(t) \\ \beta &= c / 2M \quad , \quad \gamma = \sqrt{K / M} \end{aligned} \right\} \quad (12)$$

which according to Duhamel's formula possesses the following solution

$$\left. \begin{aligned} \Pi_n(t) &= \frac{1}{\zeta} \int_0^t e^{-\beta(t-\tau)} \Phi_n(\tau) \sin \zeta(t-\tau) d\tau \\ \zeta &= \sqrt{\gamma^2 - \beta^2} \end{aligned} \right\} \quad (13)$$

Introducing the above into relations (10) and the total result into eq.(8), after some elaboration, we obtain

$$\ddot{T}_n(t) + \omega_n^2 T_n(t) = \Theta_n(t) \Rightarrow T_n(t) = \frac{1}{\omega_n} \int_0^t \Theta_n(\tau) \sin \omega_n(t-\tau) d\tau \quad (14)$$

where

$$\Theta_n(t) = \frac{2}{m\ell} \left[(M + m_0)g \sin \Omega_n t - M \sin \Omega_n t \sum_n \ddot{\Pi}_n - m_0 \sin \Omega_n t \sum_n \sin \Omega_n t \ddot{P}_n(t) \right] \quad (15)$$

Furthermore, for a random irregularity located at $x = \alpha_r = \nu t_r$, we may evidently write that

$$EIw'''' + m\ddot{w} = \bar{A}_{\nu, r} \delta(x - \alpha_r) \delta(t - t_r) \quad (16)$$

and introducing a series solution

$$w(x, t) = \sum_n X_n(x) B_n(t) \quad (17)$$

we finally find that

$$B_n(t) = \left. \begin{aligned} & \frac{2\bar{A}_{v,r}}{m\ell\omega_n} \int_0^t X_n(v\tau) \sin\omega_n(t-\tau) \delta(\tau-t_r) \\ & = \frac{2\bar{A}_{v,r}}{m\ell\omega_n} X_n(vt) \sin\omega_n(t-t_r) \text{ for } t > t_r \end{aligned} \right\} \quad (18)$$

Thus, for r irregularities due to a rough deck as in the simulation adopted, the solution takes the following final form:

$$w(x,t) = \frac{2\bar{A}_{v,r}}{m\ell\omega_n} \sum_n X_n(x) \sum_l^r \sin\Omega_n t_r \sin\omega_n(t-t_r) \quad (19)$$

with r being the integer part of the quantity $\frac{vt}{2d}$.

In the sequel, the total solution of the equation of motion given in (4) is equal to the sum of the by-products of the foregoing analytical procedure prescribed in eqs.(10), (14) and (19).

4. NUMERICAL EXAMPLE

Although a full parametric study is now in order, the length limitations of the manuscript allows us to present results regarding the effect of the deck roughness in conjunction with the vehicle speed on the dynamic response of the bridge, keeping all the other characteristics constant, but within realistic values. Consequently the exemplary bridge, impact and vehicle parameters are chosen as follows:

$\ell = 100 \text{ m}$, $m \rightarrow 40 \text{ kN/m}$, $I = 1.50 \text{ m}^4$, $m_0 \rightarrow 500 \text{ N}$, $M \rightarrow 2.5 \text{ kN}$, $\delta = 10 \text{ cm}$, $\varepsilon = 0.80$, $k_v = 60000 \text{ N/m}$, $c_v = 1000 \text{ Nsec/m}$, $R = 35 \text{ cm}$.

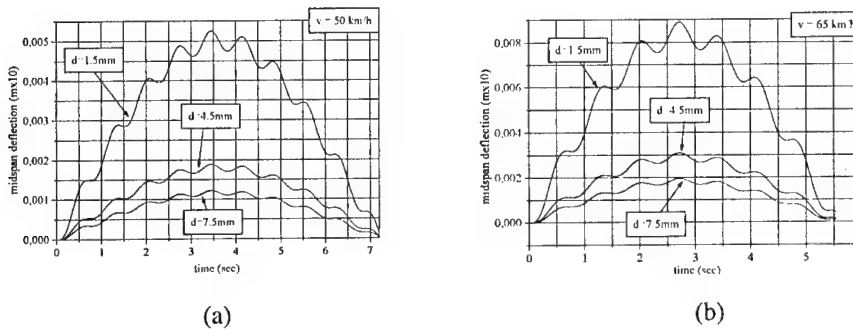


Figure 4 : Midspan deflection versus vehicle passage time t for the exemplary bridge-vehicle configuration for $v=50$ and (b) $v=65 \text{ km/h}$ and three values of the roughness parameter d .

Applying the preceding analysis and after performing cumbersome symbolic integral computations, the midspan flexural deflection of the bridge is computed, for the time required

for the vehicle to cross its span, for two vehicle velocities (50 and 65 km/h) and three values of the roughness parameter $d=1.5, 4.5$ and 7.5mm . It is found that the decrease of roughness width d (implying increase of tire impacts) has a devastating effect on the dynamic response of the bridge, since the corresponding dynamic amplification factor may as well reach the value of 5. This effect is more pronounced with increasing vehicle speed, due to the impact forces are directly proportional to it. These findings, on which a more accurate structural design of bridges with rough decks may be based, can be comprehensively perceived throughout Fig.4, depicting time-midspan deflection plots for the d, v cases considered.

5. CONCLUSIONS

The main conclusions of the present study are:

- a) Through a single axle, two-mass, spring-damper vehicle model and a saw tooth deck roughness simulation, a fully analytical modal-based treatment of the forced vibration of a bridge is evidently presented, based on the impact forces between deck and vehicle tire and the bridge-vehicle interaction.
- b) Varying the deck roughness parameter and vehicle velocity, the effect of the combination of these parameters is established. The decrease of roughness width d when accompanied with increasing vehicle velocity v drastically amplifies the flexural deformations of the bridge, a finding of great importance for structural design purposes.

6. REFERENCES

- [1] Chang, D. and Lee, H., Impact factors for simple-span highway girder bridges, *Journal of Structural Engineering* 120(3), 704-715 (1994).
- [2] Cheng, Y. S., Au, F. T. K., Cheung, Y. K. and Zheng, D. Y., On the Separation Between Moving Vehicles and Bridge, *Journal of Sound and Vibration* 222(50), 781-810 (1999).
- [3] Fafard, M., Laflamme, M., Savarad, M. and Bennur, M., Dynamic Analysis of Existing Continuous Bridge, *Journal of Bridge Engineering* 3(1), 28-37 (1998).
- [4] Huang, D. P. and Wang, T.-L., Vibration of highway steel bridges with longitudinal grades, *Computers & Structures* 69(2), 235-245 (1998).
- [5] Kou, J.-W. and DeWolf, J. T., Vibrational behavior of continuous span highway bridge-influencing variables, *Journal of Structural Engineering* 123(3), 333-344 (1997).
- [6] Yang, Y.-B., Liao, S.-S. and Lin, B.-H., Impact Formulas for Vehicles Moving over Simple and Continuous Beams, *Journal of Structural Engineering* 121(11), 1644-1650 (1995).
- [7] Wang, T.-L., Huang, D., Cable-stayed bridge vibration due to road surface roughness, *Journal of Structural Engineering* 118(5), 1354-1374 (1995).

LQR AND H^∞ OPTIMAL STRUCTURAL CONTROL IN ASEISMIC DESIGN

E.C. Zacharenakis

Department of Civil Engineering
Technological Educational Institute of Crete, GR-71500 Heraklion, Greece

K.G. Arvanitis

Department of Agricultural Engineering
Agricultural University, GR-11855 Athens, Greece

A.G. Soldatos

Department of Electrical and Computer Engineering
National Technical University, GR-15773 Athens, Greece

G.E. Stavroulakis

Department of Mathematics
University of Ioannina, GR-45110 Ioannina, Greece
Department of Civil Engineering
Carolo Wilhelmina Technical University, D- Braunschweig, Germany

1. SUMMARY

Classical linear-quadratic-regulators (LQR), provide the basis of well-known active optimal problems in mechanical engineering. They concern control of linear dynamical systems with a quadratic cost function. Their efficiency deteriorates as the uncertainty of the loading and/or of the structural system becomes higher. Robust control theories (e.g., the H^∞ control) have been developed recently to solve this problem. It is obvious that in civil engineering, and especially in aseismic design, uncertainty is higher than in other engineering applications. The present numerical comparison between two representatives of the above classes of control theories demonstrates their common points and their differences, and continues a number of recent research efforts to introduce innovative control concepts in structural dynamics for civil engineering [1,2,4,5,6].

2. LQR AND H^∞ CONTROL DESIGNS

Throughout this work, our interest is focused on linear time-invariant finite dimensional dynamical systems having the standard state space form

$$\dot{\mathbf{x}}(t) = \mathbf{A}\mathbf{x}(t) + \mathbf{B}\zeta(t) + \mathbf{D}q(t) \quad (1)$$

$$\mathbf{y}_m(t) = \mathbf{C}\mathbf{x}(t) + \mathbf{N}\mathbf{w}(t) \quad , \quad \mathbf{y}_c(t) = \mathbf{E}\mathbf{x}(t) + \mathbf{J}\mathbf{q}(t) \quad (2)$$

where, $\mathbf{x}(t) \in \mathbb{R}^n$ is the state vector, $\boldsymbol{\zeta}(t) \in \mathbb{R}^m$ is the input or control vector, $\mathbf{q}(t) \in \mathbb{R}^d$ is the external loading vector, $\mathbf{w}(t) \in \mathbb{R}^n$ is the external disturbance vector, $\mathbf{y}_m(t) \in \mathbb{R}^{p_1}$ is the vector of measurement (observed) outputs, $\mathbf{y}_c(t) \in \mathbb{R}^{p_2}$ is the controlled output vector, and where all the matrices have real entries and appropriate dimensions. A linear state feedback control law is studied, of the form:

$$\boldsymbol{\zeta}(t) = \mathbf{F}\mathbf{x}(t) \quad (3)$$

In LQR, the control is determined such that the following quadratic performance index be minimized:

$$J = \frac{1}{2} \int_0^{t_f} (\mathbf{x}^T(t) \mathbf{Q} \mathbf{x}(t) + \boldsymbol{\zeta}^T(t) \mathbf{R} \boldsymbol{\zeta}(t)) dt \quad (4)$$

with $\mathbf{Q} = \mathbf{Q}^T \geq \mathbf{0}$ and $\mathbf{R} = \mathbf{R}^T > \mathbf{0}$. The case of robust and H^∞ -controllers is more delicate. Let us consider the closed-loop system in frequency domain,

$$\mathbf{Y}_c(s) = \mathbf{E}(s\mathbf{I}_n - \mathbf{A} - \mathbf{B}\mathbf{F})^{-1} \mathbf{D}\mathbf{Q}(s) = \mathbf{H}_{qy_c}(s) \mathbf{Q}(s) \quad (5)$$

where $\mathbf{H}_{qy_c}(s) \triangleq \mathbf{E}(s\mathbf{I}_n - \mathbf{A} - \mathbf{B}\mathbf{F})^{-1} \mathbf{D}$ denotes the transfer function between the external disturbances and the controlled outputs, and $\mathbf{Y}_c(s)$ and $\mathbf{Q}(s)$ denote the Laplace transforms of $\mathbf{y}_c(t)$ and $\mathbf{q}(t)$, respectively.

The H^∞ -norm of $\mathbf{H}_{qy_c}(s)$ is defined by the following chain of relations

$$\begin{aligned} \|\mathbf{H}_{qy_c}(s)\|_\infty &= \sup_{s=j\omega} \left\{ \|\mathbf{H}_{qy_c}(s) \mathbf{Q}(s)\|_2 : \mathbf{Q}(s) \in \mathbf{H}_2, \|\mathbf{Q}(s)\|_2 = 1 \right\} = \sup_{s=j\omega} \left\{ \|\mathbf{Y}_c(s)\|_2 : \mathbf{Q}(s) \in \mathbf{H}_2, \|\mathbf{Q}(s)\|_2 = 1 \right\} \\ &= \sup_{\omega} \sigma_{\max} [\mathbf{H}_{qy_c}(j\omega)] \end{aligned} \quad (6)$$

where, in general, $\|\mathbf{F}(s)\|_2$ denotes the 2-norm of a signal $\mathbf{f}(t)$ in the frequency domain, i.e.:

$$\|\mathbf{F}(s)\|_2 = \left\{ \frac{1}{2\pi} \int_{-\infty}^{+\infty} \mathbf{F}^*(j\omega) \mathbf{F}(j\omega) d\omega \right\}^{1/2} \quad (7)$$

Here, $\mathbf{F}(j\omega)$ is the frequency domain signal, ω is the angular frequency and $(\bullet)^*$ refers to the complex conjugate transpose. Moreover, in (6), \mathbf{H}_2 is the Hardy space referring to the class of functions, which are analytic and bounded in the open right half plane, i.e.

$$\mathbf{H}_2 = \{ \mathbf{F} : \mathbf{F}(s) \text{ is analytic in } \operatorname{Re}(s) > 0 \text{ and } \|\mathbf{F}\|_2 < \infty \}$$

and $\sigma_{\max}(\bullet)$ denotes to the largest singular value of a matrix.

Relation (6) actually means that $\|\mathbf{H}_{qy_c}(s)\|_\infty$ is the maximum energy of the output $\mathbf{y}_c(t)$ for every disturbance $\mathbf{q}(t)$ with unit energy, i.e. $\|\mathbf{Q}(s)\|_2 = 1$.

The continuous-time state feedback H^∞ -disturbance attenuation problem (also called the continuous-time minimum H^∞ -norm regulation problem), can then be stated as follows:

Given a constant $\gamma \in \mathbb{R}^+$, find, a suitable control of the form (3) such that, simultaneously,

- (i) the closed-loop system is internally stable.

(ii) the H^∞ -norm of $\mathbf{H}_{q_{y_c}}(s)$ satisfies the bound $\|\mathbf{H}_{q_{y_c}}(s)\| < \gamma$.

For technological reasons we consider the case where $\mathbf{J} = \mathbf{0}$, and we study the behaviour for a small fixed θ , such that: $\mathbf{J} = \theta \hat{\mathbf{J}}$, $\theta > 0$, $\theta \rightarrow 0$, $\hat{\mathbf{J}}^T [\hat{\mathbf{J}} \quad \mathbf{E}] = [\mathbf{I} \quad \mathbf{0}]$.

3. LQR VERSUS H^∞ CONTROL FOR A SEISMICALLY EXCITED SHEAR-TYPE FRAME

In this example, continuous-time state feedback LQ regulation is compared to the continuous-time state feedback H^∞ control technique. To this end, consider the six-story full-scale shear-beam-type building with identical floors reported in [3]. In this structure, there are two actuators, one on the first floor and another on the third floor, both x-shaped active bracing systems. The mass of each floor, and the stiffness and damping coefficients of each story unit are: $m_i = 345.6 \text{ t}$, $\kappa_i = 3.404 \times 10^5 \text{ kN}$ and $c_i = 2937 \text{ kNs/m}$. According to [3], a state-space model of the form (1), (2), can be easily obtained after straightforward manipulations of the dynamical model:

$$\mathbf{M}\ddot{\mathbf{u}}(t) + \tilde{\mathbf{C}}\dot{\mathbf{u}}(t) + \mathbf{K}\mathbf{u}(t) = \mathbf{M}_0\ddot{\mathbf{u}}_g + \mathbf{B}_0\zeta(t) \quad (8)$$

where $\mathbf{M} \in \mathbb{R}^{k \times k}$ is the mass matrix, $\tilde{\mathbf{C}} \in \mathbb{R}^{k \times k}$ is the damping matrix, $\mathbf{K} \in \mathbb{R}^{k \times k}$ is the stiffness matrix, $\ddot{\mathbf{u}}_g \in \mathbb{R}^g$ is the ground earthquake acceleration vector (the load), $\mathbf{u}(t) \in \mathbb{R}^k$ is the nodal displacement vector, $\dot{\mathbf{u}}(t) \in \mathbb{R}^k$ is the velocity vector and $\ddot{\mathbf{u}}(t) \in \mathbb{R}^k$ is the acceleration vector. Moreover, $\mathbf{M}_0 \in \mathbb{R}^{k \times g}$ and $\mathbf{B}_0 \in \mathbb{R}^{k \times m}$, are the loading and control forces arrangement matrices, respectively. For the six-story shear-type frame $k=6$, $g=1$. Details can be found in Section 7 of [6]. Considering as controlled system outputs the interstory drifts, and by using the earthquake ground motion of Figure 1, representative results of the two control systems are outlined here. More detailed investigation is included in [6].

Our purpose is to design LQ and H^∞ regulators, in order to attenuate the effect of the earthquake ground motion to the interstory drifts.

We begin our analysis by first designing an LQ optimal regulator with weight matrices $\mathbf{Q} \in \mathbb{R}^{6 \times 6}$ and $\mathbf{R} \in \mathbb{R}^{2 \times 2}$ as $\mathbf{Q} = \text{diag}\{10^8\}$ and $\mathbf{R} = \mathbf{I}_2$. In this case, we obtain

$$\mathbf{F} = 10^4 \times \begin{bmatrix} -0.0147 & 3.8123 & -2.2004 & -0.0096 & -1.1796 & -1.2987 \\ -0.0096 & 3.0357 & -2.1866 & 0.0147 & -4.0439 & 1.4209 \\ -0.9498 & 0.0585 & -0.0462 & -0.0222 & -0.0379 & -0.0281 \\ 0.0215 & 0.0613 & -0.0006 & 0.8792 & -0.0327 & 0.0133 \end{bmatrix} \quad (9)$$

In Figures 2a and 2b, the first and fourth interstory drifts of both the uncontrolled and the controlled system are depicted, when the disturbance signal of Figure 1, excites the structure. Similar results can be obtained for the remaining interstory drifts. Clearly, the effect of the disturbance on the system outputs is attenuated in the controlled structure.

We are now able to proceed with the design of state feedback H^∞ regulators for the structure. To this end, observe first that, in the present case, for the open-loop system, we have

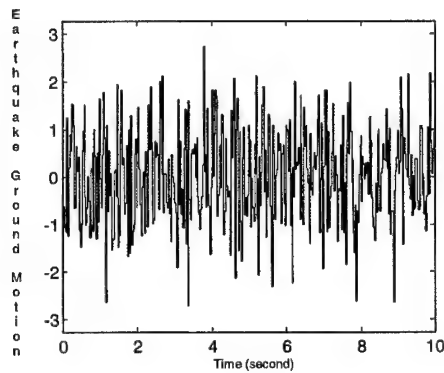


Figure 1. Earthquake ground motion considered.

$\|E(sI - A)^{-1}D\|_{\infty} = 0.147$. The above numerical value gives us the amount of the detrimental effect of the seismic load to the interstory drifts. In Figure 3a, the largest singular value of $E(sI - A)^{-1}D$ is depicted as function of the frequency ω .

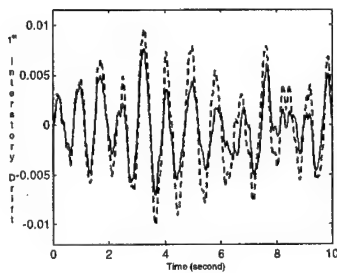


Figure 2a. First interstory drifts of the uncontrolled (dashed line) and the controlled system (solid line) with the controller (9).

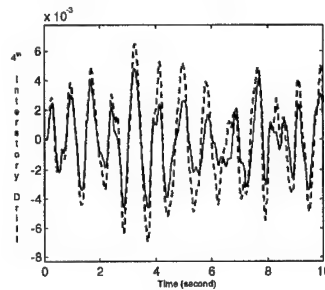


Figure 2b. Fourth interstory drifts of the uncontrolled (dashed line) and the controlled system (solid line) with the controller (9).

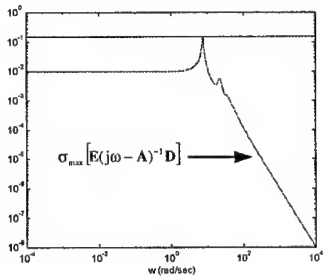


Figure 3a. The largest singular value of the transfer function of the uncontrolled system.

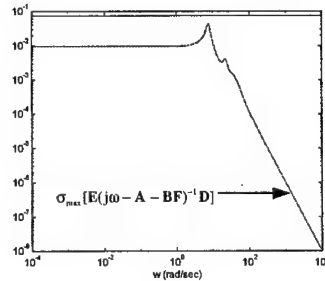


Figure 3b. The largest singular value of the closed-loop transfer function.

For $\gamma=0.075$ and $\theta=10^{-10}$ we obtain:

$$\mathbf{F} = 10^4 \times \begin{bmatrix} -1.4412 & 0.1218 & 0.0864 & 0.0299 & -0.0416 & -0.0523 \\ 0.0323 & 0.0405 & -0.0091 & 1.4390 & -0.1016 & -0.0650 \\ -0.6326 & -0.4984 & -0.3846 & -0.2823 & -0.1860 & -0.0925 \\ 0.2826 & 0.2886 & 0.3028 & 0.3296 & 0.2106 & 0.1027 \end{bmatrix} \quad (10)$$

In Figure 3b, the largest singular value of $\mathbf{H}_{qy_c}(s) = \mathbf{E}(s\mathbf{I} - \mathbf{A} - \mathbf{BF})^{-1}\mathbf{D}$ is depicted as function of ω . The desired disturbance attenuation level is satisfied. Moreover, in Figures 4a and 4b, the first and fourth interstory drifts of both controlled and uncontrolled systems are compared.

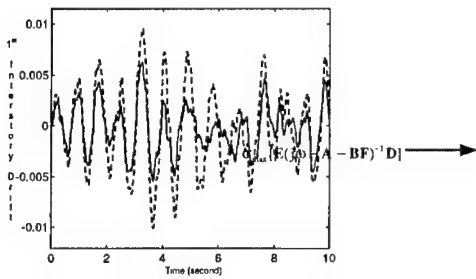


Figure 4a. First interstory drifts of the uncontrolled (dashed line) and the controlled system (solid line) with the H^∞ -controller (10).

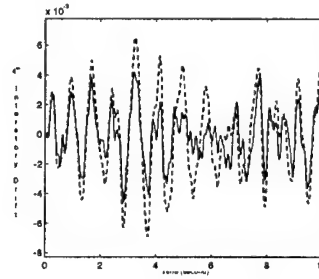


Figure 4b. Fourth interstory drifts of the uncontrolled (dashed line) and the controlled system (solid line) with the H^∞ -controller (10).

Note that, if the restrictions are contradictory no solution can be found. For example, the minimum achievable disturbance attenuation level is $\gamma=0.011$ (for $\theta=10^{-13}$), since below this level, the Riccati equation associated with the H^∞ -control problem admits no positive semi-definite solutions.

4. DISCUSSION

From the results obtained from the application of the H^∞ control technique, we arrive at the conclusion that, in the design of H^∞ controllers, similarly to that of LQ regulators, the less the effect of the disturbance on the system output we want to achieve, the largest must be the value of the control law.

It is also clear from a simple comparison of the results obtained from the application of a state feedback LQ regulator and a state feedback H^∞ controller, that an H^∞ controller attenuates system disturbances better than an LQ regulator, at the expense of almost the same (if not lower in some cases) control effort

5. REFERENCES

- [1]. Zacharenakis, E. C. and Arvanitis, K.G., H^∞ -norm regulation in structural analysis using multirate-output controllers. ZAMM 80, 363-376 (2000).
- [2]. Arvanitis, K.G., Zacharenakis, E. C. and Soldatos, A. G., Optimal noise rejection in structural analysis by means of generalized sampled-data hold functions, Journal of Global Optimization 17, 19-42 (2000).
- [3]. Jabbari, F., Schmitendorf, W. E. and Yang, J. N. H_∞ control for seismic-excited buildings with acceleration feedback, ASCE Journal of Engineering Mechanics 121, 994-1002 (1995).
- [4]. Kelly, J. M., Leitmann, G. and Soldatos, A. G., Robust control of base-isolated structures under earthquake excitation, Journal of Optimization Theory and Applications 53, 159-180 (1987).
- [5]. Zacharenakis, E. C. and Stavroulakis, G. E., On the seismic disturbance rejection of structures, Journal of Global Optimization 17, 403-410 (2000).
- [6]. Arvanitis, K. G., Zacharenakis, E. C., Soldatos, A. G. and Stavroulakis, G. E., New trends in optimal structural control, In: *Stability, Vibration and Control of Systems*, A. Guran, A. Belyaev (Eds), World Scientific Publishers (invited Chapter of ca. 100 pages, to appear).

RELIABILITY BASED OPTIMIZATION USING NEURAL NETWORKS

M. Papadrakakis and N. D. Lagaros

Institute of Structural Analysis & Seismic Research (ISASR)
National Technical University of Athens, Zografou Campus, 15780 Athens, Greece

1. SUMMARY

In this paper a robust and efficient methodology is presented for treating large-scale reliability-based, structural optimization problems. The optimization part is performed with evolution strategies, while the reliability analysis is carried out with the Monte Carlo simulation (MCS) method incorporating the importance sampling technique for the reduction of the sample size. The elasto-plastic analysis phase, required by the MCS, is replaced by a neural network predictor in order to predict the necessary data for the MCS procedure. The use of neural networks is motivated by the approximate concepts inherent in reliability analysis and the time consuming repeated analyses required by MCS. A training algorithm is implemented for training the NN utilizing available information generated from selected elasto-plastic analyses.

2. INTRODUCTION

Reliability analysis methods have developed significantly over the last decades and have stimulated the interest for the probabilistic optimum design of structures (Schueller) [1]. Despite the theoretical advancements in the field of reliability analysis serious computational obstacles arise when treating realistic problems. In particular, the reliability-based optimization (RBO) of large-scale structural systems is an extremely computationally intensive task, as shown by Tsompanakis and Papadrakakis [2]. Despite the improvement on the efficiency of the computational aspects of the reliability analysis techniques, they still require disproportionate computational effort for treating practical reliability problems. This is the reason why very few successful numerical investigations are known in the field of RBO and are mainly restricted to 2-D frames and trusses.

In the present study the reliability-based sizing optimization of large-scale multi-storey 3-D frames is investigated. The objective function is the weight of the structure while the constraints are both deterministic (stress and displacement limitations) and probabilistic (the overall probability of failure of the structure). Randomness of loads, material properties, and member geometry are taken into consideration in reliability analysis using Monte Carlo simulation. The probability of failure of the frame structures is determined via a limit elasto-plastic analysis.

The optimization part is solved using evolution strategies (ES), which in most cases are more robust and present a better global behaviour than mathematical programming methods

(Papadrakakis et. al.) [3]. The limit elasto-plastic analyses required during the MCS are replaced by NN predictions. The use of NN is motivated by the approximate concepts inherent in reliability analysis and the time consuming repeated analyses required for MCS. An NN is trained first utilizing available information generated from selected conventional elasto-plastic analyses. The limit state analysis data is processed to obtain input and output pairs, which are used to produce a trained NN. The trained NN is then used to predict the critical load factor due to different sets of basic random variables. It appears that the use of a properly selected and trained NN can eliminate any limitation on the sample size used for MCS and on the dimensionality of the problem, due to the drastic reduction of the computing time required for the repeated limit elasto-plastic analyses.

3. STUCTURAL RELIABILITY ANALYSIS

The reliability of a structure or its probability of failure is an important factor in the design procedure since it quantifies the probability under which a structure will fulfil its design requirements. Structural reliability analysis is a tool that assists the design engineer to take into account all possible uncertainties during the design, construction phases and lifetime of a structure in order to calculate its probability of failure p_f . A time invariant reliability analysis produces the following relationship

$$p_f = p[R < S] = \int_{-\infty}^{\infty} F_R(t) f_S(t) dt = 1 - \int_{-\infty}^{\infty} F_S(t) f_R(t) dt \quad (1)$$

in which R denotes the structure bearing capacity and S the external loads. The randomness of R and S can be described by known probability density functions $f_R(t)$ and $f_S(t)$, with $F_R(t) = p[R < t]$, $F_S(t) = p[S < t]$ being the cumulative probability density functions of R and S , respectively.

Most often a limit state function is defined as $G(R, S) = S - R$ and the probability of structural failure is given by

$$p_f = p[G(R, S) \geq 0] = \int_{G \geq 0} f_R(R) f_S(S) dR dS \quad (2)$$

It is practically impossible to evaluate R analytically for complex and/or large-scale structures. In such cases the integral of Eq. (2) can be calculated only approximately using either simulation methods, such as the Monte Carlo simulation method, or by using approximation methods. First and second order approximation methods (FORM and SORM) lead to formulations that require prior knowledge of the means and variances of the random variables and the definition of a differentiable failure function. On the other hand, MCS methods require that the probability density functions of all random variables must be known prior to the reliability analysis. For small-scale problems FORM and SORM implementations have been proved very efficient, but when the number of random variables increases and the problems become more complex MCS based methods have been proven more reliable.

4. BASIC STUCTURAL RELIABILITY ANALYSIS

The aim of the present study is to train a neural network to provide computationally inexpensive estimates of analysis outputs required during the MCS process. A trained neural network presents some distinct advantages over the numerical computing paradigm. It provides a rapid mapping of a given input into the desired output quantities, thereby enhancing the efficiency of the structural analysis process. This major advantage of a trained NN over the conventional procedure, under the provision that the predicted results fall within acceptable tolerances, leads to results that can be produced in a few clock cycles, representing

orders of magnitude less computational effort than the conventional computational process. The learning algorithm, which was employed for the training, is the well-known Back Propagation (BP) algorithm [4].

In the present implementation the objective is to investigate the ability of the NN to predict the collapse load for different values of the basic random variables. The calculation of the collapse load is used by the MCS method for reliability analysis. The results of the reliability analyses are used to verify the feasibility or not of the design with respect to the probabilistic constraint functions. This is achieved with a proper training of the NN. The NN training comprises the following tasks: (i) select the proper training set, (ii) find a suitable network architecture and (iii) determine the appropriate values of characteristic parameters such as the learning rate and momentum term.

The learning rate coefficient and the momentum term are two user defined BP parameters that effect the learning procedure of NN. The training is sensitive to the choice of these parameters. The learning rate coefficient, employed during the adjustment of weights, is used to speed-up or slow-down the learning process. A bigger learning coefficient increases the weight changes; hence large steps are taken toward the global minimum of error level, while smaller learning coefficients increase the number of steps taken to reach the desired error level. If an error curve shows a downward trend but with poor convergence rate the learning rate coefficient is likely to be too high. Although these learning rate coefficients are usually taken to be constant for the whole net, local learning rate coefficients for each individual layer or unit may be applied as well.

The basic NN configuration employed in this study is selected to have one hidden layer. An important factor governing the success of the learning procedure of NN architecture is the selection of the training set. A sufficient number of input data properly distributed in the design space together with the output data resulting from complete structural analyses are needed for the BP algorithm in order to provide satisfactory results. Overloading the network with unnecessary similar information results to over training without increasing the accuracy of the predictions. A few tens of limit elasto-plastic analyses have been found sufficient for the example considered to produce a satisfactory training of the NN.

In this work a fully connected network is used. The number of conventional step-by-step limit analysis calculations performed in order to built up the proper data for the training set is in the range of thirty [5]. This selection is based on the requirement that the full range of possible results should be represented in the training procedure. For the application of the NN simulation and for the selection of the suitable training pairs, the sample space for each random variable is divided into equally spaced distances. The central points within the intervals are used as inputs for the limit state analyses.

5. RELIABILITY-BASED STUCTURAL OPTIMIZATION

During the last ten years various methodologies have evolved which deal with the reliability-based optimum design of structures. These attempts are restricted to relatively moderate size truss and frame structural problems using FORM and SORM reliability analysis methods [6]. In the present study the reliability-based sizing optimization of large-scale multi-storey 3-D frames is investigated.

In sizing optimization problems the aim is to minimize the weight of the structure under

certain deterministic behavioral constraints usually on stresses and displacements. In reliability-based optimal design additional probabilistic constraints are imposed in order to take into account various random parameters and to ensure that the probability of failure of the structure is within acceptable limits. The probabilistic constraints enforce the condition that the probability of a local or the system failure is smaller than a certain value (i.e. 10^{-3}). In this work the overall probability of failure of the structure, as a result of a limit elasto-plastic analysis, is taken as the global reliability constraint.

The probabilistic design variables are chosen to be the cross-sectional dimensions of the structural members and the material properties (E , σ_y). Due to engineering practice demands the members are divided into groups having the same design variables. This linking of elements results in a trade-off between the use of more material and the need of symmetry and uniformity of structures due to practical considerations. Furthermore, it has to be taken into account that due to manufacturing limitations the design variables are not continuous but discrete since cross-sections belong to a certain set.

A discrete RBO problem can be formulated in the following form

$$\begin{aligned} &\min \quad F(s) \\ &\text{subject to} \quad g_j(s) \leq 0 \quad j=1, \dots, m \\ &\quad \quad \quad s_i \in R^d, \quad i=1, \dots, n \\ &\quad \quad \quad p_f \leq p_a \end{aligned} \quad (3)$$

$F(s)$ is the objective function (i.e. the structural weight), s is the vector of geometric design variables, which can take values only from the given discrete set R^d , $g_j(s)$ are the deterministic constraints and p_f is the probability of failure of the design. Most frequently the deterministic constraints of the structure are the member stresses and nodal displacements or inter-storey drifts. For rigid frames with I-shape cross sections, the stress constraints, under allowable stress design requirements specified by Eurocode3 [7], are expressed by the non-dimensional ratio q of the following formulas

$$q = \frac{f_a}{F_a} + \frac{f_b^y}{F_b^y} + \frac{f_b^z}{F_b^z} \leq 1.0 \quad \text{if } \frac{f_a}{F_a} \leq 0.15 \quad (4)$$

and

$$q = \frac{f_a}{F_a} + \frac{C_m f_b^y}{(1 - f_a/F_e') F_b} + \frac{C_m f_b^z}{(1 - f_a/F_e') F_b} \leq 1.0 \quad \text{if } \frac{f_a}{F_a} > 0.15 \quad (5)$$

where f_a is the computed compressive axial stress, f_b^y, f_b^z are the computed bending stresses for y and z axis, respectively. F_a is the allowable compressive axial stress, F_b is the allowable bending stresses, F_e' is the Euler stress divided by a safety factor, C_m is a coefficient depending upon element's curvature caused by the applied moments, $F_a = 0.60 \times \sigma_y$ is the allowable axial stress, $F_b = 0.66 \times \sigma_y$ is the allowable bending stress and σ_y is the yield stress. The allowable inter-storey drift is limited to 1.5% of the height of each storey.

The proposed reliability-based sizing optimization methodology proceeds with the following steps:

- 1 At the outset of the optimization procedure the member geometry, the boundaries and the loads of the structure under investigation have to be defined.

- 2 The mean values of the design variables are properly selected and the constraints are also defined in order to formulate the optimization problem as in Eq. (3).
- 3 The optimization phase is carried out with ES where feasible designs are produced at each cycle (generation). The feasibility of the designs is checked for each design vector with respect to deterministic and probabilistic constraints of the problem.
- 4 The satisfaction of the deterministic constraints is monitored through a finite elements analysis of the structure.
- 5 The satisfaction of the probabilistic constraints is realized with the reliability analysis of the structure and the MCS technique in order to evaluate the probability of failure of the structure.
- 6 If the convergence criteria for the optimisation algorithm are satisfied then the optimum solution has been found and the process is terminated, else the whole process is repeated from step 3 with the new set of design variables.

Reliability-based structural optimization using MCS, ES and NN

In reliability analysis of elasto-plastic structures using MCS the computed critical load factors are compared to the corresponding external loading leading to the computation of the probability of structural failure. The probabilistic constraints enforce the condition that the probability of a local failure of the system or the global system failure is smaller than a certain value (i.e. 10^{-5} - 10^{-3}). In this work the overall probability of failure of the structure, as a result of limit elasto-plastic analyses, is taken as the global reliability constraint. The probabilistic design variables are chosen to be the cross-sectional dimensions of the structural members and the material properties (E , σ_y).

At each ES cycle (generation) a number of MCS are carried out. In order to replace the time consuming limit elasto-plastic analyses needed by MCS for each design, a training procedure is performed based on the data collected from M conventional limit elasto-plastic analyses. After the selection of the suitable NN architecture the training procedure is performed with $M=30$ data sets, in order to obtain the I/O pairs needed for the NN training. After the training phase is concluded the trained NN replaces the conventional limit elasto-plastic analyses, for the current design.

The Algorithm

1. *Selection step* : selection of s_i ($i = 1, 2, \dots, \mu$) parent vectors of the design variables.
2. *Deterministic constraint check* : all parent vectors become feasible.
3. *Monte Carlo Simulation step* : for each parent vectors
 - 3a. *Selection of the NN training set*
 - 3b. *NN training*
 - 3c. *Perform Monte Carlo Simulations*
4. *Probabilistic constraint check* : all parent vectors become feasible.
5. *Offspring generation* : generate s_j , ($j=1, 2, \dots, \lambda$) offspring vectors of the design variables.
6. *Deterministic constraint check* : all parent vectors become feasible.
7. *Monte Carlo Simulation step* : for each offspring vectors
 - 7a. *Selection of the NN training set*
 - 7b. *NN training*
 - 7c. *Perform Monte Carlo Simulations*
8. *Probabilistic constraint check* : if satisfied continue, else change s_j and go to step 6.
9. *Selection step* : selection of the next generation parents according to $(\mu+\lambda)$ or (μ, λ) selection schemes.

10. *Convergence check* : If satisfied stop, else go to step 5.

The aim of the present study is to train a neural network to provide computationally inexpensive estimates of analysis outputs required during the MCS process. A trained neural network presents some distinct advantages

6. TEST EXAMPLE

A realistic test example has been investigated in the present study in order to illustrate the efficiency of the proposed methodology for reliability-based sizing optimization problems. The cross section of each member of the space frame considered is assumed to be an I-shape and for each member one design variable is allocated. The objective function of the problem is the weight of the structure. The deterministic constraints are imposed on the inter-storey drifts and for each group of structural members on the maximum non-dimensional ratio q of Eqs. (8) and (9) which combines axial forces and bending moments. The values of allowable axial and bending stresses are $F_a=150$ MPa and $F_b=165$ MPa, respectively, whereas the allowable inter-storey drift is limited to 1.5% of the height of each storey.

The probabilistic constraint is imposed on the probability of structural collapse due to successive formation of plastic nodes and is set to $p_a=0.001$. The probability of failure caused by uncertainties related to material properties, member geometry and loads of the structures is estimated using MCS with the Importance Sampling technique. External loads, yield stresses, elastic moduli and the dimensions of the cross-sections of the structural members are considered to be random variables. The loads follow a log-normal probability density function, while random variables associated with material properties and cross-section dimensions follow a normal probability density function. The required importance sampling function $g_x(x)$ for the loads is assumed to follow a normal distribution. The mean value of $g_x(x)$ corresponds to the failure load when all other random values are kept fixed to their mean values.

A Six-storey space frame

This example consists of 63 elements with 180 degrees of freedom as shown in Figure 1. The length of the beams and the columns of the frame is $L_1=7.32$ m and $L_2=3.66$ m, respectively. The structure is loaded with a 19.16 kPa gravity load on all floor levels and a lateral load of 110 kN applied at each node in the front elevation along the z direction. The members of the structure are divided into five groups, as shown in Figure 1, each one having one design variable. The deterministic constraints are eleven, two for the stresses of each element group and one for the inter-storey drift. The type of probability density functions, mean values, and variances of the random parameters are presented in Table 1. For each geometric variable (i.e. the cross-sectional dimensions b , h) the mean value is taken as the current value of the corresponding design variable s_i .

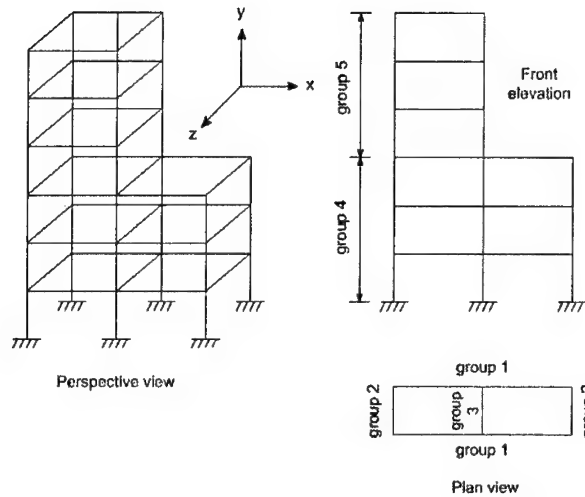


Figure 1: Description of the six-storey frame

Random variable	Probability density function (pdf)	Mean value	Standard deviation (σ)
E	N	200	20
σ_y	N	25.0	2.5
B,h	N	s_i	$0.1s_i$
Loads	Log-N	640	20

Table 1 : Characteristics of the random variables for the six-storey frame

Optimization procedure	ES cycles	p_f	Optimum weight (tn)	Time (s)
DBO	41	0.166	67.5	177
RBO	79	0.001	77.8	54,126
RBO-NN	81	0.001	77.8	9,471

Table 2 : Performance of the methods for the six-storey frame

For this test case the $(\mu+\lambda)$ -ES approach is used with $\mu=\lambda=5$, while a sample size of 500 simulations is taken for the MCS combined with the Important Sampling technique. As it can be observed from Table 2 the optimum weight achieved by the RBO is 15% more than the deterministic one. On the other hand, the probability of failure for the deterministic optimum is inapplicable since it exceeds the accepted value 10^{-3} . The proposed RBO-NN combination manages to achieve the optimum weight in one sixth of the CPU time required by the conventional RBO procedure.

7. CONCLUSIONS

The solution of realistic RBO problems in structural mechanics is an extremely computationally intensive task. In the test example considered the conventional RBO procedure was found over forty times more expensive than the corresponding deterministic optimization procedure. The aim of the proposed RBO procedure is to increase the safety margins of the optimized structures under various model uncertainties, while at the same time minimizing the weight of the structure as well as the additional computational cost. This goal was achieved using NN predictions to perform the structural analyses involved in MCS.

8. REFERENCES

- [1] G.I. Schueller, "Structural reliability – Recent advances", In the 7th International Conference on Structural Safety and Reliability (ICOSSAR '97), Kyoto, Japan, (1997).
- [2] Y. Tsompanakis and M. Papadrakakis, "Robust and efficient methods for reliability based structural optimization", In 4th International Colloquium on Computation of Shell and Spatial Structures, IASS-IACM 2000, M. Papadrakakis (Ed.), June 4-7, Chania-Crete, Greece, 2000.
- [3] M. Papadrakakis, Y. Tsompanakis and N.D. Lagaros, "Structural shape optimization using Evolution Strategies", *Engineering Optimization J.*, **31**, 515-540, (1999).
- [4] D.E. Rummelhart, and J.L. McClelland, *Parallel Distributed Processing*, Volume 1: Foundations, The MIT Press, Cambridge, (1986).
- [5] M. Papadrakakis, V. Papadopoulos, N.D. Lagaros, "Structural reliability analysis of elastic-plastic structures using Neural Networks and Monte Carlo simulation", *Comp. Methods Appl. Mech. Engrg.*, **136**, 145-163, (1996).
- [6] D.M. Frangopol and F. Moses, "Reliability-based structural optimization", in Advances in design optimization, H. Adeli (Ed.), Chapman-Hall, 492-570, (1994).
- [7] Eurocode 3, Design of steel structures, Part 1.1: General rules for buildings, CEN, ENV 1993-1-1/1992.

A NUMERICAL ESTIMATION OF THE INTERRELATION BETWEEN ACCELERATION PARAMETERS AND DAMAGE INDICATORS IN EARTHQUAKE ENGINEERING

A. Elenas, A. Liolios, L. Vasiliadis, M. Sakellari
Democritus University of Thrace, Department of Civil Engineering,
Inst. Structural Mechanics and Earthquake Engineering,
GR-67100 Xanthi, Greece

P. Koliopoulos
Technological Educational Institute, Dept. Civil Enging, Serres, Greece, and
c/o Institute of Engineering Seismology & Earthquake Engineering (ITSAK)
GR-54006 Thessaloniki, Greece

1. SUMMARY

This paper describes numerically, in form of correlation coefficients, the interdependency between several seismic acceleration parameters and the overall behaviour of reinforced concrete frame structures expressed in form of structural damage indices. After the numerical evaluation of the seismic parameters, a nonlinear dynamic analysis is carried out to provide the total damage status of a structure. The aim is to select among the parameters those, which have drastic influence on the structural destruction. Furthermore, the design philosophy of aseismic codes can be verified. The attention is focused on earthquake accelerogrammes of worldwide well-known sites with strong seismic activity.

2. INTRODUCTION

The earthquake accelerograms have inherent information which can be extracted either directly, like the peak ground acceleration (PGA) and the total duration, or indirectly using a computer supported analysis. The results of such an analysis can be classified:

- a) in peak parameters, e.g. PGA, peak ground velocity (PGV), peak ground displacement (PGD),
- b) in spectral parameters, e.g. response-, and/or energy-spectra, and
- c) in energy parameters, e.g. ARIAS intensity, strong motion duration (SMD) after Trifunac/Brady, power $P_{0.9}$, root mean square (RMS).

The definitions of these parameters have been presented in the literature [1-7]. Post-earthquake observation of building damages, as well as the numerical elaboration of structural systems exhibit a more or less interdependency between the above mentioned parameters and the structural response [8-10].

This paper provides a methodology to quantify the interrelationship between the

seismic parameters and the structural damage. First, a computer supported elaboration of the accelerograms provides several peak, spectral and energy seismic parameters. After that, a nonlinear dynamic analysis is carried out to provide the structural response for the given seismic excitations. Among the several structural response characteristics, the overall structure damage index (OSDI) is selected to represent the structural response. Finally, correlation coefficients are evaluated to express the grade of interrelation between seismic acceleration parameters and the structural damage. So the presented methodology is applied to a reinforced concrete frame building, for several seismic acceleration records, and some results useful for the structural engineering praxis are presented.

2. SEISMIC PARAMETERS

According to the first step of the methodology presented in the introduction section, here the following seismic parameters are evaluated: PGA, PGV, PGD, spectral pseudo-acceleration (SA), central period (CP), absolute seismic input energy E_{inp} , ARIAS intensity, SMD after Trifunac/Brady, power $P_{0.9}$, the term a_{max}/v_{max} and RMS. The definition of these parameters is presented in the aforementioned literature and will not be repeated here due to space restrictions (see [1-7] for details and [8,9] for a brief description).

Earthquake	Country	Date	Station	Component
Ancona	Italy	14.6.72	Rocca	EW
Friuli	Italy	6.5.76	Tolmezzo	EW
Rumania	Rumania	4.3.77	Bucharest	N0
Montenegro	Yugoslavia	15.4.79	Petrovac	NS
Argostoli	Greece	17.1.83	Argostoli	NS
Mexico	Mexico	19.9.85	Mexico City	N90W
Kalamata	Greece	13.9.86	Kalamata	EW
Spitak	U.S.S.R.	7.12.88	Gukasyan	EW
Loma Prieta	U.S.A.	17.10.89	Corralitos	0DEG
Griva	Greece	21.12.90	Edessa	NS
Pyrgos	Greece	26.3.93	Pyrgos	T
Northridge	U.S.A.	17.1.94	Jensen Filtration Plant	292
Kobe	Japan	17.1.95	Kobe	NS

Table 1: Input ground motions

Table 1 (above) shows several event data of the seismic acceleration time histories which have been selected to be used in the present analysis. The events have been chosen from worldwide well known sites with strong seismic activity.

Table 2 (below) shows the PGA a_{max} , PGV v_{max} , PGD d_{max} , SA, CP T_0 , seismic input energy E_{inp} , ARIAS intensity, SMD $T_{0.9}$, power $P_{0.9}$, a_{max}/v_{max} and RMS of the examined seismic excitations. The spectral values SA, and E_{inp} are given for the period of 1.18 s, which is identical with the first eigenperiod of the examined frame structure.

Earthquake	PGA a_{\max} (m/s ²)	PGV v_{\max} (m/s)	PGD d_{\max} (m)	SA (m/s ²)	CP T_0 (s)	E_{inp} (m ² /s ²)	ARIAS Intensity (m ² /s ⁴)	SMD $T_{0.90}$ (s)	Power $P_{0.9}$ (m ² /s ⁴)	a_{\max}/v_{\max} (g/m/s)	RMS (m/s ²)
Ancona	4.447	0.097	0.210	0.238	0.086	0.006	2.700	3.035	0.802	4.585	0.383
Friuli	3.209	1.454	2.271	6.280	0.833	1.874	15.685	5.430	2.587	0.221	0.504
Rumania	2.017	0.736	0.250	6.102	0.593	0.821	4.907	7.460	0.594	0.274	0.562
Montenegro	4.503	0.433	0.757	2.658	0.267	0.973	27.864	10.600	2.375	1.040	1.026
Argostoli	1.621	0.068	0.097	0.272	0.175	0.010	1.948	10.900	0.161	2.384	0.214
Mexico	1.679	0.619	2.206	2.684	1.569	0.496	14.655	38.840	0.340	0.271	2.911
Kalamata	2.680	0.241	0.060	2.321	0.333	0.275	4.585	6.370	0.652	1.112	0.395
Spitak	1.875	0.166	0.262	1.755	0.239	0.107	2.001	8.960	0.201	1.130	0.369
Loma Prieta	6.177	0.555	0.120	2.436	0.315	0.544	19.547	6.860	2.612	1.113	0.730
Griva	0.997	0.111	0.015	0.626	0.325	0.023	1.304	7.800	0.151	0.898	0.218
Pyrgos	4.455	0.193	0.018	0.633	0.185	0.034	2.100	4.155	0.455	2.308	0.292
Northridge	6.210	0.967	0.513	13.154	0.459	11.94	31.575	6.280	4.542	0.642	1.071
Kobe	8.206	0.924	0.469	8.729	0.302	3.713	50.735	8.320	5.556	0.888	1.120

Table 2: Strong motion parameters

3. DYNAMIC ANALYSIS OF A FRAME STRUCTURE

The 8-storey reinforced concrete frame structure shown in Figure 1 (below) has been designed according to the rules of the recent Eurocodes for structural concrete and aseismic structures, EC2 and EC8. Storey-heights are 4.5 m for the first storey and 3.5 m for the other seven ones. The cross sections of the beams are considered as T-beams with 40 cm width, 20 cm plate thickness, 60 cm total beam height and 1.45 m effective plate width. Materials-quality is C20/25 for concrete and S400 for steel. The column-sections are 60/60 (in cm) for the first three lower storeys, 50/50 for the next three and 40/40 for the last two upper ones. The distance between each frame of the structure has been chosen to be 6 m. According to the EC8 Eurocode the structure has been considered as of importance class III, ductility class M-structure. Furthermore, the subsoil was of type B and the region seismicity of category 3 (in Greece) after the EC8 Eurocode. In this procedure except the self weight and seismic loads, also the snow, the wind and the live loads have been taken into account according to the codes demand. The first eigenperiod of the frame was 1.18 s.

After the design procedure of the reinforced concrete frame structure, a nonlinear dynamic analysis has been carried out for the evaluation of the structural seismic response. For this purpose the computer program IDARC 4.0 [11] has been used.

Among the several response parameters, the focus is on the overall structural damage index (OSDI). This is due to the fact, that this parameter summarises statistically all the existing damages on columns and beams in a single value, which can be easily correlated to single value seismic parameters. The program IDARC 4.0 uses the modified damage index after Park and Ang [11]. As seismic input for the nonlinear dynamic analysis has been used the accelerograms of all the seismic excitations presented in Table 1.

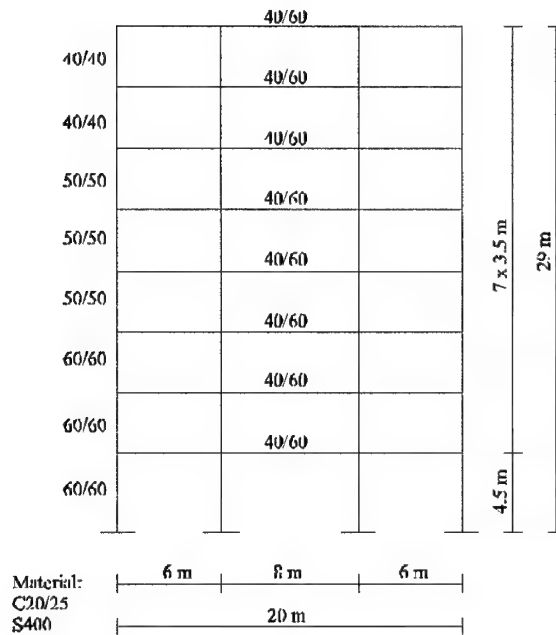


Figure 1: Reinforced concrete frame system

4. RESULTS

After a dynamic nonlinear analysis of the structure for all the examined accelerograms had been carried out, the final OSDI has been calculated for each seismic excitation.

Earthquake	OSDI
Ancona	0.000
Friuli	0.312
Rumania	0.164
Montenegro	0.198
Argostoli	0.000
Mexico	0.123
Kalamata	0.092
Spitak	0.070
Loma Prieta	0.133
Griva	0.000
Pyrgos	0.070
Northridge	0.586
Kobe	0.533

Table 3: Overall structural damage index

Table 3 presents the final overall structural damage index of the examined frame structure for each used seismic excitation. An OSDI equal 0.0 denotes that the structure remains in the elastic region during the excitation. To emphasize the grade of interrelation between seismic acceleration parameters and the OSDI, the correlation coefficient after Pearson [12] and the rank correlation coefficient after Spearman [12] have been calculated. The first correlation coefficient shows how near are the examined data to a linear relationship, while the second shows how near are the examined data to monotone ranking.

Seismic parameter	Pearson Correlation coefficient	Spearman Rank correlation coefficient
PGA	0.697	0.621
PGV	0.783	0.934
PGD	0.274	0.681
SA	0.953	0.972
CP	0.153	0.593
E_{inp}	0.849	1.000
ARIAS intensity	0.867	0.890
SMD	0.077	0.027
Power $P_{0.9}$	0.922	0.753
a_{max}/v_{max}	-0.459	-0.758
RMS	0.298	0.805

Table 4: Correlation coefficients between seismic parameters and OSDI

Table 4 presents the correlation coefficient and rank correlation coefficient between all the seismic parameters presented in the Table 2 and the OSDI in Table 3. Through the Pearson correlation coefficient it can be seen that the PGD, CP, the term a_{max}/v_{max} and RMS have poor correlation (0.153 to 0.459) with the OSDI. Next, PGA and PGV show medium (0.697 to 0.783), while the E_{inp} and ARIAS intensity show good correlation (0.849 to 0.867) with the OSDI. Finally, the power $P_{0.9}$ and the spectral parameter SA show very good correlation (0.922 to 0.953) with the OSDI. It must be pointed out that the SMD as defined by Trifunac and Brady, has very poor correlation (0.077) with the OSDI. This is due to the fact that its definition does not take into account the seismic energy content. Nevertheless, by using the SMD to define the power $P_{0.9}$ from the ARIAS intensity results into improved correlation coefficient from 0.867 to 0.922.

By examination of the Spearman's rank correlation coefficient (Table 4), we recognize that SMD has very poor correlation (0.027) with the OSDI. Furthermore, the PGA, PGD, CP, power $P_{0.9}$ and the term a_{max}/v_{max} have medium correlation (0.593 to 0.758) with the OSDI. Moreover, the PGV, SA, ARIAS intensity and RMS have very good correlation (0.805 to 0.972) with the OSDI. It must be noticed that the input seismic energy is monotone with the OSDI, which is expressed by the rank correlation coefficient equal to 1.

Finally, it must be pointed out that the design criteria of the EC2 and EC8 Eurocodes

lead to satisfactory structural behaviour for European seismic excitations, even structural damage can not be completely avoided.

5. CONCLUSIONS

In this paper a methodology for the value estimation of the interrelation between seismic acceleration parameters and the structural damage has been presented. As seismic acceleration parameters, peak, spectral and energy parameters have been used. The structural damage has been quantified as the modified Park/Ang overall structural damage index (OSDI). The degree of the interrelationship has been expressed by the linear and second order nonlinear Pearson's correlation coefficient and by the Spearman rank correlation coefficient. As the numerical results have shown, the spectral and energy parameters provide good correlation to the OSDI. On the opposite, the central period, the strong motion duration after Trifunac/Brady and the term a_{\max}/v_{\max} delivered poor correlation with the OSDI. Due to this reason, spectral and energy related parameters are better qualified to be used for the characterisation of the seismic damage potential.

6. REFERENCES

- [1] Arias, A., *A Measure of Earthquake Intensity*, in: *Seismic Design for Nuclear Power Plants*, R. Hansen (Ed.), MIT Press, Cambridge Massachusetts (1970) 438-469.
- [2] Trifunac, M.D. and Brady, A.G., *A Study on the Duration of Strong Earthquake Ground Motion*, Bulletin of the Seismological Society of America 65, 581-626 (1975).
- [3] Jennings, P.C., *Engineering Seismology*, in: *Earthquakes: Observation, theory and interpretation*, H. Kanamori and E. Boschi (Eds), Italian Physical Society, Varenna (1982) 138-173.
- [4] Meskouris, K., Kraetzig, W.B., Elenas, A., Heiny, L. and Meyer, I.F., *Mikrocomputerunterstuetzte Erdbebenuntersuchung von Tragwerken*, Wiss. Mit. SFB-Bericht Nr. 8, Ruhr-Universitaet, Bochum (1988).
- [5] Naeim, F. and Anderson, J.C., *Classification and evaluation of earthquake records for design*, EERI/FEMA NEHRP Fellowship report, PF-2/93, EERI, Berkeley (1993).
- [6] Trifunac, M.D. and Novikova, E.I., *State of the art review on strong motion duration*. In: *Proceedings of the 10th European Conference on Earthquake Engineering Vol. I*, G. Duma (Ed.), Balkema, Rotterdam (1994) 131-140.
- [7] Housner, G.W. and Jennings, P.C., *Generation of artificial earthquakes*, J. Eng. Mech. Div. 90, 113-150 (1964).
- [8] Elenas, A., *Interdependency between seismic acceleration parameters and the behaviour of structures*, Soil Dynamics and Earthquake Engineering 16, 317-322 (1997).
- [9] Elenas, A., *Interrelation between seismic acceleration parameters of european earthquakes and the structural behaviour*, European Earthquake Engineering 12, 56-63 (1998).
- [10] Elenas, A., *On the correlation between parameters of EC8 spectra compatible artificial acceleration time histories and damage indices of structures*, European Earthquake Engineering 14, 48-55 (2000).

- [11] Reinhorn, A.M., Kunnath, S.K. and Valles-Mattox, R., *IDARC 2D Version 4.0: Users Manual*, Department of Civil Engineering, State University of New York, Buffalo (1996).
- [12] Spiegel, M.R., *Theory and problems of statistics*. McGraw-Hill, London (1992).

ELASTOPLASTIC RESPONSE SPECTRA FOR THE DESIGN OF STRUCTURES SUBJECTED TO EXPONENTIAL BLAST LOADING

Nikos G. Pnevmatikos and Charis J. Gantes

Department of Civil Engineering, National Technical University of Athens
42 Patision Street, GR-10682 Athens, Greece

1. SUMMARY

The design of structures subjected to loads due to explosions is often treated by means of elastic-plastic response spectra. Such spectra that are currently available in the literature were computed on the basis of triangular shape of blast pressure with respect to time, and by neglecting the unloading stages of the structural response. In the present paper, response spectra based on a more accurate exponential distribution of blast pressure, and accounting for all stages and cycles of response, are proposed.

2. INTRODUCTION

Structures may experience blast loads due to military actions, accidental explosions or terrorist activities. Such loads may cause severe damage or collapse due to their high intensity, dynamic nature, and usually different direction compared to common design loads. Collapse of one structural member in the vicinity of the source of explosion, may then create critical stress redistributions and lead to collapse of the whole structure. A recent example of such a failure was the well-known collapse of the A.P. Murrah Federal Building in Oklahoma City, following a terrorist attack (Prendergast [1], Sozen et al. [2]).

For some structures blast resistant design may be required, if their use is such that there is a high risk for such a loading incident to be encountered. Examples include government buildings, constructed facilities in petrochemical plants or bunkers in military installations. For such structures it is desirable to establish appropriate design procedures and construction techniques (Rittenhouse [3], Ettourney et al. [4]).

This problem can be tackled in several different ways. The approach that more accurately describes the dynamic response of structures to explosive loads is via numerical analysis. Such analyses can capture the geometry of the structure, the spatial and temporal distribution of the applied blast pressure, as well as the effects of material and geometric nonlinearity, in a satisfactory manner, and have been performed by several investigators. Examples of this type are proposed by Louca et al. [5] and Otani and Krauthammer [6].

However, such analyses require highly specialized software, elaborate calibration of the models with experimental (Krauthammer et al. [7]) or other established results, and extensive computational effort. Therefore, this approach is used, for the time being, primarily for research purposes. Practice oriented design, assessment and protection methods do take advantage of advanced numerical analysis, but focus also on engineering detailing, connections and conceptual design (ASCE [8], Weidlinger Associates web page [9]).

An alternative design approach involving several approximations, rather easily applicable in routine design, is recommended by the U.S. Department of the Army TM5-1300, [10], and has been adopted by other researchers, for example Mays and Smith [11]. It is based upon substituting the structural element by a stiffness equivalent, single degree-of-freedom structural system, and using elastic-plastic response spectra to predict the maximum response. The response spectra accompanying the above methodology in the literature have been computed via numerical integration of the equations of motion, assuming triangular loading evolution with time, and applying the average acceleration method. Furthermore, these spectra do not take into account the fact that the response consists of several stages and cycles, and that the equations of motion change in each stage.

The objective of this paper is to assess the importance of these assumptions for practical design, and to provide a more accurate design tool, without sacrificing ease of use for the practicing engineer. This is achieved by deriving the equations of motion based on a more accurate exponential distribution of blast pressure, and accounting for all stages and cycles of response, obtaining analytical expressions of the solutions via symbolic manipulation software, and using these solutions to carry out an extensive parametric study, and draw a new set of response spectra.

3. IDEALIZATION OF BLAST LOADING

Chemical investigation and experimental data have shown that the evolution of blast load pressure P with time t can be simulated rather accurately by an exponential distribution with a start peak pressure P_s , as shown by the continuous line in Fig. 1 and described by the following equation (Baker et al [12], Bangash [13]), where t_d is the time of reversal of direction of pressure, and b is a shape parameter, usually taken equal to 1.

$$P(t) = P_s \left(1 - \frac{t}{t_d}\right) e^{-\frac{bt}{t_d}} \quad (1)$$

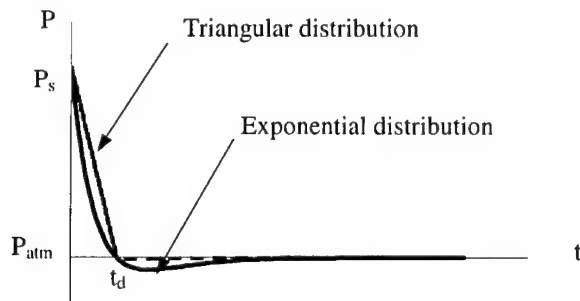


Figure 1: Exponential and triangular distribution of pressure due to blast load

The usual simple way to simulate a blast load for structural analysis and design purposes, is with a triangular distribution, which has a start peak pressure P_s and decreases linearly with time within a time period t_d , as illustrated by the dotted line in Fig. 1.

4. STATIC AND DYNAMIC ELASTIC-PLASTIC BEHAVIOR OF SDOF SYSTEMS

An elastic-perfectly plastic SDOF system without damping has the static resistance function R , shown in Fig. 2, where resistance is plotted in the vertical axis with respect to the degree-of-freedom x , plotted in the horizontal axis. The response of the system is divided in four stages, as described for example by Bangash [13] and Chopra [14]:

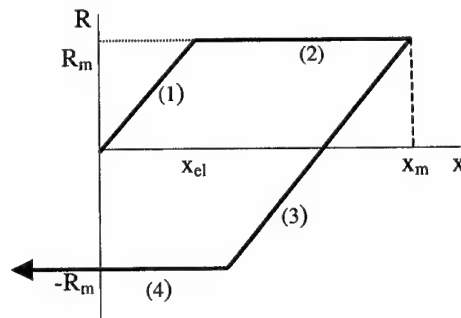


Figure 2: Elastic-perfectly plastic behavior for SDOF system

- (1) Response up to the elastic limit x_{el} , corresponding to a maximum resistance R_m , characterized by the elastic stiffness k of the system, defined as the ratio of R_m to x_{el} .
- (2) Plastic response with constant resistance R_m from the elastic limit x_{el} up to a maximum displacement x_m .
- (3) Unloading, where the response starts to decrease with the same absolute stiffness as in stage (1) up to a maximum (in absolute terms) negative resistance $-R_m$.
- (4) Plastic response during unloading, corresponding to a resistance $-R_m$.

The analytical expressions describing the response in each stage are:

$$R = \begin{cases} kx, & 0 < x < x_{el} & \text{(stage 1)} \\ R_m, & x_{el} < x < x_m & \text{(stage 2)} \\ R_m - k(x_m - x), & x_m - 2x_{el} < x < x_m & \text{(stage 3)} \\ -R_m, & x < x_m - 2x_{el} & \text{(stage 4)} \end{cases} \quad (3)$$

The response of such a system without damping subjected to dynamic excitation $P(t)$ is described by the following equations of motion:

Stage (1)

$$m \ddot{x}(t) + kx(t) = P(t) \quad (4)$$

The typical displacement in the first stage can be seen in Figs 3 and 4, corresponding to the cases when the system reaches plasticity (stage 2) before or after elastic rebounding, respectively. The displacement and the velocity at the end of this stage are the initial conditions for the second stage.

Stage (2)

In this stage the system has reached plasticity, and the equation that describes its response is:

$$m \ddot{x}(t) \pm R_m = P(t) \quad (5)$$

The sign of R_m in equation (6) depends on whether the system comes to plasticity (stage 2) before elastic rebounding (Fig. 3), in which case (-) is used, or after elastic rebounding (Fig.

4), when (+) is used. The displacement in the second stage can be seen in Figs 3 and 4, between the time t_{el} , corresponding to the first occurrence of plasticity, and the time t_m of maximum response, obtained by setting the velocity in the second stage, given by the derivative of the solution of equation (6), equal to zero. Then, the maximum response x_m can be obtained replacing time t with t_m in the solution $x(t)$ of equation (5). The new displacement x_m , and the corresponding velocity $v_m=0$ are the initial conditions for the next stage (3).

Stages (3) and (4)

A similar procedure is followed to obtain the response in the next stages (3) and (4). Graphically we can see these stages in Fig. 3 for the case when the system reaches plasticity (stage 2) before elastic rebounding. When the fourth stage finishes, then the second cycle starts and four new stages are possible to occur. The response of the second cycle can be treated with the same procedure. In Fig. 3 these four stages of the new cycle can also be seen. The absolute maximum displacement may occur either in the second or in the fourth stage of each cycle. The number of cycles depends on the ratio of maximum system resistance to external load R_m/P . As this ratio increases, the cycles decrease until the ratio becomes equal to 2, in which case there is no cycle and the system behaves elastically.

When plasticity occurs after elastic rebounding, the system usually works elastically after the third stage of the first cycle and does not enter the plasticity region again (Fig. 4). As can be observed from Fig. 4, where the total response is presented for that case, the maximum displacement could correspond either to first plasticity or to the elastic region.

The solutions of the above dynamic equations of motion of a single-degree-of-freedom system subjected to explosive loads have been obtained analytically, using the symbolic manipulation software Mathematica, Wolfram [15]. Both cases of exponential and triangular evolution of the loading function with time have been considered.

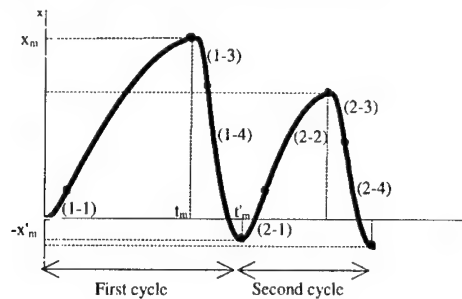


Figure 3: Response when plasticity occurs before elastic rebounding

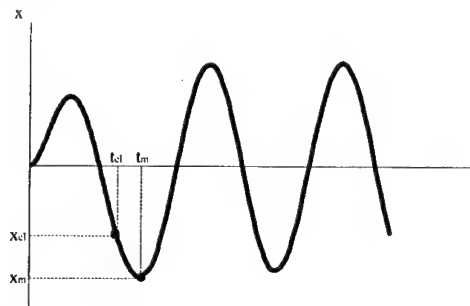


Figure 4: Response when plasticity occurs after elastic rebounding

5. ELASTIC-PLASTIC RESPONSE SPECTRA

The elastic-plastic analysis described in section 4, has been performed for a characteristic blast loading duration of $t_d=0.1\text{sec}$, and a wide range of fundamental periods of the SDOF system and range of ratios R_m/P . The maximum values of displacement ratios $\mu=x_{\max}/x_{el}$ ($x_{\max}=\max \{x_m, x_{m2}, x'_m, x'_{m2}\}$) have been plotted as response spectra for both triangular and exponential blast loading, and are shown in Figs 5 and 6.

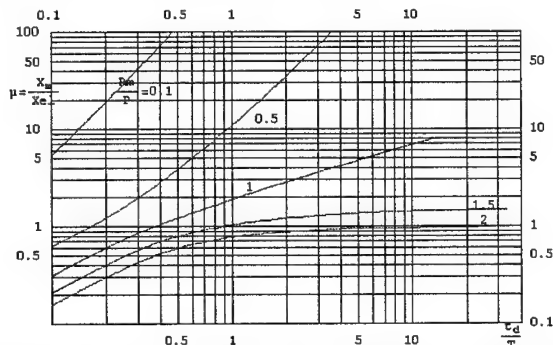


Figure 5: Response spectra for triangular blast loading and elastic-plastic behaviour

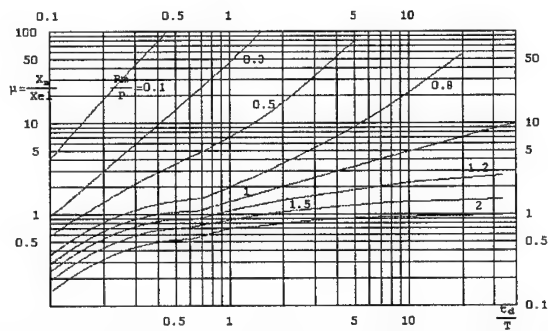


Figure 6: Response spectra for exponential blast loading and elastic-plastic behaviour

Comparing the results for exponential loading with those for triangular one, it is noted that differences do occur, which are significant in some cases. When the ratio $\mu=x_{\max}/x_{el}$ is large, ranging between 1 and 2, the response for exponential loading is less compared to the one for triangular loading. This can be explained qualitatively considering the shape of loading. The exponential loading decreases faster than the triangular one, and this has more influence in elastic-plastic situations than in purely elastic ones.

Some exceptions to this were encountered in case of low R_m/P ratios, for example for $R_m/P=0.1$ and $t_d/T=0.4$, where the exponential loading gives higher response than the triangular one. This happens in cases when the maximum response is obtained at times larger than t_d , and the exponential loading has changed sign and may be in phase with the system motion, while the triangular loading at this time is zero.

In summary, the commonly used assumption of triangular blast load evolution with time can sometimes be slightly unconservative, particularly for flexible structural systems, but can also be significantly overconservative for stiffer structures.

6. SUMMARY AND CONCLUSIONS

The response of structures subjected to loads due to explosions has been investigated. The preliminary and potentially also the final design of such structures, as well as the assessment of the bearing capacity of existing structures, is often treated by means of elastic-plastic response spectra. Such spectra that are currently available in the literature are based on triangular time evolution of the blast pressure, and neglect the possibility that the maximum response may be encountered during the unloading stages. In the present paper, response spectra based on a more accurate exponential distribution of blast pressure, and accounting for all stages and cycles of response, have been computed. This has been achieved by deriving the pertinent equations of motion, and obtaining analytical expressions of their solutions via symbolic manipulation software. A comparison of the spectra obtained by the proposed approach to the ones for triangular pressure function, led to the conclusion that design based on the commonly used assumption of triangular blast load evolution can sometimes be slightly unconservative, particularly for flexible structural systems, but can also be significantly overconservative for stiffer structures.

7. REFERENCES

- [1] Prendergast, J., Oklahoma City Aftermath, Civil Engineering, Oct. 1995, pp. 42-45.
- [2] Sozen, M.A., Thornton, C.H., Corley, W.G., and Mlakara, P.F., The Oklahoma City Bombing: Structure and Mechanisms of the Murrah Building, ASCE Journal of Performance of Constructed Facilities, Vol. 12, No. 3, Aug. 1998, pp. 120-136.
- [3] Rittenhouse, T., Designing Terrorist-Resistant Buildings, Fire Engineering.
- [4] Ettourney, M., Smilowitz, R., and Rittenhouse, T., Blast Resistant Design of Commercial Buildings, ASCE Practice Periodical on Structural Design and Construction, Vol. 1, No. 1, Feb. 1996, pp. 31-39.
- [5] Louca, L.A., Punjani, M., and Harding, J.E. Non-linear Analysis of Blast Walls and Stiffened Panels Subjected to Hydrocarbon Explosions, Journal of Constructional Steel Research, Vol. 37, No. 2, 1996, pp. 93-113.
- [6] Otani, R.K. and Krauthammer, T., Assessment of Reinforcing Details for Blast Containment Structures, ACI Structural Journal, Vol. 94, No. 2, 1997, pp. 124-32.
- [7] Krauthammer T., Flathau W.J., Smith J.L., and Betz J.F., Lessons from Explosive Test on RC Buried Arches, ASCE Journal of Structural Engineering, Vol. 115, No. 4, 1989, pp. 810-26.
- [8] ASCE, SEI, *Structural Design for Physical Security: State of the Practice*, 1999.
- [9] Weidlinger Associates, <http://www/wai.com/AppliedScience/index-blast.html>
- [10] U.S. Department of the Army Technical Manual, TM5-1300, *Design of Structures to Resist the Effects of Accidental Explosions*, Washington D.C., 1990.
- [11] Mays G.C. and Smith P.D., *Blast Effects on Buildings*, Thomas Telford, 1995.
- [12] Baker W.E., Cox P.A., Westine P.S., Kulesz J.J. and Strehlow R.A., *Explosion Hazards and Evaluation*, Elsevier, 1983.
- [13] Bangash M.Y.H., *Impact and Explosion, Analysis and Design*, Blackwell Scientific, 1993.
- [14] Chopra A.K., *Dynamics of Structures: Theory and Applications to Earthquake Engineering*, Prentice Hall, Upper Saddle River, New Jersey
- [15] Wolfram S., *The Mathematica Book*, Reference Manual, Wolfram Media and Cambridge University Press, 1996.

ANALYTICAL ESTIMATION OF TOTAL DISPLACEMENT'S COMPONENTS OF R/C SHEAR WALLS WITH ASPECT RATIO 1.0-1.5 SUBJECTED TO SEISMIC LOADS

T. N. Salonikios

Lecturer I.T.S.A.K.

P.O. Box53, GR 55102 Finikas, Thessaloniki, Greece

1. SUMMARY

In the present study is presented the algorithm that calculate the individual components of the totally imposed displacement at the top of wall specimens'. Those specimens are designed according EUROCODE 8 and have aspect ratio 1.0 or 1.5. In two of those specimens is imposed axial force with a value of 7% of the compressive strength of the wall. Five of the specimens have classical type of reinforcement (vertical or horizontal steel bars). Other four have besides the minimum classical reinforcement also bidiagonal steel bars. According the design methodology of the specimens herein is investigated the influence of the absence of axial force into the distribution of the deformations to the mechanisms of strength recovery. Those are the flexural, shear and sliding shear mechanisms. As results by the use of bidiagonal reinforcement the influence of the absence of axial force is eliminated through the limitation of the sliding shear deformations across the length of yielding of the longitudinal reinforcement. Specimens reinforced by vertical and horizontal steel bars develop the same strength as the specimens reinforced by mixed type of reinforcement (classical and bidiagonal) but their inelastic behavior is generally poor due to the existence of high sliding shear deformations at the base for medium and higher ductility level.

2. INTRODUCTION

In reinforced concrete structures, shear walls are the structural elements which resist to the deformation of the building to which they belong during the excitation of its base by an eventual earthquake. For this reason the behavior of these structural elements is being extensively investigated both experimentally and analytically [1]. During a wall's deformation three are the fundamental mechanisms which resist to the imposed deformation. These are the flexural, the shear and the sliding shear mechanisms. Although these mechanisms are assumed to act independently, during the design of the structure, it has been experimentally shown that they intensively affect each other. Especially the flexural and sliding shear mechanisms are directly linked mainly after an intense flexural cracking. As it was been determined for high ductility levels the activation and function of the sliding shear mechanism becomes more evident especially with the progress of flexural cracking and as the portion of deformation due to the yield of flexural mechanism increases. The type of flexural cracking which best activates the sliding shear mechanism is the horizontal cracking at the wall's base.

3. THEORY

In order to estimate the level of ductility at which specimens fail, as yielding displacement was used the one which corresponds to the point of section of the horizontal line which passes from the higher point of the envelop curve and the inclined line which passes from the beginning of the axes and from the point of the envelop curve corresponding to the 75% of the maximum strength. It was considered that specimen's failure happens when it's strength is decreased till the 75% of its maximum strength. The final value for the displacement ductility is the ratio of displacement for strength's decrease up to 75% of the maximum, divided by the yield displacement. The ductility versus displacement diagrams for every specimen are presented where for each level of ductility the components of the total displacement (flexural, shear, sliding shear) has been calculated. It was considered that for the achievement of each ductility level at the top, contribute the three aforementioned strength recovery mechanisms. By means of deformation observed on these mechanisms the imposed displacement on the top of the specimen is achieved. In order to estimate the proportion of contribution of every mechanism as well as its importance to the achievement of the imposed displacement at the top, for a given geometry of specimen and given conditions of support that exist we were based on the work of F. Seible and A. Igarashi [6]. These researchers were working at the department of applied mechanics of San Diego University in California, based on an earlier work of Safarini and Wilson at Berkeley 1983. They expressed the equation which describes the possible deformation modes of a disc in matrix form. According to these researchers a plane disc has five possible ways of deformation (Fig. 1): i) Shear deformation ii) Flexural deformation of its vertical sides iii) Flexural deformation of its horizontal sides iv) Horizontal axial deformation v) Vertical axial deformation

For a disc of height H and width D plane deformations in matrix form are given by the equation (1):

$$\begin{bmatrix} \gamma \\ \Delta\theta_x \\ \Delta\theta_y \\ \Delta\chi \\ \Delta y \end{bmatrix} = \begin{bmatrix} 1/2 H & -1/2 D & -1/2 H & -1/2 D & -1/2 H & 1/2 D & 1/2 H & 1/2 D \\ 1/H & 0 & -1/H & 0 & 1/H & 0 & -1/H & 0 \\ 0 & -1/D & 0 & 1/D & 0 & -1/D & 0 & 1/D \\ -1/2 & 0 & -1/2 & 0 & 1/2 & 0 & 1/2 & 0 \\ 0 & 1/2 & 0 & -1/2 & 0 & -1/2 & 0 & 1/2 \end{bmatrix} \cdot \begin{bmatrix} u_{1x} \\ u_{1y} \\ u_{2x} \\ u_{2y} \\ u_{3x} \\ u_{3y} \\ u_{4x} \\ u_{4y} \end{bmatrix} \quad (1)$$

In case we refer to an angle of a quadrangle disc (Fig. 2), at the base, where $u_{2x}=0$, $u_{2y}=0$, $u_{3y}=0$ and if matrix equation (1) is expressed in terms of the deformations of the four sides and diagonal lines of the disc, results the following matrix equation (2):

$$\begin{bmatrix} \zeta_1 \\ \zeta_2 \\ \zeta_3 \\ \zeta_4 \\ \zeta_5 \\ \zeta_6 \end{bmatrix} = \begin{bmatrix} -1 & 0 & 1 & 0 & 0 \\ 0 & 1 & 0 & 0 & 0 \\ 0 & 0 & 0 & 1 & 0 \\ 0 & 0 & 0 & 0 & 1 \\ 0 & 0 & 0.707 & 0.707 & 0 \\ -0.707 & 0.707 & 0 & 0 & 0.707 \end{bmatrix} \begin{bmatrix} u_{1x} \\ u_{1y} \\ u_{4x} \\ u_{4y} \\ u_{3x} \end{bmatrix} \quad (2)$$

For the boundary conditions of this problem due to the existence of a rigid beam at the top of specimens, ζ_1 becomes zero 0. Moreover, assuming that at the specimen's base there is no horizontal elongation, ζ_4 becomes 0 too. According to these, it is obvious that $u_{1x}=u_{4x}$ and $u_{2x}=u_{3x}=0$. By using equation (2) and the above results, $\zeta_2, \zeta_3, \zeta_5, \zeta_6$ can be defined as follows:

$$\zeta_2 = u_{1y} \quad (3)$$

$$\zeta_3 = u_{4y} \quad (4)$$

$$\zeta_5 = 0.707u_{4x} + 0.707u_{4y} \quad (5)$$

$$\zeta_6 = -0.707u_{1x} + 0.707u_{1y} + 0.707u_{3x} \quad (6)$$

Subtracting equation (6) from equation (5) results:

$$\begin{aligned} \zeta_5 - \zeta_6 &= 0.707(u_{1x} + u_{4y} + u_{1x} - u_{1y}) \Rightarrow \frac{\zeta_5 - \zeta_6}{0.707} = 2u_{1x} + u_{4x} - u_{1y} \Rightarrow \frac{\zeta_5 - \zeta_6}{0.707} - u_{4y} + u_{1y} = 2u_{1x} \Rightarrow \\ &\Rightarrow \left(\frac{\zeta_5 - \zeta_6}{0.707} - u_{4y} + u_{1y} \right) / 2 = u_{1x} \Rightarrow \left[\frac{\zeta_5 - \zeta_6}{0.707} + (u_{1y} - u_{4y}) \right] / 2 = u_{1x} \end{aligned} \quad (7)$$

Subtracting from each part of equation (7) the quantity $(u_{1y} - u_{4y})$ results:

$$\begin{aligned} \left[\frac{\zeta_5 - \zeta_6}{0.707} + (u_{1y} - u_{4y}) \right] / 2 - (u_{1y} - u_{4y}) &= u_{1x} - (u_{1y} - u_{4y}) \Rightarrow \\ \Rightarrow \left[\frac{\zeta_5 - \zeta_6}{0.707} - (u_{1y} - u_{4y}) \right] / 2 &= u_{1x} - (u_{1y} - u_{4y}) \end{aligned} \quad (8)$$

The term $(u_{1y} - u_{4y})$ represents the sum of elongation and shortening of vertical disc sides due to bending and therefore the horizontal flexural displacement on top. Subtracting this term from the total displacements on the top, the shear deformation of the disc due to the horizontal loading on top is given. When there are sliding shear deformations at the specimens base those should be subtracted by both parts of equation (8).

4. SPECIMEN DESIGN

Specimens subjected to the methodology mentioned above were designed as a part of a PhD thesis. This present thesis is mostly focused on the study and investigation of inelastic behaviour of R/C walls subjected to high cyclic shear forces. Also this study is focused on the effect that has on those specimens behaviour a set of parameters which have not been adequately investigated by other researchers such as:

- aspect ratio of walls: $H_w/L_w = 1.5$ and $H_w/L_w = 1$
- existence of main bidiagonal reinforcement in such walls
- way of arrangement of that reinforcement (in 45° angle and the steel bunch intersection

point in two specimens at the base of the wall and in other two at a distance of $0.5l_w$ from the base)

- influence of the absence and existence of low axial force
- influence of the existence of different percentages of reinforcement at the side columns and at the web
- influence of the existence of cold joint at the base of the wall without concrete roughening or additional reinforcement at the distribution of individual deformations (flexural, shear and sliding shear) among resistance mechanisms and the study of the phenomenon of sliding shear between surfaces along the flexural cracks at the specimens base. Details for the specimens are presented to the figure 3.

5. APPLICATION - RESULTS

Applying the theory described in chapter 3 to the specimens designed according chapter 4 and tested at the laboratory [2],[3],[4],[5] result the diagrams presented below (figure 4-5). These are diagrams of ductility versus individual wall deformations. From those diagrams for each ductility level the percentage of displacement is given at height equal to the wall's width, that occur to the deformation of the flexural (δ_f), shear (δ_{sh}) and sliding shear (δ_{sl}) mechanisms.

6. CONCLUSIONS

By observing the diagrams which were drawn useful conclusions are given for the inelastic behaviour of walls. Axial force of the order of 7% of the compressive strength of the wall leads to a 25% increase of the displacement ductility capacity (specimens MSW3, LSW3). In specimens with aspect ratio 1.5 (and probably greater) by means of bidiagonal reinforcement which passes through the side columns at the specimens' base, the negative influence of the absence of axial loading is totally eliminated and a capacity of ductile deformation is provided to the walls. Sliding shear deformations increases substantially for displacement ductility over 2.5. For the specimen MSW6 with cold joint at the base and reinforcement connected by side by side placement (which is the rule in real structures) the sliding shear deformations begun to increase for a displacement ductility level over 1.0. The web shear resistance mechanism did not yield in all specimens, so the shear deformations at the web were reduced after the walls' strength was decreased. This phenomenon is more evident for the MSW set of specimen.

7. REFERENCES

- [1] Penelis G.G. and A.J. Kappos (1997), "Earthquake-resistant Concrete Structures", E & FN SPON (Chapman & Hall), London (592 pp).
- [2] Salonikios, T.N., Kappos, A.J., Tegos, I. A., and Penelis, G.G. "Cyclic Load Behavior of Low-slenderness R/C Walls: Design Basis and Test Results", *ACI Structural Journal*, Vol.96, No. 4, July-August 1999, pp. 649-660.
- [3] Salonikios, T.N., Kappos, A.J., Tegos, I. A., and Penelis, G.G. "Cyclic Load Behavior of Low-slenderness R/C Walls: Failure Modes, Strength and Deformation Analysis, and Design Implications", *ACI Structural Journal*, Vol.97, No. 1, January-February 2000, pp. 132-141.
- [4] Salonikios T., Penelis G., Tegos J., Kappos A. "Squat R/C walls under inelastic shear reversals" *11 World Conference on Earthquake Engineering, Acapulco Mexico June 1996*.

-
- [5] Salonikios, T.N., Kappos, A.J., Tegos, I. A., and Penelis, G.G. " Estimation of the deformations of walls subjected to seismic loads – sliding shear strength," *13o National Concrete Conference, Rethimno 1999*, pp. 215-225.
 - [6] Seible, F., Igarashi, A., "Full scale testing of masonry structures under simulated seismic loadings", J. Donea and P. M. Jones (eds.), *Experimental and Numerical Methods in Earthquake Engineering*, 1991, pp. 119-148.

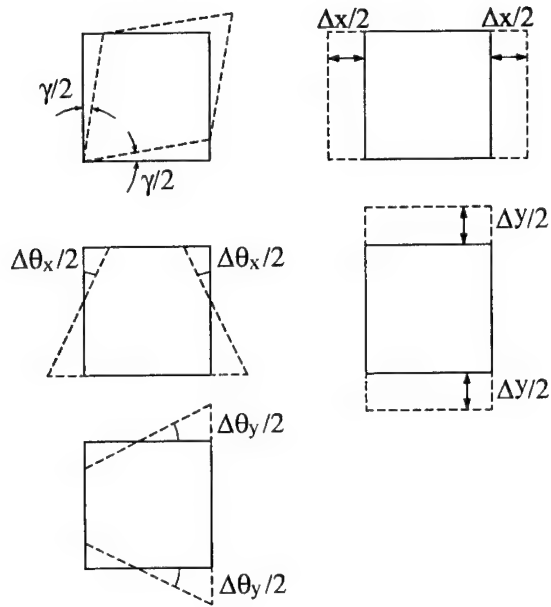


Figure 1: Possible deformation modes of flat disc

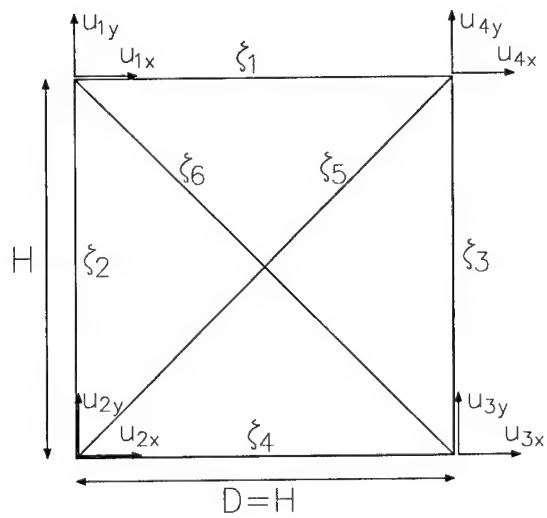


Figure 2: Definition of nodal displacements and relative deformations of disc

No	Specimen	Height	\bar{n}_h	\bar{n}_v	\bar{n}_{cc}	\bar{n}_w	\bar{n}_d	Comments
		h_w						
		cm	%	%	%	%	%	
1	LSW1	120	0.565	0.565	1.7	1.7	—	—
2	LSW2	120	0.277	0.277	1.3	1.7	—	—
3	LSW3	120	0.277	0.277	1.3	1.7	—	$N=0.07A_c f_c$
4	LSW4	120	0.277	0.277	1.3	1.7	0.416	$\delta_d=45^\circ l_d=0$
5	LSW5	120	0.277	0.277	1.3	1.7	0.416	$\delta_d=45^\circ l_d=0.8l_w$
6	MSW1	180	0.565	0.565	1.7	1.1	—	—
7	MSW2	180	0.277	0.277	1.3	1.1	—	—
8	MSW3	180	0.277	0.277	1.3	1.1	—	$N=0.07A_c f_c$
9	MSW4	180	0.277	0.277	1.3	1.7	0.416	$\delta_d=45^\circ l_d=0$
10	MSW5	180	0.277	0.277	1.3	1.7	0.416	$\delta_d=45^\circ l_d=0.8l_w$
11	MSW6	180	0.565	0.565	1.7	1.7	—	Cold Joint

$$A_{cc}=l_c \times b_w=24 \times 10=240 \text{ cm}^2, \rho_h=A_{sh}/(b_w \times s_h), \rho_v=A_{sv}/(b_w \times s_v), \rho_{cc}=A_{sc}/A_{cc},$$

$$\rho_w=(l_{stir} \times A_{sstir})/(l_c \times b_w \times s), \rho_d=A_{sd}/(b_w \times l_{web}), A_{sd}: \text{Area of total diagonal reinforcement.}$$

A_{sc} : Long. reinforcement in boundary element. A_{sh} : Horizontal web reinforcement.

A_{sv} : Vertical web reinforcement l_d : Distance between diagonal bars center axis at specimens base.

Typical cross sections at base:

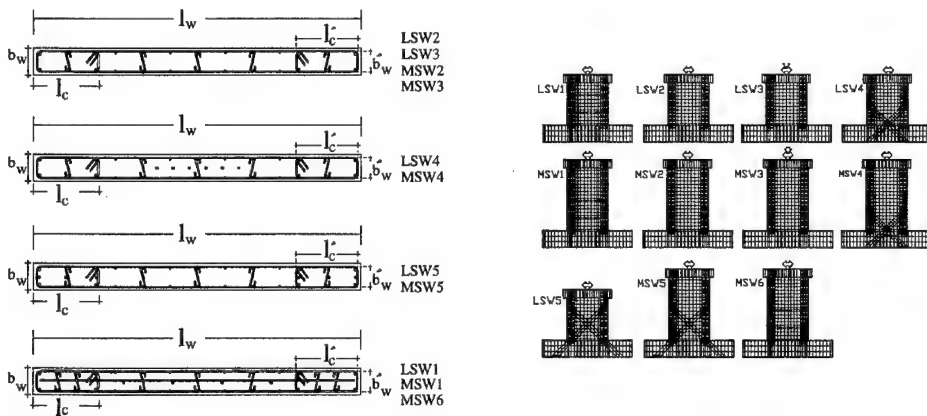


Figure 3. Main parameters of wall specimens and arrangement of reinforcement

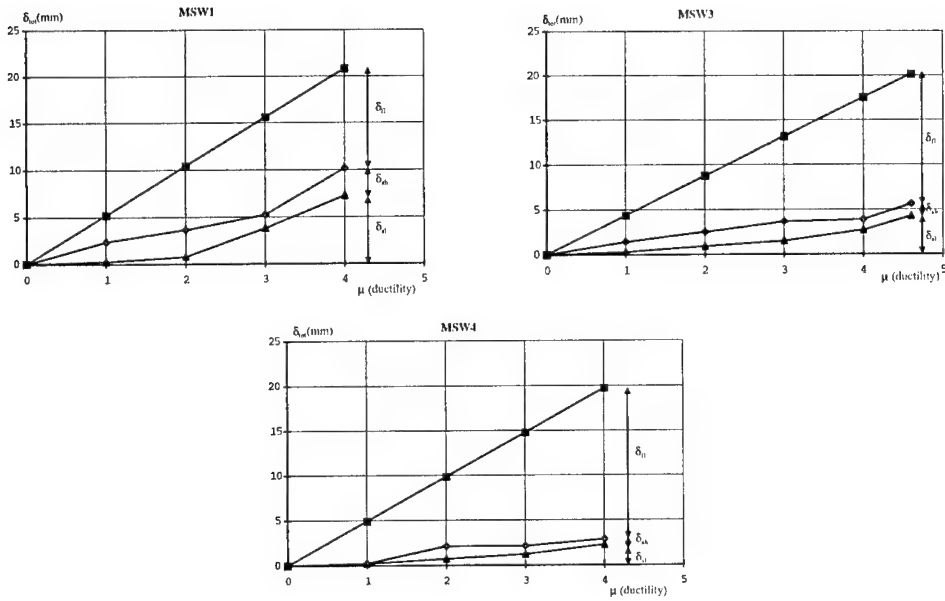


Figure 4: Diagrams of the individual components of the total deformations versus ductility for specimens MSW1, MSW3, MSW4

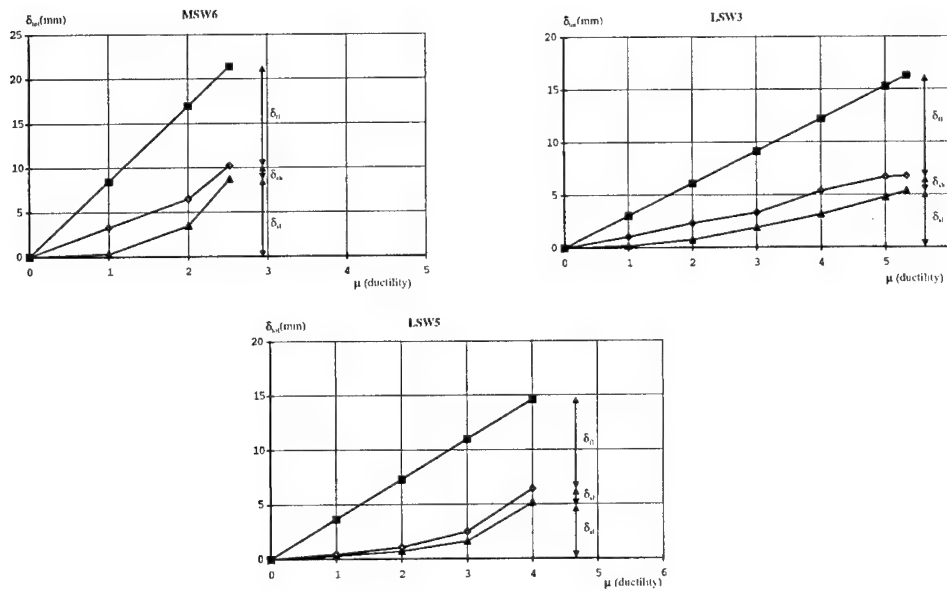


Figure 5: Diagrams of the individual components of the total deformations versus ductility for specimens MSW6, LSW3, LSW5

COMPETITION AMONG GENETIC ALGORITHMS TO IMPROVE ROBUSTNESS IN OPTIMIZATION

C. Dimou and V. Koumouis

Institute of Structural Analysis & Aseismic Research
NTUA, Zografou Campus 157 73 Athens, Greece

1. SUMMARY

Competition is introduced among the populations of a number of Genetic Algorithms (GAs). The aim is to calibrate tuning parameters of the GAs by gradually reducing the resources of the system. The evolution of the different populations is controlled on the level of metapopulation, i.e. the union of populations, on the basis of statistics and trends of the evolution of every population. The method is applied into two different problems with a number of global and near global optima. Numerical results are presented and the robustness of the proposed algorithm is discussed.

2. INTRODUCTION

Genetic Algorithms are search algorithms based on the concepts of natural selection and survival of the fittest. They guide an evolution of a set of randomly selected individuals through a number of generations that are subjected to successive reproduction, crossover and mutation, based on the statistics of each generation. The efficiency of the process is problem dependent and relies heavily on the successful selection of the number of parameters, such as population size, probability of crossover and probability of mutation, type of crossover etc. In this work a method is proposed that attempts to automate tuning of the evolution of the size of populations through an adaptive process. This is based on the competition of populations, with different sets of GA parameters, struggling for the available resources of the system.

Competition among different populations is common in natural systems. Populations evolve by adapting themselves to the environment where resources are limited. By coupling GAs with a scheme of Competing Populations (CP) a number of populations are produced in every generation. They evolve in the space of solutions guided by every GA in an adaptive way by altering their population size. By changing the available resources, the system organizes better its overall search strategy. It manages to come up with very good near optimal solutions faster as compared to the same number of standard GAs. The relative capacity of every population to adapt to the artificial habitat is used to calculate the overall fitness at a particular generation. Competition arises when the resources are insufficient to sustain the entire population. "Predator – Prey" relationships are activated, by assigning conflicts among the populations. The "predator" population is trying to survive through the extinction or drastic reduction of its "prey". The prize for the "predator" are the resources allocated for the

“prey”. The proposed method is applied to a number of different multi-modal functions used as benchmarks in optimization. Numerical results are presented that illustrate the advantages of the proposed method as compared to the standard GA.

3. GENETIC ALGORITHMS

A simple GA scheme is employed for every population [3], [5]. No mixing among individuals of different populations is allowed to preserve the characteristics of each population. Reproduction is based on a ranking scheme, while elitism is adopted allowing the best individuals to survive at the next generation. Various crossover techniques such as, single crossover, double crossover and single crossover per design variable are implemented. For the mutation probability, two decreasing functions are used. The entire system operates in two levels, the level of populations and the level of the metapopulation, where all decisions about the characteristics of the next series of populations are made. The normalized fitness of the i^{th} individual of the j^{th} population, is expressed as:

$$f_{ij}(\mathbf{x}) = \frac{\max_{i,j} \{f_{ij}(\mathbf{x})\}}{\hat{f}_{ij}(\mathbf{x})}, \quad \hat{f}_{ij}(\mathbf{x}) = \left[C_{ij}(\mathbf{x}) + \sum_{k=1}^{N_{c,i}} c_{jk} \cdot T(g_k(\mathbf{x})) \right] \quad (1)$$

where, $g_k(\mathbf{x})$ is the k^{th} inequality constraint of the individual, c_{jk} is the penalty factor assigned for the k^{th} constraint for the j^{th} population and $C_{ij}(\mathbf{x})$ is the objective function. Operator T is given as:

$$T(x) = \begin{cases} \sqrt{x - \varepsilon} & x > \varepsilon \\ 0 & x \leq \varepsilon \end{cases} \quad (2)$$

where, ε is the tolerance in violating the constraints. A soft convergence criterion is introduced that works as a trade-off between the minimum uniformity of the population, i.e. the saturation of a dominant schema per design variable of the problem, and the spatiality of the objective of the population.

4. COMPETITION

Competition is common in natural systems. Dimitrova and Vitanov

[1] study the evolution of competing populations through adaptation in a nonlinear dynamical system with limited resources. Nee et al. [2], present the important parameters of interaction among different populations in a natural environment. Populations of different species share the environment in a state of dynamic equilibrium. Competition among different species arises when they share the same resources.

Assuming the necessary computational resources per design constant within a population, the amount of resources required to process all the individuals of the metapopulation in a specific generation is given as:

$$R_{req} = \sum_{i=1}^{N_p} R_i \cdot N_i, \quad N = \sum_{i=1}^{N_p} N_i \quad (3)$$

where, R_i are the resources per individual of the i^{th} population and N_p is the number of populations in the system. The amount of available resources at generation t can be represented by a step like function with initial resources R :

$$R_{avail} = R - \sum_{i=1}^m H(t - t_i) \cdot \Delta R_i \quad (4)$$

where, m defines the number of changes of the step-like function at particular instances, i.e. at generations t_i with reduction of resources ΔR_i , and H is the Heaviside function.

The fitness of a population can be expressed as the sum of the fitness of its individuals. This favors the expansion and survival of larger populations and of populations with many "good" individuals. Alternative expressions may be used that consider the fitness of a population as the average of the fitness of its individuals. The overall fitness is expressed as:

$$\hat{F}_j = \sum_{i=1}^{N_j} f_{ij}, \quad F_j = \frac{\hat{F}_j}{\max_{i=1, N_p} \{\hat{F}_i\}} \quad (5)$$

where, N_j is the total number of individuals of the j^{th} population. The main goal at this stage is to introduce a more stringent approach, as compared to the GA, that will process the emerging data and guide the next steps taking into account the uncertainties of the system. Therefore, a diversity measure D_j of the chromosome of every population j is evaluated based on descriptive statistics of the digits appearing at every position of the chromosome. Diversity is used as an estimate of the "age" of populations. "Younger" populations exhibit higher diversity as compared to "older" ones. Moreover, "younger" populations are more prominent to adapt that "older" ones.

The amount of resources for each individual appropriately normalized, is given by:

$$R_j = \frac{\hat{R}_j}{\max_{i=1, N_p} \{\hat{R}_i\}} \quad (6)$$

The overall fitness of the j^{th} population OF_j is expressed as the ratio of the product of fitness and diversity with the resources of the population as:

$$OF_j = \frac{[F_j]^a \cdot [D_j]^b}{[R_j]^c} \quad (7)$$

where, a , b and c are parameters, that attenuate or intensify relative variations among the populations. In this analysis $a = 1.0$, $b = 2/3$ and $c = 1.0$. Equation (7) is frequently used in econometric models.

5. ENGAGEMENT RULES

The probability of conflict among different populations i and j , when shortage of resources is observed, is given by:

$$\Pr[pop_i, pop_j] = \bar{T} \left[\frac{\Delta N}{N} \right] \cdot \begin{cases} \frac{OF_i - OF_j}{OF_i} & OF_i > OF_j \\ 0 & OF_i \leq OF_j \end{cases}, \quad \bar{T}[x] = \begin{cases} 0 & x < 0 \\ \frac{x}{d} & 0 \leq x \leq d \\ 1 & x > d \end{cases} \quad (8)$$

$$\Delta N = \frac{(R_{req} - R_{avail}) \cdot E[N_i]}{E[R_i N_i]}$$

where, d is a parameter controlling the transition from a state of no conflict to a state of conflict emerging among populations, based on the magnitude of lack of resources. This equation assures that no conflict arises if the available resources are adequate. Moreover, conflicts arise in proportion of the resource deficit. Stronger populations fight only weaker ones. The probability of conflict between two competing populations increases linearly with the relative difference of their overall fitness. Only one conflict per generation per set of conflicting populations is allowed. Thus, no population is engaged in more than one conflicts per generation. Finally, conflicts cease when the available resources are adequate.

The outcome of a conflict between populations i and j , determines the size of these populations in the next generation as follows:

$$N_i = N_i + \bar{T} \left(e_{ij} \cdot \frac{OF_i - OF_j}{OF_i} \right)$$

$$N_j = N_j + \bar{T} \left(\frac{1}{e_{ij}} \cdot \left(1 - \frac{OF_i - OF_j}{OF_i} \right) \right), \bar{T}(x) = \begin{cases} \max \left\{ g \cdot \frac{\Delta N}{N_p}, 2 \right\} & 0.5 + f < x \\ 0 & 0.5 \leq x < 0.5 + f \\ -\max \left\{ g \cdot \frac{\Delta N}{N_p}, 2 \right\} & 0.5 - f \leq x < 0.5 \\ -\max \left\{ g \cdot \frac{2 \cdot \Delta N}{N_p}, 4 \right\} & x < 0.5 - f \end{cases} \quad (9)$$

where, e_{ij} is equal to:

$$e_{ij} = 1 + \frac{e \cdot (rand - 0.5)}{0.5} \quad (10)$$

and, e and f are parameters handling the fuzziness of the outcome. Furthermore, the g factor is used to regulate the velocity of variation of the size of population. Populations vanish, if their population drops to zero. Typical values of g factor are around unity.

The main ingredients of the proposed scheme at the level of metapopulation are the introduction of diversity in equation (7) obtained from the formal descriptive statistics on the different schemata, and the fuzzy outcome of the conflicts of populations. The influence of parameters e, f in equations (9) and (10) is of secondary importance.

6. CASE STUDIES - NUMERICAL RESULTS

Two multi-modal functions are used as benchmarks for the proposed method. The formal expression of the optimization problem for these functions is given respectively, as:

$$\min f(x, y) = \left\{ \sum_{i=1}^5 [i \cdot \cos((i+1) \cdot x + i)] \cdot \sum_{j=1}^5 [j \cdot \cos((j+1) \cdot y + j)] \right\} + C \quad (11)$$

$$-10 \leq x \leq 10 \quad -10 \leq y \leq 10$$

$$\min f(x, y, z, w) = \{5xy \cdot \exp[-0.5 \cdot (x^2 + y^2)] \cdot \cos(2 \cdot z) \cdot \cos(w)\} + C \quad (12)$$

$$x \leq 0 \wedge y \leq 0 \quad -3 \leq \{x, y, z, w\} \leq 3$$

where C is an arbitrary constant value. For the function of equation 11 (problem #1), the length of the chromosome per DV is taken equal to 20. The complete enumeration scheme has to investigate 1.0995 trillion possible solutions. For the function of equation 12 (problem #2), the length of the chromosome per DV is taken equal to 8. The complete enumeration scheme has to investigate 4.295 billion possible solutions. In problem #1, 5 optimum solutions exist in the design space. In problem #2, 4 optimum solutions and 16 near optimum solutions (within 1.0% of the true optimum solution) exist in the design space. In Figure 2, the objective function of problem #1 is presented. The proposed algorithm activates 18 individual populations. Three crossover probabilities (0.6, 0.75 and 0.90 respectively) are considered. Three types of crossover (single point crossover, double point crossover and single point crossover per DV) are considered. Two mutation schemes (initial probability of mutation equal to 0.1 and 0.05, final probability of mutation equal to 0.001 and 0.005 and a half-life of 10 generations) are considered. These parameters are combined to create 18 different populations. The available resources vary according to four different schemes shown in Figure 1. These problems were solved starting with initial population sizes of 40 and 60 individuals respectively [4]. For these problems, 60 simulations with random seeds are performed. The proposed algorithm was able to locate the global optimum in all cases whereas the standard GA failed to trace the global optimum for problem #1 with an initial population size of 40 individuals. The computational time needed the optimization process was a small fraction of the time necessary to investigate all possible solutions of the design

space of the order of 0.005% for problem #1 (for the entire set of 60 simulations) and of the order of 1.4% for problem #2.

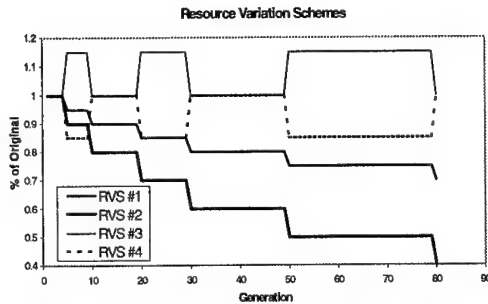


Figure 1. Evolution of Resource Variation Schemes

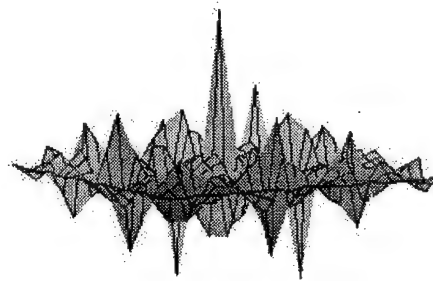


Figure 2. Objective function of problem #1.

In Figure 3 and Figure 4, the evolution of the size of the individual populations and of the objective of the best individual, for problem #1 when the RVS#1 is implemented are presented. Four populations become extinct due to strong competition in the beginning of the process. Moreover, numerous populations are forced to converge faster due to competition among the individuals of the metapopulation. The global optimum is found by population #16 (crossover probability of 0.9, single point crossover and high rate of mutation) at generation #58.

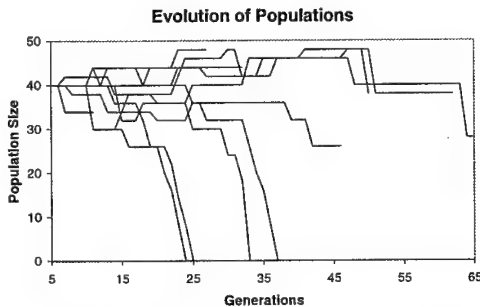


Figure 3. Evolution of the size of the population (problem #1).

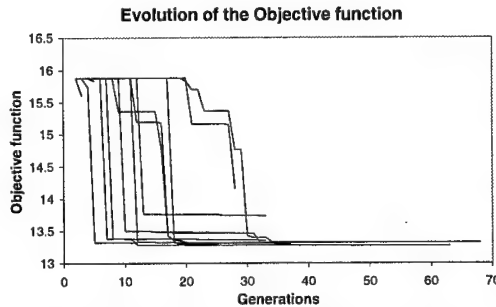


Figure 4. Evolution of the objective function (problem #1).

In Figure 5 and Figure 6, the evolution of the size of the individual populations and of the objective of the best individual, for problem #2, for RVS#1, are presented. Four populations become extinct due to strong competition. The optimum is found by population #18 (crossover probability of 0.9, single point crossover per DV and high rate of mutation) at generation #94. The size of population #18 drops rapidly after the true optimum is found due to competition with population #2 (crossover probability of 0.6, double point crossover and low rate of mutation). This is due to the convergence of population #18 resulting into a decrease of its diversity. Thus, its overall fitness drops significantly and it becomes the "prey" of the "predator" population #2.

In Figure 7 and Figure 8, the overall efficiency of the algorithm for the problems investigated, for the four different resource schemes, is presented. This is evaluated as the ratio of the number of optimum solutions found during the optimization process over the necessary computational effort. Considerable improvements are observed for an initial population size of 40 individuals. The efficiency of the algorithm drops as the number of

initial individuals increases. Still, the overall efficiency obtained, in the latter case, is at worst equal to the efficiency of the standard GA. For problem #1, the best results are obtained from RVS #3 whereas, for problem #2 RVS #1 delivers the most efficient results. The computational time of the proposed algorithm is less than the one needed for the standard GA. For RVS #1, timesavings up to 50% are observed. For RVS #2, timesavings up to 60% are observed. For RVS #3 a slight increase in time, less than 5%, is observed. For RVS #4, the computational time is roughly equal to the time needed by the standard GA.

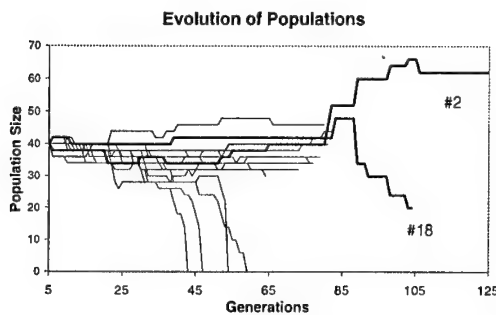


Figure 5. Evolution of the size of the population (problem #2).

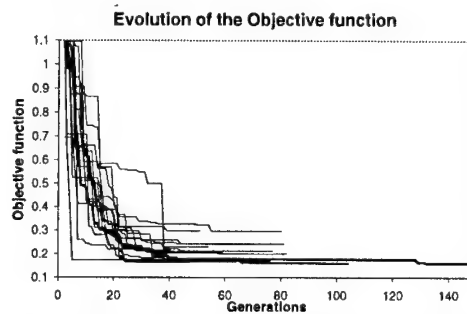


Figure 6. Evolution of the objective function (problem #2).

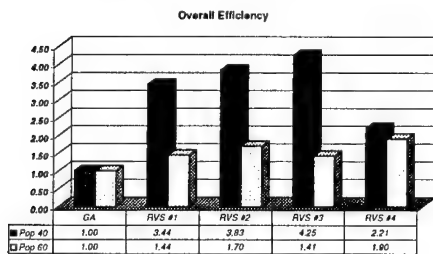


Figure 7. Comparison of overall efficiency (problem #1).

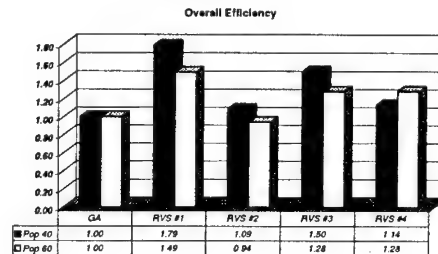


Figure 8. Comparison of overall efficiency (problem #2).

7. CONCLUSIONS

From the above analysis and the parametric studies performed it becomes evident that the proposed competitive algorithm controls satisfactorily the evolution process favoring the expansion of "promising" populations and the contraction of "weak" ones in a statistical sense. The descriptive statistics at the metapopulation level together with the rules of conflict guide the utilization of resources towards the most competent GAs. The method succeeds in finding good "near" optimal solutions in a robust way and in most cases faster than a standard GA, for two demanding multi-modal functions used as optimization benchmarks.

8. REFERENCES

- [1] Dimitrova Z. I., Vitanov N. K., "Influence of adaptation on the nonlinear dynamics of a system of competing populations" *Physic Letters A*, Vol. 272, (2000) pp. 368-380.
- [2] Hanski I. A., Gilpin M. E. (eds) "Metapopulation Biology" *Academic Press* (1997).

- [3] Goldberg, D. E., "Genetic algorithms in search, optimization, and machine learning". *Addison-Wesley, Reading, Mass* (1989).
- [4] Goldberg, D. E., Deb, K., Clark J. H., "Genetic Algorithms, Noise, and the Sizing of Populations", *Complex Systems* Vol. 6 (1992) pp. 333-362.
- [5] Koumoussis V. K., Georgiou P. G. "Genetic Algorithms in Discrete Optimization of Steel Truss Roofs" *Journal of Comp in Civil Engineering* Vol. 8, No. 3, (1994) pp. 309-325.

6th National Congress on Mechanics

Session C

Volume I

YUGOSLAV INVESTIGATIONS CONCERNING THE PATCH LOADING ON GIRDERS

Nikola Hajdin

Serbian Academy of Sciences and Arts, Belgrade, Yugoslavia

Branislav Coric

Faculty of Civil Engineering, University of Belgrade, Yugoslavia

Nenad Markovic

Faculty of Civil Engineering, University of Belgrade, Yugoslavia

Dusko Lucic

Faculty of Civil Engineering, University of Montenegro, Podgorica, Yugoslavia

1. SUMMARY

This paper describes Yugoslav experimental and theoretical investigations concerning behaviour of plate girders subjected to a localized edge load - i.e. patch load. Several aspects of this complex problem have been analyzed. In the first part local and overall stability of girders with long span is considered. The simple approximate solution for local buckling based on assumed collapse mechanism is given. The investigation of overall instability presents behaviour of slender plate girders with distortional instability. In the second part slender plate girders with short span are considered. Experimental research of the girders subjected to centric and eccentric loading is presented. The analysis of the ultimate load behaviour of plate girders with longitudinal stiffeners subjected to a patch load is also given.

2. LOCAL AND LATERAL INSTABILITY OF PLATE GIRDERS WITH LONG SPAN

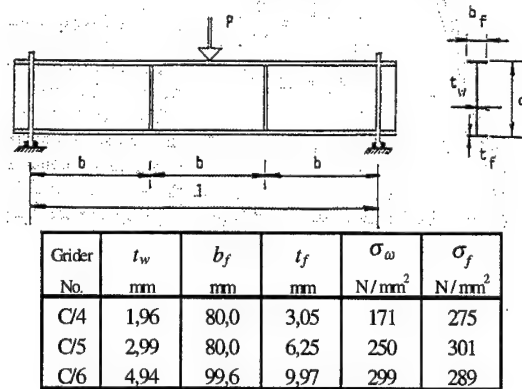
This paper describes theoretical and experimental research into the behaviour of simply supported steel plate girders subjected to a central localised load acting on the top flange. When these plate girders are subjected to such load, local and lateral instability may occur. So, the analysis of buckling of plate girders is generally concentrated on either plate buckling (local buckling) or overall buckling (lateral buckling).

Local buckling

Local buckling is a complex problem involving both material and geometric nonlinearity. During the past forty years a large number of model tests have been performed by many researches to provide a better understanding of the collapse mechanism [1] – [3]. Theoretical investigations have been concentrated on two main approaches to the problem. First approach consists of determination of an elastic critical load of web panel, with assumed idealised boundary conditions, subjected to a variety of combined loading. This approach is based on

unrealistic assumptions because it does not take into account the post buckled reserve of strength possessed by restrained thin panel and the interaction between the web and the flanges. Recent theoretical approach has been based on assumed collapse mechanism obtained from experimental investigation. Solution based on these assumed collapse mechanism have been reduced to a simple closed form. It is interesting to notice that tests have been performed on short and medium span girders. At present, very little test data is available for girders with long span and narrow flange. It is a reason why experimental analysis of three girders with long span and narrow flange is presented in this paper.

Details of loading, dimensions and material properties of the girders are given in Figure 1 and Table 1., where σ_w and σ_f are the static yield stresses of the web and flange respectively.



For all girders $L = 2300$ mm and $d = 380$ mm

Figure 1: Details of loading and dimensions

Table 1: Details of dimensions and material properties

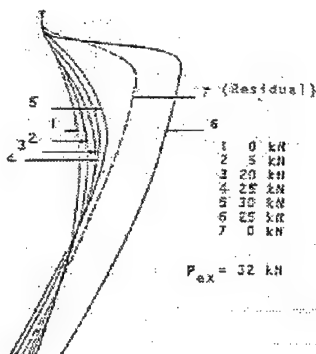


Figure 2: Lateral displacement of the vertical centreline of the girder C/4

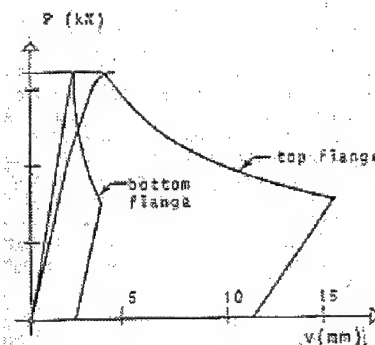


Figure 3: Vertical displacement of the top and bottom flange of the girder C/4

The load, which was applied by a hydraulic jack, was transmitted to the girders via a mechanism which prevented lateral displacement and rotation of the top flange. The tests were performed using Losenhausen equipment to control the vertical deflection of the jack.

The deflection of the jack was increased at a constant rate. The lateral displacements of the vertical centerline of the girder were measured by a transducer. Experimental results concerning lateral and vertical displacement of the girder C/4 are shown in Figure 2. and 3. Similar experimental results are obtained for girder C/5 and C/6. The corresponding collapse loads are given in Table 2.

The test results of plate girders clearly confirm that new plastic collapse mechanism is obtained, as it is shown in Figure 4.

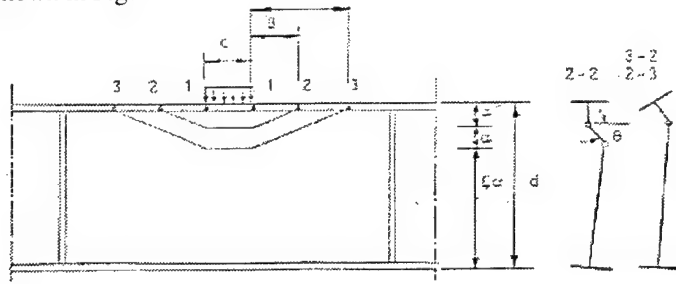


Figure 4: Obtained collapse mechanism

Following the upper bound theorem of plastic collapse and equating the work done by the applied loads to the internal dissipation of plastic energy, gives

$$P_u = \frac{4M_f}{\beta} + 2M_w\beta \frac{tg\theta}{(1+\frac{1}{\xi})\alpha} + M_w c \left[\frac{tg\theta}{\alpha(1+\frac{1}{\xi})} \left(2 + \frac{1}{\xi} \right) + 2M_w\gamma \frac{tg\theta}{\alpha} \right] \quad (1)$$

where P_u is ultimate or collapse load and M_w , M_f , are the full plastic moments of web and flange respectively. According to experimental results, expressions for α , β , γ , ξ has been found to be

$$\alpha' = \frac{c}{1,25t_w} \rightarrow \alpha = \frac{d-\alpha'}{1+\xi}, \quad \beta^2 = \frac{2M_f\alpha(1+\frac{1}{\xi})}{M_w tg\theta}, \quad \gamma = \frac{t^* \sigma^*}{t_w \sigma_w} \frac{1}{10},$$

$$\xi = \frac{\gamma}{d} \left(-0,32 \frac{d}{\gamma} - 10 \frac{\gamma}{d} + 16,8 \right)$$

where t^* is a reference thickness taken as 2,0 mm and σ^* is a reference yield stress taken as 300 N/mm². Angle θ can be obtained from the condition that deformation of the flange just prior to collapse must be compatible with deformation of the web adjacent to the flange.

Girder No.	Experiment (kN)	Theory (kN)	(Roberts & Rockey) (kN)
C/4	32,0	30,2	22,8
C/5	84,0	78,8	79,4
C/6	204,0	191,0	225,0

Table 2: Predicted and experimental collapse load

Comparison with experimental results (Table 2.) confirms that this mechanism solution gives good agreement between predicted theoretical collapse load P_U and experimental collapse load.

Lateral (distortional) buckling

The three girders tested are presented in Figure 5. The ends of the girders were constrained against rotation. Details of loading, dimensions and material properties of the girders are given in Table 3.

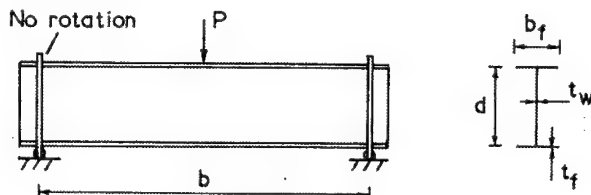


Figure 5

Girder	t_w mm	b_f mm	t_f mm	σ_w N/mm^2	σ_f N/mm^2	P_{ex} kN	P_{lat} kN
D2-3	1,96	80,0	3,05	178,0	272,0	13,0	23,0
D3-6	3,0	80,0	6,25	245,0	298,0	36,0	51,0
D5-10	4,94	100,0	10,00	292,0	305,0	94,0	172,0

Table 3

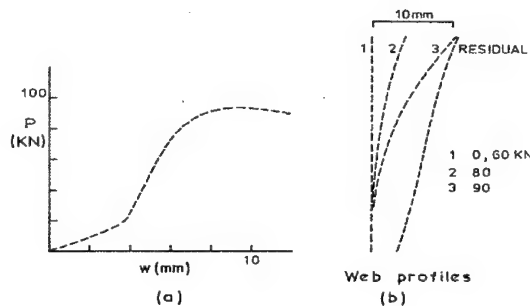


Figure 6: Results for girder D5-10

The load mechanism incorporated a knife edge to permit rotation and a layer of needle bearings to permit lateral displacement of top flange. The load P versus vertical displacement of the jack w for girder D5-10 and corresponding lateral displacement v of the vertical centreline of the girder are shown in Figure 6. The experimental failure load P_{ex} are given in Table 3.

The elastic critical load for lateral buckling P_{lat} is given in Timoshenko and Gere [4]. Comparison with experimental failure load (Table 3), shows that this classical elastic solution P_{lat} can not be used to predict real failure load. This is due to distortion of cross section, what is not taken into account in classical solution. Geometrically nonlinear finite element analysis appears able to predict the actual behaviour of such girders [5].

3. BEHAVIOUR OF THE GIRDERS WITH SHORT SPAN

Research on this problem was continued through further experimental and theoretical analyses carried out at University of Montenegro in Podgorica. There was an experimental research organized as an attempt of providing answers to some questions that have not been thoroughly investigated yet. The first issue to mention here would be the analysis of the stress state in the loaded flange. Then, the question of plastification in the flange, plastic hinges - whether they are formed or not, and where? Another question was whether the so-called tension field was formed in the flange with respect to the local collapse. A particular attention was drawn to the formation of tension fields in the web as well, along the plastification lines.

During the first part of the experiment, when the loading was centric, two parameters were varied. These two parameters are known to play an important role in determination of failure load and the buckling form: web thickness and flange thickness (flange stiffness). In the second part, the center of attention was the collapse form together with failure load in cases of eccentric loading. In order to optimize the investigations, measuring and laboratory equipment, as well as for the working team to get accustomed to working together, a preliminary investigation was carried out. It was a valuable experience as far as the plan, program, strategy and working on the main investigation, was concerned. The complete experimental research contains 36 tests (divided into three series) and eight tests in the preliminary investigation (Fig. 7).

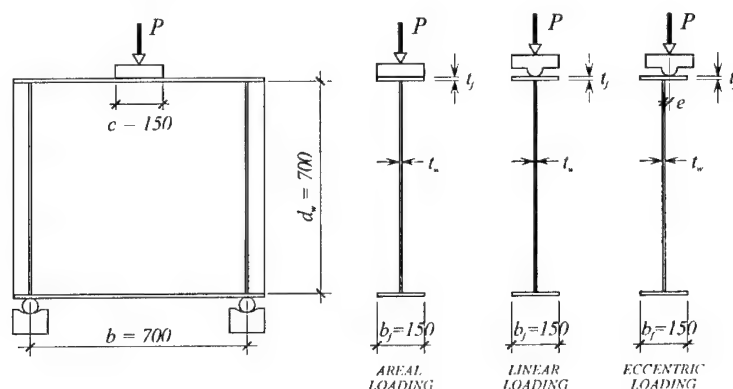


Figure 7: Girder from the experiment with the accepted denotations

The experiment was performed using a special load distribution block, distributing the load uniformly at any loading phase. This was an attempt in overcoming the evident problem of discrepancies between the load distribution block stiffness and the stiffness of the loaded flange.

With centric loading in the first and second series, the already known facts were confirmed once again: web thickness has the utmost influence on failure load, whereas, the flange thickness (stiffness) influences the increase of the critical load, but to a far lesser degree than the web thickness. In all cases, critical load is characterized by the occurrence of a buckling on the web. This kind of stability loss is of local character and it takes place right below the loading. Girder collapse is completely sudden. At the moment of critical load, a buckling outlined by two plastification lines occurs in the web. Though it is possible to determine the

positions of plastification lines in all cases, it is very difficult to state the extent of yielding lines formation until the moment of girder capacity loss (Fig. 8).

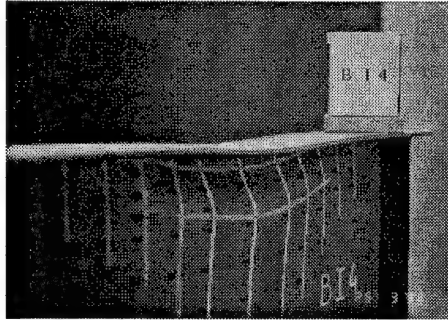


Figure 8: Residual deformations of a girder subjected to centric loading

The form of buckling depends both on the web thickness and the flange stiffness. The stiffer the flange, the closer to the flange the upper yielding line is, whereas, the lower line moves deeper downwards. Web thickness also affects the shortening of the upper line arrow. Apart from this, even the buckling curve is closer to the loaded flange. For all the girders with web thickness of $t_w = 4, 5$ and 8 mm , it can be stated that there are no signs of plastic hinges formation in the loaded flange. What is more, even the plastification is not evident, in some cases even for the loading greater than $99\% P_{ex}$. Nevertheless, in cases of web thickness of $t_w = 10 \text{ mm}$, there is plastification in the flange over the edges of load distribution block. Not even these cases can be determined by the formation of plastic hinges at the moment of reaching the critical load. Bending moments concentrate at a certain distance from the edges of load distribution block, but the intensity of these stresses is rather insignificant. Thus, it can be concluded that in this experiment, the so-called external plastic hinges on the flange do not form at all.

The third series of tests was primarily carried out with the intention of getting a better insight into the behaviour of girders, collapse form and the intensity of failure load with beams not subjected to centric loading with respect to the plane of the web, but with the load showing certain eccentricity. This investigation is among the first ones to deal with this problem. As the loading increases the most evident deformation is the bending of the flange accompanied by a slight twisting of the web following the flange deformation (Fig. 9). Collapse form of the girders differs considerably from the collapse form of the beams subjected to the centric loading. What is evident in cases of beams subjected to centric loading is the problem of elasto-plastic buckling and a local stability loss (carrying capacity loss). On the other hand, in cases of the eccentric loading, carrying capacity loss occurs due to the elasto-plastic bending (but again of local character). The question, which arises here, is about the line between these two phenomena and the extent of the eccentricity with the girder losing its carrying capacity in the same manner as it occurs with the beams subjected to the centric loading.

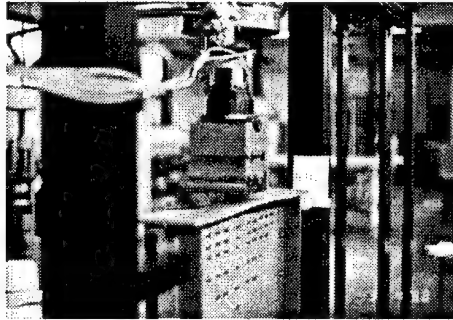


Figure 9: Flange warping of the girder subjected to eccentric loading

Failure load decreases as the eccentricity of the distributed load increases. The most significant parameters affecting the failure load are web thickness, the extent of load eccentricity (e/b_f ratio), the extent to which the flange and the web are built in, as well as the flange stiffness. Girder collapse does not occur suddenly, as in cases of centric loading. After reaching its maximum the load starts to decrease gradually. The initial deformations do not seem to affect either the development of plastification lines or the intensity of ultimate load.

In spite of a large number of mathematical expressions and models for determination of the failure load, it still cannot be claimed that there is a universal procedure which would comprise all parameters affecting the failure load, and which would, on the other hand, provide an acceptable and realistic description of the phenomenon of carrying capacity loss. Having completed the experimental research, and summarizing the experiences with regard to stress-deformation image of the girder a new mathematical model which would offer an even more realistic description of the stresses and deformations at the moment of carrying capacity loss is conceived in a rather different manner from the known ones, and it represents an initial idea for further studies and formulation of an improved mathematical model for calculating the failure load.

4. INFLUENCE OF THE LONGITUDINAL STIFFENERS

Investigations concerning the behaviour of plate girders with longitudinal stiffeners subjected to patch loading have been carried through international cooperation with University College Cardiff and T.M Roberts [6] and with Institute of Theoretical and Applied mechanics of Czechoslovak Academy of Sciences in Prag and prof M.Skaloud and further work is in progress. The influence of the longitudinal stiffeners was investigated in a series of tests on plate girders [7] and it was found that the influence of the position of longitudinal stiffener is noticeable if it is placed in the vicinity of loaded flange, especially between $0.1d - 0.4d$ and the ultimate load can be increased even for about 20%.

Theoretical work is concentrated on obtaining collapse or ultimate load. A part of the theoretical work deals with obtaining the solution using simplified model of failure. Procedure using failure model given by Roberts is adjusted to take into account the position of longitudinal stiffeners. The distance of the yield lines from the loaded flange is diminished compared with unstiffened girders and recommended value is given. Another theoretical approach is to use ultimate load solution in closed form i.e. some empirical or semi-empirical expression. An assessment of the applicability of a number of the formulae proposed by different authors for the prediction of the ultimate load for the girders without longitudinal

stiffeners was made through statistical analysis using data from experimental research. It was found that the best agreement with experimental results is obtained with Roberts formula (2). This solution includes main parameters that influence behaviour at collapse: square of thickness of the web, ratio between the thickness of the flange and the web, length of the patch load and material properties but it was needed to include the influence of the position of the longitudinal stiffener. As a result of statistical analysis a proposal is made for the modification of the existing expressions. It is suggested that the formula given by Roberts which is also used in Eurocod 3 should be slightly adjusted when applied to girders with longitudinal stiffeners by applying correction coefficient $f(s)$.

$$P_{us} = P_u \cdot f(s) = 0.5 \cdot t_w^2 \cdot \sqrt{E \cdot \sigma_w} \cdot \sqrt{t_f / t_w} \cdot \left(1 + 3 \cdot \frac{c}{d} \cdot \left(\frac{t_w}{t_f} \right)^{1.5} \right) \cdot f(s) \quad (2)$$

A simple form for taking into account the position of the longitudinal stiffeners is suggested:

$$f(s) = 1.28 - 0.7 \cdot s / d \quad \text{for } 0.1 < s / d < 0.4 \quad (3)$$

Further work is directed towards the determination of the influence of the loaded length when longitudinal stiffeners are present.

5. REFERENCES

- [1] Granholm, C.A., *Report 202*, Inst. Fur Byggnadsteknik, Gothenberg (1960)
- [2] Bergfelt, A. and Hovik, J., Thin walled deep plate girders under static loading. *Proc. 8th Congr. IABSE*, New York (1968).
- [3] Roberts, T.M. and Rockey K.C., A mechanism solution for predicting the collapse loads of slender plate girders when subjected to inplane patch loading, *Proc. Inst. Civ. Engrs.*, Part 2, 67, 155-175 (1970).
- [4] Timoshenko, S.P. and Gere, J.H., *Theory of elastic stability*, McGraw-Hill, N.Y. (1961).
- [5] Coric, B., Transversely reinforced plate girders subjected to patch load. *International Colloquium on Structural Stability*, Beijing (1989).
- [6] Roberts, T.M. and Markovic, N., Stocky plate girders subjected to edge loading, *Proc. Inst. Civil Engrs.*, London, P2, 75, 539-550 (1983).
- [7] Markovic, N. and Hajdin, N., A Contribution to the Analysis of the Behaviour of Plate Girders Subjected to Patch Loading, *J. Construct. Steel Research*, 21, 163-73 (1992).

SYNTHESIS OF NEW PHENOLIC POLYMERS VIA ENZYMATIC POLYMERIZATION AND THEIR PROPERTIES

Shiro Kobayashi

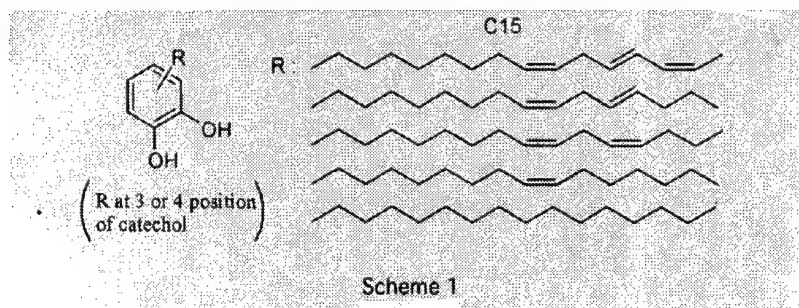
Department of Materials Chemistry, Graduate School of Engineering
Kyoto University, Kyoto 606-8501, Japan

1. SUMMARY

New "urushiol analogues" were facilely synthesized by lipase-catalyzed regioselective acylation of catechol derivatives having a primary alcohol with unsaturated fatty acids derived from plant oils. The curing via polymerization of the product catechol derivative proceeded under mild reaction conditions to produce the crosslinked film ("artificial urushi", a phenolic polymer) with high hardness and gloss surface, which are comparable with those of natural urushi coating. Similar urushiol analogues from 4-hydroxyphenetyl alcohol and unsaturated fatty acids were oxidatively polymerized by Fe-salen catalyst, yielding soluble polyphenols. Cardanol from cashew nut shell liquid, was also polymerized by peroxidase or Fe-salen catalyst to give the soluble crosslinkable polyphenol. These two phenolic prepolymers were subjected to hardening by thermal treatment or cobalt naphthenate catalyst to give a crosslinked film (also "artificial urushi") with good hardness.

2. INTRODUCTION

"Urushi" is a typical Japanese traditional coating. It shows excellent toughness and brilliance for a long period, and thus, caused much interest for organic chemists. Urushi coating is prepared from sap of Japanese lacquer tree (*Rhus vernicifera*) [1, 2], and Majima's pioneering work in the early days of the last century revealed that main important components of urushi are "urushiols", whose structure is a catechol derivative with unsaturated hydrocarbon chains consisting of a mixture of monoenes, dienes, and trienes at 3- or 4-position of catechol [3, 4]. Typical urushiols are shown as follows (Scheme 1). Crosslinking of the urushiol is supposed to be accomplished mainly by a laccase-catalyzed oxidative coupling of the phenol moiety of the urushiol and a subsequent oxidation of unsaturated alkyl chains in air.



Urushi can be regarded as the only example of practical natural paints utilizing *in vitro* enzymatic catalysis for hardening. The film-forming from the urushiol proceeds under air at room temperature without organic solvents, and hence, urushi seems very desirable for coating materials from the environmental standpoint. However, modeling study of urushi has been limited for only one paper [5]. This is mainly due to the difficulty in preparation of the urushiol.

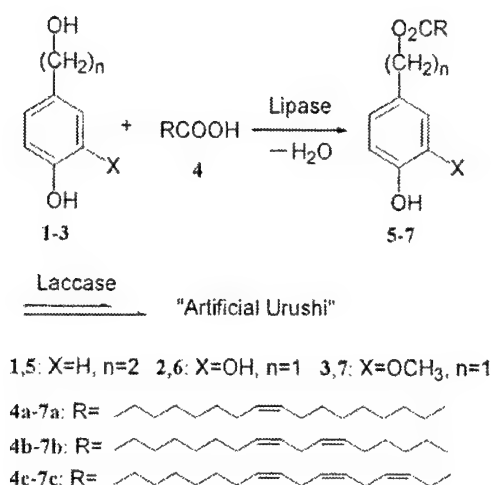
Polymerizations catalyzed by enzymes ("enzymatic polymerizations") have received much attention as new methodology of polymer syntheses [6, 7]. Characteristics of enzyme catalysis are expected to provide new polymeric materials, which are difficult to be obtained by conventional methods. Peroxidases induced the oxidative polymerization of phenol derivatives under mild reaction conditions to produce a new class of functional polyphenols in good yields [8].

Potential demands for replacing petroleum-derived raw materials with renewable plant-based ones in production of polymeric materials become worldwidely significant in the social and environmental viewpoints. Using such plant-based raw materials contributes to global sustainability without depletion of important resources. These materials are often cheaper than petrochemicals. The present lecture is concerned with our recent progress on preparation of artificial urushi, new crosslinked polymeric films, from urushiol analogues (phenols having an unsaturated group in the side chain) [9, 10]. All the monomers are derived from plant oils. In the curing stage, the crosslinked polymeric film can be obtained in the absence of organic solvents at an ambient temperature under air. Therefore, our new methodology can be regarded as an environmentally benign process of polymer coating, providing an example system of *green polymer chemistry*.

3. RESULTS AND DISCUSSION

Laccase-catalyzed hardening of urushiol analogues to artificial urushi

We designed new urushiol analogues (5~7), in which the unsaturated group is connected with the catechol or phenol group through an ester linkage [9]. The analogues were synthesized by a lipase-catalyzed esterification of phenols having a primary alcohol (1~3) with unsaturated fatty acids of different number of double bonds (4) (Scheme 2).



Scheme 2

Laccase was used for the curing, which belongs to an oxidoreductase having a copper-protein moiety as active site [6]. The curing of **5-7** was performed in the presence of acetone powder (AP, an acetone-insoluble part of the urushi sap containing mainly polysaccharides and glycoproteins) with 80% humidity at 30 °C for 24 h. AP, a third component of the sap in addition to an urushiol and laccase, is believed to act as emulsifier of oily urushiol and aqueous laccase solution. The sample film was prepared on a glass slide by using applicator for 50 μm thickness. The crosslinked film was obtained from **6b**, **6c**, **7b**, and **7c**, and other urushiol analogues were not cured. In the curing without laccase (control experiment), the film formation was not observed.

The curing of **6c** was monitored by using a dynamic microhardness tester (Figure 1). At the initial stage of the curing, the hardness value was very small and the sudden increase was observed after two weeks. Later, the value gradually increased to reach ca. 150 N/mm^2 after 5 weeks. The gloss value of the film surface was more than 100. The pencil scratch hardness reached H after 15 days, which is hard enough for practical uses. The hardness and gloss values of the present cured film are comparable to those of natural urushi coating; the curing of the urushiol analogues produced the brilliant film ("artificial urushi") with the high gloss surface. In the curing of **6b** in the presence of AP, on the other hand, the hardness value was less than 5 N/mm^2 after 6 weeks.

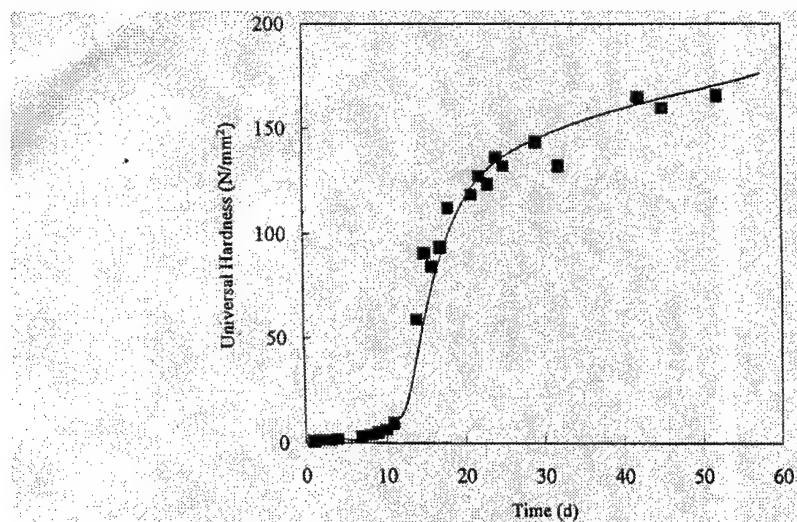
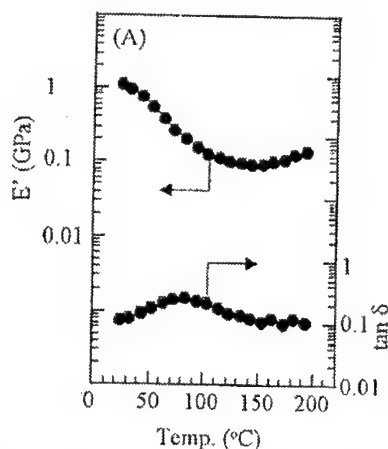


Figure 1. Time course in hardening of artificial urushi film from **6c** by using Fischer microhardness tester.

Recently, starch-urea phosphate (SP), a synthetic material, was reported to be highly effective as the third component for *in vitro* enzymatic curing of urushiols. In the curing of **6b** and **6c** in the presence of SP which is a substitute of AP (the natural sap component), the polymeric film was also obtained. However, the film hardness from **6c** was much smaller than that using AP as the third component. Interestingly, the curing of **6b** in the presence of SP produced the crosslinked film with relatively good hardness (30 N/mm² after 10 weeks); only a soft film was obtained by curing of **6b** in the presence of AP.

Figure 2 shows storage modulus (E') and dissipation factor ($\tan \delta$) of the cured films from **6c** as a function of temperature. In case of the sample obtained in the presence of AP after drying for 5 months, the glass transition temperature (T_g) was observed at 102 °C. The increase of E' in the region of high temperature indicates that the unreacted unsaturated carbon-carbon double bonds remained in the measured sample. Smooth trace of $\tan \delta$ means the homogeneous structure of the present cured film, suggesting the good miscibility between the urushiol analogue and AP. Similar traces were observed in the sample prepared by using SP as the third component. These dynamic elastic behaviors of the artificial urushi were very similar to those of natural urushi.



Preparation of soluble polyphenols from urushiol analogues and their curing
Urushiol analogue **5** was not cured via laccase catalysis. Thus, we have examined preparation of another "artificial urushi" by an oxidative polymerization of **5**, followed by curing of the resulting soluble crosslinkable polyphenols (Scheme 3).

5a, 8a: R =

5b, 8b: R =

5c, 8c: R =

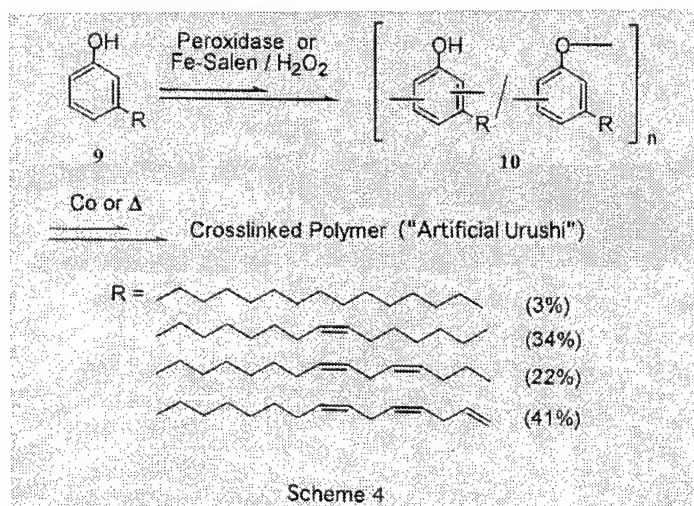
Here, iron-N,N'-ethylenebis(salicylideneamine) (Fe-salen) was used as catalyst for the oxidative polymerization of **5**. We regarded Fe-salen as model complex of peroxidase having a heme as catalytic active site. Polymerization of **5a** catalyzed by the Fe-salen produced soluble polymer **8a** with molecular weight of several thousands, whose index was relatively small (< 2). On the other hand, molecular weight and its index of polymers **8b** and **8c** were larger than those of **8a**; in some cases, the molecular weight was beyond 1×10^4 .

case of **8b** and **8c**, the hardness value of the film with thermal treatment was ca. 100 N/mm² after 3 days. The hardness of the cured film of **8c** gradually increased and reached more than 140 N/mm² after 4 weeks, whereas the hardness of the cured film of **8b** was almost constant. In the curing by cobalt naphthenate catalyst, **8b** and **8c** were also cured, however, the curing proceeded more slowly than the thermal curing. The formation of the cured film from **8a** was not observed in both curing methods. These data indicate that two or three unsaturated group in the side chain was required for the hardening. The surface gloss value of the cured film obtained by using cobalt naphthenate catalyst was more than 100, indicating the formation of the film with the high gloss surface.

Preparation of Crosslinked Polymeric Film from Cardanol

Cardanol (**9**) can also be taken as an urushiol analogue. **9**, a main component obtained by thermal treatment of cashew nut shell liquid (CNSL), is a phenol derivative mainly having the meta substituent of a C15 unsaturated hydrocarbon chain mainly with 1-3 double bonds. Since CNSL is nearly the one third of the total nut weight, much amount of CNSL is formed as by-product from mechanical processes for the edible use of the cashew kernel. Only a small part of **9** obtained in the production of cashew kernel is used in industrial field, though it has various potential industrial utilizations such as resins, friction lining materials, and surface coatings. Therefore, development of new applications for **9** is strongly desired.

Phenolic resins from **9** and formaldehyde are industrially produced as prepolymer of coating materials with high gloss surface mainly for indoor use. However, resins containing formaldehyde have much concern about toxic nature of formaldehyde in their manufacture and use. We have examined synthesis and curing of polymer **10** obtained by a peroxidase-catalyzed oxidative polymerization of **9** (Scheme 4) [11, 12]. This curing reaction is regarded as a new formaldehyde-free coating system from **9**.



We have reported that horseradish and soybean peroxidases (HRP and SBP, respectively) were efficient catalysts for oxidative polymerization of various phenol derivatives [6, 7]. As for the polymerization of **9**, SBP showed high catalytic activity to give the oily polymer **10** with molecular weight of several thousands, whereas the polymerization did not occur via HRP catalysis.

Fe-salen also catalyzed the polymerization of **9** in organic solvents as well as bulk. Using 1,4-dioxane as solvent gave soluble polymer **10** in good yields and the addition of pyridine improved the polymer yield and molecular weight. The polymerization also proceeded without organic solvent to produce the polymer **10** with molecular weight 1400-3000.

In a similar manner to **8**, the curing of **10** was examined by two methods: catalysis of cobalt naphthenate (3 weight-% for **10**) and thermal treatment (150 °C for 30 min). The curing took place within 1 h in both methods to give a yellow transparent film, which can also be regarded as "artificial urushi" in a broader sense. Such a quick hardening was not observed in monomer **9**. These data indicate that **10** is a good crosslinkable prepolymer. The hardness of the film cured by the cobalt catalyst reached nearly 100 N/mm² after 7 days. The gloss value of the film surface was higher than 100. These values are comparable to those of cardanol-formaldehyde coating materials. The resulting crosslinked film exhibited good elastic properties and its T_g was relatively high (ca. 100 °C) (Figure 3). The curing of the enzymatically obtained poly(cardanol) **10** also proceeded by cobalt naphthenate catalyst to give the crosslinked film with good hardness. FT-IR monitoring of the curing of **10** showed that the crosslinking mechanism was similar to that of the oil autoxidation.

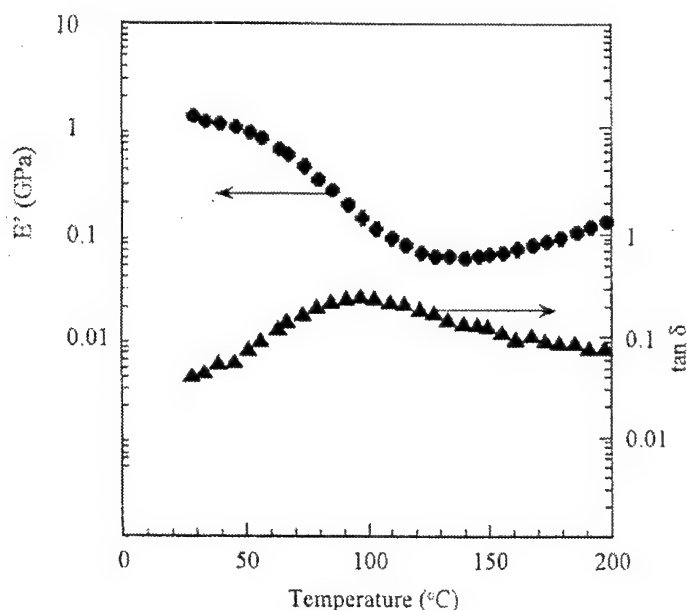


Figure 3. Dynamic viscoelasticity of crosslinked film of poly(cardanol).

4. CONCLUSION

In conclusion, "artificial urushi", a phenolic polymer, has been developed starting from three different "urushiol analogues" by using an enzymatic polymerization process. The artificial urushi showed high gloss surface and good elastic properties, which are comparable to those of natural urushi. The present method provides with an environmentally-benign process of polymer coatings.

5. REFERENCES

- [1] Rague, B. V., In *A History of Japanese Lacquer Work*, University of Toronto Press, Toronto (1976).
- [2] Kumanotani, J., In *Polymer Application of Renewable Resource Materials* (Ed. Carraher, C. E. and Sperling, L. H.), Plenum Press, New York, 225 (1983).
- [3] Majima, R., Ber. Dtsch. Chem. Ges. **42B**, 1418 (1909).
- [4] Majima, R., Ber. Dtsch. Chem. Ges. **55B**, 191 (1922).
- [5] Terada, M., Oyabu, H. and Aso, Y., J. Jpn. Soc. Colour Mater. **67**, 681 (1994).
- [6] Kobayashi, S., Shoda, S. and Uyama, H., In *Catalysis in Precision Polymerization* (Ed. Kobayashi, S.), John Wiley & Sons, Chichester, Chapter 8 (1997).
- [7] Kobayashi, S., J. Polym. Sci., Polym. Chem. Ed. **37**, 3041 (1999).
- [8] Tonami, H., Uyama, H., Kobayashi, S., Fujita, T., Taguchi, Y. and Osada, K., *Biomacromolecules* **1**, 149 (2000).
- [9] Kobayashi, S., Ikeda, R., Oyabu, H., Tanaka, H. and Uyama, H., *Chem. Lett.* 1214 (2000).
- [10] Tsujimoto, T., Ikeda, R., Uyama, H. and Kobayashi, S., *Chem. Lett.* 1122 (2000).
- [11] Ikeda, R., Tanaka, H., Uyama, H. and Kobayashi, S., *Macromol. Rapid Commun.* **21**, 496 (2000).
- [12] Uyama, H. and Kobayashi, S., *CHEMTECH* **29(10)**, 22 (1999).

ADAPTIVE FINITE ELEMENT ANALYSIS OF LIMIT-LOAD STATES IN DRY AND SATURATED SOILS

W. Wunderlich and R. Findeiß

Lehrstuhl für Statik
Technische Universität München, Germany

H. Cramer

Fachgebiet für Baustatik/Baudynamik
Universität Rostock, Germany

1. SUMMARY

The presentation deals with the analysis of strain localization in dry and water saturated granular soils. In this context a Cosserat formulation is employed to achieve a regularization and to avoid spurious mesh dependencies. The modelling of saturated soil is performed by the Theory of Porous Media. Space as well as time adaptive methods are applied using an hierarchical mesh refinement and an automatic time step adjustment in the discretization of the given problem.

The numerical examples show that reasonable discretizations may be achieved improving the efficiency of the solution technique. Localization phenomena are detected and refined properly. The resulting limit-loads may be considered as realistic, also in quantity. They were compared to the results of classical approximate methods.

2. INTRODUCTION

The treatment of zones of strain localization plays an important role in the numerical determination of limit-load states in geomechanics [3][4]. In general, shearbands connected to the limit-load state of the system are forming suddenly in time and further deformation is restricted to distinct narrow zones characterizing the type of failure. The accuracy of the finite element solution is, therefore, strongly coupled to a sufficient small mesh size in the zone of localization and reasonable time step sizes to capture the formation of the shearband. Essential ingredients of a reliable and robust finite element method are a regularization technique as well as space and time adaptive solution strategies [7].

In this presentation emphasis is given to the computation of problem dependent spatial and temporal discretizations. As estimators on a rigorous mathematical basis are difficult to obtain when non-associated flow rules are applied, the adaptive strategies are based on a combination of four different error indicators. Two of them control the space adaptive part and provide a measure for the spatial discretization error by evaluating the residuum of the extended equilibrium conditions and the error in the continuity of the fluid flows. On this

basis, the Cosserat continuum formulation and the transport subproblem may be taken into account in a straightforward manner. The time adaptive part includes two indicators for the temporal discretization error as well as for the error in the numerical integration of the constitutive equations being restricted to the zone of plastic response. With this adaptive strategy the beginning of localized failure can be captured in time and the developing of shearbands may be refined properly.

3. SPACE-TIME FINITE ELEMENT FORMULATION

In the following, soil is considered as a two phase material consisting of an elastic-plastic solid skeleton and a viscous pore fluid. Using the Theory of Porous Media [2] a homogenization may be achieved by introducing the concept of volume fractions. The local equations extended by a Cosserat formulation are then given by

$$\begin{aligned} (\sigma_{ij} + p \delta_{ij})_{,i} + \rho \bar{b}_j &= 0, \\ \mu_{ij,i} - E_{kij} \sigma_{kl} &= 0, \\ \left(\frac{\partial u_i}{\partial t} + K_{ij}^{Darcy} (p_{,j} + \rho^j \bar{b}_j) \right)_{,i} &= 0, \end{aligned} \quad (1)$$

defining the balance of momentum, balance of moment of momentum and the conservation of mass, respectively. In these equations σ_{ij} represents the effective stress tensor, p the pore water pressure, μ_{ij} the Cosserat couple stress tensor, E_{ijk} the permutation tensor and K_{ij} the Darcy permeability. The time dependence is introduced by the third equation which couples the fluid flow to the volume change. The numerical solution procedure used here may be regarded as a consistent space-time finite element method combining isoparametric elements in space with the Time-Discontinuous-Galerkin method in the time coordinate. This technique was successfully applied to the consolidation analysis by Cramer, Findeiß and Wunderlich [1]. The main advantage consists in superior stability properties, however, the discontinuities at the discrete time levels may be used to derive an error indicator for the temporal discretization error, too. The local Equations (1) are transformed into a variational form which directly supports a finite element discretization. All virtual work expressions are balanced by

$$\begin{aligned} \int_{I_n} \left\{ \int_V \delta \dot{\mathbf{u}}^T \mathbf{D}_u^T \boldsymbol{\sigma} dV + \int_V \delta \dot{\mathbf{u}}^T \mathbf{D}_u^T \mathbf{I} p dV - \int_V \delta \dot{\mathbf{u}}^T \rho \bar{\mathbf{b}} dV - \int_{O_\sigma} \delta \dot{\mathbf{u}}^T \bar{\mathbf{t}} dA + \right. \\ \left. \int_V \delta \dot{\boldsymbol{\omega}}^T \mathbf{D}_\omega^T \boldsymbol{\mu} dV + \int_V \delta \dot{\boldsymbol{\omega}}^T \mathbf{E} \boldsymbol{\sigma} dV + \right. \\ \left. \int_V \delta p \mathbf{I}^T \mathbf{D}_u \dot{\mathbf{u}} dV - \int_V \delta p \mathbf{D}_p^T \mathbf{K}^{Darcy} \mathbf{D}_p p dV + \int_{O_Q} \delta p \bar{Q} dA \right\} dt + \\ \int_V \delta p_n^+ \mathbf{I}^T \mathbf{D}_u [\![\mathbf{u}_n]\!] dV = 0 \end{aligned} \quad (2)$$

in which \mathbf{D}_u , \mathbf{D}_ω and \mathbf{D}_p are the standard gradient operators and $[\![\mathbf{u}_n]\!]$ indicates the jump in the displacement field at the discrete time t_n . Hence, the jumps are included in a variational sense. The unknown field variables are the displacement field \mathbf{u} , the field of micro-rotations

ω and field of the scalar pore water pressure p . For a combined space-time discretization shape functions are used in an appropriate product form:

$$\begin{aligned} u(x,t) &= N_u(x) N_t(t) \hat{u}, \\ \omega(x,t) &= N_\omega(x) N_t(t) \hat{\omega}, \\ p(x,t) &= N_p(x) N_t(t) \hat{p}. \end{aligned} \quad (3)$$

The discretization leads to a non-linear system of equations which has to be rewritten in an incremental form in which the rate-independent Prandtl-Reuss plasticity concept is applied:

$$\begin{bmatrix} K_{uu} & K_{u\omega} & L_{up} \\ K_{\omega u} & K_{\omega\omega} & 0 \\ L_{pu} & 0 & H \end{bmatrix}^i \begin{bmatrix} \Delta \hat{u}_n \\ \Delta \hat{\omega}_n \\ \Delta \hat{p}_n \end{bmatrix} = \begin{bmatrix} F^{u,ext} - F^{u,int} \\ F^{\omega,ext} - F^{\omega,int} \\ F^p \end{bmatrix}^i \quad (4)$$

with \hat{u}_n , $\hat{\omega}_n$ and \hat{p}_n as the discrete values at the beginning and the end of the time interval. The system is solved by a Newton-Raphson iteration where the stiffness matrices $K_{\alpha\beta}$ are assembled using a consistent tangent operator in order to ensure the stability even when limit-load states are reached.

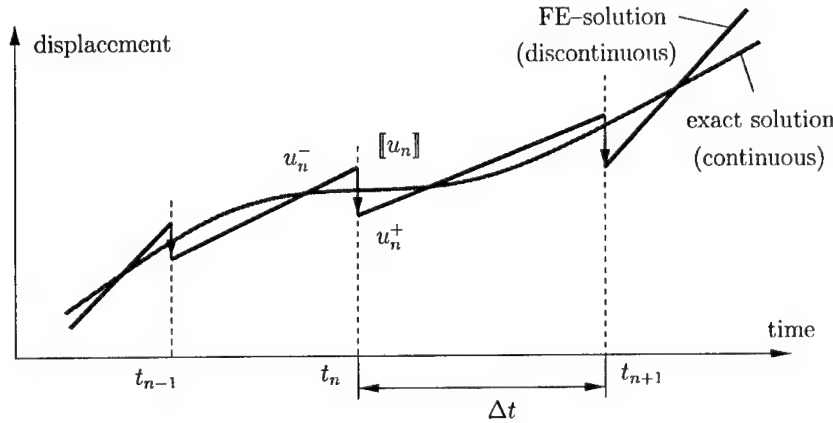


Figure 1. Illustration of the Time-Discontinuous-Galerkin method

4. ERROR INDICATORS

The coupled analysis of the multiphase problem requires independent error measures for the spatial and temporal domain. However, up to now no mathematically rigorous estimators have been proposed in the framework of non-associated plasticity. To provide a basis well suited for adaptive strategies four different indicators are developed in this section which may be used for a hierarchical mesh refinement [8] and an automatic time step control.

4.1. ERROR IN THE EQUILIBRIUM CONDITIONS

Following the approach by Johnson and Hansbo [5] a residual-type error indicator is used to capture the error in the equilibrium conditions. It is extended to the Cosserat theory by

introducing a second term of analogue structure. Instead of splitting the domain into elastic and plastic parts a weighting concept using the L_1 -norm of the incremental strains and curvatures is applied leading to the local indicator:

$$\eta_{eq,i}^2 = \underbrace{\|\Delta \varepsilon\|_{L_1(V^i)} \left(\|C_1^i h_i R(\sigma_h, p_h)\|_{L_\infty(V^i)} + \|C_2^i \frac{h_i}{h_k} J(\sigma_h, p_h)\|_{L_\infty(O^i)} \right)}_{\text{classical part}} + \underbrace{\|\Delta \kappa\|_{L_1(V^i)} \left(\|C_1^{i,c} h_i R^c(\mu_h, \sigma_h)\|_{L_\infty(V^i)} + \|C_2^{i,c} \frac{h_i}{h_k} J^c(\mu_h, \sigma_h)\|_{L_\infty(O^i)} \right)}_{\text{Cosserat part}} \quad (5)$$

in which the different parts of the residuals and the jumps across the element boundaries are defined by:

$$R(\sigma_h, p_h) = \text{div}(\sigma_h + p_h I) + \rho \bar{b}, \quad R^c(\mu_h, \sigma_h) = \text{div} \mu_h + E \sigma_h, \quad (6)$$

$$J(\sigma_h, p_h) = \begin{cases} n \cdot (\sigma_h + p_h I) - \bar{t} & \text{on } O_\sigma \\ \frac{1}{2} n \cdot \Delta(\sigma_h + p_h I) & \text{on } O^i \end{cases}, \quad J^c(\mu_h) = \begin{cases} n \cdot \mu_h - \bar{m} & \text{on } O_\mu \\ \frac{1}{2} n \cdot \Delta \mu_h & \text{on } O^i \end{cases}. \quad (7)$$

This indicator is mainly responsible for a detection and refinement of zones of strain localization. While the classical part leads to a refinement in the middle of the shearband, the Cosserat part preferably refines both edges.

4.2. ERROR IN THE CONTINUITY OF THE FLUID FLOWS

A second spatial error indicator has to be introduced to ensure a sufficient accuracy for the fluid flow subproblem. For this purpose a local super convergent patch recovery was employed to compute a smooth field of fluid flows Q^* which might be regarded as of a higher accuracy [9]. Finally, the local indicator is derived from the difference between Q^* and the finite element solution Q_h :

$$\eta_{fl,i}^2 = \int_{V^i} (Q^* - Q_h) \cdot (Q^* - Q_h) dV. \quad (8)$$

This procedure is based on the fluid flows at the end of the time interval ($t = t_{n+1}$). They are calculated in accordance to the law of Darcy:

$$Q_i = K_{ij}^{Darcy} (p_{,j} + \rho^f \bar{b}_j) \quad (9)$$

As a consequence, a purely spatial indicator is obtained which is independent of the time step size. This recovery indicator leads to reasonable results because the conservation of mass represents a linear subproblem. Within the hierarchical mesh refinement an element subdivision is performed when at least one of the two prescribed tolerances tol_{eq} and tol_{fl} is exceeded.

4.3. TEMPORAL DISCRETIZATION ERROR

Generally, the accuracy and efficiency of the numerical analysis of time dependent problems like the consolidation process is strongly coupled to an appropriate time discretization. The

indicator for the temporal discretization error proposed here is closely related to the jumps that arise at the discrete time levels in the framework of the Time-Discontinuous Galerkin method. As the size of the jumps vanishes when the step size is reduced successively, the L_2 -norm of the discontinuities in the three different fields may be directly used as an error measure:

$$\begin{aligned}\eta_{\Delta t, u} &= \| \llbracket u \rrbracket \|_{L_2(V)}, \\ \eta_{\Delta t, \omega} &= \| \llbracket \omega \rrbracket \|_{L_2(V)}, \\ \eta_{\Delta t, p} &= \| \llbracket p \rrbracket \|_{L_2(V)}.\end{aligned}\quad (10)$$

A relative local error is then derived by relating the values to the L_2 -norm of the increments. Finally, the maximum of the calculated values is taken as a basis for the time step control:

$$\eta_{\Delta t} = \text{MAX} \left(\frac{\eta_{\Delta t, u}}{\|\Delta u\|_{L_2}}, \frac{\eta_{\Delta t, \omega}}{\|\Delta \omega\|_{L_2}}, \frac{\eta_{\Delta t, p}}{\|\Delta p\|_{L_2}} \right) \quad (11)$$

The advantage of this formulation is the low computational effort to evaluate the error indicator as the jumps $\llbracket u \rrbracket$, $\llbracket \omega \rrbracket$ and $\llbracket p \rrbracket$ are directly associated to the primary unknowns of the global system of equations.

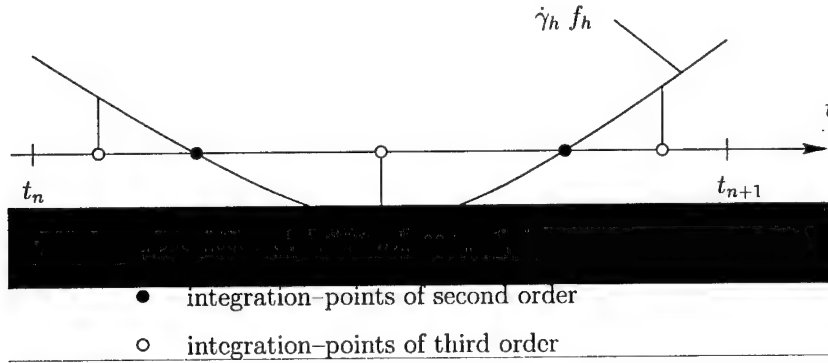


Figure 2. Gauss-point-integration of higher order over the interval I_n

4.4. ERROR IN THE INTEGRATION OF THE CONSTITUTIVE EQUATIONS

The determination of the path dependent variables is performed by a numerical integration in the context of elastic-plastic constitutive equations. Hence, another error is introduced which depends on the integration scheme as well as the time step size. In order to bound this accumulative error, the step sizes have to be controlled. The indicator proposed in this section is based on the residuum of the Kuhn-Tucker conditions:

$$\dot{\gamma} \geq 0, \quad f(\sigma, \mu, q) \leq 0, \quad \dot{\gamma} f(\sigma, \mu, q) = 0. \quad (12)$$

The application of a discontinuous time approximation prevents the use of the standard backward Euler rule. Therefore, an integration scheme has been implemented where the Kuhn-Tucker conditions are strictly enforced at two Gauss points in time. The indicator for the constitutive relations is then given by the integral of $|\dot{\gamma} f|$ over the time interval:

$$\begin{aligned}\eta_{\sigma\epsilon} &= \frac{1}{\Delta t N_{pl}} \sum_{i=1}^{N_{pl}} \int_{I_n} \underbrace{|\dot{\gamma} f(\sigma, \mu, q) - \dot{\gamma}_h f(\sigma_h, \mu_h, q_h)|}_{\rightarrow 0} dt = \\ &= \frac{1}{\Delta t N_{pl}} \sum_{i=1}^{N_{pl}} \int_{I_n} |\dot{\gamma}_h f(\sigma_h, \mu_h, q_h)| dt\end{aligned}\quad (13)$$

This results in an absolute measure $\eta_{\sigma\epsilon}$ which may be evaluated using a higher Gauss point scheme. Figure 2 illustrates the whole procedure. Of course, this indicator is restricted to zones of plastic response as an elastic stress strain relation may be integrated analytically. The time step control is based on these two temporal indicators. Therefore, two additional tolerances $tol_{\Delta t}$ and $tol_{\sigma\epsilon}$ have to be prescribed. If one of them is exceeded, the step has to be recalculated again using a smaller increment size. In the case of a purely elastic behaviour, the step size control is restricted to the evaluation of the temporal discretization error $\eta_{\Delta t}$. However, when limit-load states are reached the constitutive indicator $\eta_{\sigma\epsilon}$ becomes the restricting factor.

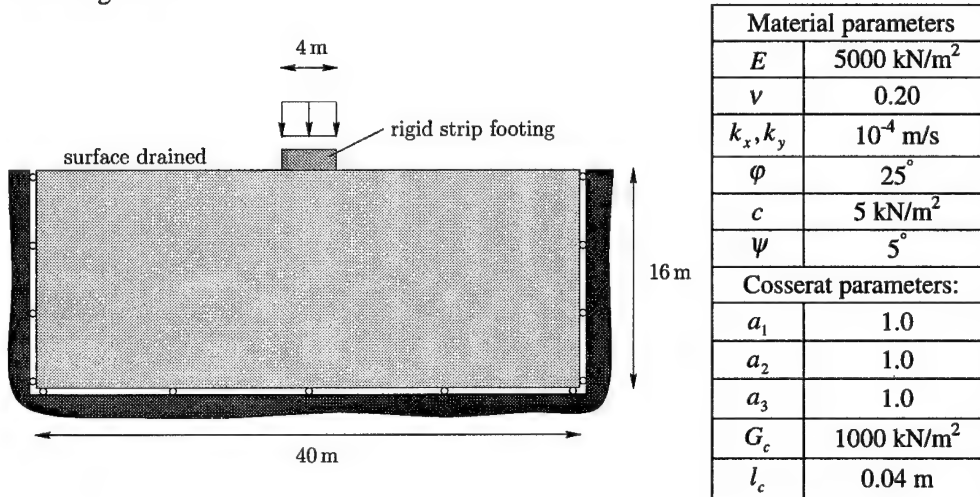


Figure 3. Geometrical and material properties of the strip footing

5. NUMERICAL EXAMPLE - STRIP FOOTING ON HALF SPACE

A standard problem in practical geomechanics is the investigation of a strip footing on a half space. A theoretical basis of the corresponding failure analysis was developed by Prandtl [6]. The numerical simulation was based on the space and time adaptive strategy proposed in this paper. The geometry of the system and the material parameters including those for the Cosserat extension are shown in Figure 3. The rigid strip footing is loaded in a displacement controlled analysis. The limit-load state is typically characterized by narrow shearbands as shown in Figure 4 and exhibits the distinct slip lines which are similar to those obtained by the analytical solution of Prandtl. The result of the space adaptive part of the computation is shown in Figure 4. Especially, the indicator η_{eq} for the equilibrium conditions is well suited to detect and refine the localization zone appropriately. An element length in the same

dimension as the internal Cosserat length ($h \approx l_c$) ensures a sufficient accurate approximation of the geometry of failure. This was achieved by a hierarchical mesh refinement. However, in this case more than 70000 degrees of freedom were necessary in the 8th level of refinement.

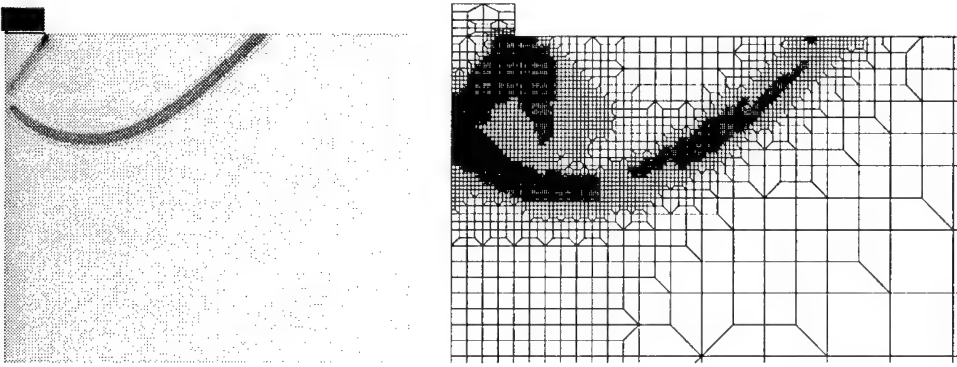


Figure 4. Incremental rotations $\Delta\omega$ and final mesh

The evolutions of the time step sizes are shown in Figure 5 where the tolerances for the constitutive error were set to $tol_{\sigma\epsilon} = 10^{-4}$, 10^{-5} and 10^{-6} . It becomes obvious that the step sizes have to be reduced in times characterized by a rapid increase in the plastic zone. But also when the shearband formation is initiated and large domains show an elastic unloading smaller step sizes are applied. In time domains which show only small changes in the stress states, the increments may be chosen larger by a factor of about 4. Thus, constant small step sizes are far from being optimal with respect to an equal error distribution over the entire time domain. It becomes obvious that a reduction of the tolerances results in a consequent adjustment to smaller time steps ensuring a higher accuracy level.

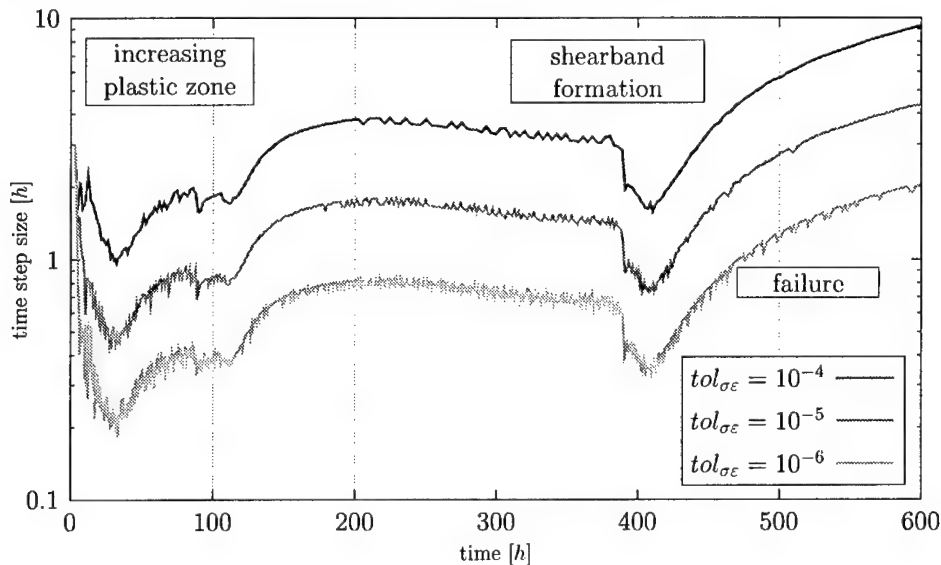


Figure 5. Time adaptivity – evolution of time step sizes

6. CONCLUSIONS

A concept for the space and time adaptive computation of localized failure in water saturated soils has been presented. The whole procedure is based on a space-time finite element formulation which couples standard finite elements in space and the Time-Discontinuous-Galerkin method. The three-field approximation for the consolidation problem includes an extension to the Cosserat theory which introduces a strong regularization effect.

A hierarchical mesh refinement and an automatic time step control are based on four different error indicators. This procedure includes an evaluation of the error in the equilibrium conditions, the error in the continuity of the fluid flows, the temporal discretization error and the error in the integration of the constitutive equations. The combination of space and time adaptive strategies lead to a significant improvement in efficiency. Zones of strain localization are detected and refined both in space and in time. An unsolved problem consists in the high number of step size changes connected to a recalculation of the current step. Therefore, the time step control has to be improved by a kind of a priori indicator.

7. REFERENCES

- [1] H. Cramer, R. Findeiß, and W. Wunderlich. Elastic-plastic consolidation analysis of saturated soil by a time discontinuous method. In W. Wunderlich, editor, *European Congress on Computational Mechanics* (CD-ROM), München, 1999.
- [2] R. de Boer and W. Ehlers. Theorie der Mehrkomponentenkontinua mit Anwendung auf bodenmechanische Probleme. Forschungsbericht aus dem Fachbereich Bauwesen 40, Universität-GH-Essen, 1986.
- [3] R. de Borst. Simulation of strain localization: A reappraisal of the Cosserat continuum. *Engineering Computations*, 8:317-332, 1991.
- [4] W. Ehlers and W. Volk. On shear band localization phenomena induced by elasto-plastic consolidation of fluid-saturated soils. In D.J.R. Owen, E. Onate, and E. Hinton, editors, *Computational Plasticity - Fundamentals and Applications*, Volume 2, pages 1657-1664. CIMNE, 1997.
- [5] C. Johnson and P. Hansbo. Adaptive finite element methods in computational mechanics. *Computational Methods in Applied Mechanics and Engineering*, 101:143-181, 1992.
- [6] L. Prandtl. Über die Härte plastischer Körper. Nachrichten der Gesellschaft der Wissenschaften, 1920.
- [7] W. Wunderlich, H. Cramer, and G. Steinl. An adaptive finite element approach in associated and non-associated plasticity considering localization phenomena. In P. Ladeveze and J.T. Oden, editors, *Advances in Adaptive Computational Methods in Mechanics*, pages 293-308. Elsevier Science, Amsterdam, 1998.
- [8] W. Wunderlich and W. Redanz. A local strategy for mesh refinement and adaptive control. In P. Ladeveze and O.C. Zienkiewicz, editors, *New Advances in Computational Structural Mechanics*, pages 233-245, Amsterdam, 1992. Elsevier Science.
- [9] O.C. Zienkiewicz and J.Z. Zhu. A simple error estimator and adaptive procedure for practical engineering analysis. *International Journal for Numerical Methods in Engineering*, 24:337-357, 1987.

MEASUREMENT OF THE MECHANICAL PROPERTIES OF MEMS MATERIALS

William. N. Sharpe, Jr.
Department of Mechanical Engineering
Johns Hopkins University,
Baltimore, Maryland, 21218, USA

1. SUMMARY

Techniques and procedures are described for the tensile testing of very small specimens of materials that are used in microelectromechanical systems (MEMS). Narrow (50 microns wide) specimens of polysilicon and wide (600 microns) specimens of polysilicon, silicon nitride, and silicon carbide are tested; these range in thickness from 0.5 microns to 3.5 microns. Larger nickel specimens are 200 microns thick and 3 millimeters long. Uniaxial and biaxial strain is measured directly on these specimens with interferometry from reflective markers. Brief descriptions of the test methods and representative results are presented.

2. INTRODUCTION

Surface micromachined MEMS are planar devices with thicknesses on the order of a few microns, widths and lengths on the order of tens of microns to millimeters, and minimum features in the plane (e.g. radius of curvature) of one micron. They are manufactured using processes common in the microelectronics industry and are indeed new materials from a mechanical performance viewpoint. It is difficult to measure Young's modulus, Poisson's ratio, and fracture strength of specimens that have the same size scale as MEMS, but considerable progress in test methods has taken place over the past half-dozen years.

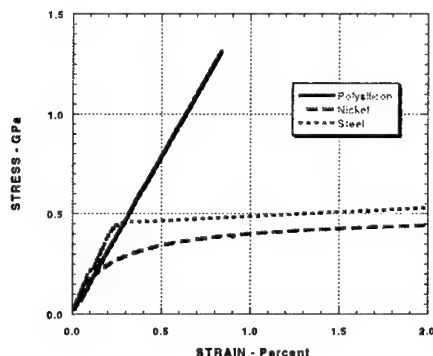


Figure 1: Representative stress-strain curves.

Polysilicon (polycrystalline silicon) is the predominant thin-film material used in MEMS at this point; the structural elements in these planar microdevices are less than 5 microns thick. More robust MEMS involving larger forces are made from electroplated nickel that is a few hundred microns thick. Figure 1 shows typical stress-strain curves for these two materials along with a common steel. These results were obtained in the author's laboratory, and the steel and nickel specimens were the same size and shape. The nickel is almost as strong as the steel and is much stronger than the bulk form of pure nickel. Polysilicon is a linear brittle material, as would be expected for a ceramic, and it is much stronger than either of the metals.

This paper is an overview of the accomplishments of the past several years. Details on the wide thin-film specimen tests can be found in [1], on the narrow specimen tests in [2], and on the nickel tests in [3]. For a comprehensive review of mechanical testing and properties of MEMS materials in general, the reader is referred to [4]. The strain measurement technique, used throughout, is described in Section 3. The next three sections describe the test methods and present typical (but not comprehensive) results for the three kinds of specimens – wide and narrow thin-films and thick-films. Section 7 offers some concluding remarks.

3. STRAIN MEASUREMENT

Strain is measured by laser-based interferometry from a set of two gold lines deposited in the center of the gage section of the tensile specimen. These lines simply need to be reflective, but gold is the last step in this particular manufacturing process. The lines are 0.5 microns thick, 20 microns wide, and spaced 200 microns apart. Figure 2 is a schematic that illustrates the optical principle and Figure 3 is a SEM photograph of two sets of gold lines on polysilicon, which enables biaxial strain measurement.

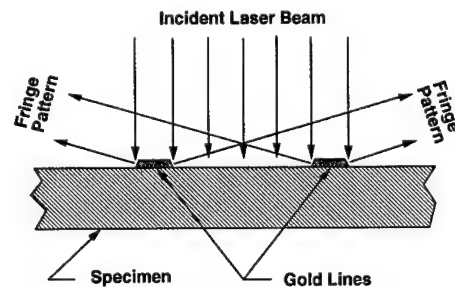


Figure 2: Schematic of interferometric strain measurement.

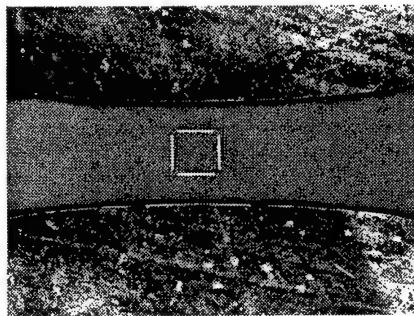


Figure 3: Photograph of gold lines on polysilicon specimen.
The width of the specimens is 600 microns.

The incident laser beam reflects (more accurately diffracts) from the edges of the two gold lines to form interference patterns. The position in space of these patterns is dependent upon the spacing between the lines, and these fringes move as the specimen is strained. Fringe motion is monitored by linear diode arrays, which feed into a computer to permit real-time strain measurement. This method is described in Sharpe et al. [1].

4. WIDE THIN-FILM SPECIMENS

A wide specimen is shown in the scanning electron micrograph of Figure 4. Polysilicon is patterned onto the die as shown and a rectangular window is etched out of the underlying silicon wafer to leave the tensile specimen supported across an opening. The die is then placed in a test machine with the large ends glued to the grips and the side support strips cut with a diamond saw. This leaves a completely free and unsupported tensile specimen mounted in the test machine. The specimen is 3.5 microns thick and 600 microns wide in the center of the test section, which has an overall length of 4 millimeters.

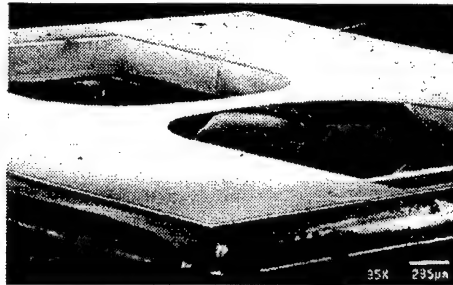


Figure 4: Photograph of a wide specimen.

Figure 5 is a schematic of the setup for testing wide specimens. The free (after the support strips are cut) end of the specimen is glued to the movable portion of a linear air bearing to reduce friction in the load train. A 4.45 N load cell measures the force applied to the specimen as a piezoelectric actuator elongates it. The arrangement for the strain measurement is also shown in the schematic. Specimens can be heated resistively for high temperature testing, and those electrical contacts are shown in the schematic.

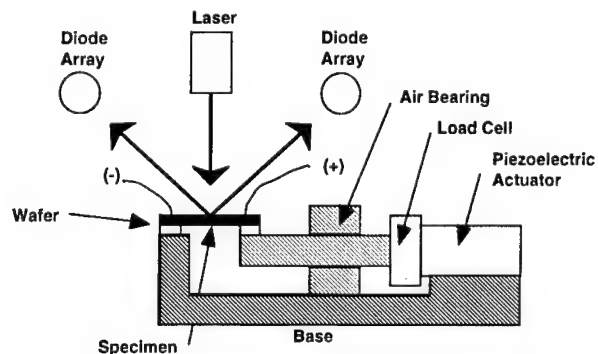


Figure 5: Schematic of the wide specimen setup.

Figure 6 is a plot of individual wide-specimen tests on three different thin-film materials. Polysilicon, which is 3.5 microns thick and is the most extensively tested material, has a Young's modulus of 169 ± 6 GPa, Poisson's ratio of 0.22 ± 0.01 , and a fracture strength of 1.20 ± 0.15 GPa [1]. The initial set of test results for 0.5 micron thick silicon nitride produce a modulus of 254 ± 3 GPa, Poisson's ratio of 0.23 ± 0.02 , and a much higher strength of 6.41 ± 1.04 GPa (note that the complete result is not plotted in Figure 6). The plot for 0.5 micron thick silicon carbide is from one early test of this material; these test methods are still under development.

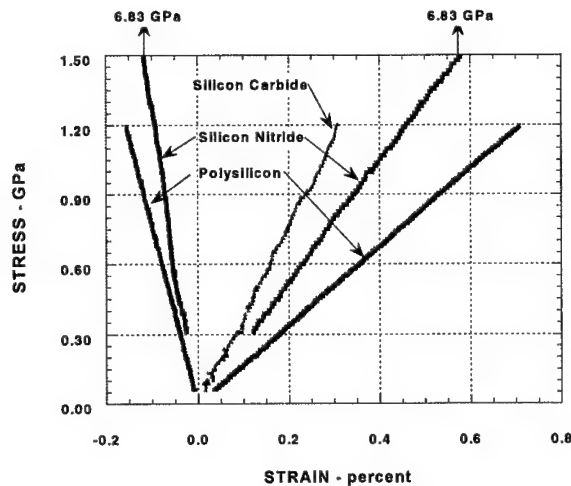


Figure 6: Stress-strain plots for three thin-film MEMS materials.

5. NARROW THIN-FILM SPECIMENS

Narrow polysilicon specimens have the advantages of providing more samples per die, and they have widths on the same scale as MEMS. A different approach is taken here in handling and gripping, and Figure 7 shows a typical specimen. One end of the specimen remains attached to the silicon substrate, but the rest of the specimen is released by etching away a 2 μm thick layer of oxide under it. The narrow straight test section (3.5 microns thick, 50 microns wide) is faired into the ends with a curvature of large radius, and the movable grip end is punctuated with holes to allow the etching to occur. Each grip end is supported by four anchors, which are broken before testing.

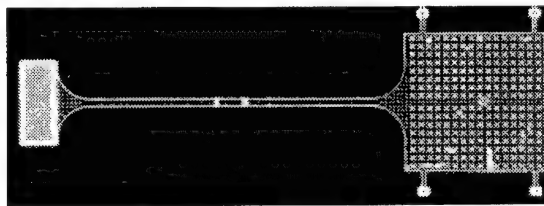


Figure 7: Photograph of a narrow thin-film specimen.

These specimens are gripped by gluing a 125 micron diameter silicon carbide fiber to the free end; the other end of the fiber is attached to a 1 N load cell as shown in the schematic of Figure 8. A small piezoelectric actuator also elongates these specimens.

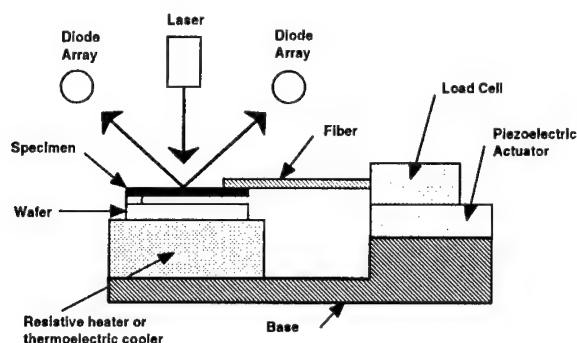


Figure 8: Schematic of the narrow specimen test setup.

Figure 9 presents a typical result for a narrow specimen test -- but at 200°C. The specimen was heated in a small resistive furnace with a quartz window to allow optical access. The silicon fiber provides the connection between the specimen and the load cell outside the furnace. The key to these tests is aligning the load cell and fiber so that the specimen is pulled straight along its axis. This requires an initial tension, which is why the plot does not start at the origin. Alignment is monitored by viewing the laser image reflected perpendicularly from the gage section and is also verified by ensuring that the loading and unloading modulus values are the same.

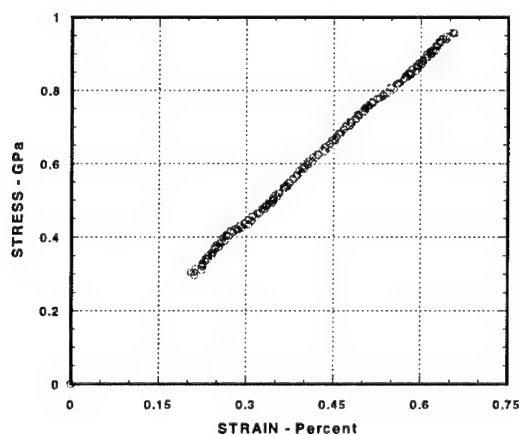


Figure 9: Stress-strain plot for a narrow polysilicon specimen tested at 200°C.

The results of modulus measurements on 13 different narrow specimens are shown in Figure 10 as a function of temperature. Room temperature measurements of Young's modulus of

polysilicon show a coefficient of variation of 5%, and the results here show a similar value at each temperature. It is clear that the decrease in Young's modulus is at most 15 GPa (less than 10% of the original value) over the entire temperature range. The fracture strengths of these specimens show no discernible trend over the temperature range.

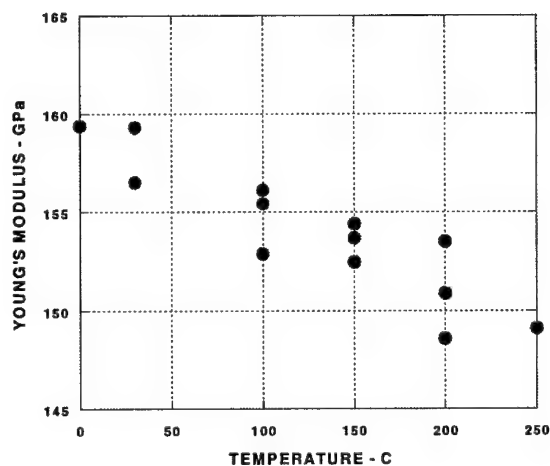


Figure 10: Young's modulus versus temperature.

6. THICK-FILM SPECIMENS

Thicker specimens of pure nickel are fabricated by electroplating into polymer molds produced by exposure to X-rays; this is the LIGA technique used to make MEMS. Figure 11 is a SEM photograph of a single specimen on a silicon substrate. These specimens can be released by etching away a thin sacrificial layer underneath the specimen, which allows one to pick them up and place them in a test machine similar in concept to the schematic of Figure 5. Uniaxial strain is measured on these ductile specimens from pyramidal indentations placed into the polished surface of the specimen with a Vickers microhardness tester.

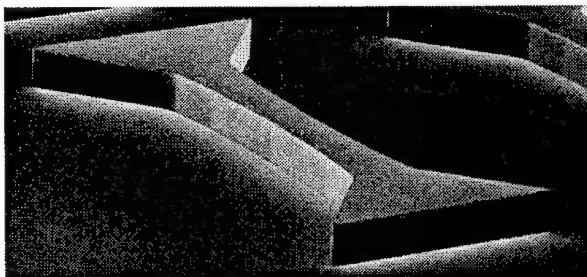


Figure 11: Nickel microspecimen produced by the LIGA method. The overall length is 3.1 millimeter, and the width at the center is 200 microns.

Electroplating is a process that can be highly variable, and Figure 12 shows the stress-strain curves for pure nickel deposited at different current densities. Strength increases with decreasing current, and one should note that this can produce an extremely strong nickel film – as strong as polysilicon.

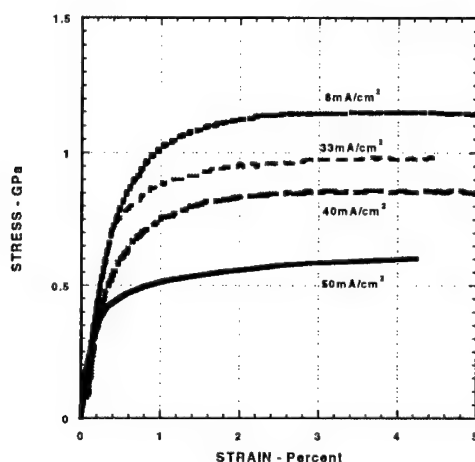


Figure 12: Stress-strain curves for nickel electroplated at different current densities.

7. CONCLUSIONS

Although not evident from this brief presentation, considerable progress has been made in the mechanical testing of these new structural materials used in MEMS. There are other indirect methods of measuring mechanical properties at this size scale. Examples are in-plane and out-of-plane bending, resonant structures, and membrane bulge tests; these are reviewed in [4]. None of those methods provide all three properties (Young's modulus, Poisson's ratio, and fracture strength), and all rely on linear behavior of the material. The tension test is the accepted standard for measuring usable mechanical properties of materials because of its simplicity (in concept) and the uniformity of the stress and strain states.

Now that test methods for thin and thick films are becoming mature, one can use them on various materials and also to explore the effect of environment on the mechanical properties. Steps in that direction have been taken with the new results for silicon nitride and silicon carbide in Figure 6 and with the temperature effects of Figure 10. Nevertheless, much more experimental research needs to be done to further develop test methods and to explore these new and interesting materials.

Acknowledgements: The author very significant contributions to all of this work by students: Bin Yuan, Andrew McAleavey, David Lavan, Kevin Turner, Kamili Jackson, and Matt Eby. Colleagues Richard Edwards and George Coles have led the efforts to develop the specimen preparation and testing methods. The nickel data of Figure 12 is courtesy of Professor Kevin Hemker and Dr. H. Cho.

Effort sponsored by the Defense Advanced Research Projects Agency (DARPA) and Air Force Research Laboratory, Air Force Materiel Command, USAF, under agreement number F30602-99-2-0553. The U. S. Government is authorized to reproduce and distribute reprints for Governmental purposes notwithstanding any copyright annotation thereon.

8. REFERENCES

- [1] Sharpe, W. N., Jr., Bin, Y., and Vaidyanathan, R., "Measurements of Young's Modulus, Poisson's Ratio, and Tensile Strength of Polysilicon," *Proceedings IEEE - The Tenth Annual International Workshop on Micro Electro Mechanical Systems*, pp. 424-429, Nagoya, Japan (1997).
- [2] Sharpe, W. N., Jr., Turner, K. T., and Edwards, R. L., "Tensile Testing of Polysilicon," *Experimental Mechanics* **39**, pp. 162-170 (1999).
- [3] Sharpe, W. N., Jr., LaVan, D. A., Edwards, R.L., "Mechanical Properties of LIGA-Deposited Nickel for MEMS," *Proceedings of International Solid State Sensors and Actuators Conference - Transducers '97*, pp. 607-610, Chicago, IL (1997).
- [4] Sharpe, W. N., Jr. "Mechanical Properties of MEMS Materials", Chapter 3 in The MEMS Handbook, CRC Press, in press.

BEHAVIOR OF PARTICLE REINFORCED COMPOSITES WITH SOFT MATRICES

C.A. Sciammarella, Federico M. Sciammarella

Department of Mechanical, Materials and Aerospace Engineering
Illinois Institute of Technology, IL, 60616, USA

1. SUMMARY

Solid propellants contain high modulus particles and a low modulus matrix made out of a mixture of rubbers. In this paper an experimental technique, holographic moiré is utilized to obtain information about the interaction between reinforcing particles and matrix. An integral definition of the quantity adherence is introduced to quantify the interfacial strains. A number of samples are studied and an adherence curve is obtained as a statistical trend of the experimental data. An independent procedure to measure adherence using the stress strain curves of the material is also introduced. Both techniques provide results that show an excellent agreement.

2. INTRODUCTION

This paper deals with the experimental determination of the interfacial adhesion of particles and matrix in a particle reinforced composite. The composite in this study consists of a rubber matrix and reinforcing particles that are made up of either potassium perchlorate or metals. The size of the particles range from 5 microns for the metallic particles to about 400 microns for the crystalline particles. In this type of material the damage process consists of the separation of the particle from the matrix as the material is loaded in tension. The experimental approach taken in this paper is to directly measure the process of separation. With this aim, regions of about 1000×1000 microns in a tensile specimen were observed with a microscope.

Figure 1 gives a schematic representation of the utilized set up. A tensile specimen is subjected

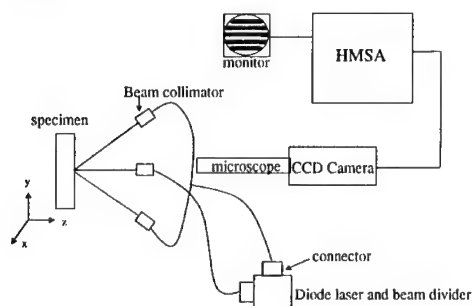


Figure 1. Testing set up.

to creep loading applied in steps and the measurements are carried out at equal intervals of time. In this way a constant average speed of loading is obtained. The Holographic moiré technique is used to measure the displacement fields and the strains. A four beam fiber optics interferometer is used to measure the displacements in two orthogonal directions. In this way full field information is obtained at each time interval. The Holo-Moiré Strain Analyzer (HMSA) a fully computerized device developed at the Experimental Mechanics laboratory is used to carry out data gathering, processing, and data analysis. The final output of the system consists of maps of the principal strains and directions in the region under observation.

3. ANALYSIS OF EXPERIMENTAL DATA

In order to evaluate the process of separation between particle and matrix an integral definition was introduced.

$$A_d = 1 - \frac{\int \epsilon_\theta(x, y) ds}{\int \epsilon_{\theta th}(x, y) ds} \quad (1)$$

The integral in the numerator represents the elongation of a closed circuit taken about 10 microns from the boundary of a particle. $\epsilon_\theta(x, y)$ is the component of the strain tensor along the tangent direction to the closed circuit. The integral in the denominator is the elongation of the same circuit computed using the modulus of elasticity and Poisson's ratio of the composite under tensile load. If we divide the numerator and denominator by the length (ℓ) of the circuit we obtain the following equation,

$$A_d = 1 - \frac{\epsilon_{avg}}{\epsilon_{th}} \quad (2)$$

where ϵ_{avg} is the average strain in the chosen circuit obtained from the actual strain distribution and ϵ_{th} is the average strain of the same circuit corresponding to the uniaxial state of stresses for the same load. If $\epsilon_{avg} = 0$, it means that the matrix sticks to the particle since the modulus of elasticity of the particles is three orders of magnitude larger than the matrix, the elongation of the contour will be negligible. In this case the adherence will be equal to one. If on the contrary $\epsilon_{exp} = \epsilon_{th}$ the adherence will be equal to zero. If ϵ_{exp} is larger than ϵ_{th} the adherence becomes negative meaning that the contour deformation is larger than the one corresponding to the tensile specimen contour, indicating the complete separation of the particle from the matrix and the increased deformation of the region due to the presence of a cavity. The definition of adhesion is related to the quantity damage in the following way,

$$D = 1 - A_d \quad (3)$$

when A_d is equal to one the damage will be zero and when $A_d = 0$ the damage will have the maximum value equal to one.

The previously introduced definition of adherence is based on a contour integral performed on the surface of the specimen based on the motion of the continuum. It can be shown mathematically that the experimentally determined contour integral provides a measure of the detachment of the particle from the matrix. As a result, the surface values can be taken as a representative measure of the process not only on the surface but also internally.

4. DAMAGE RELATIONSHIP OBTAINED FROM THE STRESS STRAIN CURVE OF MATRIX AND COMPOSITE

In the literature of composite materials it is usual to measure damage from the change of the elastic modulus of the stress strain curve. To apply this definition to the particulate composite presents the following problem. The stress strain curve of the composite has a non linear behavior due to the non linearity of the matrix material. Consequently there are two effects that produce the non linear behavior. The first effect is the non-linearity of the matrix, and the second is the separation between the particles from the matrix. Consequently to measure damage or adherence it is necessary to separate these two effects. In order to separate these two effects the following definition of adherence is introduced.

$$A_d = \frac{E_c - E_m}{E_{cth} - E_m} \quad (4)$$

where E_c is the measured composite tangent modulus for the corresponding stress level, E_m is the matrix modulus for the same stress and E_{cth} is the value of the composite modulus assuming that the adherence between the particle and the matrix is perfect.

We need to know the value of E_{cth} , an important clue towards the answer of the problem of evaluation of damage is given by Fig.2. Figure 2 shows the ratio of the modulus of elasticity of the composite and the matrix for zero stress, E_{oc}/E_{om} as a function of the volumetric matrix content, 1 indicating pure matrix.

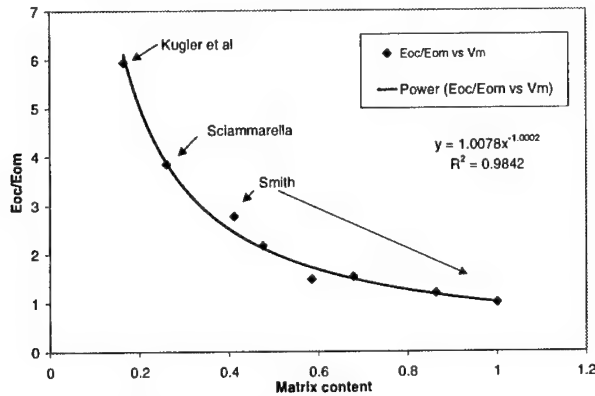


Figure 2. E_{oc}/E_{om} vs. matrix volumetric content.

The data come from references [1], [2] and [3]. In [1] and [2] the values were evaluated from the stress strain curves of the composite and the matrix material, in [3] these values are provided in tabulated form. The trend line of the experimental points is to a high degree of accuracy of the form

$$\frac{1}{E_{oc}} = \frac{V_m}{E_{om}} + \frac{V_p}{E_p} \quad (5)$$

where V_m and V_p represent the volumetric contents of the matrix and the particles respectively. In (5) the contribution of the second term is negligible because E_p is a very large value, and therefore only the first term counts. Equation (5) provides the traverse modulus of

a unidirectional composite and also is a limit form that the Halpin-Tsai equation takes for short fiber reinforced composites. If we make the hypothesis that this equation can be applied for the tangent modulus of the composite as the matrix deforms, we can obtain the composite tangent moduli for the corresponding stresses assuming that there is perfect adherence between the matrix and the particles. Actually the whole process can be expressed in dimensionless form if we divide the numerator and denominator of (5) by E_m and the corresponding stress are expressed as the ratio of the actual stresses S divided by the composite rupture stress S_r . Equation (4) becomes,

$$A_d \left(\frac{S}{S_r} \right) = \frac{\frac{E_c \left(\frac{S}{S_r} \right)}{E_m \left(\frac{S}{S_r} \right)} - 1}{\frac{1}{V_m} - 1} \quad (6)$$

We have two measures of adherence obtained from two separate procedures, the analysis of the experimental data will provide a way to compare the results coming from these two different definitions.

5. EXPERIMENTAL RESULTS

Measurements were performed on five separate specimens. In each specimen several particles were analyzed. The measurements performed need to be interpreted in the statistical sense. The adherence changes with the shape, dimensions and orientation of the particles in the strain field. Most of the particles that we have analyzed have irregular contour and therefore a large number of orientations are represented in the obtained integrals. Since we can measure only a limited number of samples of a very large population, the question to be answered is whether the obtained sample represents a meaningful trend for the whole population. This is not an uncommon situation with these kinds of problems but fortunately we have found and independent way to evaluate adherence that reflects the overall behavior of the composite. Values of adherence measured in specimens two and three have been used to obtain the trend line shown in Fig.3, together with the 95 % level of confidence interval that indicates that values within this envelope belong to the population that has the trend line indicated in Figure 3. The obtained adhesion curve goes practically to one for zero stress and to zero for a stress very close to the actual fracture stress of the composite. The trend line can be represented by the cubic equation shown in Fig. 3.

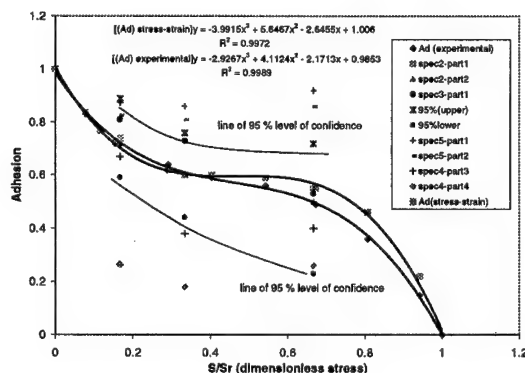


Figure 3. Adhesion curves with 95% confidence.

To implement equation (6) for our composite material, the tangent modulus of the matrix material and the composite were determined and plotted in dimensionless form in Fig. 4.

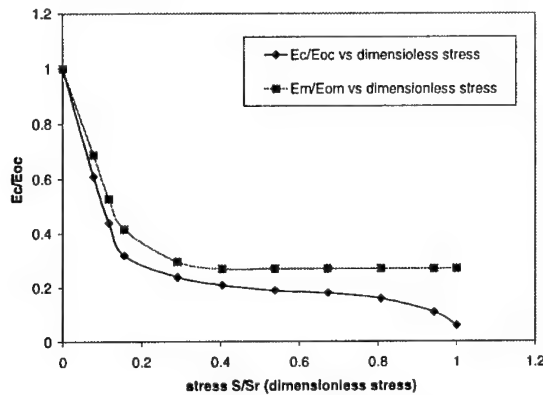


Figure 4. Modular ratios vs. dimensionless stress.

The agreement between the two trend lines is excellent particularly if we consider that the experimental values have been obtained up to $S/S_r = 0.67$. The agreement between the experimentally measured values of adhesion with the values of adhesion obtained from the stress-strain curves indicates the soundness of the model that has been used to predict adhesion from the stress-strain curves.

6. CONCLUSIONS AND OBSERVATIONS

The introduction of the definition of adhesion as a experimentally measurable quantity through a contour integral provides a unique tool to understand the behavior of the interface between particle and matrix. It can be shown theoretically that the surface measurements provide information of the events that take place in 3-D and not only on the surface. The sampling of the population of interfaces through this tool has proved to be very fruitful because it has been feasible to ascertain from a reduced number of measurements population means. These experimentally determined values lend credibility to the model of damage that has been introduced in this paper. It has been evident to us for a long time that the changes of moduli of the composite with increasing load were not only caused by gradual damage of the interfaces as many authors have modeled it but also were greatly influenced by the matrix behavior. A link was missing between these two facts and this link was provided by the experimentally obtained data that relate volumetric content of matrix of the composite and the tangent modulus at zero stress. This relationship became clear when a dimensionless plot was introduced, thus removing the dispersion of the same data when the absolute modulus was plotted vs. the volumetric content of the matrix. It is very interesting to observe that the modulus prediction follows the well-known relationship used in composites to obtain transverse moduli of uniaxially fiber reinforced composites and short fiber composites.

The difference between the predicted modulus, of the composite and the actual modulus can be attributed to the process of damage and leads to the adhesion definition given in (4). The fact that this definition of damage agrees with the definition of adhesion given in (1) indicates two important things. First the integral definition of adhesion is successful in measuring the

degree of efficiency of the particle-matrix interface. Second a reduced number of samples provides enough information to ascertain the trend of the population.

The adhesion between particle and matrix is affected by particle size, orientation in the field of stresses, geometry of the particle and therefore the observed quantity is statistical in nature. The measurement has to be performed by selecting at random a large enough number of samples so that a good estimate of the population mean can be obtained. It became clear to us, that the faces most unfavorably oriented with respect to the applied tension can separate while the other faces subjected to compressive forces can remain adherent to the particle up to very high stresses. We can conclude that to understand the evolution of the defined quantity adhesion we have two processes to analyze, separation of the matrix in the direction of tensile stress components perpendicular to the interface, and gradual sliding where compressive stress act perpendicular to the interface. The other component of adhesion, the relative sliding of the matrix and particles, seems to be a reversible process since cyclic loading after a while settles to a stable condition. The initial drop of the adhesion curve vs. stress is very likely due to mostly matrix separation. Though the techniques introduced in this paper it is possible to quantify these effects by analyzing the cyclic stress-strain curves. Summarizing the damage has a s-shape configuration. The initial part of the s represents the separation along faces that are oriented in the direction perpendicular to the applied tension. The plateau region correspond to the sliding along the faces whose orientation does not facilitate the direct separation. The final part of the s corresponds to the accelerated separation of the particles from the matrix when the sliding process has been exhausted. Numerical analysis using finite element confirm these conclusions. This analysis reproduces the stress-strain curve of the composite under increasing load. In the numerical model only the large particles are included. The small particles do not play a role as it could be anticipated by applying gradient theories.

Acknowledgments: The authors would like to express they're thanks to Dr. T.C. Liu and the United States Air force for their support to this research.

7. REFERENCES

- [1] Kugler, H.P., Stacer R.J, and C.Steimle, "Direct measurement of Poisson's ratio in elastomers, Rubber Chemistry and Technology, Vol.63, No.4, pp473-487, September, October 1990.
- [2] Sciammarella, C.A, and F.M. Sciammarella, "Damage Mechanisms in solid propellants, Fourth Report, Air force Subcontract 97-517, May 1998.
- [3] Smith, T.L., "Volume changes and dewetting in glass bead-polyvinyl chloride elastomeric composites under large deformations", Transactions of then Society of Rheology, vol.III, pp113-136, 1959.

INDENTATION FAILURE OF SANDWICH PANELS

E. E. Gdoutos, I. M. Daniel and K.-A. Wang
Departments of Civil and Mechanical Engineering
Northwestern University, Evanston, IL 60208, USA

1. SUMMARY

Indentation failure is a common problem in sandwich construction arising from localized loads, such as point loads, line loads or distributed loads over a small area. Indentation results in high local deflections of the loaded face into the core material of the sandwich panel causing high local stress concentrations. In the present work an analytical and experimental investigation of the indentation failure of a composite sandwich panel was conducted. The panel was made of a carbon/epoxy facing and a PVC foam layer. It was supported on a rigid base and indented at the center with a cylindrical indenter. The load-deflection behavior of the loaded facing was monitored during the test. Strains were also measured near the load on both surfaces of the facing using embedded strain gages. A full-field stress analysis of the in-plane displacements and stresses in the foam was conducted using moiré and birefringent coating methods. The problem was modeled as an elastic beam resting on a Winkler type elastic-plastic foundation. Initiation of indentation failure occurs when the foundation yields, while final failure takes place when the facing fractures. The experimental measurements of the critical loads for initiation and catastrophic failure of the sandwich panel were in good agreement with the analytical predictions.

2. INTRODUCTION

Sandwich structures are sensitive to failure under localized load due to the high stress concentrations induced by the indentation of the loaded facing into the core material. The indentation response of sandwich panels was first modeled by Meyer-Piening [1] assuming linear elastic bending of the loaded facing resting on a Winkler foundation (the core). Soden [2] modeled the core as an idealized rigid-perfectly plastic foundation and resulted in a simple expression for the indentation failure load corresponding to compression facing fracture. Shuaieb and Soden [3] used Zingone's equations [4] for predicting indentation failure loads for sandwich beams with glass-fiber-reinforced plastic facings and thermoplastic foam cores. The problem was modeled as an elastic beam, representing the facing, resting on an elastic-plastic foundation, representing the core. Thomsen and Frostig [5] conducted photoelastic experiments on sandwich panels with soft core and used a high-order sandwich panel theory to predict the experimental results. Thomsen [6] proposed a two-parameter elastic foundation formulation which takes into account the existence of shear interactions between the loaded facing and the core. Other works on the indentation problem are listed in references 7 and 8. For a brief review of the mechanical behavior and failure mechanisms of sandwich structures refer to references 9 and 10.

3. THEORY

The local deflection of the loaded facing of a sandwich panel into the core is modeled by treating the loaded facing as a beam resting on a foundation (Fig. 1). For linear elastic behavior, the core is modeled as continuous distributed linear tension/compression

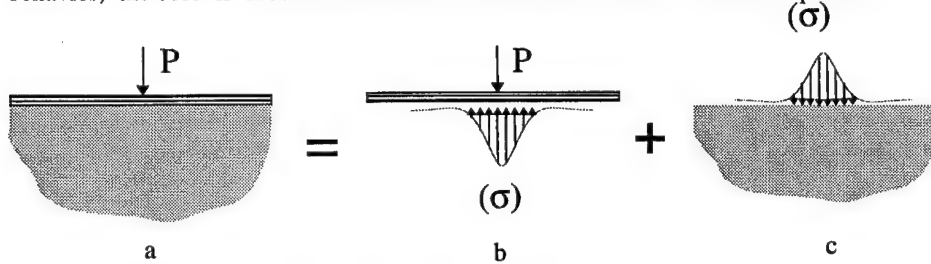


Fig. 1 Elastic beam on elastic foundation.

springs. The stress σ at the interface between core and facing is proportional to the local deflection w

$$\sigma = kw \quad (1)$$

where the foundation modulus k is given by [11]

$$k = 0.64 \frac{E_c}{h_f} \sqrt[3]{\frac{E_c}{b E_f}} \quad (2)$$

E_f, E_c = facing and core moduli, respectively

b, h_f = facing width and thickness, respectively

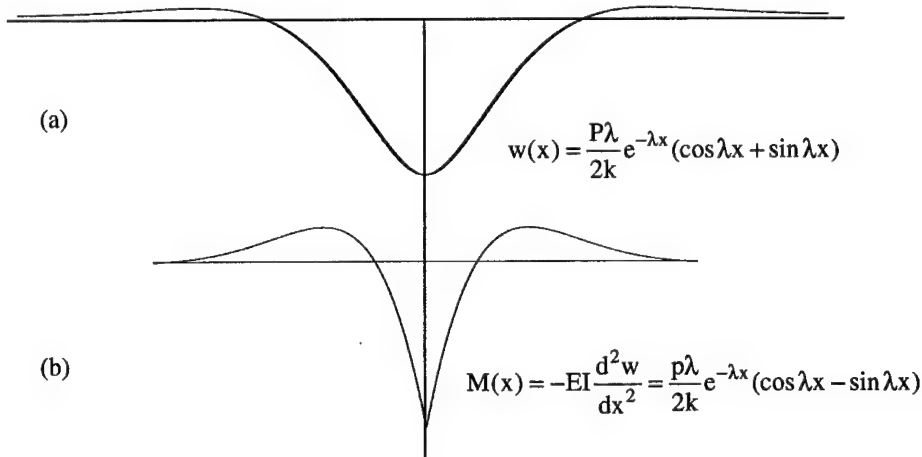


Fig. 2 Deflection (a) and moment (b) distribution in a beam resting on an elastic foundation and subjected to a concentrated load at its center.

For a long facing the deflection $w = w(x)$ is determined by [11]

$$w(x) = \frac{P\lambda}{2k} e^{-\lambda x} (\cos \lambda x + \sin \lambda x) \quad (3)$$

where P is the applied concentrated load, and

$$\lambda = \frac{1.18}{b h_f} \sqrt[3]{\frac{E_c}{E_f}} \quad (4)$$

The bending moment M of the facing is

$$M = -EI \frac{d^2 w}{dx^2} = \frac{P\lambda}{2k} e^{-\lambda x} (\cos \lambda x - \sin \lambda x) \quad (5)$$

Figure 2 shows a schematic representation of the deflection w and moment distribution along the axis of the facing.

Initiation of failure by indentation occurs when the core under the load yields. The critical load for core yielding is calculated from Eqs. (1) to (4) as

$$P_{cy} = 1.70 \sigma_{ys} b h_f \sqrt[3]{\frac{E_f}{E_c}} \quad (6)$$

where σ_{ys} is the yield stress of the core.

As the load increases beyond the core yield value, plastic deformation propagates through the core from the center to the ends of the facing (Fig. 3). Part of the core under the load deforms plastically, while the remaining part remains in the elastic region. For elastic-perfectly plastic behavior, the foundation in the first part can be modeled as rigid-plastic, while in the second part as elastic. Thus, along the plastic part the facing is subjected to a constant load q of magnitude

$$q = b \sigma_{ys} \quad (7)$$

while along the elastic part the facing is subjected to a stress proportional to the deflection, Eq. (1).

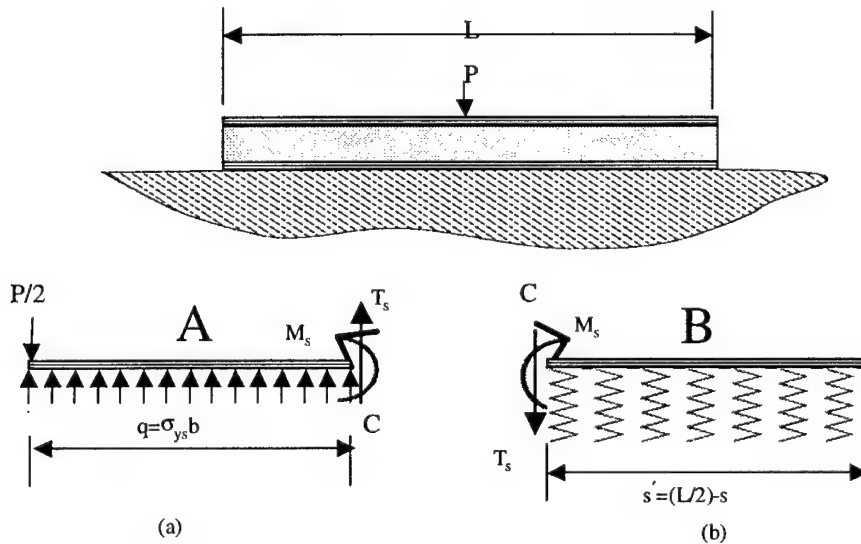


Fig. 3 Beam on elastic-plastic foundation
(a) rigid-plastic foundation, (b) linear elastic foundation.

The plastically deformed length s of the core is given in terms of the applied load P by [4]

$$\left(\frac{3\lambda}{2\sigma_{ys}b} \right) P = \frac{2z^3 (\sinh^2 z' + \sin^2 z') + 3(\sinh z' \cosh z' - \sin z' \cos z') (2z^2 - 1) - 6z}{z^2 (\sinh^2 z' + \sin^2 z') + 2z (\sinh z' \cosh z' - \sin z' \cos z') - (\cosh^2 z' + \cos^2 z')} \quad (8)$$

where $z = \lambda s$, $z' = \lambda s'$, $s' = L/2 - s$ and L is the length of the facing.

Equation (8) defines the relationship $s = s(P)$.

The critical load P for compressive failure of the facing is given by [3]

$$\left(\frac{\lambda}{\sigma_{ys}b} \right) P = \frac{\frac{2M_f \lambda}{\sigma_{ys}b} + z^2 + 2zA + B}{z + A} \quad (9)$$

where

$$\begin{aligned} M_f &= \sigma_f \frac{b h_f^2}{6} \\ A &= \frac{\sinh \lambda s' \cosh \lambda s' - \sin \lambda s' \cos \lambda s'}{\sinh^2 \lambda s' + \sin^2 \lambda s'} \\ B &= \frac{\sinh^2 \lambda s' - \sin^2 \lambda s'}{\sinh^2 \lambda s' + \sin^2 \lambda s'} \end{aligned} \quad (10)$$

and σ_f is the compressive strength of the facing. By solving Eqs. (8) and (9) the critical load P and the corresponding plastic zone length s for compressive failure of the facing are obtained.

When a rigid-perfectly plastic foundation is assumed a simplified expression for the critical load for compression facing failure is obtained as [2]

$$P = \frac{4}{3} b h_f \sqrt{\sigma_{ys} \sigma_f} \quad (11)$$

4. EXPERIMENTAL

4.1 Materials and Specimens

The sandwich panels were fabricated from 8-ply unidirectional carbon/epoxy (AS4/3501-6) facings and a PVC closed-cell foam (Divinycell H100) core. The constituent materials were fully characterized. The facing material after an initial linear part exhibits a characteristic stiffening nonlinearity in tension and a softening nonlinearity in compression. Divinycell H100 has a density of 100 kg/m³ and exhibits almost isotropic behavior. For full details of the mechanical properties of both materials refer to reference 9.

The carbon/epoxy facings were bonded to the Divinycell core with an epoxy adhesive (Hysol EA 9430). The assembly was cured at room temperature. The facing had a thickness of 1 mm. The specimens had a length of 305 mm and a height of 152 mm.

4.2 Experimental Procedure

The panels were supported on a rigid base and loaded by a cylindrical roller in an Instron servo-hydraulic testing machine. They were instrumented with four strain gages, two bonded

on the upper surface of the facing at distances of 7.1 mm and 14.5 mm from the load, and two embedded on the lower surface of the facing under the load and at distance of 14.5 mm from the loading axis. The strains were measured for progressively increasing the load on the roller.

5. RESULTS AND DISCUSSION

Figure 4 shows the load-strain curves as they were obtained by the four strain gages placed at the inner and outer surfaces of the facing of the sandwich panel. The four curves correspond to the location of the gages indicated in the figure. All four curves show an initial linear part up to a load of $P_c = 890$ N followed by nonlinear response. This load corresponds to initiation of yield in the core and is in good agreement with the

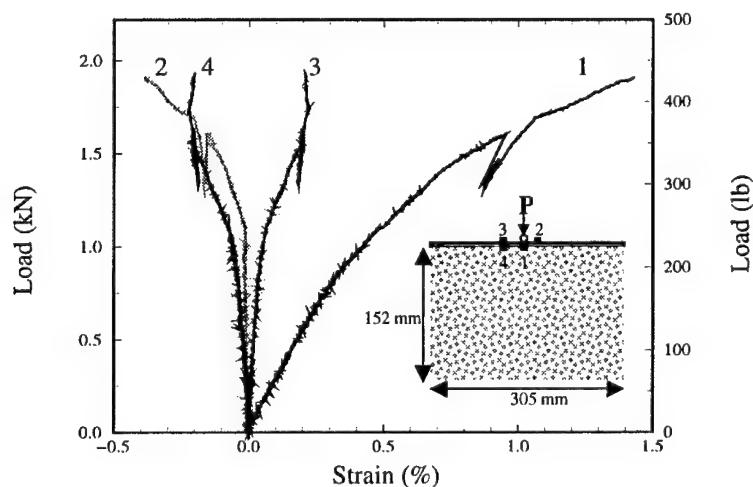


Fig. 4 Load-strain curves for a sandwich panel loaded by a cylindrical roller.

value of $P_c = 917$ N obtained from Eq. (6). Note that the strain at location 2 for linear elastic behavior is almost zero. This result is corroborated by the zero value of the deflection obtained from Eq. (4) for $x = 7.1$ mm (Fig. 2). Furthermore, curves 3 and 4 indicating strains on the upper and lower surfaces of the facing at a distance $x = 14.5$ mm from the loading axis are almost the same in magnitude but of opposite sign in the linear elastic region. The strain values are close to the predictions obtained from the value of bending moment given by Eq. (5). Fracture at the top surface of the facing occurred at a load of $P_c = 1,950$ N. The value of the critical load can be predicted from Eqs. (8) and (9). Figure 5 shows a plot of the load versus half length of the plastic zone according to these equations. The intersection of the two curves defines the critical load and the corresponding half length of the plastic zone. It was found that $P_c = 1,986$ N and $s_c = 30$ mm. The value of the predicted critical load is in good agreement with the measured value (deviation of 2%). The value of the critical load obtained from the simplified Eq. (11) based on a rigid-perfectly plastic foundation is $P_c = 1,590$ N. This value deviates from the experimental value by 20 percent. Thus, the assumption of a rigid-perfectly plastic foundation represents a crude approximation of the nonlinear behavior of the core foundation.

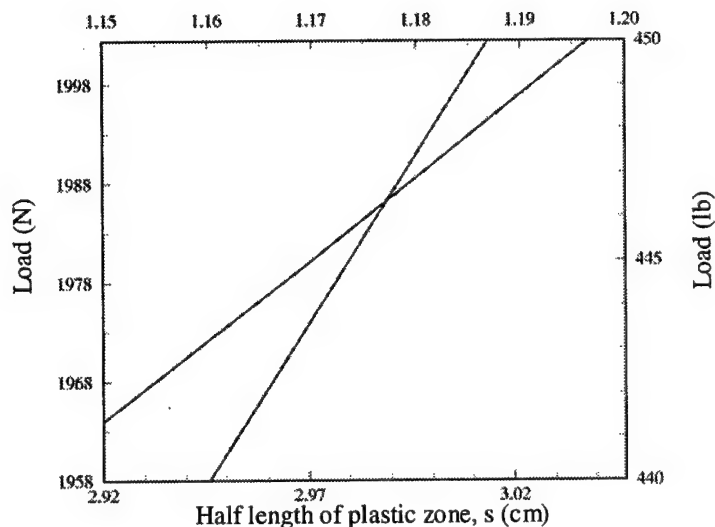


Fig. 5 Determination of critical load for fracture of the compressive facing according to Eqs. (8) and (9).

Acknowledgements: This research was sponsored by the Office of Naval Research (ONR). We are grateful to Dr. Y. D. S. Rajapakse of ONR for his encouragement and cooperation and to Mrs. Yolande Mallian for typing the manuscript.

6. REFERENCES

- [1] Meyer-Piening, H.-R., Remarks on higher order sandwich stress and deflection analyses, in *Sandwich Construction 1*, K.-A. Olsson and R. P. Reichard (Eds.), Proc. 1st Int. Conf. on Sandwich Construction, Stockholm (1989) 107-127.
- [2] Soden, P. D., Indentation of composite sandwich beams, *Journal of Strain Analysis* 31, 353-360 (1996).
- [3] Shuaieb, F. M. and Soden, P. D., Indentation failure of composite sandwich beams, *Composite Science and Technology* 57, 1249-1259 (1997).
- [4] Zingone, G., Limit analysis of a beam in bending immersed in an elasto-plastic medium, *Mechanica* 3, 48-56 (1968).
- [5] Thomsen, O. T. and Frostig, Y., Localized bending effects in sandwich panels: photoelastic investigation versus high-order sandwich theory results, *Composite Structures* 37, 97-108 (1997).
- [6] Thomsen, O. T., Analysis of local bending effects in sandwich panels subjected to concentrated loads, in *Sandwich Construction 2*, K.-A. Olsson and D. Weissman-Berman (Eds.), Proc. 2nd Int. Conf. on Sandwich Construction, Gainesville, FL (1992), 417-440.
- [7] Petras, A. and Sutcliffe, M.P.F., Indentation failure analysis of sandwich beams, *Composite Structures* 50, 311-318 (2000).
- [8] Anderson, T. and Madenci, E., Graphite/epoxy foam sandwich panels under quasi-static indentation, *Engineering Fracture Mechanics* 67, 329-344 (2000).

- [9] Gdoutos, E. E., Daniel, I. M., Wang, K.-A. and Abot, J. L., Nonlinear behavior of composite sandwich beams in three-point bending, *Experimental Mechanics*, to appear.
- [10] Daniel, I. M., Gdoutos, E. E. Wang, K.-A. and Abot, J. L., Failure modes of composite sandwich beams, *Int. J. of Damage Mechanics*, to appear.
- [11] Hetenyi, M., *Beams on Elastic Foundation*, The Univ. of Michigan Press (1946).

ESTIMATION OF THE CONCRETE CHARACTERISTICS USING PATTERN RECOGNITION METHODS

M. K. Titsias, D. I. Fotiadis and A. Likas
Dept. of Computer Science,
University of Ioannina, GR-45110 Ioannina, Greece

1. SUMMARY

We address the problem of nondestructive analysis and testing of concrete. The proposed system employs acoustic emission and pattern recognition methods of the corresponding waveforms to identify the water to cement and sand to cement ratios of a given concrete cube. For waveforms obtained experimentally using standard size concrete cubes, we study several classification methods and provide comparative results.

2. INTRODUCTION

The nondestructive testing of concrete constitutes a problem which undoubtedly is of significant importance. Our objective is to extract chemical composition characteristics of concrete, such as the ratio of water to cement (W/C) and sand to cement (S/C), and finally determine the stiffness and the microstructure of a concrete sample. Some techniques of nondestructive testing of concrete presented in the literature are based on nuclear methods and the dielectric properties of concrete [1]. The relation of the chemical composition (W/C) of the concrete using ultrasound has been also addressed [1].

The method presented in this paper is a data driven approach since we use experimentally collected data (cases of concrete cubes with known geometrical and composition characteristics) in order to construct a pattern recognition system capable of predicting the composition of unknown concrete cubes. The system is able to determine the W/C and S/C ratio of unknown concrete cubes, classifying them into a predefined set of classes. The construction of the system is based on a database of waveforms [3] which is obtained from experiments carried out using acoustic emission. Several classification methods are employed to tackle the problem. More specifically, we considered two neural network techniques, based on the multilayer perceptron and the radial basis function network [4]. We applied also a classical non-parametric method, the k nearest neighbor as well as a statistical pattern recognition method, based on probability density estimation and the Bayes decision rule [4, 5]. In addition, we provide with comparative results, identify the most promising methods and present classification results which are very encouraging.

3. ACOUSTIC EMISSION IN CONCRETE CUBES

Acoustic emission can be used for nondestructive analysis and testing of objects and aims at detecting cracks or other defects of the object. In addition, it provides information concerning the response and behavior of a object under pressure, which is associated with the object strength and chemical composition.

In this work, we use a set of waveform features produced by experiments using the acoustic emission method [2] in concrete cubes. The complete setup of these experiments is described in [3]. A typical waveform and its corresponding features are shown in Fig. 1.

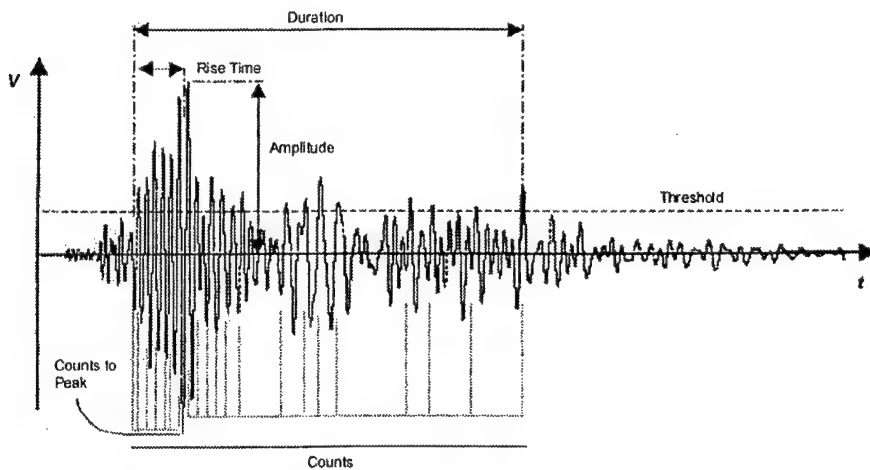


Figure 1: A typical waveform produced by acoustic emission and the corresponding features.

The terms used in Fig. 1 are explained below:

- **Threshold:** A specific signal amplitude used to separate the signal from noise. It is chosen such that to be slightly larger than the noise maximum amplitude.
- **Amplitude:** The maximum signal amplitude. This feature provides information about the intensity and the source distance.
- **Energy:** The area between the waveform and the time axis. It provides information about the intensity as well as the signal amplitude, the duration of signal and the signal its frequencies.
- **Counts:** The number of times the signal amplitude overruns the threshold. It depends on the signal intensity and frequencies.
- **Duration:** The time passed between the first the last overrun of the threshold. It provides information about the signal appropriateness in relation with the counts and the contained frequencies.
- **Rise time:** The time passed between the first threshold overrun and the occurrence of the maximum amplitude. It gives information about the intensity and the distance of the source. In addition, it can be used for noise detection.
- **Counts to peak:** The number of signal hits that overrun the threshold during rise time. It contains information, similar to the counts, for the signal part before the peak.

Note that the last six of the above terms correspond to features of the waveform and can be used by a pattern recognition method.

4. THE CLASSIFICATION PROBLEM

Our goal is to construct a classification system which will take as input concrete cube data (waveform features) of known age and provide with the ratio W/C and S/C, classifying the concrete cube into a predefined set of classes. The construction of the system is carried out using data driven methods (methods that use known data in order to train a system which can subsequently be used in unknown cases). The available waveforms have been obtained experimentally for cubes of four compositions concerning the ratio W/C and two concerning the ratio S/C, respectively (Table 1). In addition, the experiments have been performed on every concrete cube in four different ages: 1th, 7th, 28th and 90th day from production.

Table 1: The different W/C and S/C compositions of the concrete cubes and their names.

W/C \ S/C	0.50	0.55	0.60	0.65
3/1	A	B	C	D
4/1	E	F	G	H

Our classification approach is based on the fact that the total task can be partitioned into two subtasks: i) the estimation of the ratio W/C and ii) the estimation of the ratio S/C. Consequently, we could resolve the two problems independently. In such a case we can consider that the classification system consists of two classifiers which operate independently on the same input data in order to estimate W/C and S/C ratio. The estimation of the W/C ratio is a four-class problem and according to Table 1, data of compositions {A, E} correspond to the first class, {B, F} to the second class, {C, G} to the third class and {D, H} to the fourth class. Similarly, the estimation of the S/C ratio is a two-class problem and data of compositions {A, B, C, D} are from the first class, while data of compositions {E, F, G, H} are from the second class.

Now, each data point used for the construction of the classifier is essentially a feature vector with a label indicating its class. Such a feature vector can be constructed using all the waveform features described in Section 3. However, after a feature evaluation analysis applied to the total set of features, we found that the most suitable features for classification are: Energy, Counts and Duration.

5. CLASSIFICATION METHODS

We studied four classification methods. Two are based on neural networks methods, specifically on multilayer perceptron (MLP) and the radial basis function network (RBF). The third is the k -NN classifier and the fourth is a statistical pattern recognition technique which is based on probability density estimation and the Bayes decision rule. Next, we describe briefly the basic concepts of the methods and the way they have been used in our case.

The Multilayer perceptron (MLP)

The multilayer perceptron or backpropagation network [4] constitutes the most widely used neural network architecture for classification problems. Given a K -class problem with d -dimensional input data the MLP architecture includes d inputs nodes, K outputs nodes and usually one or two hidden layers of non linear (sigmoidal) activation functions. For the solution of classification problems each class i is required to be encoded with a K -dimensional indicator vector which takes zero values everywhere except for the i^{th} component which is one. The MLP network is trained to map each input data vector into its indicator vector. The training process is based on the minimization of the mean square error function estimated for the set of training data. To classify an unknown input data point, network outputs are computed and the class corresponding to the largest output value is selected.

The most common method to train an MLP network is the backpropagation algorithm which is based on the gradient descent method. However, in our case where the amount of data is small and the number of network weights is not large, it is preferable to use more sophisticated optimization techniques such as the Newton methods. In our experiments we have used a Quasi-Newton method called BFGS which gave superior results compared to gradient descent and other methods. In addition, it is well-known that models which provide sufficient representation of data and simultaneously there are not too complex (have few free parameters) give good generalization. Thus, in the training process we incorporated the concept of regularization (technique for setting constraints to the weights).

Radial basis function network (RBF)

Another major class of neural network methods is the radial basis function network [4]. The RBFs are feedforward networks with one hidden layer of units. The basic characteristic of the RBF is that a hidden activation function is determined by the distance between the input vector and a prototype vector. These activation functions are called radial basis functions and give local representation of data. The most widely used basis function is the Gaussian function. As for the output units of RBFs these are typically linear.

The typical way for adjusting the weights of a RBF network for a classification problem is based on a two-stage procedure. At the first stage unsupervised techniques, such as the k -means algorithm, are used to determine the weights associated with the basis function parameters (means and variances if Gaussian functions are used). This is achieved by considering all the training input data ignoring their class labels. At the second stage the radial basis function parameters are kept fixed and the second layer weights are adjusted using supervised learning. Typically, at this stage training is performed based on the minimization of the mean square error function with respect to the second layer weights.

In our experiments we used Gaussian functions at the hidden layer of the RBF and the first stage of training was based on probability density estimation (unsupervised technique) using Gaussian mixture models [4, 5]. The second training stage can be performed analytically (since the outputs values are linear functions of the second layer weights) by solving a linear system giving rise to mean square error solution.

The k nearest neighbor classifier (k -NN)

The k nearest neighbor classifier is a classical classification method [5]. The idea behind its use is simple: data points which are "close" under a distance measure may belong to the same class. More specifically, in order for an unknown data point to be classified, its k nearest

neighbors are found from the training set (using a distance measure) and then the class with the majority over the k neighbors is chosen. In our case we used the Euclidean distance and the parameter k takes low values (3 or 5) since a few training examples are available.

Mixture models and the Bayes decision rule (GMM)

According to the statistical approach to classification [4, 5] the goal is to find the posterior probability that an unknown data point belongs to a specific class. If we denote each class as C_k ($k = 1, \dots, K$), the posterior probability of class membership is obtained from Bayes rule

$$P(C_k | x) = \frac{P(C_k)p(x|C_k)}{\sum_i P(C_i)p(x|C_i)},$$

where $P(C_k)$ express the prior probability that class C_k is the true class of the data point x and $p(x|C_k)$ is the corresponding class conditional density function. If the prior probabilities and the class conditional densities were known, the following Bayes decision rule provides optimal results since it minimizes the misclassification error

$$\text{Choose } C_k : P(C_k | x) > P(C_i | x) \quad \text{for each } i \neq k.$$

In order to use the above rule for the classification of unknown data points, first the prior probabilities and the class conditional densities have to be determined. The prior probabilities usually take equal values ($P(C_k)=1/K$) or are easily estimated from the data as $P(C_k) = N_k / N$ where N_k is the number of data belonging to class C_k and N is the total number of training data. On the other hand, the estimation of the class conditional densities using the training examples is non-trivial and techniques of probability density estimation must be applied.

In our study we model the class densities by Gaussian mixture models, which are trained using the maximum likelihood method and the EM (Expectation-Maximization) algorithm [4].

6. EXPERIMENTAL RESULTS AND CONCLUSIONS

We applied the classification methods described above separately to the data of each of the four ages. Typically we used a training set (common for all methods) to obtain the classifiers and then a test set to measure the generalization capability, that is the classification performance for unknown data points. The results are illustrated in Fig. 2 for all ages, methods and the two classification subtasks.

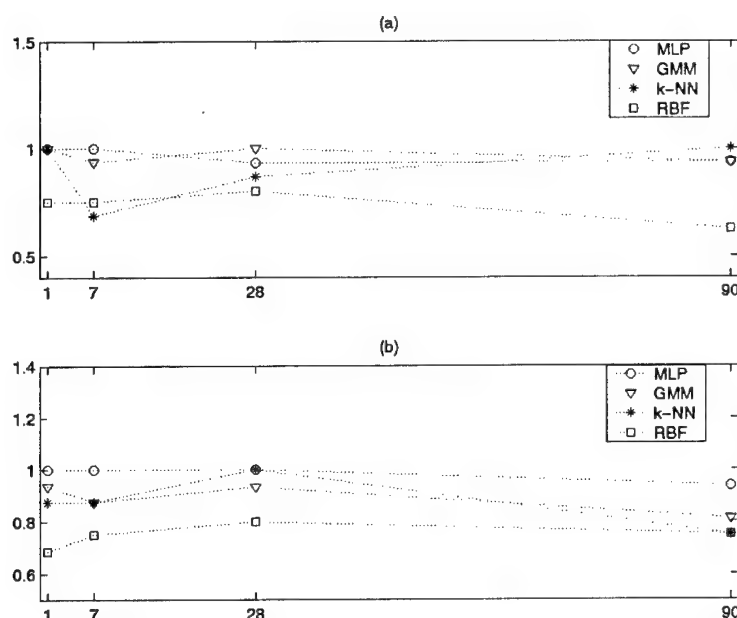


Figure 2: Representation of the generalization success rates of the methods studied for all ages: (a) results for the W/C classification problem and (b) results for the S/C classification problem.

From Fig. 2 it is obvious that some classification methods achieve high discrimination for both classification problems. The classification methods with the superior performance is the MLP and the GMM with k -NN follows, while the RBF had the worst performance. Remarkably, the MLP in the worst case concerning the different ages achieved success rate of 0.94 for both W/C and S/C problem.

Acknowledgements: This work is partially funded by the General Secretariat of Research and technology through the EPET II Project: "Mikkines: Non-Destructive Material Wave-analysis and Composition Monitoring".

7. REFERENCES

- [1] Malhorta V. M., Carino N. J. (Eds), CRC Handbook on Nondestructive Testing of Concrete, CRC Press 1991.
- [2] Vary A. The Acousto-Ultrasonic Approach, Acousto-Ultrasonics, Duke C. J. Jr. (Ed). Plenum Publishing Corporation, 1988.
- [3] Αγγέλης Δ. Γ., Πολύζος Δ., Φιλιππίδης Θ. Π., Τσιμογιάννης Α., Αναστασσοπούλου Α., Γεωργαλή Β., Καλοϊδής Β. Μη Καταστροφικός Έλεγχος Σύστασης και Εκτίμηση Αντοχής Τσιμεντοκονιάματος με την Μέθοδο Ακούστο-Υπερήχων, 1^ο Ελληνικό Συνέδριο Σύνθετων Υλικών Σκυροδέματος, Ξάνθη 2000.
- [4] Bishop C., Neural Networks for Pattern Recognition, Oxford University Press, 1995.
- [5] Duda R. O. and Hart P. E., Pattern classification and Scene Analysis, Wiley, New York, 1973.

DESTRUCTIVE AND ULTRASONIC NON-DESTRUCTIVE TESTING OF 28-DAY AND 28-YEAR OLD CONCRETE

I. N. Prassianakis

Assoc. Professor, Faculty of Applied Mathematics and Physics Sciences, Department of
Mechanics, Laboratory of Strength and Materials, Iroon Polytechniou 5,
GR-157 73, Zografou, Athens.

P. Giokas

Civil Engineer, NTUA, Laboratory of Strength and Materials, Iroon Polytechniou 5,
GR-157 73, Zografou, Athens.

1. SUMMARY

This experimental work is the continuity, the evolution development and the integration of an experimental work that was started 28 years ago by the first of the two authors, in cooperation with P.S. Theocaris, to whose memory this work is dedicated. In this paper the variation of the properties of a specific type of concrete 28-year old, whose characteristics were known on 7, 28, 36 and 90 days is controlled, [1, 2]. Beyond the destructive tests (compression, splitting tension and bending), this concrete was studied with the non-destructive testing method of ultrasounds. Moreover, the relation between the compressive strength of this concrete and the ultrasonic longitudinal waves of velocity was determined as well as the dynamic modulus of elasticity.

2. INTRODUCTION

It is well known that concrete is a composite material, which is composed of aggregates, cement and water. With the appropriate proportion and elaboration of these materials, the concrete achieves the desired mechanical properties. The quality characterization of concrete and concrete constructions, usually are accomplished by the known compressive destructive tests using cylindrical or cubic specimens [1-3].

The nondestructive testing (NDT) of concrete is of great scientific and practical importance. The subject has received growing attention during recent years, especially for the need of quality characterization of damaged constructions made of concrete, using the NDT methods.

The NDT methods used usually for the evaluation of concrete are the following: ultrasounds, industrial radiography, acoustic emission, the rebound (Schmidt) hammer test, the penetration resistance test and the pull-off test. Among them the most promising seems to be the NDT method of ultrasound, because through this method many parameters and mechanical properties of concrete, such as its dimensions, the modulus of elasticity E , the shear modulus G , the Poisson ratio ν and its fracture strength σ_f , can be determined.

The importance is that, for the application of the NDT method of ultrasound, it is not necessary to carry out destructive tests on real specimens received from concrete constructions, but only to evaluate in-situ the ultrasonic constants of this material.

Therefore, the application of the NDT methods for the quality control of concrete constructions achieve a special interest as they constitute the unique prospect for the direct, reliable, quick, safe, inexpensive and harmless method, for the quality control of buildings and other concrete constructions damaged by earthquakes, fatigue, conflagration or some other reason.

3. THE NDT METHOD OF ULTRASOUNDS FOR CONCRETE TESTING

For the ultrasonic NDT of materials, elastic waves are used, whose velocities (longitudinal c_l and transverse c_t) are related to the elastic modulus of elasticity E , shear modulus G , Poisson ratio ν and the density ρ of the material, by the following relations [4-7]:

$$E = \frac{(1+\nu)(1-2\nu)}{(1-\nu)} \rho c_l^2, \quad G = \rho c_t^2, \quad \nu = \frac{(c_l/c_t)^2 - 2}{2[(c_l/c_t)^2 - 1]} \quad (1)$$

From all NDT methods, the method of ultrasounds is the most important for concrete examination. By using this method one can determined not only the defects, cracks and other discontinuities of concrete but also many of its mechanical properties from the elastic waves velocities, such the moduli of elasticity of concrete E, G, ν , and its fracture stress σ_f [8-12].

Facaoaru [8] in 1961 estimated the relation between the compressive fracture strength of concrete and its ultrasonic longitudinal wave velocity c_l , introducing a mathematical relation of 2nd order. Experimental work executed by other researchers has also led to similar, linear and 2nd order relations [8-10], Figure 1.

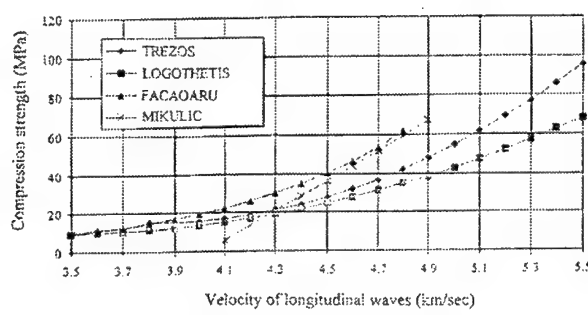


Figure 1: Compressive fracture strength versus the velocity of ultrasonic longitudinal waves.

It is not simple to introduce a basic relation connecting the quantities σ_f, c_l , as these properties are strongly affected by the porosity, the type of aggregates, the type of cement, the aggregate/cement and water/cement ratio, the conditions of concrete melting and curing, the age, etc. [8-12].

4. SPECIMENS, EXPERIMENTAL PROCEDURE AND RESULTS

All specimens used in the present experimental work were prepared in 1972 (28 years old) and had been preserved until today in a humid chamber with relative humidity of 80% and temperature of 20°C. The purpose for constructing these specimens then, was the study of the concrete behavior in multiaxial loading and specially the case of loading with axial extension and lateral compression, on standard cylindrical specimens.

The specimens used, in the present work, are cylinders (15x30 cm²), cubes (20x20x20 cm³) and beams (10x10x50 cm³). The composition, the conditions of their construction and curing and their mechanical properties at the ages of 7, 14, 28, 36 and 90 days, are included in the papers [1, 2]. Then, at the age of 28 days, this concrete had static modulus of elasticity $E_s = 40 \text{ GPa}$, Poisson's ratio $\nu = 0,26$ and fracture strength as in Table 1, [1, 2].

Before the execution of any destructive test (compression of cylindrical and cubic specimens and bending of beam specimens), the specimens were tested, using the NDT method of ultrasounds, for the determination of the elastic wave's velocity, parallel and perpendicular to the rodding direction, Table 2. Then, from the compression tests of the cylindrical specimens except the fracture stress, the initial tangent modulus of elasticity E_s and the Poisson's ratio ν , were determined and were found equal to $E_s = 39,84 \text{ GPa}$ (static) and $\nu = 0,25$, using mechanical and electrical strain gauges. Moreover, the fracture strength was also determined from splitting tension test. From the compression test of the cubic specimens and the bending (three point loading) of beam specimens, it was also possible to determine their fracture strength σ_f . All these results are included in Table 1, together with those taken from the papers [1, 2]. Figure 2 shows the variation of fracture compression strength versus the age, from 7 days to 28-year old concrete.

Table 1: Concrete specimen's strength in compression, splitting tension and bending tests.

CONCRETE AGE (days)	CYLINDERS		BEAMS	CUBS
	Compression (M.V. in kp/cm^2)	Splitting Test (M.V. in kp/cm^2)	Bending (M.V. in kp/cm^2)	Compression (M.V. in kp/cm^2)
7	192,5	21,5	52,0	291,2
28	271,2	27,0	55,1	395,0
90	330	25,8	64,3	452,0
10227	377,3	22,2	72,9	506,1

The velocities of longitudinal ultrasonic waves for frequency of 0,5MHz were evaluated, using the Krautkramer equipment USL-33 of our NDT laboratory, Table 2.

Finally, the dynamic modulus of elasticity was determined, using the first of the equations (1), equal to $E' = 42,99 \text{ GPa}$, using the Poisson ratio $\nu = 0,25$, which was computed from the compressive test, of the cylindrical specimens. The density of this concrete was found equal to $\rho = 2,45 \text{ gr/cm}^3$. The dynamic modulus of elasticity is always greater than the corresponding static modulus of elasticity and so the ratio of the dynamic to the static modulus of elasticity is always greater than unity.

Table 2: Mean values of longitudinal ultrasonic wave's velocities for concrete cylindrical and cubic specimens

Specimen	Perpendicular to the rodding direction c_1 (m/sec)	Parallel to the rodding direction c_1 (m/sec)	Total mean value c_1 (m/sec)
Cylinders	4590	4470	4530
Cubs	4810	4700	4760
M. V.	4700	4585	4645

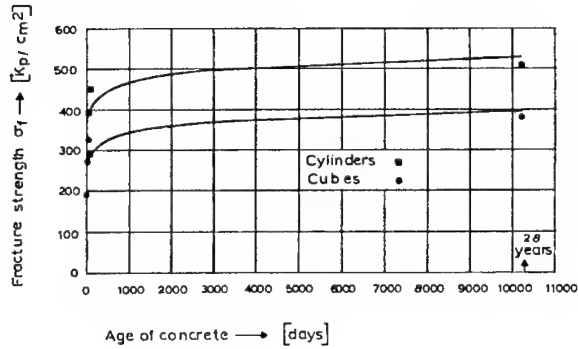


Figure 2: Variation of concrete fracture strength versus age, for different tests (for 28 years).

5. RELATION BETWEEN COMPRESSIVE STRENGTH AND ULTRASONIC PULSE VELOCITY FOR CYLINDRICAL CONCRETE SPECIMENS

A simulation model is developed to determine the relation between compressive strength and the mean value of ultrasonic pulse velocity parallel to the direction of rodding for each cylindrical specimen, as shown in Table 3. The method used for the estimation of the model parameters is the least squares (Regression Analysis). All calculations and controls were carried out by the software program SPSS Release 8.0, [13].

After the Regression Analysis, a model, out of the total developed models, was selected for the determination of the compression strength for cylindrical specimens using the ultrasonic pulse velocity. This model is shown in expression (2) and the variation the of the concrete's fracture stress, i.e. the compressive strength, versus the ultrasonic longitudinal waves velocity is shown in Figure 3.

$$\sigma_f = e^{\left(9,810 - \frac{17,713}{c_1}\right)}, \quad \mu\text{E} \quad R^2 = 0,97 \quad (2)$$

Table 3: Compressive strengths and ultrasonic velocities of longitudinal waves for concrete cylindrical specimens.

a/a	Compressive Strength σ_f (kp/cm ²)	Parallel to the rodding direction c_l (km/sec)
1	362,41	4,557
2	448,96	4,716
3	429,98	4,771
4	315,5	4,361
5	286,47	4,269
6	329,46	4,408

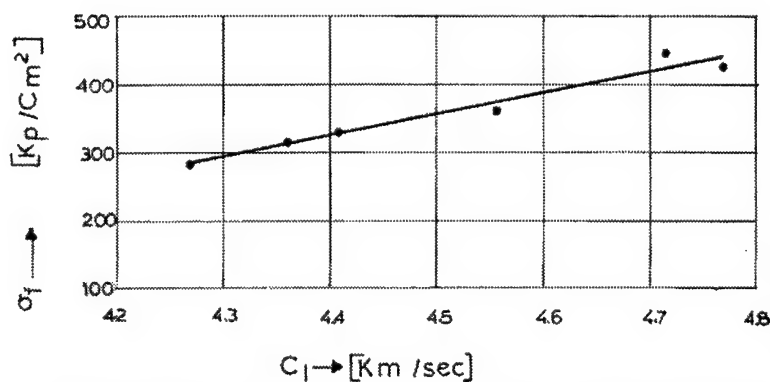


Figure 3: Variation of concrete compressive fracture stress σ_f , versus the ultrasonic longitudinal wave's velocity c_l .

6. CONCLUSIONS

From the experimental study conducted on 28-year old concrete, using destructive and the ultrasonic NDT method on concrete specimens, the following conclusions arose:

- The compressive fracture strength of concrete increases continuously by 39% for the cylindrical and by 28% for the cubic specimens, from the age of 28 days to the age of 28 years.
- Also, the fracture strength of beams, from three-point loading tests, increases by 32% , while from the splitting tests of the cylindrical specimens the fracture strength degrades by 22%, for the same time period.
- No significant changes were appeared on the static modulus of elasticity ($E_\sigma = 40,00\text{GPa}$ for 28 days and $E_\sigma = 39,84\text{GPa}$ for 28 years).
- A small decrease was observed on Poisson's ratio ν , which changed from $\nu = 0.26$ at the age of 28 days to $\nu = 0.25$ at the age of 28 years.
- On the other hand, using the NDT method of ultrasounds the modulus of elasticity for 28-year old concrete, was found equal to $E' = 43\text{GPa}$, slightly greater (7.9%) from the corresponding, as determined by the destructive tests.
- The correlation of compressive fracture stress σ_f of the concrete with the ultrasonic longitudinal wave's velocity c_l , led to the construction of a useful nommogram, which must be constructed for any type of concrete at the time of its rodding. Then, at any time, by determining the velocity of ultrasonic wave's one can evaluate the fracture strength of this concrete.

(g) Finally, another important observation related to the mode of fracture of cylindrical and cubic concrete specimens in compression, is carried out by the way of fracture of these specimens. Figure 4 shows typical photographs of concrete cylindrical and cubic concrete specimen fractures, from compressive loading, in which it is clearly seen that the fracture surfaces are almost parallel to the direction of the external compression loading.

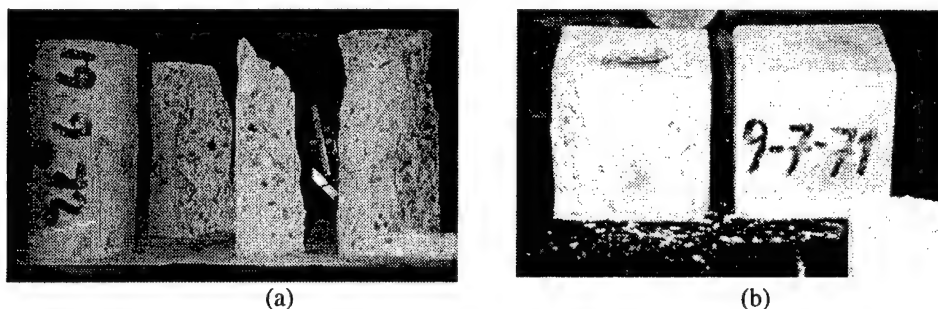


Figure 4: Typical photographs of fracture of concrete cylindrical (a) and cubic (b) concrete specimens from compressive loading

7. REFERENCES

- [1] P. S. Theocaris and I. N. Prassianakis, The Study of Concrete in Multiaxial Loading, Technika Chronika – Scientific Edition TCG, April 1974, pp. 293-302.
- [2] P. S. Theocaris and I. N. Prassianakis, The Mohr Envelope of Failure for Concrete: a Study of its Tension-Compression Part, Magazine of Concrete Research, Vol. 26, N° 87, June 1974, pp. 73-82.
- [3] A. M. Neville, Properties of Concrete, Fourth Edition, LONGMAN, England, 1999.
- [4] I. N. Prassianakis, Non Destructive Testing of Materials – The Method of Ultrasounds, N.T.U.A., 1997.
- [5] J. and H. Krautkramer, Ultrasonic Testing of Materials, Second Edition, Springer – Verlag, Berlin, 1977.
- [6] I. N. Prassianakis, Moduli of Elasticity Evaluation Using Ultrasound, Insight, Vol. 39, N° 6, June 1997, pp. 425-429.
- [7] British Standards 1881: Testing concrete, Part 201: 1986.
- [8] I. Făcăoaru, Contribution a l'étude de la Relation Entree la Resistance du Beton a la Compression et de la Vitesse de Propagation Longitudinale des Ultrasons, Rilem, N° 22, 1961, pp.125-154.
- [9] K. G. Trezos, K. Georgiou and C. Marabelias, Determination of the in-situ Strength of Concrete Using the Indirect Methods of Impact and the Ultrasounds, Technika Chronika – Scientific Edition TEE, A, Vol. 13, Issue 2, 1993, pp. 27-41.
- [10] D. Mikulić, Ž. Pauše and V. Ukrainč17. ik, Determination of Concrete Quality in a Structure by Combination of Destructive and Non-Destructive Methods, Materials and Structures, 25, 1992, pp. 65-69.
- [11] I. N. Prassianakis and P. Giokas, Non Destructive Testing of Concrete Using, 2nd National Conference of HSNT, Bolos, June 17 2000, Proceedings of Conference HSNT, Athens, September 2000.
- [12] I. N. Prassianakis and P. Gkiokas, Destructive and Non-Destructive Testing of 28-Day and 28-Year Old Concrete, Technika Chronika (submitted for publication, December 2000).
- [13] W. Mendenhal and T. Sincich, "A Second Course in Statistics – Regression Analysis", Prentice Hall, New Jersey 1996.

EXPERIMENTAL QUANTIFICATION OF CRACK TIP PARAMETERS FOR PARTICULATE METAL MATRIX COMPOSITES

S. K. Kourkoulis

Department of Mechanics, Faculty of Applied Sciences,
National Technical University of Athens, GR-15773 Athens, Hellas

V. Kytopoulos

Laboratory of Testing and Materials, Faculty of Applied Sciences,
National Technical University of Athens, GR-15773 Athens, Hellas

1. SUMMARY

The stress state in the immediate vicinity of the crack tip as well as the failure mode were investigated by experimentally quantifying some crack tip parameters, for cracked specimens made from particulate Metal Matrix Composite materials. The experiments were carried out using single edge notched specimens with the aid of scanning electron microscopy, permitting determination, on a micro-scale level, of the intensively damaged area around the crack tip. It was concluded that the void coalescence mechanism is active although void nucleation due to the presence of particles appears to be unavoidable. Finally the conditions necessary for the HRR analysis to be valid are not violated for a wide range of the crack length to specimen width values.

2. INTRODUCTION

The principal concept of the technology of composite materials is to combine certain assets of their components in order to give to the newly synthesized material unique and useful properties. Reinforcement is of either one- (fibrous) or two- (laminar) or even three- dimensional shape (particulates). The last class includes composites with more than 20% of the hard reinforcing dispersed phase. The particulate composites are non-homogeneous materials and their properties appear to be very sensitive to the constituent properties as well as to the geometric shapes of the array. The strength of particulate composites depends on the diameter of the particles, the interparticle spacing as well as on the volume fraction of the reinforcement.

Among particulate composite materials Metal Matrix Composites (MMCs) are advantageous as structural materials since they combine metallic with ceramic properties, such as high strength, high modulus of elasticity, high toughness, relatively low sensitivity to thermal shocks and temperature changes, high surface durability, low sensitivity to surface flaws, high thermal and electrical conductivity. Additionally, the ductile metal matrices, such as aluminum (used in the present work), titanium or nickel-chromium alloys, undergo energy absorbing plastic deformation under impact, which is very important in many dynamic structural applications.

On the other hand, the ductile matrix permits the blunting of cracks and relieves stress concentrations by plastic deformation. It is thus expected that the composite materials should be characterized by improved fracture toughness. However, it has been pointed out [1] that the presence of cracks strongly deteriorates the fracture strength of MMCs, in comparison to the uncracked materials, rendering the use of the matrix material more advantageous in case of presence of macrocracks. The present study consists a step towards further understanding of the processes responsible for this deterioration. This is achieved by examining, in a microscopic level, the failure mechanisms, in case of cracked specimens made from particulate MMCs and compare them with the ones activated in case of uncracked materials. Finally, the validity of the familiar HRR model for the description of the stress state around the crack tip is checked.

3. THE ELASTIC PLASTIC FRACTURE MECHANICS MODEL

The quantification of crack tip parameters is an important task in Elastic Plastic Fracture Mechanics (EPFM), since the loss of constraint, occurring with large scale yielding, is directly related to the deviation of the relationship between the J-Integral and the Crack Tip Opening Displacement (CTOD or δ_t) from the one proposed by Shih [2], even for a stationary crack:

$$J = \frac{\sigma_0 \delta_t}{d_n} \quad (1)$$

The above relationship was obtained by Shih [2] using the HRR solution for the stress and strain fields. The latter is valid within the framework of the deformation theory of plasticity and for a power law idealization of the flow behaviour of the material, generalized as:

$$\epsilon_{ij} = \frac{3}{2} \alpha \left(\frac{\sigma_e}{\sigma_0} \right)^{n-1} \frac{S_{ij}}{E} \quad (2)$$

where ϵ_{ij} and S_{ij} are the components of the strain- and of the deviatoric stress- tensor, respectively, σ_e is the effective stress, defined as $\sigma_e = [3/2(S_{ij}S_{ij})]^{1/2}$, E is the modulus of elasticity, σ_0 a reference value for stress (usually defined as the 0.2% offset yield strength) and α , n are experimentally defined constants. Assuming that the above restrictions are fulfilled, the stress field components, σ_{ij} , are described according to Shih's approach by the following equation:

$$\sigma_{ij} = \sigma_0 \frac{EJ}{\alpha \sigma_0^2 I_n r}^{1/(n+1)} \tilde{\sigma}_{ij}(n, \theta) \quad (3)$$

where, r the radial distance from the tip, I_n a dimensionless constant depending on strain hardening and $\tilde{\sigma}_{ij}$ dimensionless constants depending on strain hardening and angle θ from the crack plane. Concerning the function $d_n = d_n(n, \epsilon_0)$ of Eq.(1), which was given by Shih as a nomogramme, Omidvar's et al. [3] approximate solution, can be adopted according to which it holds that:

$$d_n(n, \epsilon_0) = \frac{\sigma_0}{E}^{1.05/(n-0.1)} \left(1 + \frac{3}{n} \right) \quad (4)$$

The previous analysis is valid as long as each material point experiences proportional loading. For cracked bodies, however, this is not the case, since an intense strain region exists, within $\sim 2\delta_i$ of the tip, that experiences highly non-proportional loading. In this case the analysis is only valid if the intense strain region is surrounded by a region in which the HRR model assumptions still prevail. This is true as long as δ_i is small compared to both the crack size and the uncracked ligament length. Otherwise fracture toughness becomes geometry dependent [4]. The validity of the above restriction will be checked in the next paragraphs.

4. EXPERIMENTAL PROCEDURE AND RESULTS

Series of experiments were carried out using single edge notched specimens for the quantification of the intense strain zone and the CTOD for specific ratios, f , of the crack length to specimen width. Scanning electron microscopy was employed, since it permits determination, on a micro-scale level, of the intensively damaged area around the tip, as well as the evolution of the CTOD, and of relevant micro-failure phenomena around the SiC particles, which are used as reinforcement in the case of the specific particulate MMC studied in the present work.

The material

The material used in the present study is the BP-2124 Al-Cu particulate MMC. It is produced by a powder metallurgy process, which reinforces aluminum-copper alloys with extremely fine SiC particles. It has excellent mechanical properties (high specific stiffness and high specific strength). The composite is obtained by adding to the matrix alloy about 20% wt. of

fine SiC of average diameter $3\text{ }\mu\text{m}$. The material was available in the form of either rolled sheets of thickness 1.20 mm or rolled plates of thickness 12.0 mm. In these forms it is slightly anisotropic.

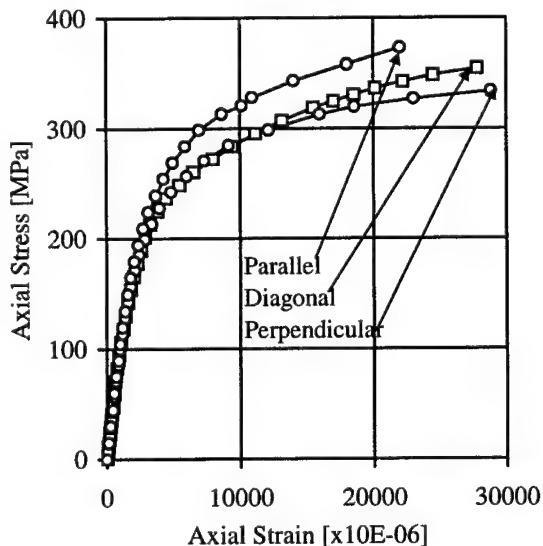


Figure 1: Axial stress versus axial strain for the three characteristic orientations

The elastic constants of the material were determined first by standardized tension tests. The specimens were cut from the rolled plates along the rolling direction, perpendicular to it and at a direction inclined 45° with respect to the rolling axis. The axial stress - axial strain curves for the three types of specimens are plotted in Figure 1. It is concluded that, the material is characterized by a common elastic modulus for all directions, equal to 80 GPa. The failure strength is reduced, as one proceeds from the rolling direction to the one perpendicular to it and the reduction is about 22%. On the contrary

the ductility increases as a function of the inclination of the specimen by an amount of about 15%. The constants necessary for the HRR analysis are directly obtained from Figure 1, since it can be proved by using any commercial curve-fitting code that the exponential law of Eq.2 fits perfectly the stress-strain curve of the material, fulfilling the initial requirements of the HRR model.

Specimens and testing procedure

The miniature specimens used in the main experimental part of the present study were cut out from the rolled sheet along the rolling direction and were formed to the familiar dog-bone like standardized geometry. Edge cracks of initial length a_0 were machined on the one side of the specimens (Single Edge Notched -SEN- specimens) by means of a rotating slow cutting diamond disc of thickness 100 μm . The specific cutting procedure was chosen since it creates cracks with minimal mechanical damage at their root. The width of the specimens was 6.5 mm, their thickness 1.2 mm while their gauge length varied between 65 and 70 mm. The initial length of the cracks varied between 1 mm and 3 mm, yielding f values in the range from about 0.15 to 0.45.

After the cracks were machined the specimens were subjected to heat treatment according to the suggestions of the manufacturer. The procedure included solution treatment for ninety minutes at 505 °C immediately followed by cold-water quench. No visible distortion or surface cracking of the specimens was observed due to the quenching. Finally, the specimens were carefully polished in order to eliminate any scratches and similar irregularities from their surface.

The heat treated specimens were then subjected to in-situ, monotonically increasing tensile loading in the Scanning Electron Microscope (SEM), Cambridge S4-10 type, available at the Laboratory of Testing and Materials of the National Technical University of Athens. The level of the tensile loading is servo-controlled (patent of the Institute of Physics, London, UK). The maximum capacity of the loading device is 2.2 kN. Following the above procedure it becomes possible to measure in-situ, with the maximum possible accuracy, the current CTOD. However, it is emphasized, that if the exact shape of the crack tip is taken into account, the term describing better the quantity measured would be "Notch Root Opening Displacement" (NROD). The measurements were carried out by means of a Gruman-type visioscopic fringe analyser, equipped with a digital electronic micropositioning system, of maximum error $\pm 0.5 \mu\text{m}$. Series of photographs were taken directly from the SEM during the loading procedure from the early loading steps up to the final failure and all measurements were made on these photographs. Finally, a fractographical study of the failure surfaces of the specimens was carried out, in order to gain a better insight into the mechanisms activated for the failure of the specific MMC.

Experimental results

In Figures 2(a,b) characteristic SEM photographs are displayed showing the unloaded tip of a crack (Fig.2a) and the same tip immediately before final failure (Fig.2b), for a crack oriented perpendicularly to the loading direction ($\beta=90^\circ$), with a crack-length to width ratio $f=0.3$. On the other hand, in Figures 3(a-c) characteristic SEM photographs are displayed showing the unloaded tip of a crack (Fig.3a) and the same tip immediately before final failure (Fig.3b), for a crack oriented at a direction $\beta=60^\circ$ with respect to the loading axis and $f=0.3$ again. The photographs of Figures 2(a,b) and 3(a,b) correspond to a magnification ratio equal to 500. However, for the case of the crack with $\beta=60^\circ$, an additional photo is given (Figure 3c) corresponding to larger magnification ($\times 1000$) in order to obtain a better view of the damaged zone around the tip.

From the series of SEM photographs taken during the loading process the CTOD was measured, adopting the procedure indicated in Figures 4(a,b). Characteristic results are shown in Figure 5, in which the CTOD is plotted versus the externally applied net stress reduced over its corresponding maximum value. In this figure filled symbols correspond to specimens with $\beta=90^\circ$ while empty symbols correspond to specimens with $\beta=60^\circ$. It is seen from this

figure that the evolution of CTOD is almost negligible for load levels lower than half the final net fracture stress and then it increases in an exponential manner until the fracture stress is reached.

Concerning the critical CTOD its average values appear to be independent of f , at least for the ratios used in the present study. The absolute value of the critical CTOD varied around $20\text{ }\mu\text{m}$ for the case of cracks with $\beta=90^\circ$, while for cracks with $\beta=60^\circ$ it was restricted to about half the respective value for cracks with $\beta=90^\circ$. The above conclusions support qualitatively the respective ones obtained by Kourkoulis [1] using a different technique for the measurement of COD, based on a modified δ_5 technique. In Figure 6 results taken from ref. [1] are shown concerning the COD values reduced over the initial width of the crack, for both the MMC and the matrix alloy, for a crack with $\beta=90^\circ$, for comparison reasons. Considering the initial width of the crack in ref. [1] ($\delta_0=0.2\text{ mm}$) the absolute COD values reported there are of the order of $80\text{ }\mu\text{m}$. Extrapolating these results at the tip of the crack the values of CTOD obtained vary in the range between $15\text{ }\mu\text{m}$ and $25\text{ }\mu\text{m}$, in good agreement with the results of the present study.

The fracture surfaces and the failure mode

In Figures 7 and 8 microfractographs are shown taken from two different locations of the fracture surface of a typical specimen with $\beta=90^\circ$ and $f=0.3$. Indeed, in Figure 9, in which the specific specimen is shown, the plane-stress "macromode" of fracture ahead of the crack tip (inclined plane of fracture) can be clearly detected. This failure mode is a combination of a shear component (distinguished by the shear lips) and a normal one (normal cone). The shear component prevails close to the surface layers whereas the normal one prevails at the mid-thickness layers of the specimen. The microfractograph of Figure 7 corresponds to points of the shear failure area while the one of Figure 8 to points of the normal failure one. From these figures it is safely concluded that the overall failure process is a ductile plane-stress one with an additional feature: The "dimple microfailure mode" is active. This is attributed to the microvoid coalescence mechanism, on which the ductile macrofracture of metals [6] is based.

Figures 7(b) and 8(b) were taken with the aid of the signal differentiation processing mode, by which contour enhancement or edge sharpening of the dimples is achieved. In this way one can better distinguish the differences in the morphologie between the two areas of the failure surface (shear lips and normal cone). It can be observed from them that the shear prevailing area is characterized by an elongated dimple pattern, in contrast to the normal cone area which is characterized by a more or less "quasi-equiaxed" dimple pattern. Such a behaviour is attributed to the loss of severity of the triaxiality of the stress state near the surface layers of the material.

5. CONCLUSIONS

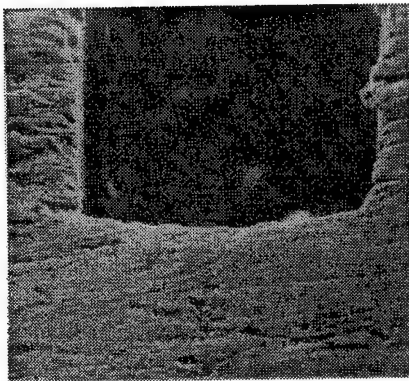
The analysis of the SEM images pointed out that the fracture process is still controlled by the void coalescence mechanism despite the presence of the reinforcing SiC particles. On the other hand, SEM analysis of the fracture surface of uncracked specimens indicates that the micro-cracks are initiated in the matrix rather than at the particle-matrix interface. This peculiar, at least for MMCs, phenomenon can be explained by the fineness of the reinforcement phase as well as by the process used for the production of the specific MMC (powder metallurgy) which is responsible for some porosity. Thus, in case of uncracked specimens void nucleation than void coalescence is the critical step for failure. When the local plastic relaxation, that relieves stress concentration becomes difficult, as in case of pre-cracked specimens, where it is concentrated in the vicinity of the tip of the macroscopic

crack, then the final failure occurs at rather low strains. It seems thus that the presence of macro-cracks changes the failure mechanism, explaining in this way the deterioration of the mechanical properties of cracked MMCs.

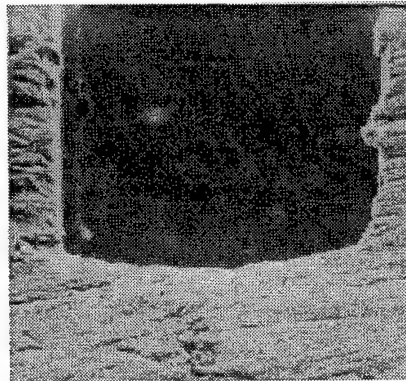
Finally, and considering that the critical CTOD is less than 20 μm , it is concluded that the intensively damaged zone surrounding the tip is restricted to about 2% of a_0 . Hence the HRR model appears to be valid, at least for the range of f values tested, although the failure mode detected is a ductile one. It means that Eqs.(1-4) can be safely used for the description of the stress field.

6. REFERENCES

- [1] Kourkoulis, S. K., The influence of cracks on the mechanical behaviour of particulate MMCs: An experimental study, Archives of Mechanics, to appear, 2001.
- [2] Shih, C. F., Relationships between the J-integral and the COD for stationary and extend-ing cracks, J. Mech. Phys. of Solids 29, 305-326 (1981).
- [3] Omidvar, B., Wnuk, M. P. and Choroszynski, M., Relationship between the CTOD and the J-integral for stationary and growing cracks, Int. J. of Fracture **87** (1997) 331-343.
- [4] Schapery, A., Report MM5762-88-1, Texas A&M University, College Station TX, 1988.
- [5] Fractography and materials science, ASTM-STP 733, 1981.

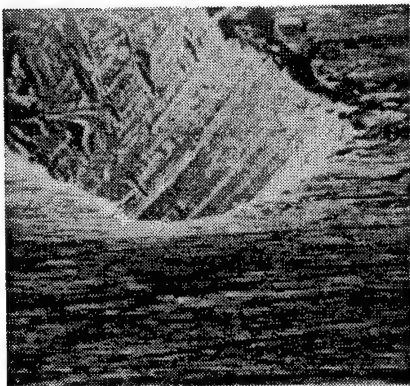


(a)

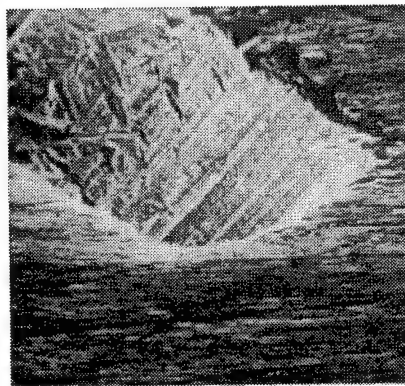


(b)

Figure 2: SEM photographs of a crack with $\beta=90^\circ$ (magnification 500x):
(a) Zero loading step. (b) Final loading step.



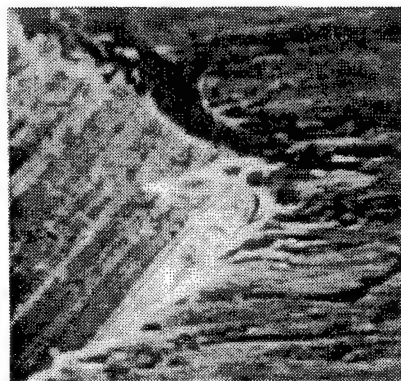
(a)



(b)

Figure 3: SEM photographs of a crack with $\beta=30^\circ$.

(a) Zero loading step (magnification 500x).
(b) Final loading step (magnification 500x).
(c) Detailed view of the crack-tip area at the final loading step (magnification 1000x). Localized damage at the "corner" of the notch root is clearly visible.



(c)

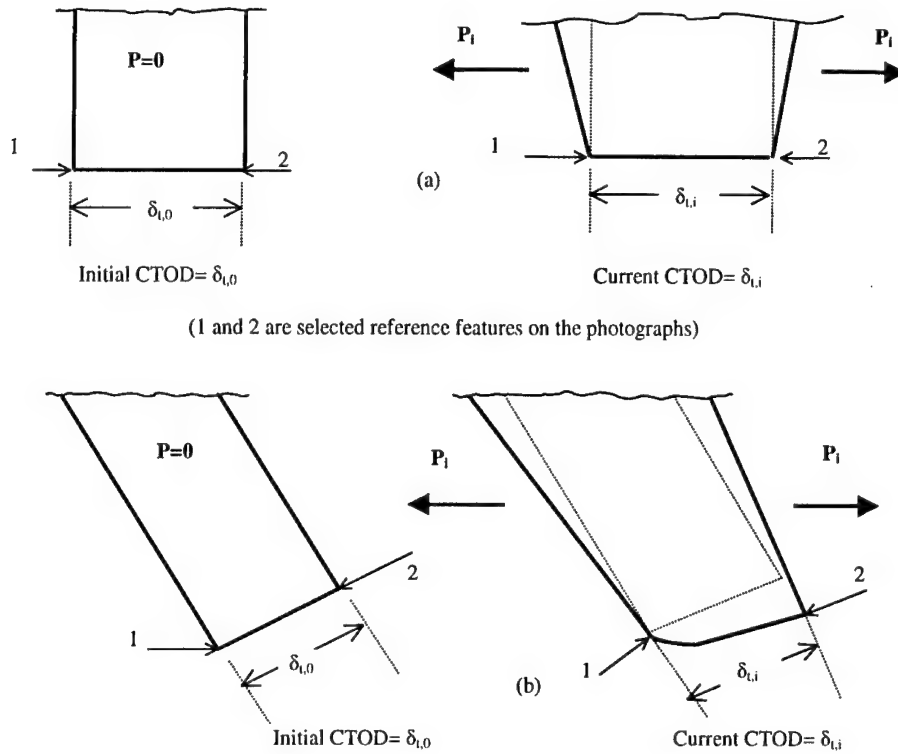


Figure 4: The procedure followed for the measurement of the CTOD from the SEM photographs.

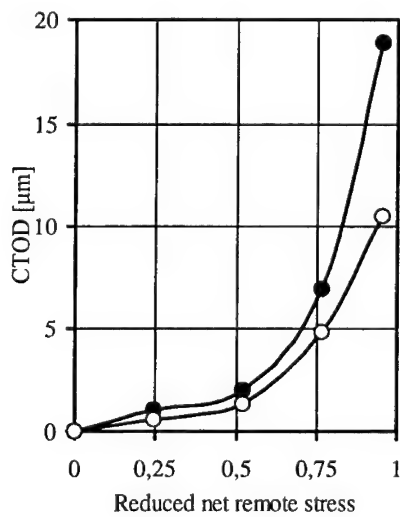


Figure 5: CTOD vs. the net remote stress for cracks with $\beta=90^\circ$ (filled symbols) and $\beta=60^\circ$ (empty symbols).

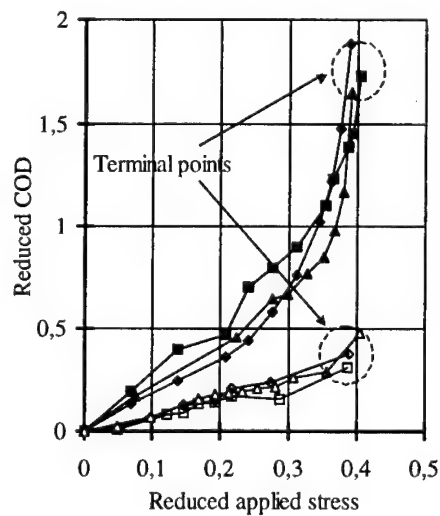
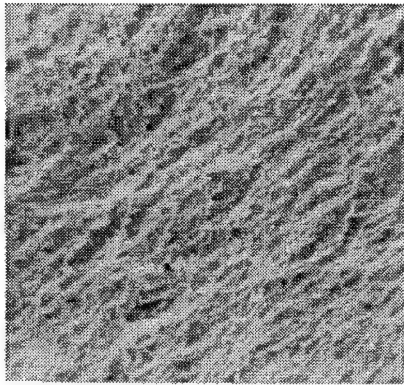
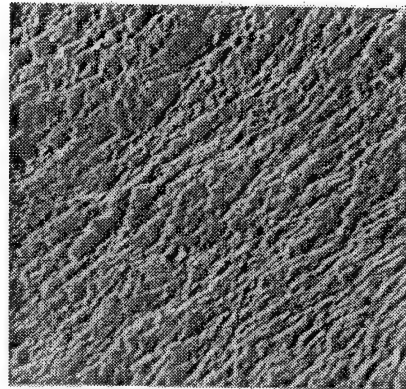


Figure 6: COD vs. applied stress for $\beta=90^\circ$. Empty symbols represent the 2124 MMC and filled ones the respective alloy.

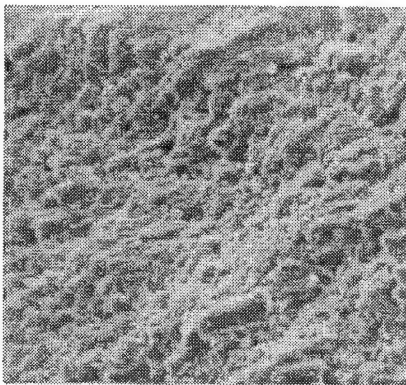


(a)

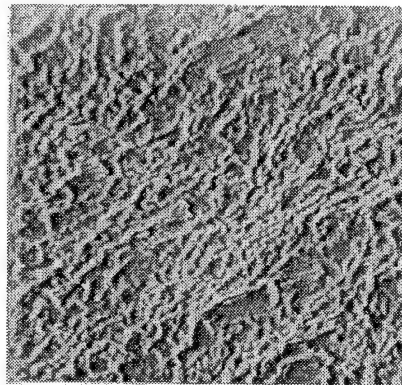


(b)

Figure 7: SEM microfractographs (magnification 500x): (a) Elongated shear dimpled surface. (b) Signal processed image for the enhancement of elongated pattern.



(a)

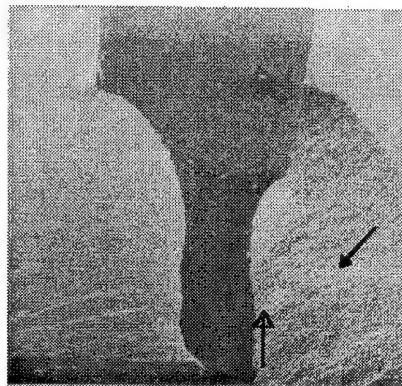


(b)

↑ Figure 8: SEM microfractographs magnification 500x): (a) "quasi-equiaxed" dimpled surface (b) Signal processed image for the enhancement of "quasi-equiaxed" pattern.

Figure 9: SEM photograph of the fractured specimen. The arrows indicate the exact points at which the photographs of Figure 7 (filled arrow) and Figure 8 (empty arrow) were taken.

→



ON SELECTING A COMPATIBLE SUBSTITUTE FOR THE KENCHREAE POROS STONE USED IN THE EPIDAUREAN ASKLEPIEION

N. Ninis

Archaeological Museum of Epidauros, GR-210 52, Ligourio, Hellas

S. K. Kourkoulis

Department of Mechanics, Faculty of Applied Sciences,
National Technical University of Athens, GR-15773 Athens, Hellas

1. SUMMARY

Various natural building stones are studied in the present work in an effort to propose the one most compatible with the material used by ancient Greeks for the erection of the monuments of the Epidaurean Asklepieion. A brief analysis of the criteria that should be fulfilled by a material used as a substitute for the restoration of ancient monuments precedes and series of experimental results are presented next concerning the mechanical properties and constants of the materials proposed so far as possible substitutes of the authentic material. Comparative study of these results indicates that only the poros stone of Kenchreae simulates the mechanical behaviour of the original material. The three new materials have a substantially different mechanical behaviour and their incorporation in the restoration should be treated with caution.

2. INTRODUCTION

Obtaining the appropriate stones for the restoration of the Asklepieion at Epidauros has long been a prime concern of the scientific committee responsible for its preservation. This paper focuses on the mechanical behaviour of the porous oolitic limestone, commonly known as the porolithos of Kenchreae, used in the upperstructure of most important buildings in the Asklepieion (Fig.1) as well as three other natural building stones that have been considered as suitable substitute for it in the restoration projects. Given the variability of texture and properties of the authentic material, the question of choosing one material becomes complex. As none of the various, commercially available, alternatives was deemed satisfactory from the aesthetical and mechanical point of view, the scientific committee's first choice has been to try and obtain the required stone from the near proximity of the ancient quarries at Kenchreae. The decision followed a first stage comprising a surface reconnaissance, a site investigation comprising a series of 19 drills and a preliminary laboratory study of samples taken from different drill cores and depths [1,2]. Unfortunately, the enterprise had to be abandoned after refusal of permission by the local authority and despite given assurances for minimum disturbance and a detailed proposal-offer for transforming the area of the ancient quarry into open, well defined, archaeological site. From the various alternatives three have been selected. A porous micritic limestone from Crete (alfopetra), a calcareous sandstone from Cyprus and a fine-grained limestone from Zakynthos.

3. PROBLEM DEFINITION – SELECTION CRITERIA

Under ideal conditions the substitute stone should react in a similar manner to environmental influence, mechanical loading and natural wear and weathering. This leads to three groups of criteria, mutually interconnected, for evaluating the compatibility between natural building stones:

The first group involves geological description, mineralogical analysis, qualitatively and quantitatively chemical analysis. The second involves the physical properties such as apparent and absolute density, porosity, water absorption permeability, and swelling. For the stones under study these are summarized in Table 1. It can be seen that the chosen three alternatives



Figure 1: Column drums of the Propylon of the Gymnasium at the Asklepieion

cover to a large extent the wide range of physical properties that are exhibited by the porolithos of Kenchreae. However, it must be pointed out that in terms of physical characteristics both alfopetra and Cyprus sandstone have a low absolute density, while alfopetra stands also apart by its dilation (13 as compared to 0 for the rest) and its relatively high permeability. It is to be noted, however, that the high permeability values of the Kenchreae stone are due to macropores of the material. Finally, the third group of compatibility criteria involves the mechanical characteristics as obtained from commercial tests, summarized in Table 2. In terms of strength, alfopetra would appear a good compromise to Kenchreae poros stone.

The above criteria describe the materials concerning their properties, but a proper evaluation of these properties in terms of compatibility involves, also, their proposed use and function in the monuments under restoration – position, size, structural requirements, weathering resistance, etc. For example for floor slabs resistance to mechanical wear is of primary importance, whereas in a lintel's case the flexural rigidity becomes the critical decision factor. This may, and must, differentiate between substitute stones depending on the specific use.

Property→ Material ↓	Apparent density [kgr/m ³]	Absolute density [kgr/m ³]	Porosity %	Absorp- tion %	Permeabil- ity x10 ⁻¹⁰ [m/s]	Swelling x10 ⁻⁶
Kenchreae	1.50-1.93	2.70	28.3-44.2	8.6-19.2	1600-28400	0
Crete	1.73	2.45	29.3	14	1200	13
Cyprus	2.04	2.54	21.1	4.4	200	0
Zakynthos	2.25	2.72	17.1	4.8-6.7	6-60	0

Table 1: Data on physical properties [1]

Property → Material ↓	Compressive strength [MPa]	Flexural strength [MPa]	Los Angeles (%)	Soundness (%)
Kenchreae	7.4 - 21.9	4.6 - 6.6	... - 61.1	... - 30
Crete	23.8	10.4	44.6	48
Cyprus	42.2	8.9	-	-
Zakynthos	51.1-76.2	9.5-12.4	31.1	33

Table 2: Data on mechanical strength [1]

4. EXPERIMENTAL PROCEDURE AND RESULTS

Series of uniaxial compression tests were carried out using a hydraulic loading frame of capacity 1000 kN. The maximum load recorded did not exceed in any case 250 kN, and thus, the stiffness of the frame can be considered infinite. This is very important if the post-peak behaviour data are to be reliable. The load was applied statically at a rate not exceeding 10^{-2} mm/min.

Cylindrical specimens were used with an aspect ratio (length, L , over diameter, D) of one. The dimensions of the specimens varied from $L=70$ mm for the ancient material, Kenchreae-, Crete- and Cyprus stones to $L=100$ mm for the Zakynthos one. Special care was taken to ensure that the bases of the cylinders were parallel to each other and perpendicular to the load direction. For this purpose a special set-up was designed permitting cover of the bases of the specimens with a thin layer of steel-putty. A semi-spherical head interposed between the loading plate and the moving piston further ensured the coaxiality between load and specimen.



Figure 2: Fractured specimen from authentic material

For the measurement of axial displacements three dial gauges of sensitivity equal to 10^{-6} m were used, placed at 120° to each other, in order to check the symmetry of the loading. The rotation of the end platens detected was negligible. In some of the tests additional dial gauges were used for the measurement of the transverse displacements for determining Poisson's ratio. Also, in a number of tests a system of four strain gauge rosettes was used, antidiagonally glued on two mutually perpendicular diameters of the specimens, for comparison reasons.

Concerning the interface between end platens and specimens the majority of tests was carried out using carefully lubricated surfaces, since Drescher and Vardoulakis [3] and Read and Hegemier [4] have pointed out that little can be inferred from non-lubricated uniaxial compression tests. Minimization of friction was achieved by interposing two sheets of Polytetrafluoroethylene (PTFE), a thick one (thickness 2 mm) and a

thin one (thickness 0.5 mm), between the base of the specimen and the respective platen. Additionally, the internal surfaces of the two sheets were covered with an amount of stearic acid, which has been proved very efficient in reducing friction under high loads [5,6]. However, for the present series of tests, the difference between the results for lubricated specimens and these for as-received ones was not important.

Authentic material

The authentic material both ancient and new comes from the Kenchreae quarries. It is a porous oosparite of "sandstone-like" appearance due to its high porosity (about 35% to 40%). It is a more or less homogeneous material, of layered structure, with complex nets of internal pores and surface vents, sometimes running through the whole width of the specimens (as it can be seen from the photograph of Figure 2), rendering the scattering of the results unavoidable. Frequent calcite veins or small calcite accumulations appear within it. The texture ranges from massive to very thin-bedded and the colour varies from a whitish-gray to grayish-beige (rarely light yellow). The dimensions of the pores and the vents vary between a few millimeters and a few centimeters. This kind of structure imposes to the material a rather anisotropic character of the transverse type. The material appears to be extremely friable and it is very difficult to prepare specimens suitable for accurate Strength of Materials tests. Its mechanical properties exhibit strong variation depending on the exact point of sampling and the age of the material [7].

Specimens of the ancient material were taken from amorphous blocks with the permission of the archaeological authorities. The average values of the elasticity modulus, E , compressive strength, σ_c , failure strain and Poisson's ratio are tabulated in Table 3, together with the respective values of the materials proposed as possible substitutes. In Figure 3 the complete stress-strain diagram of a characteristic test is plotted. It can be seen that after a more or less linearly increasing portion the diagram exhibits an abrupt drop. Then the curve rises again, sometimes exceeding the initial peak. From this point on, the graph follows a smooth path with very small slope before the final destruction of the specimen. The failure mode can be

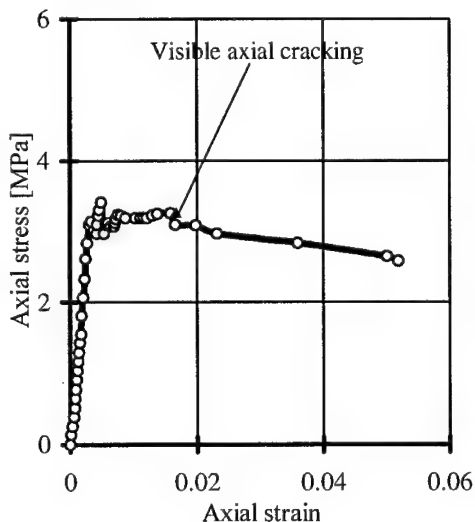


Figure 3: Axial stress vs. axial strain for the ancient material of the monuments.

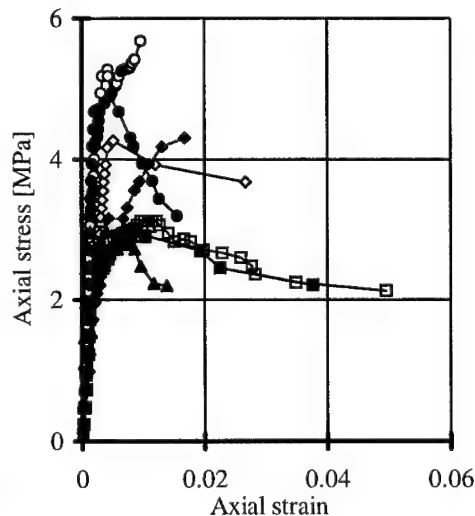


Figure 4: Axial stress vs. axial strain for fresh Kenchreae poros stone.

described as a combination of axial cracks with parallel crushing of weak material layers. The familiar Mohr's cone was not detected, indicating that the conventional failure theories cannot be applied for such type of materials [8,9]. The first visible cracks appear at strain levels equal to about 0.016. However, the final destruction of the specimens (depending on the lubrication conditions) takes place at strain levels corresponding to a height reduction of about 5%.

Detailed investigation has, also, been carried out on Kenchreae stone, either freshly quarried or drilled from the wider area of the ancient quarries at Kenchreae. Preliminary experimental work [7] pointed out that it simulates qualitatively in a very satisfactory manner the physico-mechanical properties of the ancient material and can be, thus, safely recommended for use in the restoration works. In Figure 4 the complete axial stress - axial strain diagram has been plotted for a number of characteristic tests. It is to be noted, however, that the texture of the fresh Kenchreae poros stone strongly depends on the depth of sampling from the various drill cores. In Figure 4 the empty symbols correspond to specimens with relatively massive texture, while the filled ones correspond to specimens with more porous and layered texture. This dependence covers almost all aspects of the stress-strain curve with the exception of only Young's modulus, which for the initial portion of the linear part of the graphs (stress levels lower than 1 MPa) is practically identical for all specimens, equal to about 2 GPa.

At this point it could be argued that the results of detailed testing using small size specimens are doubtful due to the macropores, layering and inhomogeneities of the material. However, the tests so far have shown that this influence is restricted to mechanical parameters such as the peak load and the extend of the post-peak deformation. On the other hand, the qualitative appearance of the stress-strain curves is very consistent, thus implying that it represents true material behaviour irrespectively of size. Moreover, the overall mechanical behaviour is close enough to the respective ones of the ancient material.

Substitution materials

Unfortunately, for reasons already mentioned in the introductory paragraph, it will not be possible to obtain fresh Kenchreae poros stone for the restoration, at least in the immediate future. So the three stones, previously mentioned, from Crete (alfopetra), Cyprus and Zakynthos, respectively, are considered as possible alternatives, with the last one being the most likely due to its better resistance to chemical weathering. Macroscopically all three of them appear to be of much more compact structure compared to that of the Kenchreae, as it can be concluded, also, from their apparent specific weight (Table 3).

Property→ Material ↓	Failure stress [MPa]	Young's modulus [GPa]	Poisson's ratio [-]	Failure strain [-]	Specific weight [kN/m ³]
Ancient	3.5	1.8	0.26	0.050	14.8
Kenchreae	4.2	2.0	0.26	0.035	15.3
Crete	34.2	12.5	0.27	0.004	17.8
Cyprus	33.4	7.2	0.26	0.006	19.3
Zakynthos	26.5	12.0	0.27	0.003	21.4

Table 3: Mechanical properties and constants of the ancient, authentic and substitute materials

However, the differences between the materials are not limited in the physical range. As it can be seen from Figure 5, the strength and the stiffness of the candidate substitute materials differ significantly from those of the authentic material. The same is true for the post-peak portion of the stress-strain curve as well as for the failure mode. All three materials fail in a very brittle (almost explosive) manner and the familiar Mohr's cone was consistently detected in all tests.

5. COMPOSITE SPECIMENS

In order to verify the above conclusions concerning the compatibility of the substitute materials with the authentic one, two types of composite cylindrical specimens were tested, composed of equal parts of Kenchreae poros stone and alfopectra: For the first type the adhesion plane was parallel to the loading direction (Figure 6), while for the second one the adhesion plane was perpendicular to the loading direction.

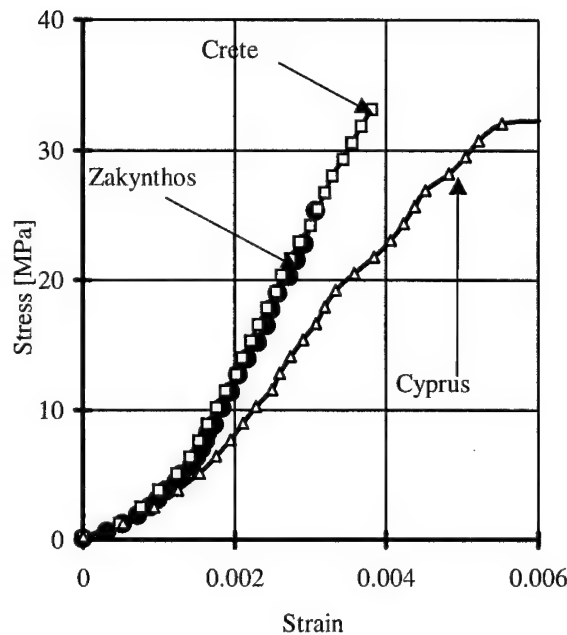


Figure 5: The stress – strain curves for Crete-, Cyprus- and Zakynthos poros stones

For the first type of specimens the failure started from the authentic material in the form of crushing a material layer, almost perpendicularly to the loading axis, at an overall stress level equal to about 5.5 MPa. Then at a stress level equal to 6.0 MPa axial cracks appeared, again in the authentic material, and finally at a stress level equal to 11.2 MPa the failure propagated in the substitute material in the form of surface axial cracks. However, if the ratio of the elasticity moduli of the two materials is taken into account ($E_{\text{alfopetra}}/E_{\text{ancient}} \cong 6.2$) then it is concluded that the first failure of the authentic material took place at a stress level equal to 3.2 MPa and the axial cracks appeared at a stress level of 3.5 MPa. On the other hand, the failure of the substitute material took place at about 35.0 MPa. It is thus seen that the failure of the two materials takes place at their respective failure stresses and the substitute material cannot protect the authentic material, at least for the specific configuration.

On the other hand for the second type of specimens, as it was expected, the authentic material failed first at 5.6 MPa. However, it is very important to note that this stress is relatively higher compared to the failure stress of the authentic material. The failure of the substitute material took place at about 7.7 MPa, considerably lower compared to the failure stress of the alfopectra. In means that for the specific configuration (load perpendicular to adhesion plane) the substitute material constrained the generation of cracks within the mass of the authentic material increasing its apparent strength. However, once the first cracks appeared within the mass of the authentic material, they propagated within the mass of the substitute material and its strength was reduced to less than one fourth of its true failure stress.

It is clear that the above conclusions are valid exclusively for the specific geometry studied, i.e. identical parts of authentic and substitute materials. A much more detailed investigation is required in order to take into account both the dimensions of the patch in respect to the dimension of the authentic material as well as the orientation of the adhesion plane.

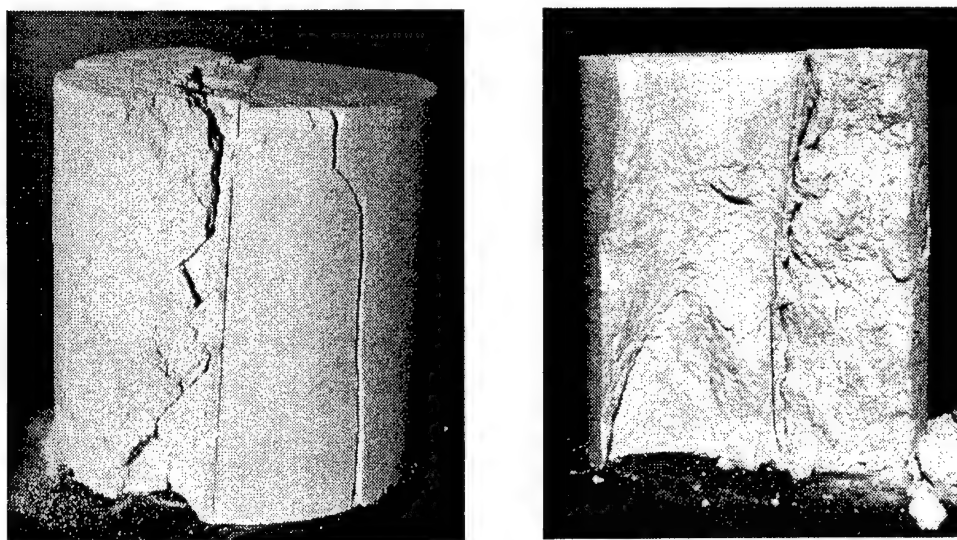


Figure 6: A tested composite specimen of the first type. The different failure modes are clearly visible.

Concerning the failure mode of the composite specimens it was concluded that for both types the authentic material failed in a combined mode (crushing of a layer almost perpendicular to the loading direction and generation of axial cracks immediately afterwards), while the substitute material failed under the formation of the familiar Mohr's double cone configuration. The two failure modes are clearly visible in Figure 6, where a tested specimen of the first type is exhibited.

6. DISCUSSION AND CONCLUSIONS

Compatibility between natural building stones is based on macroscopic and geological description, physical properties and mechanical strength. These criteria should be applied in relation to the function and the position of each particular architectural member in the building.

Comparison based on standard commercial testing (Tables 1 and 2) needs careful evaluation as to the materials concerned and the properties investigated both in terms of physical properties and mechanical strength (Table 3). For example, based on a direct comparison of their physical properties it may appear that a stone such as alfopetra from Crete could be a reasonable substitute for the Kenchreae poros stone. However, when comparing apparent and absolute density for the two stones and relating them to porosity and permeability, it becomes clear that porosity for the Kenchreae poros stone is at macrostructural level while that for alfopetra is at microstructural level. Detailed mechanical testing under static loading conditions reveals the differences in character of the materials concerning their maximum strength, modulus of

elasticity and mode of failure. Kenchreae poros stone is of low strength and high ductility while the other three stones are of medium strength and brittle nature.

Strain rate is, also, an important parameter for the range of porous limestones examined here. Peak strength data obtained from static deformation-controlled tests may change and even reverse the relative picture obtained from fast load-controlled tests (75% decrease in case of Kenchreae poros stone, 40% increase in alfopeira from Crete, 25% decrease in Cyprus sandstone and 50% decrease in Zakynthos limestone. On the other hand for all materials studied here, external overall measurements (using dial gauges) correspond with strain gauge ones at least up to the point of first visible cracks. So use of the latter appears not obligatory.

Long-term weathering seems to produce in the porous stone of Kenchreae a kind of residual behaviour. Specimens cut from ancient Kenchreae poros stone, which has been exposed for more than 2000 years yielded a lower boundary of the observed mechanical behaviour of the material.

Concerning the behaviour of composite specimens, at least for the geometries studied, it was concluded that in both cases the authentic portion of the specimens failed first, at stress levels either identical to the failure strength of the authentic material or slightly higher (in case the adhesion plane is perpendicular to the loading axis). Thus, it can be said that the principal requirement of the restoration process from the substitute material, i.e., to fail first protecting the ancient material is violated.

From the above, it is concluded that the Kenchreae poros stone cannot be really substituted by any of the investigated alternatives in the sense of true mechanical compatibility. Their incorporation in the restoration alongside the stone of Kenchreae should be considered carefully.

Acknowledgements: The financial support of the Committee for the Preservation of the Epidauros Monuments is acknowledged. The authors would, also, like to acknowledge the contribution of Dr Sakellariou as well as the willing assistance of Mr G. Karydas and Mr Th. Gerakis during the experimental procedure.

7. REFERENCES

- [1] Sakellariou, A., The physico-mechanical characteristics of the natural building stones of the Epidaurean Asklepieion, 1st and 2nd Interim reports. Testing, Research and Standards Center, Public Power Corporation, Athens, Greece (In Greek), (2000).
- [2] Ninis, N., Papakostopoulos, N. & Tsikouras, B. A new quarry at Kenchreae of Corinth designed to serve the needs of a restoration in the Epidaurean Asklepieion, in *Geological and Geotechnical Influences in the Preservation of Historical and Cultural Heritage*, G. Lollino (Ed), CNDICI Publishing, Torino (2000) 705-713.
- [3] Drescher, A. and Vardoulakis, I., Geometric softening in triaxial test on granular materials, *Geotechnique*, 32, 291-303, (1982).
- [4] Read, H. E. and Hegemier, G. A. (1984). Strain softening of rock, soil and concrete - A review article, *Mechanics of Materials*, 3, 271-294 (1984).
- [5] Van Vliet, M. R. A and Van Mier, J. G. M, *Concrete under uniaxial compression*, Report 25/5-95-9. TU Delft, Faculty of Civil Engineering, The Netherlands (1995).
- [6] Vardoulakis I., Exadaktylos G., Kourkoulis S. K. and Papadopoulos C., Characterization of mechanical properties and damage of natural building stones in historical monuments,

- in *Proceedings of the IV Int. Symp. On the Conservation of Monuments in the Mediterranean Basin*, A. Moropoulou et al (Ed), *Technical Chamber of Greece, Athens* (1997), 193-205.
- [7] Kourkoulis S. K., Vardoulakis I. and Ninis N., Evaluation and theoretical interpretation of mechanical properties of porolithoi used in the restoration of the Epidaurean Asklepieion, in *Geological and Geotechnical Influences in the Preservation of Historical and Cultural Heritage*, G. Lollino (Ed), *CNDICI Publishing, Torino* (2000) 831-839.
- [8] Vardoulakis, I., Kourkoulis, S. K., and Skjaerstein A., Post-peak behaviour of rocks and natural building stones in uniaxial compression, in *Material Instabilities in Solids*, R. de Borst and E. van der Giesen (Eds), *John Wiley & Sons, New York* (1998) 207-226.
- [9] Vardoulakis, I., Kourkoulis, S. K. and Zambas, C., Modeling of the mechanical behaviour of a conchyliates shellstone, in *Proceedings of the 2nd International Symposium on Hard Soils Soft Rocks*, A. Evangelista and L. Picarelli (Eds), *A. A. Balkema, Rotterdam* (1998) 911-922.

NON-LINEAR MECHANICS AND BUCKLING ANALYSIS OF COMPOSITE SHELLS WITH EMBEDDED PIEZOELECTRIC ACTUATORS AND SENSORS

Dimitris Varelis and Dimitris A. Saravanos

Department of Mechanical Engineering & Aeronautics
University of Patras, GR-26500 Patras, Greece

1. SUMMARY

Mechanics for laminated piezoelectric shells including non linear effects due to large displacements and rotations are presented, and a non-linear finite element formulation is developed. The problem of initial buckling due to mechanical and electric loading is formulated. Results quantify the mechanical buckling of cylindrical panels with various electric conditions on piezoelectric layers, as well as the case of active piezoelectric buckling.

2. INTRODUCTION

The analysis of smart composite laminates with embedded piezoelectric actuators and sensors has received substantial research attention. Smart shell structures are among the more challenging to study both analytically and experimentally, yet, are commonly used in aeronautical, aerospace, automotive and other engineering applications. One issue which has surfaced so far, is that the severity and type of electromechanical loading may exceed the range of linear theories, thus mandating the development of non linear techniques for correct prediction of the structural response.

Most theoretical and computational models that have been proposed for the static and dynamic analysis of piezoelectric composite shells have been limited in the linear region. Analytical solutions for electromechanical static and dynamic response have been developed¹⁻³ and computational models using various linear theories have been published⁴⁻¹². Coupled theories for laminated piezoelectric shell structures have been also presented¹³⁻¹⁵. A small number of papers has included non-linear effects due to large displacements and rotations for circular plates¹⁶⁻¹⁸

The present paper presents coupled non linear mechanics due to large displacements and rotations while the material behaviour is assumed linear. The kinematic assumptions of the mixed field laminate theory are used. A finite element formulation based on the non-linear piezolaminate mechanics is described. Subsequently, the problem of electromechanical buckling is formulated and its solution is presented. Results from various application cases of mechanical and electrical buckling are shown.

3. PIEZOELECTRIC LAMINATED SHELLS

An orthogonal curvilinear coordinate system $O\xi\eta\zeta$ is used such that ξ, η axes lie on reference surface A_0 , while ζ axis remains straight and perpendicular at each point of A_0 .

Governing equations. The material of each ply that compose the piezoelectric laminate is assumed to remain within the range of linear piezoelectricity with constitutive equations on the curvilinear system,

$$\begin{aligned}\sigma_i &= C_{ij}^E S_j - e_{ik} E_k \\ D_i &= e_{ij} S_j + \epsilon_{ik}^S E_k\end{aligned}\quad (1)$$

where $i, j = 1, \dots, 6$ and $k, l = 1, \dots, 3$; σ_i and S_j are the mechanical stresses and engineering strains in vectorial notation, C_{ij} is the elastic stiffness tensor, e_{ik} is the piezoelectric tensor E_k is the electric field tensor, D_i is the electric displacement vector and ϵ_{ik} is the electric permittivity tensor. The Green's strains in the ply level are described below, where the first and second RHS describe linear and non-linear components respectively :

$$\begin{aligned}S_1 &= \left[\frac{I}{g_{11}} \left(u_{,\xi} + \frac{g_{11,\eta}^0}{g_{22}^0} v \right) + \frac{w}{R_1} \right] + \frac{I}{2} \left[\frac{w^2}{R_1^2} + \frac{u^2}{R_1^2} + \frac{w_{,\xi}^2}{g_{11}^0} - \frac{u w_{,\xi}}{R_1 g_{22}^0} \right] \\ S_2 &= \left[\frac{I}{g_{22}} \left(v_{,\eta} + \frac{g_{22,\xi}^0}{g_{11}^0} u \right) + \frac{w}{R_2} \right] + \frac{I}{2} \left[\frac{w^2}{R_2^2} + \frac{v^2}{R_2^2} + \frac{w_{,\eta}^2}{g_{11}^0} - 2 \frac{v w_{,\eta}}{R_2 g_{22}^0} \right] \\ S_6 &= \left[\frac{I}{g_{11}} \left(v_{,\xi} - \frac{g_{11,\eta}^0}{g_{22}^0} u \right) + \frac{I}{g_{22}} \left(u_{,\eta} - \frac{g_{22,\xi}^0}{g_{11}^0} v \right) \right] + \frac{I}{2} \left[\frac{w_{,\xi} w_{,\eta}}{g_{11}^0 g_{22}^0} + \frac{uv}{R_1 g_{22}} - \frac{u w_{,\eta}}{R_1 g_{22}^0} - \frac{v w_{,\xi}}{R_2 g_{11}^0} \right] \\ S_4 &= \beta_{\eta} + \frac{w_{,\eta}}{g_{22}^0} - \frac{v}{R_2}, \\ S_5 &= \beta_{\xi} + \frac{w_{,\xi}}{g_{11}^0} - \frac{u}{R_1}\end{aligned}\quad (2)$$

Kinematic assumptions. The mixed field laminate theory is used¹⁵ that combines a linear displacement field with layerwise electric potential field for capturing all state variables through the thickness. The discrete-layer theory divides the laminate in $N-1$ sub-laminates. The assumed displacements and electric potential take the following form through the thickness:

$$\begin{aligned}u(\xi, \eta, \zeta, t) &= u^0(\xi, \eta, t) + \zeta \beta_{\xi}(\xi, \eta, t) \\ v(\xi, \eta, \zeta, t) &= v^0(\xi, \eta, t) + \zeta \beta_{\eta}(\xi, \eta, t) \\ w(\xi, \eta, \zeta, t) &= w^0(\xi, \eta, t) \\ \phi(\xi, \eta, \zeta, t) &= \sum_{m=1}^N \phi^m(\xi, \eta, t) \Psi^m(\zeta)\end{aligned}\quad (3)$$

The electric field vector becomes¹⁵:

$$E_i(\xi, \eta, \zeta, t) = \sum_{m=1}^N E_i^m(\xi, \eta, t) \Psi^m(\zeta) \quad i = 1, 2$$

$$E_3(\xi, \eta, \zeta, t) = \sum_{m=1}^N E_3^m(\xi, \eta, t) \Psi^m(\zeta)$$
(4)

where \bar{E}^m are generalized electric field vectors. Substituting eq. (3) into eq. (2) the strains take the following general form:

$$\begin{Bmatrix} S_1 \\ S_2 \\ S_6 \end{Bmatrix} = \begin{Bmatrix} S_1^0 \\ S_2^0 \\ S_6^0 \end{Bmatrix} + \zeta \begin{Bmatrix} k_1^0 \\ k_2^0 \\ k_6^0 \end{Bmatrix} + \begin{Bmatrix} S_{1L} \\ S_{2L} \\ S_{6L} \end{Bmatrix}$$
(5)

where the S_i^0, k_i^0 , are the linear generalized strains (see Ref. 15) and S_{Li} are the generalized non-linear strains

$$S_{1L} = \frac{1}{2} \left[\frac{w_0^2}{R_1^2} + \frac{u_0^2}{R_1^2} + \frac{w_{0,\xi}^2}{g_{11}^0} - 2 \frac{u_0 w_{0,\xi}}{R_1 g_{22}^0} \right]$$

$$S_{2L} = \frac{1}{2} \left[\frac{w_0^2}{R_2^2} + \frac{v_0^2}{R_2^2} + \frac{w_{0,\eta}^2}{g_{11}^0} - 2 \frac{v_0 w_{0,\eta}}{R_2 g_{22}^0} \right]$$

$$S_{6L} = \frac{1}{2} \left[\frac{w_{0,\xi} w_{0,\eta}}{g_{11}^0 g_{22}^0} + \frac{u_0 v_0}{R_1 g_{22}^0} - \frac{u_0 w_{0,\eta}}{R_1 g_{22}^0} - \frac{v_0 w_{0,\xi}}{R_2 g_{11}^0} \right]$$
(6)

Generalized Equations of motion. The mechanical and electrical response of the piezoelectric material can be represented by the stress equilibrium and the conservation of electric-charge respectively:

$$\rho_- \ddot{u}_i = \sigma_{ij,j} + \bar{f}_i$$

$$D_{ii} = 0 \quad i, j = 1, \dots, 3$$
(7)

Through the use of the divergence theorem, equilibrium equations can be expressed over the volume of the piezoelectric laminated shell in an equivalent variational form as:

$$\delta u \Psi_1 = - \int_V \delta S_{ij} \sigma_i dV + \int_V \delta u_j b_{jdV} + \int_{\Gamma_\tau} \delta u_j \tau_j d\Gamma = 0$$

$$\delta u \Psi_2 = - \int_V \delta E_j D_j dV + \int_{\Gamma_q} \delta \phi q d\Gamma = 0 \quad i = 1, \dots, 6 \quad , \quad j = 1, \dots, 3$$
(8)

where τ_j are the surface tractions on the bounding surface Γ_τ , b_j is the inertial force per unit volume, q is the electrical charge applied on the surface Γ_q , and V represents the whole volume including both composite and piezoelectric layers.

Finite element formulation

A finite element formulation for a composite piezoelectric shell is obtained encompassing the previous non linear mechanics. An eight node element with five degrees of freedom of the

Serendipity family is used. The state variables are approximated from quadratic interpolation functions into the element on the reference surface A_0 and take the form:

$$\begin{aligned} u_j^o(\xi, \eta, t) &= \sum_{i=1}^M u_j^{oi}(t) N^i(\xi, \eta), & j = 1, \dots, 3 \\ \beta_j^o(\xi, \eta, t) &= \sum_{i=1}^M \beta_j^i(t) N^i(\xi, \eta), & j = 1, \dots, 2 \\ \phi_j^m(\xi, \eta, t) &= \sum_{i=1}^M \phi_j^{mi}(t) N^i(\xi, \eta), & m = 1, \dots, N \end{aligned} \quad (9)$$

where N indicates the number of discrete layers that the laminate is subdivided, and M the number of nodes. Substituting eqs. (1-6) and eq. (9) into eq.8, the incremental equilibrium equations are obtained in the form of a coupled system:

$$\begin{aligned} (\bar{K}_{uu}^0 + \bar{K}_{uu}^\sigma + \bar{K}_{uu}^L) \delta u + (\bar{K}_{ue}^0 + \bar{K}_{ue}^L) \delta \phi &= -[M_{uu}] \delta \ddot{u} + \Psi_1 \\ (\bar{K}_{eu}^0 + \bar{K}_{eu}^L) \delta u + \bar{K}_{ee}^0 \delta \phi &= \Psi_2 \end{aligned} \quad (10)$$

where all the sum of matrices in parentheses are tangential structural and piezoelectric matrices indicated by overbar. Subscripts uu, ue, ee indicate linear elastic, piezoelectric and permittivity matrices respectively; superscripts $0, \sigma, L$ respectively indicate linear, initial stress and nonlinear components and Ψ_1, Ψ_2 are differences between internal and external nodal forces and charges. Three new matrices are introduced, the initial stress matrix \bar{K}_{uu}^σ , the nonlinear stiffness matrix \bar{K}_{uu}^L and the nonlinear piezoelectric matrix \bar{K}_{ue}^L . The terms of initial stress matrix depend on initial laminate force N_i which includes the effect of external mechanical loads or applied electrical voltages, and has the following form:

$$[K_{\sigma}^{ij}] = \int_A R^i \begin{bmatrix} N_1 & N_6 \\ N_6 & N_2 \end{bmatrix} R^j \quad (11)$$

where R is a proper matrix of shape functions. N_i are the in-plane laminate forces described below:

$$N_i = \int_0^h \sigma_i d\zeta = A_{i,j} S_j^0 + B_{i,j} k_j^0 - \sum_{m=1}^N \bar{E}_{3i}^m E_3^m \quad i, j = 1, 2, 6 \quad (12)$$

where the first two RHS terms are the average mechanical stress components while the third term is the average piezoelectric stress.

Initial Buckling. Neglecting the non-linear stiffness matrices (indicated by superscript L), eq (14) results:

$$\begin{aligned} (\bar{K}_{uu}^0 - \lambda \bar{K}_{uu}^\sigma) \delta u + \bar{K}_{ue}^0 \delta \phi &= 0 \\ \bar{K}_{eu}^0 \delta u + \bar{K}_{ee}^0 \delta \phi &= 0 \end{aligned} \quad (13)$$

where λ is the critical factor on the applied mechanical load or electrical voltage that will initiate buckling. The solution of the buckling problem is based on two incremental steps. In the first step, a unit load is subjected to the structure and from static solution, the average stresses are calculated at the laminate. The corresponding stress matrix \bar{K}_{uu}^σ is subsequently formulated and the eigenvalue problem (13) is solved.

Numerical results

Evaluations of the developed models are presented for simply supported plates and cylindrical

shells. A [p/Al/p] piezoelectric laminate plate with a 0.5mm thick aluminium layer and two 0.25mm thick continuous piezoceramic layers of PZT5 attached on the upper and lower surface is examined. The hoop is $L_\xi = 200\text{mm}$ and the width of the panel is $L_\eta = 200\text{mm}$.

Table 1 Critical mechanical buckling loads for piezoelectric laminated cylindrical shell [p/Al/p] under a concentrated force at center

Order	Critical mechanical load F (Nt) 8x8 mesh	
	Opened circuit	Closed circuit
shell ($\theta=15^\circ$)		
1	275	214
2	329	246
3	615	466
shell ($\theta=45^\circ$)		
1	982	749
2	1180	908
3	2087	1562

Mechanical buckling. Two curvatures are considered, $1/R=0.76394$ ($\theta=15^\circ$) and $1/R=0.25464$ ($\theta=45^\circ$). For all cases, a transverse concentrated force is applied at the center of the shell for two cases: (a) all electric terminals at piezoelectric layer are grounded, and (b) the inner terminals remain closed while the outer ones are open. The predicted critical mechanical loads are provided in Table 1, where the influence of piezoelectric conditions is apparent. The first buckling mode for the 15° panel is shown in Figure 1.

Piezoelectric buckling. Buckling can be also induced through the application of electric potential on piezoelectric actuators. Table 2 illustrates the critical electric potential when a sinusoidal electric potential $\Phi=\Phi_0\sin 3\pi\xi/L_\xi\sin\eta/L_\eta$ is applied on the outer terminals of each piezolayer. Figure 2 shows the first electric buckling mode for a 15° panel.

Table 2. Critical electric potential for piezoelectric laminate plate and shell [p/Al/p] under sinusoidal electric potential $\Phi_0\sin 3\pi\xi/L_\xi\sin\eta/L_\eta$

Order	Critical electric potential Φ_0 (V) 8x8 mesh
plate ($\theta=0^\circ$)	
1	1209
2	1477
3	2107
shell ($\theta=15^\circ$)	
1	3422
2	3781
3	4000

shell ($\theta=45^\circ$)	
1	11247
2	11431
3	12198

4. CONCLUSION

Non linear mechanics including non linear effects due to large displacements and rotations for laminated piezoelectric shells were presented. Based on them, an eight node finite element was developed to predict the initial mechanical and electric buckling of plates and shells. Applications have indicated the dependence of mechanical buckling loads on the electric conditions of piezolayers. The feasibility of piezoelectric buckling was also illustrated.

5. REFERENCES

- [1] Mitchel, J.A. and Reddy, J.N., "A Study of Embedded Piezoelectric Layers in Composite Cylinders," *ASME Journal of Applied Mechanics*, Vol.62, 1995, pp.166-173
- [2] Xu, K.M. and Noor, A.K., "3-Dimensional Analytical Solutions for Coupled Thermoelastoelectric Response of Multilayered Cylindrical-Shells," *AIAA Journal*, Vol.34, 1996, pp.802-812
- [3] Heyliger, P.R., "A Note of the Static Behavior of Simply-Supported Laminate PiezoelectricCylinders," *International Journal of Solids and Structures*, Vol.34, 1997, pp.3781-3794
- [4] Tzou, H.S. and Garde, M., "Theoretical Analysis of a Multi-Layered Thin Shell Coupled with Piezoelectric Shell Actuators for Distributed Vibration Controls@," *Journal of Sound and Vibration*, Vol.132, 1989, pp.433-450
- [5] Tzou, H.S. and Zhong, J.P., "Electromechanics and Vibrations of Piezoelectric Shell Distributed Systems," *Journal of Dynamics Systems, Measurement and Control*, Vol.115, 1993, pp.506-517
- [6] Lammering, R., "The Application of a Shell Finite Element for Composites Containing Piezoelectric Polymers in Vibration Control," *Computers and Structures and Structures*, Vol.41, 1991, pp1101-1109
- [7] Docmesi, M.C., "Shell Theory for Piezoceramics Under a Bias," *IEEE Transactions on Ultrasonics*, Vol.37, 1990, pp.369-385
- [8] Koconis, D.B., Kollar, L.P. and Springer G.S., "Shape Control of Composite Plates and Shells with Embedded Actuators," *Journal of Composite Materials*, Vol.28, 1994, pp.415-458
- [9] Tzou, H.S. and Bao, Y., "Theory on Anisotropic Piezothermoelastic Shell Laminates with Sensor/Actuator Applications@," *Journal of Sound and Vibration*, Vol.184, 1995, pp.453-473
- [10] Shen, Y.P. and Cheng, C.Q., "Stability Analysis of Piezoelectric Circular Cylindrical Shells@," *Journal of Applied Mechanics*, Vol.64, 1997, pp.847-852
- [11] Sonti, V.R. and Jones, J.D., "Curved Piezoactuator Model for Active Vibration Control of Cylindrical Shells@," *AIAA Journal*, Vol.34, 1996, pp.1034-1040
- [12] Tzou, H.S. and Ye, R., "Piezothermoelasticity and Precision Control of Piezoelectric Systems: Theory and Finite Element Analysis@," *Journal of Vibration and Acoustics*, Vol.116, 1994, pp.489-495

-
- [13] Tzou, H.S. and Ye, R., "Analysis of Piezoelectric Structures with Laminated Piezoelectric Triangle Shell Elements", *AIAA Journal*, Vol.34, 1996, pp.110-115
 - [14] Heyliger, P., Pei, K.C., and Saravanan, D.A., "Layerwise Mechanics and Finite Element Model for Laminated Piezoelectric Shells", *AIAA Journal*, Vol.34, 1996, pp.2353-2360
 - [15] Saravanan, D.A., "Coupled Mixed-Field Laminate Theory and Finite Element for Smart Piezoelectric Composite Shell Structures", *AIAA Journal*, Vol.35, 1997, pp.1327-1333
 - [16] Tzou, H.S. and Bao, Y., "Nonlinear Piezothermoelasticity and Multi-Field Actuations, Part1: Nonlinear Anisotropic Piezothermoelastic Shell Laminates", *Journal of Vibration and Acoustics*, Vol.119, 1997, pp.374-381
 - [17] Tzou, H.S. and Zhou, Y.H., "Nonlinear Piezothermoelasticity and Multi-Field Actuations, Part2: Control of Nonlinear Deflection Buckling and Dynamics", *Journal of Vibration and Acoustics*, Vol.119, 1997, pp.382-389
 - [18] Tzou, H.S. and Zhou, Y.H., "Active Control of Nonlinear Piezoelectric Circular Shallow Spherical Shells", *International Journal of Solids and Structures*, Vol.37, 2000, pp.1663-1677

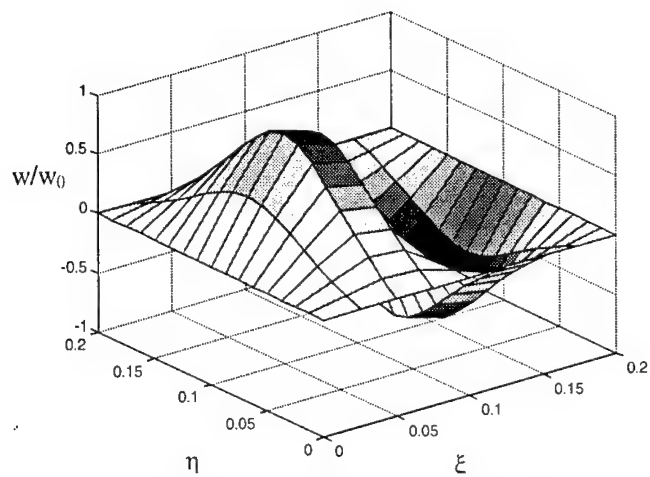


Figure 1. First critical buckling mode of a cylindrical panel (15°) [$p/Al/p$], under transverse mechanical force at center

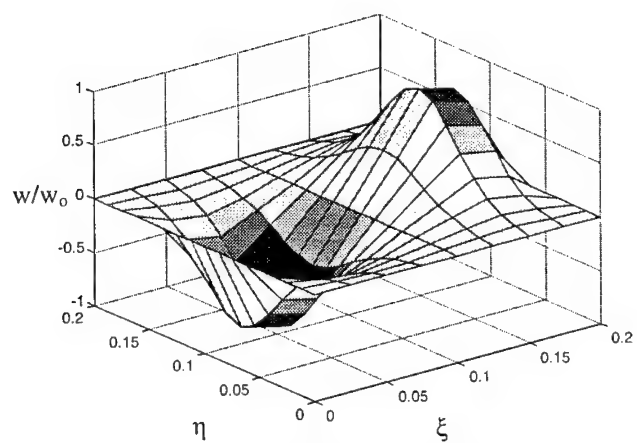


Figure2. First critical buckling mode of a cylindrical panel (15°) [$p/Al/p$], under sinusoidal potential $\Phi_0 \sin 3\pi\xi/L_\xi \sin \eta/L_\eta$

**A NEW DESIGN METHODOLOGY FOR HIGH TEMPERATURE STRUCTURAL
COMPONENTS MADE OF CONTINUOUS FIBER CERAMIC COMPOSITES
EXHIBITING THERMALLY INDUCED ANISOTROPIC DAMAGE**

D.E. Vlachos¹, Y.Z. Pappas¹, R. De Stefano² and V. Kostopoulos¹

¹Applied Mechanics Laboratory, University of Patras and ICE-HT/FORTH,
GR-265 00 Patras, Greece

²Nuovo Pignone, Via F. Matteucci 2, 50127 Florence - Italy

1. SUMMARY

Continuous Fiber Ceramic (Matrix) Composites (CFCCs) have found during the last decade numerous industrial applications in a variety of technological areas, where structural components are subjected to high temperature combined with significant mechanical loading. The present work deals with the application of innovative design methodologies for the development of an industrial gas turbine combustor chamber made of oxide/oxide composite materials.

Oxide/oxide composites offer high-temperature structural stability without the need of any kind of oxidation protection and thus permit the increase of the working temperature of the gas turbines, increasing the efficiency of the system and decreasing the need for cooling air and NO_x emissions.

Since, oxide/oxide composites degrade their structural properties as a function of the operating temperature (for temperature higher than 1000° C) and the exposure time, an incremental approach has been introduced for the solution of the problem and each increment represents a thermal exposure stage. The structure has been divided in temperature zones and a mean working temperature was considered for each zone. The data set required for the application of the present design methodology, was obtained through an extensive material characterization program based on the measurement of the anisotropic properties of oxide/oxide composites using ultrasonic techniques.

2. INTRODUCTION

Gas turbines for both simple and combined cycles had in the last five years a market of 30 GW/annum and the expectations are for 40 GW/annum, for the running decade. Within this market there is a tremendous commercial pressure on gas turbine manufacturers to increase plant efficiency and reduce specific costs, whilst continuing to meet the ever more stringent emission limits. From several key technology areas, all the gas turbine manufacturers have identified CFCCs as the key material to fulfil the imposed targets and consequently CFCCs are aggressively pursued with aim of full engine test in the very near future [1].

The basic parameter, which supports the use of CFCCs in high temperature engineering components, is their improved fracture toughness, compared to monolithic ceramics, due to the activation of various stress redistribution mechanisms in the material structure [2]. Thus CFCCs have the ability to withstand damage without immediate catastrophic rupture.

The present work deals with the application of innovative design methodologies for the development of an industrial gas turbine combustor chamber made of oxide/oxide composite materials [3].

Oxide/oxide composites offer high-temperature structural stability without the need of any kind of oxidation protection and thus permit the increase of the working temperature of the gas turbines, increasing the efficiency of the system and decreasing the need for cooling air and NO_x emissions.

However, in the long run oxide/oxide composites indicate a reduction of their structural performance, as a function of the working temperature and the duration of high temperature exposure, for temperature higher than 1000° C.

Among the limitations in applying CFCCs in structural components is the uncertainty in using well-documented design methodologies. Up to now, the most of the existing design approaches suffer from the presence of a strong metal culture on the final products. In other words, some basic design methodologies, based on a database of life and stiffness data, have been used together with a strain or time/cycle based life prediction philosophy [3]. Then, after conducting a thermal analysis, a linear static stress analysis follows, using stiffness information for the given composite system. The obtained stresses can be used to find the life under a given thermo-mechanical loading.

The proposed procedure, in the present work design, involves stress redistribution and this is achieved through the development of a lamina stiffness evolution law that includes all the major factors contributing to stiffness reduction as a consequence of the developed anisotropic damage. This approach, certainly more accurate as it allows for stress transferring of the more damaged parts of the structure where stiffness is lower, involves:

- Completely new design of the combustor chamber which makes use of the material capacity and takes into consideration the manufacturing limitations
- Thermo-mechanical analysis of the component and calculation of the temperature and the stress profiles for the given thermo-mechanical loading and boundary conditions.

At this preliminary phase, an operational life of 1500 h duration is demanded for the combustor chamber.

Since, oxide/oxide composites indicate anisotropic degradation of their structural properties [4], an incremental approach has been introduced for the solution of the problem and each increment represents a thermal exposure stage. The structure has been divided in temperature zones and a mean working temperature was considered for each zone. During each increment the material properties were considered constant and they changed through the successive increments.

For the analysis of the problem the commercially available FE code ANSYS was used [5].

The data set required the application of the above-described approach was obtained through an extensive material characterization program. The material characterization process involves typical quasi-static tests and an extensive set of 'stop and go' thermal exposure-fatigue experiments of the oxide/oxide composite, at different temperature levels. At each stage of the thermal exposure experiments, advanced ultrasonic measurements of the composite stiffness matrix were conducted. Then, all the elements of the stiffness matrix of oxide/oxide composite were known as functions of the applied temperature and the thermal exposure duration, and these properties were transformed to lamina stiffness evolution law.

The stresses and the displacements results obtained from the combustor chamber made of oxide/oxide composites by the application of the proposed design methodology were compared against the conventional design of the same component and the results are discussed analytically.

3. MATERIAL CHARACTERIZATION

The complete set of the mechanical properties of the single lamina, which are necessary for the design of the laminate structure, are not available since unidirectional material is very difficult to manufacture and its properties do not represent the actual lamina properties within the laminate.

For the purpose of the present work the following strategy has been adopted:

- Calculation of the laminate mechanical properties for a given laminate using ultrasonic velocity measurements.
- Inversion of the laminate mechanical properties for the determination of the actual lamina properties.

The determination of the elastic properties of a laminate structure can be achieved by calculating the coefficients of the propagation equation of an elastic plane wave, from a set of properly chosen velocity measurements along known material directions. These measurements are carried out using a special experimental setup that is described below [6].

A thin specimen with plan parallel faces is immersed in an acoustically coupling fluid (water). The specimen is placed between a transmitter (E) and a receiver (R), which are rigidly connected to each other through a supporting arm. Both the specimen and the arm, holding the two probes, can rotate as seen in Fig. 1. Using appropriate signal processing devices, the phase velocities of each of the propagated waves within the specimen are calculated for a number of specimen/probes relative orientations.

Depending on the angle of incidence, the pulse sent by transmitter E is refracted within the material in one, two or three bulk waves (one quasi longitudinal wave QL, one quasi transverse wave QT, or two quasi transverse waves QT₁, QT₂) that propagate in the anisotropic solid at different phase velocities and in different directions.

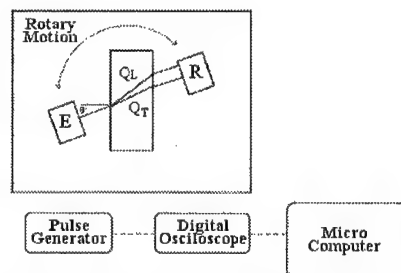


Figure 1: Experimental setup for the ultrasonic velocity measurements

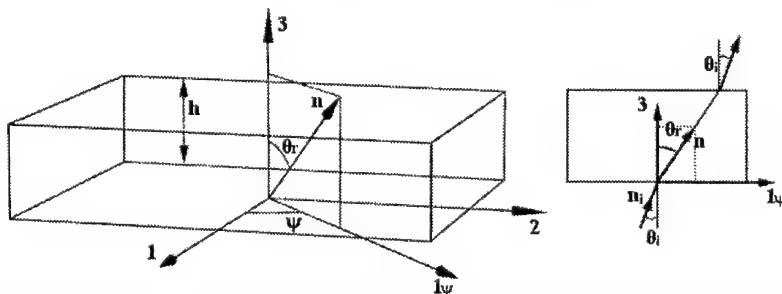


Figure 2: Typical geometry of the specimen used for ultrasonic velocity measurements

The difference in the propagation time of each the waves and the propagation time of the emitted signal in the coupling fluid without the specimen, is measured.

The evaluation procedure is based on the measurement of the time difference of the longitudinal and one or both transverse waves, and is only valid when the QL and the QT waves are appropriately separated.

The components of the elasticity tensor are obtained from the propagation velocities through a least square regression analysis, which minimizes the residuals of the wave propagation equations.

After the calculation of the components C_{ij} of the elasticity tensor, the engineering constants of the laminate structure (orthotropic in general) are determined by the following relations:

$$\begin{aligned} S_{11} &= (C_{22} \cdot C_{33} - C_{23}^2) \cdot C^{-1} & S_{44} &= C_{44}^{-1} \\ S_{22} &= (C_{11} \cdot C_{33} - C_{13}^2) \cdot C^{-1} & S_{55} &= C_{55}^{-1} \\ S_{33} &= (C_{22} \cdot C_{11} - C_{12}^2) \cdot C^{-1} & S_{66} &= C_{66}^{-1} \\ S_{12} &= (C_{13} \cdot C_{23} - C_{12} \cdot C_{33}) \cdot C^{-1} \\ S_{13} &= (C_{12} \cdot C_{23} - C_{13} \cdot C_{22}) \cdot C^{-1} \\ S_{23} &= (C_{12} \cdot C_{13} - C_{23} \cdot C_{11}) \cdot C^{-1} \end{aligned} \quad (1)$$

where:

$$C = C_{11} \cdot C_{22} \cdot C_{33} - C_{11} \cdot C_{23}^2 - C_{22} \cdot C_{13}^2 - C_{33} \cdot C_{12}^2 + 2 \cdot C_{12} \cdot C_{23} \cdot C_{13}$$

and finally

$$\begin{aligned} E_1 &= S_{11}^{-1} & G_{12} &= S_{66}^{-1} & \nu_{12} &= -S_{12} \cdot E_1 \\ E_2 &= S_{22}^{-1} & G_{23} &= S_{44}^{-1} & \nu_{23} &= -S_{23} \cdot E_2 \\ E_3 &= S_{33}^{-1} & G_{13} &= S_{55}^{-1} & \nu_{13} &= -S_{13} \cdot E_3 \end{aligned} \quad (2)$$

Table 1 shows the conditions under which the ultrasonic tests were performed, while Table 2 summarizes the calculated laminate properties for the $\text{Al}_2\text{O}_3/\text{Al}_2\text{O}_3$ laminate of $[0,90]_{6S}$ configuration.

Material	Thickness (mm)	Density (kg/m^3)	Water Temperature ($^{\circ}\text{C}$)	Frequency (MHz)
$\text{Al}_2\text{O}_3/\text{Al}_2\text{O}_3$	2.56	2313	23	5

Table 1: Ultrasonic test conditions and material geometry

E_1 (GPa)	E_2 (GPa)	E_3 (GPa)	G_{12} (GPa)	G_{13} (GPa)	G_{23} (GPa)	ν_{12}	ν_{13}	ν_{23}
75.8	73.2	14	14.2	7.5	7.2	0.08	0.26	0.25

Table 2: Engineering constants of $[0, 90]_{6S}$ $\text{Al}_2\text{O}_3/\text{Al}_2\text{O}_3$ laminate.

As it is expected due to the symmetric structure of the laminate, the modulus of elasticity is almost identical in the directions 1 and 2, while is much lower in the 3rd direction (normal to the plate thickness). In addition these values are very close to the ones measured under quasi-static loading.

This testing procedure was applied to a series of material samples that had been exposed to a simulated turbine engine environment inside a specially designed furnace. Different test durations were used up to 500 hours, allowing for the measurement of the degradation of the elastic properties of the oxide/oxide material, due to the sustained microstructural damage

under operating conditions. Table 3 shows the lamina properties of $\text{Al}_2\text{O}_3/\text{Al}_2\text{O}_3$ at the various steps/time of the thermal exposure as they have been calculated by inverting the measured laminate properties to the respective lamina ones for a given laminate structure.

For the purpose of the present analysis it was assumed that the developed damage does not affect the degree of anisotropy. All the thermal exposure experiments were conducted at 1100°C and the evolution laws of the various stiffness components, with no lack of generality, were assumed constant with respect to temperature. Thus, after an initial thermal analysis step, where the actual temperature of the component was identified, the combustor was divided to temperature zones and the stiffness degradation laws were applied to the temperature zones that exceed 1000°C .

4. MODEL DESCRIPTION

The outer liner of the combustion chamber was modelled using 4414, 8-node SHELL99 layered elements [5]. Reduced modelling was used since the component exhibits rotational symmetry. Thus, only the 1/16 of the whole chamber was introduced in the model along with the appropriate symmetry conditions, in order to reduce run time. The liner is held on its supports with 16 screws. This condition was transferred into the numerical model using appropriate nodal displacement constraints on the area of contact between the liner and the supports. A 15 bar pressure was uniformly applied on the liner.

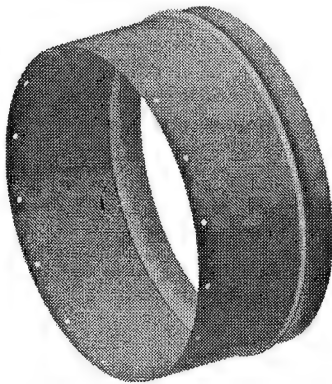


Figure 3: View of the geometric model using symmetry expansion.

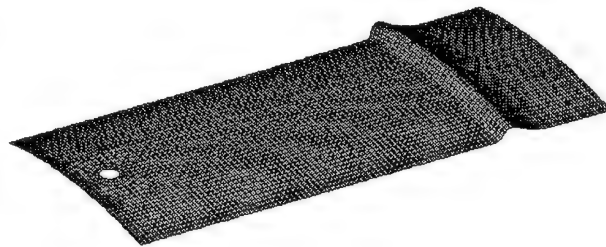


Figure 4: The finite element mesh.

Thermal loads were neglected at this stage in order to simplify the analysis and to focus on the influence of the anisotropic stiffness degradation on the mechanical response of the combustor liner.

The lay up sequence used for the layered material was $(0/\pm 45/90)_2$. This results to a 4mm thickness for the component. The material properties used were calculated from a series of tests conducted on the $\text{Al}_2\text{O}_3/\text{Al}_2\text{O}_3$ ceramic material as described in the previous section.

Ten sets of material properties were used in equal analyses to depict the degradation sustained by the material, due to the microstructural damage developed during its exposure to the extreme temperature environment of the combustion chamber.

Operation Time (hours)	E_1 (GPa)	$E_2=E_3$ (GPa)	$G_{12}=G_{13}$ (GPa)	G_{23} (GPa)	$n_{12}=n_{13}$	n_{23}
0	118.768	20.959	20.000	8.000	0.15	0.25
25	112.660	19.881	19.400	7.760		
50	108.588	19.163	18.800	7.520		
75	104.855	18.504	18.350	7.340		
100	101.801	17.965	18.000	7.200		
150	96.711	17.067	17.500	7.000		
200	93.318	16.468	17.200	6.880		
300	90.773	16.019	16.900	6.760		
400	89.076	15.719	16.800	6.720		
500	88.228	15.570	16.700	6.680		

Table 3: Material properties used in the analysis

5. NUMERICAL PROCEDURE

The stiffness degradation of the ceramic material cannot be simulated with standard material models. In order to avoid the complicated procedure of developing a new material model, a simple procedure was selected for the analysis. The analysis was conducted in ten steps in order to simulate the non-linear behaviour of the material in the presence of microstructural damage. The overall procedure is based on a Newton-Raphson approach for the solution of the non-linear problem, being applied using multiple analysis runs. For each analysis step the deformed geometry resulting from the previous step, was used to update the model to the current deformation condition. In this way, displacement continuity was achieved. The results of the last analysis step show the condition of the liner at the end of the 500-hour operation time.

6. RESULTS

Displacement and stress data were recorded for each analysis step. The evolution of the maximum displacement in the form of radial expansion is presented in Figure 5 against the operation time in hours. A second curve that represents the variation of E_1 stiffness component of the single lamina versus the operation time in hours is also given in the same Figure. For each stress component, the evolution of the maximum values, with respect to the engine operation time, is plotted for the respective critical locations. Figure 6 shows the critical nodes for which the stress components will be given in the next. The use of layered elements in the analysis allows for the computation of the stress distribution through the laminate thickness.

Figure 7 presents the through thickness variation of the axial stress component at the node 13027, which is the node where the maximum values for the axial stresses appear.

Figure 8 plots the variation of the maximum axial stress, which has been monitored at the outer layer (0° degree layer) versus the operation time of the gas turbine.

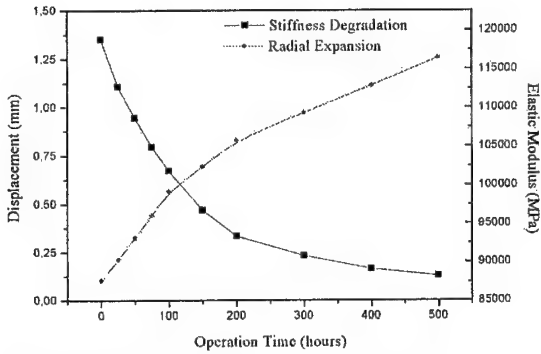


Figure 5: Radial expansion and stiffness degradation of the liner versus engine operation time.

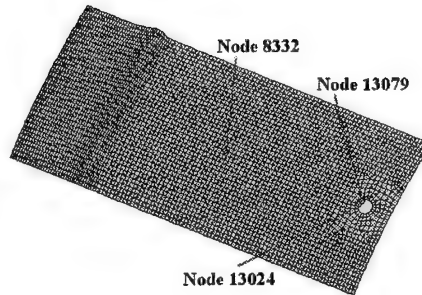


Figure 6: Locations of maximum stress

As it is shown, there is a 10% increase of the maximum axial stress experienced by the material at the said point, due to the anisotropic degradation of the lamina properties caused by thermally induced damage.

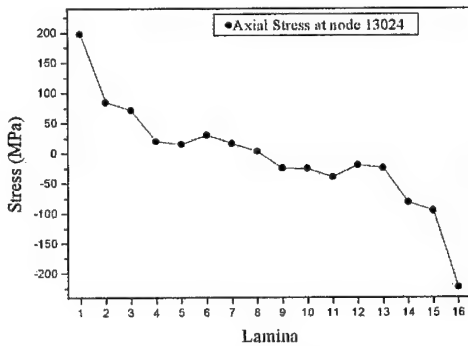


Figure 7: Axial stress distribution through the laminate at node 13024

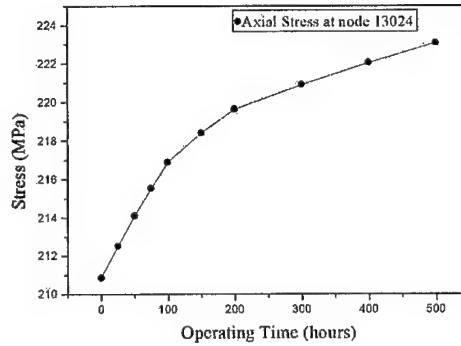


Figure 8: Axial stress at node 13024 vs. engine operation time

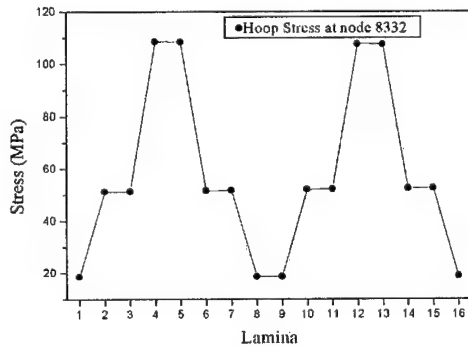


Figure 9: Hoop stress distribution through the laminate at node 8332

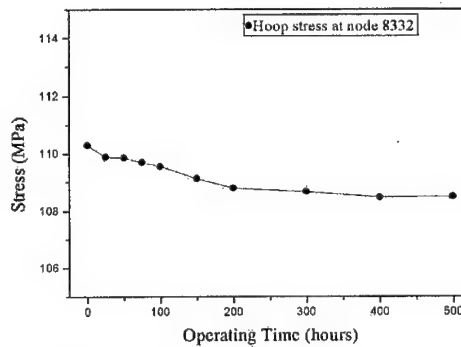


Figure 10: Hoop stress at node 8332 vs. engine operation time

Figure 9 shows the through thickness variation of the hoop stress component at the node 8332, which is the node where the maximum hoop stresses appear.

Figure 10 presents the variation of the maximum hoop stress versus the operation time of the gas turbine. In this case, the decrease of the maximum hoop stress appears to be of 3%, as a result of the thermally induced damage within the material structure and the increase of the axial monitored stress.

Figure 11 shows the through thickness variation of the shear stress component at the node 13079, which is the node where the maximum shear stresses appear.

Figure 12 presents the variation of the maximum shear stress, which has been monitored at the outer layer (0° degree layer) versus the operation time of the gas turbine. In this case an increase of the maximum shear stress of about 5% appears as a result of the thermally induced damage within the material structure.

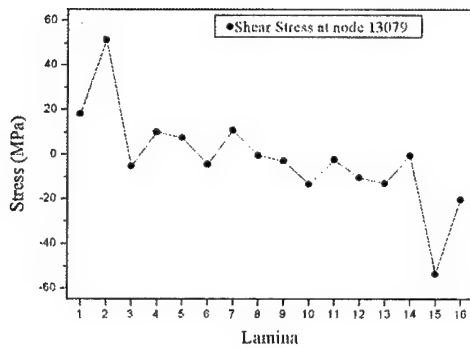


Figure 11: In plane shear stress distribution through the laminate at node 13079

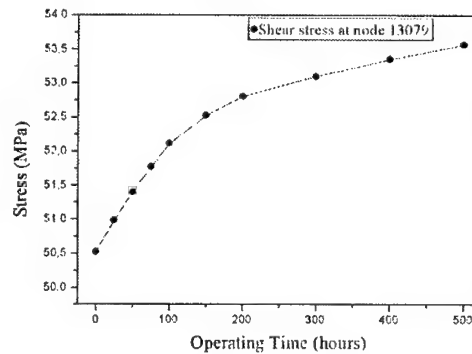


Figure 12: In plane shear stress at node 13079 vs. engine operation time

Figure 13 shows the deformable shape of the analysed component and the corresponding displacement contours of the outer lamina, while Figure 14 presents the axial stress contours that correspond to the outer-critical lamina. Under the given loading conditions the maximum monitored displacement is of the level of 0.17 mm.

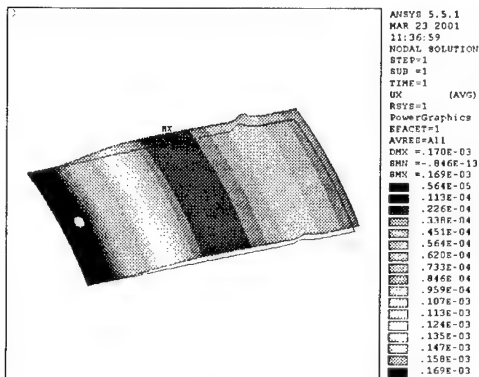


Figure 13: Displacement contour

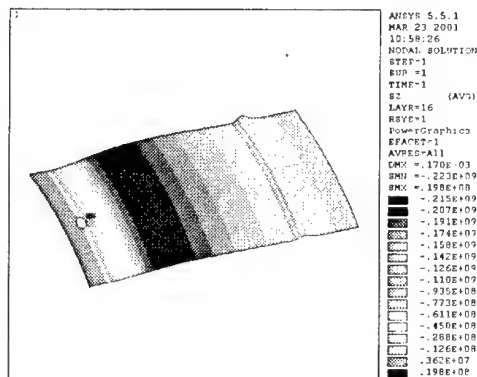


Figure 14: Axial stress contour at lamina 16

Finally, Figure 15 shows the hoop stress contours monitored at the lamina 4 while the shear stress contours developed at the lamina 15 are given in Figure 16.

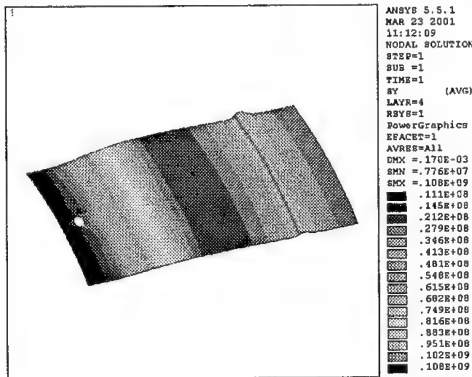


Figure 15: Hoop stress contour at lamina 4

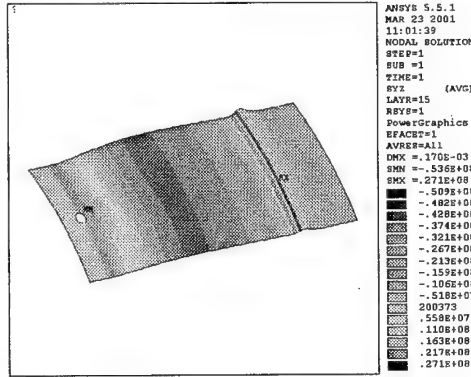


Figure 16: In plane shear stress contour at lamina 15

7. CONCLUSIONS

An Oxide/Oxide composite material was used for the design and the manufacturing of the combustor liner of an industrial gas turbine system.

Analytical characterization of the material was conducted at ambient and high temperature. Additional characterization of the material at ambient temperature was also made using ultrasonic waves. Since the exposure of the Oxide/Oxide composite at high temperature (over 1000° C) results to the development of anisotropic damage within the material structure, it concludes to anisotropic degradation of the composite properties. Using ultrasonic waves, the complete characterization of the Oxide/Oxide lamina properties at different high temperature exposure time is available.

For the design of the combustor liner a series of FE analysis was applied using a give, easy to manufacture stacking sequence for the laminated structure. Results showed that the Oxide/Oxide composite fulfils the design requirements for high temperature structural applications and may be considered as a very promising candidate material in future application. In addition, for design of high temperature components using CFCCs, innovative design methodologies that take into consideration the anisotropic damage, which is developed within the material structure under operation conditions, is necessary.

Future work that has been already planned includes coupled thermo-mechanical analysis and the introduction of material models that permit anisotropic damage and properties degradation with respect to exposure time and working temperature.

8. REFERENCES

- [1] Lamicq, P., Boury, D., "Ceramic Matrix Composite Parts Design", AGARD REPORT 795 "Introduction of Ceramics into Aerospace Structural Composites", Nov. 1993.
- [2] Kostopoulos, V., Pappas, Y.Z., "Toughening Mechanisms in Long Fiber Ceramic Matrix Composites", In "Comprehensive Composite Materials" Vol. 4, Elsevier Science Ltd, Ed. A. Kelly & C. Zweben, 2000
- [3] Sygulla, D., Mührlatzer, Agathovic, P., "Integrated Approach in Modelling, Testing and Design of Gradient-CVI Derived CMC Components" AGARD REPORT 795 "Introduction of Ceramics into Aerospace Structural Composites", Nov. 1993.

-
- [4] Baste, S., Audoin, B., "On Internal Variables in Anisotropic Damage", European Journal of Mech., A/Solids, vol. 10, 6, 1991.
 - [5] ANSYS, Operation Manual, ANSYS Release 5.4, Nov. 1997
 - [6] CEN Technical Committee 184, SubCommittee 1, 'Advanced Technical Ceramics,- Ceramic Matrix Composites - Mechanical Properties at Room Temperature - Determination of Elastic Properties by an Ultrasonic Technique', WI 114, March 2001.

EXPERIMENTAL AND THEORETICAL STRESS ANALYSIS OF INCOMPRESSIBLE BONDED ELASTOMERIC DISCS SUBJECTED TO COMPRESSION

P.A. Kakavas

Technological Educational Institute, Department of Architecture: Reconstruction &
Restoration of Buildings, 1 M. Alexandrou str., 26334, Koukouli, Patras, Greece
e-mail:kakavas@teipat.gr

1. SUMMARY

The aim of this article is to derive the distribution of stress and strain in bonded rubber discs subjected to uniaxial compression. The axial stress was analytically computed using a neo-Hookean strain energy function. The testing material is Hyperelastic and incompressible and the equilibrium equations lead to the solution of two separate ordinary differential equations. Their solution yields the radial profile of displacement and the distribution of pressure as a function of the axial coordinate within the compressed sample. Using the condition that the free surface of the cylindrical samples is stress free, the pressure term was explicitly determined. The axial stress was also determined using the equilibrium equations of the deformed material and taken its mean value along the radial direction. The theoretical predicted axial stress was compared to experimental data for reinforced elastomeric samples subjected to compression.

2. INTRODUCTION

The importance to understand the micro-fracture process, reinforcement, adhesive joint strength and explosive decompression in rubbers, extensive experimental studies were contacted previously by the author using the Acoustic Emission Technique [1]. Various theoretical approaches to evaluate the stress and displacement fields within bonded elastomeric discs subjected to uniform tension and/or compression were adduced by Blatz and kakavas [2]. An effective material property, ν_{eff} , was derived which is consistent with the measured values of the normalized volumetric contraction, $\gamma = -u_0(a)/a\epsilon$ and the initial modulus from the triaxial tests on compression and tension.

The geometry of the testing samples were bonded circular discs the so-called '*poker chip*', where their chemical composition was described in previous articles published by the author and co-workers [1,2,3]. Analytical expressions for the axial stress in bonded elastomer discs subjected to triaxial stress were derived using a *neo-Hookean* strain energy function and an

algebraic equation was developed to correlate the diametrical contraction of the testing 'poker chip' samples with the applied strain [4]. A theoretical equation of the nominal stress based on the average value of the axial component of stress was also developed and the derived numerical values were compared to experimental data [5,6].

In the present paper, after the introduction of basic equations of nonlinear rubber elasticity, the deformation gradient tensor \mathbf{F} , was developed for incompressible bonded circular discs subjected to uniaxial compression along the axial direction. The axial components of the Piolla stress were derived for 'poker chip' type of samples by assuming that the material is incompressible and a neo-Hookean strain energy function was assumed for the derivation of the stresses.

3. DESCRIPTION OF THE PROBLEM

The geometry of the testing specimens was a circular cylindrical disc of radius $R=A$ and thickness $Z=2H$ where the ratio $\alpha = A/H$ is called *aspect ratio*. For a circular cylindrical coordinate system in the undeformed state, the coordinates are denoted by (R, Θ, Z) and their corresponding deformed by (r, θ, z) . Along this analysis the following assumptions hold [5,6] (1) In the deformed configuration planes normal to the direction of the applied load remain planes (2) The volume change is uniform throughout the body and depends upon the Poisson ratio, the aspect ratio and the applied compression. (This assumption is more accurate when the aspect ratio is large.)

By virtue of the first assumption, and the cylindrical symmetry of the problem, the deformed coordinates with respect to its undeformed are defined by:

$$r = r(R, Z), \vartheta = \Theta, z = \zeta(Z) \quad (1a)$$

where the function $\zeta(Z)$ on the upper and lower surfaces of the sample satisfies the condition:

$$\zeta(\pm H) = \pm h \quad (1b)$$

Since, at $r(R=0)=0$, holds [5,6]:

$$r = R\chi(Z), \chi(\pm H) = 1 \quad (2)$$

It can be proved that the Piolla stress tensor is given by[4]:

$$\frac{T}{\mu} = \begin{bmatrix} \chi - p\chi^{-1} & 0 & pR\chi\chi' \\ 0 & \chi - p/\chi & 0 \\ R\chi' & 0 & \chi^{-2} - p\chi^2 \end{bmatrix} \quad (3)$$

Substitution the stress tensor into equilibrium equations yields:

$$\frac{\partial p}{\partial \Theta} = 0 \Rightarrow p \neq p(\Theta) \quad (4)$$

i.e. the pressure p is independent of the tangential coordinates.

Also, holds that [4]:

$$-\frac{p_R}{\chi} + R\chi'' = 0 \text{ and } R p_R \chi' - \frac{2\chi'}{\chi^3} - \chi^2 p_z = 0 \quad (5)$$

$$\chi' \chi'' - \chi \chi''' = 0, \quad p_0(Z) = -\frac{2\chi'}{\chi^5} \quad (6)$$

The solution of the ordinary differential equation (6a) yields the $\chi(Z)$, i.e.

$$r = R \frac{\cos(mZ)}{\cos(mH)} \quad \forall m = 0, 1, 2, 3, \dots \quad (7)$$

A plot of the normalized profile r/R as a function of the axial coordinate z is shown in Fig. 1.

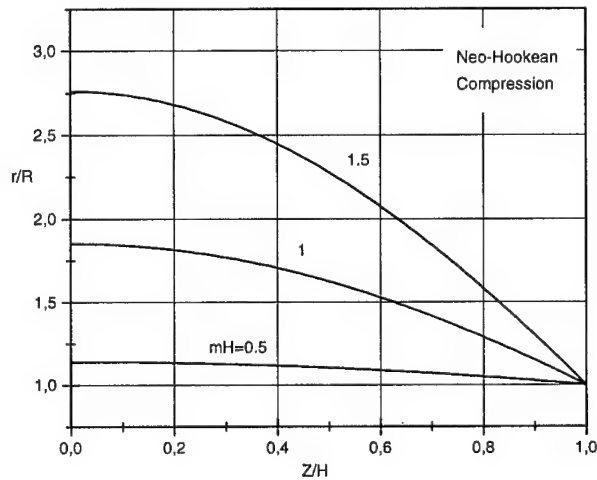


Figure 1: Profile of the normalized radial displacement r/R as a function of the normalized z coordinate

And the pressure term is given by:

$$p(R, Z) = p_{oo} + \frac{1 \cos^4(mH)}{2 \cos^4(mZ)} - \frac{R^2 m^2 \cos^2(mZ)}{2 \cos^2(mH)} \quad (8)$$

The component of the radial stress is:

$$\frac{T_r^R}{\mu} = \frac{\cos(mZ)}{\cos(mH)} - \frac{\cos(mH)}{\cos(mZ)} \left[p_{00} + \frac{1}{2} \frac{\cos^4(mH)}{\cos^4(mZ)} - \frac{R^2 m^2 \cos^2(mZ)}{2 \cos^2(mH)} \right] \quad (9)$$

where μ defines the shear modulus of the material.

The outer surface of the 'poker chip' sample is considered stress free, i.e.

$$\int_{-H}^H \frac{T_r^R}{\mu} \Big|_{R=A} dZ = 0 \quad (10)$$

Replacing eqn (9) into eqn (10) and integration yields the value of p_{00} , i.e.

$$p_{00}(w, \alpha) = \left\{ \frac{2 \tan(w)}{\cos(w)} - \frac{\sin(w)}{4} - \frac{3}{8} \tan(w) \cos^3(w) \right. \\ \left. - \frac{3}{16} \cos^4(w) \ln \left(\frac{\tan(\frac{\pi}{4} + \frac{w}{2})}{\tan(\frac{\pi}{4} - \frac{w}{2})} \right) + \alpha^2 w^2 \tan(w) \right\} / \ln \left(\frac{1 + \sin(w)}{1 - \sin(w)} \right) \quad (11)$$

where $w = mH$

A plot of the parameter p_{00} as a function of mH is shown in Fig. 2

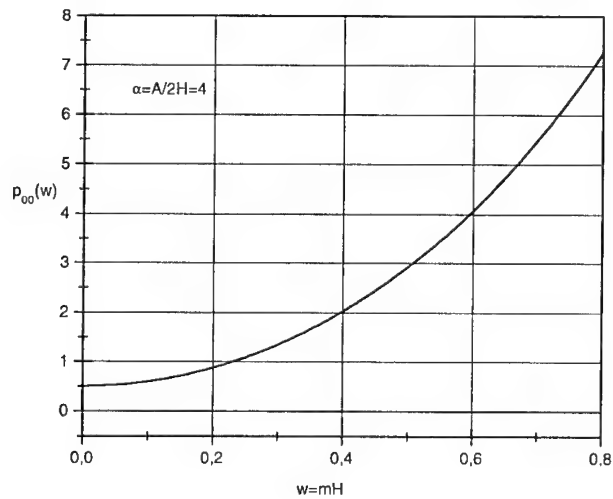


Fig. 2 P_{00} vs. mH

It can also be proved that the axial stress is:

$$\frac{T_z^r}{\mu} = \frac{1}{2} \frac{\cos^2(mH)}{\cos^2(mZ)} - \frac{\cos^2(mZ)}{\cos^2(mH)} [p_{00} - (\frac{R}{H})^2 (mH)^2 \frac{\cos^2(mZ)}{\cos^2(mh)}] \quad (12)$$

By taken the mean value of eqn (12) along the axial direction yields:

$$\left\langle \frac{T_z^r}{\mu} \right\rangle = \frac{1}{2H} \int_{-H}^{+H} \frac{T_z^r}{\mu} dZ = \frac{1}{2(w)} \tan(w) \cos^2(w) - \frac{p_{00}}{2\cos^2(w)} \left(1 + \frac{\sin(2w)}{2w}\right) + \frac{1}{4} r^2 \frac{(w)^2}{\cos^4(w)} \left[\frac{3}{2} + 2 \frac{\sin(2w)}{(2w)} + \frac{1}{2} \frac{\sin(4w)}{(4w)} \right] \quad (13)$$

where $w = mH$ and $r = R/H$

The value of the normalized stress upon the bonded surfaces in z-direction are given by:

$$\frac{T}{\mu} = \frac{1}{\pi A^2} \int_0^A \left\langle \frac{T_z^r}{\mu} \right\rangle 2\pi R dR \quad (14)$$

where A denotes the radius of the bonded rubber sample.

Hence,

$$\frac{T}{\mu} = \frac{1}{2(2w)} \sin(2w) - \frac{p_{00}}{2\cos^2(w)} \left(1 + \frac{\sin(2w)}{2w}\right) + \frac{1}{8} \frac{(\alpha w)^2}{\cos^4(w)} \left[\frac{3}{2} + 2 \frac{\sin(2w)}{(2w)} + \frac{1}{2} \frac{\sin(4w)}{(4w)} \right] \quad (15)$$

where the function $p_{00}(w)$ is given by eqn (11).

For incompressible materials ($J=1$), the function $\zeta(Z)$ is given by:

$$\zeta(Z) = \frac{1}{m} \tan(mZ) \cos^2(mH) \quad (16)$$

where $\zeta(H) = \lambda H$, λ being the compression ratio.

Hence,

$$\lambda = \frac{\tan(mH) \cos^2(mH)}{(mH)} = 1 - \varepsilon \Leftrightarrow \varepsilon = 1 - \frac{\sin(2mH)}{(2mH)} \quad (17)$$

where ε is the applied compression strain.

Equation (17) correlates the applied compression on the specimen to the product mH . A plot of the theoretically predicted stress in the axial direction T/μ , as a function of strain is shown in Fig. 3.

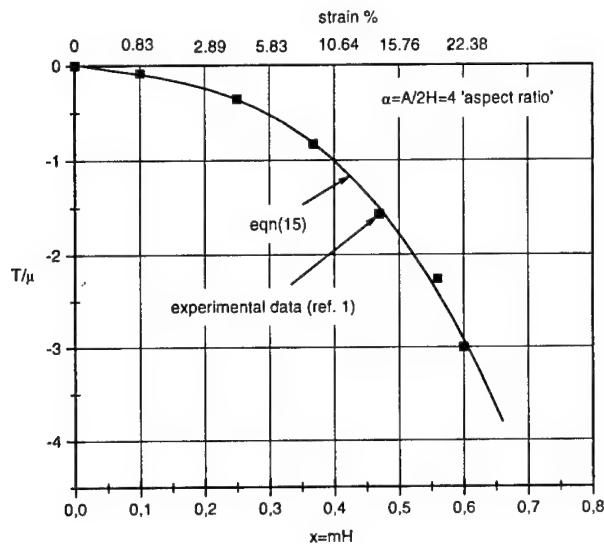


Figure 3: Normalized stress T/μ as a function of applied strain on the bonded cylinders.

As it is clear for Fig. 3 the *axial* stress distribution in 'poker-chip' samples the experimental data[1] were fitted theoretically up to applied strain 25%. The present problem is currently under investigation using a new strain energy function for Hyperelastic solids proposed by the author[7].

4. REFERENCES

- [1] Kakavas P.A. and Chang W.V., Acoustic Emission in Bonded Elastomer Discs Subjected to Compression, J. Appl. Polym. Sci. Vol. 45, 865-869 (1992)
- [2] Blatz P.J. and Kakavas P.A. : A Geometric Determination of Void Production in an Elastic Pancake. J. Appl. Polym. Sci. **49**, 2197-2205 (1993)
- [3] Kakavas P.A.: Mechanical Properties of Bonded Elastomer Discs Subjected to Triaxial Stress. J. Appl. Polym. Sci. **59**, 251-261 (1996)
- [4] Kakavas P.A.: Prediction of the Stress Distribution in an Elastic Pancake Using a neo-Hookean Strain Energy Function. Pol. Eng. & Sci., **37**(2), 428-435, (1997)
- [5] Petrie C.J. & Shariff M. : Finite Deformation of Compressible Bonded Rubber Mounts. J. of Strain Analysis. **27**(3), 157-169 (1992)
- [6] Shariff M. : An Approximate Analysis of Infinitesimal Deformations of Bonded Elastic Mounts. J. of Strain Analysis. **23**, 115-120 (1988)
- [7] Kakavas P.A. A New Development of the Strain Energy Function for Hyperelastic Materials Using a Logarithmic Strain Approach. J. Appl. Polymer Sci. vol. 77, 660-672 (2000)

OPTICAL DEVICE FOR PROSTATE CANCER DETECTION

G. T. Anastassopoulos - J.G. Lytras - M.M. Sunaric - V.C. Moulianitis - S.D. Panteliou¹
Machine Design Lab., Dept. of Mechanical Engineering & Aeronautics, University of Patras,
GR-265 00 Patras, GREECE

A. Bekos - N. Kalinderis - D. Hatzichristou
Department of Urology and Center for Sexual and Reproductive Health,
Aristotle University of Thessaloniki, GR-540 06 Thessaloniki, GREECE

1. SUMMARY

Prostate cancer is the most prevalent male cancer. The existing testing methods are subjective and not quantitative (Digital Rectal Examination) or not sufficiently accurate or expensive (ultrasound, biopsy). There is a need for a simple, yet accurate method to detect changes in the mechanical properties of the prostate as a replacement of the DRE. We developed a new device, which is able for geometric representation and objective measurements of the stiffness of the prostate tissue, based on image processing of data taken with a micro camera from an inflated balloon inserted in the rectal area and touching the prostate.

Computer based digital image processing applied consists of: transformation of image data (captured by micro camera) to intensity matrix, image enhancement (contrast, brightness), block processing and relative distance calculation (shape from shading method), calculation of relative stiffness value corresponding to each block and objective data mapping (containing geometric representation of the prostate, calculation of prostate area and stiffness map). For this purpose a genuine algorithm was developed.

The research prototype built was successfully applied to models for prostate diseases and cadaveric tissues for preliminary assessment. The results encouraged the first clinical application in vivo, which has demonstrated that there were no side effects mentioned by the doctors or the subjects examined. The reproduction of the stiffness map enables the assessment of the changes in mechanical properties of each prostate surface. In all cases, results can be compared and are in agreement with the results of conventional methods (DRE, ultrasound). Hence the proposed design is feasible and can lead to a diagnostic tool. This design will be used to validate in clinical setting the sensitivity and specificity of the device developed.

¹ Contact Person: S.D. Panteliou, Machine Design Lab. Dept. of Mechanical Engineering & Aeronautics,
University of Patras, Patras, Greece, Phone: 30-61-997206, Fax: 30-61-997207,
email: panteliu@mech.upatras.gr

2. INTRODUCTION

Physical examination is one of the principle physician's sources of information for patient's evaluation in the everyday clinical practice and is based on manual examination of different organs and systems. Its importance is based on information on the physical and mechanical properties of living tissues, detecting pathological signs of disease, as the mechanical properties of biological tissues depend on their morphological structure, circulation architecture and neuromuscular status. Physical examination however, relies on physician's experience and the tactile properties of the human fingers. Human tactile sensors in the skin recognize the characteristics of an object by using the sense of touch and/or tactility in coordination with the movements of the hand and/or finger. Human touch provides the necessary feedback to identify the object in question and the collected data contain qualitative information about their textural patterns, such as shape, hardness or softness. Part of these data is qualitative and the reminder is semi quantitative. Such limitations make the examination's results subjective and non-reproducible. It is evident that objective quantitative and reproducible measurement of even the simple mechanical parameters, such as stiffness, is of critical importance for every physician, regardless of his specialty.

The structures of the urogenital system are of particular importance in that their dysfunction constitutes a significant part of male pathology. Specifically the prostate gland (Carter H.B., Coffey D.S., 1990) is subject to ultra structural changes due to benign prostate hyperplasia (the most common benign disease of the male)(Barry M.J. et al., 1993) and cancer of the prostate (the most common cancer of the male) (Wingo P.A., Tong T., Bolden S., 1995). Physical examination of the prostate relies on the digital rectal examination of the prostate; physicians examine the mechanical properties of the gland by inserting the finger in the rectum and palpating the gland. Enlargement of the gland is evidence of benign prostate hyperplasia, while detection of areas with increased stiffness is suspicious for prostate cancer. It is clear that DRE plays a key role, at least for the decision for further diagnostic testing of the organ, although the human finger may not detect minor changes in stiffness –associated with early stage disease-, or fibrotic nodules associated with inflammatory disease and not cancer (Carvalho G.F., Smith D.S., Mager D.E., Ramos C., Catalona W.J., 1999), (Catalona WJ, Richie JP, Ahmann FR et al., 1994). Human hand sense of hardness for soft tissues however depends on: a) the thickness of the tissue (as the thickness of the tissue is reduced, the felt hardness increases), b) the contracting area and c) the contract pressure. Such sensory performance is inappropriate for medicine, a science dealing with human life (Sarvazyan et al. 1998). Over the past few years, there have been numerous studies on tactile sensors for object recognition. An artificial tactile sensor therefore, in order to possess human hand-like characteristics may imitate these conditions. Unfortunately, conventional tactile sensors, consisting of miniature micro switch, strain gauge, resistive sensor and pressure sensitive piezoelectric element, do not satisfy the above conditions (Omata S., Terunuma Y., 1992). In particular, previous work to develop sensor technology to provide calibrated physical values of tissue compliance in a noninvasive manner, were not successful in vivo (Constantinou C.E., Omata S., 1996).

During the last year, we developed a methodology based on image processing techniques [A. Bovik, 2000], for a qualitative and quantitative assessment of the prostate.

3. DESCRIPTION OF THE DEVICE

An optical method is applied (Fig. 1). In the rectal area 1, an Anoscope Tube with an inflatable balloon 3 is used against the prostate gland 2 (with or without tumor). The balloon is inflated to a desired pressure by a connection 4 to a regulated air pressure supply source, through a tube 5. The same tube conveys light that has been modulated to light the balloon in the prostate area. The balloon is sealed with a seal 7 against air leaks. The tube 5 also contains a video micro-camera 6 at its distal end, which can transmit pictures of the observed balloon surface to an electronic controller, such as a PC computer, through the tube 5 and cables 8. Every point on the surface of the prostate is under a certain pressure that is approximately equal to the air pressure inside the balloon.

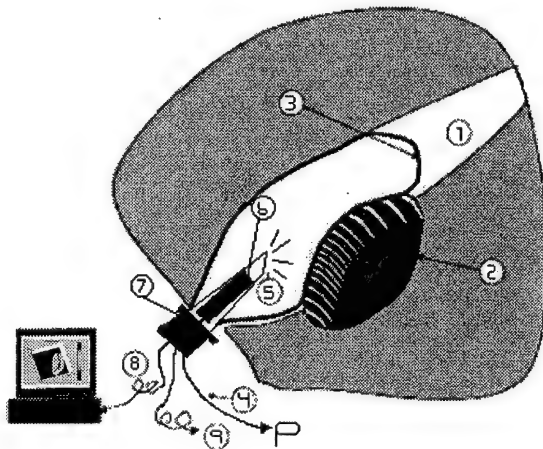


Figure 1. Optical Prostate Geometric Imaging and Prostate Stiffness Imaging

The measuring procedure consists of a first step of introducing the balloon 3 with the measuring head that consists of tube 5 and the video micro-camera 6, inside the rectal cavity 1, inflating the balloon to sufficient pressure P_2 so that the balloon contacts the prostate over the desired surface, lighting the balloon inside surface, transmitting the image of the inner surface of the balloon at the area of contact with the prostate tissue under investigation to the computer 8. Then, the air pressure in the balloon is released to P_1 and the new image of the soft tissue or tumor is recorded. From the difference in brightness of these two images, the displacement of each point in a direction perpendicular with the surface, due to the change in pressure, can be computed. From these data, stiffness per unit of surface area can be obtained. The user can get both the 3D representations of intensity images and the 3D stiffness map on a PC. The distribution of stiffness values and their percentage are also obtainable. The described images can be compared with standard images to yield the diagnosis of a malignant prostate tissue if the differences are medically significant.

4. IMAGE PROCESSING

The optical method used is based on digital images of the inner surface of the balloon in contact with the prostate surface, captured by the micro-camera, that are processed by means of sequential filtering and identification of the prostate volume. This is done through software

developed for this purpose capable to compare two pictures corresponding to the different pressures P1 and P2 (Figure 2). The method called shape-from-shading is one of shape-from-X methods, which are well known in image processing environment [Tsai P.S., Shah M., 1994]. This method is based on representing the height of the point on the surface by the pixel value in that point on the image taken by the device. It is assumed that brighter points are closer to the camera, hence higher, while darker points are more distant from the camera, hence lower. The first step is to transform the image into 2D array, the intensity matrix, containing information about intensity value for every pixel of the image. By applying shape-from-shading algorithms and image processing techniques, it is possible to obtain the 3D representation that is very close to the real shape. The idea of this method is to take the two images at pressures P1 and P2 (Figure 2), then produce their 3D representations (Figure 3), and then, by subtracting the 3D representations, that is subtracting the intensity matrix of the second image from the intensity matrix of the first image, to recover changes in shape and to obtain the stiffness per unit of surface area from these changes, as it was described previously (Figure 4). This procedure will enable the user to identify the prostate boundaries, thus producing its geometric representation, as well as areas on the prostate that exhibit stiffness values above normal, hence suspicious for cancerous developments. This is done through assessment of the intensity of the brightness of each point and is due to the pressure addressed on the prostate area through the inflated balloon, thus permitting the user to identify stiffer and less stiff areas, which are expected to guide the medical personnel to more detailed detection methods (i.e. U/S, biopsy). From then on, elaboration of information of such graphs will lead to production of prostate maps distinguishing stiffer than less stiff areas. This will be achieved through comparison of the extracted information with controls.

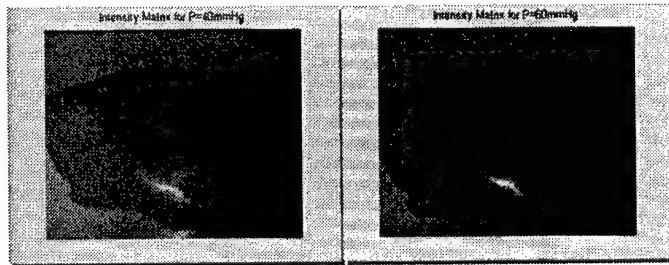


Figure 2. Images of the prostate at pressures P1 and P2 captured by micro-camera.

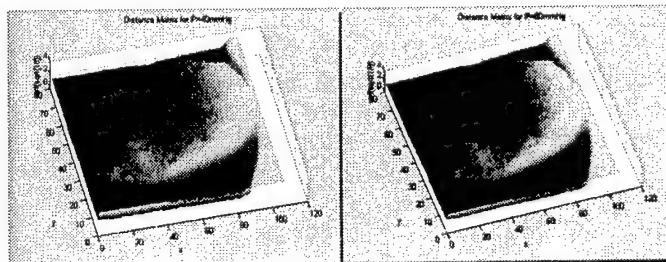


Figure 3. 3D representations of Images (brighter areas represent higher points).

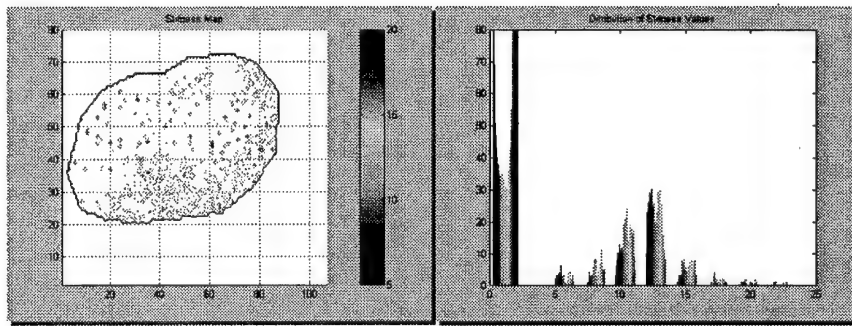


Figure 4. Geometric Representation and Stiffness Calculation and Distribution

5. CLINICAL APPLICATION

After the successful experimentation (Panteliou et al 2000, Παντελιού κ.α. 2000, Sunaric et al 2000) on prostate models used for training of medical students, the next step was the in vivo application of the device. More than 60 measurements in vivo were performed on 29 informed volunteer patients. Frames were taken with the micro-camera in a pressure range of 16 and 100 mm Hg. A typical set of images and results taken from these tests are showed in Fig. 5,6.

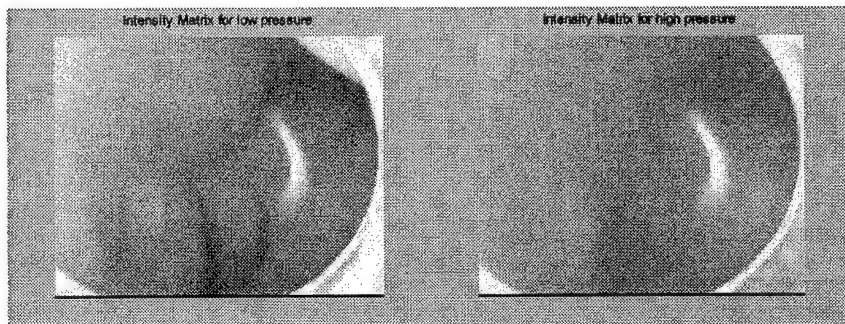


Figure 5. Images Captured with the Micro-camera during in vivo Application.

Despite the technical difficulties raised during the standardization of the procedure, the method was able to identify differences in the stiffness of the points of each prostate, while it was in agreement with DRE results in 70% of the cases.

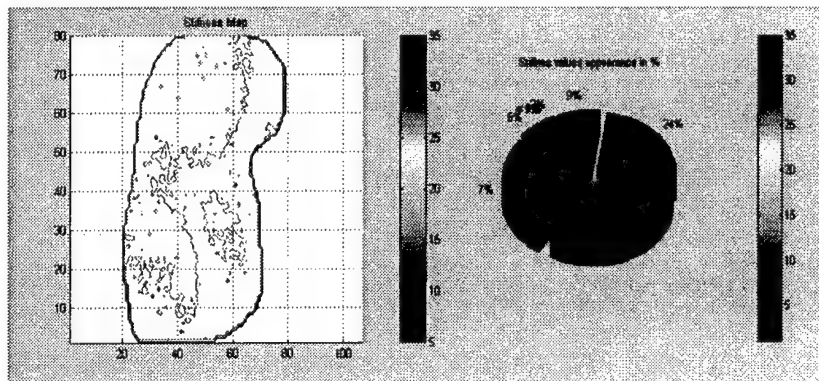


Figure 6. Geometric Representation - Stiffness Calculation and Distribution (data in vivo).

6. CONCLUSIONS

The design and development of the above mentioned device, based on image processing of pictures taken at the inside of an inflated balloon inserted in the rectal area and touching the outer surface of the prostate, is expected to lead after evaluation to an accurate method for the assessment of the mechanical properties of the prostate gland, through its geometric and stiffness representation.

In comparison with the DRE (Digital Rectal Examination) the proposed device will be:

- a. Objective and establish a permanent record of the examination for future comparisons. Present method is subjective and not unambiguously recordable.
- b. More acceptable to both patients and physicians.
- c. Totally non-invasive due to minimal disturbance of the prostate.
- d. Less costly as compared to other imaging techniques, such as ultrasonography.

Besides this, the device seems to have a variety of other biomedical applications, where the characteristics of soft or hard tissue need to be evaluated.

7. REFERENCES

- [1] Barry M.J. et al: Epidemiology and Natural History of BPH in Proceedings of the 2nd International Consultation on Benign Prostate Hyperplasia (BPH), Paris, pp 17-34, 1993.
- [2] Bovik A., Handbook of Image and Video Processing, Academic Press, Harcourt Publishers Limited, 2000.
- [3] Carter H.B., Coffey D.S.: The prostate: An increasing medical problem. Prostate 1990; 16:39-48.
- [4] Carvalhal G.F., Smith D.S., Mager D.E., Ramos C., Catalona W.J., Digital rectal examination for detecting prostate cancer at prostate specific antigen levels of 4 ng./ml. or less. J Urol 1999;161:835-9.
- [5] Catalona W.J., Richie J.P., Ahmann F.R. et al: Comparison of digital rectal examination and serum specific antigen in the early detection of prostate cancer: results of a multicenter clinical trial of 6630 men. J Urol 1994; 151:1283-1290.

- [6] Constantinou C.E., Omata S., Analysis of the relative biomechanical effects of a1 and a2 antagonists in modifying the compliance of the prostate and micturition parameters of the hormonally manipulated male rat. *Neurourology and Urodynamics*, 1996, 15: 85 -101.
- [7] Omata S., Terunuma Y., New tactile sensor like the human hand and its applications. *Sensors and actuators*, 35:9-15, 1992.
- [8] Panteliou S.D., Sunaric M.M., Sarris J., Anastassopoulos G., Lytras J., Hatzichristou D.G., Design of a Device for the Objective Assessment of the Mechanical Properties of the Prostate Gland. *Mechanics 2000, International Conference on Role of Mesomechanics for the Development of Science and Technology*, Xi'an, China, June 13-16, 2000.
- [9] Sarvazyan et al., 11th IEEE Symp. Comp-Based Med Sys, 1998, Lubbock, TX, page 110 and US patent 5,524,636.
- [10] Sunaric M.M., Anastassopoulos G., Lytras J., Panteliou S.D., Hatzichristou D.G., Tzortzis V., Melachrinou M., Device for the objective Assessment of the Mechanical Properties of Tissues. *2nd European Symposium in Biomedical Engineering and Physics*, 6-8 October, 2000, Patras, Greece.
- [11] Tsai P.S., Shah M., Shape from Shading Using Linear Approximation, *Image and Vision Computing Journal*, 12(8): 487 498, 1994.
- [12] Wingo P.A., Tong T., Bolden S., *Cancer statistics*, 1995, *Cancer J Clin* 1995, 45:8-31.
- [13] Παντελιού Σ., Τζώρτζης Β., Sunaric M., Σαρρής Ι., Παπατσώρης Α., Νικολαΐδου Φ., Αποστολίδης Α., Παπακωνσταντίνου Ν., Χατζηχρήστου Δ., Ανάπτυξη συστήματος για την αντικειμενική εκτίμηση των μηχανικών ιδιοτήτων του προστάτη. 15ο Πανελλήνιο Ουρολογικό Συνέδριο, Κέρκυρα, 27-30 Σεπτεμβρίου 2000.

EXPERIMENTAL VERIFICATION OF SHEAR WALL MODELING USING FINITE ELEMENT ANALYSIS

A. G. Papachristidis

Institute of Structural Analysis & Seismic Research
National Technical University of Athens, GR-15773 Athens, Greece

G. N. Badaloukas

4M – VK Engineering Research and Services
Mykinon 9 & Kifisias, GR-15233 Athens, Greece

B. G. Badalouka

Department of Engineering Science, Section of Mechanics
National Technical University of Athens, GR-15773 Athens, Greece

1. SUMMARY

A three – storey building structure from elastic material is modeled using Lexan and its behavior under an external static loading is examined. Using the photoelastic method we inspect the stresses at shear walls and the experimental results are compared with the corresponding results of a computational model by finite element method application which was developed to describe the problem.

2. INTRODUCTION

The experimental model is a three storey (level) 3D building, having three flat shear walls and one of a “Π” – shape, used for the elevator, at every level. The framework plan of the typical level of the building is shown in Fig. 1. Point “A” represents the point in witch the external loading is applying. Points “B” and “C” at levels 3 and 2, respectively are the exact points where the displacement is measured.

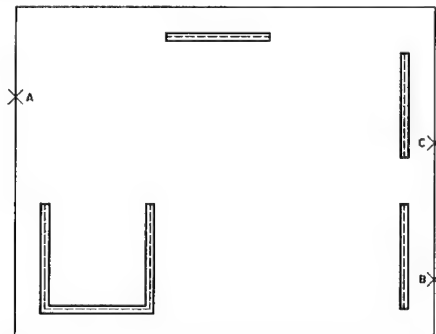


Figure 1: Framework plan of the typical level

Photoelastic analysis is widely used for problems in which stress or strain information is required for extended regions of the structure. It provides quantitative evidence of highly stressed areas and peak stresses at surface and interior points of the structure.

3. FINITE ELEMENT ANALYSIS METHOD

For the finite element analysis of the building we used a four node quadrilateral thin flat shell element, which has six degrees of freedom (dof) per node. The sixth dof is obtained by combining a membrane element with a normal rotation θ_z , the so-called the drilling degree of freedom, and a discrete Kirchhof plate element. The drilling dof is introduced via the variational formulation. The variational formulation employs enforcement of equality of the independent rotation field and skew-symmetric part of the displacement gradient.

In small displacement models of flat shell elements, the effects of membrane and bending strain are not coupled in the energy expression within the elements. Coupling occurs only on the interelement boundary. Therefore, we consider a flat shell element as combination of a plane stress element and a plate bending element. In the combined element subject to membrane and bending actions, the displacements prescribed for 'in-plane' forces do not affect the bending deformations, and vice versa.

The drilling degree of freedom may be physically interpreted as a true rotation of the vertex bisecting the angle between adjacent edges of the finite element. A schematic of the angle bisector and associated partial derivatives in element displacements is shown in Fig. 2.

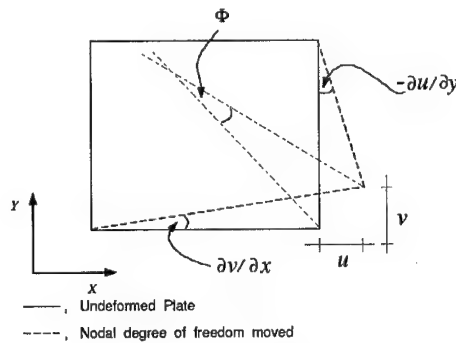


Figure 2: Physical interpretation of the drilling degree of freedom

The drilling degree of freedom is defined as:

$$\Phi = \frac{1}{2} \left(\frac{\partial v}{\partial x} - \frac{\partial u}{\partial y} \right) \quad (1)$$

Flat shell finite elements may be formulated through the use of a variational formulation that includes an independent rotation field for the drilling degree of freedom. The variational formulation is due to Hughes and Brezzi [1, 2]. It employs the skew-symmetric part of the stress tensor as a Lagrange multiplier to enforce the equality of independent rotations with the skew-symmetric part of the displacement gradient. Taylor subsequently combined the variational formulation with an Allman-type interpolation for the displacement field with an independent interpolation field of rotation [3].

The variational formulation suggested by Hughes and Brezzi [1, 3], can be described as

$$\Pi_p(\bar{u}, \bar{\Phi}) = \frac{1}{2} \int_{\Omega} \text{symm}(\nabla \bar{u}) : C : \text{symm}(\nabla \bar{u}) d\Omega + \frac{1}{2} \rho \int_{\Omega} \left| \text{skew}(\nabla \bar{u}) - \bar{\Phi} \right|^2 d\Omega - \int_{\Omega} \bar{u} \cdot f d\Omega \quad (2)$$

where \bar{u} , $\bar{\Phi}$ are trial displacements and rotations of the region Ω , f is the external general forces, and ρ is a penalty. The corresponding variational formulation is:

$$0 = D\Pi_{\rho}\left(u, \Phi\right)\left(\bar{u}, \bar{\Phi}\right) = \int_{\Omega} \text{symm}\left(\nabla \bar{u}\right) \cdot C \cdot \text{symm}\left(\nabla u\right) d\Omega + \rho \int_{\Omega} \left[\text{skew}\left(\nabla \bar{u}\right) - \bar{\Phi} \right]^T \left[\text{skew}\left(\nabla u\right) - \Phi \right] d\Omega - \int_{\Omega} \bar{u} \cdot f d\Omega \quad (3)$$

The first term in the variational equations produces the element stiffness matrix,

$$[K] = \int_{\Omega} [\bar{B}]^T [C] [\bar{B}] d\Omega \quad (4)$$

The plate bending component of the shell element corresponds to the 12 dof discrete Kirchhoff quadrilateral plate element (DKQ), and is derived in detail using the discrete Kirchhoff technique. The DKQ element formulation is based on the discretization of the strain energy. The model neglects the transverse shear strain energy.

4. FINITE ELEMENT ANALYSIS MODEL

The corresponding model is shown in Fig. 3a. It consists of 3496 nodes and 3346 elements. We have tried several mesh sizes and in this paper we present a medium one. The deformed shape of the model is shown in Fig. 3b. The model's elastic isotropic material has a Young modulus of $E = 280000 \text{ N/cm}^2$, and a Poisson rate of $\nu = 0.36$.

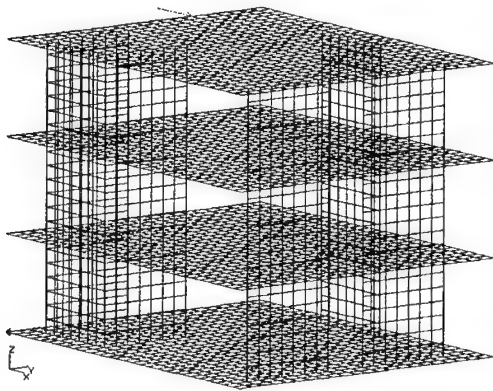
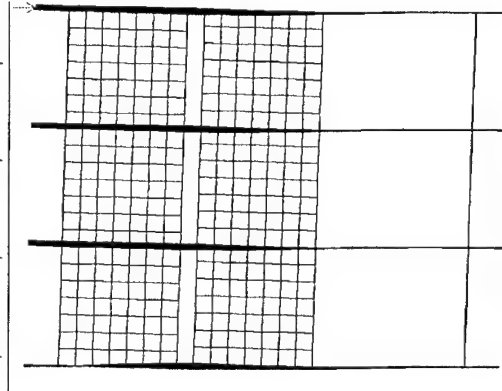


Figure 3a: Finite element analysis model,



3b: Deformed shape of the building

5. EXPERIMENTAL ARRANGEMENT

The specimen was made of Lexan of thickness 6 mm. This material is suitable for both photoelastic and caustic optical method techniques. According to the photoelastic method the specimen is placed between the plates of a circularly polarized field, so that isochromatic fringes patterns can be taken. These fringes give the principal stress difference of an existing stress field. The experimental model is shown in Fig. 4.

The external load is applied at point "A". The starting value is zero and gradually reaches 600N when the joining between the parts of the specimen starts failing. We have also measured the displacements at points "B" and "C" shown in Fig. 1.

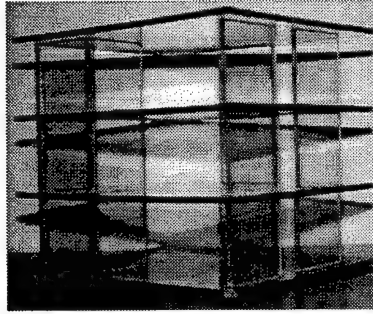


Figure 4: Experimental model

6. EXPERIMENTAL RESULTS – COMPARISON

The isochromatic pattern is related to the principal stresses by the stress – optic law:

$$\sigma_1 - \sigma_2 = 2\tau_{max} = \frac{C}{b} \cdot N \quad (5)$$

where σ_1 , σ_2 are algebraically the maximum and minimum principal stresses, respectively, τ_{max} is the maximum shear stress, C is the stress – optic coefficient and N is the relative retardation of rays forming the pattern, also known as isochromatic fringe order.

In terms of the isochromatic pattern, the isochromatic fringe order, N , at a point is specifically defined as the number of fringes that pass through the point during the application of the external loads. The isochromatic pattern of this experimental model is shown in Fig. 5.



Figure 5: Isochromatic pattern

Therefore, in Fig. 6d we count 4 fringes. Taken that the stress – optic coefficient of Lexan is $16.42 N/cm$ the principal stresses difference is $109.47 N/cm^2$. We studied both the shear walls that belong to the elevator and the flat shear wall at the top of the framework plan of the typical level (Fig.1). At the next photographs we present the behavior of the flat shear wall at the top of the floor plan, as the value of the external loading is being increased from zero to $600N$. The direction of the principal stresses as they are obtained by the finite element analysis are shown in Fig. 7.

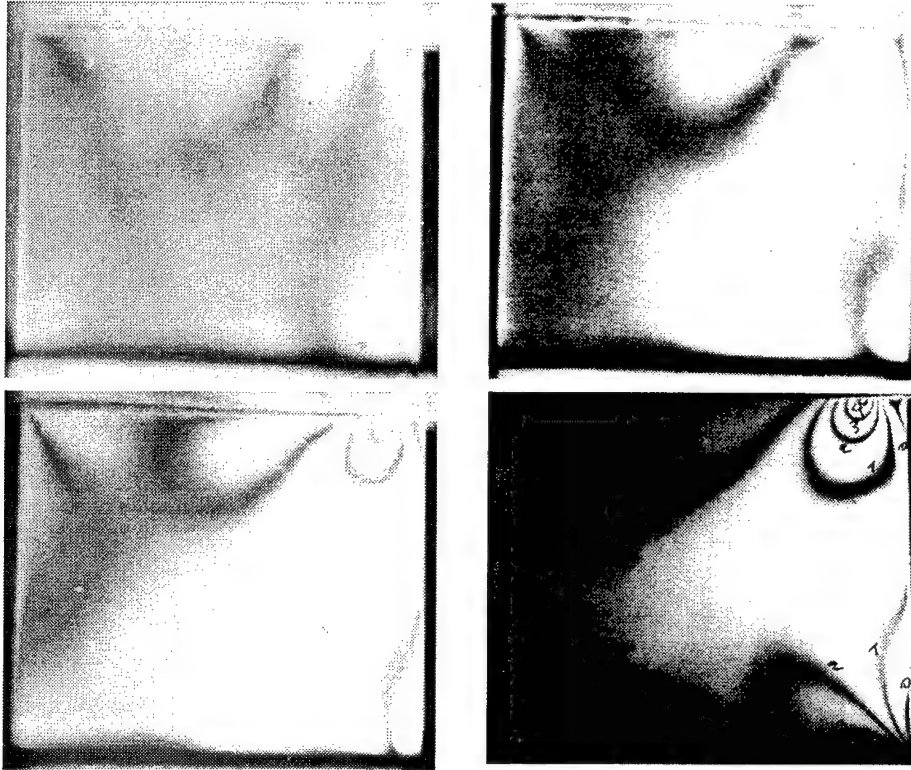


Figure 6: Photoclastic pattern for externally applied load equal to a) 0N, b) 200N, c) 400N and d) 600N

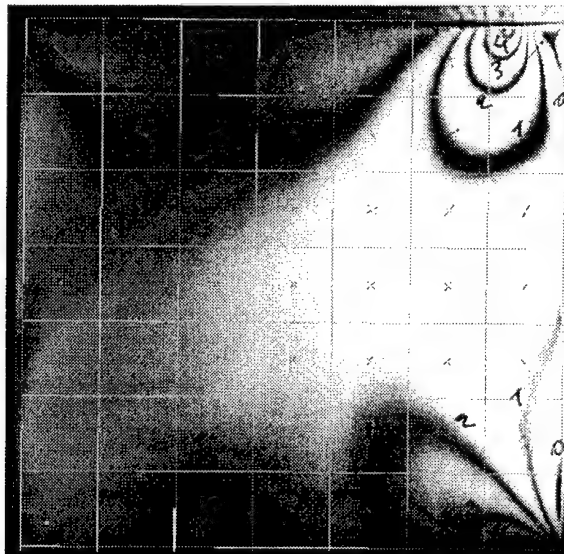


Figure 7: Principal stresses F.E.A.

The comparison between the displacements measured at point B (Level 3), C (Level 2) and those from the finite element analysis are presented at Fig. 8b.

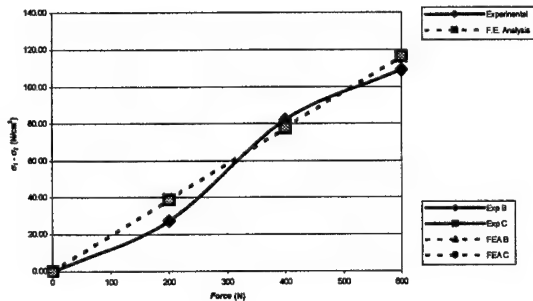
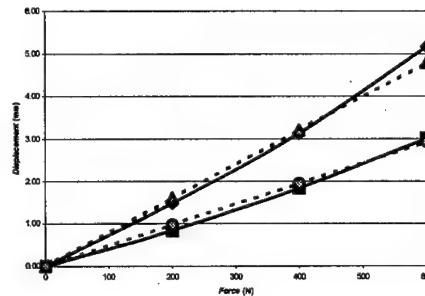


Figure 8a: Experimental principal stresses - F.E.A. ,



8b: Experimental displacements - F.E.A.

7. CONCLUSIONS – FUTURE WORK

The concluding result is that the specific element type can be used to model the experimental specimen in a very satisfactory degree, which is not far enough from a real life building structure. The main assumption that the building's behavior falls into the elastic area will be soon raised as we have already proceeded developing the plastic formulation of the specific element and we shall present it soon.

8. REFERENCES

- [1] Hughes T.J.R., "On Drilling Degrees of Freedom", *Computer Methods in Applied Mechanics and Engineering*, Vol. 72, (1989), pp 105-121.
- [2] Hughes T.J.R., Brezzi F., Masud A. and Harari I., "Finite Elements with Drilling Degrees of Freedom: Theory and Numerical Evaluations", *Proceedings of the Fifth International Symposium on Numerical Methods in Engineering*, Computational Mechanics Publications, Ashurst, U.K., (1989), pp 3-17.
- [3] Ibrahimbegovic A., Taylor R.J. and Wilson E.L., "A Robust Quadrilateral Membrane Finite Element with Drilling Degrees of Freedom", *International Journal for Numerical Methods in Engineering*, Vol. 30, (1990), pp 445-457.
- [4] Jin, L. "Analysis and Evaluation of a Shell Finite Element with Drilling Degree of Freedom", University of Maryland at College Park, (1996).
- [5] Papachristidis A., "Mesh Generation, Modeling and Solving Structures using Finite Element Analysis", Post Graduate Thesis supervised by Prof. M.Papadrakakis, National Technical University of Athens, Athens, (2000).
- [6] Papachristidis A. and Vadaloukas G., "mySTRAD FE 2000, Finite Element Analysis Toolkit", 4M – VK Research and Services, Athens, (2000).
- [7] Dally J.W. and Riley W.F., "Experimental Stress Analysis", *McGraw-Hill Book Co.*, (1965).
- [8] Kuske A. and Robertson G., "Photoelastic Stress Analysis", *Joghn Wiley and Sons*, New York, (1974).
- [9] Badalouka, B.G., Papadopoulos, G.A. and Badaloukas, G.N. "An experimental study of pre-stressed beam by means of optical methods", *3rd National Conference on Computational Mechanics*, University of Thessaly, Volos, Greece (1999).

FAILURE OF A COMPOSITE WITH A BROKEN FIBER

D.A. Zacharopoulos and E.E. Gdoutos

School of Engineering

Democritus University of Thrace, GR-671 00 Xanthi, Greece

D. Karalekas

University of Piraeus

GR-185 34, Piraeus, Greece

1. SUMMARY

An analytical investigation of the failure behavior of a composite material with a broken fiber was undertaken. The problem was modeled as a cylindrical element of matrix with a single fiber subjected to uniform axial displacement along the fiber axis. The stress field near the fiber break was determined by a finite element code. The results of the stress analysis were combined with the strain energy density and the strain energy release rate failure criteria to study initiation of failure from the fiber break. Results for crack growth into the matrix or along the fiber-matrix interface were presented for various combinations of material properties and geometrical dimension of the composite cylindrical model.

2. INTRODUCTION

Failure of fiber reinforced composites is generally preceded by an accumulation of different types of internal damage. Failure mechanisms on the micromechanical scale include fiber breaking, matrix cracking and interface debonding. They vary with type of loading and are intimately related to the properties of the constituents, i.e., fiber, matrix and interface/interphase. While failure mechanisms are common in most composites, their sequence and interaction depend on the type of the loading and the properties of the constituents. Study of the progressive degradation of the material as a consequence of growth and coalescence of internal damage is of utmost importance for the understanding of failure.

The problem of stress distribution in a composite consisting of a single fiber embedded in a matrix was first studied by Cox [1], for the case where both the fiber and the matrix are linear elastic. It was assumed that the fiber is perfectly bonded to the matrix and the Poisson's ratio of the fiber and the matrix are equal. Other early studies referred to the problem of stress transfer from the matrix to fibers in a composite were presented by Dow [2], Rosen [3] and Kelly and Tyson [4]. In the above simplified models only the fiber axial stress and fiber-matrix interfacial shear stress are determined. An approximate closed form solution that gives the axisymmetric stress distribution in a system consisting of a single broken fiber surrounded

by an unbounded matrix was presented by Whitney and Drzal [5]. For a thorough study of the various forms of failure mechanisms of fiber reinforced composite refer to [6].

In the present work the stress distribution in a cylindrical element of matrix with a single fiber subjected to a uniform axial displacement along the fiber axis is analyzed. The results of the stress analysis are coupled with the strain energy density and the strain energy release rate failure criteria to study crack growth into the matrix or along the fiber-matrix interface in the cylindrical model.

3. CYLINDRICAL MODEL

Consider a cylindrical element of matrix with a single broken fiber (Fig. 1). Let r_f and r_m represent the radius of the fiber and the outer cylinder respectively, and $2d$ the distance between the two ends of the broken fiber. The element is subjected to a uniform displacement of 0.05 cm at its upper surface. Numerical results are presented for $d = 0, 0.5$ and 2 cm, $r_f = 0.2$ cm and 1 cm and $r_m = 10$ cm. A crack of length a ($a = 0.05, 0.2$ and 0.4 cm) is considered along the matrix-fiber interface.

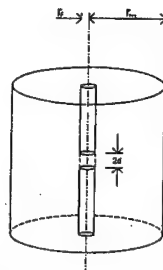


Figure 1: Cylindrical element of composite.

The material of the matrix is an epoxy resin with Young's modulus $E = 3,400$ MPa and Poisson's ratio $\nu = 0.34$. The ratio of the moduli of elasticity E_f/E_m of the fiber and matrix takes the values of 2, 5 and 10.

For the finite element analysis, due to symmetry, one quadrant of the element needs to be modeled. Axisymmetric quadrilateral eight-node elements were used. The number of elements varied between 2598 and 2958, which the number of nodes varies between 775 and 875 depending on the geometry of the problem. The finite element code ABAQUS was used.

4. STRESS ANALYSIS

From the finite element analysis the stress distribution in the fiber and matrix of the cylindrical element were determined. Fig. 2 presents the variation of the normalized normal stress σ_1/σ_{\max} along the axis of the fiber for $r_f = 0.2$ cm, $E_f/E_m = 2$ and $d = 0, 0.6$ and 2 cm. σ_{\max} represents the maximum value of σ_1 that takes place far away from the broken fiber end. Note that the normal stress increases from zero at the broken fiber end to σ_{\max} at a distance of approximately $4d_1$. Figure 3 presents the variation of the normalized shear stress τ/τ_{\max} along the fiber-matrix interface for the same values of r_f , E_f/E_m and d as in Fig. 2. τ_{\max} is the maximum value of the shear stress at the fiber break. The interfacial stress decreases from a maximum value of the broken fiber end to zero at a distance of approximately $4d$. Fig. 2 and 3 establish that the transfer of load between the fiber and matrix takes place by the interfacial

shear stress along a critical transfer length. These results are qualitative in agreement with the shear lag analyses of [1-4].

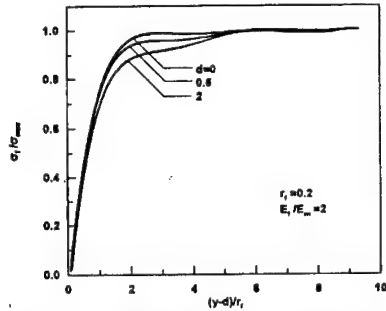


Figure 2: Normalized normal stress σ_1/σ_{\max} versus distance $(y-d)/r_f$ for $r_f=0.2$ cm, $E_f/E_m=2$ and $d=0, 0.5$ and 2 cm.

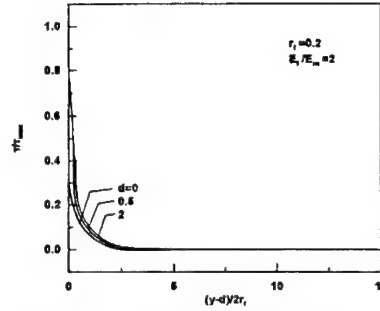


Figure 3: Normalized shear stress τ/τ_{\max} versus distance $(y-d)/2r_f$ for $r_f=0.2$ cm, $E_f/E_m=2$ and $d=0, 0.5$ and 2 cm.

5. FAILURE ANALYSIS

For an increasingly applied normal load failure initiation from the fiber break takes place. Two cases are considered: crack growth into the matrix or crack growth along the matrix fiber interface. They are studied separately in the following sections.

5.1 Crack Growth into the Matrix

For the study of crack growth from the fiber break into the matrix the strain energy criterion is used [7]. The fundamental quantity is the strain energy density function, dW/dV , which for crack problems takes the form

$$\frac{dW}{dV} = \frac{S}{r} \quad (1)$$

where S is the strain energy density factor and r the radial distance measured from the site of failure initiation. Crack propagates along the direction of relative minimum strain energy density and occurs when dW/dV reaches its critical value $(dW/dV)_c$. For the case of the epoxy matrix considered in this work $(dW/dV)_c=2.66$ MPa.

From the stress analysis coupled with the strain energy density theory the critical load, P_c and angle, ϕ_c , for initiation of crack growth from the fiber break into the matrix are obtained. Results are shown in Table 1 for $d=0$ and 2 cm. Note that the crack propagates into the matrix at an angle ϕ_c ranging between 41 and 70 degrees. This indicates the mixed-mode loading conditions dominate at the crack tip.

Table 1: Calculated results

	$d = 0$				$d = 2$			
	$E_f/E_m=2$		$E_f/E_m=10$		$E_f/E_m=2$		$E_f/E_m=10$	
	$r_f=0.2$	$r_f=1$	$r_f=0.2$	$r_f=1$	$r_f=0.2$	$r_f=1$	$r_f=0.2$	$r_f=1$
(N) P_c	130751	124256	39572	46445	485466	309692.9	172637	369549
(N/cm ²)	112.9	137.6	1258.3	1478.3	8.2	22	66	220.1
$(dW/dV)_{\min}$								
$\Gamma \omega \alpha \phi_c$	45	45	43	41	69	52	70	55

5.2 Crack Growth Along the Interface

The study of crack growth along the fiber-matrix interface was conducted by using the strain energy release rate criterion. The strain energy release rate, G , was calculated for different lengths of the interfacial crack. For details about the calculation of G refer to [8]. Figure 4 presents the variation of G versus crack length for a fiber volume ratio $V_f=0.01$, $d=0$, an applied displacement 0.05 cm and $E_f/E_m=2, 5$ and 10. The values of opening-mode, K_I , and sliding-mode, K_{II} , stress intensity factors are shown in Figs 5 and 6. Note that G as well as K_I and K_{II} remain almost constant for crack lengths larger than 2 mm (except for $E_f/E_m=10$).

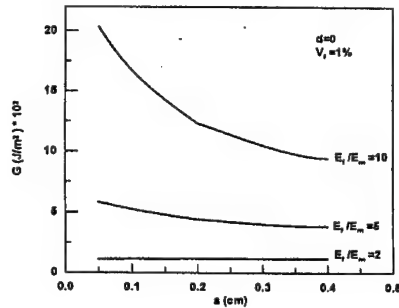


Figure 4: Variation of strain energy release rate G versus crack length a for $d=0$, $V_f=1\%$ and $E_f/E_m=2, 5$ and 10. Applied displacement 0.05 cm.

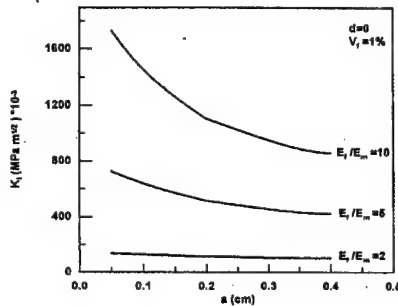


Figure 5: Variation of opening-mode stress intensity factor, K_I , versus crack length a for $d=0$, $V_f=1\%$ and $E_f/E_m=2, 5$ and 10. Applied displacement 0.05 cm.

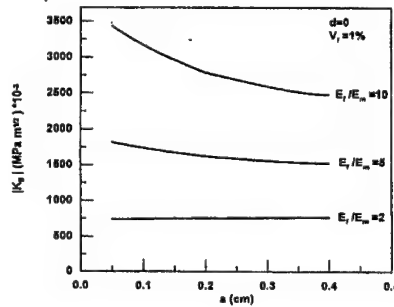


Figure 6: Variation of sliding-mode stress intensity factor, K_{II} , versus crack length a for $d=0$, $V_f=1\%$ and $E_f/E_m=2, 5$ and 10. Applied displacement 0.05 cm.

5.3 Failure Mode Prevalence

Crack growth into the matrix or along the interface from the fiber break depends on the relative values of the strain energy density factor, S , and the strain energy release rate, G . Thus, crack growth along the interface occurs when

$$\frac{S_m}{G_i} < \frac{S_{mc}}{G_{ic}} \quad (2)$$

where

S_m : strain energy density factor for crack growth in the matrix

S_{mc} : critical strain energy density factor for the matrix

G_i : strain energy release rate for crack growth along the matrix-fiber interface

G_{ic} : critical strain energy release rate for matrix-fiber interface

When the inequality of relation (2) is reversed the crack propagates into the matrix. The strain energy release rate G is obtained from the function $G=G(a)$ by letting a to tend to zero. The critical value G_{ic} of G_i is a characteristic of the matrix-fiber system. The critical value S_{mc} of S_m is obtained by

$$S_m = r_0 \left(\frac{dW}{dV} \right)_c \quad (3)$$

where $(dW/dV)_c$ is the area under the true stress-strain curve of the matrix material in tension and r_0 is a material constant given by $r_0 = 2.65 \times 10^{-4}$ cm.

Results for the prevalent failure mode of crack growth in the matrix or along the matrix-fiber interface were obtained as a function of the bimaterial constant α ,

$$\alpha = \frac{\bar{E}_f - \bar{E}_m}{\bar{E}_f + \bar{E}_m} \quad (4)$$

where for conditions of plane strain $\bar{E} = E/(1 - \nu^2)$.

Figs 7 and 8 present the variation of S_m/G_i versus α for various values of d and V_f . The curves of the figures separate the plane of S_m/G_i - α into two regions, one above and another below the curve. For those combinations of S_m/G_i and α that fall above the curve crack growth takes place along the matrix-fiber interface; for the others the crack propagates into the matrix.

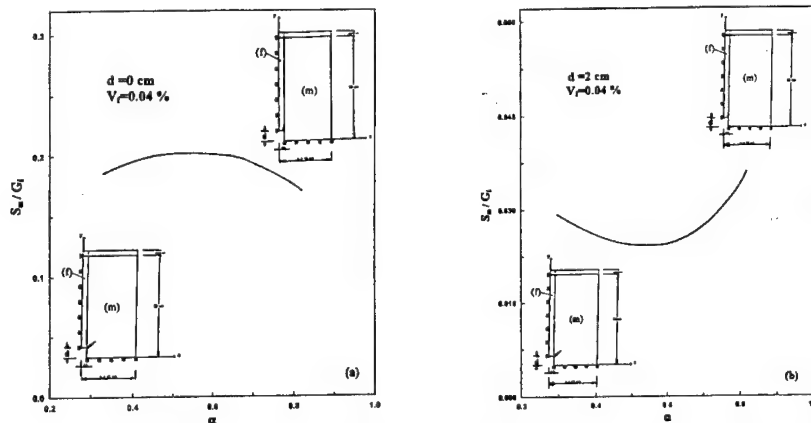


Figure 7: Variation of S_m/G_i versus α for $V_f=0.04\%$ and (a) $d=0$ cm, (b) $d=2$ cm. Crack growth takes place along the interface or in the matrix for combinations of S_m/G_i , α above or below the curve of figure, respectively.

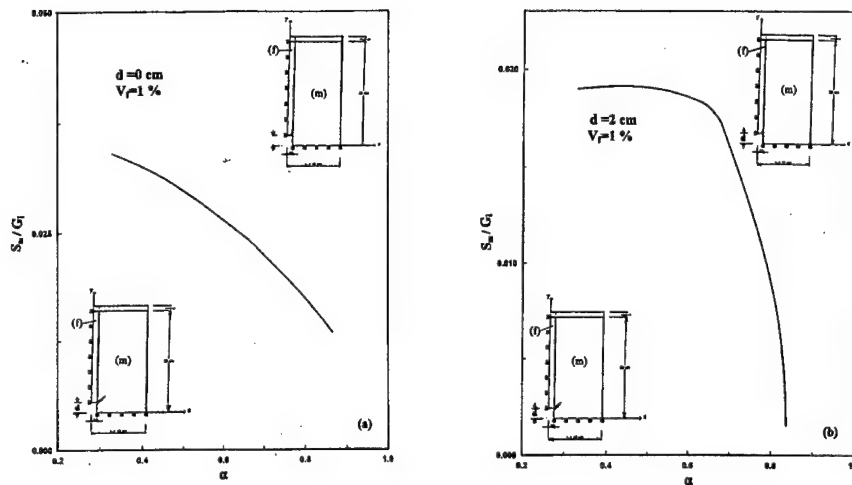


Figure 8: Variation of S_m/G_i versus α for $V_f=1\%$ and (a) $d=0$ cm, (b) $d=2$ cm. Crack growth takes place along the interface or in the matrix for combinations of S_m/G_i , α above or below the curve of figure, respectively.

6. ACKNOWLEDGEMENTS

The authors would like to express their thank to engineers Th. Grammeno and M. Papablasopoulou.

7. REFERENCES

- [1] Cox, H.L., The elasticity and strength of paper and other fibrous materials, *British Journal of Applied Physics* 3, 72-7, (1952).
- [2] Dow, N.F., Study of stresses near a discontinuity in a filament-reinforced composite metal, Space Mechanics Memo 102, General Electric Space Sciences Lab, Report No. 63SD61 (1961).
- [3] Rosen, B.W., Mechanics of composite strengthening, in *Fiber Composite Materials*, American Society for Metals, Metals Park, OH (1965) 37-75.
- [4] Kelly, A. and Tyson, W.R., Tensile properties of fibre reinforce metals: Copper/tungsten and copper/molybdenum, *Journal of the Mechanics and Physics of Solids* 13, 329-350 (1965).
- [5] Whitney, J.M. and Drzal, L.T., Axisymmetric stress distribution around an isolated fiber fragment, in *Toughened Composites*, N.J. Johnson (Ed.) ASTM STP 937, American Society for Testing and Materials (1987) 179-196.
- [6] Gdoutos, E.E., Failure mechanisms and failure criteria of fiber reinforced composites, in *Failure Analysis of Industrial Composite Material*, E.E. Gdoutos, K. Pilakouta and G.A. Rodopoulos (eds), McGraw-Hill (2000) 51-108.

- [7] Sih, G.C., Strain-energy-density factor applied to mixed-mode crack problems, *International Journal of Fracture* 10, 305-321 (1974).
- [8] Gdoutos, E.E., Giannakopoulou, A. and Zacharopoulos, D.A., Stress and failure analysis of brittle matrix composites. Part II: Failure analysis, *Inter. J. of Frac.* 98, 279-291 (1999).

MICROMECHANICS OF CARBON FIBRE MODEL COMPOSITES UNDER TENSILE, COMPRESSIVE AND FATIGUE LOADING CONDITIONS

C. Koimtzoglou, S. Goutianos and C. Galiotis

Institute of Chemical Engineering and High Temperature Chemical Processes
Foundation of Research and Technology – Hellas
P.O. BOX 1414, Patras 265 00, Greece

1. SUMMARY

Raman spectroscopy was used to get an insight into the microstructural aspects of the mechanical response of carbon fibre composites under various loading conditions (tension, compression and fatigue). This is done by an assessment of the stress transfer efficiency in single-fibre (continuous or discontinuous) model composites. It was found that in the elastic regime no actual difference exists between tensile and compressive behaviour. However, compressive failure is quite different, fibre fragments past each other and remain in contact, thus they can still bear load. Concerning cycling loading, the results showed that the main fatigue damage parameter that affected the stress transfer efficiency at the interface was the fibre fracture process itself and not the degradation of the interface.

2. INTRODUCTION

Composite materials are anisotropic solids, which exhibit complex mechanical behaviour. In general, the tensile behaviour is better defined compared to the compressive and fatigue behaviour. Their numerous internal boundaries and interfaces which separate the different constituent materials or even building blocks (plies) respond differently to an applied cycling load. The propagation of damage in each case and the interaction between dissimilar failure modes is still the subject of intense investigation [1]. In addition there is little information as to how the failure modes of the constituent materials interact with each other and induce areas of stress concentration that may, in turn, affect the integrity of a component [2]. For example, fibre fracture and consequent recoiling resulting from fatigue loading may initiate interfacial damage, which can propagate either as conical shear crack or as a fibre/matrix debond and affect the local stress transfer efficiency of the system.

Concerning the compressive behaviour of these systems it is well known that the compressive strengths are often less than 60% of their tensile strengths [3]. Early investigations associated compressive failure with a fibre buckling process in an elastic foundation (matrix) [4], however predictions were 3-4 times higher than the measured values. Today, the initial fibre waviness and the matrix shear yield strength are believed to be the main factors controlling compressive strength [5]. However, there is experimental evidence that highly anisotropic

fibres like carbon show themselves a non-linear response in compression and soften at higher strains.

Fatigue life prediction of composite materials has generally not been a major issue in the design of composite structures, which has been limited by impact and static notch performance. At present the ultimate design strain levels are kept low, in the region of 4000 $\mu\epsilon$, where composite materials can withstand large numbers of fatigue cycles without failing, thus at this strain level damage growth is not seen as a major problem [6]. To use composite structures to their full potential, design strain levels will have to rise and an accurate fatigue methodology needs to be established. Key to this is the understanding of the effects of various damage mechanisms on fatigue life. On other words we need to establish links between observable damage/failure mechanisms and fatigue life [6].

The aim of this work is to get an insight into the micromechanical behaviour of carbon/epoxy composites by employing a single-fibre model composite. The only available experimental technique that can provide information (axial fibre stress/strain) at microscopic level is the laser Raman spectroscopy (LRS). The interfacial shear stress distribution (τ_{rx}) is evaluated by means of a balance of forces argument:

$$\tau_{rx} = -\frac{r_f}{2} \frac{\partial \sigma_f}{\partial x} \quad (1)$$

where r_f is the fibre radius, σ_f is the fibre axial stress and x the distance along the length of the fibre.

3. EXPERIMENTAL

3.1 Laser Raman spectroscopy experimental set-up

A remote laser Raman microprobe, which was built in our laboratory [7], was used in this work. The main feature of the probe is the use of flexible fibre for laser delivery and collection, which brings about a complete separation of the spectroscopic and the testing stages and therefore allows *in-situ* measurements. More details can be found in ref. [8].

3.2 Materials and specimen geometry

The materials used were an Epikote 828/Ankamine 1618 (Shell) epoxy resin and M40-40B carbon fibres (Toray). The resin/hardener mixture was 100/60 parts by weight and after mixing the system was cured for one week at room temperature. In the case of specimens tested in fatigue a post curing cycle was applied: 24 h at 50 °C followed by 24 h at 70 °C and, finally 10 h at 90 °C.

The fibres were surface treated, by the manufacturer, and had a nominal Young's Modulus of 390 GPa. The Raman wavenumber stress sensitivity of the fibres was $\alpha_\sigma = -3.0 \text{ cm}^{-1}/\text{GPa}$ and the corresponding strain sensitivity was $\alpha_\epsilon = -11.4 \text{ cm}^{-1}/\%$ [9]. The fibre diameter was found to have an average value of $D = 6.6 \text{ }\mu\text{m}$.

Two different specimen geometries were employed, namely: dogbone geometry used in tension and fatigue (tension-tension) experiments and prism geometry for the case of compression tests.

The fatigue experiments designed here involved the imposition of a tension-tension load during cycling to both matrix and fibre. Therefore, in order to avoid the development of thermal residual -compressive- stresses in the fibre after curing [9,10] the fibres were pre-strained -prior to mould filling- at a level, ε_{fibre}^* , greater than 0.5% but less than the fibre fracture strain, ε_{fibre}^* , of ~1%. The strain cycle varied from 0 % to 0.5 % (Fig. 1) which assured loading below the critical fatigue limit of the matrix material and the cyclic frequency was 2Hz in order to avoid thermal curing of the epoxy resin due to cyclic loading [11]. Two cases were studied, one with fibre strain -after curing and post curing- of 0.3% (Case A) and another one with 0.4% (Case B). It is therefore obvious that the fibre in Case A is subjected to a cycle from 0.3% - 0.8% while in Case B and more severe one, from 0.4% - 0.9%, close to fibre static strength (Fig. 1).

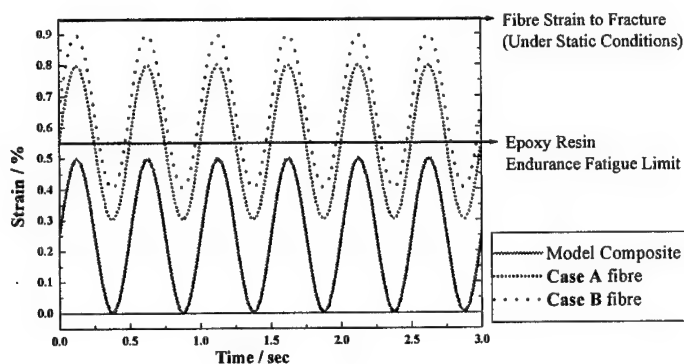


Figure 1: Cyclic loading of the model composites and the subsequent loading cycle of the embedded fibres

4 RESULTS

4.1 Comparative assessment of tensile and compressive behaviour

The different trends in compression and tension are presented in Fig.2 and, as can be seen, in the elastic regime (Fig. 2a) the strain profiles are almost identical in both cases. Upon increasing the applied strain (Fig. 2b) a deviation from linearity is observed in the case of compression as manifested by the multiple fibre fractures (shear breaks). It is worth noting that fibre failure is not observed in tension. In Fig. 3 the associated interfacial shear stresses are presented, from the ISS profiles it is clear that the stress is transferred from the fibre ends through shear at the interface for both loading conditions. Tensile failure was observed at higher applied strain levels (1.25%), whereas interfacial damage occurred at ~1.1% applied strain (the onset of the tensile nonlinear behaviour occurred at ~0.8%). The strain profile of a fragmented fibre loaded in compression is in distinct contrast with those observed in tension [12]. After fibre failure, fibre fragments remain in contact (sliding past each other, see Fig 4) and, therefore, the derivation of interfacial shear stress profiles at these locations by use of balance of forces argument can lead to erroneous results. This is why the ISS are not calculated in the vicinities of compressive fibre breaks as can be seen in Fig. 3. The cause of the nonlinear behaviour is different in compression and in tension. The fairly non-linear tensile behaviour observed at high strains ($\varepsilon > 0.8\%$) can be viewed as a result of the interfacial damage occurred above this critical strain (for this fibre/matrix combination). A degraded interface affects the stress transfer from the matrix to the fibre and the more the

interface is damaged the less the load is transferred to the fibre. On the other hand, in compression things are quite different since no interfacial damage was observed prior to fibre shear breaks (see Fig. 3).

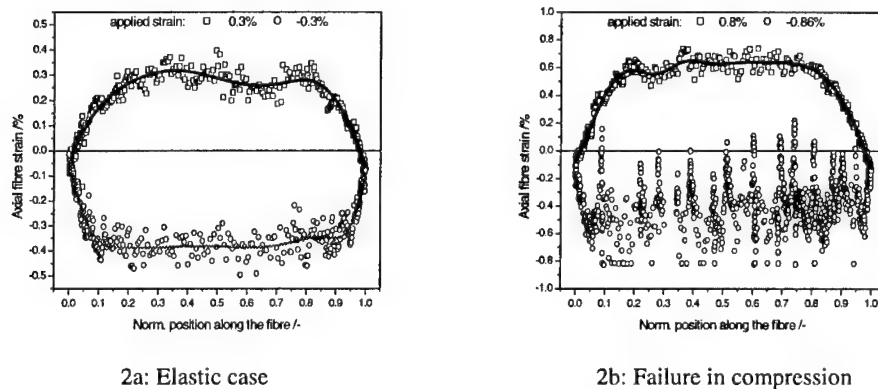


Figure 2: Fibre strain measurements (tension – compression). Continuous lines represent the cubic spline fit of the experimental data.

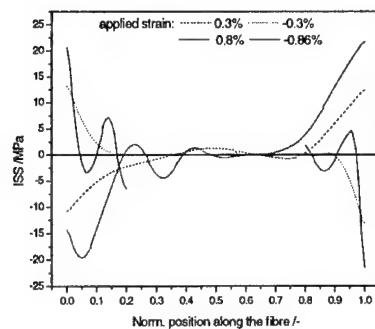


Figure 3: Corresponding interfacial shear stresses of the data presented in Fig. 2. (For the case of applied compressive strain equal to -0.86% ISS are calculated only in the fibre end regions)

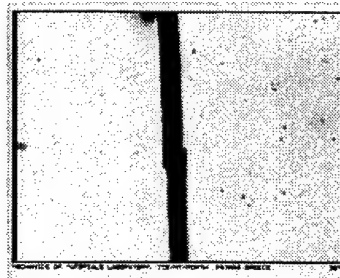


Figure 4: Typical shear break of a high modulus carbon fibre embedded in an epoxy matrix under compressive loading.

4.2 Fatigue behaviour

4.2.1 Effect of the fatigue history on the fibre

By design, the fatigue experiment imposes more severe conditions for the embedded fibre of case B (0.4% - 0.9%) than that of case A (0.3% - 0.8%). The effects of cyclic loading are presented in Fig. 5 as a function of number of observed fibre breaks, with the number of cycles within the 2000 μm observation window. For case A, the fibre had 3 breaks just after the first imposition of tensile load up to 0.5% strain of model composite. This number of breaks was altered with cyclic loading indicating no actual effects on the fibre properties.

On the contrary, for case B a completely different evolution can be observed, where the fibre was cycled from an average pre-strain of 0.4 % to a maximum strain level of 0.9%, which is just below the tensile strength for the 2000 μm length of observation. The observed behaviour between the number of fibre fractures and the number of cycles expressed by the equation in Fig. 5 indicates that, in absolute terms, the rate of fibre fracture decreases with life and a tension-tension fatigue degradation of carbon fibres themselves under the effect of an axial load. This is important since cyclic work on carbon fibres performed in air by Bunsell and Somer [13] has failed to identify a clear fatigue pattern possibly due to the complexities of the experimentation involved.

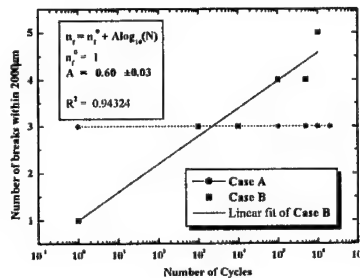


Figure 5: Number of observed fibre breaks, within the 2000 μm window, as a function of number of cycles plotted on a logarithmic scale for both cases of specimens.

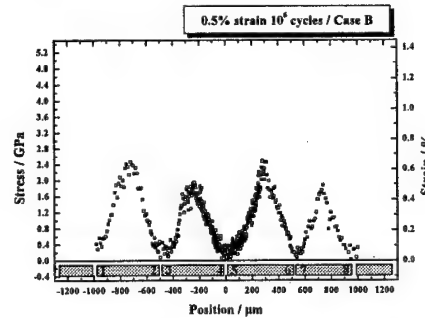


Figure 6: Normal fibre stress (left) and fibre strain (right) along the fibre length after 10^6 cycles for case B.

4.2.2 Effect of fatigue history on the stress transfer efficiency

The cyclic experiment presented here was designed in such a way to resemble the stress state encountered in a full volume fraction composite. The strain field does not exceed the elastic limits of the matrix and this is exactly what is observed in full unidirectional composites incorporating similar fibre/ matrix combinations [14].

The average maximum stresses (strains) observed from the profiles along the fibre length within a window of 2000 μm (Fig. 6) appear to be different in the two cases examined. Concerning case A, it starts with 3.5GPa (0.9%) at 0 cycles and decreases to 2.7GPa after 2×10^6 cycles and this is attributed to the viscoelastic behaviour of the matrix [15]. On the contrary, for case B, the value of 3.5GPa did not change with the number of cycles as long as the fibre length remained greater than 1000 μm .

By using equation (1) the Interfacial Shear Stress (ISS) distributions have been derived (Fig. 7) and the behaviour of three significant parameters with the cyclic loading have been chosen to describe the fatigue effect on the stress transfer efficiency: ISS_{max} , b and L_t (Fig. 7). Therefore, for case A, the change shown in Fig. 8 is attributed to the viscoelastic response of the matrix while for case B the fibre fracture process with the number of cycles dominates the change of their values.

To conclude, the results obtained here for the interfacial parameters ISS_{max} , b and L_t indicate that for case A the reduction of ISS_{max} observed is due to the reduction of resin modulus with life. While, for case B, at least up to 5×10^5 cycles the effect of fibre fracture upon the integrity of the interface is by far greater than the progressive deterioration of the stress

transfer efficiency with number of cycles in existing fractures. This reinforces the finding that in unidirectional composites under loading parallel to the fibres, the fibre fracture and the associated interface weakening, here for an area of about $b=90\text{--}160\text{ }\mu\text{m}$, are the major damage components.

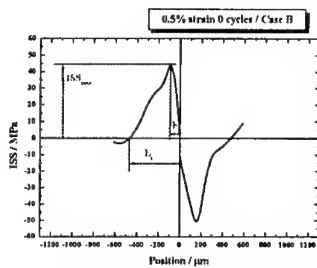


Figure 7: Interfacial Shear Stress (ISS) distribution along the fibre length at 10^0 cycles for case A.

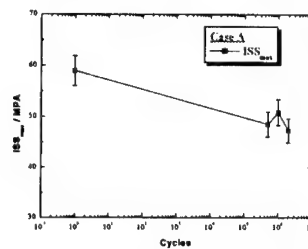


Figure 8: Maximum ISS, for case A, as a function of a number of cycles for one fibre end and at all different fatigue levels. The results were recorded at the peak of the fatigue cycle at 0.5% applied strain.

5. REFERENCES

- [1] Reifsnider, K. L., Fatigue of composite materials, in *Composite material series 4*, K. L. Reifsnider (Ed), Amsterdam: Elsevier, 1991 (chap. 1).
- [2] Talreja, R., Fatigue of composite materials. Zurich, Switzerland: Technomic, 1986.
- [3] Budiansky, B. and Fleck, N. A., Compressive failure of fibre composites, in *Journal of the Mechanics and Physics of Solids*, 41, 183-211 (1991).
- [4] Rosen, B. W., Mechanics of composite strengthening, in *Fiber Composite Materials*, American Society of Metals, Metals Park, Ohio, 37-75 (1965).
- [5] Budiansky, B., Micromechanics, in *Computers & Structures*, 16 (1-4), 3-12 (1983).
- [6] Curtis, P.T., Davies, A.J., Fatigue Life prediction of Polymer Composite Materials, in *Proc. of ECCM-9*, Brighton (2000).
- [7] Paipetis, A., Vlittas, C. and Galiotis, C., Remote laser Raman microscopy (ReRaM). 1. Design and testing of a confocal microprobe, in *Journal of Raman Spectroscopy*, 27, 519-526 (1996).
- [8] Kointzoglou, C., Kostopoulos, V. and Galiotis, C., Micromechanics of reinforcement and damage initiation in carbon fibre/epoxy composites under fatigue loading, in *Composites*, 32A, 457-471 (2001).
- [9] Chohan, V. and Galiotis, C., Interfacial Measurements and Fracture Characteristics of 2D Microcomposites Using Remote Laser Raman Microscopy, in *Composites*, 27A (1996), 881-888.
- [10] Galiotis, C. and Paipetis, A., Definition and Measurement of the Shear-Lag Parameter Beta as an Index of the Stress Transfer Efficiency in Polymer Composites, in *J. Mat. Sci.*, 33/5 (1998), 1137-1143.
- [11] Kointzoglou, C., Kostopoulos, V., Melanitis, N.E., Paipetis, S.A., The effect of cyclic loading on the micromechanics of the interface, in *Adv. Comp. Let.*, 4/ 5 (1995), 151-155.

-
- [12] Chohan, V. and Galiotis, C., Effects of interface, volume fraction and geometry upon stress re-distribution in polymer composites under tension, in *Composites Science and Technology*, 57/8, 1089-1101 (1997).
 - [13] Bunsell, A.R. and Somer, A., The tensile and fatigue behaviour of carbon fibres, in *Plastics, Rubber and Comp. Proc. and Appl.*, 18/ 4 (1992), 263-267
 - [14] Chohan, V. and Galiotis, C., Effects of Interface, Volume Fraction and Geometry upon Stress Re-Distribution in Polymer Composites under Tension, in *Comp. Sci. & Tech.*, 57/8 (1997), 1089-1101
 - [15] Koimtzoglou, C., Kostopoulos, V., Galiotis, C., Effect of fatigue loading upon the stress transfer efficiency in carbon fibre composites, in *Proc. Of ECCM-9*, Brighton (2000).

DYNAMIC BEHAVIOR OF A HANGED CABLE FOR DEEP WATER APPLICATIONS

I. K. Chatjigeorgiou

Dept. of Naval Architecture and Marine Engineering
National Technical University of Athens

S. A. Mavrakos

Dept. of Naval Architecture and Marine Engineering
National Technical University of Athens

1. SUMMARY

The present study examines the dynamic behavior of a marine cable having attached in its lower end a free vibrating body. The governing equations of dynamic equilibrium in 2-D space are presented for both cable and the attached body. The solution method is based in an efficient finite differences numerical scheme. The numerical calculations concern a particular cable-body assembly and the numerical predictions are plotted suitably in order to obtain important conclusions for the behavior of the dynamic system and to study several aspects of the dynamic response.

2. INTRODUCTION

Marine cable systems are used in a wide variety of offshore operations. These include the deployment and the recovery of instrumentation packages, salvage operations, underwater construction, scientific deep ocean coring studies and deep ocean mining activities. These systems utilize wire rope, chain or synthetic rope, and are sometimes used in combination with slender pipe sections. The cable portions are configured with either single or multiple lines depending upon the particular application.

The present paper is a contribution to the direction of studying the dynamic behavior of a cable, hanged from a floating offshore structure having attached in the lower end a free vibrating body. The study intends to analyze the surge and heave response behavior associated with the lowering and raising of large packages to sea floor in regular seas. The dynamic system configuration of this type, may experience cancellation of tension in the cable-body attachment point, which is followed by cable's re-tensioning, resulting in sever impact load, which is referred to as snap loading. Niedzwecki and Thampi [1], focused their attention exclusively in the heave response behavior by describing the cable with a sequence of one-degree of freedom oscillators. In the present contribution the cable-body assembly, is

treated as a continuous system by introducing the full set of differential equations, which govern the dynamic equilibrium of both cable and the hanged body in 2D space. The dynamic model is fully described by applying proper boundary conditions at both cable ends. The system of differential equations is being solved in time domain by applying an efficient implicit finite differences numerical scheme. The method has been already successfully applied for the prediction of the dynamic behavior of catenary-type mooring lines (Chatjigeorgiou and Mavrakos, [2], [3]), and it is now extended to the case of hanged cables with a suspended weight at their lower end.

3. DYNAMIC EQUILIBRIUM OF THE CABLE IN 2-D SPACE

The cable is modeled as a slender rod without bending stiffness. Let s denote the unstretched Lagrangian co-ordinate measured from the lower cable end up to a material point of the cable; $\mathbf{v}(u, v)$ its velocity vector; m the mass per unit unstretched length; T the tension along the cable; ϕ the angle which is formed between the tangent of the line at any point along it, and the horizontal; and ε the local strain. Assuming that the tension along the line can be expressed in terms of its elastic strain in the form:

$$T = f(\varepsilon) \quad (1)$$

the equations of motion of a cable in 2D-space can be expressed along the local tangential, \mathbf{t} and normal, \mathbf{n} , directions of its moving configuration (moving dynamic reference) as (Chatjigeorgiou and Mavrakos, [3]; Triantafyllou et al., [4]):

$$m \left(\frac{\partial u}{\partial t} - v \frac{\partial \phi}{\partial t} \right) = f'(\varepsilon) \frac{\partial \varepsilon}{\partial s} - w_0 \sin \phi - \frac{1}{2} \rho_w D_0 C_{Dr} \pi u_r |u_r| \quad (3)$$

$$m \left(\frac{\partial v}{\partial t} + u \frac{\partial \phi}{\partial t} \right) + m_a \frac{\partial v_r}{\partial t} = f(\varepsilon) \frac{\partial \phi}{\partial s} - w_0 \cos \phi - \frac{1}{2} \rho_w D_0 C_{Dn} v_r |v_r| \quad (4)$$

$$\frac{\partial u}{\partial s} - \frac{\partial \phi}{\partial s} v = \frac{\partial \varepsilon}{\partial t} \quad (5)$$

$$\frac{\partial v}{\partial s} + \frac{\partial \phi}{\partial s} u = (1 + \varepsilon) \frac{\partial \phi}{\partial t} \quad (6)$$

$$u_r = u - U \cos \phi \quad (7)$$

$$v_r = v + U \sin \phi \quad (8)$$

where m_a is the added mass, w_0 the submerged weight, both defined per unit of unstretched cable's length; U is the current velocity having direction parallel to horizontal x -axis of the inertial co-ordinate system and finally C_{Dr} and C_{Dn} are the tangential and normal drag coefficients respectively.

Since a general form of stress-strain relation has been assumed, the governing Eqs. (3)-(6), describe the 2D dynamics of both synthetic and steel wire cables.

4. DYNAMIC EQUILIBRIUM OF THE HANGED BODY

Let us denote x_1 and z_1 , the horizontal and vertical motions of the cable's point, which is attached to the hanged body and p_1 and q_1 the respective tangential and normal motions of the same point with respect to the Lagrangian coordinate system. We further define: ϕ_1 the angle which is formed between the tangential of the cable in the body-touch point and the horizontal, W_b the weight of the body in the air, B_b the buoyancy force and finally D_{bx} and D_{bz} the nonlinear drag forces in x and z direction respectively (see Fig. 1).

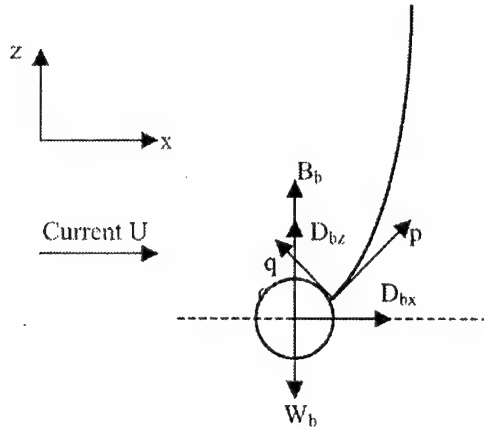


Figure 1. Dynamic Equilibrium of the hanged body in 2-D space.

The equations of motion which govern the dynamic equilibrium of the hanged body in 2-D space are:

$$(M + M_{ax})\ddot{x}_1 = T_1 \cos \phi_1 + D_{bx} \quad (9)$$

$$(M + M_{az})\ddot{z}_1 = T_1 \sin \phi_1 + D_{bz} + B_b - W_b \quad (10)$$

where

$$D_{xb} = \frac{1}{2} \rho C_{bd} A_x (U - \dot{x}_1) \sqrt{(U - \dot{x}_1)^2 + \dot{z}_1^2} \quad (11)$$

$$D_{zb} = \frac{1}{2} \rho C_{bd} A_z (-\dot{z}_1) \sqrt{(U - \dot{x}_1)^2 + \dot{z}_1^2} \quad (12)$$

In Eqs. (9)-(12) M , M_{ax} and M_{az} represent the mass and the added masses of the body in x and z direction respectively, T_1 is the tension of the cable in the attachment point, D_{xb} and D_{zb} , are the drag forces in horizontal and vertical direction respectively, and finally A_x , A_z , C_{bd} are the projected areas in horizontal and vertical direction and the drag coefficient of the body. Eqs. (9) and (10) can be matched with the system of differential Eqs. (3)-(6) by expressing

$\dot{x}_1, \dot{z}_1, \ddot{x}_1, \ddot{z}_1$ in terms of the tangential and normal velocities u_I and v_I and their time derivatives.

5. FINITE DIFFERENCES APPROXIMATION SCHEME

The solution method used in the present contribution for the treatment of the governing differential Eqs. (3)-(6), is the so-called Keller Box finite differences method (Hoffman, [5]). This method was first applied in cable dynamics by Ablow and Schechter, [6] and expanded by Milinazzo et al., [7], who introduced a number of modifications to improve the efficiency and the algorithm's numerical stability characteristics as applied to towed cable systems. The application of the Box method is extended in the present contribution to problems associated with fully submerged cable-attached bodies vibrating freely due to motions imposed in the point of suspension. According to this method, the time t and the Lagrangian coordinate s can be discretized using either uniform or non-uniform discretization schemes, the later being more suitable when bending effects are incorporated in the governing equations. As in the present contribution bending effects have been neglected, higher-order spatial derivatives are not present in the governing equations, and thus it is more convenient to utilize uniform discretization for the independent variables of the problem. Assuming that the variation in time and space is expressed through the indices i and j , respectively (see Fig. 2), the derivatives of the vector $\mathbf{Y}^T(u, v, \varepsilon, \phi)$ that contains the unknowns of the problem can be approximated as follows:

$$\frac{\partial Y}{\partial t} = \frac{Y_j^{i+1} - Y_j^i}{\Delta t} \quad (13)$$

$$\frac{\partial Y}{\partial s} = \frac{Y_{j+1}^i - Y_j^i}{\Delta s} \quad (14)$$

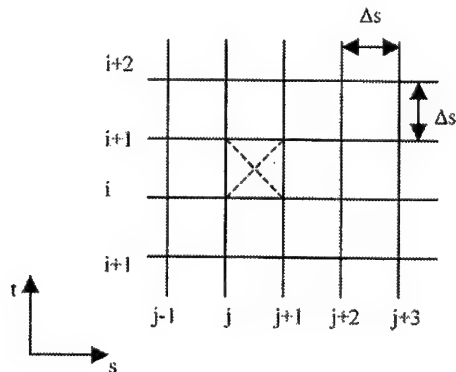


Figure 2. Stencil of Keller-Box Method

Next, substituting Eqs. (13) and (14) into Eqs. (3)-(6) and evaluating the equations in the middle of $[i, i+1]$ and $[j, j+1]$, i.e., in the point $[i+1/2, j+1/2]$ (Fig. 2), we can derive the system of nonlinear algebraic equations (Chatjigeorgiou and Mavrakos, [8]), which delivers the unknown dynamic components of the vector $\mathbf{Y}^T(u, v, \varepsilon, \phi)$ at each discretization point and

time step. The first discretization point coincides with cable-body attachment point; the last one with the connection of the line to the floating structure.

Boundary Conditions

The boundary conditions are implemented at the upper and lower end points of the cable. The connection of the floating structure with the cable is being considered as the location of the excitation, in which the following equations must be satisfied:

$$u_n \cos \phi_n - v_n \sin \phi_n = \dot{x}_{top} \quad (15)$$

$$u_n \sin \phi_n + v_n \cos \phi_n = \dot{z}_{top} \quad (16)$$

where the subscript n denote the line's top-terminal-point. Moreover, \dot{x}_{top} and \dot{z}_{top} denote the imposed external velocities in the horizontal and vertical direction at the cable's upper end. On the other hand, the motions of the cable-body attachment point must satisfy Eqs. (13) and (14). Thus Eqs. (13) and (14) (after being treated with the finite differences approximation scheme described before), consist the two boundary conditions, which must be satisfied in the lower end of the cable.

6. NUMERICAL RESULTS AND DISCUSSION

In order to express numerically the behavior of the dynamic system, which is examined in the present study, and to obtain conclusions in regards to the features of it's dynamic response, the mathematical formulation outlined above was applied to a particular cable-mass assembly.

Tables 1 and 2 list the physical and geometrical properties of the cable and the hanged mass under consideration, respectively.

Table 1. Physical and Geometrical Properties of the Cable

Description	Symbol	Cable
Unstretched Diameter	D_0 (m)	0.062
Suspended Length	L (m)	100
Young's Modulus of Elasticity	E (N/m ²)	$0.7 \cdot 10^{10}$
Submerged Weight per Unit Length	w_0 (N/m)	169.61
Mass per Unit Length	m (Kg/m)	20.38
Added Mass per Unit Length	m_a (Kg/m)	3.090
Tangential Drag Coefficient	C_{Dt}	1.2
Normal Drag Coefficient	C_{Dn}	0.01

Table 2. Physical and Geometrical Properties of the Hanged Body

Description	Symbol	Hanged Body
Weight in Air	W_b (N)	44119
Buoyancy	B_b (N)	42119
Mass plus Added Mass in x- Direction	$M + M_{ax}$ (Kg)	8790
Mass plus Added Mass in z- Direction	$M + M_{az}$ (Kg)	8790
Projected Area in x-Direction	A_x (m ²)	3.14
Projected Area in z-Direction	A_z (m ²)	3.14
Drag Coefficient	C_{bd}	0.8

The imposed harmonic motion in the upper cable's end was either horizontal or vertical with amplitude equal to 1 m, and with various excitation frequencies. The results of the numerical simulations, which were performed for the purposes of the present contribution, are given graphically in Figs. 3-8. In time $t = 0$, the cable is being considered totally vertical and the angle which is formed in any point along the cable with the horizontal, is 90° . The tension along the cable is varying linearly from $W_b - B_b$ (the net weight of the hanged mass) in the point of attachment, up to $W_b - B_b + w_0 * L$ (the total submerged weight of the system) at the upper cable's end. The initial conditions are zero motions and velocities in all discretization points along the cable at time $t = 0$.

An important aspect, which is experienced in dynamic systems such the one examined in the present, is the cancellation of the tension at the free end. For cables not carrying loads at the free end the tension is always zero at any time step. For cables having loads attached in this particular point, the cancellation of tension may occurs under certain conditions depending on the motions of the hanged load. The feature of the zero tension is apparently shown in Fig. 3. The load is severely vibrating due to high frequency vertical motion imposed at the cable's top end, allowing the variation of tension in wide range. Due to the fact that the cable is not capable to undertake bending effects, the tension equals to zero until the motion of the hanged body causes the appearance of positive tension in the load attachment location. This feature is accompanied with sudden change in the value of the angle in the attachment point, which lasts during all zero tension time intervals, whereas in the other time steps the cable in the location of attachment remains vertical, Fig. 4. The body loses balancing and falls down because of its own weight, initiating the so-called "snap loading behavior". The same is valid for the cable's length, which is close to the cable-mass connection point, as indicated by the highly vibrating lines in the lower portions of curves plotted in Fig. 7. These curves represent the dynamic configuration of the cable for various time steps during one period of excitation.

As expected, the horizontal motions of the load are insignificant for vertical excitations contrary to the horizontal ones imposed at the top of the cable. For horizontal excitations there is a time lag until the hanged load starts moving. This is clearly visible in Fig. 5, in which it is shown that the angle at the location of attachment starts to change after termination of a certain time interval during which every point along the cable has been moved.

The body motions are considerable only for small frequencies of horizontal excitation, Fig. 8. Then, the cable and the body are actually performing a horizontal translation, parallel to the direction of the imposed motion. As the frequency of excitation increases, the horizontal displacement of the hanged body reduces amplitude, see Fig. 8. For top end fast motions, the body remains actually stable (Fig. 8), whereas in the same time there is a significant and continuous shift in the direction of motion along the cable.

Although the most important contribution to the variation of the total tension comes from the vertical motions, the effect of horizontal motions to this feature cannot be considered as negligible. As indicated in Fig. 6, there is an apparent effect of the horizontal motions to the total tension acting at the top of the cable. This effect is more important at the body's attachment point because the total tension at this point has the smaller value, and, thus, cancellation of tension can be occur. As the frequency of imposed harmonic horizontal motion increases, the tension at the cable-mass connection point does not follow the sinusoidal mode of the excitation. Although the response maintains periodicity, the nonlinear effects become significant and the harmonic feature vanishes.

7. CONCLUSIONS

The paper deals with the dynamic response of a hanged cable having attached a free vibrating mass at its lower end. The system of dynamic equilibrium for the cable in 2-D space is accompanied with the set of differential equations of dynamic equilibrium for the attached body, the later being considered as the boundary conditions, which must be satisfied in the lower end of the cable. The dynamic system is fully described by applying appropriate boundary conditions in the upper cable's end, which determine the external imposed excitation. The dynamic behavior predictions obtained through numerical simulations describe explicitly the zero tension feature, which is experienced by dynamic system configurations such the one examined in the present contribution. The cancellation of tension, which may be experienced in the cable's lower end, is accompanied with a sudden change in the value of the angle in the location of attachment. During horizontal excitation there is always a time lag until the cable-mass connection point starts moving. The magnitude of the body's motion, caused due to cable's upper end imposed horizontal excitation, is significant only for small excitation frequencies and seems to vanish for fast top-end movements. Finally, horizontal excitations could be an important contributor in the total tension along the cable indicating that even with the absence of vertical motions the effect on the variation of tension caused due to horizontal top-end displacements should not be considered negligible.

8. REFERENCES

- [1] Niedzwecki, J.M., Thampi, S.K., Snap Loading of Marine Cable Systems, *Applied Ocean Research* (1991), Vol. 3, No. 5, 210-219.
- [2] Chatjigeorgiou, I.K., Mavrakos, S.A., Non - Linear Contributions in the Prediction of the Dynamic Tension on Mooring Lines, for High and Low Frequencies of Excitation, *Proc 7th Int Offshore and Polar Eng Conf*, Honolulu, Hawaii, ISOPE (1997), Vol. II, 192-199.
- [3] Chatjigeorgiou, I.K., Mavrakos, S.A., Comparative Study on the Efficiency of Improved Numerical Solutions Schemes in the Prediction of the Dynamic Behavior of Mooring Lines, *Proc 9th Int Offshore and Polar Eng Conf*, Brest, France, ISOPE (1999), Vol. II, 332-339.
- [4] Triantafyllou, M.S., Bliet, A., Shin, H., Dynamic Analysis as a Tool for Open Sea Mooring System Design, *Trans SNAME* (1985), Vol. 93, 303-324.
- [5] Hoffman, J.D., *Numerical Methods for Engineers and Scientists*, (1993) McGraw-Hill.
- [6] Ablow, C.M., Schechter, S., Numerical Simulation of Undersea Cable Dynamics, *Ocean Eng* (1983), Vol. 10, No. 6, 443-457.
- [7] Milinazzo, F., Wilkie, M., Latchman, S.A., An Efficient Algorithm for Simulating the Dynamics of Towed Cable Systems, *Ocean Eng* (1987), Vol. 14, No. 6, 513-526.
- [8] Chatjigeorgiou, I.K., Mavrakos, S.A., Comparative Evaluation of Numerical Schemes for 2D Mooring Dynamics, *Int Journal of Offshore and Polar Eng* (2000), Vol. 10, No. 4, 301-309.

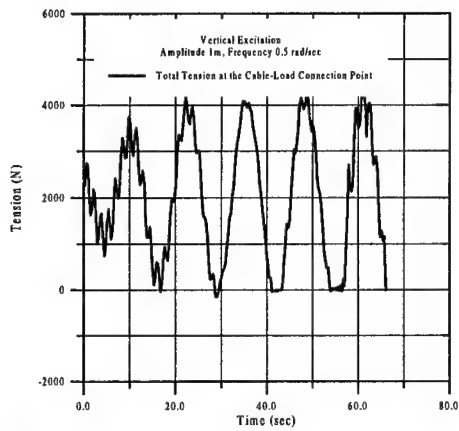


Fig. 3

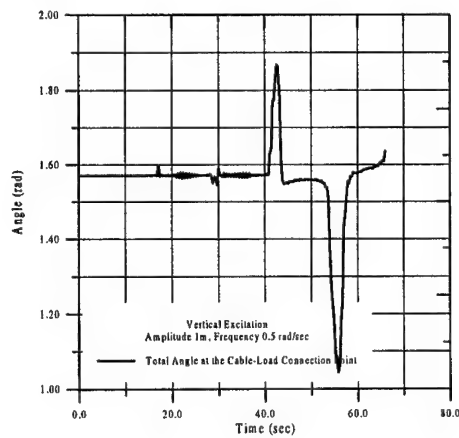


Fig. 4

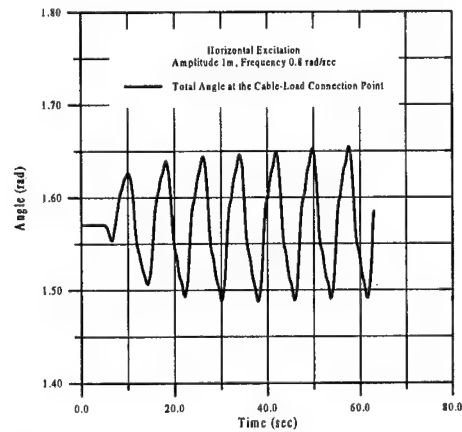


Fig. 5

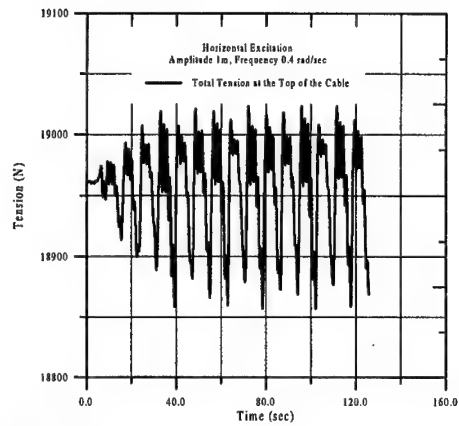


Fig. 6

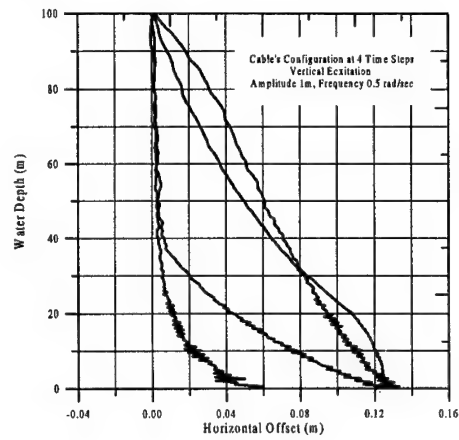


Fig. 7

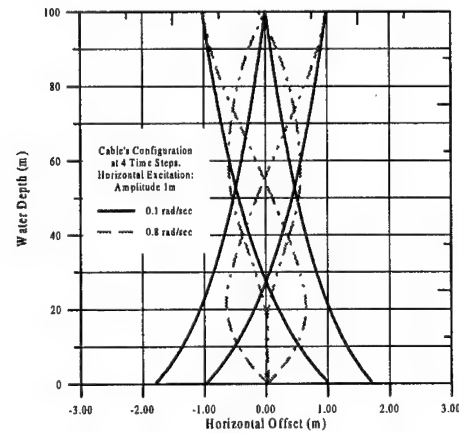


Fig. 8

EXPERIMENTS FOR THE ESTIMATION OF UNSATURATED HYDRAULIC CONDUCTIVITY

G. K. Arampatzis

Department of Rural and Surveying Engineering
Aristotle University of Thessaloniki, GR-54006 Thessaloniki, Greece

Ch. D. Tzimopoulos

Department of Rural and Surveying Engineering
Aristotle University of Thessaloniki, GR-54006 Thessaloniki, Greece

1. SUMMARY

The aim of this paper is to present experiments for the determination of unsaturated hydraulic conductivity in porous media. For the determination of unsaturated hydraulic conductivity a dosimeter pump, a system of tensiometers with pressure transducers and a γ -ray absorption instrument were used. This way the determination of experimental values (θ_i , Ψ_i) and (θ_i , K_i) is possible and the curve $K(\Psi)$ can be determined.

2. INTRODUCTION

In order to simulate the unsaturated water flow it is necessary to know the unsaturated hydraulic conductivity as a function of suction or of soil moisture and the soil moisture characteristic curve. The hydraulic conductivity is one of the most important hydraulic properties and it is determined by direct and indirect methods or using numerical and analytical prediction models. The soil moisture characteristic curve is determined usually experimentally in the field or in the laboratory, which is time-consuming and expensive. As a result, many methods have been developed to estimate unsaturated hydraulic conductivity from empirical equations (e.g. Irmay, 1954; Brooks and Corey, 1964; Gardner, 1958; Campbell, 1974) or from statistical models (e.g. Childs and Collis - George, 1950; Marshal, 1958; Millington and Quirk, 1961; Kunze et.al, 1968). Mualem (1976) presented an integral form as predictive model and other researchers, substituting in this form a functional relationship of $\theta(\Psi)$, proposed new prediction models (e.g. van Genuchten, 1978; Tzimopoulos and Sakellariou - Makrantonaki, 1996).

This paper presents experiments for the determination of unsaturated hydraulic conductivity in porous media, undertaken in the Laboratory of Agricultural Hydraulic in the Department of Rural and Surveying Engineering in A.U.Th. (direct method). For the determination of unsaturated hydraulic conductivity a dosimeter pump, a system of tensiometers with ceramic cups and pressure transducers and a γ -ray absorption instrument were used. The dosimeter

pump supplied water at the top of an experimental column in small quantities (submultiples of the saturated hydraulic conductivity). The soil water content was measured using γ -ray absorption method and the negative water pressure in the pore media was measured using the system of tensiometers with ceramic cups and pressure transducers. This way the determination of experimental values (θ_i , Ψ_i) and (θ_i , K_i) is possible and the curve $K(\Psi)$ can be determined.

3. EXPERIMENTAL METHOD

The experiments were performed in the laboratory using a Plexiglas cylindrical vertical column, 60-cm length and 6 cm internal diameter. The column was packed using a soil raising method with free-falling soil passing through a sequence of 2-mm sieves. With this method, a good homogeneity of soil packing can be achieved. All experiments were conducted at a constant temperature of 21 ± 1 °C.

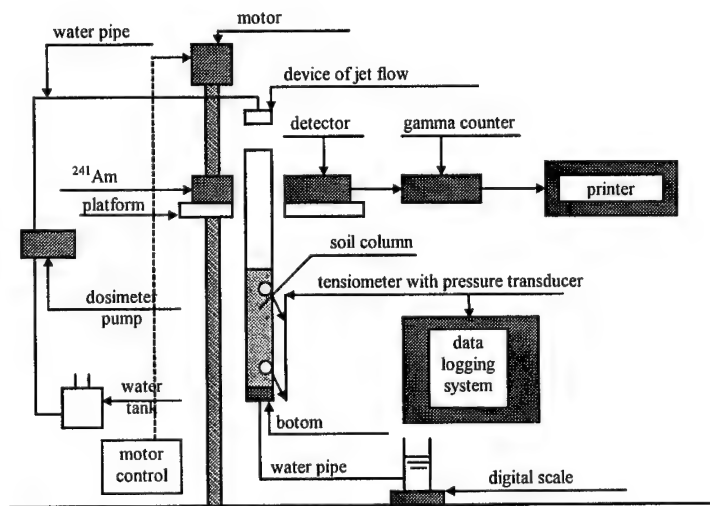


Figure 1: Schematic diagram of the experimental setting.

Two sand samples of 30-cm length were used. The experiments were repeated for each sample separately. The average dry bulk density for the first sample was 1.377 ± 0.018 gr/cm³ and for the second sample was 1.44 ± 0.021 gr/cm³. This indicates the good homogeneity of the samples.

The dry bulk densities and the water content were measured by γ -ray absorption method, as described by Arampatzis (1996). The device of γ -ray contained a 300-mCi Americium -241 source. The Americium -241 source and the photomultiplier detector (including a NaI crystal and preamplifier) were positioned on a horizontal platform moved by an electric motor. In this way the development of water profile in the column can be followed over time.

The water pressure was measured at the same time at two different depths in the column using tensiometers with ceramic cups and pressure transducers. Each tensiometer was connected to its own pressure transducer. Pressure transducers were connected by a multichannel data acquisition system to a digital voltmeter and then to a printer. The accuracy

of the pressure transducers was within 1.5 % and the response time was 1 ms. The position of the tensiometers corresponded respectively to depths of 6 and 16 cm from the soil surface. The assumption that the tensiometers measure the average pressure at the point of insertion was made in order to process the measurements.

The characteristic curve was obtained by wetting and draining the soil column from the bottom by means of a Mariotte burette. This method was followed for two reasons:

- To prevent the air to be caged into the soil pores.
- To have a slow flow as the gravity was negative.

The unsaturated hydraulic conductivity was estimated using a dosimetric pump that fed the soil column with distilled water from the top. In order to determine the hydraulic conductivity at the appropriate soil moisture, the moisture must be stabilized at the same value at an upper and a lower level of each soil layer. This experimental procedure is based on Darcy 's law:

$$q(\theta) = -K(\theta) \left[\frac{d\Psi(\theta)}{dz} - 1 \right], \quad (1)$$

where q is Darcy 's velocity [L/T], K is the unsaturated hydraulic conductivity [L/T], θ is the soil moisture [L^3/L^3], Ψ is the suction [L] and z is the level measured from an arbitrary control surface [L]. In equation (1) the vertical axis z has a positive direction downwards. Assuming that the soil moisture θ is constant along the soil column at each layer, then $d\Psi/dz = (d\Psi/d\theta)(d\theta/dz) = 0$ and equation (1) becomes:

$$q(\theta) = |K(\theta)|. \quad (2)$$

The saturated hydraulic conductivity was approximated as a fitting parameter using the Brooks and Corey 's empirical equation (Touma, 1984; Arampatzis, 2000).

4. APPLICATION

The soil moisture as a function of the suction is given by van Genuchten 's equation (1978) (figure 2):

$$\frac{\theta - \theta_r}{\theta_s - \theta_r} = \frac{1}{[1 + (a\Psi)^n]^m}, \quad (3)$$

where θ is the soil moisture (L^3/L^3), θ_s is the saturated soil moisture (L^3/L^3), θ_r is the residual soil moisture (L^3/L^3), Ψ is the suction (L) and a , n and $m = 1-1/n$ are coefficients. The saturated soil moisture was measured by γ - ray absorption method as the average value of θ_s when all positions at the column were in the saturated condition. The residual soil moisture was measured by the same way, when the sample was drained and the value of θ_r was the same in all positions for a few days. The parameters a and n were estimated by fitting the experimental values (table 1).

Also van Genuchten (1978) gives a predictive model for the determination of unsaturated hydraulic conductivity as a function of suction:

$$K = K_s \frac{\left\{ 1 - (a \Psi)^{n-1} \left[1 + (a \Psi)^n \right]^{-m} \right\}^2}{\left[1 + (a \Psi)^n \right]^{m/2}}, \quad (4)$$

In equation (4) K is the unsaturated hydraulic conductivity (L/T), K_s is the saturated hydraulic conductivity (L/T). The coefficients a , n and m are using the same values as estimated in the equation (3) and the K_s is using the same value as estimated in the equation (5) (table 1 and fig. 3).

Table 1: Coefficients of van Genuchten (1978), Brooks and Corey (1964) and Gardner (1958) equations.

	First sample		Second Sample	
θ_s	0.43		0.34	
θ_r	0.12		0.02	
	Infiltration	Drainage	Infiltration	Drainage
van Genuchten 's equation $\theta(\Psi)$ (1978)				
a	0.48102	0.02585	0.07356	0.055211
n	1.99825	6.87915	4.59636	6.91369
van Genuchten 's predictive model $K(\Psi)$ (1978)				
Mean square error	$8.2 * 10^{-4}$	$7.2 * 10^{-3}$	$5.7 * 10^{-3}$	$1.8 * 10^{-2}$
Coef. correlation	0.990	0.932	0.995	0.987
Brooks and Corey 's empirical equation $K(\theta)$ (1964)				
K_s (cm/min)	0.462		1.72	
B	9.2373		4.98615	
Gardner 's empirical equation $K(\Psi)$ (1958)				
α	1.2317	0.0369	0.1059	0.0713
b	2.8689	10.44	6.5527	9.9795
Mean square error	$5 * 10^{-5}$	$7 * 10^{-5}$	$7.2 * 10^{-4}$	$7.8 * 10^{-4}$
Coef. correlation	0.999	0.999	0.998	0.998

The next point of interest was to fit experimental data (θ_i , K_i) using the following relationship, given by Brooks and Corey (1964):

$$K = K_s \left(\frac{\theta - \theta_r}{\theta_s - \theta_r} \right)^B, \quad (5)$$

where B is coefficient. The values of K_s and B were estimated as fitting parameters by experimental values (table 1).

From the above the relationship between hydraulic conductivity K_i and suction Ψ_i can be determined by Gardner 's empirical equation (1958):

$$K = \frac{K_s}{1 + (\alpha\Psi)^b}, \quad (6)$$

where α and b are coefficients. The results are presented at table 1 and figure 3.

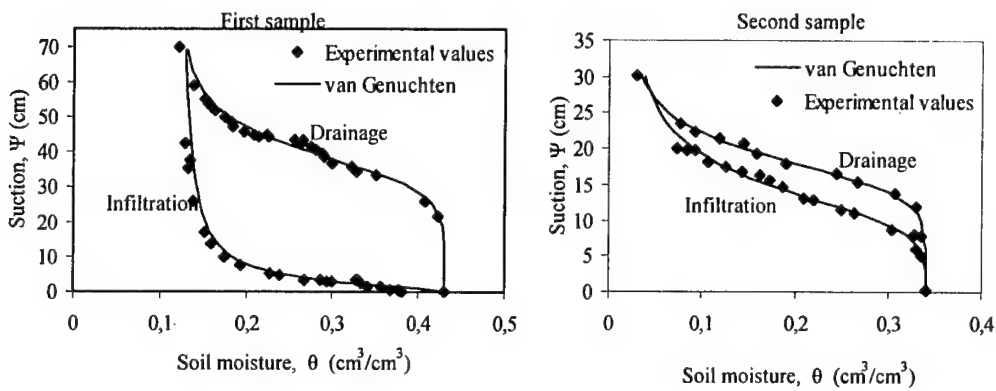


Figure 2: Characteristic curves of the two soil samples.

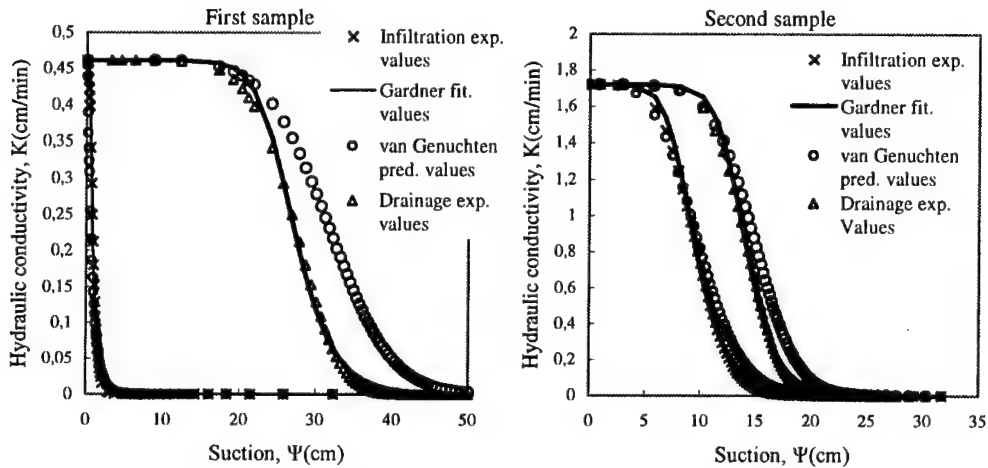


Figure 3: The hydraulic conductivity as a function of suction.

5. CONCLUSION

The above method of determining the unsaturated hydraulic conductivity as a function of suction, although is an indirect method, gives satisfactory results in the cases where experimental values of (Ψ_i, K_i) are not determined. The suction for a specific value of unsaturated hydraulic conductivity is difficult to measure accurately and so the determination of (Ψ_i, K_i) with direct methods is not used.

The curve (Ψ_i , K_i) shows very strong hysteresis (figure 3) in contrast to the curve (θ_i , K_i).

Gardner 's empirical equation fits satisfactorily the experimental values since mean square error is between 10^{-3} and 10^{-5} and the correlation coefficient is between 0.999 and 0.998.

Van Genuchten 's predictive model, with m.s.e. between 10^{-2} and 10^{-4} and a correlation coefficient between 0.932 and 0.995, does not give good results as shown in figure 3.

6. REFERENCES

- [1] Arampatzis, G., *Estimation of hydraulic conductivity in unsaturated condition. Experiment Procedure - Prediction Model*, M.Sc. Thesis, A.U.Th., Thessaloniki, pp. 140, (1996).
- [2] Arampatzis, G., *Laboratory research of infiltration and drainage in layered soils. Simulation of the natural problem with finite control volume method*, Ph.D. Thesis, A.U.Th., Thessaloniki, pp.215, (2000)
- [3] Brooks, R. A. and Corey, A. T., *Hydraulic properties of porous media*, Colorado State University, Hydrology Paper 3, 1-27, (1964).
- [4] Campbell, G., *A simple method for determining unsaturated conductivity from moisture retention data*, Soil Sci., 117(6), 311-314, (1974).
- [5] Childs, E. C. and Collis - George, N., *The permeability of porous materials*, Proc. Roy. Soc., London, Ser. A 201, 392-405, (1950).
- [6] Gardner, W. R., *Mathematics of isothermal conduction of water in unsaturated soils*, Highway Res. Board Spec. Rep. 40, 78-87, (1958).
- [7] Irmay, S., *On the hydraulic conductivity of unsaturated sands*, Trans. Amer. Geophys. Union, 35(3), 463-467, (1954).
- [8] Kunze, R. J., Uehara, G. and Graham, K., *Factors important in the calculation of hydraulic conductivity*, Soil Sci. Soc. Amer. Proc., 32, 760-765, (1968).
- [9] Marshall, T. J., *A relation between permeability and size distribution of pores*, J. Soil Sci., 9(1), 1-8, (1958).
- [10] Millington, R. J. and Quirk, J. P., *Permeability of porous solids*, Trans. Faraday Soc., 57, 1200-1206, (1961).
- [11] Mualem, Y., *A new model for predicting the hydraulic conductivity of unsaturated porous media*, Water Resour. Res., 12(3), 513-522, (1976).
- [12] Tzimopoulos, C. and Sakellariou - Makrantonaki, M., *A new analytical model to predict the hydraulic conductivity of unsaturated soils*, Water Resour. Manag., 10, 1-18, (1996).
- [13] Van Genuchten, R., *Calculating the unsaturated hydraulic conductivity with a new closed form analytical model*, Dep. Civ. Eng. Princeton Univ., Princeton, N. J., Water Resour. Prog., Res. Rep. 78 - WR - 08, 63, (1978).
- [14] Touma, J., *Etude critique de la caractérisation hydrodynamique des sols non saturés: rôle de l' air, influence de l' écoulement multidimensionnel de l' eau*, Thèse de Docteur es - Sciences Physiques, Université de Grenoble, Grenoble, pp.187, (1984).

AUTHOR INDEX

Volume I

- | | |
|---|---|
| <p>Z. Agioutantis, 191
 P. Anagnostopoulos, 39, 66
 G. Anastassopoulos, 381
 G. Arampatzis, 416
 K. Arvanitis, 240
 V. Assouti, 72
 A. Avdelas, 228
 B. Badalouka, 388
 G. Badaloukas, 388
 R. Barber, 52
 A. Bekos, 381
 D. Beskos, 210
 V. Bontozoglou, 33
 A. Boudouvis, 21
 I. Chatjigeorgiou, 408
 B. Coric, 282
 H. Cramer, 298
 I. Daniel, 320
 J. Demetriou, 102, 108, 121
 Y. Dimakopoulos, 84
 D. Dimitriou, 102
 C. Dimou, 275
 A. Elenas, 254
 R. Findei, 298
 D. Fotiadis, 327
 K. Gagas, 72
 C. Galiotis, 401
 C. Gantes, 261
 E. Gdoutos, 320, 394
 K. Giannakoglou, 72
 P. Giokas, 333
 T. Goudoulas, 27
 S. Goutianos, 401
 M. Hadjinicolaou, 59
 N. Hajdin, 178, 282
 D. Hatzichristou, 381
 G. Hatzigeorgiou, 210
 P. Kakavas, 375
 N. Kalinderis, 381
 A. Kaounis, 72</p> | <p>D. Karalekas, 394
 E. Kastrinakis, 27, 96
 J. Katsikadelis, 172, 204, 222
 I. Kevrekidis, 21
 S. Kobayashi, 290
 C. Koimtzoglou, 401
 P. Koliopoulos, 254
 E. Koronaki, 21
 V. Kostopoulos, 365
 V. Koumousis, 275
 C. Kouris, 45
 S. Kourkoulis, 339, 348
 S. Kourtakis, 184
 A. Koutras, 66
 D. Krajcinovic, 155
 J. Kratochvil, 14
 V. Kytopoulos, 339
 P. Ladeveze, 140
 N. Lagaros, 246
 J. Lemaitre, 163
 A. Likas, 327
 A. Liolios, 254
 V. Loukopoulos, 90
 D. Lucic, 282
 J. Lytras, 381
 I. Mademlis, 228
 N. Malamataris, 33
 R. Mandic, 178
 D. Margaritis, 114
 Lj. Markovic, 146
 N. Markovic, 282
 S. Marnoutsidis, 228
 G. Maugin, 1
 S. Mavrakos, 408
 G. Michaltsos, 234
 V. Moulianitis, 381
 H. Mpimpas, 39
 K. Nanou-Giannarou, 121
 N. Ninis, 348
 S. Nychas, 27, 96</p> |
|---|---|

- Th. Panidis, 127
 S. Panteliou, 381
 A. Papachristidis, 388
 M. Papadrakakis, 246
 Y. Pappas, 365
 G. Paschalis, 191
 N. Pelekasis, 78
 N. Pnevmatikos, 261
 C. Pourliotis, 108
 I. Prassianakis, 333
 C. Providakis, 184
 D. Ruzic, 146
 M. Sakellari, 254
 T. Salonikios, 267
 E. Sapountzakis, 222
 P. Sarantos, 108
 D. Saravanos, 357
 R. Schapery, 134
 C. Sciammarella, 314
 F. Sciammarella, 314
 S. Seitani, 66
 M. Sfakianakis, 210
 W. Sharpe Jr., 306
 G. Sideridis, 96
 D. Smyrnaio, 78
 K. Soldatos, 216
 A. Soldatos, 240
 D. Sophianopoulos, 234
 C. Sophocleous, 216
 K. Spiliopoulos, 198
 G. Stavroulakis, 240
 R. de Stefano, 365
 C. Stiakakis, 191
 M. Sunaric, 381
 D. Theodorakopoulos, 210
 C. Theodoropoulos, 21
 M. Titsias, 327
 J. Tsamopoulos, 45, 78, 84
 G. Tsiatas, 172
 Ch. Tzimopoulos, 416
 P. Vafeas, 59
 K. Valanis, 9
 D. Varelis, 357
 L. Vasiliadis, 254
 M. Vlachogiannis, 33
 D. Vlachos, 365
 N. Volakos, 52
 K.-A. Wang, 320
 W. Wunderlich, 298
 J. Yiotis, 204
 E. Zacharenakis, 240
 D. Zacharopoulos, 394
 T. Zervogiannis, 72

Volume II

- M. Abellan, 365
 E. Amanatidou, 149
 I. Andreadis, 177
 N. Anifantis, 52
 H. Antes, 28
 N. Aravas, 149
 Y. Bamnios, 342
 C. Baniotopoulos, 70, 78
 A. Bardzokas, 13
 D. Bardzokas, 22
 J. Bergheau, 365
 D. Beskos, 163, 328
 M. Betti, 78
 D. Bolas, 63
 C. Borri, 78
 D. Briassoulis, 57
 A. Carpinteri, 349
 N. Charalambakis, 276
 A. Charalambopoulos, 216
 C. Charitidis, 40
 B. Chiaia, 349
 K. Chong, 391
 P. Cornetti, 349
 C. Dascalu, 233, 239
 G. Dassios, 109
 D. Davis, 391
 R. de Borst, 365
 B. Demakos, 102
 R. Desmorat, 318
 A. Diamantopoulou, 46

- K. Dimitrakopoulou, 301
 R. Dorgan, 309
 E. Douka, 335
 E. Douka, 342
 P. Entchev, 120
 G. Exadaktylos, 140, 155, 189
 M. Filshtinsky, 22
 D. Fotiadis, 216
 G. Foutsitzi, 216
 G. Frantziskonis, 359
 C. Galiotis, 63
 H. Georgiadis, 289, 295
 D. Georgiou, 90
 E. Gerde, 1
 J. Gilarranz, 371
 P. Grammenoudis, 263
 P. Gupta, 33
 Y. Haddad, 245
 E. Hadjigeorgiou, 239
 D. Homentcovschi, 233, 239
 J. Huyghe, 365
 S. Ichtiaroglou, 379
 J. Jaric, 115
 X. Jiang, 170
 N. Kafoussias, 227
 V. Kalpakides, 126, 239
 T. Kalvouridis, 385
 G. Kamvyssas, 222
 T. Karakasidis, 177, 183
 C. Karakostas, 280
 F. Kariotou, 222
 D. Katsareas, 52
 A. Kekatou, 52
 K. Kishimoto, 115
 M. Kontoleon, 70, 78
 V. Koukouloyannis, 379
 S. Kourkoulis, 140
 D. Lagoudas, 120
 S. Logothetidis, 40
 G. Lykotrafitis, 295
 G. Manolis, 280
 M. Marder, 1
 R. Masiani, 257
 C. Massalas, 216
 A. Massih, 7
 G. Maugin, 126
 A. Mavraganis, 301
 E. Meletis, 33
 E. Mistakidis, 84, 90, 96
 X. Nie, 33
 M. Omiya, 115
 M. Pagitsas, 46
 O. Panagouli, 84
 D. Panayotounakos, 189, 196
 S. Papargyri-Beskou, 163, 328
 J. Parthenios, 63
 N. Politis, 90
 D. Polyzos, 163, 328
 B. Polyzos, 335
 G. Psarras, 63
 F. Psarros, 385
 O. Rediniotis, 371
 D. Sazou, 46
 E. Schettini, 57
 D. Schick, 269
 V. Sfakiotakis, 52
 V. Singh, 33
 P. Sofronis, 251
 K. Soldatos, 209
 J. Staboulglou, 133
 G. Stavroulakis, 28
 S. Subramanian, 251
 D. Sumarac, 397
 E. Theotokoglou, 133
 A. Trochidis, 335, 342
 P. Trovalusci, 257
 G. Tsaklidis, 209
 Ch. Tsakmakis, 263, 269
 K. Tsepoura, 163, 328
 E. Tzirtzilakis, 227
 A. Vakakis, 170, 189
 I. Vardoulakis, 140, 289
 A. Varias, 7
 E. Velgaki, 289
 G. Voyiadjis, 309
 T. Wang, 115
 C. Younis, 196
 A. Zobnin, 13
 M. Zygomalas, 70

Volume III

- | | |
|----------------------------------|------------------------|
| E. Aifantis, 29, 35, 67, 73, 102 | M. Latzel, 53 |
| H. Ait-Amokhtar, 22 | S. Lisina, 90 |
| H. Askes, 1 | S. Luding, 53 |
| K. Chihab, 22 | G. Maugin, 67 |
| F. Chmelik, 16 | E. Meletlidou, 67 |
| R. de Borst, 1 | H. Neuhauser, 9, 16 |
| B. Devincre, 47 | A. Nortmann, 9 |
| H. Dierke, 9 | A. Potapov, 85, 90, 96 |
| A. Fernandes, 61 | J. Pouget, 61, 67, 73 |
| I. Groma, 35 | V. Rodyushkin, 85 |
| S. Gromov, 96 | G. Stagika, 35 |
| M. Gutierrez, 1 | P. Sutcliffe, 79 |
| S. Ichtiaroglou, 35 | A. Tokiy, 40 |
| T. Ioannidou, 73 | N. Tokiy, 40 |
| V. Kazhaev, 96 | G. Utkin, 90 |
| F. Klose, 9 | V. Varyukhin, 40 |
| T. Konstantinova, 40 | G. Wells, 1 |
| L. Kubin, 47 | M. Zaiser, 102 |
| D. Kugiumtzis, 29 | A. Ziegenbein, 9, 16 |